MDOF RESPONSE OF LOW-RISE BUILDINGS

Final Report

Project ST-5
Mid-America Earthquake Research Center

By

Sang-Cheol Kim
PostDoctoral Research Associate

and

Donald W. White
Associate Professor

Georgia Institute of Technology

November 4, 2003

ABSTRACT

In current practice, many approaches for building structural analysis focus on two-dimensional and/or linear elastic idealizations of the response. Nevertheless, the earthquake behavior of low-rise shear wall buildings with non-rigid diaphragms can be highly three-dimensional, and the performance of these systems can depend significantly on the inelastic response of their components. Key modes of response may include both in-plane and out-of-plane wall deformations, and combined diaphragm flexural deformations in two principal directions with diaphragm shear raking displacements. The diaphragm flexibility can significantly influence the out-of-plane wall displacements. The distribution of lateral loads to the structural walls and the degree of torsional coupling between the wall systems can be strongly dependent on the flexibility of the diaphragms and the inelastic system behavior.

This research investigates the seismic assessment of shear wall buildings with non-rigid diaphragms. The focus of this work includes the creation and investigation of a simplified multiple degree-of-freedom (MDOF) linear or nonlinear three-dimensional analysis approach that accounts for diaphragm flexibility in buildings of rectangular plan geometry. The number of degrees-of-freedom in the simplified analysis approach is kept as small as possible while still permitting capture of the three-dimensional effects mentioned above. A computer graphics system is developed for visualizing the physical three-dimensional behavior predicted by the simplified MDOF models.

The above analysis tools are applied to a two-story historic unreinforced masonry building from which earthquake field data is available, and to a half-scale one-story reinforced masonry building that has been subjected to shaking table tests in prior research. These studies focus on defining appropriate structural properties for accurate prediction of the dynamic responses using the proposed simplified MDOF procedure.

This research concludes with the investigation of a simplified linear static methodology applicable for flexible diaphragm structures. The advantages and limitations of this methodology are assessed by comparison of its predictions to experimental and time history analysis results.

Acknowledgments

This research was done as part of project ST-5 of the Mid-America Earthquake (MAE) Center which is supported primarily by the Earthquake Engineering Research Centers Program of the National Science Foundation under Award Number EEC-9701785. The authors would like to thank the MAE center for their assistance in this research. The opinions, findings and conclusions expressed in this paper do not necessarily reflect the views of the above individuals, groups or organizations.

TABLE OF CONTENTS

LIST OF TABLES

LIST OF FIGURES

CHAPTER I

INTRODUCTION

Masonry is a widely used material for building construction because of its versatility and appearance. According to Shing (1998), approximately 70 percent of the building inventory in the United States employs masonry walls in some capacity as lateral-load resisting elements. French and Olshansky (2000) categorize 33 percent of the essential facilities within a study area of the New Madrid fault zone as unreinforced masonry (URM), while eight percent of the essential facilities within this area are categorized in their research as reinforced masonry. On this basis, an early decision of the Mid-America Earthquake (MAE) Center Essential Facilities Program was to focus on masonry building construction, particularly unreinforced masonry. The MAE Center was formed in the fall of 1997 with the goal of helping to reduce significant economic losses that are expected with a future earthquake in Mid-America. The purpose of the specific research addressed in this dissertation is to develop and apply simplified analytical models for seismic assessment of low-rise buildings with nonrigid floor and/or roof diaphragms. A key focus of this work is on the modeling of low-rise masonry buildings. However, the approaches investigated have some potential for other low-rise building types as well.

1.1 Research Objectives

In prior research, numerous approaches have been employed for analysis of the dynamic response of low-rise shear wall building structures. These approaches range from

refined finite element models of the in-plane behavior of individual walls and diaphragms to various types of coarse "lumped parameter" (or "discrete element") models. Many of the three dimensional building analysis models have focused primarily on elastic, or linearized, building responses.

The primary objectives of this research are:

1. To develop, test and validate a simplified three-dimensional linear and nonlinear multiple degree-of-freedom (MDOF) analysis approach for low-rise buildings (e.g., up to four stories) with nonrigid diaphragms, and

2. To develop associated guidelines for linear static seismic evaluation of flexible diaphragm structures (i.e., buildings in which the diaphragm stiffness is small enough such that torsional coupling effects can be neglected).

The following essential response characteristics are addressed:

- Diaphragm flexibility and nonlinear hysteretic response.
- Wall in-plane hysteretic response.
- Out-of-plane displacement of walls due to diaphragm flexibility.
- Stiffness, and strength associated with flange effects from out-of-plane walls.
- Influence of diaphragm response on the distribution of lateral forces to the structural walls.
- Influence of diaphragm response on torsional coupling between the structural walls.

With respect to the first objective, emphasis is placed on capture of the three-dimensional response as well the effects of potential significant nonlinearities using a small number of degrees of freedom. It is intended for the methodologies developed in this research to be useful for on-going and potential future studies pertaining to:

1. Reliable and rapid evaluation of the seismic vulnerability of specific buildings,

2. Analysis of the influence of nonrigid diaphragms on the response of low-rise masonry buildings in general, and

3. Development of comprehensive guidelines for seismic evaluation of buildings with nonrigid diaphragms.

1.2 Background and Problem Statement

There is a dearth of experimental and analytical work on the seismic performance of low-rise buildings with nonrigid diaphragms. The lack of information on the dynamic characteristics of nonrigid diaphragms and their influence on the seismic response of low-rise buildings is evidenced in a lack of comprehensive guidance for seismic assessment of these types of structures in FEMA 273 (FEMA 1997) and 356 (ASCE 2000a). This section summarizes some of the research needs with respect to development of analysis models and with respect to seismic assessment of the above types of structures.

1.2.1 Research needs with respect to development of analysis models

Key structural components in the simplified analysis approach addressed in this work are the shear walls and diaphragms. In masonry buildings, wall hysteretic models should incorporate the effects of pier rocking, bed-joint sliding, toe crushing and diagonal tension failure. Diaphragm hysteretic models should account for stiffness degradation, strength deterioration and pinching characteristics in diaphragms. A detailed literature review is outlined in Chapter 2. A few key previous studies are summarized below.

Flexible diaphragms have been idealized as beams by Shepherd and Donald (1967), Lee and Moon (1989), Dolce et al. (1994), and Masi et al. (1997). Dolce et al.

(1994) idealized the floor diaphragm as a beam with its own elastic and elasto-plastic hysteresis curve. Masi et al. (1997) investigated the seismic response of irregular multi-story reinforced concrete buildings with flexible inelastic diaphragms. The vertical elements were idealized as shear springs and the diaphragm elements were idealized as beams. Both the beam and spring elements had a capability to represent stiffness degradation.

Rutenberg (1980) used a deep-beam idealization to investigate laterally-loaded flexible-diaphragm buildings. Kunnath et al. (1990, 1991, 1994) developed a special-purpose hysteresis model to study the behavior of inelastic flexible concrete floor diaphragms. Kunnath's idealization is based on beam theory. Tena-Colunga and Abrams (1992a, 1992b, and 1996) used shear springs to model flexible diaphragms in two-dimensional analyses. Beam models may be suitable for long narrow buildings with nonrigid diaphragms (Jain and Jennings 1985 and Button et al. 1984). However the above types of beam models do not consider explicitly the various three-dimensional effects (bending in two orthogonal directions and overall raking of the diaphragms as "shear panels" between the walls). These effects may have a significant influence on buildings with nonrigid diaphragms with small to moderate aspect ratios in plan.

A finite element model that predicts the cyclic in-plane behavior of slabs was formulated by Chen (1986). Refined finite elements were also used to model floor slabs by Saffarini and Qudaimat (1992), Lopez et al. (1994), and Costley and Abrams (1996). Kunnath et al. (1991) found that the element developed by Chen could not be readily applied to an entire building. Costley and Abrams (1996) suggested that there is a need for improved simplified models for estimating response maxima of URM buildings with flexible diaphragms.

The number of degrees of freedom in the analytical model of low-rise buildings with nonrigid diaphragms should be kept small for efficiency in rapid evaluation of physical buildings or test designs, as well as in conducting large numbers of analyses in simulation studies of low-rise shear wall buildings with nonrigid diaphragms.

1.2.2 Research needs in seismic assessment

The FEMA 357 *Global Topics Report on The Prestandard and Commentary for The Seismic Rehabilitation of Buildings* (ASCE 2000b), outlines several issues in which research on the inelastic performance of the buildings with nonrigid diaphragm is needed. A few of the needs, which are still largely unresolved in 2002, are:

- "Some building types, such as URM or tilt-up structures, may be more appropriately evaluated as systems rather than components. Flexible wood diaphragms in rigid wall buildings may need special treatment…. The response amplification of ground motion occurs in the diaphragm of rigid wall flexible diaphragm systems. As such, the behavior of individual components such as wall anchors depends on the overall system behavior" (Global Issues 3-8 in FEMA 357, ASCE 2000b).

- "The definition of torsion and the procedure for amplification of torsion need further clarification. … The current definition does not discuss dynamic torsion, or torsion due to rotational modes of building response. This is a dynamic characteristic of the system that may produce torsion in excess of that due to eccentricity between the center of mass and center of rigidity. Currently the Guidelines only require accidental torsion to be amplified" (Global Issues 3-22 in FEMA 357, ASCE 2000b).

- "Procedures for torsional amplification do not account for torsional degradation and are not conservative in determining increased forces and displacements for this effect. … Reportedly there have been recent studies in Japan indicating that further amplification of forces and displacements is required to properly account for torsion as the stiffness of the structure degrades in the direction perpendicular to the direction under consideration" (Global Issues 3-38 in FEMA 357, ASCE 2000b).

- "Further guidance is required on the proper application of the NSP [Nonlinear Static Procedure] in buildings with nonrigid diaphragms. … In buildings with nonrigid dia-

phragms, some of the deformation demand can be taken up in diaphragm deflection. This could be unconservative in estimating deformation demands on vertical seismic framing elements. To approximately account for this, FEMA 273 included provisions for amplifying the calculated target displacement by the ratio of the maximum diaphragm displacement to the displacement at the center of mass. However, pushing the vertical elements to the full target without consideration of diaphragm deflections is overconservative. Development of methods to explicitly apply the NSP to nonrigid diaphragms is recommended…." (Global Issues 3-36 in FEMA 357, ASCE 2000b).

There is little information on the three-dimensional behavior of shear wall buildings with nonrigid diaphragms (Abrams 2001). Although there have been several experimental tests of low-rise shear wall buildings with flexible diaphragms, many questions remain regarding the behavior and analysis of these types of buildings. No attempt has been made to perform extensive numerical studies of the three-dimensional inelastic response of these types of structures.

1.3 Contributions of this research

This research addresses the development of simplified methods of analysis and seismic assessment for shear wall type building structures with nonrigid diaphragms.

The work focuses on low-rise wall-type buildings with rectangular plan geometry. A three-dimensional linear and nonlinear analysis approach is created to allow for accurate and rapid seismic assessment for these types of buildings. The suggested approach is efficient enough for the rapid evaluation of physical buildings or test designs, and for conducting large numbers of analyses within simulation studies. The approach utilizes new diaphragm and wall elements developed in this research. The diaphragm element is based on a flexibility (equilibrium) based formulation to calculate its stiffness and overall nonlinear force deformation response. Strength and hysteretic properties of the diaphragm

element are estimated from the results of experimental tests conducted in previous research. The wall element involves a simple shear spring idealization. In order to most accurately estimate the initial stiffness coefficients of shear walls, a flexibility approach is recommended using the results of plane stress finite element analysis. Simple equations based on mechanics of materials are also considered for calibration of the wall stiffnesses.

As noted at the beginning of this chapter, unreinforced masonry is a major construction material in existing essential facilities in mid America. Thus, an early decision of this research was to focus on the nonlinear characteristics of these types of buildings. The hysteretic properties of the structural components of these buildings are approximated in this work based on previous experimental tests. The wall and diaphragm elements are implemented with computer graphics visualization, as a post-processing tool, to manage the massive analysis outputs for better understating of the behavior of these buildings.

The MDOF model discussed above can be used for simplified three-dimensional nonlinear time history analysis of low-rise shear wall rectangular building structures. Comparisons of analytical studies to experimental tests can be valuable for understanding the seismic response of these types of buildings and for determining the qualities and limitations of simplified models. To this end, the proposed simplified MDOF analysis approach is applied to a two-story unreinforced masonry historic building with interior walls and multiple diaphragms in each story, and to a half-scale single-story reinforced masonry test building with a single diagonally-sheathed diaphragm. The two-story building was instrumented within the California Strong Motion Instrumentation Program (CSMIP) and withstood the Loma Prieta earthquake in 1989. This building, which is referred to as the Gilroy Firehouse, was previously studied extensively by Tena-Colunga and Abrams (1992). The single-story building was constructed and tested on the shaking table at the United States Army Construction Engineering Research Laboratory (CERL), and was subsequently studied by Cohen (2002a). The structural properties of the Gilroy Firehouse are calculated based on extensions to various current methods prescribed in

FEMA 273 (FEMA 1997) and 356 (ASCE 2002a) as well as other publications and developments from this research. The structure is analyzed based on these properties, and modifications necessary to obtain improved predictions relative to the field test data are discussed. For the single story test building, a model calibration process is performed in this work to determine the required structural properties based on the elastic and inelastic test responses. This approach is necessary since it is difficult to determine accurately the in-plane and out-of-plane stiffness, strength, and hysteresis using simplified equations specified in current seismic codes and standards. The comparison between the structural properties obtained by this calibration process and by various simple strength of materials type procedures are discussed.

Lastly, a simplified linear static procedure is proposed for low-rise buildings with flexible diaphragms. This method involves the consideration of the individual diaphragms and the associated out-of-plane walls within a building via separate idealized single degree of freedom models. The shear forces calculated from the separated models are combined to obtain wall shear forces. The final forces and displacements determined using this simplified linear static procedure are compared with linear time history analysis results for the one- and two-story buildings discussed in this research, and conclusions regarding the use of this approach are discussed.

1.4 Overview of proposed simplified three-dimensional MDOF analysis approach

In the three-dimensional analysis approaches developed in this work, a building subdivided into its horizontal roof or floor diaphragms and their supporting vertical elements as shown in Fig. 1.1. This figure illustrates the general deformation of buildings with nonrigid diaphragms. These figures show the three key idealized modes of diaphragm displacement: an out-of-plane bending mode in the N-S direction (Fig. 1.1(b)); an out-of-plane bending mode in the E-W direction (Fig. 1.1(c)); and a shear raking mode

(Fig. 1.1(d)). The distribution of the horizontal forces to the vertical elements depends on the geometry and the rigidity of the nonrigid diaphragm. Floor diaphragms can be classified as flexible, stiff and rigid (ASCE 2000a). The prediction of the behavior of a structure with rigid diaphragm is relatively easy compared to that of structures with nonrigid diaphragm because the three key modes of diaphragm deformation shown in Fig. 1.1 do not exist in this case.

As the rigid diaphragm does not deform appreciably, it is assumed that its behavior remains elastic and the earthquake-induced internal forces are generally distributed to the vertical resisting elements in direct proportion to the relative rigidities of these elements. Conversely, in nonrigid diaphragm structures, the horizontal force within the vertical elements due to the lateral excitation depends on the rigidity and strength of the diaphragms.

In this section, the essential components that comprise the proposed MDOF analysis approach are summarized. These are: (1) the degree-of-freedom idealization of horizontal roof and/or floor diaphragms, (2) the degree-of-freedom idealization of shear walls, (3) lumping of masses, (4) extensions to the basic model to include out-of-plane wall stiffness and strength and diaphragm-to-wall anchorages, (5) idealization of foundation conditions, (6) idealization of ground motions, and (7) damping assumptions.

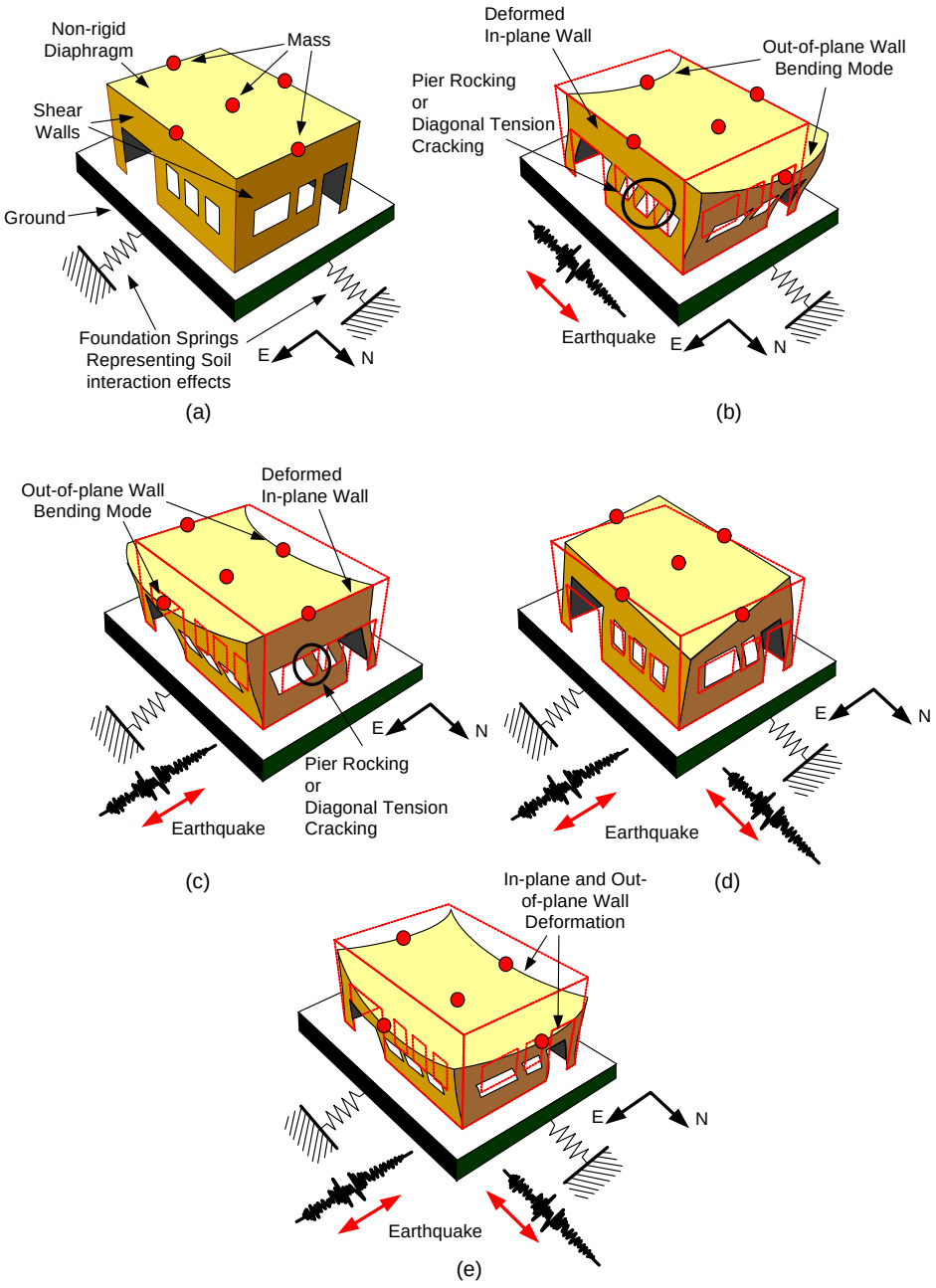

Figure 1.1: Low-rise shear wall building with a nonrigid diaphragm: (a) Structural components and undeformed shape; (b) Bending mode in N-S direction; (c) Bending mode in E-W direction; (d) Shear raking mode in both direction; (e) Combined bending and shear raking modes in both directions.

1.4.1 Low degree-of-freedom idealization of diaphragms

To idealize the behavior of nonrigid diaphragms, it is assumed that, in terms of its bending response, the diaphragm behaves essentially as a horizontal plate girder, in which the boundary members or chords serve as the girder flanges, and the sheathing or decking functions as the web to transfer the flexural shear force. The flange of the diaphragms is assumed to resist the flexure in the diaphragm; thus, the bending contribution of the web is ignored. The diaphragm webs are assumed to be subjected only to shearing actions. A flexibility-based diaphragm model is developed to incorporate deformations due to this bending in two orthogonal directions along with the shear raking associated with coupling of lateral-load resisting wall systems. The basic diaphragm element proposed in this work consists of six DOFs: three DOFs in the x direction and three in the y direction, as shown in Fig. 1.2. This element can be used to represent various types of wood and metal deck diaphragms. In addition, diaphragm hysteretic models are addressed that account for stiffness degradation, strength deterioration and pinching characteristics in diaphragms.

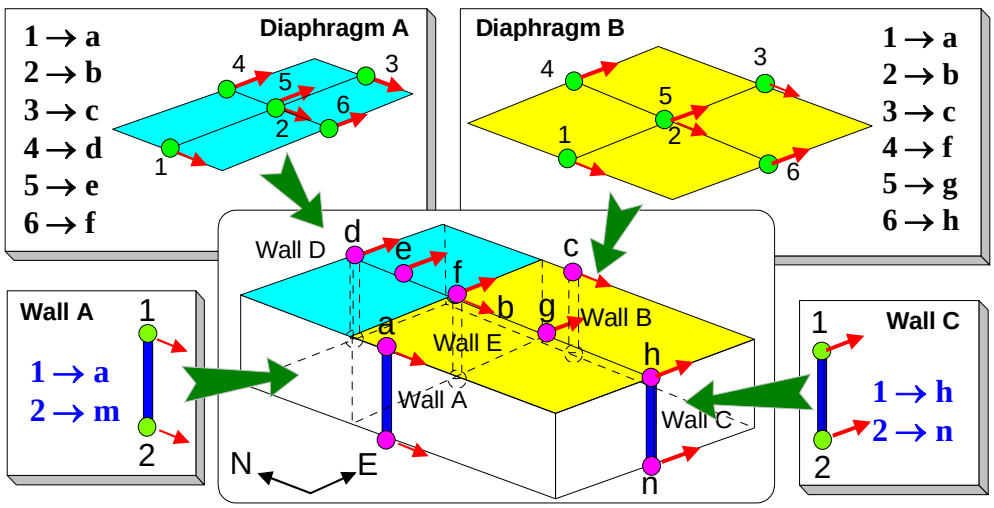

Figure 1.2: Assembly of diaphragm and wall element DOFs to global DOFs.

1.4.2 Low degree-of-freedom idealization of walls

The proposed basic wall element has two DOFs, one DOF at each floor or roof level. Each story of each in-plane wall may be represented by a single wall element, or multiple wall elements may be used to model directly the response of individual wall components. A flexibility approach is suggested to obtain the elastic stiffness of perforated shear walls, based on the results of FEM plane stress analyses. Although the stiffness of individual piers can be easily calculated based on simplified strength of materials idealizations, this approach has been shown to give results of limited accuracy for perforated shear walls (Tena-Colunga and Abrams 1992). Details about the flexibility approach are discussed in Chapter II. In addition, hysteretic models for unreinforced masonry (URM) walls incorporating the effects of pier rocking, bed-joint sliding, toe crushing and diagonal tension failure are addressed to predict the nonlinear behavior of these components.

Out-of-plane walls are affected by the out-of-plane bending associated with the diaphragm deformation and displacements of the in-plane walls. It is difficult to idealize the complex behavior of the out-of-plane walls. In this research, the effect of out-of-plane-walls is modeled as a shear wall element connected to the center of the diaphragm. This captures the aspect that the behavior of the out-of-plane walls depends highly on the bending deflection of the diaphragms in addition to the in-plane wall lateral displacement.

1.4.3 Assembly of diaphragm and wall element DOFs to global DOFs

A single diaphragm element with wall elements on each side can be used to model a single story structure with exterior structural walls. Figure 1.2 illustrates the assembly of the diaphragm and wall element DOFs to the global DOFs for a building with more than one diaphragm and with an interior shear wall. In order to assemble the two diaphragm stiffnesses at the same level (having a common boundary and a common degree-of-freedom), the element local DOFs 1 through 6 of diaphragms A and B are transformed

the structure global DOFs, as shown in Fig. 1.2. The central local DOFs 2 of each diaphragm are assigned to the global DOF b, which corresponds to mid-diaphragm displacements in the N-S direction. Global DOFs a and c represent N-S in-plane displacements at the tops of the walls A and B. The local DOFs 1 of both diaphragms are assigned to global DOF a and DOFs 3 are assigned to global DOF c. Global DOFs d, f, and h represent E-W in-plane displacements at the tops of the walls D, E, and C respectively. Global DOFs e and g accommodate E-W bending deformation of the diaphragms and the corresponding out-of displacement of the walls A and B. Global DOF b accommodates the bending and shear deformation of the diaphragms A and B and the corresponding out-of plane displacements of the walls C, D, and E. The above idealization assumes that the responses are captured adequately by assuming equal wall out-of-plane displacements in each side of the diaphragms in a given direction. Alternatively, separate global DOFs can be maintained, or used for the out-of plane displacement of the walls, or these DOFs can be tied by axial springs.

1.4.4 Lumping of masses

The diaphragm response can be represented in general by multiple intermediate lumped masses. However, the use of only one intermediate mass to model a diaphragm's response is sufficient for practical purposes. For the simplified MDOF model, masses are lumped at the location of each degree-of-freedom of the wall and diaphragm elements, and at the center of each diaphragm. Each lumped mass represents the effects of the distributed mass within the corresponding diaphragm area as well as the tributary mass of the attached side wall. The above lumped masses may be calculated by first determining nine concentrated masses, as shown in Fig. 1.3. When a uniform distributed mass is specified over the floor or roof area, the lumped masses of the element, based on Fig. 1.3, are calculated and assigned to the corresponding DOF of the element. Equation 1.1 is used to

define the lumped mass associated with each DOF. In addition, the lumped mass due to the out-of-plane wall is included in M_{u2} and M_{v2}. For the example shown in Fig. 1.2, lumped masses in E-W direction are located at global DOFs d, e, f, g, and h. Lumped masses in N-S direction are also located at global DOFs a, b, and c.

$$[M] = \begin{bmatrix} M_{u1} & 0 & 0 & 0 & 0 & 0 \\ & M_{u2} & 0 & 0 & 0 & 0 \\ & & M_{u3} & 0 & 0 & 0 \\ & & & M_{v1} & 0 & 0 \\ & Sym & & & M_{v2} & 0 \\ & & & & & M_{v3} \end{bmatrix} \tag{1.1}$$

where

$$M_{u1} = m1 + m2 + m3$$
$$M_{u2} = m4 + m5 + m6$$
$$M_{u3} = m7 + m8 + m9$$
$$M_{v1} = m1 + m4 + m7$$
$$M_{v2} = m2 + m5 + m8$$
$$M_{v3} = m3 + m6 + m9$$

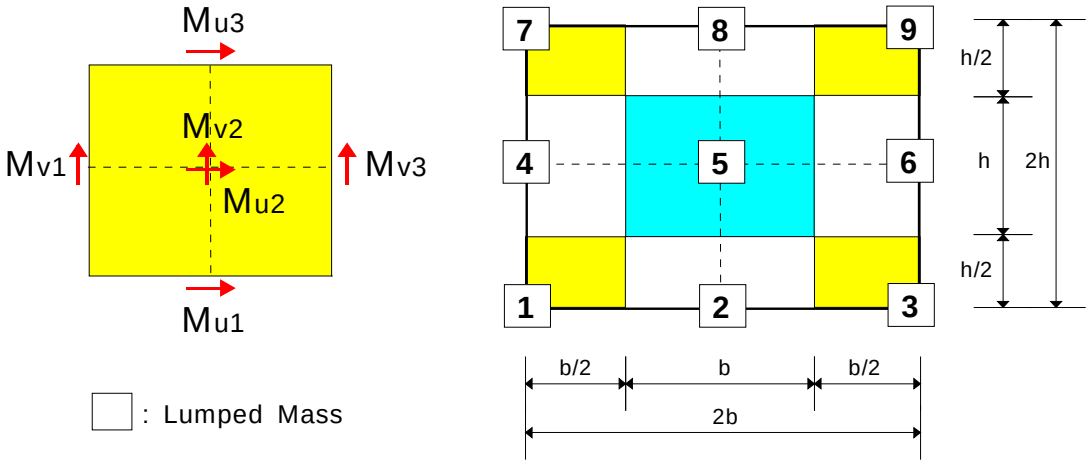

Figure 1.3: Distributed Area and Lumped Mass Configuration.

1.4.5 Idealization of foundation conditions

As compared to the rigid base, the effect of flexible base can be an important factor causing a decrease in the natural frequency of the structure (Hjelmstad et al., 1988). The flexibility of the base can greatly affect the fundamental frequency if the stiffness of soil is relatively small compared to the stiffness of the rigid support. A substantial part of the vibration energy may be dissipated into the supporting medium by radiation of waves and by hysteric action in the soil. In this work, soil-structure interaction is modeled where necessary by using equivalent linear springs under each wall corresponding to the direction of ground motion.

1.4.6 Idealization of ground motions

The recorded motions utilized in the studies by Tena-Colunga and Abrams (1992a) and the artificial ground motions proposed by Wen et al. (1999) are used in this research. For the Gilroy firehouse studied by Tena-Colunga and Abrams (1992a), both single and multiple recorded ground accelerations from the Loma Prieta earthquake are applied. Because of the lack of significant ground motion records in the mid-America region, synthetic ground motions generated by Wen are used to evaluate the performance of the half-scale test building (Cohen 2000). For the non-linear time history analysis, the ground motion of representative soil in Carbondale, Illinois site at the 2% in 50 years level is used in these shaking table tests.

1.4.7 Damping Assumptions

Among many different damping assumptions, Rayleigh damping is the most popular for the structure-damping matrix because of its simplicity and computational advantages. In this approach, the damping matrix is taken proportional to the stiffness and to the mass matrices, i.e.,

$$C = a_0 M + a_1 K \tag{1.2}$$

where

C = Rayleigh Damping Matrix

a_0 = Mass proportional damping influence coefficient

a_1 = Stiffness proportional damping influence coefficient

M = Mass Matrix

K = Stiffness Matrix

Rayleigh damping is assumed throughout this research. Issues associated with this simplified damping model within the context of nonlinear dynamic analysis are discussed in Section 4.3.6.

1.5 Overview of proposed linear static methodology for structures with flexible diaphragms

Current seismic codes and standards generally use a single degree-of-freedom (SDOF) model for low-rise buildings with rigid diaphragms, as shown in Fig. 1.4(a). However, flexible diaphragm structures behave in general in the manner of a MDOF model, as is shown in Fig. 1.4(b). A proposed simplified linear static methodology, applicable to buildings with flexible diaphragms (i.e., applicable to buildings in which the diaphragm stiffness is small enough such that torsional coupling effects may be neglected) is summarized in this section.

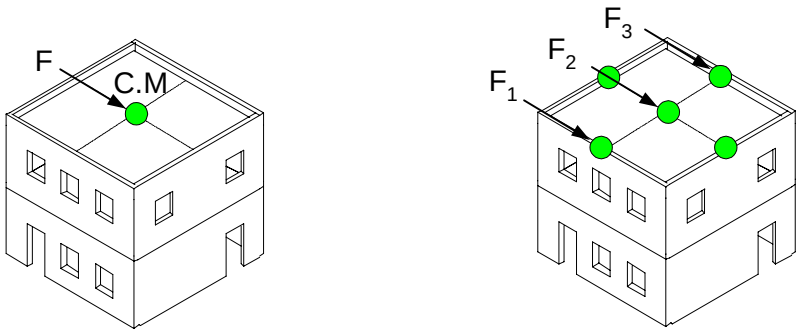

(a) Rigid diaphragm (b) Flexible diaphragm

Figure 1.4: Inertial force of rigid and flexible diaphragm.

An example single-story MDOF system with two flexible roof diaphragms is shown in Fig. 1.5(a). Figure 1.5(b) shows the two likely dominant modes of vibration of the structure in the direction considered. Because of small diaphragm stiffness relative to the stiffness of the walls, the first and second modes of vibration are associated predominantly with bending in each of the diaphragms. During an earthquake excitation, each of these flexible diaphragms will tend to respond independently of one another, and thus the behavior of each diaphragm can be assessed using separate subassemblies models, as shown in Fig. 1.5(c). Because the displacement of the in-plane walls is typically small compared to that of the flexible diaphragms, a simplified estimate of the period of a diaphragm can be obtained by assuming that the walls are rigid. However, the method does not require the in-plane walls to be modeled as rigid elements. The periods of in-plane walls can be obtained by summing the masses from the adjacent diaphragm subassemblies with the masses due to the direct inertial effects within each wall. When the walls are assumed to be rigid, the accelerations at the top of the in-plane walls are equal to the acceleration at the base.

Based on these assumptions, the natural periods of the separate models are calculated using the diaphragm stiffness and a lumped mass at the center of the diaphragm. The

lateral inertia forces at the center of the diaphragms are calculated from the period of the separate models using the spectral acceleration. The lateral inertia forces of the in-plane walls are calculated based on the peak ground acceleration and the lumped mass at the top of the walls. The lateral forces at the center of the diaphragms are distributed to the adjacent in-plane walls. The reaction forces at the base of the walls are taken as the sum of the lateral forces from the diaphragms plus the lateral forces of the in-plane walls. This method is referred to in this research as the structural separation method.

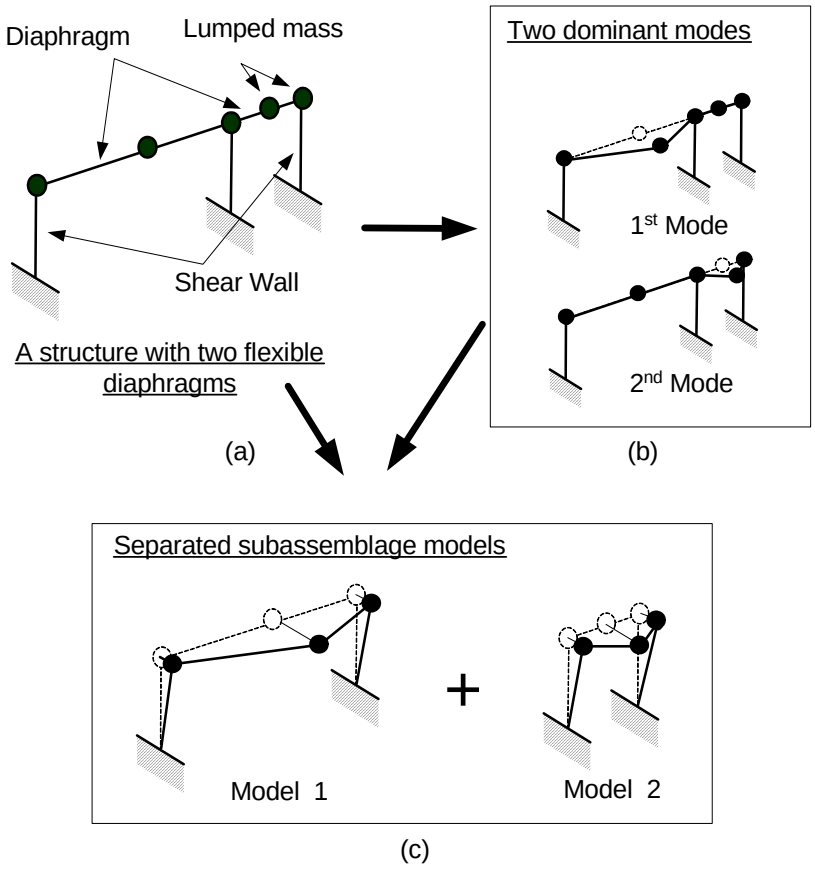

Figure 1.5: Structural separation method for a story building with two flexible diaphragms.

1.6 Organization

The main body of the report is subdivided into four chapters. Chapter II summarizes the implementation of the proposed MDOF analysis approach. Horizontal roof and floor diaphragms, shear walls, and general hysteretic models for the wall and diaphragm elements are considered. This chapter discusses wall and diaphragm element formulations, and the strength, stiffness, and hysteretic response of the structural elements.

Chapter III applies the simplified MDOF model to a two-story historic building with multiple diaphragms from Tena-Colunga and Abrams (1992). The main objective is that the simplified multiple-degree-of-freedom (MDOF) models discussed in Chapter I can be used for structural assessment of low-rise buildings with flexible floor diaphragms. Time history analysis results are compared to measured field data.

Chapter IV provides a detailed analysis of the simplified MDOF model for a half-scale one-story test building with a single nonrigid diaphragm from Cohen (2000a). A calibration process is introduced and applied with the non-linear time history analyses of the building to determine the model's structural properties. After finishing the model calibration process, sensitivity analyses are performed to ascertain the influence of variations in key parameters on the dynamic response.

Chapter V describes the simplified linear static procedure to assess low-rise buildings with flexible diaphragms. This chapter investigates structural separation procedure using the two-story building discussed in Chapter III. The simplified procedure is applied to linear elastic seismic assessment of the two-story and one-story buildings discussed in Chapters III and IV, respectively. The resulting values are compared to those of linear time history analysis for the buildings and implications relative to the inelastic seismic response are addressed.

The research results are summarized and recommendations for seismic assessment are provided in Chapter VI.

CHAPTER II

SIMPLIFIED ANALYSIS OF LOW-RISE BUILDINGS WITH NON-RIGID DIAPHRAGMS

2.1 Introduction

Prediction of the behavior of structures with rigid diaphragms is relatively easy compared to that of the structures with flexible diaphragms. When the diaphragms do not deform appreciably, horizontal forces are distributed to the lateral load resisting elements in direct proportion to their relative rigidities. On the other hand, in building structures with flexible diaphragms, the distribution of horizontal forces to the lateral load resisting elements can depend significantly on the rigidity of the diaphragms.

One goal of this research is the development of simplified multiple-degree-of-freedom (MDOF) models that can be used for structural assessment of low-rise buildings with flexible floor diaphragms. Subsequently, these models can be used to develop guidelines for evaluating the response of these types of structures, or potentially as assessment tools along with guidance documents. The simplified linear/nonlinear three-dimensional analysis approach presented here captures the essential response characteristics of low-rise shear wall buildings with flexible floor diaphragms discussed in Chapter I.

Particular emphasis is placed on how three-dimensional torsional response of the structural system can be addressed, as well as how the effects of potential significant nonlinearities can be included within the analysis. The suggested approach is essentially as efficient as possible for rapid evaluation of physical buildings or test designs, and for conducting large numbers of analyses within simulation studies, while capturing the three-

dimensional response characteristics discussed in Chapter I.

One wall and one diaphragm element are developed for the suggested simplified MDOF approach. These elements can be applied generally to various types of low-rise shear wall buildings, but in this research, the modeling is focused mainly on masonry buildings with nonrigid diaphragms. The nonlinear wall element is capable of capturing in-plane diagonal tension, bed joint sliding, rocking and toe crushing limit states in URM shear walls under lateral loadings. Three representative hysteresis models: a general purpose linear kinematic hardening model, a rocking model, and a general purpose three parameter model that includes stiffness degradation, strength deterioration, and pinching, are implemented for use within the wall and/or diaphragm elements. The formulation of the wall and diaphragm elements is presented in this chapter. Section 2.2 presents a literature review of previous analysis models for buildings with nonrigid diaphragms. Section 2.3 derives the diaphragm model and discusses the calculation of the diaphragm stiffness and strength. Section 2.4 explains the formulation of the wall models, including the calculation of the wall stiffness and strength. The primary focus is on unreinforced masonry walls, since the assessment of unreinforced masonry structures is of key importance in the MAE Center research program.

2.2 Literature Review

Low-rise masonry shear wall buildings with nonrigid diaphragms have been constructed extensively in many active seismic areas. However, few research studies have been conducted to gain a detailed understanding of the behavior of these types of buildings. The majority of prior studies have been limited to flexible diaphragms or masonry shear wall structural components. Prior studies of masonry building structural systems with flexible diaphragms have focused primarily on linear elastic analysis models. The prior research is summarized in this section to provide the authors' motivation for the pro-

posed three-dimensional simplified nonlinear analysis model.

2.2.1 Experimental basis for analysis modeling of buildings with nonrigid diaphragms

This section focuses on several areas of prior experimental tests that provide important information for understanding the behavior of shear wall buildings with non-rigid diaphragms. For purposes of discussion, these experimental tests are subdivided into the following categories: flexible diaphragms, in-plane unreinforced masonry walls, and masonry buildings with flexible diaphragms.

Experimental tests of flexible diaphragms

Current APA design procedures for horizontal plywood diaphragms are based in large part on tests by Countryman (1952), Stillinger and Countryman (1955), and Tissell (1966). Carney (1975) presented a bibliography that includes references on test results and design procedures for straight-sheathed and diagonally-sheathed wood diaphragms and plywood diaphragms.

Due to the addition of Seismic Design Zone 4 to the Uniform Building Code (ICBO 1976), and the resulting greater design accelerations, Tissell (1979) conducted eleven tests to check if the above design procedures would accurately predict the performance of diaphragms designed for much higher loads. These tests included cases with a high density of fasteners, openings, glued plywood diaphragms, and two-layer diaphragms (plywood overlay). Tissell and Elliot (1983) summarized these test results and proposed corresponding design procedures.

A major experimental program of 14 diaphragm tests subjected to simulated earthquake loading was conducted by ABK (1981). The tested diaphragms included a steel deck with a concrete slab, two steel decks without a concrete slab, five plywood diaphragms, three wood diaphragms composed of straight sheathing, and three diagonally-sheathed wood diaphragms. These dynamic component tests were designed to incorporate

the nonlinear dynamic interaction between the mass of the out-of-plane walls and the horizontal diaphragm of typical URM buildings. The diaphragms, 20 ft. x 60 ft. in dimension, were excited in the direction orthogonal to the out-of-plane walls. The unfilled steel deck diaphragms, in general, responded elastically with the exception of seam and weld failures, whereas the other tests exhibited significant nonlinearity.

Tissell and Rose (1993) tested five full-scale roof diaphragms. The intent of these tests was to develop empirical relationships for predicting diaphragm performance and determining diaphragm design recommendations, with an emphasis on construction similar to that used in single- and double-wide manufactured homes. These diaphragms were unblocked, and four of the tests had length/width ratios larger than 4:1.

Although the tests referenced above generally involve repeated loading, none of the tests in any of the above references include cyclic loading reversals.

Falk and Itani (1987) tested two plywood-sheathed walls, two gypsum board sheathed walls, three plywood floor diaphragms, and three gypsum board sheathed ceilings. The purpose of the tests was to determine the basic natural frequencies, damping ratios, and nonlinear load-deflection characteristics of plywood and gypsum diaphragms with and without openings. It was found that the diaphragm natural frequency decreases and the damping ratio increases as the displacement of the diaphragm is increased. Calculated values of the damping ratio ranged from 9 to 34 percent of critical damping. It was also found that the reduction in the stiffness of wall diaphragms with openings is approximately proportional to the fraction of the wall area occupied by the openings.

Since the late 1940s, numerous composite diaphragm tests (steel deck with concrete topping) have been performed for several steel deck manufacturers (Easterling and Porter 1994a). However, most of these tests were proprietary, and thus there are few published results. Subsequently, Easterling and Porter (1994a) performed cyclic static tests of 32 full-size steel-deck-reinforced concrete floor diaphragms to determine their behavioral and strength characteristics. A sample hysteresis response is shown in this reference, and

complete hysteresis data is catalogued in referenced research reports upon which this paper is based. Six diaphragms within this series were subjected to both in-plane and vertical load. The tests were conducted in a cantilever configuration. Based on the results of these experiments, the authors developed expressions for the strength and stiffness of the diaphragms. These expressions are specific to the configurations tested, and incorporate the strength and stiffness of edge connectors specific to steel frames. However, these test results and models can potentially be extended to cases having other boundary conditions.

Nakashima et al. (1982) tested several reinforced concrete beam-supported floor slabs. These tests were scale models of a portion of the floor system in a typical medium- to high-rise reinforced concrete building, and were subjected to monotonic loading as well as symmetric cycles of increasing amplitude to failure. The purpose of these tests was to evaluate the in-plane strength, stiffness and deformation characteristics of these types of diaphragms, and to perform a comparison with the results of analysis models. Hysteresis results for one of the tests are shown in the paper. The paper also correlates the experimental results with a detailed nonlinear finite element model composed of rigid triangular elements connected by springs.

Peralta et al. (2000) investigated experimentally the in-plane performance of reduced scale existing and rehabilitated wood floor and roof diaphragms with elements and connection details typical of pre-1950's construction. The tests provided fundamental information for definition of the yield strength and displacement, effective stiffness, and post-yield stiffness in bi-linear representations of the response. It was observed that the recommendations in FEMA 273 and FEMA 356 did not predict the backbone curves of the diaphragm tests accurately.

In general, the following characteristics are exhibited within at least some of the diaphragm tests referenced above, for each of the major diaphragm types (plywood, straight- and diagonally-sheathed wood, steel deck with concrete topping, and concrete slab):

1. Strength deterioration, i.e., a loss in maximum load capacity with cycling at a constant range of displacement.

2. Stiffness degradation, i. e., a loss in unloading stiffness with an increasing number of cycles and/or with cycling at larger displacement amplitudes.

3. Pinching, i.e., development of a plateau or near plateau in the load-displacement response within a given half-cycle, followed by a subsequent increase in the stiffness and load resistance at larger displacement levels within the half-cycle.

Experimental tests of masonry walls

Experimental testing and analytical modeling of multistory URM walls with openings have been conducted in prior research. However, the experimental studies in this field have been less extensive than analytical studies (Anand 1996). A major experimental test program involving unreinforced masonry (URM) walls subjected to earthquake loading was conducted by ABK (1981). These tests showed that the resistance to collapse depends more on the peak velocity input at the base and top of the walls than on the peak relative deformations induced between the top and bottom of the walls. Pomonis (1992) performed six shaking table tests on various types of unreinforced masonry walls. These tests investigated the damage related to the effects of strong ground motion parameters. Abrams (1992) tested a series of unreinforced brick walls. He discussed that masonry walls or piers need not be considered brittle, but can possess a large inelastic deformation capacity if they fail in a rocking mode. It was also noted that the behavior of walls under in-plane cyclic loading was not influenced by previous damage due to rocking, that is, essentially zero strength deterioration and stiffness degradation were observed. Leiva and Klingner (1994) tested six full-scale two-story reinforced concrete masonry walls with openings under in-plane seismic loading. They compared the effectiveness of two different models -

a pier and a multiple story type collapse model - for determining the collapse mechanism of perforated walls. Thirty-two equally reinforced masonry walls, subjected to different imposed lateral displacement - monotonic and cyclic, static and dynamic - were tested by Tomazevic et al. (1996a). As vertical load increased, lateral resistance of the walls was increased. It was also reported that the values of lateral resistance obtained by imposing the same displacement pattern dynamically were higher than those obtained by static loading, and that the ultimate displacement and resistance obtained by monotonic loading is higher than that obtained by cyclic loading.

Erbay and Abrams (2002) tested three full-scale, clay-unit masonry walls subjected to slowly applied reversals of lateral displacement. The results showed that unreinforced masonry walls can have substantial amount of inelastic deformation and energy dissipation capacity. Behavior of the URM walls tested was dominated by sliding shear behavior at the wall base. One of the walls was rehabilitated using the Center-Core Technique. This rehabilitation scheme improved the sliding shear capacity through dowel action as much as 20%. The authors suggested that the lateral-force behavior of the walls rehabilitated with this method can be assumed to be the same as that for reinforced masonry walls.

It is difficult to specify detailed information on the properties of URM walls because these properties differ from region to region (Scawthorn 1986; Paulson 1990; Abrams 1992; Page 1998). These types of walls often have been assumed to be brittle (Abrams 1992). In order to predict the lateral resistance and the nonlinear behavior of URM walls or pier elements, the behavior is typically idealized as one of the following types of failure: pier rocking, bed-joint sliding, toe crushing and diagonal tension. In a pier rocking mode, a slender wall rocks on its base and behaves as a rigid body. Bed-joint sliding is governed by a large fracture of the mortar joint at the bed joints when cracks propagate from one interface to other along the mortar joint. Toe crushing occurs when the vertical compressive stress of the URM wall is larger than the masonry compressive

strength and the bottom corner of the wall is crushed. Diagonal tension failure occurs when diagonal cracks form in the wall, due to large tension stresses.

Experimental tests of masonry buildings

Due to the limited capabilities of laboratory facilities and testing equipment, detailed information on full size building response is still very limited (Paulson and Abrams 1990).

Tomazevic (1990) studied the influence of structural layout and reinforcement on the seismic behavior of a three- to four- story residential masonry building. A small-scale masonry building was tested by Tomazevic and Velechovsky (1992). Tomazevic and Weiss (1994) tested two typical Central European three-story plain- and reinforced-masonry buildings containing a reinforced concrete ribbed slab. The plain masonry tests showed that cracks occurred between the walls and slabs.

In cooperative research between U.S. and Japan, a 5-story full-scale prototype structure was tested in both countries. Yamazaki (1988a and 1988b) reported on the Japanese 5-story full scale reinforced concrete masonry test. As the final validation of the TCCMAR/US (U.S. Technical Coordinating Committee for Masonry Research) design philosophy and analytical models, Seible (1994) reported on the U.S. full-scale five-story building test. The U.S. test consisted of fully grouted masonry walls and precast pre-stressed hollow-core plank floors with reinforced concrete topping, subjected to simulated seismic loads.

Costley and Abrams (1996) investigated the dynamic behavior of two reduced-scale single bay two-story URM buildings with flexible diaphragms. The test buildings had steel floor systems which were designed to simulate the wood diaphragms. Approximately 40 channels of data from accelerometers and displacement transducers were collected on each test structure. A total of 12-earthquake simulations, which were taken from the Nahanni Earthquake, were performed with the first test structure. The last five studies

used a filtered displacement time history. Each earthquake simulation increased the intensity of the base motion with respect to the previous simulation with the accelerations ranging from 0.15g to 1.8g. Four earthquake simulations were performed with the second structure. The intensity of the motion was increased from 0.2 g to 1.1 g in this test. The test results and comparisons with various analytical models were reported.

Tomazevic and Klemenc (1997) performed two shaking table tests of a typical confined masonry building. These tests were intended to confirm Eurocode 8. Modeling the confined masonry shear walls as frames was considered as a rational analytical method.

Paquette and Bruneau (2000) tested a single-story full-scale unreinforced brick masonry building with wood diaphragms. They assessed the effectiveness of fiberglass strips to improve the rocking behavior and compared the results with predictions from existing seismic evaluation methodologies.

Cohen et al. (2000 a and b) tested two single-bay one-story half-scale reinforced masonry buildings with flexible roof diaphragms. The first test had a diagonally sheathed lumber diaphragm, and the second had a corrugated metal deck diaphragm. The structures were subjected to artificial ground motions developed for the Mid-America region. The test results showed that the structures did not behave as a single degree-of-freedom system. The flexible roof diaphragms tended to behave independently of the two side in-plane shear walls in these tests.

2.2.2 Prior and potential models for analysis of buildings with nonrigid diaphragms

In order to investigate the effect of the diaphragm flexibility on low-rise shear wall buildings with nonrigid diaphragms, a wide range of analysis models have been developed in prior research. Some of the most relevant models pertaining to the present work are summarized below.

A detailed lumped parameter model was created in (ABK 1981) to characterize the

experimental diaphragm tests discussed in Section 2.2.1. This model has five degrees-of-freedom distributed over one-half of the width of the diaphragm and connected by springs and viscous dampers to represent the internal diaphragm response. The model is based on assumed symmetry about the mid-span of the diaphragms, and includes lumped masses from the diaphragm and the out-of-plane walls. Detailed plots of the experimental and analytical diaphragm hysteresis behavior are provided in the report.

Cohen et al. (2000 a and b) developed a two degree-of-freedom idealized model of their test buildings, also discussed in Section 2.2.1. The first DOF of the model is associated with the in-plane deformation of the narrow end shear walls (assumed equal due to symmetry), and the second DOF is associated with the flexural deformation of the diaphragm (and the corresponding out-of-plane deformation of the longer walls). This model can be represented as shown in Fig. 2.1(a). The calculated responses from this simplified model are compared with the measured responses in the reports. This two-DOF model cannot capture the significant contribution of the out-of-plane walls to the building lateral stiffness and strength and torsional effects associated with incidental or intentional non-symmetry of the stiffness and/or mass.

Practical modeling of URM buildings for design and/or assessment purposes has been carried out by a number of investigators using two-dimensional discrete models. Tena-Colunga and Abrams (1992a, 1992b, and 1996) examined the dynamic response of a two-story URM building (a former firehouse in Gilroy, California) and a two-story reinforced masonry building located at Palo Alto during the Loma Prieta Earthquake. Data was collected for the response of both buildings. Because the buildings were strong and the earthquake motions were moderate, these structures remained predominantly within the proportional limit. The accuracy and ease of use of a number of computational techniques were evaluated, including the simple two-dimensional discrete linear-elastic MDOF analytical model shown in Fig. 2.1(b) and a three-dimensional finite element model such as illustrated in Fig. 2.1(d). Two-dimensional plane stress finite element mod-

els were used to estimate the stiffness of the in-plane masonry walls. In the discrete models, the in-plane masonry walls were modeled as condensed beam elements. The in-plane stiffness coefficients of these beams were obtained from the two-dimensional plane stress finite element analyses. The in-plane actions of the diaphragms were considered as elastic shear springs in the direction of loading, considering in-plane shear resistance.

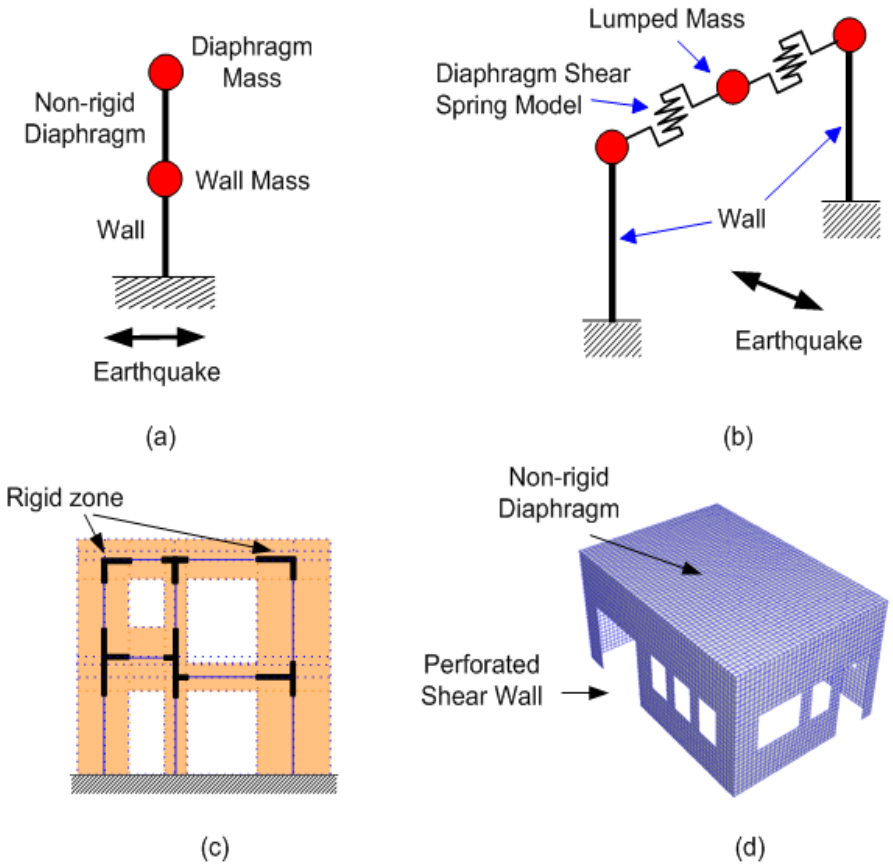

Figure 2.1: Analytical models: (a) Two DOFs model (Cohen 2000 a and b); (b) Lumped parameter model (Tena-Colunga and Abrams 1992a, 1992b, and 1996); (c) Equivalent frame model (Costley et al. 1996 and Kappos et al. 2002); and (d) Three-dimensional Finite Element Model (Tena-Colunga et al. 1992 and Kappos 2002).

In the above studies, when the model shown in Fig. 2.1(b) is symmetric, it is identical with the one shown in Fig. 2.1(a).

An equivalent frame method (Tena-Colunga 1992, Kappos 2002), shown in Fig. 2.1(c), has been used by some investigators to model perforated shear walls. Kappos (2002) performed two-dimensional nonlinear static pushover analyses using both Finite Element and equivalent frame models to investigate the nonlinear behavior of perforated walls. His equivalent frame model is composed of equivalent columns and beams with rigid end zones. This method may not be accurate in some cases. The zones that are assumed to be rigid often deform and crack (Tena-Colunga 1992).

Costley and Abrams (1996) investigated a number of conventional methods of analysis to determine their applicability and accuracy in conjunction with their two reduced-scale experimental tests (see Section 2.2.1). Beam and solid finite elements were applied to determine the natural frequencies. To investigate the flexibility of the diaphragm, an isolated diaphragm model consisting of eleven floor beams was created to represent the experimental system. The experimental system involved steel bars that were framed into the masonry with pinned ends, and each of these components were represented explicitly in the diaphragm model. The diaphragm model was used to check how the diaphragm would behave within the overall structure. To represent the masonry portion of the test buildings, eight-node solid elements were used. Two common analysis methods, response spectrum and pushover analysis, were used. Also, a lumped parameter three degree-of-freedom nonlinear dynamic model, similar in form to the one shown in Fig. 2.1(b), was developed to estimate the post-cracking response of the structures. Costley and Abrams suggested that there was a need for improved simplified models for estimating the response maxima of URM buildings.

Shing and Klingner (1998) used a state-of-the-art finite element program to investigate possible failure mechanisms of URM walls in a qualitative manner and to provide guidance for the repair and retrofit of existing structures.

All of the above simplified MDOF models are two-dimensional lumped parameter models. In all of these models, the nonrigid diaphragms and shear walls are idealized as

beams or shear springs. The only three-dimensional models involve the use of solid finite elements, and these models are linear elastic. Isolated components have been modeled by more complex two-dimensional nonlinear finite element capabilities. However, the extension of these sophisticated nonlinear models to general three-dimensional building response is difficult both due to the lack of consideration of three-dimensional effects in their development as well as the associated computational expense. Many of the prior studies of overall structural systems have focused primarily on elastic, or linearized, building responses.

In order to improve the seismic assessment of shear wall structures with nonrigid diaphragms, a new simplified three-dimensional nonlinear MDOF modeling approach is proposed in this Chapter. The general characteristics of this model have been summarized in Chapter I, Section 1.4.

2.3 Diaphragm Models

A building generally consists of horizontal floor and roof diaphragms and vertical elements. The floor and roof diaphragms, which are typically assumed in design to behave as horizontal deep beams or plate girders, distribute the lateral forces among the vertical lateral-load resisting elements. The distribution of the horizontal forces to the vertical elements depends on the geometry and the rigidity of the diaphragms. Diaphragms can be classified as nonrigid or rigid. Section 2.3.1 discusses how flexible diaphragms have been idealized in prior research and practice. Section 2.3.2 presents the formulation of a new diaphragm element. The element has six DOFs and is based on a force (equilibrium) approach. An equivalent shear modulus is used in calculating the diaphragm stiffness. Section 2.3.3 explains the idealization of multiple diaphragm structures in this work, i.e., the assumed connectivity between adjacent diaphragm elements. Section 2.3.4 discusses the two basic types of diaphragm force-deformation models utilized in this work, i.e., non-

linear hysteretic models and equivalent linear models, and the basic properties associated with each of these models. Section 2.3.5 discusses specific equivalent linear properties for different diaphragm types, as well as the implications of various diaphragm approximations.

2.3.1 Proposed diaphragm idealization

As shown in Fig. 2.2, diaphragms are typically modeled using a plate girder analogy to idealize their behavior (ATC 1981). The boundary members of the diaphragm serve as the girder flange and are termed the chords of the diaphragm. The deck or sheathing functions as the web.

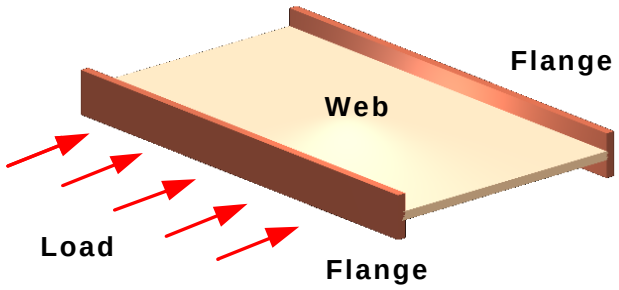

Figure 2.2: Plate girder under the horizontal loading.

In this approach, the diaphragm chord is typically assumed to provide the only contribution to bending resistance, i.e., the bending contribution of the web is ignored. The compression or tension force in the chord is calculated by dividing the moment in the diaphragm by the distance between centerlines of the chord elements. The "flange" force determined by this procedure is conservative.

The web carries the shear forces induced by the horizontal loadings. Based on mechanics of materials and the assumption of a homogeneous isotropic elastic material, the web shear stress exhibits a parabolic, but typically near uniform, distribution through

the web depth. Nevertheless, the webs of wood and steel deck diaphragms are not one piece. The largest contribution to the deformation typically comes from nail slip in wood diaphragms (ATC 1981), and from connector slip and distortion of the deck cross-section profile in steel decks (SDI 1995). In plywood diaphragms, the shear stress conditions in the web depend on the thickness and boundary nailing of plywood panels. In practice, the shear force (load per unit length) is assumed to distribute uniformly across the width of the diaphragm, and thus the shear stress (load per unit length divided by the equivalent thickness) is assumed to be uniform across width of the web. For the MDOF model considered in this work, an equivalent shear modulus of the web and an equivalent tangent modulus of the chord are calculated from established diaphragm design equations.

2.3.2 Diaphragm element formulation

The new diaphragm element developed in this work is shown in Fig. 2.3. This element consists of six DOFs: three in the u direction and three in the v direction. The boundary degrees of freedom capture the in-plane wall displacements at the edges of the diaphragm, and the middle DOFs capture the diaphragm deformation associated with out-of plane wall displacements. The diaphragm element is based on a force (equilibrium) approach. This approach is necessary to capture the combined two- and three-dimensional effects discussed in Section 1.4 with the limited number of degrees of freedom of the element. The element develops bending moments via its chord members and shears via its web.

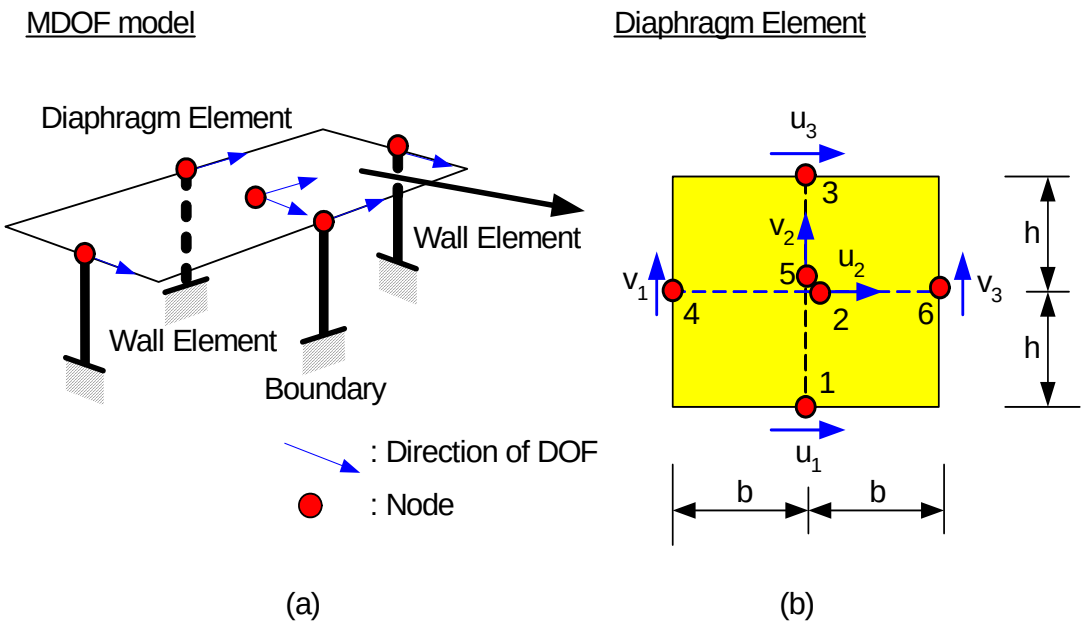

Figure 2.3: (a) MDOF model of one bay one-story building with four in-plane shear walls, (b) Six degree-of-freedom diaphragm element.

The element has four sampling points, one for each quadrant of the diaphragm as shown in Fig. 2.4(a). Different uniform shear stresses exist in each quadrant due to the lumped horizontal loadings at each of the DOFs. Specifically, the different shear stresses in each quadrant are caused by the lumped loadings at DOFS u_2 and v_2 shown in Fig. 2.3.

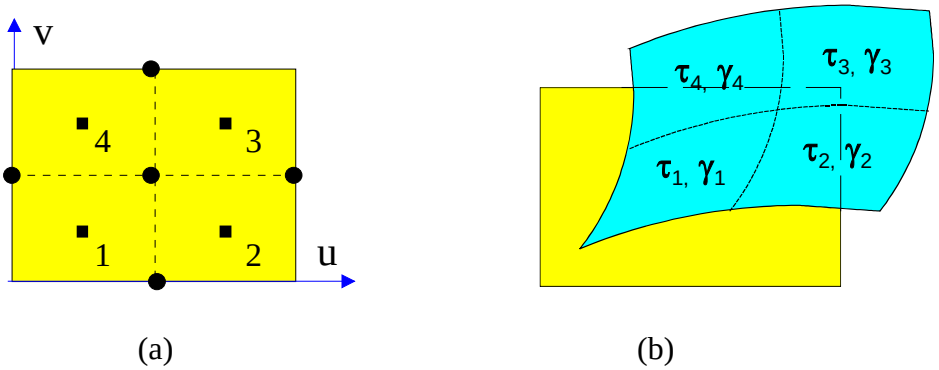

Figure 2.4: (a) Mesh of diaphragm element showing 4 sampling points in each quadrant (b) General deformation of diaphragm element.

Also, the shear stresses may differ in each quadrant because the properties of the diaphragm may not be uniform due to openings, cutouts and changes in diaphragm thickness or type. Openings through diaphragms for stairways, shafts, skylights, etc., can cause a reduction in the stiffness and capacity of the diaphragms to resist lateral forces. In the proposed approach, diaphragm openings are addressed by use of a reduced stiffness contribution from the quadrants in which the openings are contained. Furthermore, in a nonlinear analysis, the shear stresses (and shear stiffnesses) within each quadrant may differ in the post-elastic range of the response even if the initial properties are the same.

It is assumed that uniform shear strains are produced over the entire diaphragm area by shear raking distortions associated with relative in-plane wall displacements in the u and v directions. Figure 2.4 (b) illustrates the combination of this shear raking deformation with the bending deformations in the u and v directions. If the diaphragm properties are the same within each of its quadrants, the shear raking distortions of course produce a corresponding uniform shear stress throughout the diaphragm. However, if the diaphragm properties are different in each quadrant, the idealized uniform shear raking distortions produce different shear stresses in each quadrant.

To minimize the number of degrees-of-freedom, axial elongation and shortening of the diaphragm is neglected in this research. These deformations may be included in general by the use of independent axial springs between the out-of-plane walls and the middle diaphragm DOFs.

Section 2.3.2.1 discusses the transformation between the global displacements of the six-DOF diaphragm element and its three independent natural or deformational modes of displacement (two bending modes and a shear raking mode). Section 2.3.2.2 presents the formulation of the natural flexibility matrix, which is based on the above three natural modes. Section 2.3.2.3 summarizes the calculation of the element stiffness matrix from the flexibility matrix of Section 2.3.2.2 and the transformation matrix of Section 2.3.2.1. Section 2.3.2.4 discusses the state determination procedure for nonlinear static and

dynamic analysis.

2.3.2.1 Transformation matrix

Consider the diaphragm element shown in Fig. 2.3(b). The nodal displacements of this element can be subdivided into six independent modes $\{d_i\}$ (see Fig. 2.5). The first three modes, labeled as 1, 2 and 3 in Fig. 2.5, are referred to as deformational or natural (Argyris et al. 1979) modes. The next three (labeled as 4, 5 and 6) are rigid body modes. The three natural modes may be written as

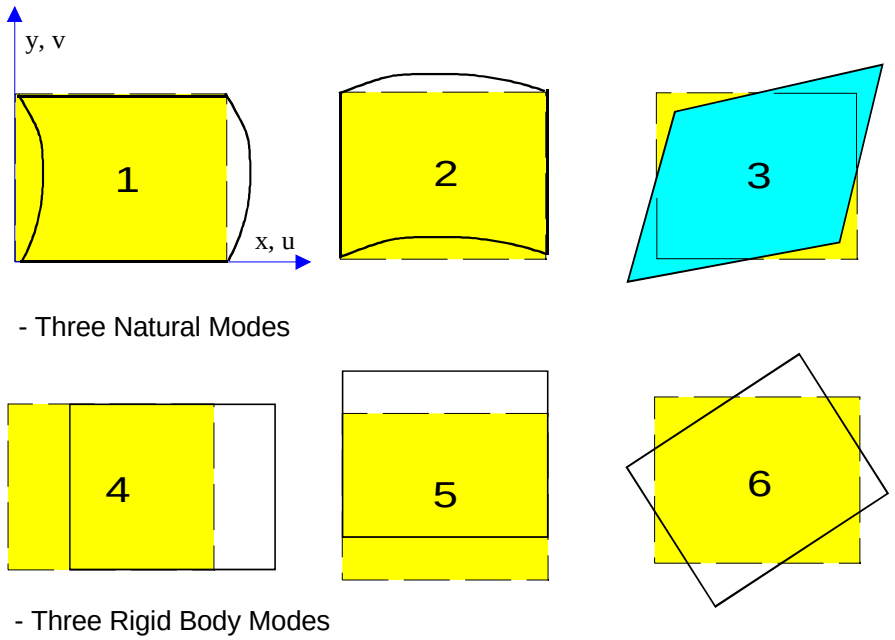

Figure 2.5: Independent displacement modes of a diaphragm element (three natural modes and three rigid body modes).

$$\{d_1\} = \begin{Bmatrix} 0 \\ u_N \\ 0 \\ 0 \\ 0 \\ 0 \end{Bmatrix} \qquad \{d_2\} = \begin{Bmatrix} 0 \\ 0 \\ 0 \\ 0 \\ v_N \\ 0 \end{Bmatrix} \qquad \{d_3\} = \begin{Bmatrix} -\gamma_N h \\ 0 \\ \gamma_N h \\ -\gamma_N b \\ 0 \\ \gamma_N b \end{Bmatrix} \tag{2.1}$$

and the three rigid body modes may be expressed as

$$\{d_4\} = \begin{Bmatrix} u_R \\ u_R \\ u_R \\ 0 \\ 0 \\ 0 \end{Bmatrix} \qquad \{d_5\} = \begin{Bmatrix} 0 \\ 0 \\ 0 \\ v_R \\ v_R \\ v_R \end{Bmatrix} \qquad \{d_6\} = \begin{Bmatrix} \theta_R h \\ 0 \\ -\theta_R h \\ -\theta_R b \\ 0 \\ \theta_R b \end{Bmatrix} \tag{2.2}$$

where

$$u_N = u_2 - \frac{u_1 + u_3}{2} \tag{2.3}$$

$$u_R = \frac{u_1 + u_3}{2} \tag{2.4}$$

$$v_N = v_2 - \frac{v_1 + v_3}{2} \tag{2.5}$$

$$v_R = \frac{v_1 + v_3}{2} \tag{2.6}$$

$$\gamma_N = \frac{1}{2}\left(\frac{v_3 - v_1}{2b} + \frac{u_3 - u_1}{2h}\right) \tag{2.7}$$

$$\theta_R = \frac{1}{2}\left(\frac{v_3 - v_1}{2b} - \frac{u_3 - u_1}{2h}\right) \tag{2.8}$$

2b = diaphragm width in the u direction (see Fig. 2.3)

2h = diaphragm span length in the v direction (see Fig. 2.3)

The terms u_N and v_N in Eqs. 2.1, 2.3 and 2.5 are element natural displacements, or element deformations, associated with diaphragm bending. These deformations are obtained as the difference between the total displacement at the middle of the diaphragm

and the average of the corresponding displacements at the diaphragm edges (see Fig. 2.6). The third natural displacement, γ_N, is associated with the shear raking in mode 3 of the diaphragm as shown in Fig. 2.5. The total shear strain induced by this mode is equal to $2\gamma_N$, where γ_N is defined by Eq. 2.7.

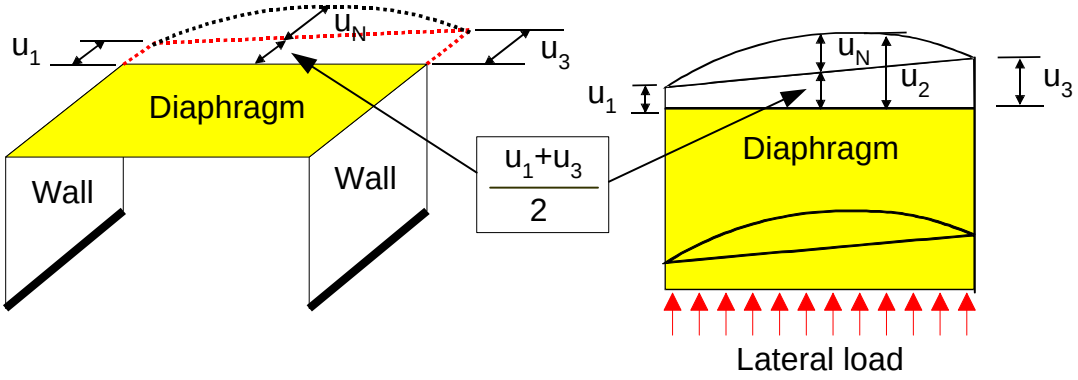

Figure 2.6: Calculation of the diaphragm deflection.

Given the above relationships, the natural displacements may be related to the total displacements by the following matrix form:

$$\{d_N\} = [T]\{d\} \quad \text{or} \tag{2.9}$$

$$\begin{Bmatrix} u_N \\ v_N \\ \gamma_N \end{Bmatrix} = [T] \begin{Bmatrix} u_1 \\ u_2 \\ u_3 \\ v_1 \\ v_2 \\ v_3 \end{Bmatrix} \tag{2.10}$$

where

$\{d_N\} = \begin{bmatrix} u_N & v_N & \gamma_N \end{bmatrix}^T$; Element natural displacement vector

$\{d\} = \begin{bmatrix} u_1 & u_2 & u_3 & v_1 & v_2 & v_3 \end{bmatrix}^T$; Element total nodal displacement vector

$$[\mathrm{T}] = \underset{3 \times 6}{[T]} = \begin{bmatrix} -\frac{1}{2} & 1 & -\frac{1}{2} & 0 & 0 & 0 \\ 0 & 0 & 0 & -\frac{1}{2} & 1 & -\frac{1}{2} \\ -\frac{1}{4h} & 0 & \frac{1}{4h} & -\frac{1}{4b} & 0 & \frac{1}{4b} \end{bmatrix} \tag{2.11}$$

Given Eq. 2.10, the force components must obey the following transformation rules (Cook 1989):

$$\{r\} = [T]^T \{r_N\} \tag{2.12}$$

where

$\{r_N\} = \begin{bmatrix} U_N & V_N & S_N \end{bmatrix}^T$; Element natural force vector

$\{r\} = \begin{bmatrix} U_1 & U_2 & U_3 & V_1 & V_2 & V_3 \end{bmatrix}^T$; Element total nodal force vector

U_N = x - directional natural force corresponding to mode 1

V_N = y - directional natural force corresponding to mode 2

S_N = Natural shear force corresponding to mode 3

2.3.2.2 Natural Flexibility Matrix

The natural flexibility matrix is formulated based on the 3 natural modes in Fig. 2.5. The coefficients of the natural flexibility matrix

$$[F_N]_{3\times 3} = \begin{bmatrix} F_{N11} & F_{N12} & F_{N13} \\ F_{N21} & F_{N22} & F_{N23} \\ F_{N31} & F_{N32} & F_{N33} \end{bmatrix} \tag{2.13}$$

are obtained by subjecting the element to a unit load at each of the natural DOFs, with the displacements in the three rigid-body modes held to zero. The flexibility coefficient F_{Nij} is the i^{th} displacement due to a unit load at the j^{th} natural DOF. The following subsection derives the diagonal flexibility coefficients corresponding to the element bending modes (the first and second columns of Eq. 2.13). This is followed by the derivation of the diagonal flexibility coefficients corresponding to the element shear raking mode (column three of Eq. 2.13).

Flexibility coefficients corresponding to the diaphragm bending modes.

Consider the diaphragm deformations in mode 1 of Fig. 2.5 induced by a unit force applied at the center of the diaphragm, as shown in Fig. 2.7. This force produces uniform shear stresses in each of the diaphragm's quadrants as shown on the right side of Fig. 2.7. The resulting total displacement at the center of the diaphragm can be expressed as the sum of the bending displacement due to shear deformation of the diaphragm web plus the displacement due to flexural deformation of the diaphragm chords. That is,

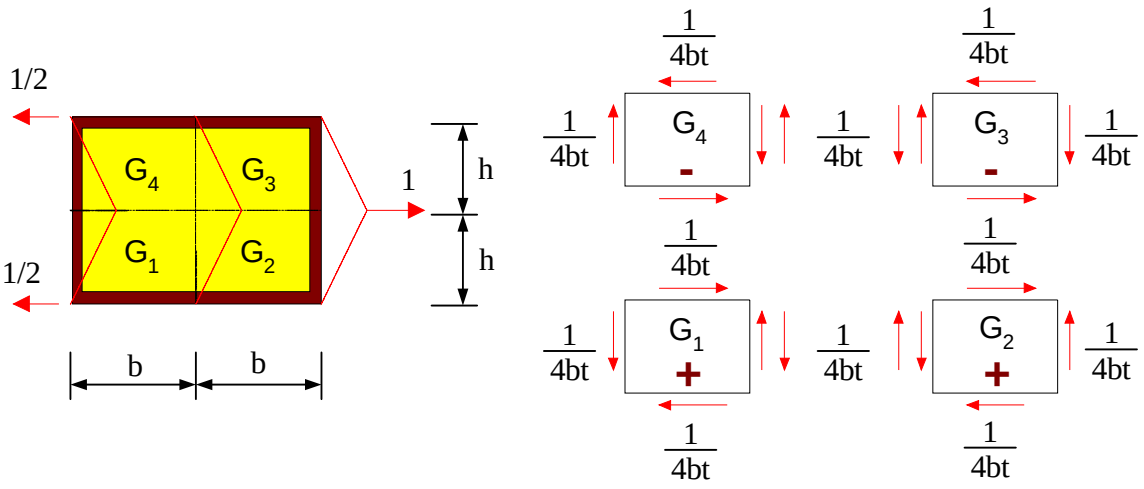

Figure 2.7: Internal stress distributions due to horizontal unit force, $U_N = 1$.

$$F_{N11} = \Delta_S + \Delta_C \tag{2.14}$$

where

Δ_S = bending deflection due to web shear deformation

Δ_C = bending deflection due to chord deformation

For a diaphragm with uniform properties throughout its area ($G = G_1 = G_2 = G_3 = G_4$), the diaphragm center-span displacement can be calculated (from virtual work) as

$$\Delta_S = \int_0^b \int_0^h \frac{1}{(4bt)^2}\left[\frac{1}{G_1} + \frac{1}{G_2} + \frac{1}{G_3} + \frac{1}{G_4}\right] t\,dx\,dy = \frac{h}{4btG} \tag{2.15}$$

where

G_i = shear modulus of the web for quadrant i = 1, 2, 3, 4.

In the context of linear analysis, these coefficients are the elastic (or equivalent elastic)

shear moduli within each of the diaphragm quadrants. In the context of a nonlinear analysis, these coefficients are the tangent shear moduli corresponding to the current state within each of the diaphragm quadrants.

As noted previously, the shear modulus of each diaphragm quadrant may be different due to openings in the diaphragm, irregular diaphragm properties, or diaphragm nonlinearity. In this general case, the diaphragm bending deflection due to web shear is calculated as

$$\Delta_S = \int_0^b \int_0^h \frac{1}{(4bt)^2}\left[\frac{1}{G_1} + \frac{1}{G_2} + \frac{1}{G_3} + \frac{1}{G_4}\right] t\,dx\,dy$$

$$= \frac{h}{(16bt)}\left[\frac{1}{G_1} + \frac{1}{G_2} + \frac{1}{G_3} + \frac{1}{G_4}\right] \tag{2.16}$$

The displacement due to diaphragm chord deformation may be expressed in general as the sum of the effects due to the flexural strains generated in the chords plus that due to slippage within the chord splices (ATC 1981), i.e.,

$$\Delta_C = \Delta_{cb} + \Delta_{cs} \tag{2.17}$$

where

Δ_{cb} = bending deflection due to flexural strains in the chord members

Δ_{cs} = bending deflection due to the chord splice slip in the chord members

The bending deflection due to flexural strains within the chord members is

$$\Delta_{cb} = \frac{(2h)^3}{48EI} = \frac{h^3}{6EI} \tag{2.18}$$

where

E = elastic modulus of the chord members

$I = 2Ab^2$ = moment of inertia contribution from the chord members

2h = diaphragm span length in v direction

Based on virtual work principles, the bending deflection due to slip at a single chord splice location may be written as

$$\Delta_{cs} = \Delta_{slip}\left(\frac{X_s}{4b}\right) \tag{2.19}$$

where

Δ_{slip} = slip at the chord splice location

X_s = location of chord splice relative to the end of the diaphragm

The total deflection due to slip at all the chord splices is obtained by summing the contributions from each of the chord splice locations. Therefore, for the example shown in Fig. 2.8, the bending deflection due to slip is

$$\Delta_{cs} = (\Delta_{elongation} + \Delta_{shortening})\left(\frac{X_s}{4b}\right) \tag{2.20}$$

The reader should note that Eqs. 2.19 and 2.20 are used to obtain an equivalent elastic (secant) stiffness associated with an anticipated or specified slip at the chord splices. Non-linear chord deformations are not considered in the present research. If chord inelastic response is considered, tangent relationships for the chord flexural deformations and for chord splice slip are needed.

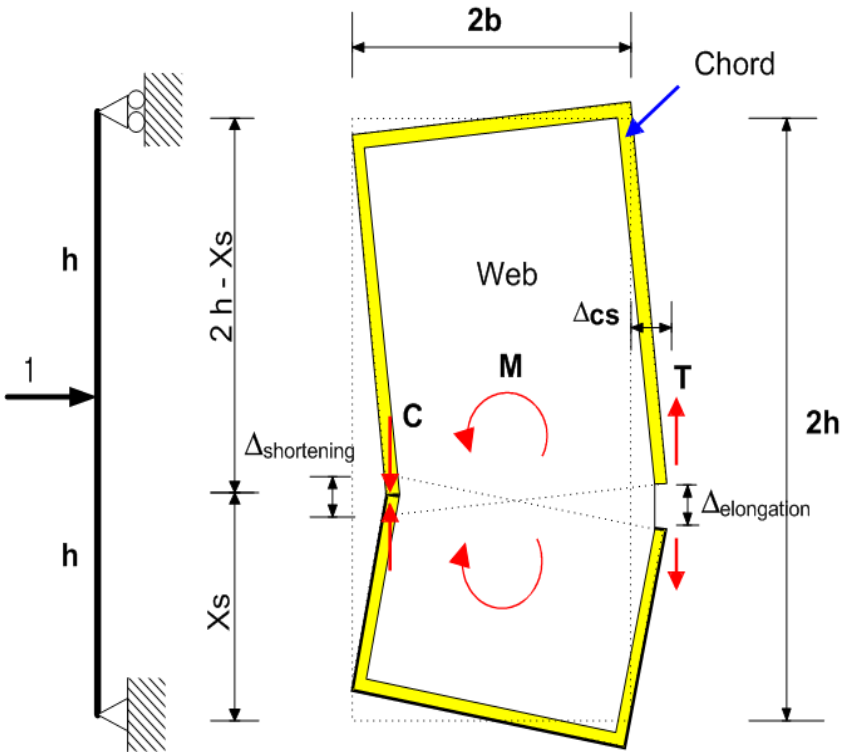

Figure 2.8: Example bending deflection Δ_{cs} due to chord splice slip.

For a diaphragm with uniform shear properties (i.e., $G_1 = G_2 = G_3 = G_4$ and constant effective thickness), the off diagonal flexibility coefficients in Eq. 2.13 are zero. However, in the general case in which these properties differ between any of the quadrants of the diaphragm, displacements are produced at all of the natural degrees of freedom due to a force at any one of these degrees of freedom. Based on virtual work and considering Figs. 2.7 and 2.9, the off-diagonal flexibility coefficient F_{N12} is derived as follows:

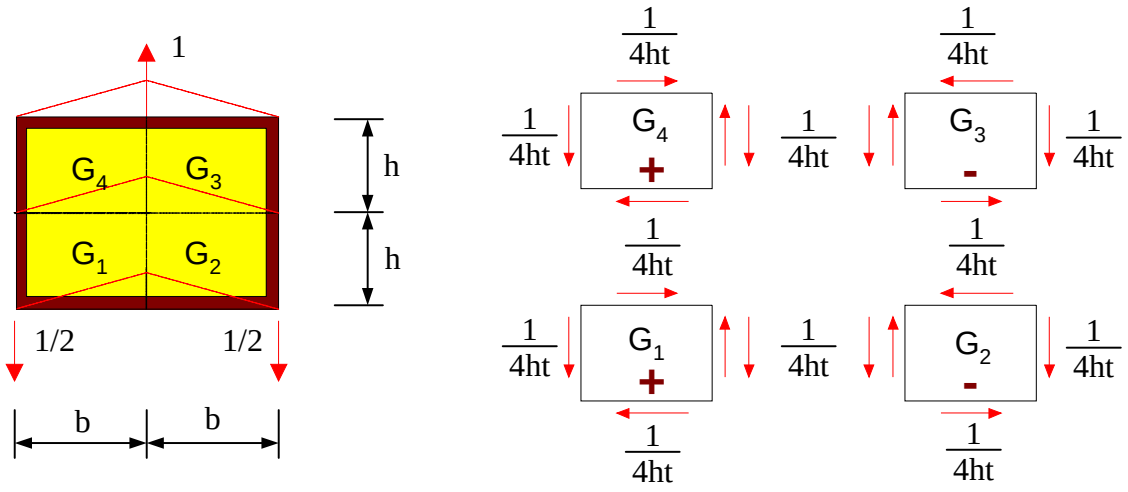

Figure 2.9: Internal stress distributions due to vertical unit force, $V_N = 1$.

$$F_{N12} = \int_0^b \int_0^h \frac{1}{(4bt)(4ht)} \left[\frac{1}{G_1} - \frac{1}{G_2} + \frac{1}{G_3} - \frac{1}{G_4} \right] t\,dx\,dy$$

$$= \frac{h}{(16t)} \left[\frac{1}{G_1} - \frac{1}{G_2} + \frac{1}{G_3} - \frac{1}{G_4} \right] \qquad (2.21)$$

The flexibility coefficient F_{N21} is equal to F_{N12} by symmetry.

Flexibility coefficients corresponding to the shear raking mode.

For the third natural mode in Fig. 2.5, the nodal forces due to a given natural shear force S_N may be calculated as:

$$\begin{Bmatrix} U_1 \\ U_2 \\ U_3 \\ V_1 \\ V_2 \\ V_3 \end{Bmatrix} = [T]^T \begin{Bmatrix} 0 \\ 0 \\ S_N \end{Bmatrix} = \begin{Bmatrix} -\frac{S_N}{4h} \\ 0 \\ \frac{S_N}{4h} \\ -\frac{S_N}{4b} \\ 0 \\ \frac{S_N}{4b} \end{Bmatrix} \tag{2.22}$$

The nodal forces at the middle of the diaphragm, U_2 and V_2, are zero in Eq. 2.22. The other nodal forces are illustrated in Fig. 2.10. The associated internal shear stresses are shown in Fig. 2.11.

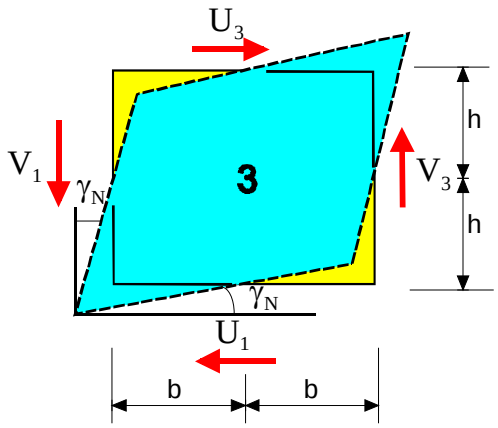

Figure 2.10: Element shear raking mode and corresponding nodal forces.

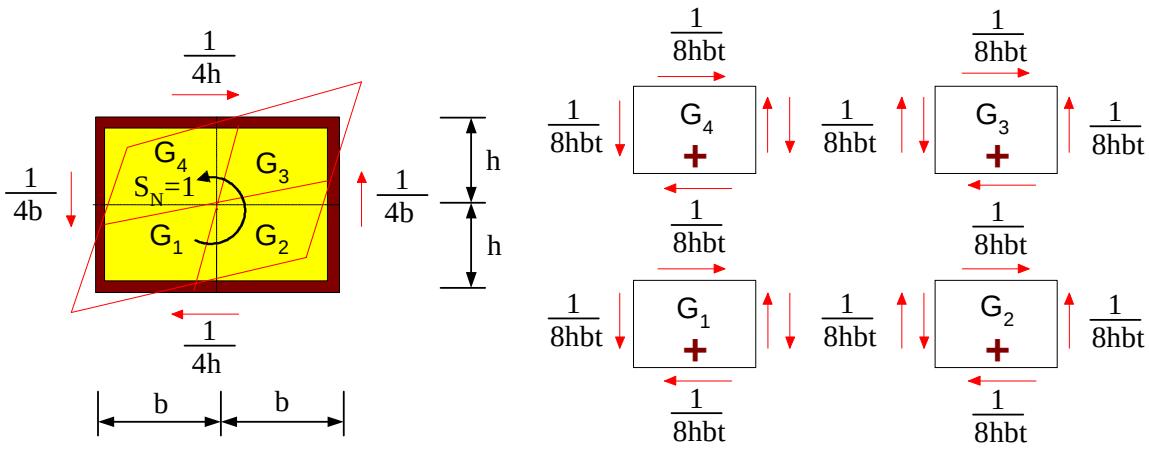

Figure 2.11: Internal shear stress distribution in four quadrants of the diaphragm element for S_N=1.

The diagonal flexibility coefficient associated with the shear raking natural mode, F_{N33}, is obtained for the general case of an irregular diaphragm (i.e., $G_1 \neq G_2 \neq G_3 \neq G_4$), as

$$F_{N33} = \int_0^b \int_0^h \frac{1}{(8bht)^2}\left[\frac{1}{G_1}+\frac{1}{G_2}+\frac{1}{G_3}+\frac{1}{G_4}\right] t\,dx\,dy$$

$$= \frac{1}{64\,bht}\left[\frac{1}{G_1}+\frac{1}{G_2}+\frac{1}{G_3}+\frac{1}{G_{e4}}\right] \tag{2.23}$$

The off-diagonal flexibility coefficient F_{N31} is obtained for the general case in which the diaphragm has nonuniform properties in a similar fashion to the derivation of F_{N12} of the previous section. Based on virtual work, and considering Figs. 2.7 and 2.11, one obtains:

$$F_{N31} = \int_0^b \int_0^h \frac{1}{(8bht)(4bt)} \left[\frac{1}{G_1} + \frac{1}{G_2} - \frac{1}{G_3} - \frac{1}{G_4} \right] t\,dx\,dy$$

$$= \frac{1}{32bt} \left[\frac{1}{G_1} + \frac{1}{G_2} - \frac{1}{G_3} - \frac{1}{G_4} \right] \tag{2.24}$$

The off-diagonal flexibility coefficient F_{N32} is derived in exactly the same manner based on virtual work, and considering Figs. 2.9 and 2.11.

$$F_{N32} = \int_0^b \int_0^h \frac{1}{(8bht)(4ht)} \left[\frac{1}{G_1} - \frac{1}{G_2} - \frac{1}{G_3} + \frac{1}{G_4} \right] t\,dx\,dy$$

$$= \frac{1}{32ht} \left[\frac{1}{G_1} - \frac{1}{G_2} - \frac{1}{G_3} + \frac{1}{G_4} \right] \tag{2.25}$$

Finally, coefficients F_{N13} and F_{N23} are obtained by symmetry.

Flexibility Matrix

Based on the above developments, the 3 x 3 diaphragm natural flexibility matrix can be summarized as

$$[F_N]_{3\times 3} = \begin{bmatrix} \frac{h}{16bt} D_1 + \frac{h^3}{6EI_u} + \Delta_{csu} & \frac{h}{16t} D_2 & \frac{1}{32bt} D_4 \\ & \frac{b}{16ht} D_1 + \frac{b^3}{6EI_v} + \Delta_{csv} & \frac{1}{32ht} D_3 \\ Sym & & \frac{1}{64bht} D_1 \end{bmatrix} \tag{2.26}$$

where

$$D_1 = \frac{1}{G_1} + \frac{1}{G_2} + \frac{1}{G_3} + \frac{1}{G_4} \tag{2.27}$$

$$D_2 = \frac{1}{G_1} - \frac{1}{G_2} + \frac{1}{G_3} - \frac{1}{G_4} \tag{2.28}$$

$$D_3 = \frac{1}{G_1} - \frac{1}{G_2} - \frac{1}{G_3} + \frac{1}{G_4} \tag{2.29}$$

$$D_4 = \frac{1}{G_1} + \frac{1}{G_2} - \frac{1}{G_3} - \frac{1}{G_4} \tag{2.30}$$

Δ_{csu} = x-directional displacement due to the chord splice slip

Δ_{csv} = y-directional displacement due to the chord splice slip

E = elastic modulus of the chord members

I_u = x- directional moment of inertia from the chord members

I_v = y- directional moment of inertia from the chord members

t = effective thickness of diaphragm web.

2.3.2.3 Element stiffness matrix

The 3 x 3 natural stiffness matrix $[K_N]$ is determined from the flexibility matrix $[F_N]$ as

$$\left[K_N\right] = \left[F_N\right]^{-1} \tag{2.31}$$

Given the natural stiffness, the 6 x 6 element global stiffness is obtained by fundamental principles (Cook 1989) as

$$\left[K\right] = \left[T\right]^T \left[K_N\right] \left[T\right] \tag{2.32}$$

2.3.2.4 State determination process

For nonlinear static or dynamic analysis, the diaphragm internal forces and the stiffness matrix $[K_N]$ are evaluated and updated by tracking the state within each quadrant of the diaphragm. This process, which is referred to as element state determination, is summarized in this section.

Given the incremental diaphragm displacements

$$\{\Delta d\} = \left[\Delta u_1 \ \Delta u_2 \ \Delta u_3 \ \Delta v_1 \ \Delta v_2 \ \Delta v_3\right]^T \tag{2.33}$$

which are obtained from the solution of the global tangent stiffness equations, the incremental natural displacement vector is obtained as

$$\{\Delta d_N\} = [T]\{\Delta d\} \tag{2.34}$$

The element incremental natural forces are then calculated via

$$\{\Delta r_N\} = \left[K_N\right]\{\Delta d_N\} \tag{2.35}$$

where

$\{\Delta r_N\} = \left[\Delta U_N \ \Delta V_N \ \Delta S_N\right]^T$; incremental natural forces

Based on these incremental natural forces, the incremental shear strains are calculated in each of the diaphragm quadrants as:

$$\Delta\gamma_1 = \frac{\Delta U_N}{4btG_1} + \frac{\Delta V_N}{4htG_1} + \frac{\Delta S_N}{8bhtG_1} \tag{2.36}$$

$$\Delta\gamma_2 = \frac{\Delta U_N}{4btG_2} - \frac{\Delta V_N}{4htG_2} + \frac{\Delta S_N}{8bhtG_2} \tag{2.37}$$

$$\Delta\gamma_3 = -\frac{\Delta U_N}{4btG_3} - \frac{\Delta V_N}{4htG_3} + \frac{\Delta S_N}{8bhtG_3} \tag{2.38}$$

$$\Delta\gamma_4 = -\frac{\Delta U_N}{4btG_4} + \frac{\Delta V_N}{4htG_4} + \frac{\Delta S_N}{8bhtG_4} \tag{2.39}$$

These equations can be represented in matrix form as

$$\{\Delta\gamma\} = \begin{bmatrix} \frac{1}{4btG_1} & \frac{1}{4htG_1} & \frac{1}{8bhtG_1} \\ \frac{1}{4btG_2} & \frac{1}{4htG_2} & \frac{1}{8bhtG_2} \\ \frac{1}{4btG_3} & \frac{1}{4htG_3} & \frac{1}{8bhtG_3} \\ \frac{1}{4btG_4} & \frac{1}{4htG_4} & \frac{1}{8bhtG_4} \end{bmatrix} \{\Delta r_N\} \tag{2.40}$$

Using Eq. 2.40, with $\{G\} = \begin{bmatrix} G_1 & G_2 & G_3 & G_4 \end{bmatrix}^T$, the quadrant incremental shear stresses are

$$\{\Delta\tau\} = \begin{bmatrix} G_1\Delta\gamma_1 \\ G_2\Delta\gamma_2 \\ G_3\Delta\gamma_3 \\ G_4\Delta\gamma_4 \end{bmatrix} \tag{2.41}$$

and if the response in a given quadrant is linear during this increment, the total shear stresses may be updated using the equation

$$\{\tau_{cur}\} = \{\tau_{prev}\} + \{\Delta\tau\} \tag{2.42}$$

where

$\{\tau_{prev}\}$ = shear stress in the quadrant at the beginning of the increment

If nonlinearities occur within the increment, the following sub-incrementation process is employed to obtain the state at the end of the increment.

Sub-incrementation

Consider Figs. 2.12 and 2.13. Figure 2.12 shows the notation and sign convention employed for the stresses and strains in each quadrant of the diaphragm. Within this work, diaphragm nonlinear shear response is represented in a multi-linear fashion. Any number of the quadrants of a diaphragm may experience some nonlinearity during a given increment. Figure 2.13 shows a hypothetical increment in which the stress-strain response is nonlinear within the 1st, 2nd and 3rd quadrants. The subincrementation process starts by calculating the fraction of the increment required to reach the first point of nonlinearity (or change in stiffness) within all of the quadrants. This fraction is

$$\alpha_i = \frac{\Delta\tau_{yi}}{\Delta\tau_i} \tag{2.43}$$

in each quadrant

where

α_i = a ratio of shear stress to trial shear stress for i^{th} quadrant

i = 1, 2, 3, 4 for four quadrants

$\Delta\tau_i$ = trial shear stress increment for i^{th} quadrant

$\Delta\tau_{yi}$ = $\tau_{yi} - \tau_{prev\_i}$ for i^{th} quadrant

The trial stress increment $\Delta\tau_i$ is initially taken as the value from Eq. 2.41.

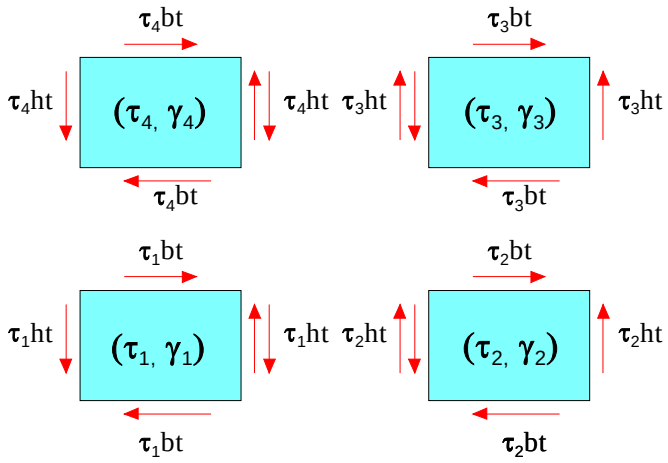

Figure 2.12: Stresses and strains for each quadrant of a diaphragm.

The magnitude of the subincrement is taken as

$$\beta_m = min(\alpha_{m1}, \alpha_{m2}, \alpha_{m3}, \alpha_{m4}) \le 1.0 \tag{2.44}$$

Given this subincrement size, the shear stresses and strains in each of the quadrants are updated using

$$\{\tau\}_m = \{\tau\}_{m-1} + \beta_m \{G_{em}\}\{\Delta\gamma\} \tag{2.45}$$

and the element natural forces are updated using

$$\{\Delta r_N\}_m = \{\Delta r_N\}_{m-1} + \beta_m \left[K_N\right]_m \{\Delta d_{Ns}\} \tag{2.46}$$

where

m = sub-incremental step (1, 2, 3, ..., m).

$\{\tau\}_m$ = accumulated shear stress at the end of the mth sub-increment

$\{\tau\}_{m-1}$ = accumulated shear stress at the beginning of the mth sub-increment

$[K_N]_m$ = natural tangent stiffness at the beginning of the mth sub-increment

The above process is repeated until the complete $\{\Delta\gamma\}$ of Eq. 2.40 is applied. The quadrant shear stiffnesses G_i and the element natural stiffness $[K_N]$ are updated throughout the subincrementation process based on the nonlinearity that is encountered within each of the quadrants. At the end of this process, the current total nodal forces are calculated from the element natural force vector using Eq. 2.12. This nodal force vector is then exported to the global nonlinear incremental iterative solution algorithm.

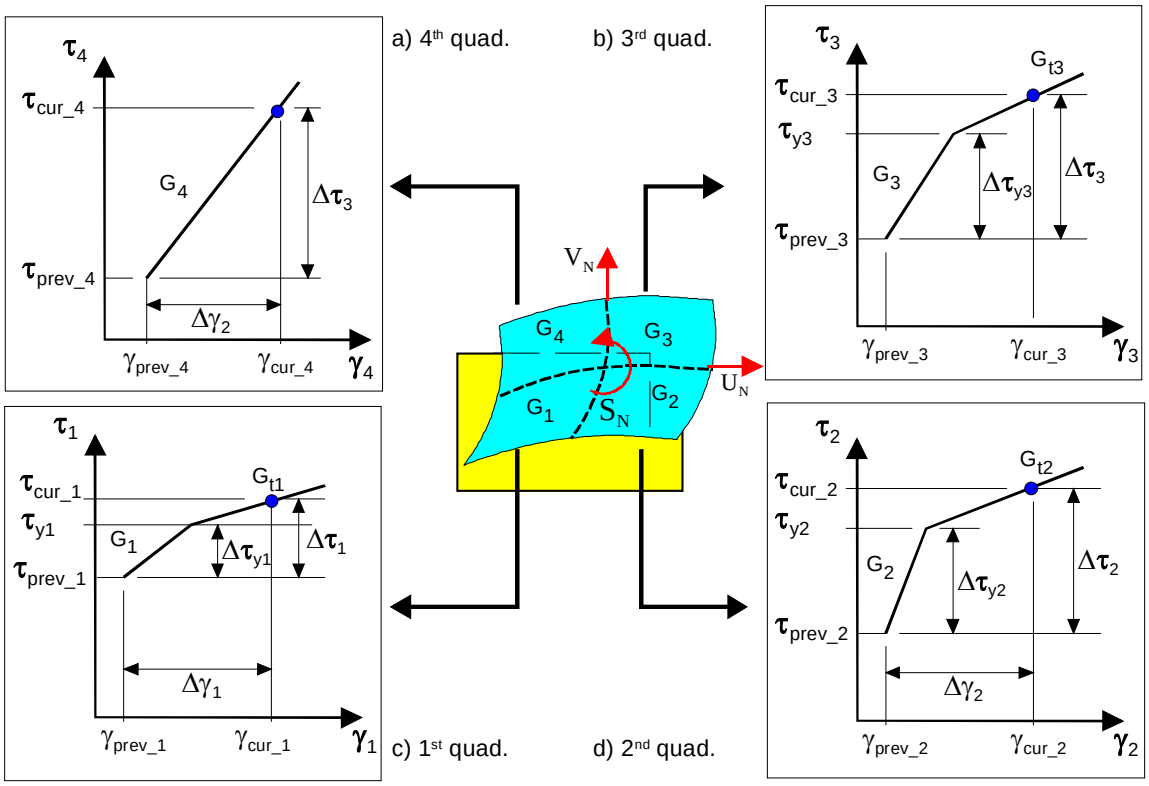

Figure 2.13: Stress-strain diagram example for each quadrant of a diaphragm.

2.3.3 Idealization of multiple diaphragms

The proposed diaphragm element, which has six DOFs, is discussed in Sections 2.3.1 and 2.3.2. When this element is used to model multiple adjacent diaphragms, the associated idealizations may be explained as follows. Figure 2.14 (a) shows two adjacent diaphragm elements, representing two adjacent floor or roof diaphragms with one interior wall between them and exterior walls on their outside edges. DOF numbers 1 through 6 are assigned to the diaphragm on the left, and DOF numbers 7 through 12 are assigned to the diaphragm on the right. DOFS 1, 2, 3, 7, 8, and 9 are in the x (or u) direction and nodes 4, 5, 6, 10, 11, and 12 are in the y (or v) direction.

When the structure containing these diaphragms is loaded in the y direction, it is assumed that the diaphragms will deform as shown in Fig. 2.14(b). That is, each of the above diaphragms deforms effectively as a simply-supported beam between the interior wall and the associated exterior wall. Continuity of the flexural deformations between the two diaphragms is neglected. This assumption is considered to be appropriate for typical masonry buildings with nonrigid diaphragms, since the in-plane wall displacements tend to be small compared to the diaphragm displacements, and the diaphragm displacements tend to be dominated by shear deformations. Also, these types of buildings would not necessarily have any physical continuity of a diaphragm chord member across the interior wall. Due to the significant flexural shear deformations within each of the diaphragm elements, any displacement discontinuities at the interior wall are expected to be small.

If deformations within the anchorages between the diaphragms and the interior wall are small, neglected, or included implicitly within the description of the overall diaphragm force-deformation relationships, DOFS 6 and 10 may be shared as the same global DOF. If the stiffness of the interior wall is reduced, e.g., due to damage or nonlinearity, the displaced shape of the two diaphragm elements may become more like that shown in Fig. 2.14(c). The resistance from the diaphragms to the y direction displacement of the

interior wall is solely due to the shear raking stiffness of each of the diaphragms. This idealization is again believed to be appropriate for the types of buildings considered here. It would not be appropriate for extremely long and thin buildings with end walls serving as the only primary lateral load resisting elements, e.g., the types of buildings considered by Jain and Jennings (1985).

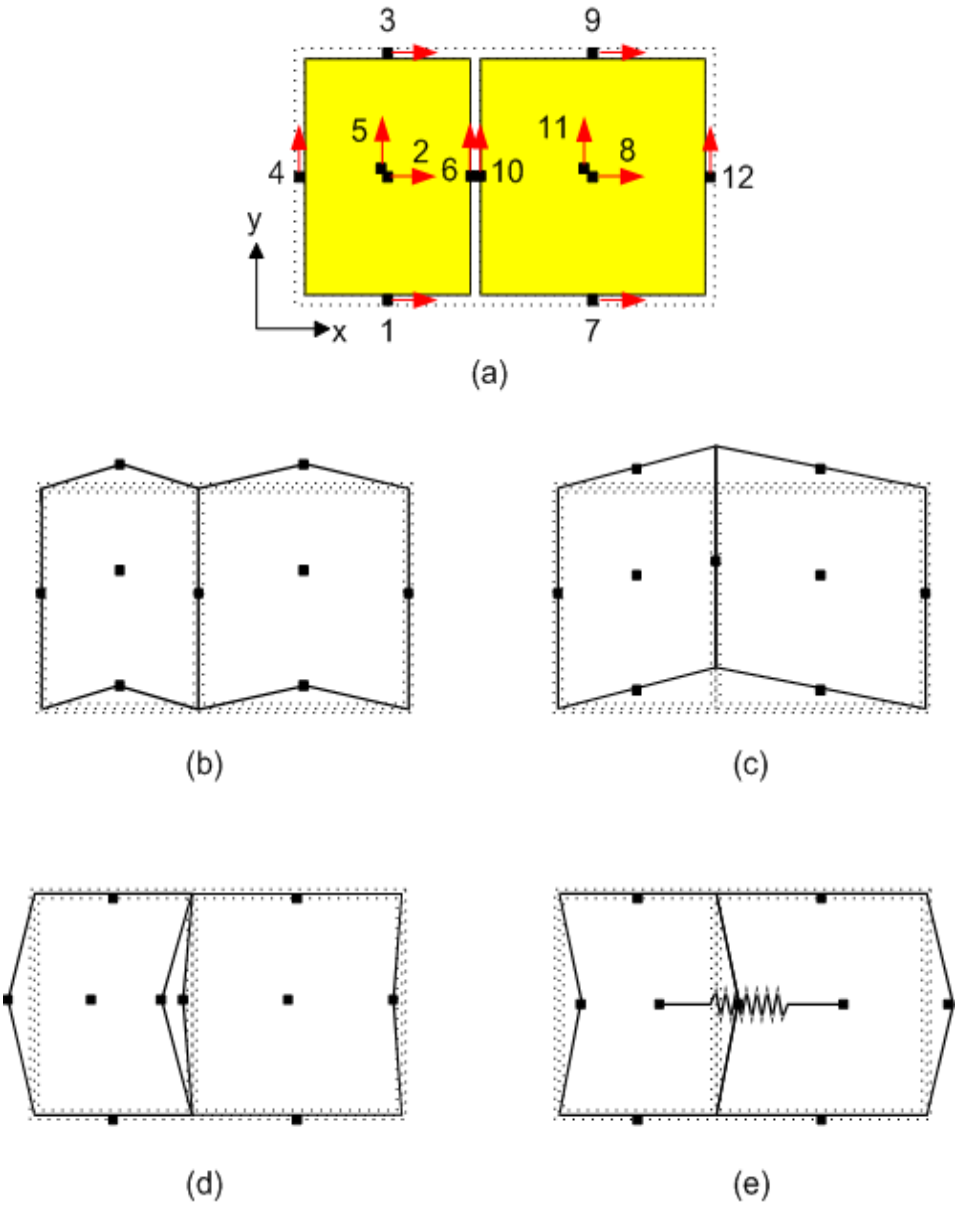

Figure 2.14: Adjacent elements of diaphragm element.

When the above structure is loaded in the x direction, the deflected shapes of the diaphragms might appear as shown in Fig. 2.14(d) unless the continuity of the mid-diaphragm u displacements is addressed. That is, a gap or overlap could occur between the diaphragms. The continuity of the x direction displacements of the two diaphragms, and the fact that some axial shortening or extension of the diaphragms may occur between the walls, can be addressed by specifying an axial spring between the x-direction DOFS at the middle of the diaphragms, as shown in Fig. 2.14 (e). This type of idealization was employed by Tena-Colunga and Abrams (1992) within a two-dimensional analysis approach. Alternately, a simpler MDOF model is obtained by assuming that the diaphragm middle DOFS are rigidly constrained to have the same displacement in the x direction. This idealization is employed in this work for structures containing multiple diaphragms. As previously explained in Section 1.4.3, the x direction wall degrees of freedom, 1 and 7, and 3 and 9, are constrained to have equal displacements in this work.

2.3.4 Diaphragm force-deformation relationships

In the previous sections, a diaphragm idealization has been introduced and an associated diaphragm element has been derived. The basic idealization is that the diaphragm behaves as a deep plate girder with respect to bending deformations and as a uniformly strained shear panel with respect to coupling of the walls at the diaphragm boundaries. As noted in the above discussions, there are essentially two types of diaphragm force-deformation models that are used in the context of this idealization: (1) a general nonlinear hysteretic model and (2) an equivalent linear model. The key concepts and properties associated with each of these models are discussed below.

2.3.4.1 Nonlinear force-deformation model

A typical nonlinear hysteretic response of a wood diaphragm, taken from (ABK 1981), is shown in Fig. 2.15(a). The diaphragm is subjected to static cyclic loadings as illustrated in Fig. 2.15(b). The main phases of the cyclic behavior are loading, unloading with stiffness degradation, pinching, and reloading with strength deterioration. The initial loading path typically follows the virgin envelope determined by a monotonic loading test.

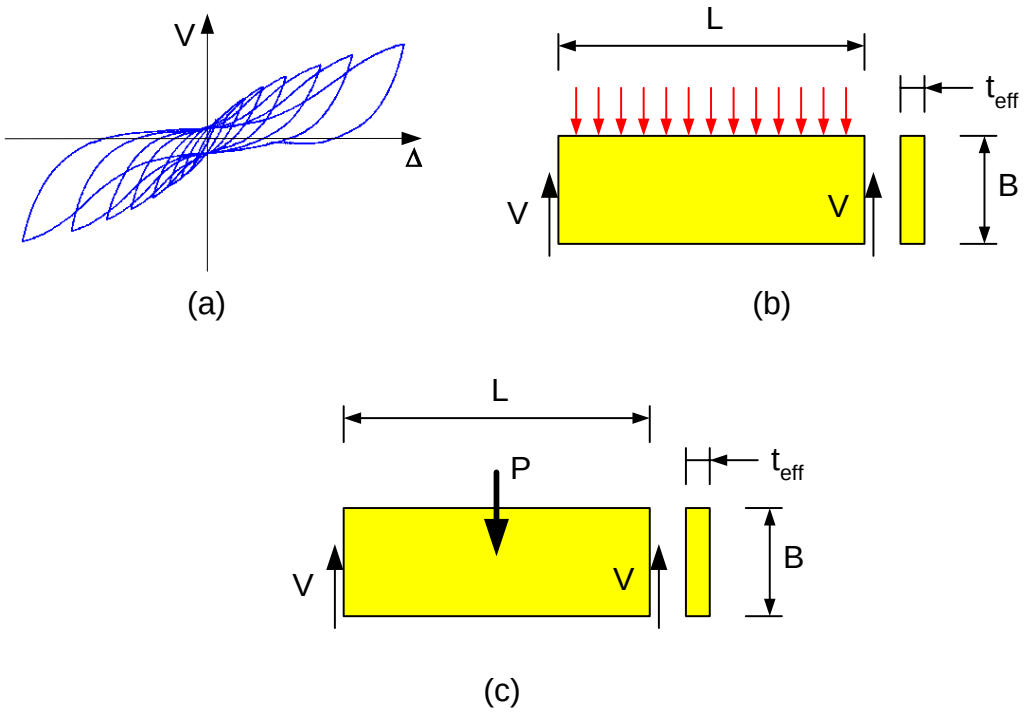

Figure 2.15: (a) Typical cyclic force-deformation model (ABK 1981); (b) Diaphragm subjected to distributed loading; and (c) Diaphragm subjected to lumped loading.

In this research, a three-parameter model similar to those developed by Kunnath et al. (1991, 1994) is implemented to characterize the general diaphragm hysteresis behavior. This model is also used to represent certain types of wall hysteresis. In this model, stiffness degradation, strength deterioration and pinching are each described by a single parameter or property. Stiffness degradation is characterized by a parameter symbolized

by the term α, strength deterioration is represented by a parameter symbolized by the term β, and pinching addressed by a parameter symbolized by the term γ. The influence of each of these parameters on the behavior of the nonlinear hysteresis model is explained in detail in Appendix A.

Figure 2.16 gives a simple illustration of the concepts associated with the above nonlinear hysteretic model. Figure 2.16(a) shows a trilinear representation used by the model to represent the force-deformation response from a monotonic test. It is assumed that this curve also represents the nonlinear backbone curve for the cyclic response with sufficient accuracy (see Section 2.8.3 of FEMA 356 (ASCE 2000a) for discussion of the backbone curve). Five properties of the nonlinear model are determined based on the results of a monotonic test and are illustrated in Fig. 2.16(a): V_o, V_1, K_0, K_1 and K_2. One can observe that K_0 is the initial tangent stiffness of the virgin diaphragm, and V_o is the proportional limit associated with the monotonic response. The term V_1 might be referred to as the ultimate strength of the diaphragm, although diaphragm forces greater than this value are produced within the model. The terms K_1 and K_2 are post-elastic tangent stiffnesses associated with the trilinear representation of monotonic load-deformation response.

Figure 2.16(b) shows an example cyclic prediction by the three-parameter hysteresis model, and illustrates the significance of the three hysteresis parameters α, β and γ. As the reader might expect, it can be difficult to characterize the complex nonlinear hysteretic response of general diaphragms and other structural components by the use of only three parameters. Example experimental results from a recent cyclic diaphragm test (Peralta et al. 2000) are shown in Fig. 2.17. The prediction of the response for diaphragm MAE-2B is shown in Fig. 2.18. The pinching parameter γ is equal to infinity for this case, indicating zero pinching. An example determination of the above three parameters based on a cyclic diaphragm test, including pinching effects, is explained in Section 4.3.2.

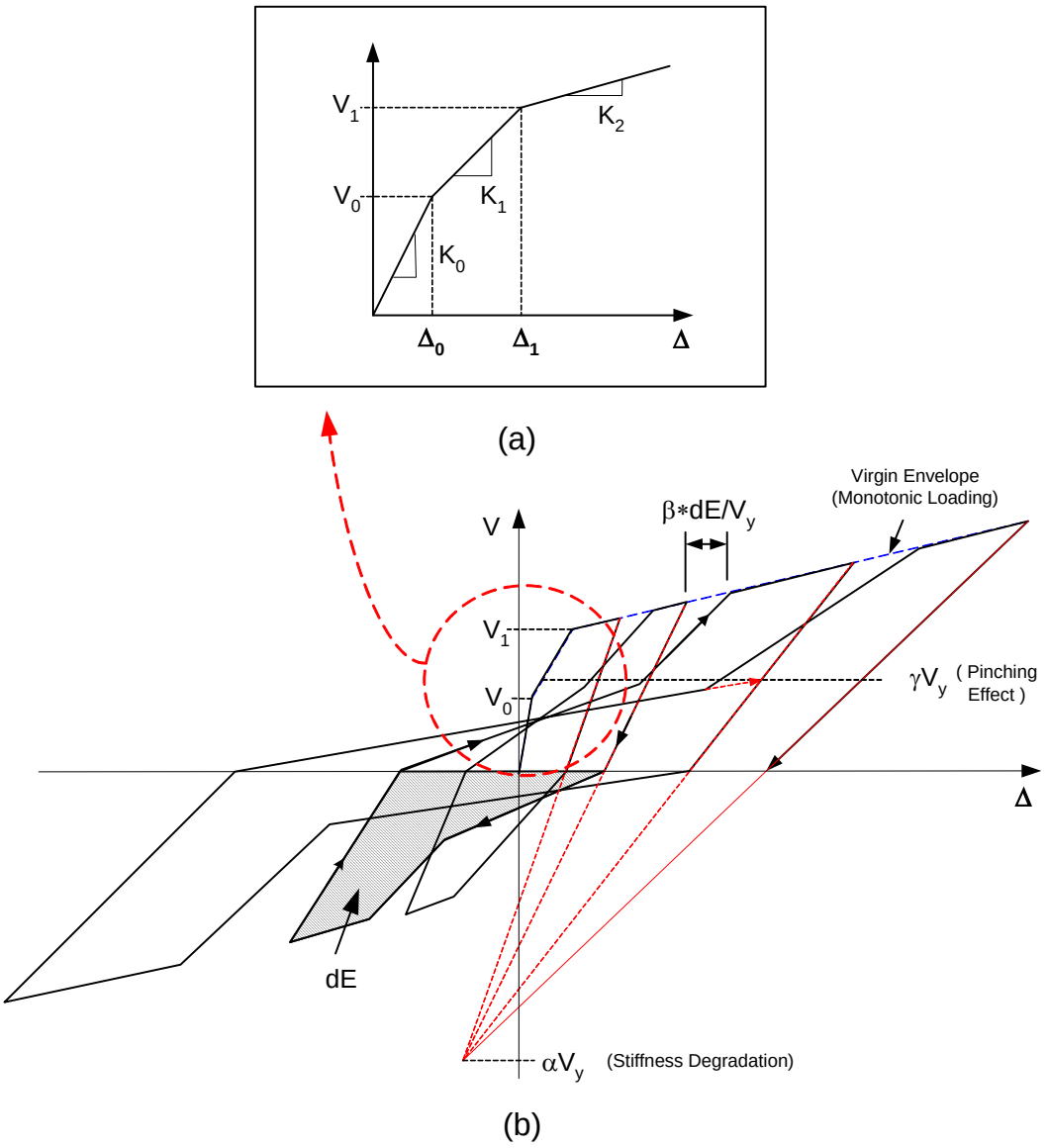

Figure 2.16: Typical cyclic load deflection model using three parameter model: (a) A trilinear representation and (b) Three parameter model (See Appendix A).

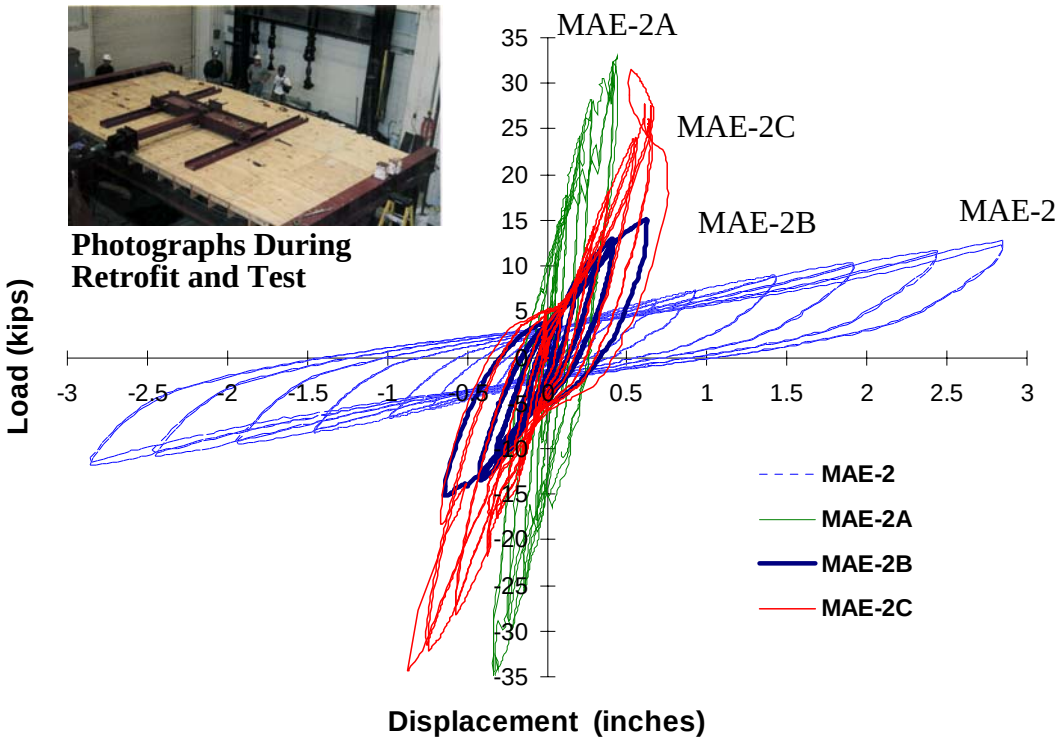

Note:

1. MAE-2 - 24'x12' Roof diaphragm: 2"x10" joists with 1"x6" straight sheathing
2. MAE-2A - Steel truss underneath the diaphragm
3. MAE-2B - 3/8" Plywood overlay nailed on decking
4. MAE-2C - Blocking added and heavier nailing pattern

Figure 2.17: Specimen MAE-2. Load vs. displacement at loading points (Peralta et al. 2000).

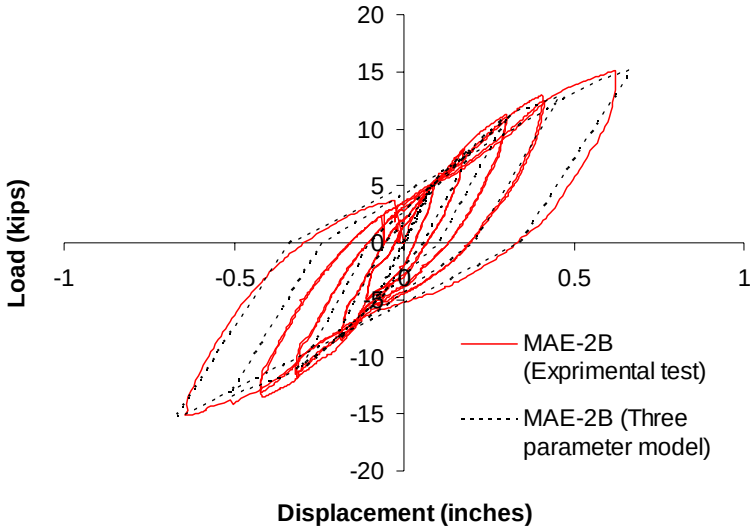

Figure 2.18: Experimental test and predicted force and displacement force and displacement relationship using three parameter model($\alpha = 6.0$, $\beta = 6.0$, and $\gamma = \infty$).

Diaphragm force-deformation models are typically expressed in terms of the maximum diaphragm shear force and a corresponding maximum diaphragm bending displacement. That is, the nonlinear response associated with the shearing deformations within the diaphragm web and the flexural deformations with the diaphragm chords (including nail slip, chord splice slip, etc.) are all lumped into a single force-deformation relationship. This is somewhat problematic if one wishes to determine a "rigorous" diaphragm force-deformation relationship for combined bending in two orthogonal directions along with diaphragm shear raking displacements.

For many of the diaphragm types used in masonry building structures, the diaphragm is dominated by the shear response of its web. This assumption is implicit within the development of the diaphragm element proposed in this work. It is assumed in this work that the chord flexibility can be represented sufficiently by an elastic or equivalent elastic model. In many situations, the chord stiffness is even large enough relative to the stiffness of the diaphragm in shear such that the chord can effectively be modeled as rigid. Based on these assumptions, the diaphragm shear force (per unit length) versus shear

strain relationship, which is required within the proposed element, can be derived from test results by representing the test by the associated lumped parameter idealization as shown in Fig. 2.15(c). The idealization of the chord response is established first, and the shear-force shear-strain relationship is then obtained by equating the predicted displacements in the analysis model, based on the lumped loading at the middle of the diaphragm, to the measured displacements. The resulting shear-force shear-strain model is then applied for general three-dimensional analysis in which diaphragm shear forces are developed due to flexure in the two orthogonal directions of the diaphragm plus shear raking associated with coupling between the walls on the diaphragm boundaries.

The wood diaphragm tests of ABK TR-03 (ABK 1981b) were designed to produce force-deformation data for static monotonic and cyclic loadings on diaphragms, as well the dynamic response. These tests, based on applied lateral loadings, as shown in Fig. 2.15(b), demonstrated that most of diaphragm specimens were relatively undamaged for all levels of earthquake ground motion, and when damage occurred, the diaphragms were still serviceable and the damage was repairable. Equation 2.47 was selected to represent the force-deflection envelope of the diaphragm (ABK 1981):

$$V(\Delta) = \frac{V_u \Delta}{\frac{V_u}{K_i} + |\Delta|} \tag{2.47}$$

where

$V(\Delta)$ = maximum shear force in the diaphragm tests, equal to the reactions at the ends of the diaphragm

Δ = deflection at the center of the diaphragm

V_u = ultimate capacity of diaphragm at large values of deflection

K_i = initial diaphragm stiffness

The force-displacement relationship in Eq. 2.47 is illustrated in Fig. 2.19. One can

observe that for low values of K_i , this model asymptotes to V_u only at extremely large values of displacement.

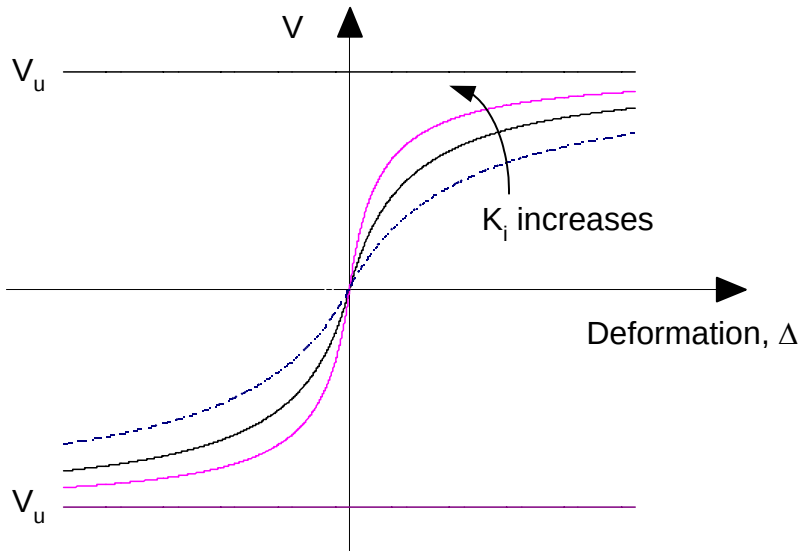

Figure 2.19: Force-deflection envelope of model (ABK 1981).

2.3.4.2 Equivalent linear force-deformation model

The other type of diaphragm force-deformation model considered in this work is the equivalent linear model shown in Fig. 2.20. The key properties associated with this model are the maximum strength, often written as v_y, and the corresponding displacement Δ_y. Given these two properties, the equivalent linear stiffness is typically calculated as $K_{eq} = v_y/\Delta_y$. Code and guideline documents generally provide substantial recommendations pertaining to the values that Engineers should use in linear static and linear dynamic procedures for v_y and K_{eq}. For diaphragms, these quantities are typically expressed in terms of the maximum shear force (units of force per unit length across a diaphragm width) and the flexural displacement at the middle of the diaphragm. In tests to determine these values, the diaphragms are often loaded by a distributed loading along an edge of the diaphragm as shown in Fig. 2.15(b), although in some cases, e.g., (Peralta et al. 2000), the diaphragm may be subjected to a concentrated load at is mid-span.

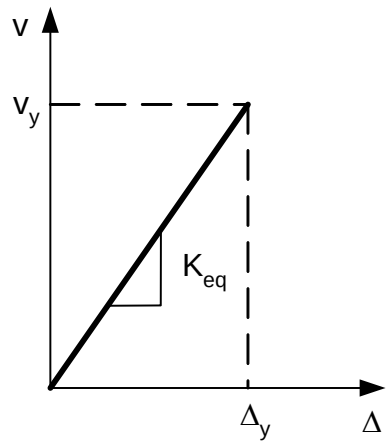

Figure 2.20: Equivalent linear force-deformation model.

The diaphragm equivalent linear response may involve explicit contributions from the web as well as from the chord elements (e.g., see the discussions pertaining to plywood diaphragms in Section 2.3.5.2), or it may involve a coarser idealization in which all the contributions to the deformations are considered together in arriving at the equivalent linear stiffness and the shear strength. In many cases, the equivalent linear properties appear to be obtained largely based on judgement. The equivalent linear properties are discussed for various types of diaphragms in Section 2.3.5.2. Section 2.3.5.4 explains how the stiffness parameters for the proposed diaphragm element can be obtained (if desired) from recommended code and guideline values.

2.3.5 Diaphragm equivalent linear properties per current codes and guidelines

Present code and guideline documents generally do not directly address nonlinear hysteretic diaphragm responses. Rather the focus is on the stiffness and strength associated with equivalent linear models. This section discusses the calculation and use of the equivalent linear stiffness and strength properties per current codes and guidelines.

Section 2.3.5.1 first discusses the categorization of diaphragms based on the level of the computed diaphragm bending displacements, via equivalent elastic models, relative

to the wall displacements in a given direction. Section 2.3.5.2 discusses the recommended diaphragm equivalent linear stiffness properties and displacement calculations in current guidelines. Recommended stiffness values are compared to the results from a number of recent experimental tests. Section 2.3.5.3 discusses recommended diaphragm strength values. Section 2.3.5.4 explains the calculation of the chord and shear modulus values of the proposed diaphragm element, E_e and G_e, based on stiffnesses reported in code and guideline documents. Section 2.3.5.5 gives illustrative example calculations, and investigates when it is appropriate to neglect the chord flexibility, i.e., to assume that the chord elements (if they exist) are rigid.

2.3.5.1 Categorization of diaphragms in current codes and guidelines

FEMA 356 (ASCE 2000a) gives provisions for categorizing diaphragms as either rigid, stiff or flexible. These rules are based on the ratio between the diaphragm displacements associated with out-of-plane wall deformation Δ_d and the average in-plane wall displacements at the sides of the diaphragm in the direction under consideration $(\Delta_{w1} + \Delta_{w2})/2$ (using the notation in FEMA 356). The deflection Δ_d is the diaphragm natural bending displacement discussed in the previous developments, i.e., $\Delta_d = u_N$ in Fig. 2.6. If the above ratio is greater than two, the diaphragm is assumed to be flexible, and if it is less than 0.5, the diaphragm is assumed to be rigid. The lateral forces applied to the diaphragm and to the walls in the calculation of these deflections are to be consistent with the distribution of mass within the system. In FEMA 356, if a diaphragm is considered as flexible, coupling between the wall elements of the structural system may be neglected within the analysis of the structure. If a diaphragm is considered as rigid, then diaphragm deformations may be neglected within the analysis model and coupling between the wall elements is generally accounted for based on the relative wall stiffnesses. The response of a structure with stiff diaphragms is obviously between these two extremes. FEMA 356 (ASCE 2000a) does not provide any direct guidance for seismic

assessment of buildings with stiff diaphragms.

The Steel Deck Institute Diaphragm Design Manual (SDI 1995) itemizes diaphragms into four groups as shown in Table 2.1, based on the ratio between the maximum shear force per unit length and the diaphragm mid-span bending displacement. Based on the values reported in this table, wood diaphragms typically belong to the flexible category and steel deck diaphragms belong to the flexible or semi-flexible category. (SDI 1995) does not discuss any implications of these categorizations.

Table 2.1: Definition of diaphragm types in (SDI 1995).

Diaphragm	**Shear Stiffness (kips/in)**
Flexible	6.67 ~ 14.3
Semi-Flexible	14.3 ~ 100
Semi-Rigid	100 ~ 1000
Rigid	over 1000

2.3.5.2 Equivalent linear stiffness of diaphragms

This section discusses recommended diaphragm equivalent linear stiffness properties and calculations in current guidelines. Detailed equations for blocked and chorded plywood diaphragms are considered first, followed by coarser approximate equations for other general types of diaphragms. Recommended stiffness values are compared to the results from a number of recent wood diaphragm experimental tests.

Equivalent linear stiffness of blocked and chorded plywood sheathed diaphragms

The equivalent linear stiffness of a blocked and chorded plywood sheathed diaphragm depends on the properties of the wood structural panels, the nail spacing (assumed

constant) on the panel edges, the chord properties, and the characteristics of any chord splices. (APA 1983), (FEMA 1997a) and (ASCE 2000a) give the following formula for calculation of the mid-span bending displacements in these types of diaphragms, subjected to an assumed uniformly distributed transverse loading, as shown in Fig. 2.21:

$$\Delta_y = \frac{5 v_y L^3}{8 E A_c B} + \frac{v_y L}{4 G t} + 0.188 L e_n + \frac{\Sigma(\Delta_c X)}{2B} \tag{2.48}$$

where

Δ_y = diaphragm mid-span deflection at "yield," i.e., at the diaphragm maximum shear strength, in

v_y = shear yield (i.e., strength) in the direction under consideration, lb/ft

L = diaphragm length, ft

B = diaphragm width, ft

A_c = area of chord cross section, in^2

E = elastic modulus of the chord, psi

G = shear modulus of the plywood panels, psi

t = effective plywood thickness, in

e_n = nail deformation at the maximum shear strength, in

$\Sigma(\Delta_c X)$ = sum of individual chord-splice slip values on both sides of the diaphragm, each multiplied by its distance to the nearest support.

One can observe that this model conforms to the general conceptual approach illustrated in Fig. 2.19 and discussed in Section 2.3.4.2.

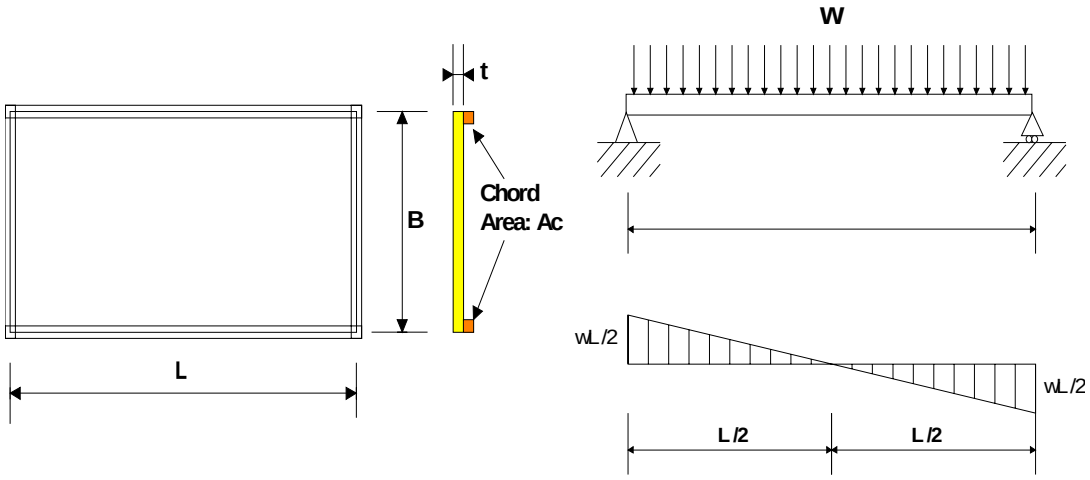

Figure 2.21: Plywood sheathed diaphragm and load case.

Equivalent linear stiffness for general diaphragms

FEMA 273 (FEMA 1997a) provides the following general formula for calculation of diaphragm bending deflections:

$$\Delta_d = \frac{vL^4}{G_{d\_\mathrm{FEMA273}}\, b^3} \tag{2.49}$$

where v is the shear in units of force per unit length at the ends of the diaphragm span, L is the span length of the diaphragm, *b* is the diaphragm width, and G_{d_FEMA273} is the diaphragm stiffness parameter associated with this equation. FEMA 273 (FEMA 1997a) and 356 (ASCE 2000a) suggest diaphragm stiffness values, G_{d_FEMA273} and G_{d_FEMA356}, as shown in Table 2.2, for different diaphragm types. The stiffnesses G_{d_FEMA356} are applied with a different equation than Eq. 2.49 as discussed subsequently.

Table 2.2: Diaphragm shear stiffness properties specified in FEMA 273 (FEMA 1997a) and FEMA 356 (ASCE 2000a).

Wood Diaphragms		G_{d_FEMA273} (kips/in)	G_{d_FEMA356} (kips/in)
Single Straight Sheathed Diaphragm	With/without chorded	200	2
Double Straight Sheathed Diaphragm	Chorded	1,500	15
	Unchorded	700	7
Single Diagonally Sheathed Diaphragm	Chorded	500	8
	Unchorded	400	4
Diagonal Sheathing with Straight Sheathing or Flooring Above Diaphragm	Chorded	1,800	18
	Unchorded	900	9
Double Diagonally Sheathed Diaphragm	Chorded	1,800	18
	Unchorded	900	9
Wood Structural Panel Sheathed Diaphragm	Unblocked, chorded	800	8
	Unblocked, unchorded	400	4
Wood Structural Panel Overlays on Straight or Diagonally Sheathed Diaphragm	Unblocked, chorded	900	9
	Unblocked, unchorded	500	5
	Blocked, chorded	1,800	18
	Blocked, unchorded	700	7

The derivation of Eq. 2.49 is outlined in (Tissel and Rose 1993). Unfortunately, there is a significant error in this derivation. The derivation is based on the Euler-Bernoulli beam theory equation

$$\Delta_d = \frac{5\,wL^4}{384\,EI} \tag{2.50}$$

in which shear deformations are assumed to be negligible, and where *w* is an equivalent uniformly distributed load, *L* is the diaphragm span, and *EI* is the diaphragm flexural rigidity. After substitution of $w = W/L = 2v(b/L)$ and $I = (tb^3)/12$, where W is the total lateral load transmitted by the diaphragm, and *t* is the diaphragm equivalent thickness (in concept, this is the approach taken in (Tissel and Rose 1993)), this equation may be expressed as:

$$\Delta_d = \frac{vL^3}{3.2Etb^2} = \frac{vL^3}{\overline{G}_{d\_\mathrm{FEMA273}}\,b^2} \tag{2.51}$$

where $\overline{G}_{d\_\mathrm{FEMA273}}$ is the appropriate stiffness term associated with this "corrected" equation, which would of course be different than the reported values in FEMA 273. In other words, based on the approach taken by (Tissel et al. 1993), the diaphragm bending displacement should be a function of L^3/b^2, not L^4/b^3. The form of Eq. 2.49 results from an error in the substitution of the terms. Nevertheless, it is important to emphasize that neither of these equations should be taken too literally. In other words, Eq. 2.49 (or alternatively Eq. 2.51) is applied to estimate the deflections in a wide variety of diaphragm types, many of which are either dominated by shearing deformations or in which, strictly speaking, Euler-Bernouli beam theory does not apply (Kim and White 2001).

The values of G_{d_FEMA273} were specified based on limited test data and expert judgment. Nevertheless, the form of Eq. 2.49 developed in (Tissel et al 1993) is derived erroneously, and to the knowledge of the authors, has no rational basis. This causes prob-

lems when Eq. 2.49 is applied to diaphragms with varying aspect ratios *L/b*. The greatest difficulty is when the results of diaphragm tests that have typically been conducted at values of *L/b* = 3 (or at similar values) are extended to diaphragms having a small aspect ratio, say *L/b* = 1 (which is not uncommon in masonry buildings). These problems will be explained subsequently, after discussion of a new equation for calculation of diaphragm deflections, specified in FEMA 356 (ASCE 2000a).

FEMA 356 gives the following equation for calculation of deflections in general diaphragms:

$$\Delta_d = \frac{vL}{2G_{d\_\mathrm{FEMA356}}} \tag{2.52}$$

where G_{d_FEMA356} is an appropriate specified diaphragm stiffness for use with this equation (see Table 2.2). Equation 2.52 is based on a shear deformable beam theory in which the shear deformations are assumed to dominate the response of the system to the extent such that the contributions from the chord flexibility to the diaphragm deflections (if a chord exists) may be neglected. In other words, in Eq. 2.52, the flexural rigidity *EI* is assumed to be infinite (i.e., the chords are assumed to be rigid). This is in contrast to Eq. 2.51, in which the shear flexibility of the diaphragm is assumed to be zero, and thus the diaphragm deflections are assumed to come entirely from bending deformations. In the view of the authors, Eq. 2.52 is a more appropriate equation for calculation of diaphragm deflections in masonry building systems, since as noted previously, shear deformations are typically the major contributor to the diaphragm flexibility in these systems.

Comparison to experimental results

Peralta et al. (2001) report recent test results for several representative wood floor diaphragms. It is interesting to consider how the recommended equivalent linear (i.e.,

secant) stiffness values from these tests compare to the current G_{d_FEMA356} values as well as the initial tangent stiffness values from these tests. Table 2.3 shows these comparisons in the context of Eq. 2.52. One should note that the secant stiffness properties recommended by Peralta et al. (2001) are based on the shear force and mid-span deflection at the end of the first branch of a bilinear representation of the backbone curve. Peralta et al. (2001) express the deflection at this point as

$$\Delta_y = \frac{V_y}{K} \tag{2.53}$$

where V_y is the actuator force at the middle of the diaphragm (the diaphragms were loaded by a concentrated force at their mid-span). By equating this expression to Eq. 2.52, recognizing that $v_y = V_y/2b$, and noting that $L/b = 2$ for the diaphragms tested in this research, the appropriate G_d values in the context of Eq. 2.52 are simply $K/2$.

With the exception of their tongue and groove single straight-sheathed diaphragm test, the secant stiffnesses in Peralta et al. (2001) are significantly higher than the stiffnesses specified in FEMA 356. This might be expected since, based on the derivation of the equivalent linear stiffness for a plywood diaphragm, the implied stiffness values in FEMA 356 are secant values to a larger maximum strength level. Furthermore, as would be expected, the diaphragm initial stiffnesses are significantly higher than the recommended design secant stiffness values.

Peralta et al. (2000) calculate their recommended secant stiffness values based on a bilinear representation of the experimental backbone curve, with the second branch set as a tangent to the backbone curve at large diaphragm displacements (the experimental backbone curves were approximately linear in this range), and with the first "secant" branch of the bilinear representation set to obtain equal area under the experimental and bilinear backbone curves. All sources of deformation (shear and flexural deformations of the floor system, deformation of the anchorages at the diaphragm boundaries, etc.) are included

within the stiffness values derived from Peralta's tests. The reader is referred to (Peralta et al. 2001) for details of the diaphragm characteristics and test results.

Table 2.3: Comparison of FEMA 356 expected and experimental (Peralta et al. 2001) stiffness values for wood diaphragms.

Diaphragm Designation and Type		$G_{d\_FEMA356}$ kips/in	G_{di} [a] kips/in	G_{d_Secant} [b] kips/in	Δ_y / L [c]
1A: Single Straight Sheathed (1x4 in. tongue and groove decking w/ 2x10 in. joists)		2	3.3	1.4	0.0020
MAE-2: Single Straight Sheathed (1x6 in. boards w/ 2x10 in. joists)[d]		2	10	6.0	0.0022
MAE-2B and 2C: Wood Structural Panel Overlay on Straight Sheathing[d]	Unblocked, Unchorded	5	30	24	0.0008
	Blocked, Unchorded	7	67	33	0.0008

a. G_{di} = approximate initial tangent stiffness of back-bone curve from experiment (Peralta et al. 2001) based on Eq. 2.52.

b. G_{d_Secant} = secant stiffness of first branch of a bilinear representation of the backbone curve, determined as defined by (Peralta et al. 2001) based on Eq. 2.52.

c. Δ_y / L = diaphragm "yield deflection" divided the diaphragm span length, where yield is defined at the transition to the second branch of the bilinear representation of the backbone curve (Peralta et al. 2001).

d. See Fig. 2.17.

One observation regarding the data in Table 2.3 should be considered by the engineer in applying the FEMA 356 equations. FEMA 356 does not distinguish between different types of straight-sheathed diaphragms. Peralta's study illustrates the fact that the stiffness properties of diaphragms categorized as the same type in FEMA 356 may be significantly different. The 1x4 in. tongue and groove and 1x6 in. board single straight-

sheathed diaphragms tested in (Peralta et al. 2001) have secant stiffness values of G_{d_Secant} = 1.4 kips/in and 6.0 kips/in respectively, compared to a recommended value of 2 kips/in in FEMA 356. Depending on one's perspective, it may be argued that the recommended FEMA 356 values are a reasonable coarse approximation of the broad range of diaphragm stiffnesses which may exist for this type of diaphragm in practice, or alternatively, it may be argued that the FEMA 356 equation predictions may be inaccurate by a significant factor relative to the physical response.

One attribute of the wood diaphragm responses discussed by Peralta et al. (2000), similar to the observations from (ABK 1981b) discussed in Section 2.3.4.1, is that the diaphragms generally were able to accommodate large deformations without significant degradation of the cyclic response.

2.3.5.3 Recommended diaphragm strengths in current guideline documents

(APA 1997) details a commonly accepted procedure for design of plywood diaphragms and presents the effects of openings in the diaphragm and field gluing of plywood sheathing. Table 1 of this report gives recommended design shear strengths for these diaphragm types, derived from prior test results. It is noted that the allowable shear values vary from other reports depending on the type of framing, splices, ties, hold-downs and other connections. It is also noted that the controlling diaphragm shear capacity is based on the type and spacing of the anchorages at the boundary (APA 1997). Table 2306.3.1 of IBC 2000 (ICC 2000) gives recommended design shear strengths for new plywood sheathed floors or roofs with blocking at panel edges. Sections 8.6.8 and 8.3.2.5 of FEMA356 refer to the yield capacity of wood structural panel diaphragms, but do not provide specific values for these strengths.

Table 2.4 summarizes recommended diaphragm shear strengths v_y from (ABK 1984) and Table 2.5 gives recommended strength values for a number of general dia-

phragm types from FEMA 356 (ASCE 2000a).

Table 2.4: Diaphragm strengths from (ABK 1984).

Description	Strength v_y (lb/ft)
Straight sheathing	300[a] 650[b]
Unblocked plywood sheathing with roofing applied on the sheathing	400
Diagonal sheathing with roofing applied on the sheathing	750
Double board systems with finish flooring laid over diagonal sheathing or multiple board systems with board edges offset	1,800
Metal roof deck systems designed for minimal lateral load capacity; Metal deck with minimal welding	1,800
Metal roof deck systems designed for lateral load capacity; Metal deck welded for seismic resistance	3,000

a. with roofing applied on the sheathing or a single layer of tongue and groove sheathing without roofing.
b. straight sheathing with plywood overlay.

Table 2.5: Diaphragm strengths v_y from FEMA 356 (ASCE 2000a).

Description		Strength v_y (lb/ft)
Single straight sheathing[a]		120
Double straight sheathing	Chorded	600
	Unchorded	400
Single Diagonally Sheathing	Chorded	600
	Unchorded	420
Diagonal Sheathing with Straight Sheathing or Flooring Above	Chorded	900
	Unchorded	625
Double Diagonal Sheathing	Chorded	900
	Unchorded	625
Wood Structural Panel Overlays on:Straight or Diagonal Sheathing or Existing Wood Structural Panel Sheathing	Unblocked, Chorded	450
	Unblocked, Unchorded	300

a. for single straight sheathing, yield capacity shall be multiplied by 1.5 when built-up roofing is present. The value for stiffness shall not be changed.

2.3.5.4 Calculation of equivalent E_e and G_e values for the proposed diaphragm element based on recommended code and guideline stiffnesses

This section explains the calculation of the chord and shear modulus values of the proposed diaphragm element, E_e and G_e, based on stiffnesses reported in code and guideline documents. The calculation of these values from specific equations for blocked and

chorded plywood diaphragms and metal deck diaphragms are discussed first, followed by the calculation of these values from general equations for other diaphragm types.

Blocked and chorded plywood diaphragms

Based on Eq. 2.15 and considering a lumped transverse loading at the center of the diaphragm of $W/2 = wL/2 = v$, where

W = total load in the direction under consideration, in pounds per foot

w = uniformly distributed force, in pounds per foot

v = maximum shear due to loads in the direction under consideration, in units of force per unit length

L = diaphragm length, in feet

the shear contribution to the mid-span deflection of an equivalent elastic diaphragm with uniform shear properties throughout may be written as

$$\Delta_s = \frac{vL}{4G_e t} \tag{2.54}$$

where G_e is the equivalent elastic shear stiffness. By equating Eq. 2.54 to the shear contribution to the deflection in Eq. 2.48, i.e.,

$$\frac{vL}{4G_e t} = \frac{vL}{4Gt} + 0.188Le_n \tag{2.55}$$

(where all the terms are expressed in units of *lbs* and *in*) the equivalent shear modulus for a plywood diaphragm can be derived as

$$G_e = \frac{vG}{v + 0.0627e_n Gt} \tag{2.56}$$

Similarly, an equivalent elastic chord modulus for the proposed diaphragm element, including the effects of both the chord flexibility as well as chord splice slip, may be derived by equating Eq. 2.18 to the flexural contributions to the displacement in Eq. 2.48. This gives

$$E_e = \frac{5\,vEL^3}{5\,vL^3 + 48\Sigma(\Delta_c X)EA_c} \tag{2.57}$$

Metal deck

Due to their corrugated profile, steel deck sections exhibit anisotropic behavior (Easterling 1994b). Also, the shear stiffness of these types of diaphragms is influenced significantly by distortion of the deck profile under the action of shear forces. (SDI 1995) bases its suggested equations for diaphragm shear stiffness on a more fundamental test than considered in the previously discussed wood diaphragm research. The test configuration considered by (SDI 1995) is illustrated in Fig. 2.22. If the proposed diaphragm element is applied to the analysis of this test, the shear deflection is obtained as

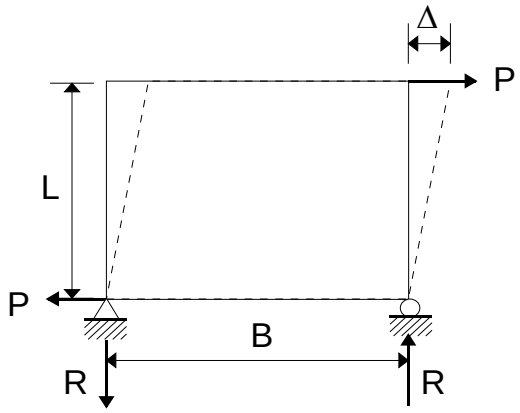

Figure 2.22: Schematic layout for metal deck diaphragm.

$$\Delta_s = \frac{vL}{G_e t} \tag{2.58}$$

(SDI 1995) gives a similar equation for this deflection, and defines an equivalent shear modulus of the diaphragm, considering the effects of corrugations, warping relaxation, and discrete connections at panel side laps as

$$G' = \frac{E}{2(1+\nu)\frac{S}{d} + D_n + C} \tag{2.59}$$

where:

E = modulus of elasticity, kips/in^2

ν = Poisson's ratio, 0.3

D_n = warping constant

S = girth of corrugation per rib, in

C = connector slip parameter

d = corrugation pitch, in

The reader is referred to (SDI 1995) for specific values of these constants.

The equivalent stiffness for the proposed diaphragm element is obtained simply as $G_e = G'$.

Metal deck with concrete topping

For diaphragms with concrete topping over a corrugated steel deck, the shear capacity increases proportionally with the added concrete. In addition, the concrete top-

ping eliminates the panel end warping effect for loads within the design range (SDI 1995). Thus, the warping constant term of Eq. 2.59 approaches zero. Finally, the total effective modulus is increased by adding second term in Eq. 2.60:

$$G_e = \frac{E}{2(1+\nu)\times\frac{S}{d}+C} + \frac{3.5\,d_c(f_c')^{0.7}}{t} \tag{2.60}$$

where

d_c = concrete cover depth

f_c' = concrete compressive strength, psi

General diaphragms

The equivalent elastic stiffnesses G_e and E_e for the proposed diaphragm element may be determined for general diaphragms from the FEMA 356 (ASCE 2000a) stiffness values G_{d_FEMA356} as follows. Based on the idealization of the diaphragm as being rigid in flexure and deformable only in shear (see the discussion of Eq. 2.52), E_e may be set effectively to infinity. That is, the flexural contributions to the diaphragm flexibility coefficients are taken as zero. Subsequently, Eq. 2.54 may be equated to Eq. 2.52 to obtain

$$G_e = \frac{G_{d\_\mathrm{FEMA356}}}{2\,t} \tag{2.61}$$

Similarly, again assuming that the diaphragm response is dominated by shearing type deformations, the equivalent shear modulus for the proposed diaphragm element corresponding to the FEMA 273 (FEMA 1997a) general diaphragm stiffness equation is

$$G_e = \frac{G_{d\_\mathrm{FEMA273}}B^3}{4L^3t} \tag{2.62}$$

2.3.5.5 Example calculations

In this section, the relative contribution of bending and shear deformations to the deflections in representative plywood and steel deck diaphragms are examined. The purpose of this study is to investigate when the bending deformations may be neglected. The following assumptions are invoked: (1) The area of the chord member is constant in all the studies. (2) Only the chord member at the outer edge of diaphragm is considered in calculating the bending stiffness, i.e, the potential contribution of the walls to the chord stiffness is not included. (3) The stiffness of walls subjected to out-of-plane bending is neglected. (4) The lateral load is uniformly distributed.

Wood Diaphragm

Consider the plywood diaphragm from (Tissell and Elliot 1983) shown in Fig. 2.23. Various properties of this diaphragm required for the diaphragm displacement calculations are shown in Table 2.6. The bending and shear contributions to the displacements for this diaphragm are determined from the fundamental equation

$$\Delta = \frac{5wL^4}{384E_eI} + \alpha_s \frac{wL^2}{8G_eA_w} \tag{2.63}$$

where E_e and G_e are determined from Eqs. 2.56 and 2.57, I is taken as $A_cB^2/2$, and $A_w = Bt$. The first term in Eq. 2.63 is the flexural or bending contribution to the displacement Δ_b and the second term is the shear contribution to the displacement Δ_s. The following assumptions from (Tissell and Elliot 1983) are invoked to determine the chord splice contribution to E_e along with Eq. 2.57:

- Each chord of the diaphragm in Fig. 2.23 is composed of four 12 ft long segments. Therefore, there are three internal splices in each segment.
- Tension chord: The splice slip Δ_c is assumed to be 0.011 in for both of the outer splices and 0.015 in for the center splice.
- Compression chord: The splice slip Δ_c is assumed to be 0.002 inches at all of the splice locations.

In the discussions below, the aspect ratio of this diaphragm L/B is varied from 1 to 5 at increments of one. For L/B values other than the value of three for the diaphragm shown in Fig. 2.23, the chords are still assumed to be composed of 12 ft long segments. The splice slip values are taken as described above, with the tension chord splice slips taken as 0.011 in only at the outer splices and 0.015 in for all interior splices. The tension chord splice slip is taken as 0.011 in for L/B = 2.

Based Eq. 2.63, one can write

$$\frac{\Delta_b}{\Delta_s} = \frac{5}{24}\left(\frac{G_e A_w}{E_e A_c}\right)\left(\frac{L}{B}\right)^2 \tag{2.64}$$

and

$$\frac{\Delta_S}{\Delta} = \frac{1}{1 + \frac{5}{24}\frac{G_e A_w}{E_e A_c}\left(\frac{L}{B}\right)^2} \tag{2.65}$$

Table 2.7 shows the corresponding computed total displacement Δ, shear contribution to this total displacement Δ_s, the bending contribution Δ_b, and the ratios $\frac{\Delta_s}{\Delta}$ and $\frac{\Delta_b}{\Delta}$ for this diaphragm if its aspect ratio L/B is varied from 1 to 5. Fig. 2.24 shows the plot of the corresponding total displacement, and the flexural and shear contributions to this displacement as a function of the diaphragm aspect ratio. As the aspect ratio increases from 1 to 5,

the ratio of $\frac{\Delta_b}{\Delta}$ increases from 9% to 32%. One can observe that even at an aspect ratio of 3, the contribution of the chord flexural deformations to the total diaphragm bending displacement is less than 20%. If the structural walls also provide some contribution to the chord stiffness, the flexural contribution to the total displacement is reduced further.

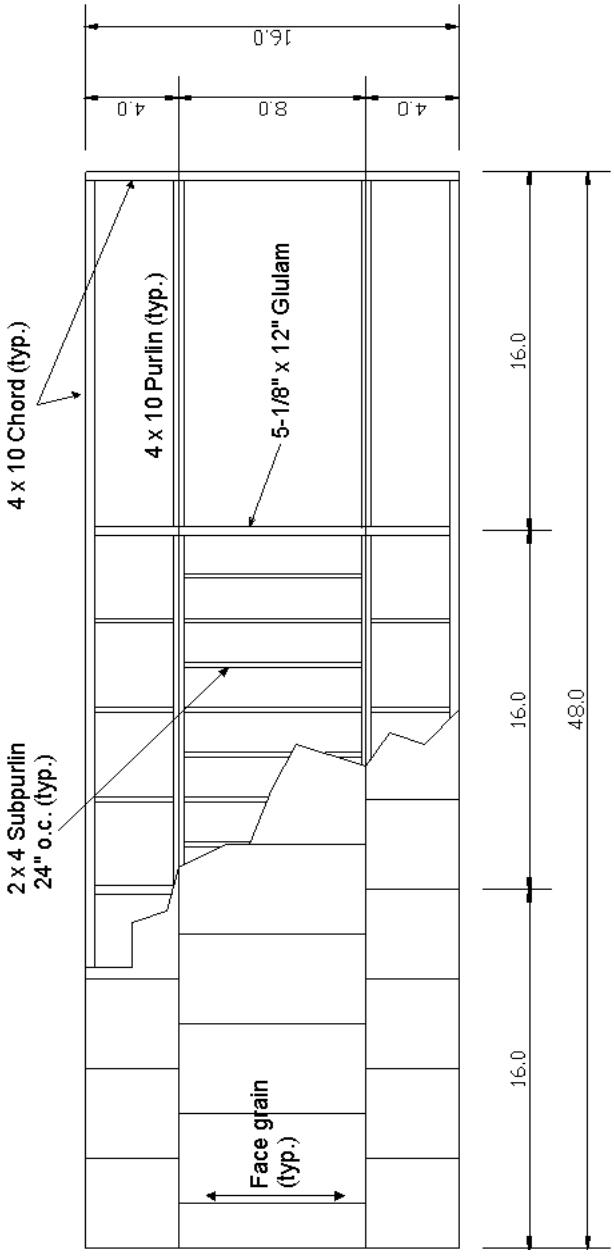

Figure 2.23: Framing details and panel layout for a representative plywood diaphragm (Tissell and Elliott 1983).

Table 2.6: Values for example plywood diaphragm deflection calculations (APA 1983).

Variable		Value
Shear in the direction under consideration	v_y	35.42 lb/in
Length of Diaphragm	L	576 inch (L/B = 3)
Width of Diaphragm	B	192 inch
Young's Modulus (Chord Member)	E	$1.7x10^7$ psi
Shear Modulus (Panel)	G	$9.0x10^4$ psi
Area of Chord Cross Section	A_c	32.375 in^2
Effective Plywood Thickness	t	0.535 inch
Nail Deformation	e_n	$\left(\frac{v}{1538}\right)^{3.276}$
Shear Coefficient	α_s	1.0

Table 2.7: Total displacements, shear and bending contributions to the total displacements and ratios of these contributions to the total for a representative wood diaphragm.

Diaphragm aspect ratio (L/B)	Displacement (in)				
	Δ	Δ_s	Δ_b	$\frac{\Delta_s}{\Delta}$	$\frac{\Delta_b}{\Delta}$
1	0.088	0.080	0.008	0.907	0.093
2	0.183	0.160	0.024	0.871	0.129
3	0.294	0.239	0.055	0.814	0.186
4	0.423	0.319	0.103	0.756	0.244
5	0.582	0.399	0.183	0.685	0.315

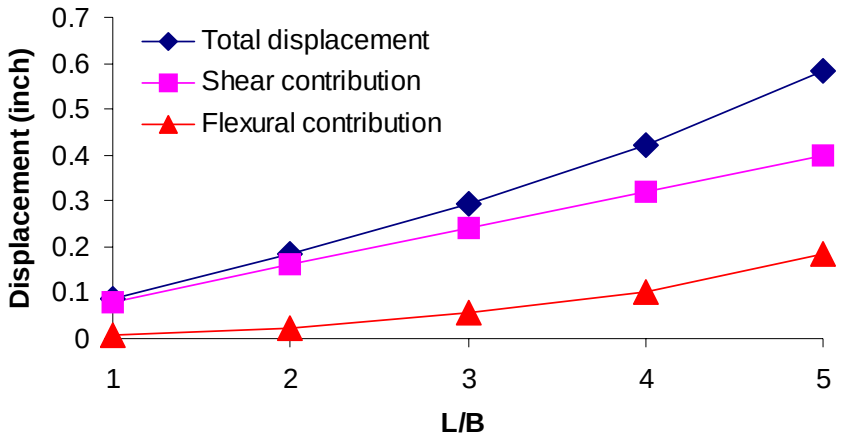

Figure 2.24: Example plywood diaphragm displacements.

Steel deck diaphragm

Consider the steel deck diaphragm from (SDI 1995) shown in Fig. 2.25. Various properties of this diaphragm required for the displacement calculations are shown in Table

2.8. The displacements of this diaphragm may also be calculated from Eq. 2.63. Table 2.9 shows the corresponding computed total displacement Δ, the bending contribution in this total displacement Δ_b, the shear contribution Δ_s, and the ratio of $\frac{\Delta_s}{\Delta}$ and $\frac{\Delta_b}{\Delta}$ for this diaphragm if its aspect ratio is varied from 1 to 5. Fig. 2.26 shows the plot of the corresponding total displacement, and the flexural contribution and shear contributions to this displacement as function of steel deck diaphragm aspect ratio.

Table 2.8: Values for calculation of deflections in an example steel deck diaphragm (SDI 1995).

Variable		Initial Value
Uniform Lateral Load	w	16.67 lb/in
Length of Diaphragm	L	120 ft (L/B = 3)
Width of Diaphragm	B	40 ft
Young's Modulus (Joist Member)	E	29,500 ksi
Effective Shear Modulus	G_e	1000 ksi
Section Area of Joist Member	A_c	10 in^2
Thickness	t	0.03 inch
Shear Coefficient	α_s	1.0

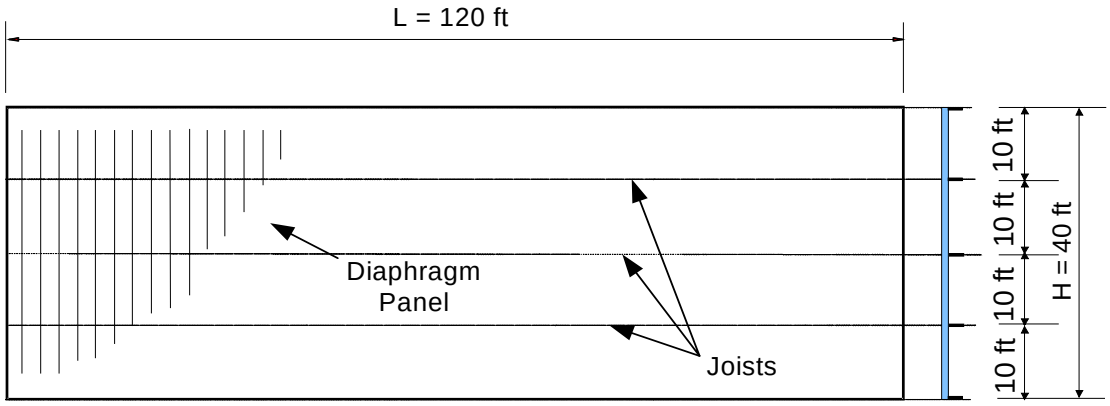

Figure 2.25: Representative steel deck diaphragm (SDI 1995).

Table 2.9: Total displacements, shear and bending contributions to the total displacements, and ratios of these contributions to the total for a representative steel deck diaphragm.

Diaphragm aspect ratio (L/B)	Displacement (inch)				
	Δ	Δ_s	Δ_b	$\frac{\Delta_s}{\Delta}$	$\frac{\Delta_b}{\Delta}$
1	0.034	0.034	0.0003	0.991	0.009
2	0.139	0.134	0.005	0.964	0.036
3	0.327	0.300	0.027	0.917	0.083
4	0.62	0.533	0.087	0.860	0.140
5	1.045	0.833	0.212	0.797	0.203

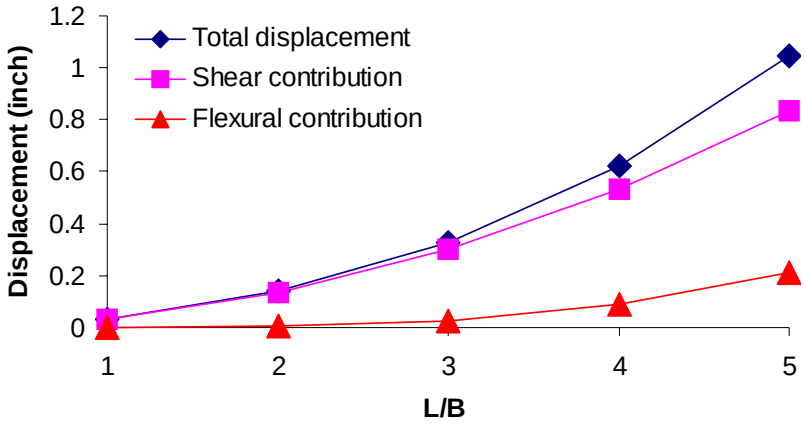

Figure 2.26: Example steel deck diaphragm displacements.

Comparison of two diaphragms

Figure 2.27 compares the ratio of the shear contribution to the displacement to the total displacement, $\frac{\Delta_S}{\Delta}$, for the plywood and steel deck diaphragms (calculated per Eq. 2.65). The value of $\left(\frac{G_e A_w}{E_e A_c}\right)$ is constant for all the aspect ratios in the steel deck diaphragm. However, because of the assumption of chord splices at every 12 ft in the plywood diaphragm, the $\left(\frac{G_e A_w}{E_e A_c}\right)$ varies as a function of the aspect ratio in this case.

Figure 2.27 shows that the ratio of $\frac{\Delta_S}{\Delta}$ is greater than or equal to 0.8 for the steel deck diaphragm. Because of the effects of the chord splices on the chord flexibility, $\frac{\Delta_S}{\Delta}$ is as low as 0.69 for an aspect ratio of 5 in the wood diaphragm. However, as noted previously, $\frac{\Delta_S}{\Delta}$ is greater than 0.8 for L/B $\leq$ 3 in this diaphragm.

Based on the above results, one can conclude that in many practical cases, it is sufficient to neglect the contributions from the chord flexibility altogether in approximating the diaphragm responses. That is, in many cases, the diaphragm response can be idealized as rigid with respect to the flexure and only the diaphragm shear deformations need be considered in determining the bending and shear raking displacements. It is again noted that this idealization is invoked in the general FEMA 356 equation for the diaphragm

bending displacements, Eq. 2.52.

,

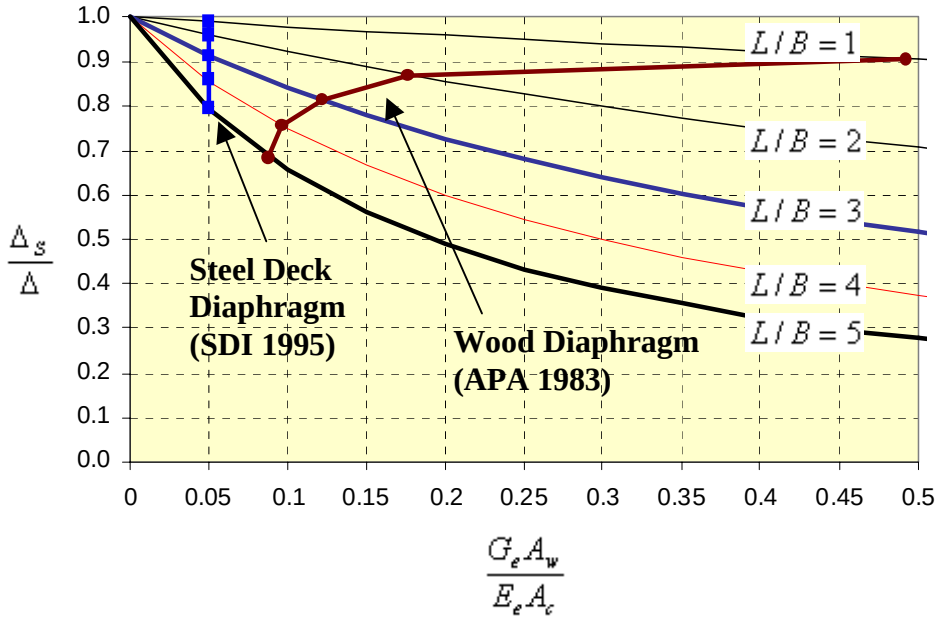

Figure 2.27: Comparison of deflection ratios.

2.4 Wall models

As discussed in Chapter I, the proposed modeling approach uses two degree-of-freedom shear spring elements within each story to analyze the wall responses. Each in-plane wall is represented by a single degree of freedom at each story level. These degrees of freedom are connected by one or more shear springs. A single shear spring element may be used as shown in Fig. 2.28 (a) if the engineer wishes to characterize the overall behavior of the wall within a given story using a single hysteretic model. Multiple shear spring elements as shown in Fig. 2.28 (b) may be connected in parallel to the corresponding story DOFs to track the behavior of each of the wall components directly. In this case, the overall wall hysteretic response is obtained by summing the responses from each of the components. In cases where the wall behavior is elastic, or if the engineer can approx-

imate the overall hysteretic response of the wall via a single hysteretic curve, only one element is needed per wall.

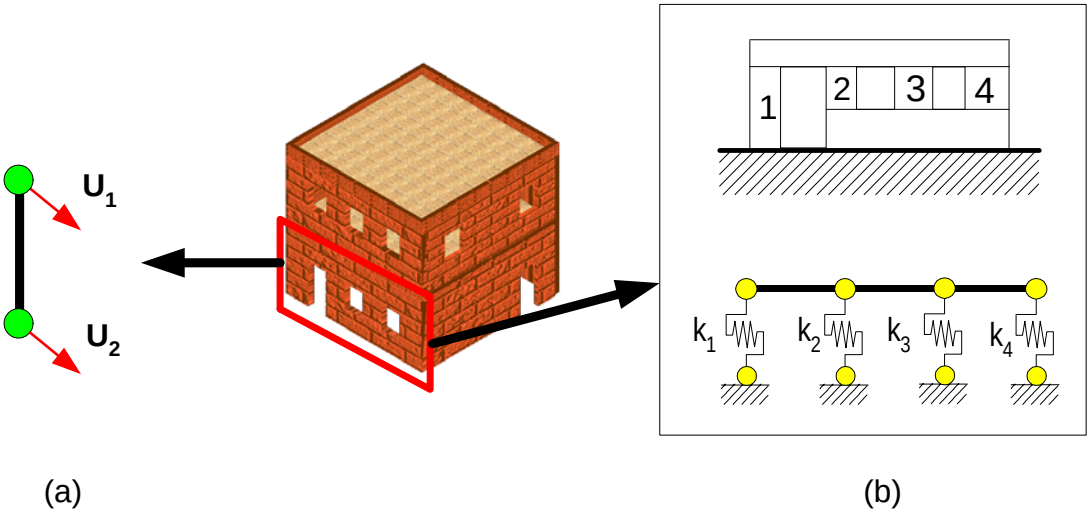

Figure 2.28: Shear wall element: (a) single shear spring element and (b) multiple shear spring elements.

As noted previously, the primary focus of the current research is on unreinforced masonry structures. The material properties for calculation of initial elastic wall stiffnesses in these types of buildings are discussed in Section 2.4.1. The initial elastic stiffness of each of the in-plane walls is determined in this work using either a finite element plane stress analysis and a flexibility approach, or by simplified strength of materials approaches. These calculations are presented in Section 2.4.2. The overall wall strength is determined by summing the strengths determined from each of the wall components. These strength calculations are discussed in Section 2.4.3.

As noted above, the overall wall hysteretic response may be approximated by a single hysteretic curve, based generally on judgment, or by the use of multiple wall elements, connected in parallel to the corresponding story degrees of freedom, each with their own independent hysteretic model. The hysteretic models that may be utilized for the walls include the three-parameter model discussed previously with respect to the anal-

ysis of the diaphragm responses, as well as a rocking model and a bed-joint sliding model. The three-parameter model is useful for representing the behavior of walls or piers that exhibit a diagonal tension mode of failure.

Section 2.4.4 discusses the inclusion of flange effects from the out-of-plane walls in the modeling of in-plane walls. Section 2.4.5 discusses a special case of the basic pier rocking models addressed earlier in Section 2.4.3: the modeling of piers that fail by a multiple story rocking mechanism. Section 2.4.6 addresses the calculation of individual component stiffnesses when an in-plane wall is represented by multiple parallel spring elements. Section 2.4.7 discusses the modeling of out-of-plane walls.

2.4.1 Wall material properties in code and guideline documents

The behavior of masonry walls is more complex than that of concrete shear walls (Shing 1998). This is due to the nonhomogeneous nature of unreinforced masonry, involving the interaction of the constituent materials, i.e., brick, mortar, and grout, The influence of mortar joints as weak planes is a significant feature that is not present in concrete. Masonry walls do not fail immediately after cracks develop. They can possess a gradual softening until the ultimate limit state is achieved, and they can be deformed considerably (Abrams 1992).

A representative masonry strain-strain response curve from a compression prism test (MSJC 1999c) is shown in Fig. 2.29. This figure shows one definition of the elastic modulus for masonry in compression, E_m. The commentary to ACI 530-99 (MSJC 1999b) explains that the elastic modulus in compression of masonry has been traditionally taken as 1000 f_m', but indicates that lower values are more typical. FEMA 356 (ASCE 2000a) suggests

$$E_m = 550 \times f_m' \tag{2.66}$$

as an expected value for the elastic modulus of masonry in compression, where f_m' is the masonry compressive strength.

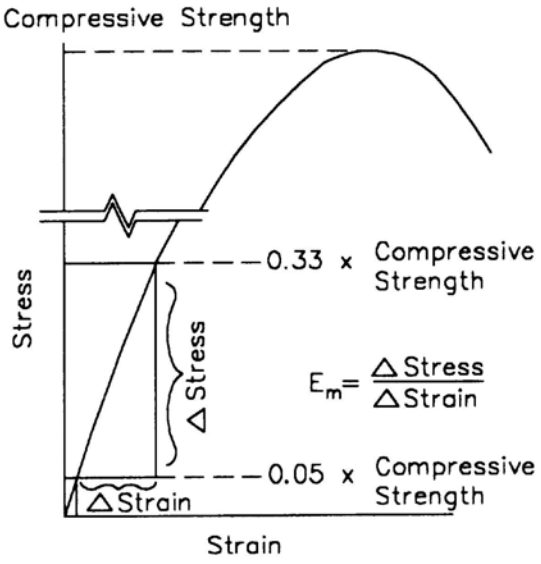

Figure 2.29: Compressive stress-strain response of masonry (MSJC 1999b).

Table 2.10 gives expected values for f_m' suggested by FEMA 273 (FEMA 1997), and the corresponding values for E_m for masonry in good, fair and poor condition.

Table 2.10: Summary of elastic modulus with compressive strength in FEMA 273 (FEMA 1997) and FEMA 356 (ASCE 2000a).

Condition	f_m' (FEMA273 and FEMA 356 Masonry compressive strength)	E_m (FEMA 273 Masonry elastic modulus)
Good	< 900 psi	< 495 ksi
Fair	< 600 psi	< 330 ksi
Poor	< 300 psi	< 165 ksi

ACI 530-99 (MSJC 1999a) suggests the following expected values for E_m:

$$E_m = 700 \times f_m' \quad \text{for clay masonry} \tag{2.67}$$

$$E_m = 900 \times f_m' \quad \text{for cement masonry} \tag{2.68}$$

and IBC 2000 (ICC 2000) suggests a design value of

$$E_m = 750 \times f_m' \quad \text{3,000 ksi max. for clay, shale, or cement unit masonry} \tag{2.69}$$

The ACI 530-99 (MSJC 1999a) and UBC 1997 (ICBO 1997) codes specify the modulus of elasticity of grout as

$$E_g = 500 \times f_g \tag{2.70}$$

where f_g is the grout compressive strength.

Common practice is to use the E_m value from one of the above approaches as the elastic modulus, along with an effective wall thickness, for structural analysis. FEMA273, ACI 530-99, and UBC 1997 suggest that the shear modulus of unreinforced masonry may be taken as

$$G_m = 0.4 E_m \tag{2.71}$$

This corresponds to a Poisson's ratio of 0.25.

2.4.2 Determination of wall initial elastic stiffness

The lateral displacement of a single shear wall without openings may be calculated using simple flexural theory. However, openings are often introduced in shear walls, thereby reducing their effectiveness and altering their deformation characteristics. Simplified methods that give reliable estimates for the lateral stiffness of perforated shear walls are not available at this time (December 2002). Given an accurate characterization of the material stiffness and effective thickness, a flexibility approach based on the use of plane-stress finite element analysis has been shown by Tena-Colunga and Abrams (1992a) to provide a significant improvement in the overall accuracy of the analysis relative to typical simplified methods.

The next subsection discusses two typical simplified methods for calculating elastic wall stiffnesses. This is followed by an explanation of the above flexibility approach and a comparison of the results from this approach to those of the simplified calculations for an example wall.

2.4.2.1 Initial stiffness calculation based on strength of materials type analysis

Schneider and Dickey (1994) suggest several simplified methods for the elastic stiffness of single-story masonry walls. These models are explained in the following subsections using the perforated wall shown in Fig. 2.30.

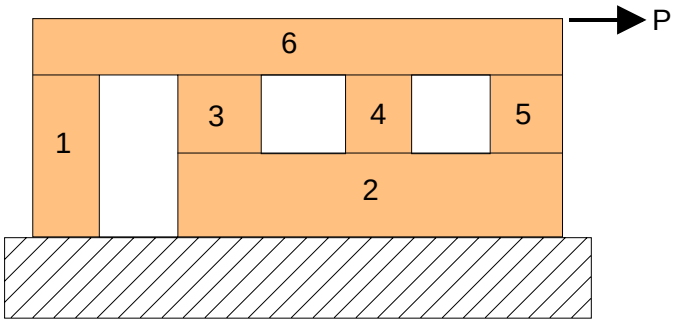

Figure 2.30: Example perforated wall (Schneider and Dickey 1994).

Method 1

The procedure of method 1 is:

1) The deflection of the wall under a unit lateral load is calculated assuming that the wall is a solid cantilever (no openings). The following equation is used for this calculation:

$$\Delta_C = \Delta_B + \Delta_S = \frac{Ph_{eff}^3}{3E_m I} + \frac{1.2Ph_{eff}}{G_m A_v} \tag{2.72}$$

where

I = moment of inertia for the gross section representing uncracked behavior

h_{eff} = wall height

A_v = shear area

P = lateral force on wall, taken equal to a unit value.

2) The deflection under a unit for a cantilever strip having a height equal the height of the tallest opening in the wall and a width equal to the total width of the wall is calculated using Eq. 2.72.

3) The deflection of the cantilever strip calculated from step 2 is subtracted from wall deflection determined in step 1.

4) The strip in step 2 is subdivided into several areas composed of one or more openings *of the same height* and the portions of the walls adjacent to these openings.

5) For each of the areas determined in step 4, the lateral deflection under a unit load is determined. These deflections are determined assuming fixed boundary conditions at the top and bottom of the area.

6) Each of the deflections obtained in step 5 are added to the deflection from step 3.

7) The stiffness of the wall is obtained by taking the reciprocal of the displacement from step 6.

In step 5, the deflections are calculated for each of the wall areas in a fashion similar to the procedure for the total wall. The deflection is first calculated assuming that the wall is solid within the area under consideration (no openings). Second, the deflection of a strip having a height equal to the height of the openings in this area is subtracted from the above. Finally, the deflection of each of the piers of height equal to the height of the openings is calculated an added to the above result. The deflection equation used in these area calculations is

$$\Delta_F = \Delta_B + \Delta_S = \frac{Ph_{eff}^3}{12E_mI} + \frac{1.2Ph_{eff}}{G_mA_v} \tag{2.73}$$

where P is again taken as a unit load, and the dimensional parameters correspond to the area under consideration.

Method 2

The stiffness using method 2 is determined simply by summing the stiffnesses of the individual piers between the openings within the wall, i.e.,

$$K = \sum_{i=1}^{n} k_i = \sum_{i=1}^{n} \frac{1}{\Delta_i} \quad \text{for} \quad i = 1, 2, 3, \ldots, n \tag{2.74}$$

where the individual pier stiffnesses k_i are obtained from Eq. 2.73.

2.4.2.2 Initial stiffness by flexibility approach, using plane stress finite element analysis

The calculation of the lateral stiffness by the flexibility approach can be explained using the representative two-story perforated wall shown in Fig. 2.31. The general proce-

dure is as follows:

1) The perforated wall is discretized using plane stress finite elements.

2) A unit load, P_j, is applied at the diaphragm level at each story.

3) The corresponding displacements at each diaphragm level i associated with each of the unit loads P_j are determined. These displacements are denoted by the symbol U_{ij}.

4) The displacements U_{ij} are assembled to form the flexibility matrix of the wall. For the two-story example in Fig. 2.31, this matrix may be written as

$$[U] = \begin{bmatrix} U_{11} & U_{12} \\ U_{21} & U_{22} \end{bmatrix} \tag{2.75}$$

5) The condensed wall stiffness matrix is obtained by inverting the above flexibility matrix:

$$[K] = [U]^{-1} = \begin{bmatrix} K_{11} & K_{12} \\ K_{21} & K_{22} \end{bmatrix} \tag{2.76}$$

Tena-Colunga and Abrams (1992a) use Eq. 2.76 directly within their simplified elastic analysis approach, discussed in Section 2.2.2. However, in order to approximate the inelastic response of a wall such as the one shown in Fig. 2.31, it is desirable to subdivide the wall into multiple elements. In the context of this research, shear spring elements are utilized to represent each story of the wall. The 2 x 2 stiffness matrix for the example wall can be expressed in terms of stiffnesses of the shear springs in the first and second stories as

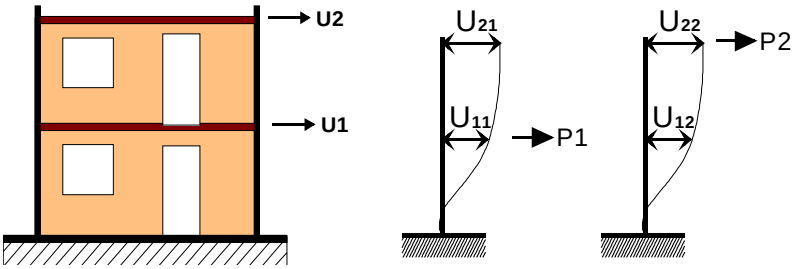

Figure 2.31: Representation of a perforated cantilever wall (Tena-Colunga and Abrams 1992a).

$$[K] = \begin{bmatrix} K_1 + K_2 & -K_2 \\ -K_2 & K_2 \end{bmatrix} \tag{2.77}$$

where K_1 and K_2 are the stiffnesses of the shear springs within the first and second stories respectively. The fundamental formulation of this stiffness matrix is illustrated in Fig. 2.32.

Given Eqs. 2.76 and 2.77, the elastic stiffness of the second story is calculated by equating diagonal coefficients in the second row of the matrices, i.e.,

$$K_2 = K_{22} \tag{2.78}$$

Once K_2 is determined, K_1 is calculated by equating the diagonal coefficients in the first row of the above equations. This gives

$$K_1 = K_{11} - K_2 \tag{2.79}$$

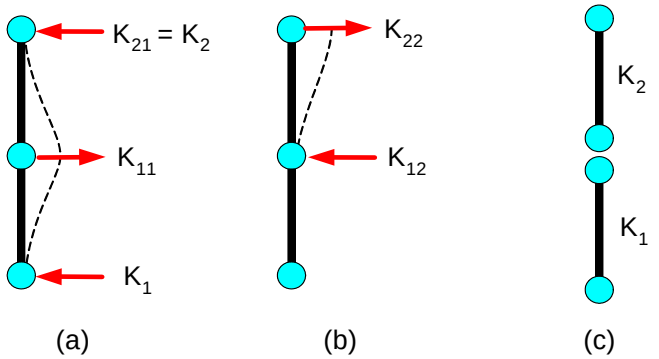

Figure 2.32: Calculation of story stiffness.

A similar approach is employed for walls with more than two stories. The shear spring stiffnesses are obtained by equating the diagonal coefficients of the stiffness matrix obtained by plane stress finite element analysis to the corresponding diagonal coefficients associated with the shear spring idealization.

The above procedure of course gives only an approximation of the elastic stiffness matrix for the complete wall obtained from the plane stress analysis. The diagonal coefficients obtained from the plane stress analysis are matched exactly, but the off-diagonal stiffness terms are generally not the same. Also, the elastic stiffness from the plane stress analysis is generally full. That is, all of the story degrees of freedom are coupled. A non-zero force is produced at any story level i due to a unit deflection at any story level j. However, only the adjacent story degrees of freedom are coupled using the shear spring idealization, as illustrated in Fig. 2.32. By equating the diagonal coefficients, a suitable approximation of the "exact" wall stiffness is obtained that satisfies equilibrium in the context of the story-by-story shear spring idealization.

2.4.2.3 Comparison of methods

Figure 2.33 shows the plane stress finite element discretization and deformed geometry for two perforated walls from Schneider and Dickey (1994) and Tena-Colunga

and Abrams (1992a) (labeled as walls B and C in these references). A four-node plane-stress element is used for the analysis using ABAQUS Version 5.8 (HKS 1998). The elastic modulus of the wall is taken as E_m = 1200ksi, G_m is determined per Eq. 2.71, and the equivalent wall thickness is taken as 8.5 in. A lateral load of P = 1,000 kips is applied at the top of the wall. Since this problem involves only a single story, the "exact" stiffness per the plane stress analysis is used directly within the shear spring idealization. The deflections predicted by this recommended approach are compared to the corresponding predictions using Methods 1 and 2 from Section 2.4.2.1 in Table 2.11. Similar results are reported by Tena-Colunga and Abrams (1992a).

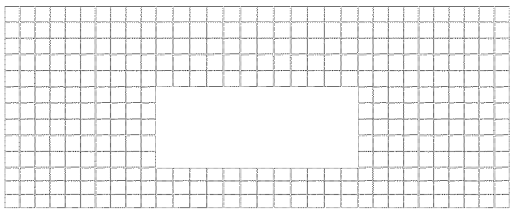

(a) Wall B: Undeformed mesh

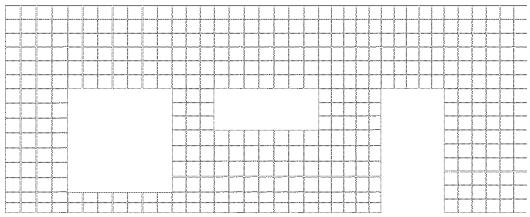

(b) Wall C: Undeformed mesh

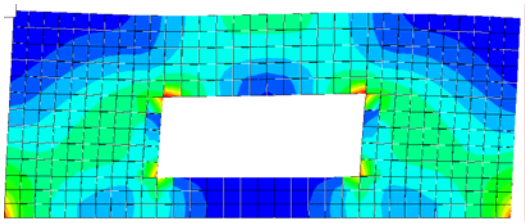

(c) Wall B: Deformed mesh and minimum principal stress

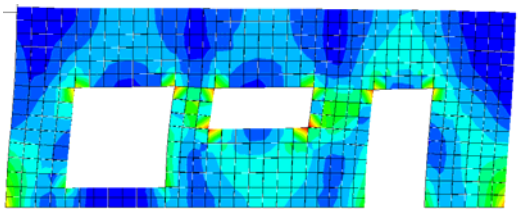

(d) Wall C: Deformed mesh and minimum principal stress

Figure 2.33: Perforated walls for the comparison between the simplified and the FEM analysis.

Both of the simplified methods tend to underestimate the lateral deflections in this problem. Method 1 gives the best predictions of these two approaches for these walls. The predicted lateral displacements only 0.25 and 0.26 of the values obtained from finite

element analysis using Method 2.

Table 2.11: Comparison of the displacement of the perforated cantilever walls by FEM vs. Method I and II (Tena-Colunga and Abrams 1992a).

WALL	FEM (ABAQUS) in	Method 1 in	Method 2 in
B	0.2832	0.152	0.071
C	0.3483	0.201	0.091

2.4.3 Wall strength and hysteresis models

The physical behavior of general perforated masonry walls is complex. Many types of failure are possible and the strength and hysteretic response can vary significantly as a function of the failure mode. The failure mode can be influenced by the nonhomogeneous nature of these wall types. As the lateral force on a wall or pier increases, flexural or shear cracking - or a combination of both - occurs. Shear failures, i.e., diagonal tension or bed-joint sliding limit states, are common types of failure of masonry walls (Zhuge 1998). In this research, simplified equations specified in FEMA 273, FEMA 356 and EC 6 are adapted to calculate the strength of walls as a whole and of individual wall components.

According to FEMA 274 (FEMA 1997b), four different failure modes can occur in masonry walls and/or their components: diagonal tension, bed-joint sliding, toe crushing, and rocking. It is well known that the strength and hysteresis behavior of masonry shear walls depends predominantly on the length-to-height aspect ratio (L/H) and the amount of vertical compressive stress overall and within the individual components of the wall. FEMA 274 categorizes rectangular walls or piers according to L/H as shown in the first two columns of Table 2.12. The most common modes of failure for each of the categories are described in the third column of the table. Table 2.13 gives the characterization of the failure modes adopted in this research based on the combined rules in FEMA 273 (FEMA

1997a) and EC6 (CEN 1995). The categorization of the behavior into two types of diagonal tension failure, per EC6, is adopted here. FEMA 273 lists only the four basic failure modes discussed above.

The behavior of stocky walls (L/H greater than 1.5) is typically governed either by diagonal tension or bed-joint sliding. The crack pattern associated with diagonal tension can develop in either a stair-step pattern through the mortar head and bed joints, or along a straight diagonal path through the masonry units. For taller more slender walls or piers, the strength and hysteresis behavior is typically governed either by rocking or toe-crushing. As the lateral force approaches to PL/2H, a wall or pier will start to rock about its toe. Walls and piers with an intermediate aspect ratio (L/H between 1.0 and 1.5) are more apt to be governed by toe crushing, which occurs after flexural cracks form at the heel of a wall. Slender walls (L/H < 1.0) loaded by relatively light vertical compressive forces are typically governed by rocking. Although the above modes of failure (listed also in Table 2.12) are the most common for each of the wall types, in general the strength associated with each of the five damage models listed in Table 2.13 must be checked. The controlling damage model is taken as the one that gives the smallest strength.

Table 2.12: Categorization of rectangular masonry walls and piers (FEMA 1997b).

Wall Type	L/H	Typical Failure Mode
Stocky walls	> 1.5	Diagonal tension cracking or bed-joint sliding
Moderate walls	> 1.0 and < 1.5	Rocking or toe crushing
Slender walls	< 1.0	Rocking

Table 2.13: Characterization of failure modes in rectangular masonry walls and piers, adapted from (FEMA 1997b) and (CEN 1995).

Failure Mode	Description of Damage	Damage Model Index
Diagonal tension crack	Stair-step pattern	1
	Straight diagonal pattern	2
Bed-joint sliding	Sliding at one or several bed joints	3
Toe crushing	Flexural cracking at the heel of the wall and crushing at the toe	4
Rocking	Flexural cracks along a bed joint near the base of the wall	5
	Bed-joint crack will develop across almost all of the wall base	

Simple hysteresis models can be constructed to represent bed-joint sliding and rocking, since experimental tests show little stiffness degradation, strength deterioration or pinching associated with these limit states. However, the hysteretic responses associated with diagonal tension and toe crushing are not well established at the present time. The three parameter model discussed in Section 2.3.4.1 is expected to give a reasonable approximation of hysteresis response for walls that fail by diagonal tension or toe crushing. This model captures the essential characteristics associated with these modes of failure, i.e., stiffness degradation, strength deterioration and pinching.

Recommendations are provided for calculation of the strength and hysteresis of rectangular walls and piers in the following subsections. The recommended strength equations are adapted from FEMA273 (FEMA 1997a) and EC6 (CEN 1995). For purposes of discussion, the recommendations are organized using the damage index numbers shown in the last column of Table 2.13. Generally, the total shear strength of a perforated wall is obtained by summing the strengths from its components.

2.4.3.1 Damage models 1 and 2: Diagonal tension cracking

When a wall is subjected to a combination of vertical and lateral load as shown in Fig. 2.34, diagonal cracks may pass through the masonry units or through the mortar joints. FEMA 356 (ASCE 2000a) specify a wall shear strength equation that is effectively based on the maximum principal tensile stress reaching the diagonal tension strength within an idealized element at the middle of the wall (Turnsek 1980).

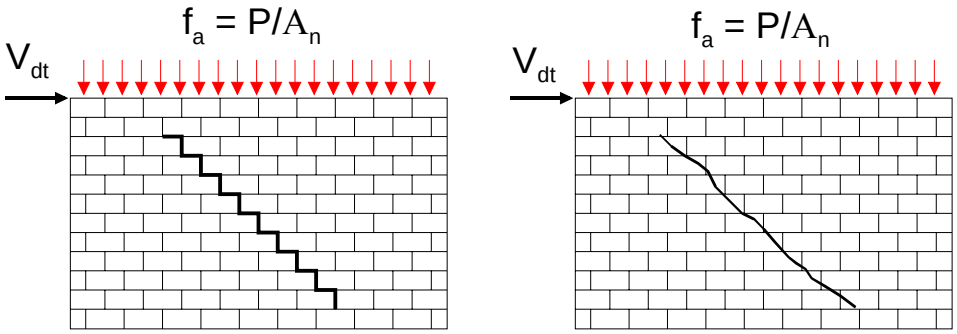

(a) crack through mortar joints (b) crack through masonry units

Figure 2.34: Diagonal tension cracking.

The total gravity load P as shown in Fig. 2.34 is taken as the sum of the dead load, effective live load, and effective snow load contributions. The vertical compressive stress in the wall f_a is taken as the 1.1 times this force at the wall mid-height divided by the horizontal net mortared/grouted section of the wall A_n. The shear stress τ is calculated as the total shear force at the wall mid-height divided by A_n, as shown in Fig. 2.35. The principal diagonal tension stress at the middle of the wall, f_t, is then calculated as follows:

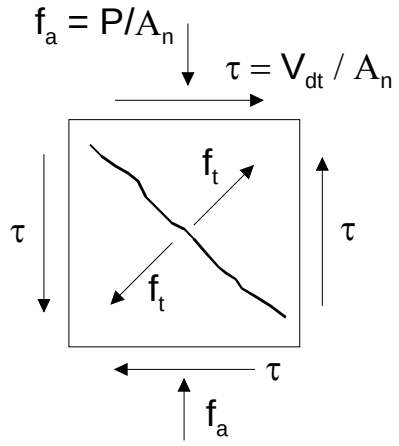

Figure 2.35: Principal stress for unit area.

$$f_t = \sqrt{\left(\frac{f_a}{2}\right)^2 + (b\tau)^2} - \frac{f_a}{2} \tag{2.80}$$

where

$b = \frac{h_{eff}}{L}$ = shear stress distribution factor, which depends on the geometry of wall

h_{eff} = height from the base of the wall to the resultant of the applied lateral force

This equation is obtained from Mohr's circle, except that the shear stress is modified by the shear stress distribution factor *b*. Equation 2.80 was developed originally by (Turnsek 1980) and is also discussed in (Tomazevic 1999).

By equating f_t to the lower-bound diagonal tension strength of the masonry f'_{dt} and solving Eq. 2.80 for τ, the lateral shear resistance may be expressed as

$$V_{dt} = \frac{f_{dt}' A_n L}{h_{eff}} \sqrt{1 + \frac{f_a}{f_{dt}'}} \tag{2.81}$$

where, V_{dt} = lateral strength limited by diagonal tension

FEMA 356 do not recommend any specific values for f'_{dt}, but state, "Substitution of the bed-joint shear strength, v_{me}, for the diagonal tension strength f'_{dt} in Equation (7-5) [Equation 2.81 in the above] shall be permitted." The bed-joint shear strength is discussed in the next subsection. FEMA 356 state that Eq. 2.81 is applicable only for $0.67 < \frac{L}{h_{eff}} < 1.00$. No recommendations are provided for walls or components that do not meet these limits.

As noted previously, EC6 considers two different potential diagonal tension failure modes for URM, denoted by indices 1 and 2 in Table 2.13. The lateral shear resistance for damage model 1 (which involves stair-step diagonal tension cracking) is expressed in EC6 as (Tomazevic 1999)

$$V_{dt} = \frac{(v_{to} + \mu_c \sigma_d) t L_c}{\gamma} \tag{2.82}$$

where

v_{to} = shear strength under zero compression stress

μ_c = slip coefficient, assumed equal to 0.75

σ_d = vertical design compression stress

γ = material partial safety factor

L_c = length of the compressed part of the wall

This equation is applied in this research by taking $\gamma = 1$ and $\sigma_d = f_a$.

The shear resistance for damage model 2 (a straight diagonal tension crack through the mortar and masonry units) is calculated in EC6 using Eq. 2.81, but the nominal strength is divided by the partial safety factor γ, and is multiplied by 0.9 if the hysteretic response is idealized as bilinear. The FEMA 356 equation is used directly for damage model 2 in this research.

EC6 does not specify any limitations on the usage of the above formulas.

There is little information about the hysteresis behavior associated with diagonal tension failures. Benedetti and Castellani (1980) explain that significant energy dissipation occurred in their tests, but do not show any hysteresis results. A representative nonlinear response of brick masonry walls (Magenes and Calvi 1997) shown in Fig. 2.36 is characterized by strength deterioration, stiffness degradation, and moderate energy dissipation. In this research, the three-parameter model discussed previously in Section 2.3.4 is used to represent the nonlinear responses of walls and components that fail in a diagonal tension mode. The three-parameter model post-elastic properties are established based on judgment.

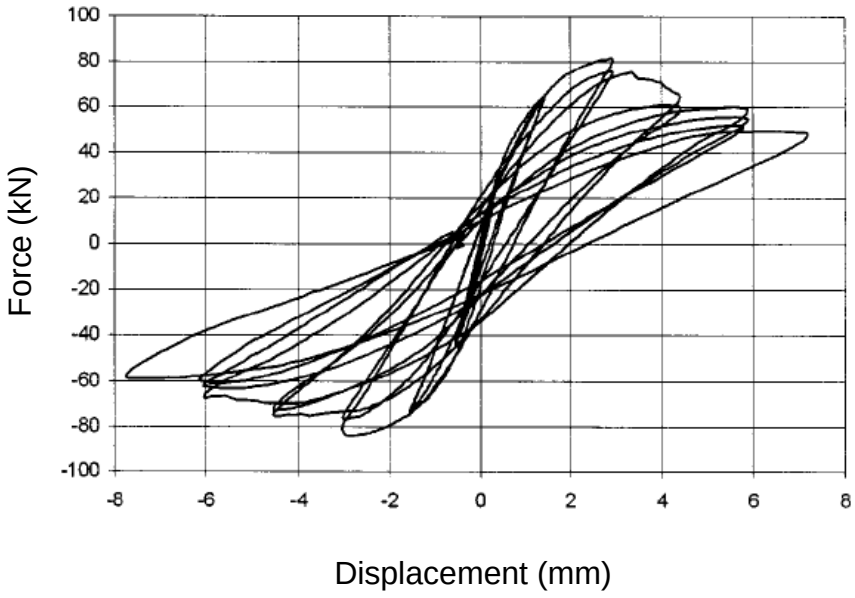

Figure 2.36: Example of diagonal tension cracking response of simple piers (Magenes and Calvi 1997).

2.4.3.2 Damage model 3: Bed joint sliding

Bed joint sliding involves the development of a fracture across the entire wall or

component at a mortar joint (see Fig. 2.37). The strength in this failure mode depends on the shearing strength of the mortar joints in the absence of axial compression, but is influenced significantly by the axial compression at the joints (Shing 1998).

The shear resistance in FEMA 356 is expressed as

$$V_{bjs} = \left(0.375\, v_{te} + 0.5\frac{P_{CE}}{A_n}\right) A_n \tag{2.83}$$

where

V_{bjs} = lateral strength based on bead joint shear strength

v_{te} = average bed-joint shear strength

P_{CE} = expected gravity compressive force due to gravity and earthquake loads combined as specified in the FEMA 356 Articles on deformation-controlled design actions and force-controlled design actions.

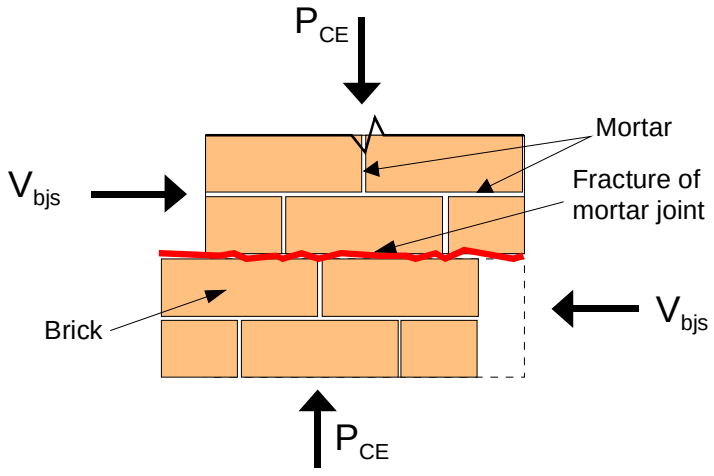

Figure 2.37: Bed joint sliding.

The expected gravity load P_{CE} explicitly includes an estimate of the force from vertical acceleration, while the gravity load used for the calculation of the diagonal tension cracking shear strength does not.

For cases involving low vertical load and high seismic acceleration, the shear

resistance in EC6 is represented by the friction of masonry relative to mortar joint and expressed as

$$V_{bjs} = \mu_c P_{CE} \tag{2.84}$$

where, μ_c = constant defining the contribution of compression stresses, assumed equal to 0.75. Therefore, for small v_{te}, the EC6 model is 50 percent stronger than the FEMA 356 model.

URM wall tests (Shing 1998) indicate that cyclic bed-joint sliding behavior can be represented by an elasto-plastic hysteresis rule as shown in Fig. 2.38. Due to the loss of cohesive force, the shear resistance drops rapidly after the peak shear force is reached. The subsequent residual shear force is provided by the friction depending on the compressive force in the wall. The strength in Fig. 2.38 is calculated from Eqs. 2.83 and 2.84. The elastic stiffness, K_e, is discussed in Section 2.3.4, and the post elastic tangent stiffness is typically chosen as a small value for purposes of numerical stability.

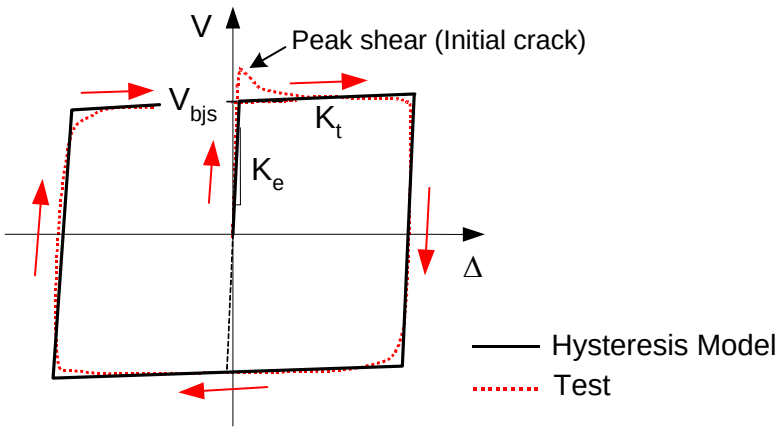

Figure 2.38: Bed joint sliding behavior (Shing 1998) and uniaxial bed-joint sliding hysteresis model.

2.4.3.3 Damage model 4: Toe crushing

Figure 2.39 illustrates the idealized behavior associated with toe crushing. As the lateral load *V* increases, flexural cracking occurs at the right side of the pier wall and the width of the effective shear zone (taken as the width of the wall that remains under compression) decreases (Abrams 1992). At the shear associated with the toe crushing strength, V_{tc}, the vertical compressive stress in the extreme compression fiber at the base reaches the lower bound masonry compressive strength f_m' and the compressed corner at the base is crushed.

By assuming that the behavior in compression is linear within effective shear zone and neglecting the flexural cracking section, the lateral strength V_{tc} associated with this failure mode can be derived simply. The resultant force is calculated from the triangular compression stress block. The distance *e* from the location of the resultant force to the centerline of the wall is $\frac{L}{2} - \frac{d}{3}$. The equilibrium equations for the masonry wall shown in Fig. 2.39 are expressed as

$$V_{tc} h_{eff} = Pe \tag{2.85}$$

$$\frac{1}{2} f_m' dt = P \tag{2.86}$$

where

V_{tc} = lateral strength limited by toe crushing

f_m' = lower bound of masonry compressive stress

t = thickness of wall

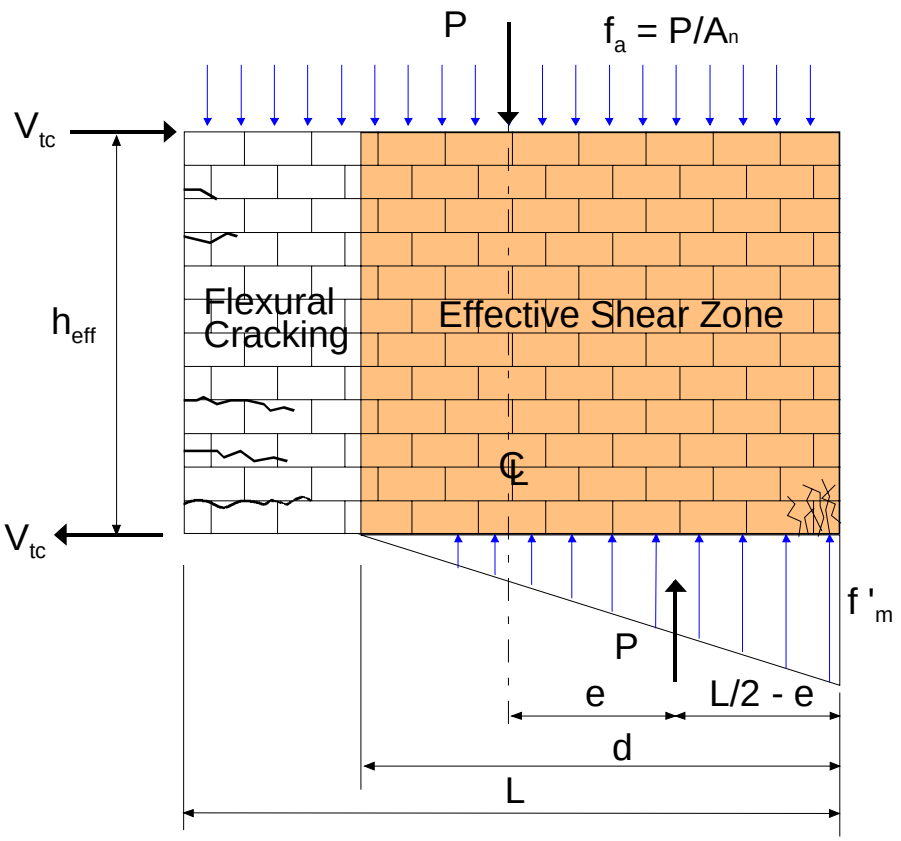

Figure 2.39: Assumed effective shear zone and free body diagram of wall cracked at base.

By equating Eqs. 2.85 and 2.86, the lateral force is expressed as

$$V_{tc} = \frac{1}{2} P \left(\frac{L}{h_{eff}} \right) \left(1 - \frac{4 f_a}{3 f_m'} \right) \tag{2.87}$$

The lower bound lateral strength V_{tc} in FEMA 356 is calculated as

$$V_{tc} = \alpha P_L \frac{L}{h_{eff}} \left(1 - \frac{f_a}{0.7 f_m'} \right) \tag{2.88}$$

where

α = factor equal to 0.5 for a cantilever wall, or equal to 1.0 for fixed-fixed pier.

f_a = axial compressive stress calculated from 1.1 times the total gravity loads discussed in Section 2.4.3.1

P_L = lower bound axial compressive force 0.9 times gravity load associated with dead load.

FEMA 356 limits the use of this equation to $0.67 < \frac{L}{h_{eff}} < 1.00$.

It should be noted that $f_a = P/A_n$ in the development of Eq. 2.87. However, FEMA 356 specifies two different gravity load combinations in the application of Eq. 2.88. The axial compressive stress f_a is calculated from the total gravity load (multiplied by 1.1) whereas the axial compressive force P_L is calculated only from the dead load (multiplied by 0.9).

The expected hysteresis behavior of this failure mode may be characterized by moderate energy dissipation and by strength and stiffness degradation. Initiation of the first flexural cracks may be characterized by moderate energy dissipation with negligible strength and stiffness degradation. The post-peak response may be characterized by higher energy dissipation but with extensive strength and stiffness degradation. The hysteresis behavior of this failure mode may be represented by the three parameter hysteresis model discussed previously, with pinching effects neglected.

2.4.3.4 Damage Model 5: Rocking failure

Figure 2.40 illustrates the idealized behavior associated with rocking. In a rocking mode of failure, tension cracking occurs across a major portion of the bed joint, the compression block moves toward the extreme compression fiber, and the lateral force is carried by the compressed masonry. At the rocking strength V_r, an isolated wall essentially

rotates as a rigid body about its toe, as shown in Fig. 2.40 (b), and simultaneously the bottom compressed corner tends to crush (Magenes and Calvi 1997). However, when the wall is a part of a structural system, unconstrained rigid body motion is prevented and additional force is needed to cause crushing of masonry (Tomazevic 1999).

The lateral load V_r and the total gravity load P_{CE} discussed in Section 2.4.3.1 are assumed to be applied at the slender wall shown in Fig. 2.40(b). By summing moments about the line of action of the compressive force P_{CE} in Fig. 2.40 (b), the lateral strength is obtained as

$$V_r = P_{CE}\frac{L-d}{h_{eff}} \tag{2.89}$$

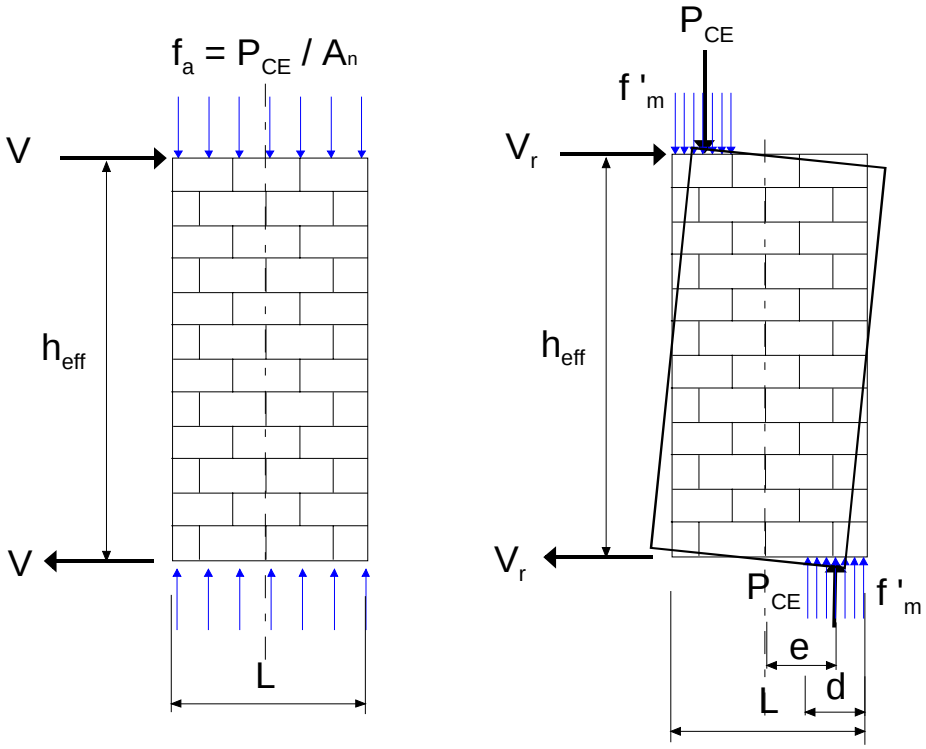

(a) (b)

Figure 2.40: Equilibrium of masonry pier.

The expected rocking strength in FEMA 273 and FEMA 356 is modified from the above equation as follows:

$$V_r = 0.9\alpha P_{CE}\frac{L}{h_{eff}} \tag{2.90}$$

The α value is the same as specified previously for the toe crushing strength calculation. The length of compression zone d is assumed to be $0.1L$ (see Eq. 2.89).

In EC6, the rocking strength is calculated as

$$P_{CE}e = \frac{P_{CE}L}{2}\left(1 - \frac{f_a}{f_m'}\right) \tag{2.91}$$

That is, $e = \frac{L}{2}\left(1 - \frac{f_a}{f_m'}\right)$. By equating Eq. 2.91 to the moment due to the lateral load V_r x h_{eff}, the lateral resistance of the wall may be expressed as

$$V_r = \frac{P_{CE}L}{2h_{eff}}\left(1 - \frac{f_a}{f_m'}\right) \tag{2.92}$$

The hysteretic energy dissipated in a typical rocking mode response is generally small as shown in the test results (Erbay and Abrams 2002) of Fig. 2.41. There is low energy dissipation in the tests. However, when the damage is concentrated in a bed-joint and significant vertical loads are present, high energy dissipation is possible (Magenes and Calvi 1997). When vertical loads are relatively low, the shaking table tests on brick masonry walls (Magenes and Calvi 1994) show that rocking and bed joint sliding typically take place together. The uniaxial rocking hysteresis model shown in Fig. 2.41 is used to represent the rocking behavior. One can observe from the figure that this model assumes zero energy dissipation. The rocking strength in Fig. 2.41 is calculated from Eqs. 2.89 and

2.92. The stiffness, K_e, is taken as the wall elastic stiffness discussed Section 2.4.2, and the post-elastic tangent stiffness shown in Fig. 2.41 is approximately zero (i.e., constant strength). However, the test results (Magenes and Calvi 1997) show significant post-elastic tangent stiffness and increasing lateral strength after the rocking strength V_r is reached.

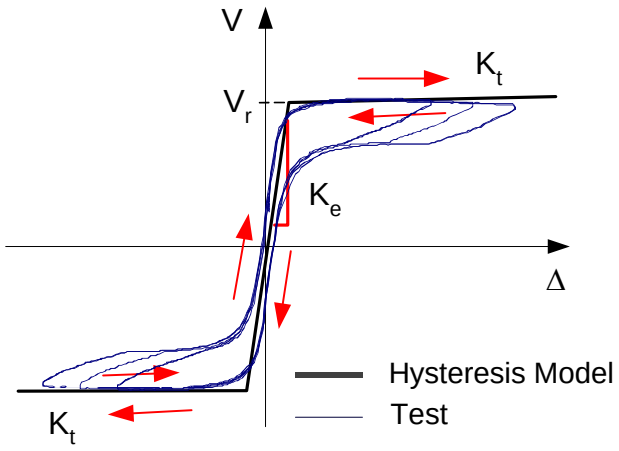

Figure 2.41: Load history for masonry wall test (Erbay and Abrams 2002) and the assumed uniaxial rocking hysteresis model.

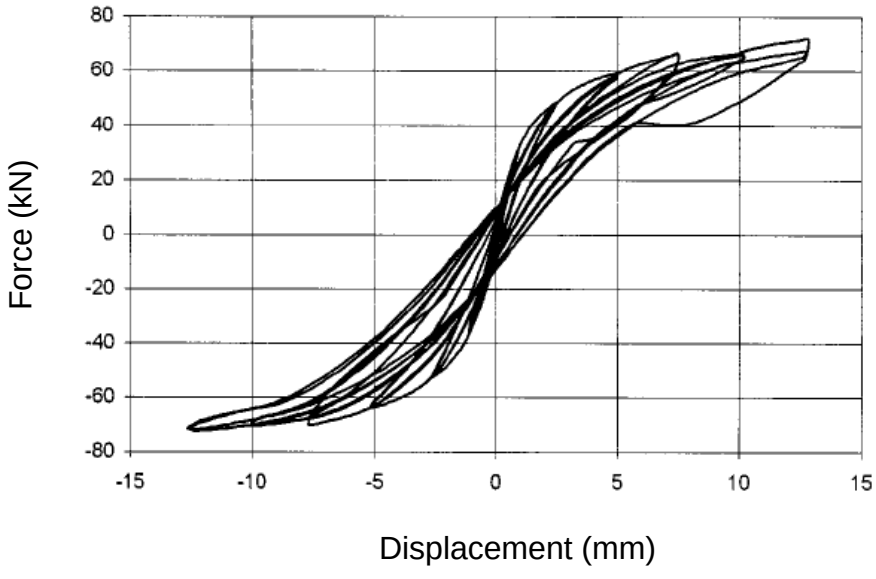

Figure 2.42: Example of rocking response of simple piers (Magenes and Calvi 1997).

2.4.4 Flange effects

FEMA 356 (ASCE 2000) recommends strength consideration of flange effects in masonry walls, when the following three conditions are satisfied: 1) The face shells of hollow masonry units are removed and the intersection is fully grouted; 2) Solid units are laid in running bond, and 50% of the masonry units at the intersection are interlocked; and 3) Reinforcement from one intersecting wall continues past the intersection a distance not less than 40 bar diameters or 24 inches. Flange effects increase the in-plane strength and stiffness of shear walls. The influence of the orthogonal walls acting as flange elements is generally different in tension than in compression. This influence is also a function of the load level and any nonlinearity in the wall components. When loaded in significant tension, flexural cracking is apt to occur. In this case, the orthogonal wall may contribute significantly to the rocking resistance, but otherwise will tend to be less effective than if it is placed in compression. When loaded in compression, the orthogonal wall will likely provide a significant increase in the toe crushing strength. At the present time (December 2002), there is little quantitative data on flange effects in masonry walls. FEMA 356 suggests that the flange effect should be considered only where the resulting flange element is placed in compression, and that the effective flange width on each side of an in-plane wall shall be take as the lesser of six times the thickness of the in-plane wall, half the distance to the next wall, or the actual width of the orthogonal wall. Flange effects are modeled in this work by assuming an in-plane wall thickness equal to the total width of the effective flange at the location of the orthogonal wall.

2.4.5 Strength associated with a multiple story failure mode involving damage within the lintel beams

Section 2.4.3 discusses the strength and hysteresis behavior based on pier type collapse mechanisms. However, in some cases the maximum strength of a wall may be governed by a mode of failure involving substantial damage within the lintel beams along

with a multiple story pier failure type mechanism. The hypothetical wall shown in Fig. 2.43 is chosen as an example of this failure mode. A specific example involving this failure mode is discussed in Chapter III. The current code and guideline documents do not give any guidance on the influence of damage within the lintel beams on wall strengths. Figure 2.43 (b) illustrates a preliminary multiple-story rocking model developed in this work to account for this potential type of failure. This model may be located at any position within a masonry wall (for example, position A, B or C of the wall shown in Fig. 2.43(a)). The pier may be flanged or unflanged, with the flange effects being handled in a fashion similar to that discussed in the previous section.

The wall shear strength in the above multiple-story rocking model may be determined as follows. The uniform vertical loads (f_{a1} and f_{a2}), determined from the distributed gravity loads from each floor plus the lumped wall self-weight, increase the shear rocking strength as discussed in Section 2.4.3. However, the vertical shear forces (V_{a1}, V_{a2}, V_{b1} and V_{b2}) and moments (M_{a1}, M_{a2}, M_{b1} and M_{b2}) from the connected lintels also affect the collapse behavior of the pier. The maximum moment resistance from the lintel shown in Fig. 2.44 is calculated based on flexural cracking as

$$M_{lintel} = \frac{f_t \cdot h_{eff} \cdot t}{6} \tag{2.93}$$

where,

h_{eff} = effective height of lintel

t = thickness of lintel

Equation 2.93 is expected to provide a lower-bound estimate of the contribution of the lintel beams to the strength.

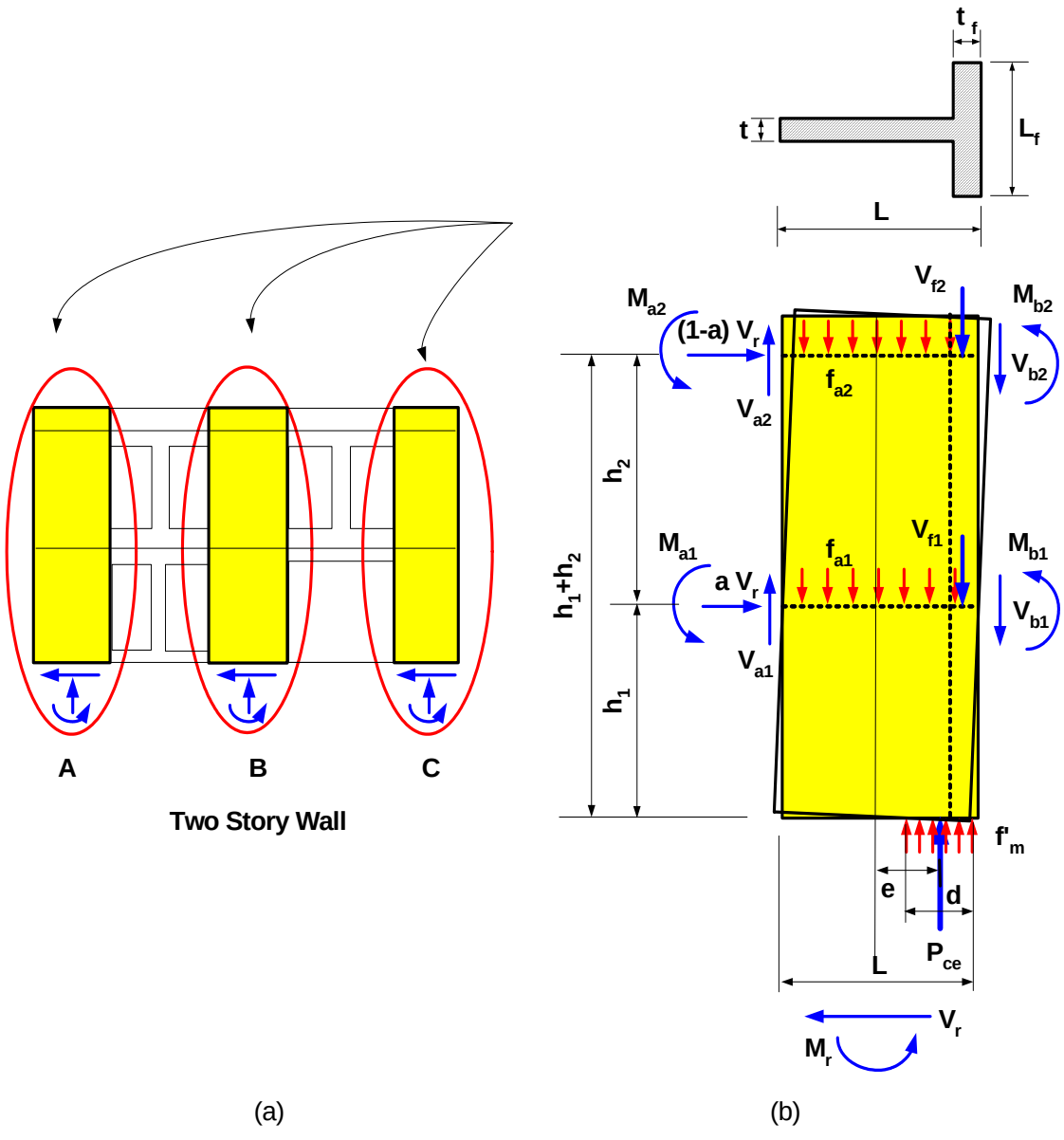

Figure 2.43: Assumed free body diagram of a two-story pier associated with a multiple-story rocking failure.

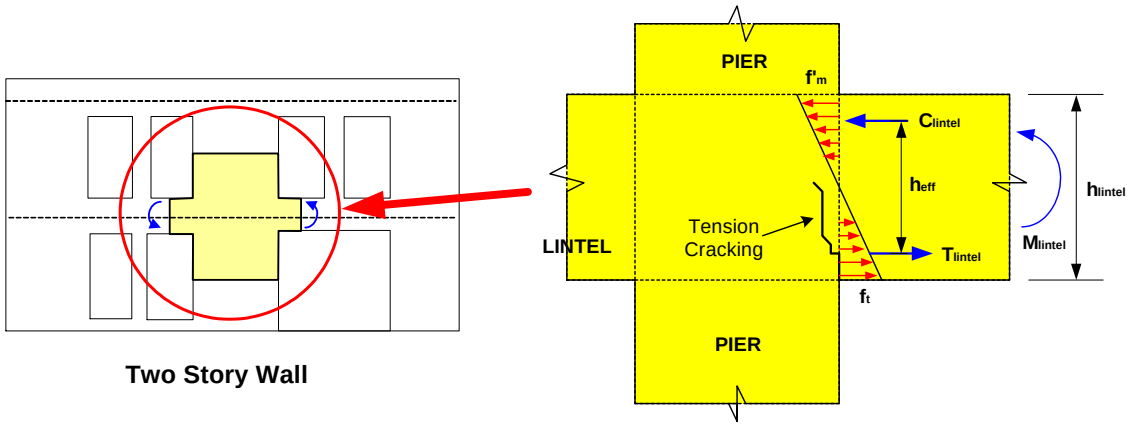

Figure 2.44: Assumed stress distribution at the interface between a lintel and a pier, based on an idealized flexural cracking model.

When the flange of the pier is under compression, the rocking shear strength associated with the above model is

$$V_r = \frac{P_{ce}e - (V_a + V_b)\frac{L}{2} - V_f\left(\frac{L}{2} - \frac{t_f}{2}\right) + M_a + M_b}{h_1 + h_2 - ah_2} \tag{2.94}$$

where,

a = lateral load distribution factor, 0 < a < 1 (see Fig. 2.43)

f_{a1} = uniform load from second floor and upper wall weight

f_{a2} = uniform load from roof floor and upper wall weight

$f_a = f_{a1} + f_{a2}$

f_{f1} = compressive uniform load from second floor and upper wall weight at the flange area

f_{f2} = compressive uniform load from roof floor and upper wall weight at the flange area

V_{a1}, V_{a2} = shear force from left lintel at the second floor and roof levels

V_{b1}, V_{b2} = shear force from right lintel at the second floor and roof levels

$V_a = V_{a1} + V_{a2}$

$V_b = V_{b1} + V_{b2}$

A_{n_flange} = area of flange

$V_{f1} = f_{f1} A_{n\_\text{flange}}$ = shear force from the flange at the second floor level

$V_{f2} = f_{f2} A_{n\_\text{flange}}$ = shear force from the flange at the roof level

$V_f = V_{f1} + V_{f2}$

M_{a1}, M_{a2} = ultimate moment from left lintel at second floor and roof levels, calculated from Eq. 2.93

M_{b1}, M_{b2} = ultimate moment from right lintel at the second floor and roof levels, calculated from Eq. 2.93

$M_b = M_{b1} + M_{b2}$

$M_a = M_{a1} + M_{a2}$

$P_{ce} = f_a L t + V_a + V_b + V_f$ = lower bound of vertical compressive force

$e = 0.5\left(L - \frac{P_{ce}}{f_m'}\right)$

When the flange is in tension, its contribution is neglected (i.e., it is assumed that $V_f = 0$), and thus Eq. 2.94 simplifies to

$$V_r = \frac{P_{ce} e - (V_a + V_b)\frac{L}{2} + M_a + M_b}{h_1 + h_2 - a h_2} \tag{2.95}$$

The calculation of V_a and V_b in Eqs. 2.94 and 2.95 generally requires considerable judgement. It is recommended that these values may be calculated by summing the downward shear contribution from the lintel beams due to gravity load with the upward or downward shear due to lateral loading. The lintel beam shears due to lateral load may be estimated from a free-body diagram of the lintel beams, with the lintel end moments calculated per Eq. 2.93.

For the two-story example illustrated in Fig. 2.43, the shear strength contributions

are taken as V_r for the bottom story and *(1-a)* V_r for the top story.

2.4.6 Calculation of individual component stiffnesses within a parallel spring wall idealization

Each of the wall components shown in Fig. 2.28 (b) is represented by a separate model. This analysis idealization is based on the assumption that the wall can be subdivided into independent isolated components, and that these components act in parallel within each story and in series from story-to-story. As noted at the beginning of Section 2.4, the purpose of using a separate model for each of the components is to obtain a more quantitative representation of a perforated wall. However, the total lateral stiffness per strength of materials models and Eq. 2.74 is typically estimated poorly as discussed in Section 2.4.2.3. Therefore, the elastic stiffness of each wall component calculated from the strength materials type models is modified by a single scale factor such that the total lateral stiffness of the wall is the same as that from the plane stress analysis approach discussed in Section 2.4.2.2. The overall procedure for calculating the elastic stiffness contribution from each of the components of a perforated wall is summarized in Fig. 2.45.

In the parallel spring model, the effect of the nonlinearity of each component, i.e, the damage patterns: diagonal cracking, bed joint cracking, rocking, and toe crushing discussed in Section 2.4.3, is assumed to be localized within each component. The contributions of the other components are assumed to not be affected by the nonlinearity of a given component.

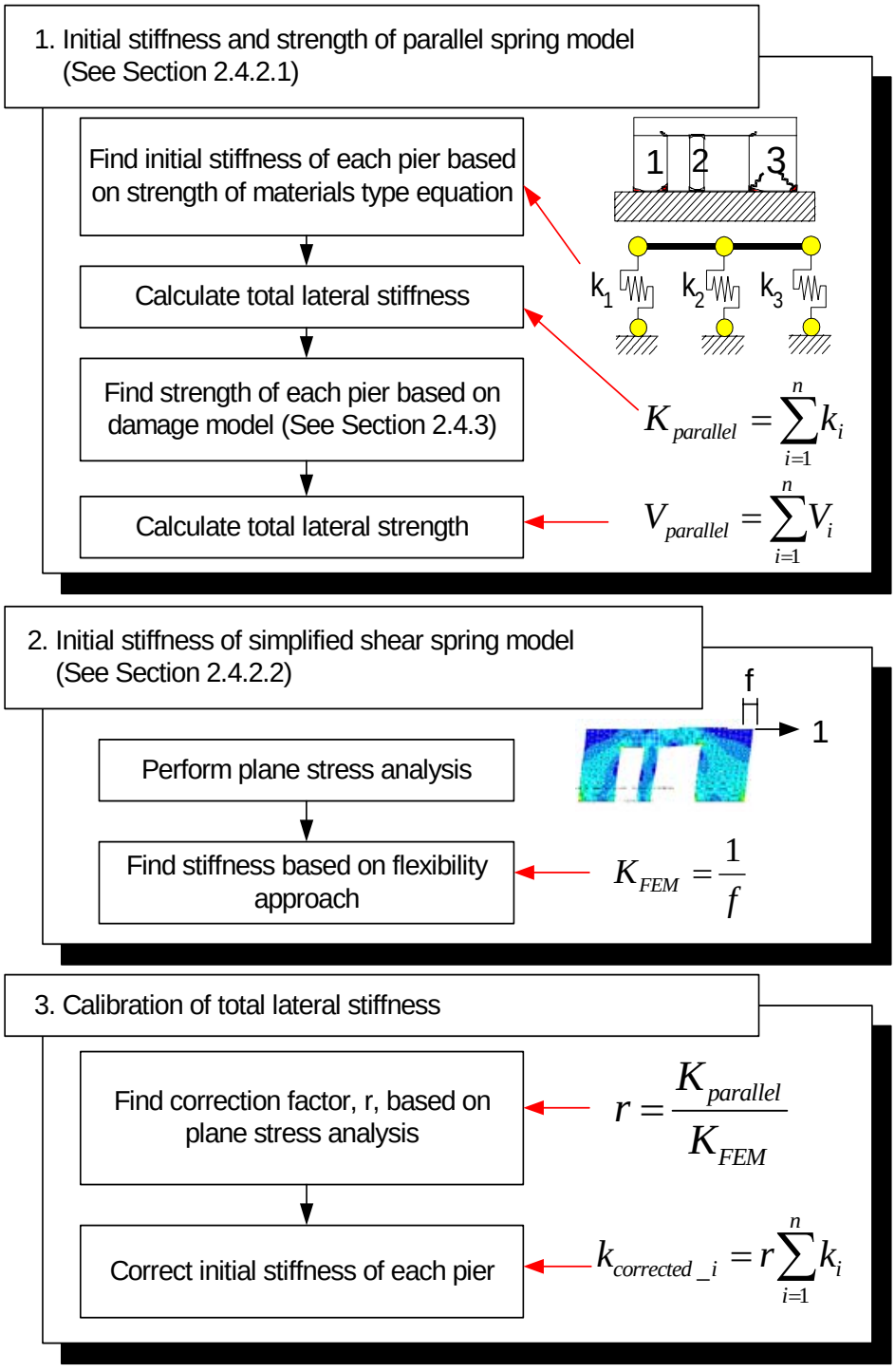

Figure 2.45: The procedure of calculating the elastic stiffness contribution of the each components of a perforated wall.

2.4.7 Modeling of out-of-plane walls

FEMA 356 (ASCE 2000) suggests that the out-of-plane contributions from unreinforced masonry walls shall not be included in the overall modeling of the building. However, the contributions of the out-of-plane walls to the stiffnesses and strength of reinforced masonry structures should be considered. The stiffness and strength contributions from out-of-plane walls should be calculated in general based on these walls acting as isolated components spanning between floor levels, and/or spanning horizontally between the in-plane walls (ASCE 2000). The relative magnitude of these two contributions depends on the width versus the height of the walls, the anchorages between the diaphragm and out-of-plane walls, and the rigidity of the flexible diaphragm. The effects of the out-of-plane walls spanning in the horizontal direction between adjacent in-plane walls is often small compared to the effects of the out-of-plane walls spanning in the vertical direction between the diaphragms.

Figure 2.46 shows an example of out-of-plane wall modeling. The spanning of the out-of-plane-walls between the diaphragm levels is modeled using the shear wall element discussed previously. The deflection at the center of the flexible diaphragm in the direction of the ground motion shown in the figure is associated with the out-of-plane deformation of walls C and D. The DOFs of the out-of-plane walls are connected to the central DOF of the diaphragm element in the proposed simplified three-dimensional model. The out-of-plane effects from walls C and D may be modeled using a single element for convenience.

The out-of-plane behavior of walls C and D is considered as uncoupled with the in-plane behavior of these walls. That is, the influence of in-plane deformations in walls C and D on the out-of-plane response of these walls, and the influence of the out-of-plane bending of these walls on their in-plane response, is neglected. Also, any coupling between the behavior of walls C and D acting as flange elements for the in-plane walls with the above in-plane and out-of-plane behavior is not considered.

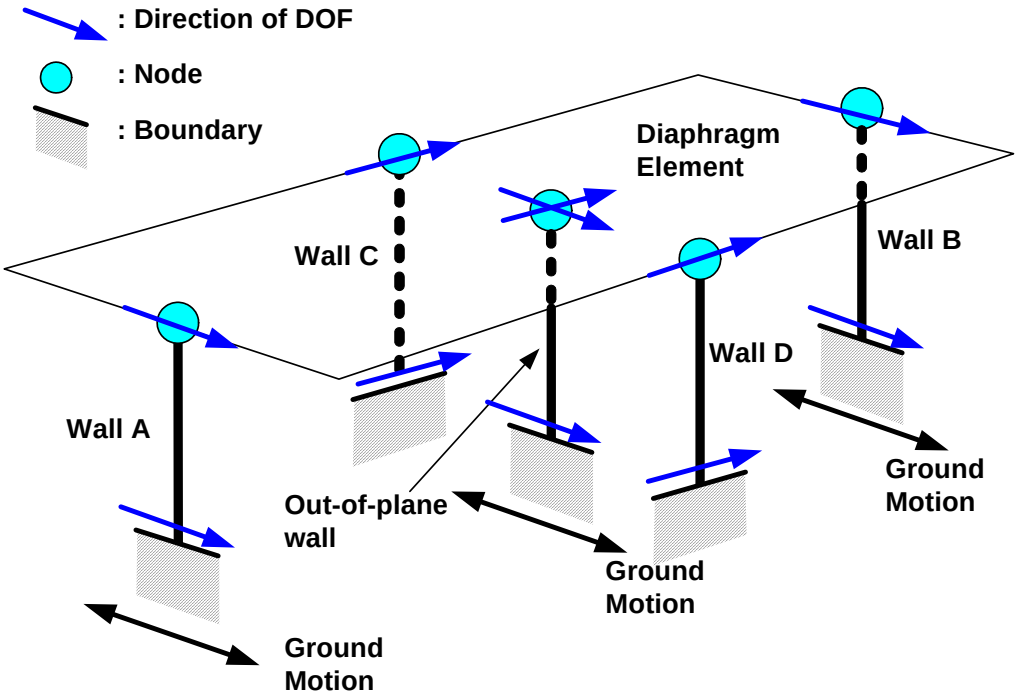

Figure 2.46: Three dimensional model with one diaphragm, four in-plane and one out-of-plane walls.

In the modeling of out-of-plane walls, it is assumed that the deformation of the anchorages is negligible and that no gaps form between the out-of-plane wall and the diaphragm structure. If there is significant deformation of the anchorages, a appropriate spring element can be inserted between the wall and diaphragm element to represent the connection. The presence of deformations between the out-of-plane walls and floor/roof diaphragms can significantly reduce the performance of the out-of-plane walls (Paquette et al 2001).

If the out-of-plane walls are perforated, the calculation of the stiffness and strength is difficult due to the complex behavior. The general calculation of the out-of-plane stiffness and strength in these cases is not addressed directly in this research. A flexibility based approach similar to that employed in this work for calculation of the in-plane wall stiffnesses could be used as a potential method of determining the initial elastic out-of-

plane stiffness of these types of walls.

2.5 Summary

Details of the simplified three dimensional MDOF modeling approach proposed in this work are presented in this Chapter. The essential analytical components of this approach, i.e., the structural elements and procedures for calculation of the associated stiffnesses and strengths for nonrigid diaphragms and shear walls, are discussed.

The diaphragm bending behavior of nonrigid diaphragms is assumed to be similar to that of a horizontal plate girder. The flanges of the diaphragms resist the flexure and the webs of the diaphragms are considered to carry the shear induced by the horizontal forces. It is found that the bending behavior of typical diaphragms in the types of buildings considered in this research is dominated by shear. Generally, the diaphragms also provide coupling between the walls of the structure by acting approximately as shear panels, subjected to shear raking deformations.

The proposed diaphragm element consists of six DOFs: three DOFs in the x direction and three in the y direction. An equivalent shear model is developed to provide a useful and practical characterization of the diaphragm properties, and to calculate the stiffness of the various types of horizontal wood and metal deck diaphragms in accordance with FEMA 273 (FEMA 1997a), FEMA 356 (ASCE 2000a) and the SDI manual (SDI 1995). The nonlinear hysteresis model specified for diaphragms accounts in general for stiffness degradation, strength deterioration and pinching characteristics.

Two concepts for simplified wall modeling, one using a single element for each wall and the other using multiple component elements for each wall, are discussed. A flexibility based approach, based on elastic plane stress finite element analysis, is recommended for accurate calculation of the initial elastic wall stiffnesses in each of these approaches. The lateral shear strengths of in-plane walls are calculated in each of the

above approaches by summing the strength contributions from each of the wall components. If a single element approach is utilized to model a complex perforated in-plane wall, the post-elastic hysteresis response must be specified largely based on judgment. For these cases, the wall may be modeled explicitly by separate component models connected in parallel within each story, and connected in series from story-to-story. Strength and hysteresis models for unreinforced masonry walls from FEMA 356 (ASCE 2000a) and EC6 (CEN 1995) are discussed and recommendations are provided for use with the proposed three-dimensional MDOF modeling approach. The strength and hysteresis models for the walls are based on the limit states of pier rocking, bed-joint sliding, toe crushing and diagonal tension failure. Also, a preliminary model is developed that accounts for a potential multiple-story pier rocking mode of failure involving damage within the adjacent lintel beams.

CHAPTER III

SEISMIC ASSESSMENT OF A TWO-STORY LOW-RISE MASONRY BUILDING WITH FLEXIBLE DIAPHRAGMS

3.1 Introduction

This chapter addresses the seismic assessment of a two-story historic building located in Gilroy, California, using the simplified three-dimensional analysis approach discussed in Chapter II. This building, referred to herein as the Gilroy Firehouse, was previously studied in detail by Tena-Colunga and Abrams (1992a). In (Tena-Colunga and Abrams 1992a), a two-dimensional discrete linear-elastic MDOF dynamic model was developed and analyses were performed. The Gilroy Firehouse is selected for further study in this work since its detailed as-built information is available and its strong motion data was recorded during the Loma Prieta earthquake, which struck the San Francisco Bay Area on October 17, 1989. Three motions at the ground floor slab and three motions at the roof level were recorded at this building during the Loma Prieta earthquake. The building withstood the ground shaking with little damage. Although the firehouse is located in California, its structural system is similar to typical essential buildings in Mid America. Therefore, the study of its survival during the Loma Prieta earthquake can enhance the understanding of essential URM buildings in Mid America.

The goals of this study are:

1. To demonstrate the use of the suggested simplified three-dimensional MDOF approach discussed in Chapter II for a representative multiple story building with multiple floor and roof diaphragms.

2. To investigate the qualities and limitations of the modeling approach discussed in Chapter II by comparing calculated and measured results.
3. To investigate reasons why the firehouse withstood the ground shaking with little damage.

These goals are accomplished by conducting three-dimensional linear and nonlinear analyses of the Gilroy Firehouse subjected to the horizontal motions in two orthogonal directions measured at its ground floor slab. Section 3.2 describes the building, the observed damage, and the measured motions during the earthquake. Section 3.3 explains the modeling of the building and the calculation of the wall and diaphragm stiffnesses and strengths based on the best available procedures as captured within the three-dimensional analysis approach discussed in Chapter II. Section 3.4 then presents linear analysis results based on the above properties and compares the calculated responses to measured data.

The responses at two of the three monitored degrees of freedom are predicted reasonably well by the model developed in Section 3.3. However, it is found that the correlation between the calculated and measured results at one of the monitored degrees of freedom can be improved by modifying the roof diaphragm flexural stiffness in one direction. Therefore, an additional flexural stiffness contribution is proposed in one direction at the roof diaphragm level. Potential reasons for this increased stiffness are discussed. Section 3.5 discusses the linear analysis results for the above modified model of the building.

Section 3.6 presents nonlinear analysis results using the wall strengths calculated with the procedures from Chapter II. Since the physical structure sustained little damage during the Loma Prieta earthquake, an accurate three-dimensional nonlinear analysis model should also exhibit only minor damage. Such is the case in the model per Section 3.3 with the exception of the weakest wall of the building. Whereas minor damage was observed in this wall within the physical structure, the model per Section 3.3 predicts substantial nonlinearity in this wall. Therefore, additional analyses are conducted to deter-

mine the strength required for the weakest wall such that only a modest amount of damage is predicted.

One option that is often considered in the seismic rehabilitation of flexible diaphragm structures such as the Gilroy Firehouse is the stiffening and/or strengthening of the diaphragms. Also, the diaphragm flexibility is a significant variable considered in this research. Therefore, a useful application of the proposed three-dimensional approach is for analysis of the sensitivity of building responses to variations in the diaphragm flexibility. Section 3.7 presents the results of sensitivity analyses in which the diaphragm stiffnesses of the Gilroy Firehouse are varied.

3.2 Description of the Structure

The Gilroy Firehouse, shown in Fig. 3.1, is a box-type structure with a lateral force resisting system composed of unreinforced masonry brick walls together with flexible wood diaphragms. The building has one interior masonry wall, as shown in Fig. 3.2. The original structure was constructed in 1890 and survived the 1906 earthquake. The portion of the structure to the north of the central wall was added after 1906. The central wall and the exterior walls on the west and north side of the structure have relatively few openings compared to the exterior walls on the south and east side of the building. Figures 3.3 and 3.4 show schematic elevations of the south and east walls. A one in. mortar joint exists between the new portion of the east and west walls and the original structure. Three interior wood stud load bearing walls span between the second floor and roof diaphragms north of the central wall as shown in Fig. 3.2.

Detailed plans and elevations for the firehouse are provided in Appendix B. Key attributes of the structural system are described below.

The structure has plan dimensions of 40.1ft x 62.4 ft as shown in Fig. 3.2. The total height of the structure is 29.17 ft as shown in Figs. 3.3 and 3.4. All the walls except

for the south wall are three wythe 12 in thick unreinforced brick walls. The south wall is three wythe and is 12 in thick at the window openings, but is to 16 to 17 in thick at the exterior piers.

The south diaphragms are almost square whereas the north diaphragms have an aspect ratio of approximately two. The second floor diaphragms consist predominantly of a 1/2 in. plywood overlay on 1 in. by 4 in. timbers running in the diagonal direction, nailed to timber joists (see Fig. 3.2). A small area of the diaphragm on the northwest corner of the second floor has 1 in tongue and groove sheathing over the diagonal timbers. The south and north roof diaphragms have a small slope of 1:85 and 1:40, respectively. They intersect the central wall at 25 in below the top of the wall, and they intersect the north and south walls at 31 in below the top of the wall. The south roof diaphragm consists of built-up roof trusses under 1 in.in. by 4 in. timbers running in the diagonal direction. The north diaphragm is composed of timber sheathing running in the N-S direction. The roofing consists of asphalt sheets totaling 3 in in thickness.

The diaphragms and the walls are tied with 3/4 in. diameter steel rods anchored in the outside wythe of the walls by a hook. These ties are nominally placed every 5 ft - 1 in at the east and west walls and every 6 ft at the south, center and north walls.

The first floor slab is 36 in thick (Tena-Colunga and Abrams 1992a). This large thickness is a result of the ground floor being raised a number of times to match the increasing grade elevation of the street. The building is supported on spread footings, the dimensions and depth of which are not available. Although no specific information is available pertaining to the type of soil, Tena-Colunga and Abrams (1992a) infer that the site has a natural stiff soil based on inspection of the response spectra for the recorded ground motions.

Figure 3.1: Firehouse at Gilroy, CA.

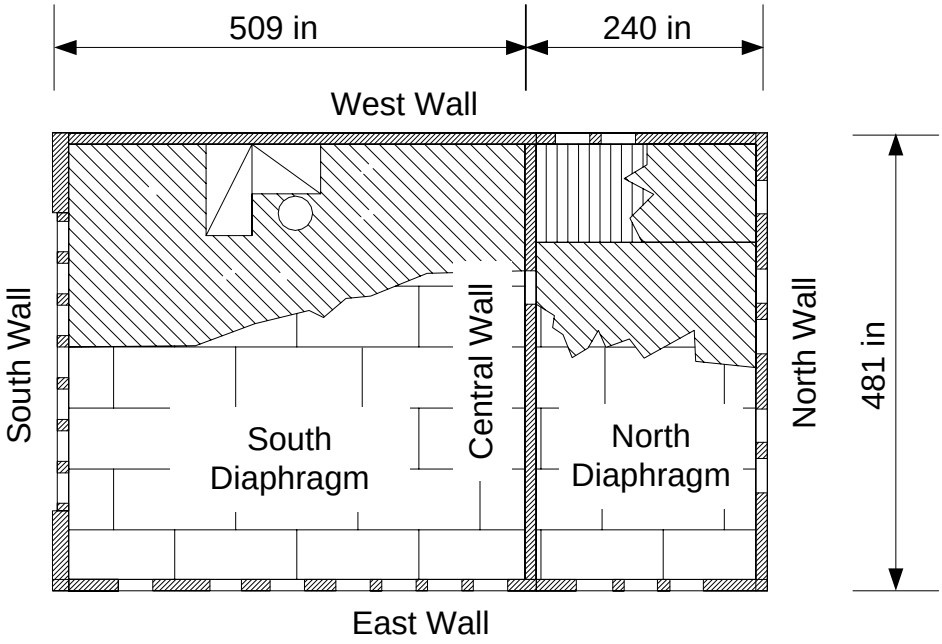

Figure 3.2: Second floor plan.

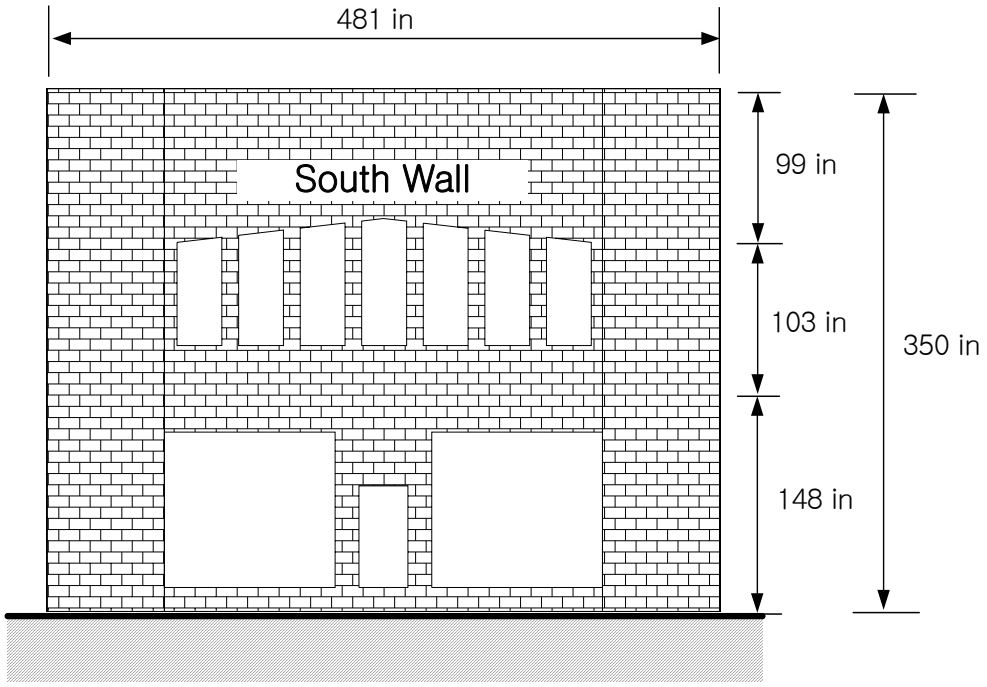

Figure 3.3: South wall.

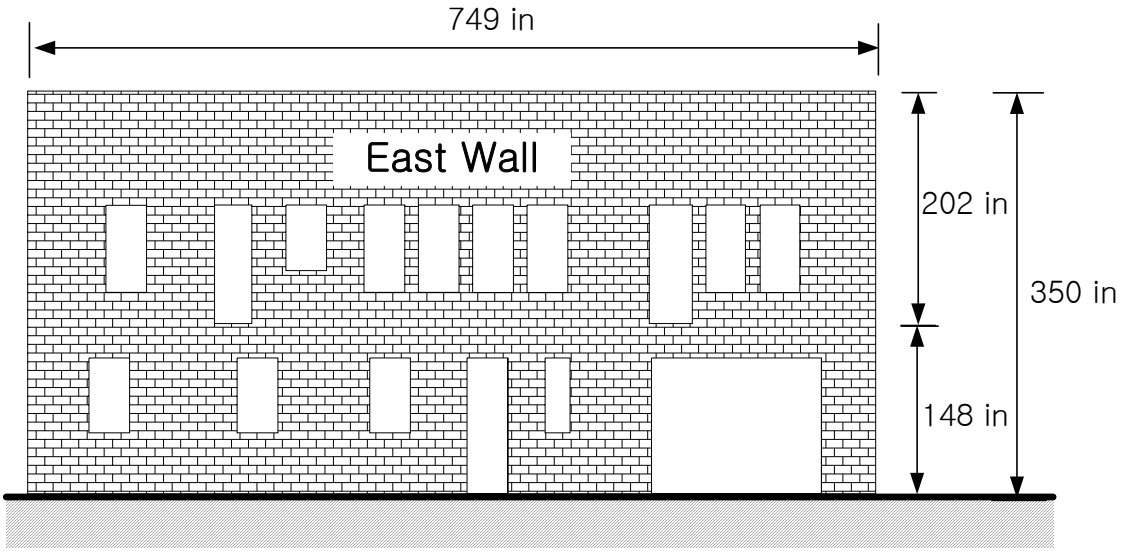

Figure 3.4: East wall.

Observed damage

During the earthquake, the building suffered little damage. The observed damage included a few cracks at the top and bottom piers between window openings in the south wall, as shown in Fig. 3.5, and initial shear cracks at the south and north corners of the second story in the east wall. However, it is possible that the walls may have experienced mild damage that could have not been observed. The small level of damage observed suggests that the structure responded primarily in an elastic fashion during the earthquake (Tena-Colunga and Abrams 1992a).

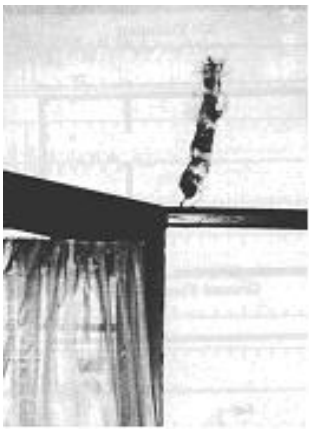

Figure 3.5: Damage on the southeast corner of south wall. (Tena-Colunga and Abrams 1992a).

Recorded motions

Figure 3.6 shows the locations and orientations of six sensors placed on the Gilroy Firehouse via the California Strong Motion Instrumentation Program (CSMIP). Three sensors, corresponding to the N-S, vertical and E-W motions, were placed on the ground floor slab just outside the large opening in the bottom level of the east wall. Also, the horizontal motion in the E-W direction on the south diaphragm adjacent to the middle of the central wall, and the E-W and N-S motions at the middle of the south roof diaphragm were recorded.

The measured ground floor slab horizontal motions in the N-S and E-W directions are shown in Figs. 3.7 and 3.8. It should be noted that the roof records were not synchronized with the ground floor records (Tena-Colunga and Abrams 1992a). The roof records are 1.78 sec out-of-phase with the ground floor records. This shift is can be observed by comparing the motion adjacent to the central wall at the roof level (U_4), shown in Fig. 3.9, to the ground floor slab motions.

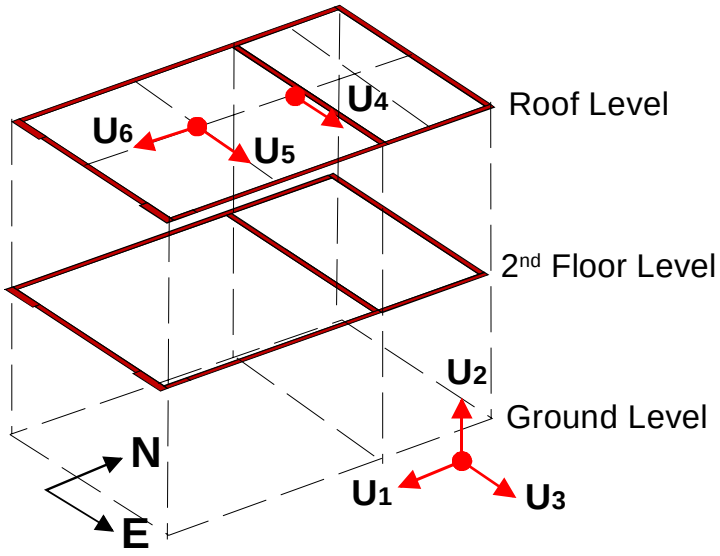

Figure 3.6: Location of sensors at the firehouse at Gilroy.

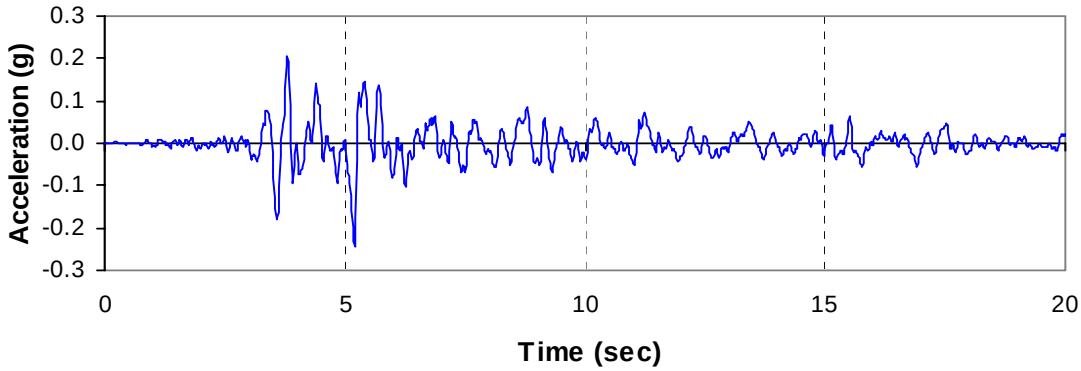

Figure 3.7: N-S direction acceleration at the ground floor slab (U_1), PGA = 0.24g at 5.2 sec.

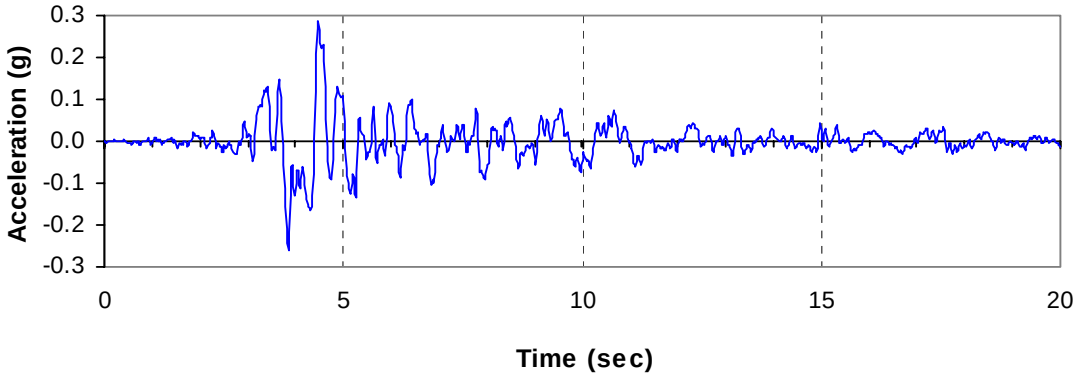

Figure 3.8: E-W direction acceleration at the ground floor slab (U_3), PGA = 0.29g at 4.48 sec.

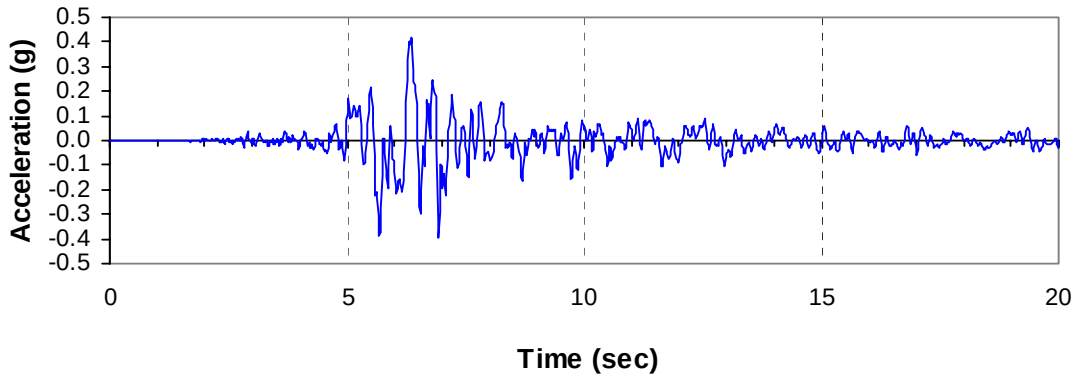

Figure 3.9: E-W direction acceleration adjacent to the central wall (U_4).

3.3 Base model (Simplified three dimensional analysis)

This section describes the application of the proposed simplified three-dimensional modeling approach of Chapter II to the Gilroy Firehouse. Section 3.3.1 discusses details of the flexible diaphragm models for this building. Section 3.3.2 presents the calculation of the stiffness and strength of the in-plane walls. Section 3.3.3 discusses the calculation of the mass properties. Section 3.3.4 explains the damping assumptions used for this example.

Figure 3.10 shows an overall simplified three-dimensional MDOF model of the

building. Each story is modeled in a fashion similar to that shown in Fig. 1.2 except that building has two stories.

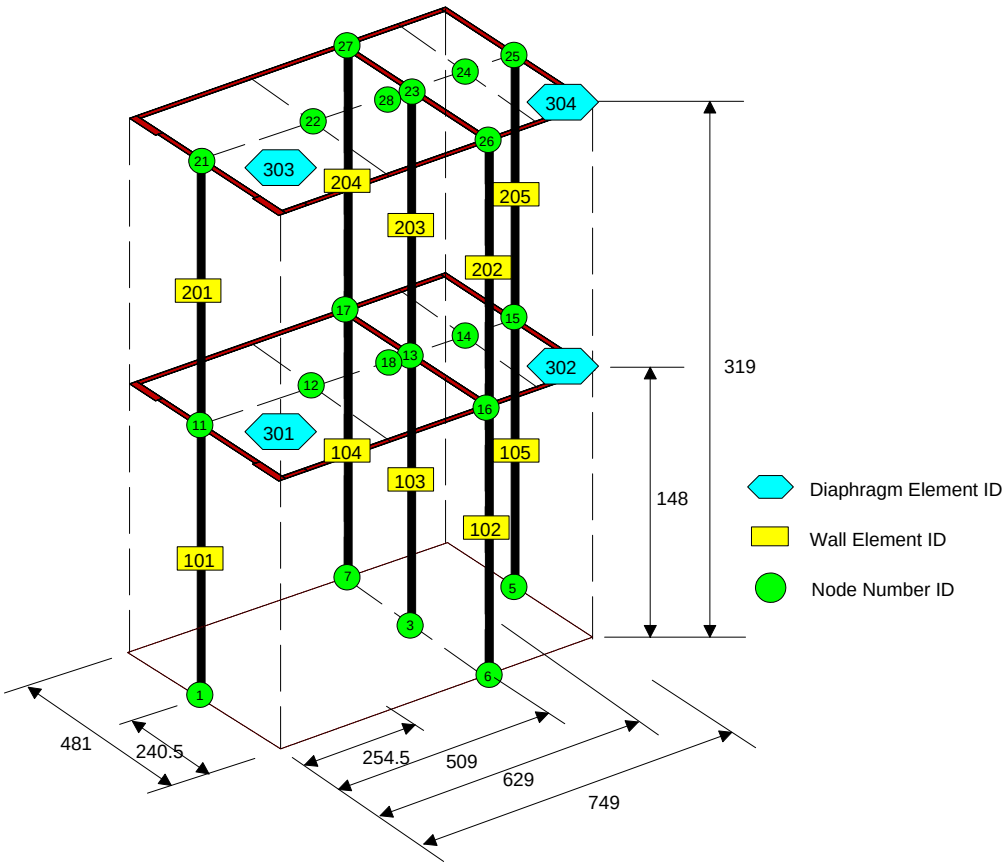

Figure 3.10: Three-dimensional analysis model of Gilroy firehouse.

The diaphragm elements 301 and 303 represent the south diaphragms at the second floor and roof, respectively. Diaphragm elements 302 and 304 represent the north diaphragms at the second floor and roof, respectively. As discussed in Section 1.4.3, each of the nodes in this model have only one degree of freedom. The wall degrees of freedom are associated with in-plane wall displacements. Separate nodes, each with one degree of freedom capture the diaphragm displacements associated with out-of-plane motion of the walls.

3.3.1 Diaphragm modeling

Section 3.3.1.1 presents the diaphragm stiffness values obtained using the FEMA 273 and 356 procedures detailed in Section 2.3.5. The diaphragm stiffnesses estimated by Tena-Colunga and Abrams (1992a) are compared to these stiffnesses in Section 3.3.1.2. Section 3.3.1.3 draws conclusions regarding the above stiffnesses and explains the rationale for the diaphragm stiffness values used in this research.

3.3.1.1 Equivalent shear stiffness calculation based on FEMA 273 and 356

Section 2.3.5.4 explains how to calculate the equivalent shear modulus (stiffness) of flexible diaphragms for the proposed 3D modeling approach. Table 2.2 summarizes the shear stiffness values (G_d) specified for various diaphragm configurations in FEMA 273 and 356. Based on the assumption that the diaphragm responses are dominated by shearing type deformations, the equivalent shear moduli for the proposed modeling approach (G_e) may be calculated from the FEMA273 and 356 stiffnesses using Eqs. 2.61 and 2.62. Given a computed G_e value, the diaphragm bending deflection for specified lateral loading in one direction is obtained using Eqs. 2.54. Therefore, G_e can be used as a common measure of the diaphragm stiffnesses predicted by the different approaches.

Table 3.1 lists the characteristics of the different diaphragms within the Gilroy Firehouse, and gives the corresponding G_d values from FEMA 273 and 356 as well as the resulting $G_e t$ values based on Eqs. 2.61 and 2.62. The joists within the second floor of the building are generally supported on a ledger beam on two sides of the diaphragm, and are anchored within wall pockets on the other two sides. Detailed information regarding blocking within the diaphragms is not available. Four different values from FEMA 273 and 356 are reported for these diaphragms, depending on the interpretation of whether they are blocked and/or chorded.

Table 3.1: Equivalent shear modulus, G_e, calculation using FEMA 273 and FEMA 356.

Diaphragm	Diaphragm categorization	FEMA 273			FEMA 356	
		$G_{d\_FEMA273}$ (kips/in)	G_et (kips/in)		$G_{d\_FEMA356}$ (kips/in)	G_et (kips /in)
			EW	NS		
2nd floor south diaphragm (1/2" Plywood over 1" Diag. Sheathing)	Blocked, chorded	1,800	380	533	18	9
	Unblocked, chorded	900	190	267	9	5
	Blocked, unchorded	700	148	207	7	4
	Unblocked, unchorded	500	105	148	5	3
Roof south diaphragm (Built-up Roofing Over 1xDiag. Sheathing)	Single diagonal sheathing, chorded	500	105	148	5	3
2nd floor north diaphragm (1/2" Plywood over 1" Diag. Sheathing)	Blocked, chorded	1,800	3,623	56	18	9
	Unblocked, chorded	900	1,811	28	9	5
	Blocked, unchorded	700	1,409	22	7	4
	Unblocked, unchorded	500	1006	16	5	3
Roof north diaphragm (1 x Straight Sheathing)	Straight sheathed diaphragm with or without chords	200	403	6	2	1

One can observe that the comparable diaphragm stiffnesses from FEMA 273 and 356, expressed here as the equivalent shear moduli times the equivalent thickness of the diaphragm $G_e t$, are dramatically different from one another. This should not come as a significant surprise, since Section 2.3.5.2 has already discussed a number of problems associated with the FEMA 273 approach. The FEMA 356 characterization of the diaphragm stiffness is more representative of the physical response for diaphragms with relatively small aspect ratios (e.g., $L/b \leq 3$) since it is based essentially on an idealized beam that is rigid in flexure and flexible only in shear. Based on the FEMA 356 model, equal values are obtained for $G_e t$ in both the E-W and N-S directions. However, the FEMA 273 characterization, which is based essentially on Euler-Bernoulli beam theory, predicts that $G_e t$ would differ significantly in the two orthogonal directions for the North diaphragms.

3.3.1.2 Equivalent shear stiffness calculation based on (Tena-Colunga and Abrams 1992a)

In (Tena-Colunga and Abrams 1992), the flexible diaphragms were represented by elastic shear springs (K_s) as shown in Fig. 2.1(b). The stiffnesses (K_s) of the shear springs for the second floor diaphragms were determined using the APA plywood diaphragm equation (Tissell and Elliott 1997) shown in Eq. 2.48, which is based on the assumption that the diaphragm is blocked and chorded. The Young's modulus of the chord was taken as 1,700ksi (Tena-Colunga and Abrams 1992a) and the shear modulus was assumed to be 60 ksi (Tena-Colunga 1998). The detailed contributions to the flexibility and stiffness from the chord, chord splice, and nail slip were not stated by Tena-Colunga and Abrams (1992a). Specifics of the original calculations for the straight-sheathed and diagonally-sheathed roof diaphragms are also not available. However, it should be noted that the stiffness values selected for the north roof diaphragm are identical to those for the north second-floor diaphragm. The south roof diaphragm stiffness values are 0.87 to 0.88 of the south second-floor diaphragm values. Table 3.2 summarizes the diaphragm stiffnesses K_d

from Tena-Colunga and Abrams (1992a) along with the corresponding $G_e t$ values associated with the proposed 3D modeling approach.

The diaphragm stiffness (K_d) in Table 3.2 is calculated based on the fact that the elastic shear springs shown in Fig. 2.1(b) act in parallel (i.e., $K_d = 2K_s$). Based on Eq. 2.15, the equivalent shear stiffness can be expressed in terms of Tena-Colunga and Abrams's K_d values as

$$G_e t = \frac{hK_d}{4b} \quad \text{and} \quad G_e t = \frac{bK_d}{4h} \tag{3.1}$$

for the N-S and E-W directions, respectively, where:

b = 509 in /2 for south diaphragm and 240 in / 2 for north diaphragm (See Fig. 2.3)

h = 481 in /2 (See Fig. 2.3)

Table 3.2: Summary of shear spring stiffness (K_d) and equivalent shear stiffness ($G_e t$) for the discrete model of the Gilroy firehouse (Tena-Colunga and Abrams, 1992a).

Modeling Direction	Diaphragm	Stiffness, K_d (kips/in)	$G_e t$ (kips/in)
E-W	2nd floor south diaphragm	72.82	19
	2nd floor north diaphragm	117.28	15
	Roof south diaphragm	63.66	17
	Roof north diaphragm	117.28	15
N-S	2nd floor south diaphragm	77.06	18
	2nd floor north diaphragm	58.52	29
	Roof south diaphragm	67.80	16
	Roof north diaphragm	58.52	29

3.3.1.3 Discussion of diaphragm stiffnesses

The suggested values in FEMA 273 are not applicable as discussed in Section 3.3.1.1. The diaphragm stiffnesses suggested in FEMA 356 are smaller than the values estimated by Tena-Colunga and Abrams (1992a). For example, the FEMA 356 G_et values for the 2nd floor south diaphragm (ranging from 3 to 9 kips/in) are smaller than the equivalent shear stiffness (19 kips/in) from (Tena-Colunga and Abrams 1992a) (see Tables 3.1 and 3.2). Based on the analysis results reported subsequently in this chapter, it is apparent that diaphragm stiffness values similar to those selected by Tena-Colunga and Abrams are required to obtain accurate predictions of the measured building response. For this reason, the equivalent stiffnesses shown in the fourth column (N-S direction) of Table 3.2 are chosen as the diaphragm properties of the base simplified MDOF model.

The reader should note that the G_et values based on (Tena-Colunga and Abrams 1992a) are similar in the E-W and N-S directions for the south second floor and roof diaphragms. This is expected since these diaphragms are nearly square. However, G_et = 15 and 29 kips/in are obtained in the E-W and N-S directions respectively for both of the north diaphragms. For an analysis idealization in which the diaphragm response is assumed to be dominated by shearing deformations, it can be argued that a single value is appropriate for G_et for plywood diaphragms, straight sheathing diaphragms and the combination of the two based on the fundamental mechanics of the diaphragm shearing behavior (ATC 1981). For diagonally-sheathed diaphragms, the fundamental mechanics of the diaphragm response are more complex (ATC 1981), but it is apparent that beam shear models with equal values for G_et for the two orthogonal bending directions gives a reasonable coarse representation of the diaphragm bending stiffnesses. The FEMA 356 equations for these diaphragm types matches with this assumption about the behavior. The larger of the two G_et values determined from Tena-Colunga and Abrams's stiffnesses is used for the base model of the Gilroy firehouse in this work.

3.3.2 Wall modeling

All the in-plane walls of the Gilroy firehouse are perforated unreinforced masonry shear walls. The flexibility approach discussed in Section 2.4.2 is used to determine the in-plane stiffnesses of the perforated shear walls. Section 3.3.2.1 discusses the results of the plane stress analysis of the in-plane masonry walls to obtain the flexibility coefficients. Section 3.3.2.2 explains the in-plane wall stiffnesses calculated from the flexibility coefficients. Section 3.3.2.3 discusses the strength of the in-plane masonry walls based on the damage models discussed in Sections 2.4.3 and 2.4.5.

3.3.2.1 Plane stress analysis of walls

Two–dimensional isoparametric plane stress finite element analyses are used to determine flexibility coefficients for the in-plane masonry walls. The ABAQUS (HKS 1998) eight-node biquadratic plane-stress element is used for the two-dimensional finite element wall models. The elastic modulus of the wall is taken as 515ksi. The Poison's ratio for the analysis is 0.25. The deformed shapes and minimum principal stress contours (i.e., maximum compressive principal stress or minimum tensile principal stress) from these analyses for a unit load at the roof diaphragm level are shown in Figs. 3.11 to 3.15.

A unit load is applied to each diaphragm level and the corresponding displacements at the second-floor and roof levels are determined as discussed in Section 2.4.2. These computed displacements are summarized in Tables 3.3 and 3.4. The south and north portions of the east and west walls are modeled separately to account for the mortar joint between these parts (see Section 3.2), based on the assumption that the lateral deflections in each of these parts are equal but otherwise the walls are unconnected.

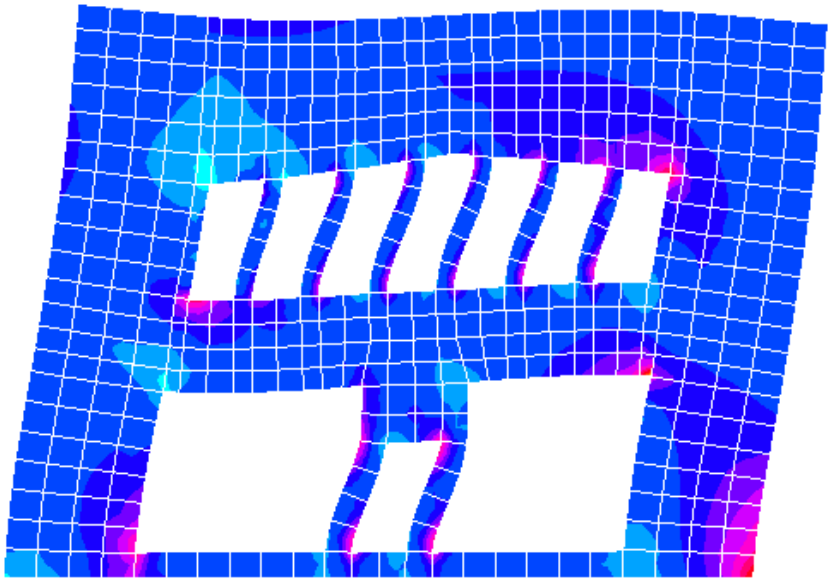

Figure 3.11: Deformed shape and minimum in-plane principal stress plot for south wall.

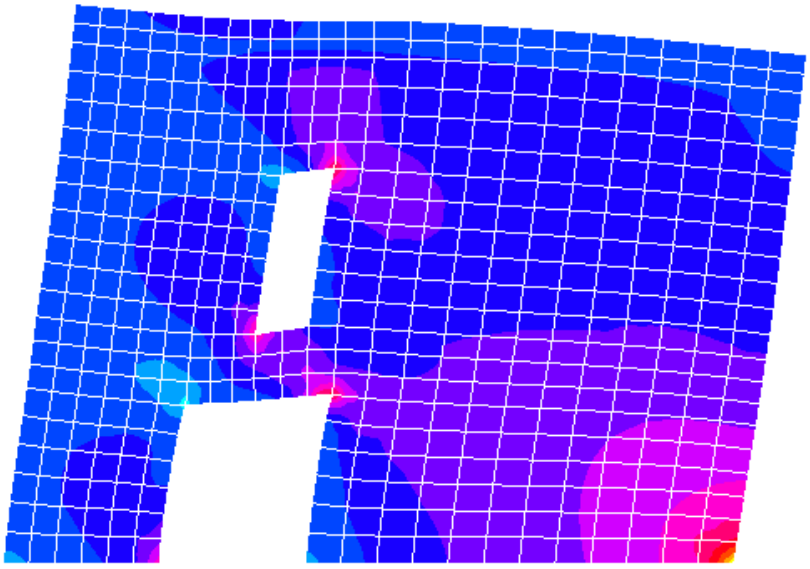

Figure 3.12: Deformed shape and minimum in-plane principal stress plot for central wall.

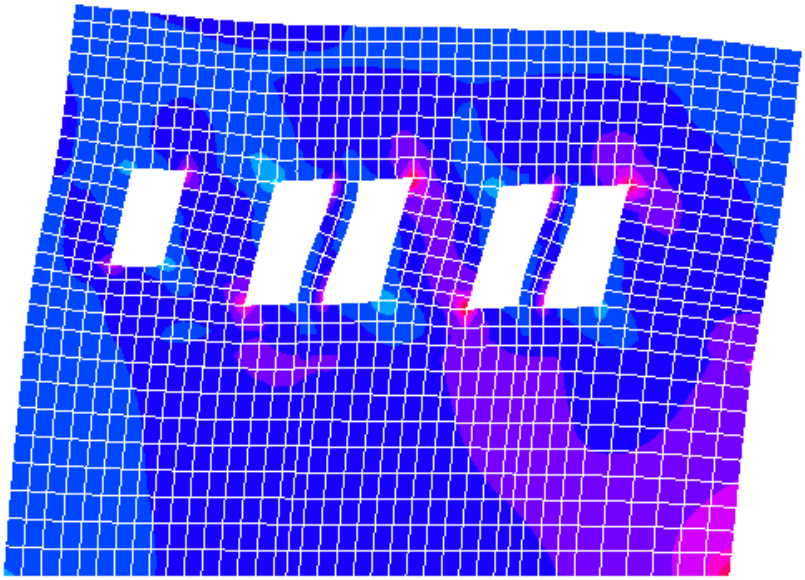

Figure 3.13: Deformed shape and minimum in-plane principal stress plot for north wall.

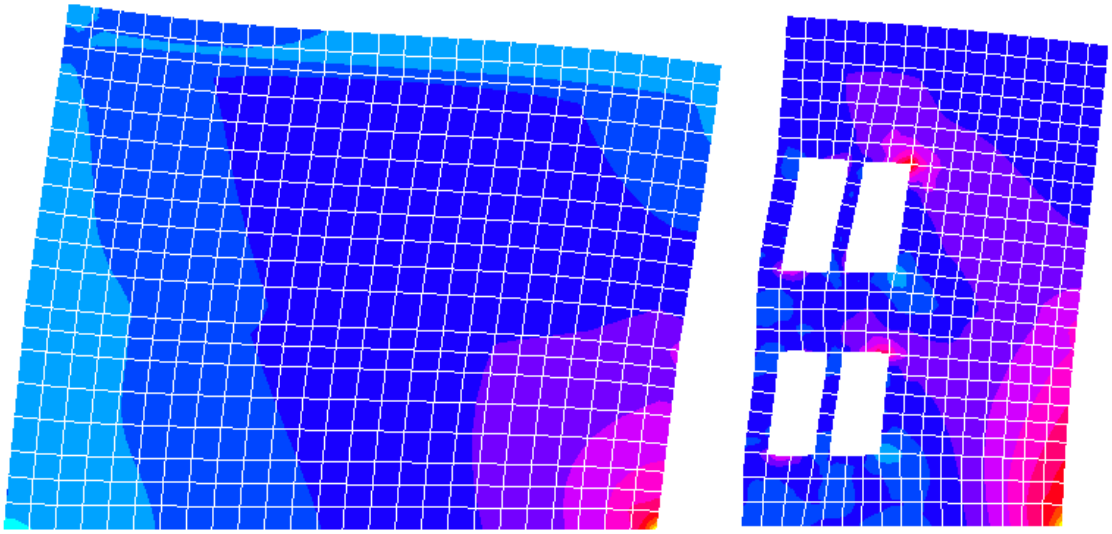

Figure 3.14: Deformed shape and minimum principal stress plot for east wall.

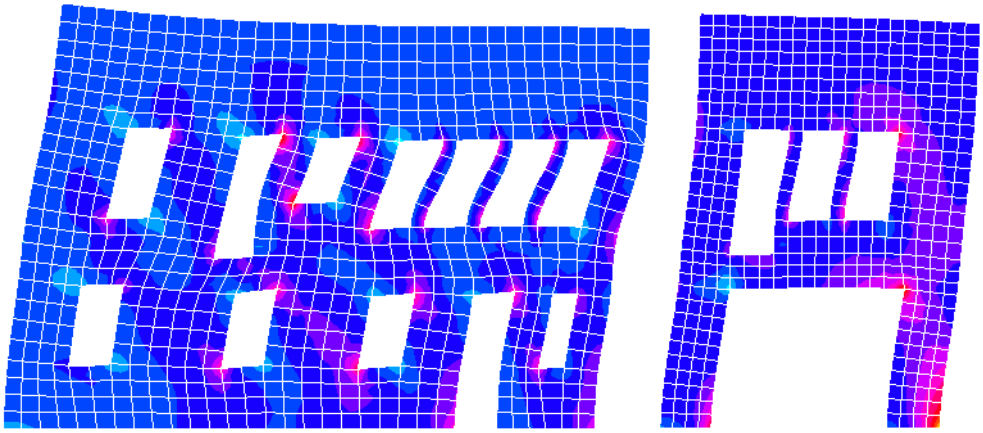

Figure 3.15: Deformed shape and minimum principal stress plot for west wall.

Table 3.3: Summary of displacements from plane stress analysis of the walls loaded in the E-W direction.

Wall Name	Applied Load Case	DOFs shown in Fig. 2.31	Displacement (Unit: in.)
South	2nd floor	U_1	7.216×10^{-4}
		U_2	9.929×10^{-4}
	roof	U_1	9.929×10^{-4}
		U_2	2.198×10^{-3}
Central	2nd floor	U_1	2.277×10^{-4}
		U_2	2.807×10^{-4}
	roof	U_1	2.807×10^{-4}
		U_2	6.757×10^{-4}
North	2nd floor	U_1	1.566×10^{-4}
		U_2	2.013×10^{-4}
	roof	U_1	2.013×10^{-4}
		U_2	8.511×10^{-4}

Table 3.4: Summary of displacements from plane stress analysis of the walls loaded in the N-S direction.

Wall	Applied Load Case	DOFs shown in Fig. 2.31	Displacement (Unit: in.)
East South	2nd floor	U_1	3.169×10^{-4}
		U_2	3.843×10^{-4}
	roof	U_1	3.843×10^{-4}
		U_2	1.322×10^{-3}
East North	2nd floor	U_1	3.574×10^{-3}
		U_2	4.281×10^{-3}
	roof	U_1	4.281×10^{-3}
		U_2	7.985×10^{-3}
West South	2nd floor	U_1	1.454×10^{-4}
		U_2	1.755×10^{-4}
	roof	U_1	1.755×10^{-4}
		U_2	4.495×10^{-4}
West North	2nd floor	U_1	7.584×10^{-4}
		U_2	1.201×10^{-3}
	roof	U_1	1.201×10^{-3}
		U_2	3.557×10^{-3}

3.3.2.2 Stiffness of walls

The stiffness matrices of the walls are calculated from the flexibility coefficients shown in Tables 3.3 and 3.4 using Eqs. 2.75 through 2.79. In order to consider the mortar joint for the east and west wall, the stiffness of south and north part of east/west wall are

calculated separately as discussed in the previous section. The total stiffnesses of east and west wall stiffnesses are summed from the south and north part of the walls. The final shear stiffness of each wall is shown in Table 3.5.

Table 3.5: Wall stiffness.

Wall	Story	Stiffness (kips/in)
South	1st	2,008
	2nd	1,654
Central	1st	5,263
	2nd	3,739
North	1st	7,005
	2nd	2,170
East	1st	3,820
	2nd	1,835
West	1st	9,806
	2nd	6,038

3.3.2.3 Wall strength calculations

Two types of failure mechanisms, the pier type mechanism discussed in Section 2.4.3 and the multiple-story mechanism (involving damage within the lintel beams) discussed in Section 2.4.5 are considered to determine the in-plane lateral shear strength of the south and central walls. The other wall strengths are calculated only based on the pier type limit states. The two types of models for the south wall are illustrated in Figs. 3.16 and 3.17. For all the wall calculations, the compressive strength is taken as 1,325 ksi. This is the average compressive strength of prism tests for the Gilroy Firehouse (Tena-Colunga and Abrams 1992a). This strength is much higher than the recommended values in FEMA

356 shown in Table 2.10. The tensile strength is taken as a representative value of 40 psi based: flexural prism tests and bond wrench tests conducted by Erbay and Abrams (2002).

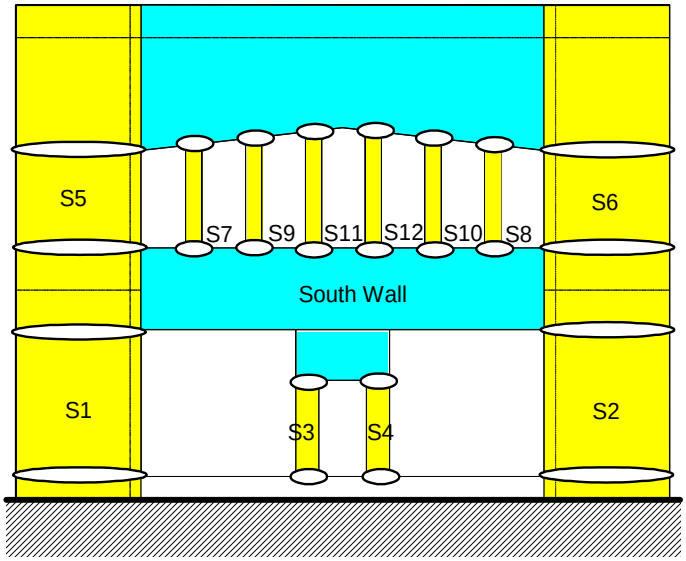

Figure 3.16: Pier-type collapse mechanism.

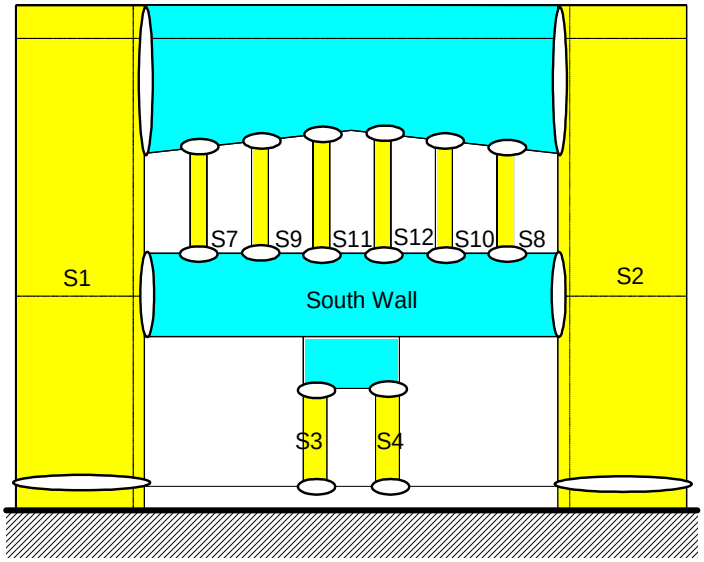

Figure 3.17: Multiple story type collapse mechanism.

The piers of the south wall are labeled as shown in Figs. 3.16 and 3.17 for purposes of discussing the above two alternative strength models. The pier discretization for the

other walls are shown in Figs. B.8 through B.12 in Appendix B. The height of the piers is taken as the height of the window and door openings in each wall. The lateral strengths of the piers are calculated using the equations discussed in Section 2.4.3. Four different failure modes are considered: diagonal tension, bed-joint sliding, toe crushing, and rocking for each pier strength calculation. The minimum lateral strength from these models is taken as the strength for a given pier.

For the multiple-story type collapse mechanism shown in Fig. 3.17, the right and left side pier strengths of the south wall are calculated by using Eqs. 2.94 and 2.95. Figure 3.18 illustrates the left side pier of the south wall with the assumed lateral load distribution. Equation 2.94 is used to calculate the strength of the pier with the flange wall in compression and Eq. 2.95 is used for the pier with the flange wall in tension. The variables in these equations are summarized in Tables 3.6 and 3.7. Since the south wall is symmetric, the total contribution from the left and right side piers is the same for lateral deflections to the east or west.

The total lateral shear strengths of the walls are summarized in Tables 3.8 through 3.12. These strengths are obtained as the sum of the pier shear strengths.

All the piers of the south wall are governed by the rocking strength. The strength of piers S1 and S2 of the south wall, 33.08 kips, is calculated from Eq. 2.90 (rocking strength) based on the pier type collapse mechanism. The rocking strength of these piers based on the multiple-story type collapse mechanism is 15.34 kips using Eq. 2.94 (for the case of the flange wall in compression) and 15.64 kips using Eq. 2.95 (for the case of the flange wall in tension). The strength of the pier with the flange wall in compression is smaller than that of the pier with the flange wall in tension because the vertical load from flange reduces the rocking strength. The minimum strength calculated for the two collapse mechanisms is reported as shear wall strength in Table 3.8. All the piers of the other walls are governed by rocking except pier (C2) of the central wall. This pier exhibits a bed joint sliding behavior as indicated in Table 3.9.

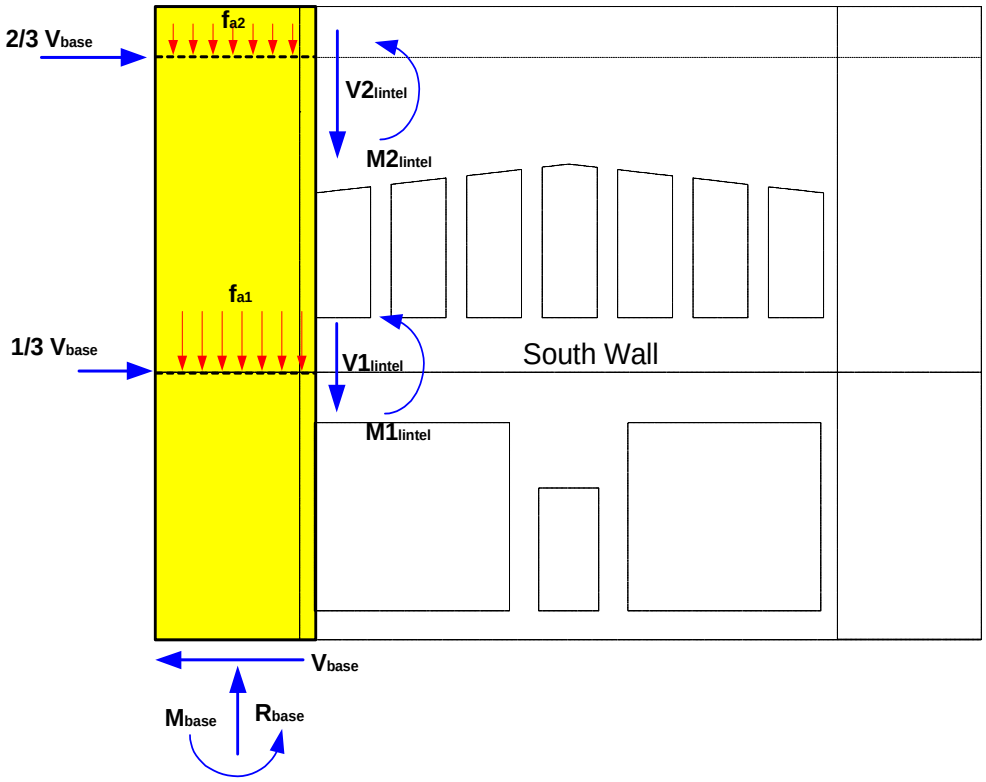

Figure 3.18: Right side pier of the south wall.

Table 3.6: Variables for the pier strength in Fig. 3.17 when the flange wall is in compression.

Variable	Value	Variable	Value
f_{a1}	0.009 ksi	t	12 in
f_{a2}	0.017 ksi	f_t	0.04 ksi
$f_a = f_{a1} + f_{a2}$	0.026 ksi	h_{eff}	58 in for M_{a1} 103 in for M_{a2}
f_{f1}	0.014 ksi	$M_{a1} = \frac{f_t \cdot h_{eff} \cdot t}{6}$	269.12 kips*in
f_{f2}	0.014 ksi	M_{a2}	848.72 kips*in
V_{a1}	11.34 kips	$M_a = M_{a1} + M_{a2}$	1,118 kips*in
V_{a2}	6.085 kips	$P_{ce} = f_a L t + V_a + V_b + V_t$	78.35 kips
$V_a = V_{a1} + V_{a2}$	17.43 kips	$e = 0.5\left(L - \frac{P_{ce}}{f_m'}\right)$	41.33 in
$L_f = 6 t_f$	72 in	L	84 in
A_{n_flange}	456 in^2	t_f	12 in
$V_{f1} = f_{f1} A_{n\_flange}$	11.7 kips	h_1	132 in
$V_{f2} = f_{f2} A_{n\_flange}$	12.12 kips	h_2	202 in
$V_f = V_{f1} + V_{f2}$	23.82 kips	a	1/3

Table 3.7: Variables for the pier strength in Fig. 3.17 when the flange wall is in tension.

Variable	Value	Variable	Value
V_{a1}	10.425 kips	M_{b2}	848.72 kips*in
V_{b2}	3.198 kips	$M_b = M_{b1} + M_{b2}$	1,118 kips*in
$V_b = V_{b1} + V_{b2}$	13.62 kips	$P_{ce} = f_a L t + V_a + V_b + V_f$	63.63 kips
Other values are as in Table 3.6		$e = 0.5\left(L - \frac{P_{ce}}{f_m'}\right)$	41.33 in

Table 3.8: Shear strength and stiffness of south wall.

Wall (Wall ID)	Stiffness (kips/in)	Pier	Shear strength (kips)	
			Pier type mechanism for end piers[a]	Multi-story type mechanism for end piers
1st Story (101)	2,008	S1	33.08	15.34 [b]
		S2	33.08	15.64 [b]
		S3	1.84	1.84 [a]
		S4	1.84	1.84 [a]
		Total	69.84	34.66
2nd Story (201)	1,654	S5, S6	13.54	-
		S7, S8	0.21	
		S9, S10	0.20	
		S11,S12	0.19	
		Total	28.28	

a. The strength is governed by rocking (Eq. 2.90) in all of the piers
b. Calculated from the multiple story type collapse mechanism discussed in Section 2.4.5.

Table 3.9: Shear strength and stiffness of central wall.

Wall (Wall ID)	Stiffness (kips/in)	Pier	Shear strength (kips)	
			Pier type mechanism for end piers	Multi-story type mechanism for end piers
1st Story (103)	5,263	C1	36.71[a]	19.06
		C2	182.17[b]	95.04
		Total	218.88	114.10
2nd Story (203)	3,739	C3	33.07 [a]	
		C4	142.50 [a]	
		Total	175.57	

a. The strength is governed by rocking (Eq. 2.90)
b. The strength is governed by bed joint sliding strength (Eq. 2.83)

Table 3.10: Shear strength and stiffness of north wall piers.

Wall (Wall ID)	Stiffness (kips/in)	Pier	Shear strength[a] (kips) Pier type mechanism
1st Story (105)	7,005	N1	259.98
2nd Story (205)	2,170	N2	6.86
		N3	9.85
		N4	1.12
		N5	8.38
		N6	1.12
		N7	22.03
		Total	49.38

a. The strength is governed by rocking (Eq. 2.90) in all of the piers.

Table 3.11: Shear strength and stiffness of east wall piers.

Wall (Wall ID)	Stiffness (kips/in)	Pier	Shear strength[a] (kips) Pier type mechanism
1st Story (102)	3,820	SE1	16.59
		SE2	43.49
		SE3	38.15
		SE4	20.77
		SE5	5.43
		SE6	4.43
		NE1	7.97
		NE2	10.97
		Total	147.8
2^{nd} Story (202)	1,835	SE7	9.75
		SE8	11.25
		SE9	4.26
		SE10	4.75
		SE11	0.89
		SE12	0.74
		SE13	0.68
		SE14	2.05
		NE3	3.70
		NE4	0.74
		NE5	0.92
		NE6	10.84
		Total	50.57

a. The strength is governed by rocking (Eq. 2.90) in all of the piers.

Table 3.12: Shear strength and stiffness of west wall.

Wall (Wall ID)	Stiffness (kips/ in)	Pier	Shear strength[a] (kips) Pier type mechanism
1st Story (104)	9,806	SW	208.45
		NW1	1.90
		NW2	1.33
		NW3	64.04
		Total	275.72
2nd Story (204)	6,038	SW	167.05
		NW4	0.97
		NW5	0.70
		NW6	32.74
		Total	201.46

a. The strength is governed by rocking (Eq. 2.90) in all of the piers.

3.3.3 Mass modeling

The masses of the building are obtained from the information provided by Tena-Colunga and Abrams (199a). Table 3.13 shows the dead and live loads of the Gilroy Fire-house. Figures 3.19 and 3.20 show the lumped mass locations at the roof and 2nd floor level. These masses are lumped at the intersection of the centroidal axes of walls and dia-phragms, and at the center of each diaphragm. The lumped mass distribution for the dia-

phragms is discussed in Section 1.4.4. The gravity loads from the diaphragm are calculated from the tributary strip areas shown in Fig. 3.19 and 3.20. The tributary masses of the masonry walls are added to the lumped masses at the wall locations. The resulting lumped masses used in this study are summarized in Table 3.14. The total mass of the building is estimated as 2,745 lb-sec2/in as shown in Table 3.15.

Table 3.13: Weight consideration of the structure (Tena-Colunga and Abrams 1992a).

Description	Weight
Self weight of the brick masonry wall	10psf /in. of thickness
Self weight of glass	8 psf
Uniform DL+LL (2nd floor level)	67.5 psf
Uniform DL+LL including Ceiling Load (roof level)	50 psf

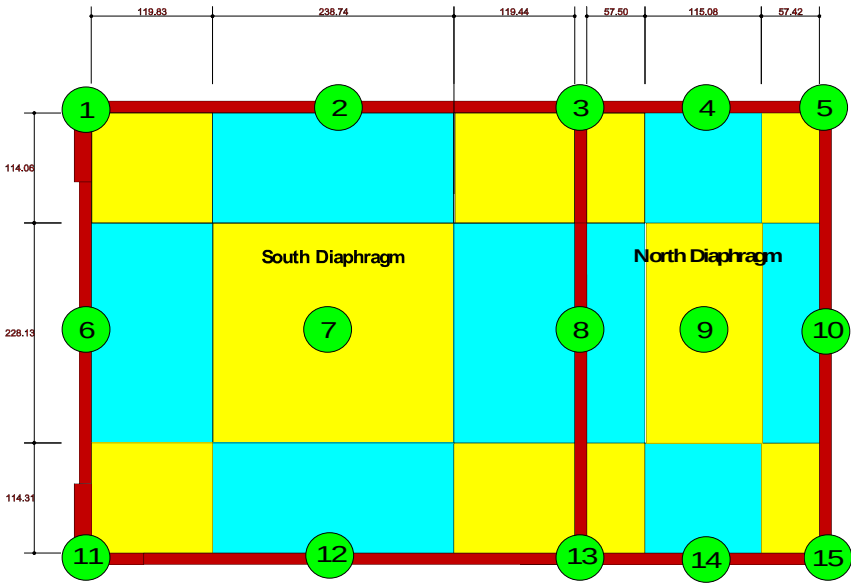

Figure 3.19: Lumped mass ID at 2nd floor diaphragm.

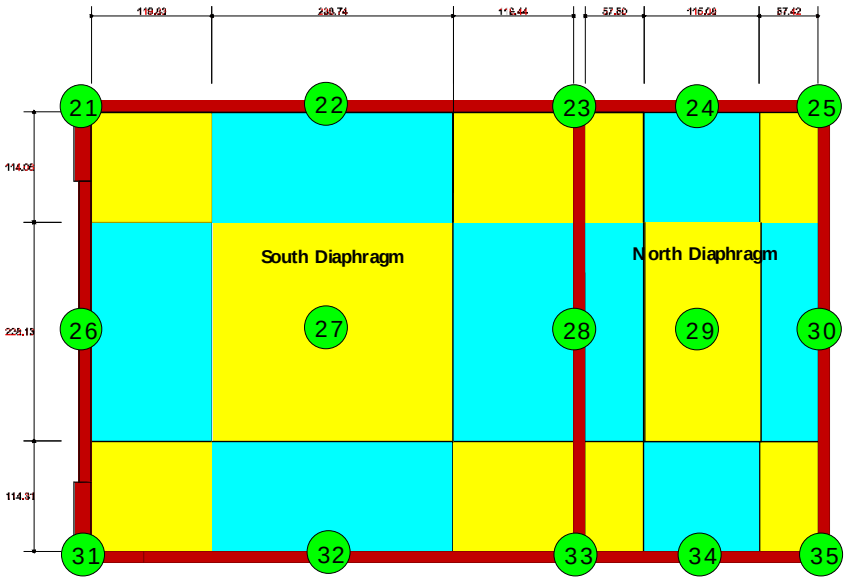

Figure 3.20: Lumped mass ID at roof diaphragm.

Table 3.14: Lumped mass calculations.

Direction	Floor	Mass ID	Mass (lb-sec^2/in)
E-W	2nd	1+6+11	279
		2+7+12	318
		3+8+13	339
		4+9+14	144
		5+10+15	208
	Roof	21+26+31	280
		22+27+32	270
		23+28+33	342
		24+29+34	128
		25+30+35	203
	Total		2,512
S-N	2nd	11+12+13+14+15	403
		6+7+8+9+10	435
		1+2+3+4+5	450
	Roof	31+32+33+34+35	412
		26+27+28+29+30	395
		21+22+23+24+25	417
	Total		2,512

Table 3.15: Summary of masses.

Note	Mass (lb-sec2/in)
At roof level	1223
At 2nd floor level	1288
Total mass (roof level + 2nd floor level)	2512
Total mass of the building	2745

3.3.4 Damping assumption

Rayleigh damping is the most popular procedure because of its simplicity and the computational advantage that it offers. Rayleigh damping is used to construct the structure-damping matrix in this study.

The damping influence coefficients in Eq. 1.2 are obtained for the first and second modes. The structural damping factor ζ_i is assumed as 0.1(10%), a typical value for unreinforced masonry structures. The damping influence coefficients are calculated using the first and second Eigenmode values, which are 14.69 and 15.78 Hz. Since the structure responded primarily in an elastic fashion during the earthquake, the same damping ratios are applied to the walls and diaphragms. However, for nonlinear dynamic analysis, there are problems to apply this proportional damping matrix. These issues within the context of nonlinear dynamic analysis are discussed in Section 4.3.6.

3.3.5 Soil structure interaction modeling

Soil-structure interaction in general can have an important effects on the dynamic response. A flexibly supported structure differs from a rigidly supported one in that a substantial part of the vibration energy may be dissipated into the supporting medium by radiation of waves and by hysteretic action in the soil. A shallow foundation as illustrated in Figure 3.21 is considered in this study. The foundation elements of this type are usually

stiff relative to the soil. Therefore, the three equivalent springs shown in this figure are often suitable to represent the soil-structure interaction effects for simplified analysis.

In this study, the effects of soil structural interaction are neglected. The rationale for this decision is that the soil stiffness is much larger than the stiffnesses of the in-plane walls and diaphragms (Tena-Colunga and Abrams 1992a). Moreover, the recorded motions were measured on the ground floor slab as shown in a SDOF model including soil-interaction effects in Fig. 3.22. Therefore, the recorded ground motion can be applied directly to the building without considering soil-interaction effects.

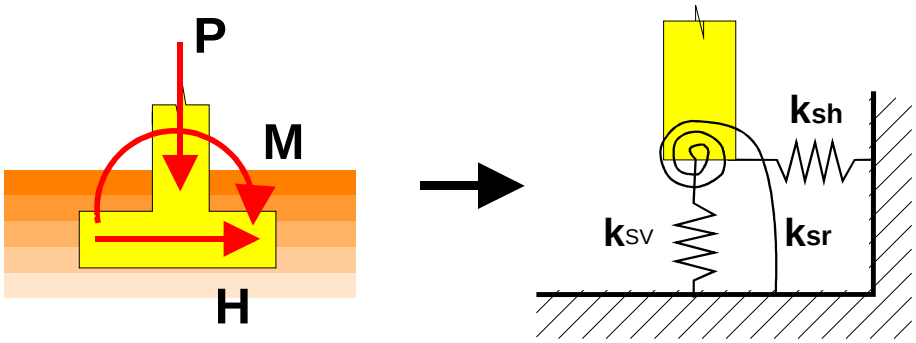

Figure 3.21: Foundation load and Uncoupled Spring Model.

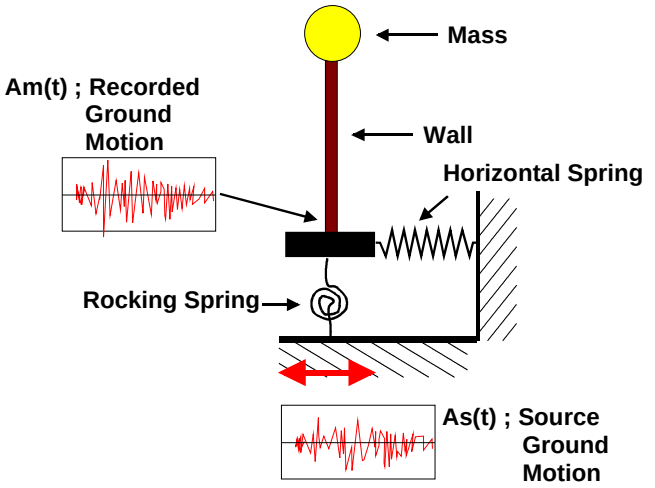

Figure 3.22: SDOF model including soil-interaction effects and ground motions.

3.4 Elastic analysis results (base model)

In this section, linear analyses are performed using the proposed MDOF model. As discussed Section 3.2, Tena-Colunga and Abrams (1992a) also assumed that the structure responded elastically in their analyses. The purpose of this section is to assess how the responses of the analysis model based on the estimated properties discussed in Section 3.3 match with the measured field data. Section 3.4.1 shows the results of frequency analysis. Section 3.4.2 compares linear time history analysis responses using the base model to measured field data.

3.4.1 Frequency analysis

The results of frequency analysis are shown in Table 3.16. The first four mode shapes from the Eigenvalue analysis of the building are shown in Fig. 3.23. The measured natural periods at the roof diaphragm of the building are 0.45 and 0.33 sec. the E-W and N-S directions, respectively. In the first mode of the building shown in Fig. 3.23, the second floor diaphragm moves predominantly in the N-S direction, and the south roof diaphragm moves in the E-W direction for the second mode, the north roof diaphragm moves in the E-W direction for the third mode, and the roof diaphragm moves in the N-S direction for the fourth mode. Therefore, in Table 3.17, the natural period of the second mode is compared to the measured natural period in the E-W direction, and the natural period of the fourth mode is compared to the measured natural period in the N-S direction. The reason that the natural periods of this analysis are slightly higher than the ones of Tena-Colunga and Abrams is that the N-S directional roof diaphragm stiffnesses (see Table 3.2) are used for this analysis. The N-S directional roof diaphragm stiffnesses are smaller than the ones of the E-W directional stiffness. Therefore, these periods (0.417 and 0.354 sec in the E-W and N-S directions, respectively) match well with the measured ones (0.45 and 0.33 sec in the E-W and N-S directions, respectively).

Table 3.16: Results of frequency analysis.

Eigenmode	Period (sec)
1st mode	0.428
2nd mode	0.417
3rd mode	0.359
4th mode	0.354

Table 3.17: Comparison of recorded vs. computed period (sec).

Location	Direction	Measured[a]	Tena-Colunga and Abrams's results	Results from this study
Roof diaphragm	E-W	0.45	0.36	0.417
	N-S	0.33	0.29	0.354

a. Obtained from normalized Fourier amplitude spectra (Tena-Colunga and Abrams, 1992).

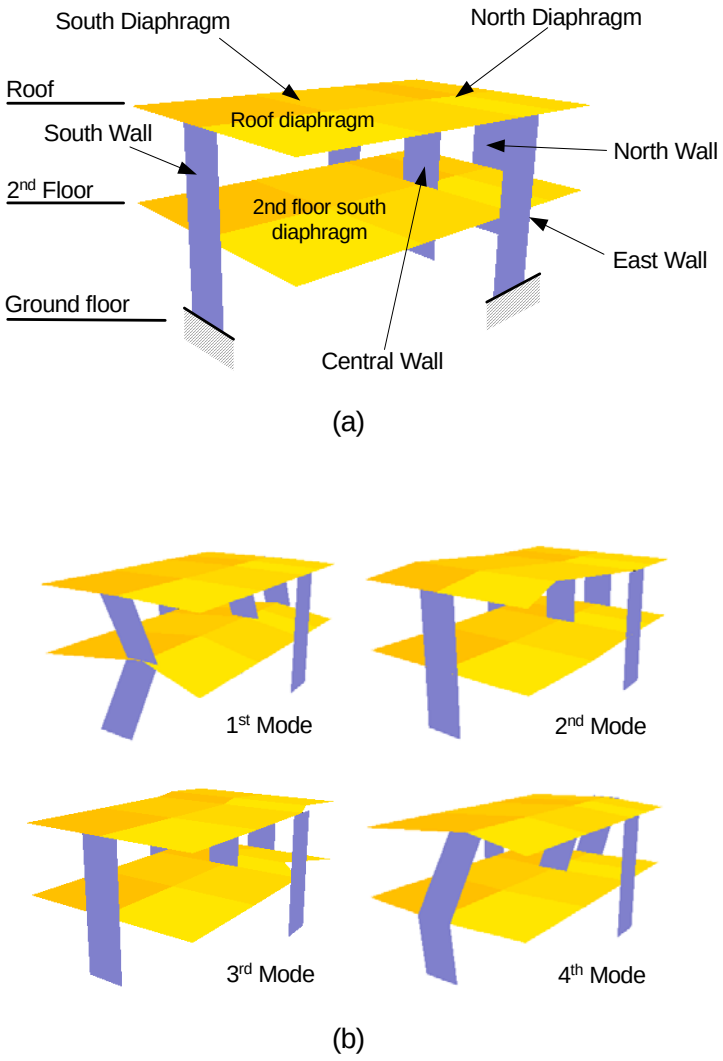

Figure 3.23: (a) Undeformed three-dimensional model and (b) Key mode shapes of Gilroy Fire House.

3.4.2 Time history analysis

Linear time history analysis is performed to identify the response of the structure. The diaphragm and wall properties of the base model discussed in Sections 3.3.1 and 3.3.2 are used in this analysis. Two ground accelerations as shown in Fig. 3.7 and 3.8 are applied at the base of the walls simultaneously in the N-S and E-W directions. For the time history analysis, the assumed effective viscous damping is assumed as 10% based on ATC 3-06 (ATC 1978).

The computed peak responses are summarized in Table 3.18. The computed peak displacements and accelerations in the E-W direction match well with the measured responses at the center of the south roof diaphragm. However, the calculated peak responses in the N-S direction at the center of south diaphragm and the responses in the E-W direction at the top of central wall do not match well with the measured responses.

Table 3.18: Comparison of recorded vs. computed response.

Parameter		Measured[a]	Tena-Colunga's results	Results from this study
Center of south diaphragm at the roof level (E-W) U_5-U_3	Accel (g).	0.79	0.74	0.694
	Drift (in)	1.30	1.25	1.217
Center of south diaphragm at the roof level (N-S) U_6-U_1	Accel (g).	0.55	0.44	0.493
	Drift (in)	0.46	0.87	0.626
Top of Central Wall (E-W)U_4-U_3	Accel (g).	0.41	0.06	0.328
	Drift (in)	0.56	0.08	0.044

a. Displacements U_1 through U_5 are illustrated in Fig. 3.6.

Discussion of the south roof diaphragm displacement in the N-S direction.

The calculated displacement of 0.626 in, at the center of the roof diaphragm in the N-S direction is overestimated compared to the measured value, 0.46 in. It is expected that the actual stiffness in the N-S direction is higher than the properties used in this analysis. This discrepancy may be due to the influence of the trusses spanning in the N-S direction under the roof diaphragm; combined with interior load bearing walls between central and north walls; or out-of-plane stiffnesses of the south, central, and north walls. In order to increase the roof diaphragm stiffness, two shear springs are added to the roof diaphragm in

the N-S direction (see Fig. 3.24). The estimated shear spring stiffness, K_{add}, is 24 kips/in.

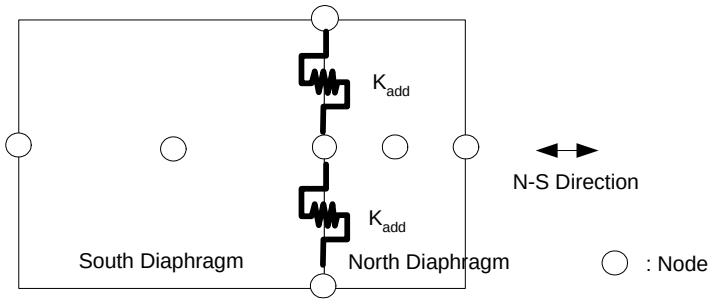

Figure 3.24: Added shear spring model at roof diaphragm in the N-S direction.

Discussion of central wall E-W displacements and accelerations

The measured maximum for U_4 - U_3 of 0.56 in. (drift of the interior wall) is much larger than the corresponding computed value of 0.044 in. The relative displacement (U_4 - U_3 = 0.56 in.) corresponds to 0.18% drift. Since this exceeds the immediate occupancy drift ratio of 0.1% from FEMA 356, some damage would be expected. However, no damage was observed within the interior wall. The above discrepancy might have resulted due to slip between the roof diaphragm and the central wall, assuming the accelerometer was placed on the diaphragm adjacent to the wall.

3.5 Elastic analysis results (modified base model)

The N-S directional diaphragm stiffness is modified as discussed in Section 3.4.2 and the linear analyses are repeated. Section 3.5.1 shows the results of frequency analysis. Section 3.5.2 compares the corresponding linear time history analysis results to measured data.

3.5.1 Frequency analysis

The computed periods are summarized in Table 3.19. The computed periods with the modified stiffness are not significantly different from those shown in Table 3.16. except for the 4th mode. which is related to the modified roof diaphragm stiffness. The natural period of the 4th mode, 0.354 sec in Table 3.16, is decreased to 0.31 sec, due to the shear springs. The natural periods of the Gilroy firehouse from eigenvalue analysis are 0.42 sec in the E-W direction and 0.31sec in the N-S direction, as shown in Table 3.20. These correspond to measured natural periods of 0.45 sec in the E-W and 0.33 sec in the N-S direction reported by Tena-Colunga and Abrams (1992a).

Table 3.19: Natural period including the diaphragm shear springs in the N-S direction.

Eigenmode	Natural Period (sec)
1st mode	0.428
2nd mode	0.417
3rd mode	0.358
4th mode	0.310

Table 3.20: Comparison of recorded vs. computed period.

Location	Direction	Measured[a]	Tena-Colunga's results	Results from this study
Roof dia-phragm	E-W	0.45	0.36	0.42
	N-S	0.33	0.29	0.31

a. Obtained from normalized Fourier amplitude spectra (Tena-Colunga and Abrams, 1992a).

3.5.2 Time history analysis

The wall displacements and accelerations at the roof level are compared with measured values in Table 3.21 and Fig. 3.25 to 3.30. The computed peak displacements and accelerations match well with the measured response. The maximum computed relative displacements of the roof south diaphragm and the base are 1.27 and 0.46 in the E-W and N-S directions, respectively (see Fig. 3.25). These calculated values are match well with the measured responses (1.3 and 0.46 in. in the E-W and N-S directions, respectively). The measured peak acceleration for the center of the south diaphragm is 0.55g compared to the calculated one, 0.51g. The amplitude of the movement of the diaphragm (1.27 in) is high compared to the amplitude calculated at the top of the central wall (0.05in.), as shown in Table 3.21.

However, the measured maximum for U_4 - U_3 of 0.56 in (drift of the interior wall) is still much larger than the corresponding computed value of 0.05 in. As discussed in Section 3.4.2, the measured data at the top of the central wall may not represent the response of the central wall. The calculated and measured displacements at the top of central wall are compared in Fig. 3.27.

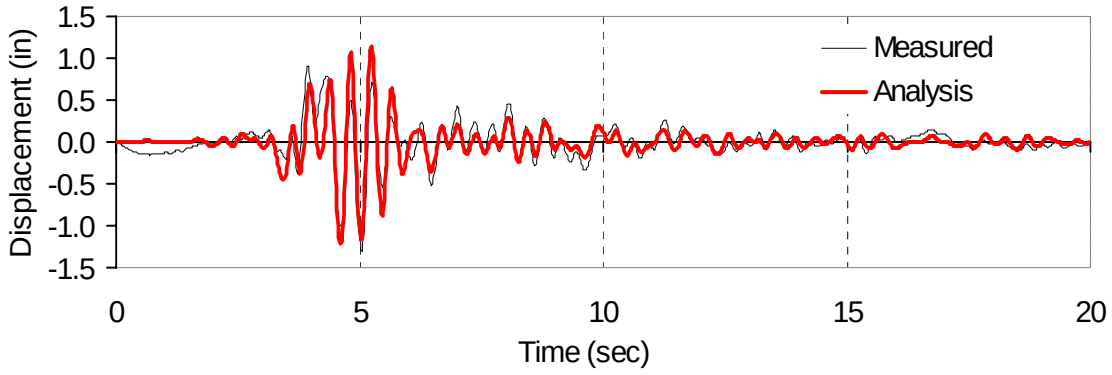

Figure 3.25: Comparison of measured and computed displacement response of roof diaphragm displacement in the E-W direction (U_5-U_3).

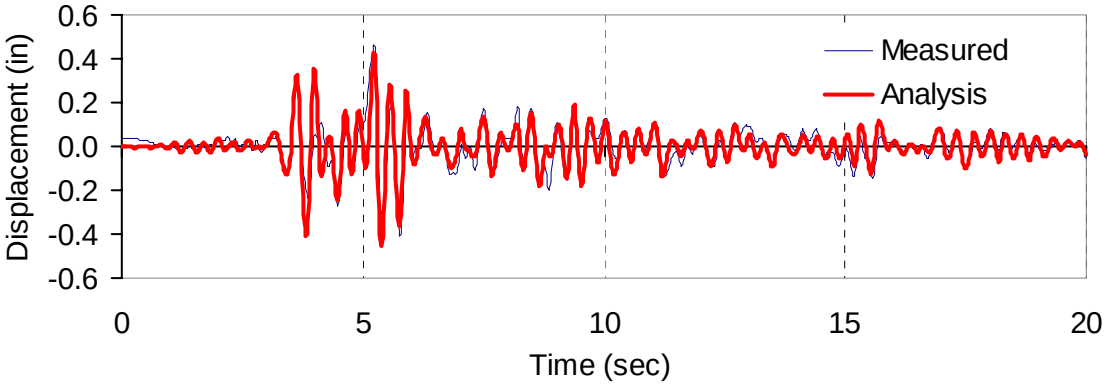

Figure 3.26: Comparison of measured and computed displacement response of roof diaphragm displacement in the N-S direction (U_6-U_1).

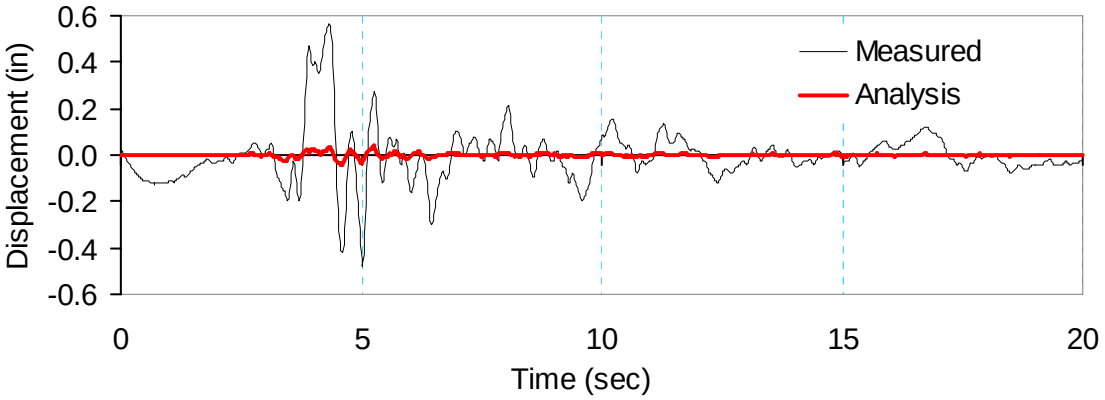

Figure 3.27: Comparison of measured and computed displacement response of in-plane drift of interior wall at the roof level in the E-W direction (U_4-U_3).

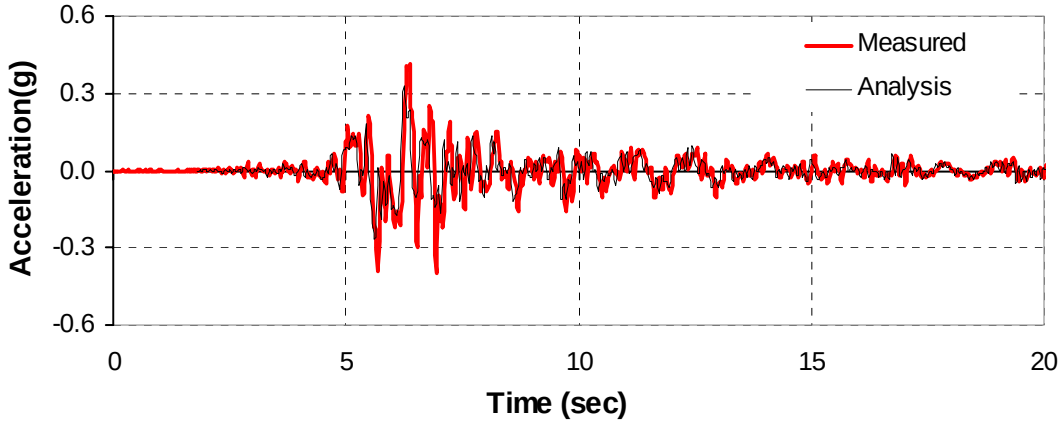

Figure 3.28: Comparison of measured and computed acceleration at the top of central wall in the E-W direction (U_4).

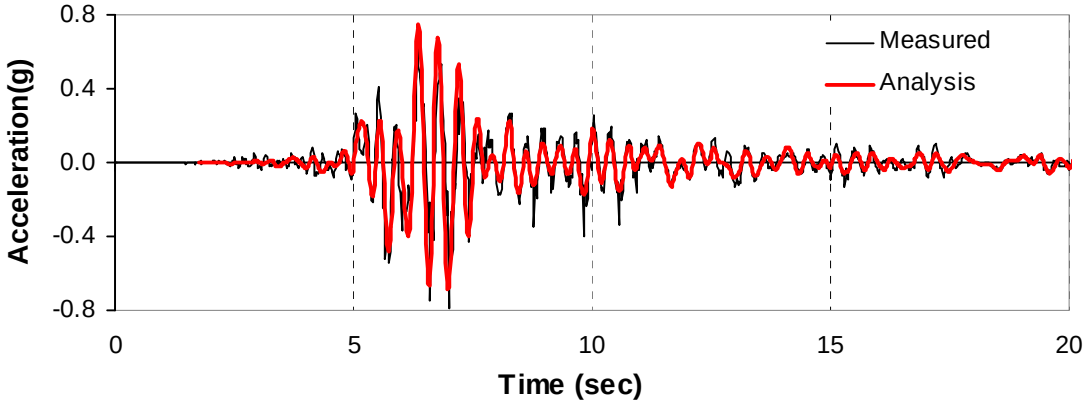

Figure 3.29: Comparison of measured and computed acceleration at the center of south diaphragm in the E-W direction (U_5).

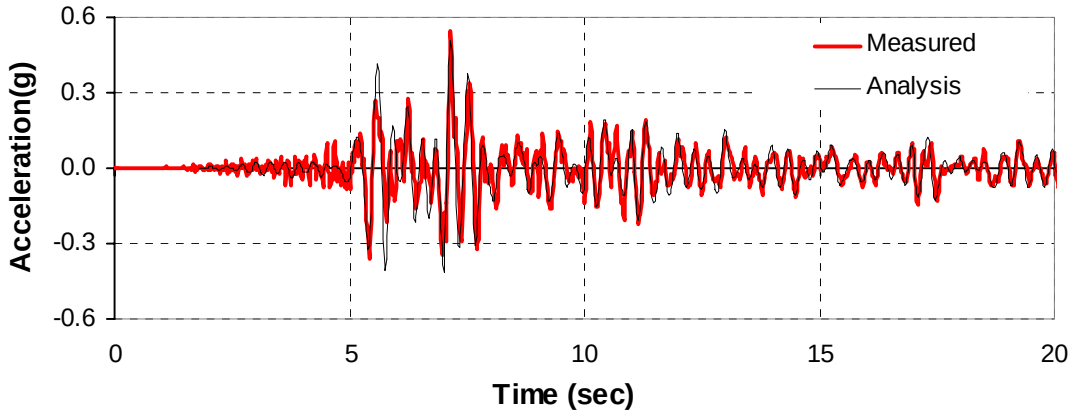

Figure 3.30: Comparison of measured and computed acceleration at the center of south diaphragm in the N-S direction (U_6).

Table 3.21: Updated comparison of recorded vs. computed response of the Gilroy Firehouse.

Parameter		Measured[a]	Tena-Colunga's results	Results from this study
Center of south diaphragm at the roof level (E-W) U_5-U_3	Accel (g).	0.79	0.74	0.69
	Drift (in)	1.30	1.25	1.27
Center of south diaphragm at the roof level (N-S) U_6-U_1	Accel (g).	0.55	0.44	0.51
	Drift (in)	0.46	0.87	0.46
Top of Central Wall (E-W)U_4-U_3	Accel (g).	0.41	0.06	0.33
	Drift (in)	0.56	0.08	0.05

a. Displacements U_1 through U_5 are illustrated in Fig. 3.6.

3.6 Evaluation of wall strength

As discussed in Section 3.2, the observed damage involved a few cracks at the top and bottom of the piers between the window openings on the south wall as well as incipient shear cracks at the southeast and northeast corners of the second story (Tena-Colunga and Abrams, 1992a). The south wall and east wall are investigated here to judge the estimated in-plane shear wall strengths discussed in Section 3.3.2.3 based on the above observed damage. However, it must be recognized that the estimated shear strengths in this section are based on the assumption that the in-plane shear forces cause the observed cracks on the south and east walls. Alternative source of the damage may be due to the effects of out-of-plane behavior of the south and east walls.

Section 3.6.1 discusses the nonlinear time history analysis using the in-plane wall strength calculated from FEMA 356 as noted in Section 3.3.2.3. Section 3.6.2 presents the

results of the nonlinear time history analysis using modified strengths. Section 3.6.3 discusses the out-of-plane responses associated with the diaphragm behavior.

3.6.1 Nonlinear time history analysis (base model with additional shear springs in the N-S direction at the roof)

For the nonlinear time history analysis, the contributions from the individual components are summed to calculate the shear strength of each masonry wall as explained in Section 3.3.2.3. Due to the large openings in the south wall (see Fig. 3.3), its lateral shear strength (34.66 kips) is smaller than that of the other walls (see Tables 3.8 to 3.12). When the walls begin to damage, lateral loads tend to be redistributed to the neighboring components along the boundaries of the flexible diaphragm. When the south wall is first damaged, as shown in Fig. 3.31, lateral loads are redistributed to the east, west and central walls due to torsional effects. The east wall on the second story and the central wall on the first story are damaged slightly thereafter. The overall response of the building is not changed significantly because the other walls remain elastic, as shown in Table 3.22 and Fig. 3.31. However, there must be no damage in central wall and small displacements in the south and east walls. It is judged that the shear strength of south wall in Table 3.8 is underestimated based on the observed damage. The rocking strength, 34.66 kips, which is based on the multiple story type collapse mechanism, is smaller than the 69.84 kips, which is calculated based on the sum of the first story pier strengths. However the strengths of south and east walls based on the pier type mechanism model are also underestimated. It is also found that the strength of the central wall based on the multi-story mechanism is underestimated. The nonlinear analyses are repeated to prevent significant damage on the south and east walls and to have zero damage on the central wall by increasing the in-plane shear strengths of these walls.

The shear strengths of the above walls necessary for the model to give results comparable to the observed response of the physical structure are summarized in Table 3.23.

The modified shear strength of the first story south wall is approximately 80 kips. The modified strength of the first story central wall must be greater than 130 kips to prevent damage. As discussed previously in Section 3.3.2.3 and shown in Table 3.9, the estimated strength of the central wall is 218.88 kips based on the pier type model, and 114.1 kips based on the multi-story mechanism. The modified strength of the second story south and east walls are 55 and 80 kips, respectively.

Table 3.22: Comparison of recorded vs. computed response using shear strengths in Tables 3.8 and 3.12.

Parameter		Measured[a]	Tena-Colunga's results	Results from this study
Center of south diaphragm at the roof level (E-W) U_5-U_3	Accel (g).	0.79	0.74	0.555
	Drift (in)	1.30	1.25	1.194
Center of south diaphragm at the roof level (N-S) U_6-U_1	Accel (g).	0.55	0.44	0.510
	Drift (in)	0.46	0.87	0.461
Top of Central Wall (E-W)U_4-U_3	Accel (g).	0.41	0.06	0.312
	Drift (in)	0.56	0.08	0.047

a. Displacements U_1 through U_5 are illustrated in Fig. 3.6.

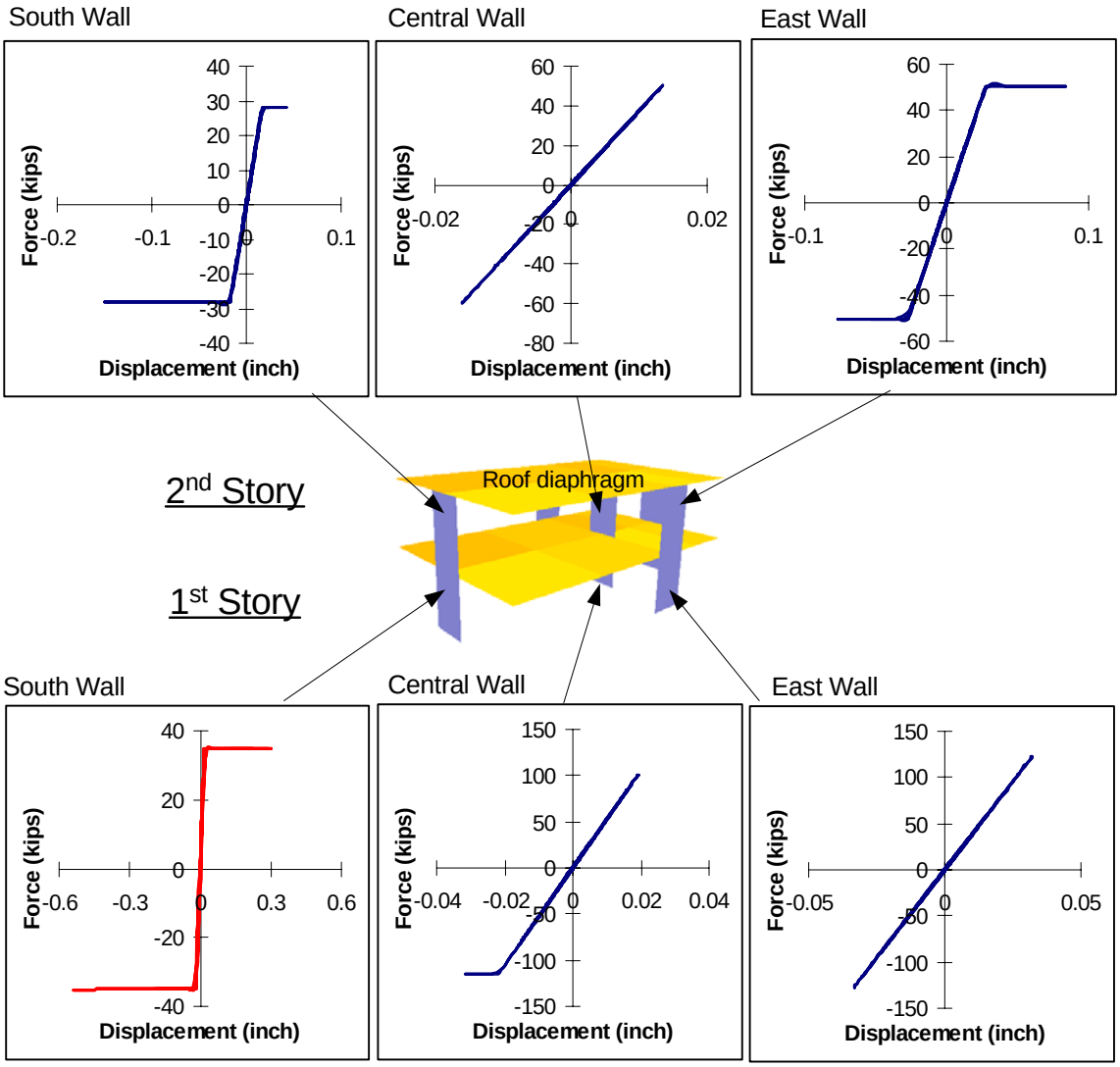

Figure 3.31: Nonlinear time history response of the building using shear strength in Tables 3.8 through 3.12.

Table 3.23: Modified shear strengths.

Story	Wall (ID)	Shear strength (kips)
1st Story	South (101)	80
	Central (103)	>130
2nd Story	South (201)	55
	East (202)	80

3.6.2 Nonlinear time history analysis (base model with modified wall strengths)

The non-linear time history analysis results are presented in this section to identify the response of the structure using the modified shear strengths shown in Table 3.23. The results of this analysis are not significantly different from the elastic response shown in Table 3.21. The overall response of the building is predominantly elastic due to the slight damage on the south and east walls, and that this damage does not significantly affect the diaphragm responses.

Figure 3.32 shows that the south and east walls are slightly damaged and the other walls are not damaged. It is hard to see the damage of the east wall because the strength of the second story east wall is almost equal to the strength capacity of the wall.

Table 3.24: Comparison of recorded vs. computed response using the modified shear strength in Table 3.23.

Parameter		Measured[a]	Tena-Colunga's results[b]	Results from this study
Center of south diaphragm at the roof level (E-W) U_5-U_3	Accel (g).	0.79	0.74	0.70
	Drift (in)	1.30	1.25	1.22
Center of south diaphragm at the roof level (N-S) U_6-U_1	Accel (g).	0.55	0.44	0.50
	Drift (in)	0.46	0.87	0.46
Top of Central Wall (E-W)U_4-U_3	Accel (g).	0.41	0.06	0.32
	Drift (in)	0.56	0.08	0.044

a. Displacements U_1 through U_5 are illustrated in Fig. 3.6.
b. Tena-Colunga and Abrams (1992a).

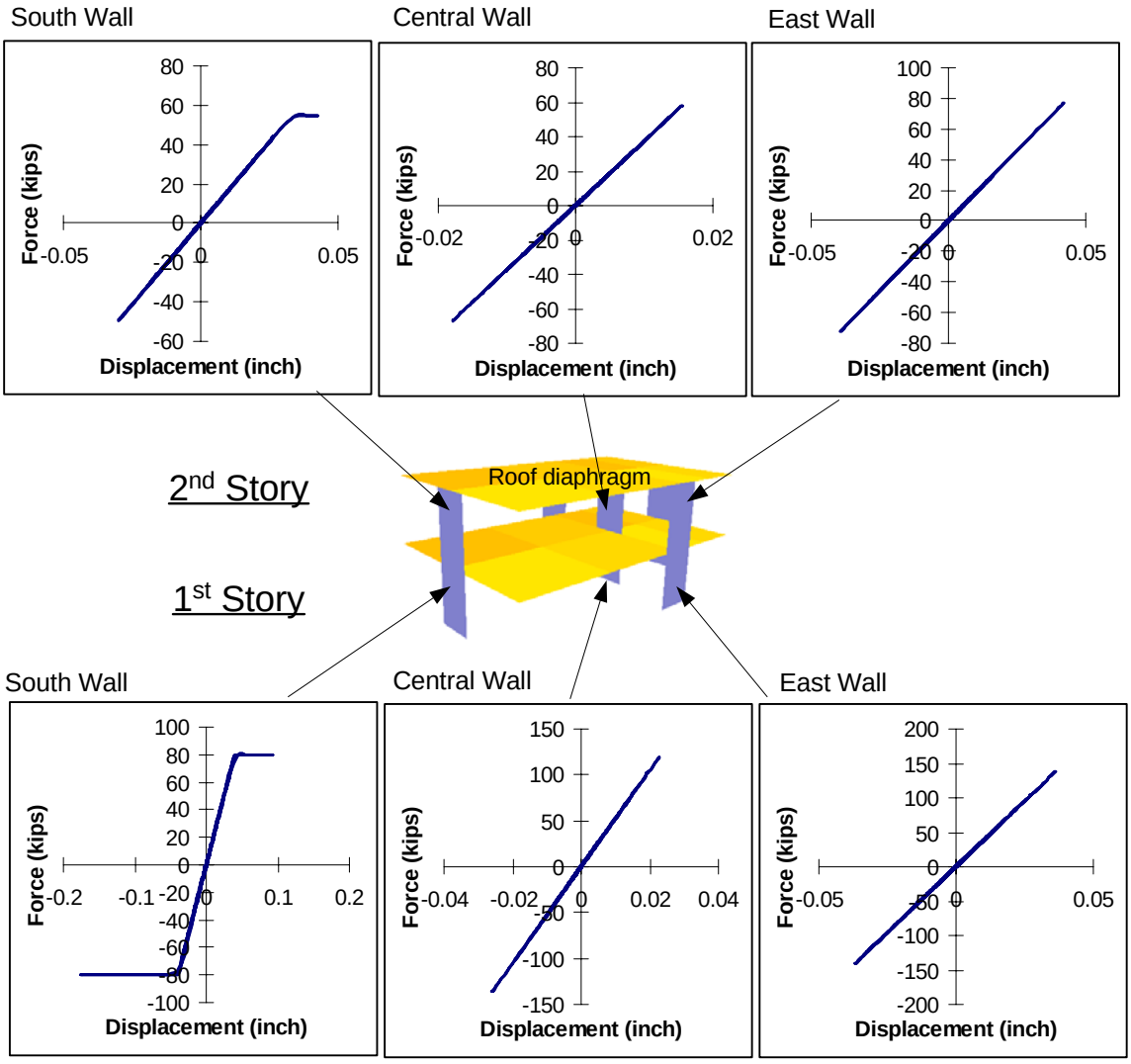

Figure 3.32: Nonlinear time history response of the building using updated strength shear strength.

3.6.3 Out-of-plane response

Figure 3.33 shows one example of bi-directional deformation of the diaphragms and in-plane and out-of plane deflection of the walls taken five seconds into the time history analysis. This figure shows the significant out-of-plane movements of the diaphragm in the E-W and N-S direction. Although out-of-plane failures are common in URM build-

ings (ATC 1998), FEMA 356 currently does not provide any limits on out-of-plane wall deformations for various conditions such as collapse prevention or immediate occupancy. Such limits, or alternative checks to ensure the integrity of the walls and floors need to be defined. Issues that need to be considered in establishing these limits include the potential effects of bi-directional movement of walls and vertical seismic excitation of the wall elements. The peak out-of plane drift ratios of the south and east walls are 0.14% and 0.4%, respectively, within the analysis corresponding to Fig. 3.33.

It should be noted that the out-of-plane stiffness of the URM walls is neglected in this model as per FEMA 356 recommendations. The effects of potential contributions from the out-of-plane wall stiffness were not studied for this building. If out-of-plane wall stiffnesses were included, the above drifts would tend to be reduced. However, these drifts would tend to be increased if diaphragm stiffnesses smaller than those recommended by Tena Colunga and Abrams (1992) and closer to FEMA 356 recommended values were used. The potential contributions from out-of-plane wall stiffness are considered within the study presented in Chapter IV.

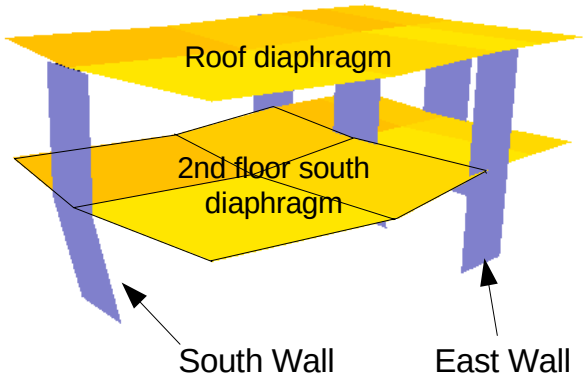

Figure 3.33: Displaced shape including both in-plane and out-of-plane wall deformations at 5.2 second during the time history analysis.

3.7 Effects of diaphragm stiffness

In this section, three different diaphragms; flexible diaphragm using stiffness of $G_e t$ (see Table 3.2), diaphragm using stiffness of ($3G_e t$), and rigid diaphragm, are investigated to check the responses of the building. It assumed the diaphragms remain elastic. However, the modified strength of south and east walls and the estimated strengths of other walls shown in Table 3.23 are used to investigate the non-linear characteristics of the building stiffening the diaphragms. Due to stiffening of the diaphragms, the overall behavior of the structure is changed. The detailed results are discussed in the following sections. Section 3.7.1 compares the calculated shear wall force and displacements. Section 3.7.2 shows the nodal responses due to the diaphragm stiffness.

3.7.1 Comparison of shear wall force and displacement

As the diaphragm stiffness, $G_e t$, in Table 3.2 are increased to 3 $G_e t$, the shear forces of walls are not changed significantly. However, the lateral forces are distributed to the shear walls according to the relative wall stiffnesses for the rigid diaphragm structure. Figure 3.34 compares the responses for the flexible ($G_e t$) and rigid diaphragm structures. As discussed in Section 3.6.2, the south and east walls of the structure with flexible diaphragm are damaged. However, there are no noticeable damaged walls (see Fig. 3.34) for the structure with rigid diaphragms. When the shear force of the first story south wall reaches to its strength capacity (80 kips), the lateral shear forces are redistributed to the west and north walls due to the torsional effect of the rigid diaphragms. This effect increases the north wall shear force from 62 kips to 95 kips, and the west wall shear force from 143 kips to 191 kips. However, the shear forces of east and central walls are reduced to 110 kip and 117 kips, respectively. From Table 3.25 and Fig. 3.35, it is found that, due to the increased diaphragm stiffness, the lateral loads are redistributed to the stronger walls (the north and west walls). These walls have small openings compared to the other walls. It is also concluded that increasing the diaphragm stiffnesses three times does not

change significantly the lateral wall shear forces of the building compared to the rigid diaphragm structure. This attribute of the behavior is taken advantage of in the development of the simplified procedures discussed in Chapter V.

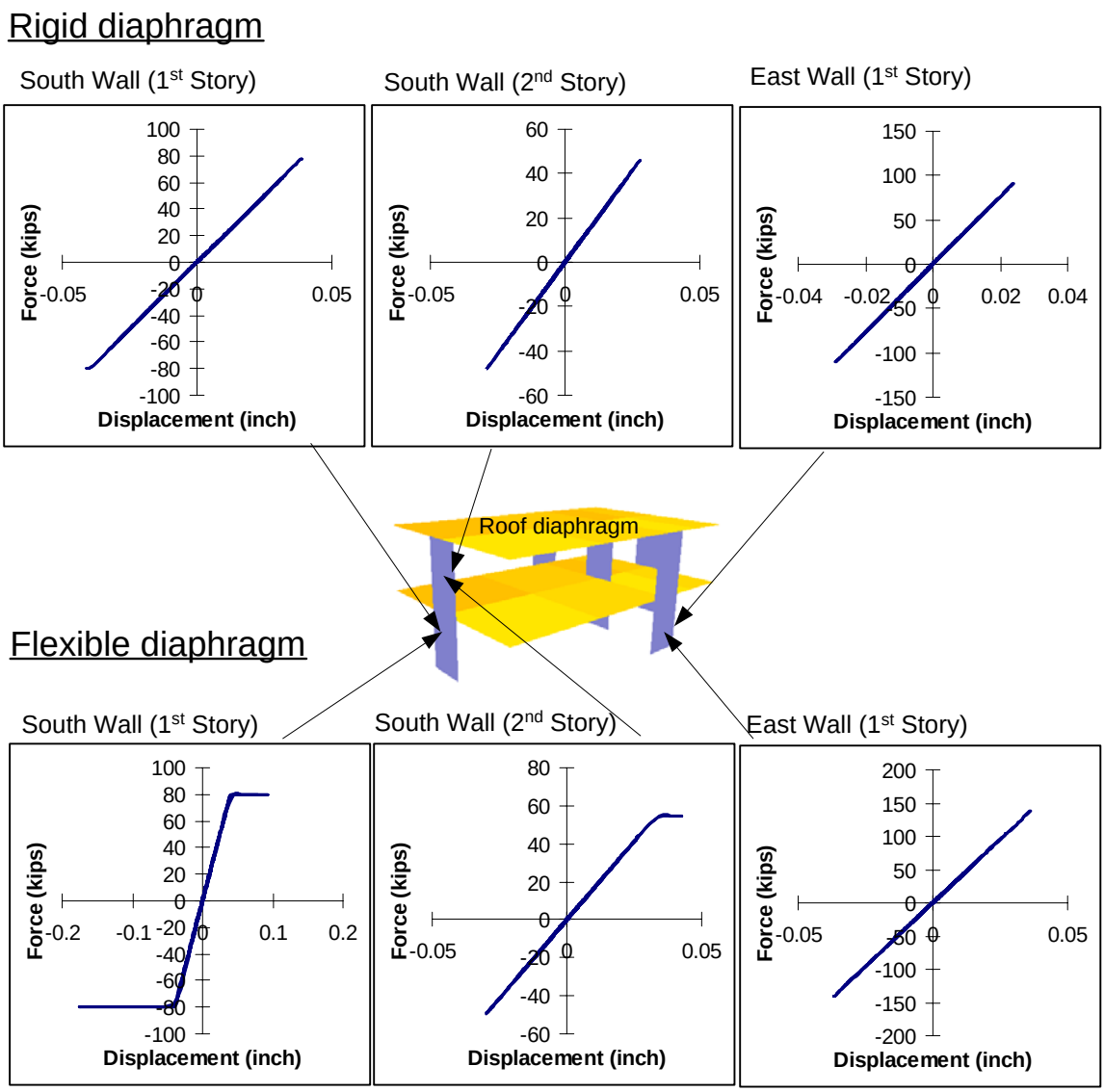

Figure 3.34: Comparison of wall force and displacement between the flexible ($G_e t$) and rigid diaphragm structure.

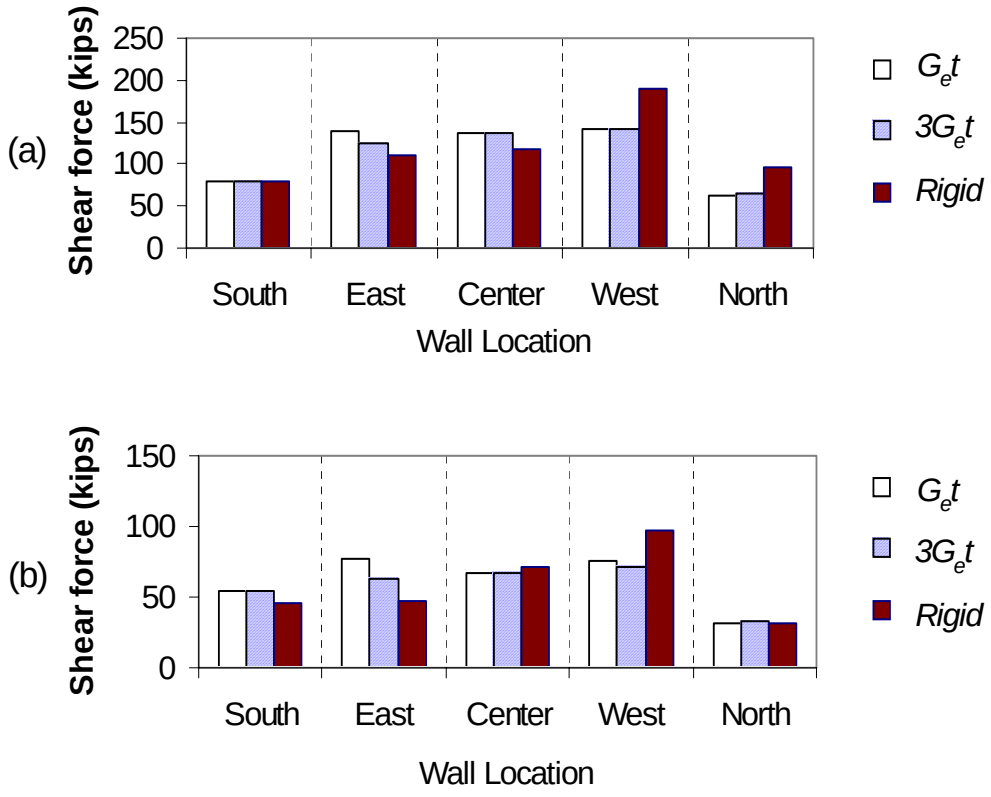

Figure 3.35: Comparison of in-plane shear forces using three different diaphragms: (a) first story and (b) second story.

Table 3.25: Comparison of peak wall displacement and shear force using three different diaphragms.

Wall ID	Wall Location (Element ID[a])	Flexible diaphragm model ($G_e t$) per Section 3.6.2		Flexible diaphragm (3 $G_e t$)		Rigid diaphragm	
		Disp. (in)	Force (kips)	Disp. (in)	Force (kips)	Disp. (in)	Force (kips)
1st Story	South (101)	0.17	80	0.16	80	0.039	80
	East (102)	0.037	140	0.033	126	0.029	110
	Center (103)	0.026	136	0.026	136	0.022	117
	West (104)	0.015	**143**	0.015	**143**	0.013	**191**
	North (105)	0.009	**62**	0.009	**64**	0.013	**95**
2nd Story	South (201)	0.043	55	0.033	55	0.029	46
	East (202)	0.042	77	0.034	63	0.025	47
	Center (203)	0.018	67	0.018	67	0.019	72
	West (204)	0.013	76	0.012	71	0.016	97
	North (205)	0.014	31	0.015	33	0.015	32

a. See Fig. 3.10.

3.7.2 Comparison of nodal responses

Increased diaphragm stiffness significantly affects the displacements and accelerations at the center of the diaphragms. Fig. 3.36 and Table 3.26 compares the nodal responses associated with stiffening of the diaphragms. The responses at the center of the diaphragm are emphasized using bold character in the table. When the diaphragm stiff-

nesses G_et are increased to $3G_et$, the shear wall forces are essentially unchanged, as discussed in the previous section; however, this change affects the nodal displacements and accelerations at the center of the diaphragms significantly (see Fig. 3.36 and Table 3.26). The displacement in the E-W direction at the center of the south roof diaphragm is decreased from 1.221 (G_et) to 0.413 in ($3G_et$), and the displacement in the N-S direction is decreased from 0.453 to 0.163 in. The out-of-plane displacement of the east and west walls connected to the second floor south diaphragm is reduced from 1.22 (G_et) to 0.395 in ($3G_et$).

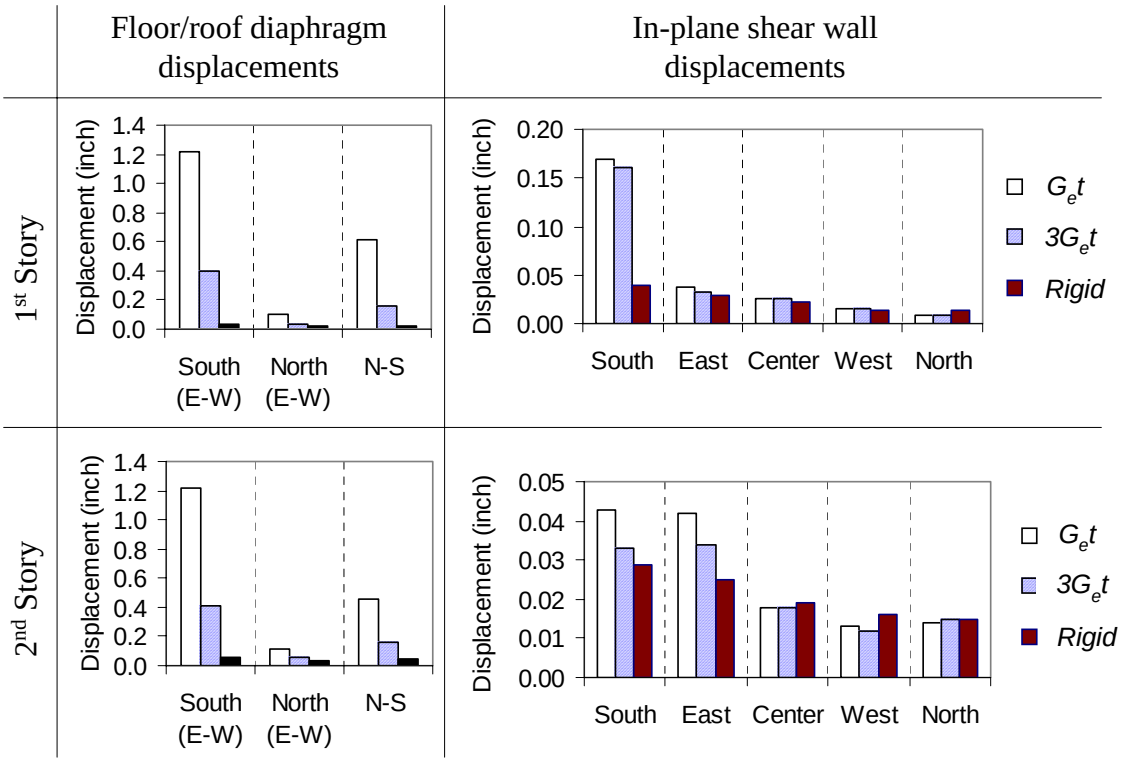

Figure 3.36: Comparison of displacement response using three different diaphragm stiffnesses.

Table 3.26: Comparison of peak nodal response using three different diaphragms.

Story	Element	Node[d]	Flexible diaphragm model (G_et) per Section 3.6.2		Flexible diaphragm (3 G_et)		Rigid diaphragm	
			Disp. (in)	Acc. (g)	Disp. (in)	Acc. (g)	Disp. (in)	Acc. (g)
2nd Floor Level	South wall	11	0.176	0.465	0.160	0.406	0.041	0.371
	South dia.[a]	**12**	**1.220**	**0.657**	**0.395**	**0.600**	**0.032**	**0.345**
	Central wall	13	0.026	0.299	0.026	0.308	0.022	0.319
	North dia.[b]	**14**	**0.104**	**0.431**	**0.039**	**0.340**	**0.018**	**0.307**
	North Wall	15	0.009	0.293	0.009	0.294	0.014	0.295
	East wall	16	0.036	0.261	0.033	0.253	0.029	0.255
	West wall	17	0.015	0.248	0.015	0.247	0.020	0.259
	Dia in N-S[c]	**18**	**0.613**	**0.478**	**0.156**	**0.373**	**0.022**	**0.257**
Roof Level	South wall	21	0.200	0.535	0.185	0.549	0.071	0.449
	South dia.[a]	**22**	**1.221**	**0.689**	**0.413**	**0.630**	**0.056**	**0.399**
	Central Wall	23	0.044	0.312	0.044	0.327	0.042	0.349
	North dia.[b]	**24**	**0.110**	**0.445**	**0.054**	**0.361**	**0.035**	**0.326**
	North Wall	25	0.023	0.309	0.024	0.315	0.028	0.304
	East wall	26	0.078	0.290	0.068	0.265	0.054	0.298
	West wall	27	0.027	0.254	0.026	0.252	0.036	0.274
	Dia in N-S[c]	**28**	**0.453**	**0.496**	**0.163**	**0.413**	**0.042**	**0.272**

a. Center of the south diaphragm in the E-W direction.
b. Center of the north diaphragm in the E-W direction.
c. Center of the diaphragm in the N-S direction.
d. See Fig. 3.10.

The nodal responses of the in-plane shear walls depend on their nonlinear hyster-

etic behavior. For example, the displacement of the first story south wall is reduced from 0.176 ($G_e t$) to 0.041 in ($3G_e t$) for the rigid diaphragm case, because this wall is damaged for the flexible diaphragm structures ($G_e t$ and $3G_e t$) but is not for the rigid diaphragm structure. The nodal responses of the undamaged walls for the flexible diaphragm structure are not changed significantly. The displacement of the first story west wall is 0.015 in for the flexible diaphragm ($G_e t$) and 0.02 in for the rigid diaphragm structure.

3.8 Summary

The Gilroy firehouse is investigated using a simple three-dimensional time history analysis model discussed in this Chapter. The calculated responses of the building are compared with the measured responses during the Loma Prieta Earthquake. The suggested simplified three-dimensional MDOF model predicts well the measured response and the observed damage with the exception of the top of the central wall. It is concluded that the source of this disparity may have been some movement between the roof diaphragm and the top of the central wall. Because the flexible diaphragm stiffnesses are much smaller than those of the walls, the flexible diaphragms dominate the dynamic response of the firehouse in both the E-W and N-S directions. Each of the four diaphragms in the building move largely in an independent fashion.

Based on comparison to the measured responses in the physical structure, it appears that the estimated diaphragm stiffnesses and wall strengths based on FEMA 356 are smaller than the physical values. This is consistent with the results of the diaphragm tests conducted by Peralta et al. (2000) and discussed in Section 2.3.5.2. The sensitivity studies conducted in this chapter indicate that the nonlinear responses of the structures with flexible and hypothetical rigid diaphragms are significantly different. The shear wall forces are distributed according to the relative stiffness of the walls in the hypothetical rigid diaphragm structure. The out-of-plane displacements of the diaphragms are reduced

significantly when the diaphragm stiffnesses are increased three times that of the recommended model for the physical structure; however, the shear wall forces are not affected significantly. Unfortunately, appropriate drift or other limits for the out-of-plane wall response have not been quantified at the present time (December 2002) and are not provided in FEMA 356. Therefore, it is difficult to say whether the stiffening of the diaphragms in the Gilroy firehouse would be appropriate or not. Obviously, the building withstood the Loma Prieta earthquake with diaphragm displacements very similar to those predicted by the 3D MDOF model.

CHAPTER IV

ANALYSIS OF A ONE-STORY LOW-RISE MASONRY BUILDING WITH A FLEXIBLE DIAPHRAGM

4.1 Introduction

Recently, two single-story single-diaphragm half-scale reinforced masonry buildings were tested jointly by researchers at the University of Texas at Austin and the United States Army Construction Engineering Research Laboratory (CERL) (Cohen 2001 and Cohen and Klingner 2001a). These experimental tests were conducted at the CERL shaking table facility, and considered the seismic response under elastic conditions, moderate damage and extensive damage. The first specimen had a diaphragm with a single layer of diagonal-lumber sheathing. The second had a corrugated metal deck diaphragm. The first of these tests is studied in this chapter.

The purpose of the study presented in this chapter is to assess the ability of the general model presented in Chapter II for capture of the linear and nonlinear response of a flexible-diaphragm building in which there are significant contributions from the out-of-plane walls. Due to its elongated rectangular plan (L/B = 4), the seismic responses in the E-W (short) direction were significant compared to those in N-S (long) direction. The test results show significant nonlinear behavior of out-of-plane and in-plane walls, including flange effects from the out-of-plane walls for shaking in the E-W direction. These and other characteristics are not easily captured by the simple models currently provided in code and guideline documents (Abrams 2001). Since the most significant responses in

the experimental tests were in the E-W direction, only the shaking in this direction is considered in this chapter.

It is difficult to determine accurately the in-plane and out-of-plane stiffness, strength, and hysteresis using simplified equations specified in current seismic codes and standards. In particular, it is difficult to estimate out-of-plane wall flange effects on the response of the in-plane walls since the behavior of the out-of-plane walls is also related to the diaphragm flexibility. Therefore, model calibration approach is adopted to predict the structural properties. The overall geometry and topology of the building model is first established per the concepts proposed in Chapter II. The required stiffnesses and strengths of the components within this model are then determined by calibration to the experimental test results. The diaphragm properties are established by comparing to separate isolated tests of the building diaphragm. The wall elastic stiffness properties are determined based on one of the early shaking table tests, the strength and post-elastic stiffness properties of the out-of-plane walls are estimated based on one of the intermediate tests, and finally the strength and post-elastic stiffness properties of the in-plane walls are computed using the results from one of the latter CERL tests that involved significant damage to the structure. The properties determined by this approach are compared with those calculated from simple code and guideline type models.

After determining the model properties, sensitivity analyses are performed to determine the influence of variations in the diaphragm flexibility, particularly the influence of the diaphragm flexibility on the in-plane and out-of-plane wall behavior.

Section 4.2 describes the test structure and summarizes the shaking table test results. A general model based on the simplified approach from Chapter II is developed in Section 4.3. Since the wall modeling procedures discussed in Chapter II are focused on unreinforced masonry walls, additional studies are conducted to determine the strength required for the reinforced masonry walls. Section 4.4 presents the model calibration process. Sensitivity analyses are performed based on the structural properties obtained from

the calibration process in Section 4.5. Section 4.6 summarizes the general observations obtained from the model calibration study and from the sensitivity analyses.

4.2 Summary of shaking table tests

The experimental test results of the building are summarized in detail by Cohen (2001a). All experimental results in this chapter are obtained from electronic files of the recorded test data (Cohen and Klingner 2001b and c).

4.2.1 Description of the structure

Figure 4.1 shows a schematic of the half-scale test structure. The building consisted of a single wood diaphragm supported by four reinforced masonry shear walls. A photograph of the specimen is shown in Fig. 4.2. As-built dimensions (Cohen 2001) are shown in Figs. D.1 through D.4 of Appendix D. The height (H), length (L), and width (B) of the building were 84, 264, and 55 in, respectively, measured from the outer-lines of walls. The walls were composed of four-inch concrete masonry units (CMU) reinforced vertically with #3 bars at 24 inches on center per grouted cell and reinforced horizontally with two #3 bars at each bond beam. Bond beams were located at the tops of the openings and in the top course of the wall. The wood diaphragm consisted of spruce-pine-fur (SPF) 3/8 in. x 3-1/4 in. diagonal lumber sheathing and SPF 3/4 in. x 5-1/2 in. roof rafters (Cohen 2001).

4.2.2 Recorded data

Two different types of instruments -accelerometers and displacement transducers- were used to capture the response of the building. The accelerations in the E-W direction at the roof diaphragm were captured at five sampling locations: two locations at the top of

the north and south walls, and one at the center of the diaphragm, as shown in Figs. 4.3 and 4.4. The displacements in the east-west direction were captured at the top and bottom of the west walls (see Fig. 4.4).

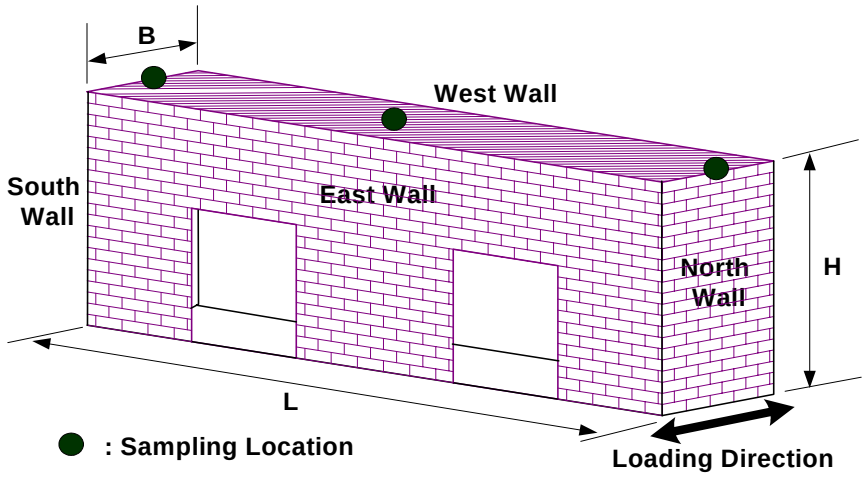

Figure 4.1: Overall view of test building and nodal locations for the analytical model.

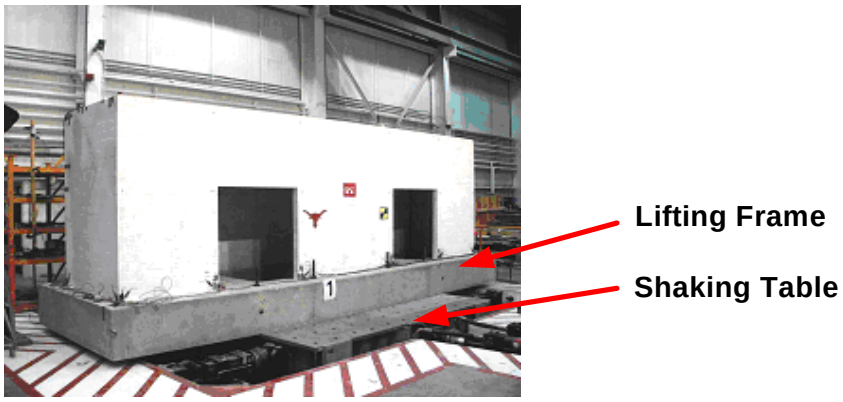

Figure 4.2: Overall photograph of specimen (Cohen 2001).

4.2.3 Overview of input base motions and observed damage

Tests 1, 3, 5, 9, and 10 of the 11 tests were in the E-W direction and corresponded to progressively higher maximum input accelerations ranging from 0.1 to 1.33 g. Tests 2, 4 and 6 were in the N-S direction. These tests also involved progressively higher maximum input accelerations. The excitation in the E-W direction was the artificial ground motion (C02_09s) for Carbondale, IL, developed by Wen and Wu (1999), modified to achieve similitude (Cohen 2001). The original input time step, 0.01 sec, was reduced to 0.005 sec to maintain dynamic similitude between the half-scale structure and the full-scale prototype (Cohen 2001). Test 5 represents the 1.0 of the C02_09s ground motion. The excitation in the N-S direction was the artificial ground motion (C02_03s) from Wen and Wu (1999). Test 6 corresponds to 1.0 of this ground motion. The ground motions in all the other tests were simply scaled from those of Tests 5 and 6. Tests 7 and 8 involved combined shaking in both the E-W and N-S directions, first with 50% of the maximum accelerations from Tests 5 and 6 and then with 100% of these accelerations in both directions. For the analyses conducted in this dissertation, tests 3, 5, 9, and 10 are chosen from the 11 tests results summarized by Cohen (2001).

Table 4.1 summarizes the measured peak responses, and observed damage during Tests 3, 5, 9 and 10. Test 3 with PGA of 0.5g provides the basis for the linear elastic analytical modeling. Test 5 with PGA of 0.67g showed slight cracking in the east and west (out-of-plane) walls. Test 9 was intended as the first test at which substantial damage to the building would be induced. Tests 9 and 10 with PGA of 1.0g and 1.33g, respectively, showed extensive damage of the E-W out-of-plane walls. Diagonal cracks formed at both ends and a vertical crack formed at the center of the wall in these tests, as shown in Fig. 4.5 (Cohen 2001). When PGAs greater than 1.0g were applied to the building, significant bed-joint cracking, characteristic of wall rocking, developed along the bottom of the north and south in-plane walls (Cohen 2001).

Test 6, which had a PGA of 0.55g in the N-S direction exhibited some additional

cracking along the base of the center pier in the perforated (East) wall, and along the base of one of the transverse (N-S) walls (Chon 2001). The data from Tests 7 and 8 is not considered within (Cohen 2001). Apparently the additional damage to the building during these tests was small. In this chapter, the additional damage to the building within Tests 6 through 8 is assumed to be associated with the excitation in Test 9.

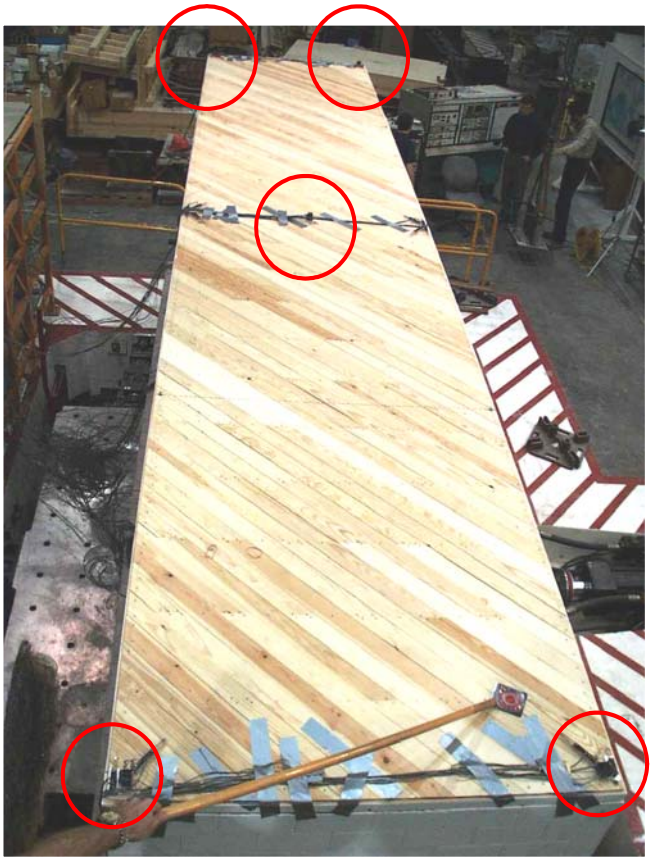

Figure 4.3: Photograph of diaphragm showing the location of accelerometers (Cohen 2001).

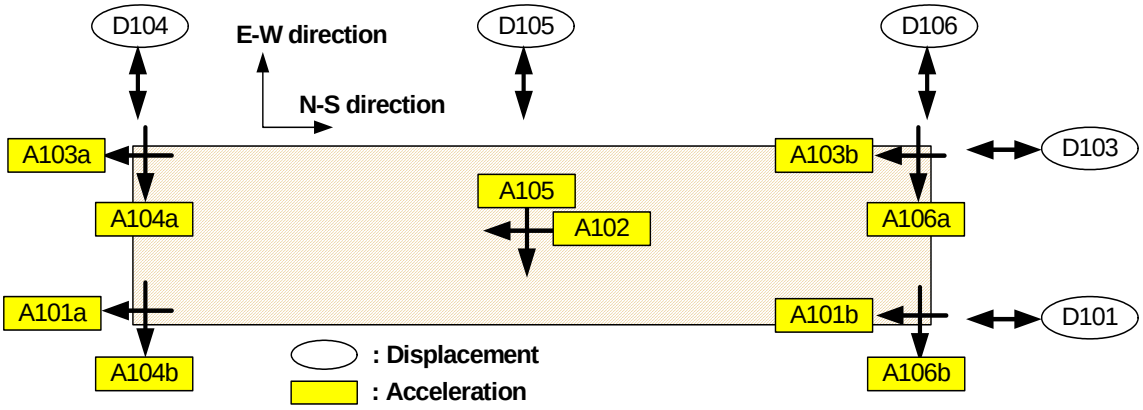

Figure 4.4: Instrumentation for measuring horizontal accelerations and global point displacements at roof diaphragm.

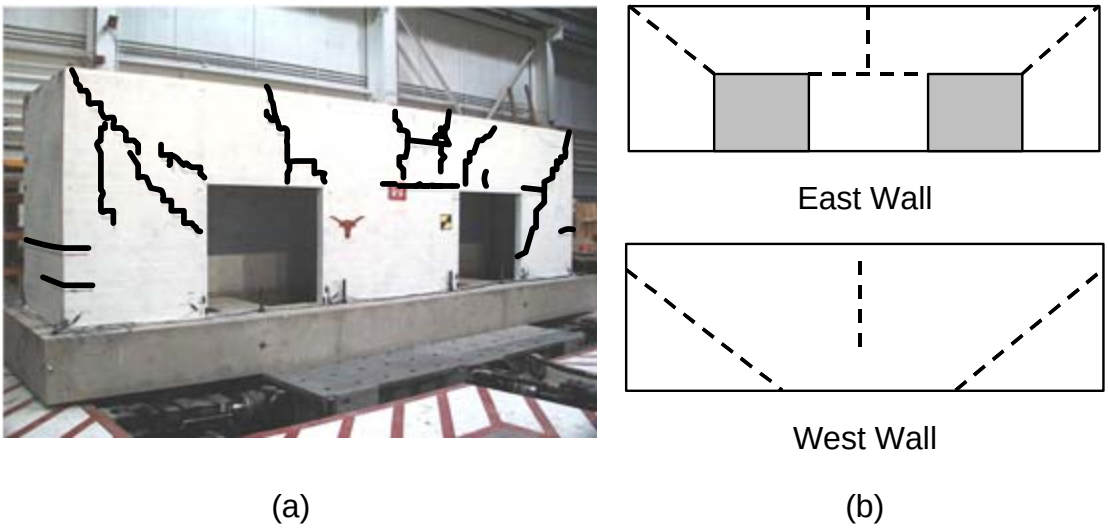

Figure 4.5: Damage to east and west walls from E-W shaking: (a) Photograph and (b) Idealized crack patterns of east and west walls (Cohen 2001).

Table 4.1: Summary of observed drift and damage (Cohen 2001).

Test		3	5	9	10
PGA		0.50 g	0.67 g	1.00 g	1.33 g
Diaphragm Drift Ratio		0.08%	0.2%	0.35%	0.7%
out-of-plane Wall Drift Ratio (%)		0.14% (0.12 in)	0.27% (0.225in)	0.54% (0.456in)	1.1% (0.92 in)
In-Plane Wall Drift Ratio (%)	South wall	0.03% (0.026in)	0.04% (0.036 in)	0.06% (0.053 in)	0.09% (0.076 in)
	North wall	0.03% (0.026in)	0.03% (0.028 in)	0.06% (0.053 in)	0.086% (0.072 in)
Damaged Elements		N/A	- East and west walls (Slight cracking)	- East and west walls (Extensive cracking) - South wall (bed joint cracking)	- East and west walls (Extensive cracking and hinging) -South wall (bed joint cracking) -Diaphragm (Splitting, nail pulling)

4.3 Analytical modeling

The proposed simplified modeling approach discussed in Chapter II is applied to the test building. Section 4.3.1 gives an overview of the idealized analysis model. Section 4.3.2 presents how the diaphragm model properties are obtained from a diaphragm test. Section 4.3.3 discusses how the reinforced in-plane and out-of-plane masonry walls are modeled. Section 4.3.4 discusses issues associated with the modeling of the input ground motions applied to the base of the building. Section 4.3.5 describes the calculation of the building masses. Section 4.3.6 discusses the damping model used in the analysis. Section

4.3.7 discusses other detailed issues associated with the execution of the linear and nonlinear time history analysis.

4.3.1 Overview of analysis model

In order to investigate the response of the test building in the E-W direction, one diaphragm element, four in-plane wall elements (one on each side of the diaphragm), and one out-of-plane wall element (representing the combined effect of the East and West walls in their out-of-plane direction) are used to model the test structure. Figure 4.6 shows the simplified MDOF model. Each of the in-plane shear wall elements is linked to the boundary DOFs of the diaphragm element.

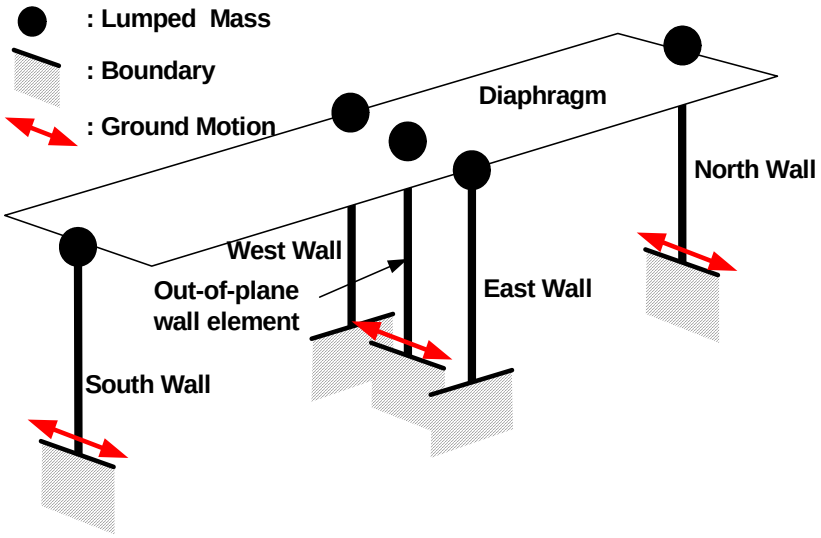

Figure 4.6: Analytical model.

The out-of-plane wall element is connected to the middle DOF of the diaphragm element, as discussed in Section 2.4.7. Section 3.2.2.1 of FEMA 356 states that for nonlinear dynamic analysis, a connection between the wall and diaphragm shall be explicitly modeled if the connection is weak and is not considered as a rigid connection (ASCE

2000). However, the diaphragm was positively anchored to all the walls and no failure of the connections was observed in the shaking table tests (Cohen 2001). Therefore, it is assumed that the walls are anchored to the diaphragm by rigid connections. The masses are lumped at the corresponding degrees-of-freedom of the wall and diaphragm element. The E-W ground motion is applied to the base of the in-plane north and south walls and to the base of the single element model of the out-of-plane (east and west) walls (see Fig. 4.6). Detailed modeling of each of the structural components - diaphragm, in-plane walls, and out-of-plane walls - is discussed in the next several sections.

4.3.2 Diaphragm modeling

The diaphragm element, explained in Section 2.3, consists of six degrees-of-freedom (DOFs): three degrees of freedom in the E-W direction and three in the N-S direction as shown in Fig. 4.7. The diagonal lumber sheathed wood diaphragm of the test structure is idealized as a plate girder for calculation of the diaphragm bending response as discussed in Section 2.3.1. The diaphragm element can capture three key modes: the E-W and N-S directional bending mode; and shear raking mode. However, in the tests considered in this chapter, only the E-W bending mode is excited significantly.

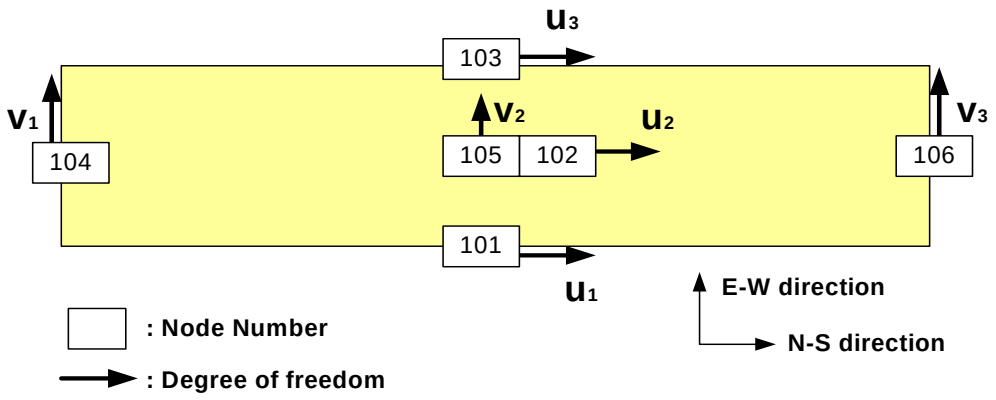

Figure 4.7: Node number and the associated degree-of-freedom of diaphragm element.

The boundary walls and chord members at the tops of the east and west walls connected to the diaphragm serve as the flange of the idealized plate girder. The diagonal sheathing functions as the web. The E-W directional bending mode is significant for this particular test building due to its long rectangular plan. The experimental tests of the diaphragm show that these bending displacements are dominated by shear (Cohen 2001). Therefore, the diaphragm chord is assumed to be rigid. The web carries the shear forces induced by the horizontal loadings. The boundary DOFs (u_1, u_3, v_1 and v_3), as shown in Fig. 4.7, capture the in-plane wall displacements. Node 105 (v_2) represents the E-W directional behavior of the diaphragm associated with the out-of-plane behavior of east and west walls. Node 102 (u_2) captures the N-S directional behavior of the diaphragm. Node 104 captures the south in-plane wall deflection and Node 106 captures the north in-plane wall deflection.

For the diaphragm model, an equivalent shear stiffness of the diaphragm element is obtained from the results of quasi-static diaphragm tests reported in (Cohen and Klingner 2001a). A summary of these test results is presented and the estimated diaphragm stiffness and strength are discussed in Section 4.3.2.1.

4.3.2.1 Summary of diaphragm test results

After the shaking table tests (see Section 4.2) were completed, the wood diaphragm was removed from the half-scale masonry structure (Cohen and Klingner 2001a). The damaged components of the diaphragm (five pieces of sheathing lumber) were removed and replaced (Cohen and Klingner 2001a). The diaphragm was supported by a steel test frame, as shown in Fig. 4.8. It was loaded at its quarter points using two actuators (see Figs. 4.9 and 4.10). A sequence of displacement controlled loads were applied by monotonically, increasing the maximum displacement in what are referred to as major cycles, each followed by several smaller-amplitude cycles, which are called minor cycles (Cohen and Klingner 2001a). One major cycle with the following minor cycles is labeled

as one test number. The diaphragm was subjected to nine tests, i.e., sequences of a major cycle followed by minor cycles.

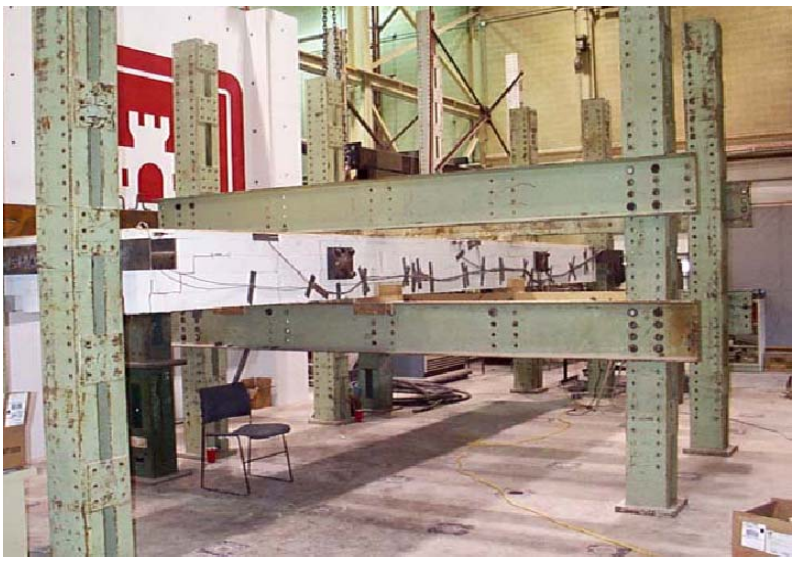

Figure 4.8: Photograph of diaphragm test setup (Cohen and Klingner 2001a).

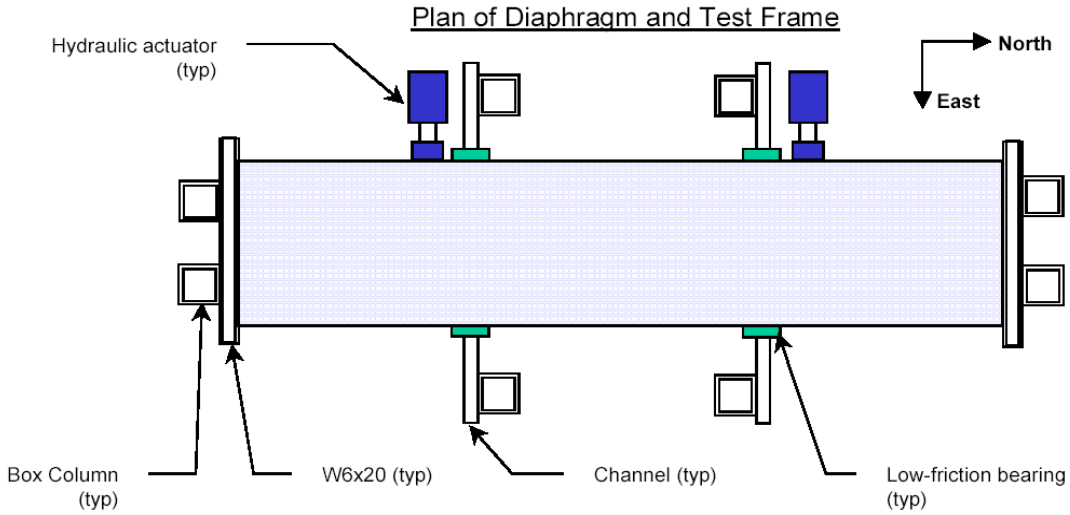

Figure 4.9: Plan drawing of test set up for the diaphragm (Cohen and Klingner 2001a).

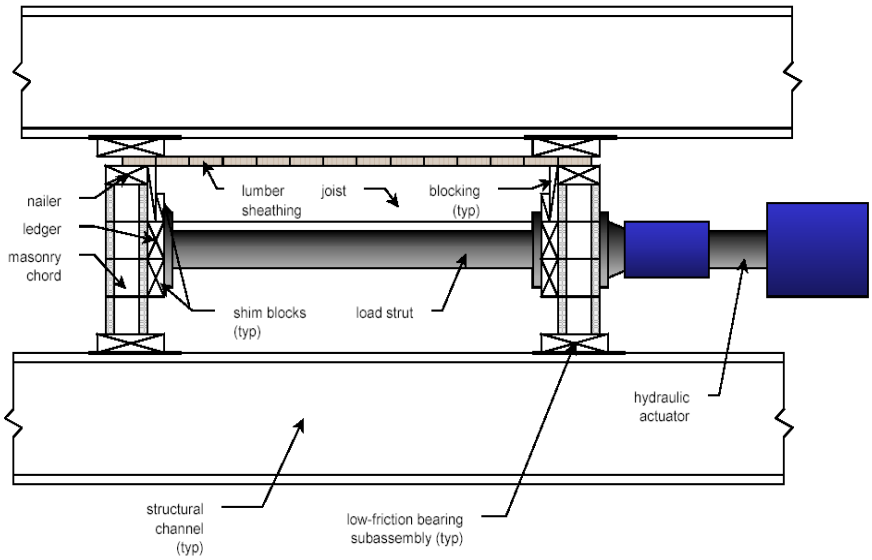

Figure 4.10: Typical cross-section of test setup at loading points (Cohen and Klingner 2001a).

The diaphragm was displaced symmetrically in the E-W direction at its quarter points. Figures 4.11 and 4.12 show the hysteretic relationship between the applied load and the diaphragm drift ratio for Tests #1 - #5 and Tests #6 - #9, respectively. The diaphragm drift ratio in these figures is defined by

$$\delta_{diaphragm} = \frac{\Delta_{diaphragm}}{0.5L} \tag{4.1}$$

where, $\Delta_{diaphragm} = \Delta_{Out-of-plane-wall} - \frac{\Delta_{north-wall} + \Delta_{south-wall}}{2}$. The figure for Tests #1- #5 shows little degradation in stiffness or strength. However, Tests #6 - #9 show considerable stiffness degradation and pinching effects due to the damage including nail slipping, splitting of sheathing boards, and cracks in the masonry chord (Cohen and Klingner

2001a).

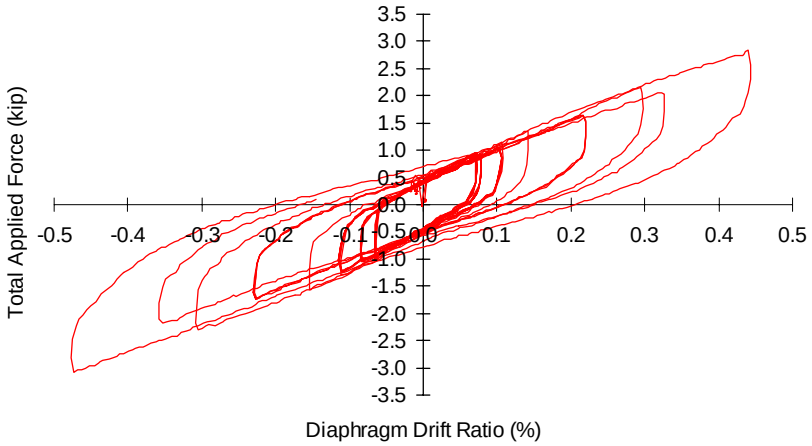

Figure 4.11: Relationship between applied load and diaphragm drift ratio for low diaphragm drift ratios (Tests #1 - #5) from the diaphragm test (Cohen and Klingner 2001a).

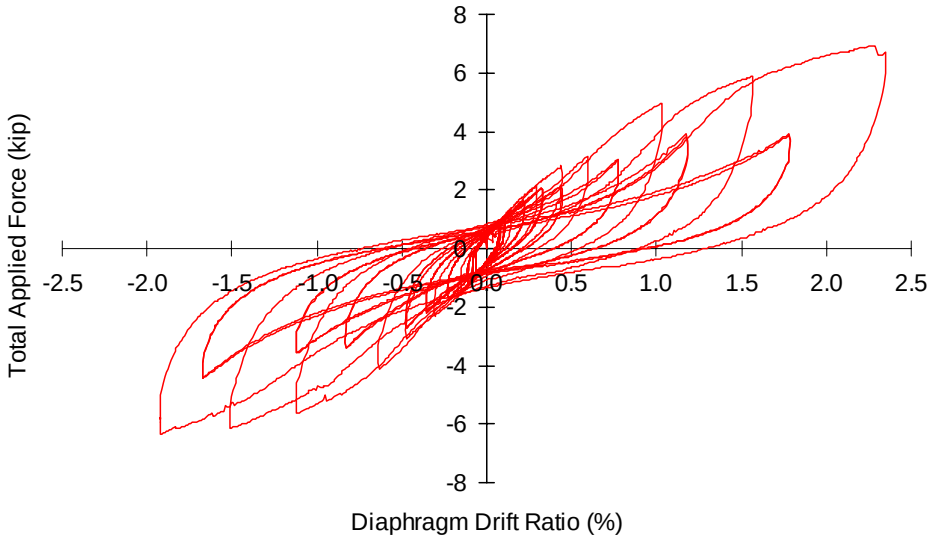

Figure 4.12: Relationship between applied load and diaphragm drift ratio for high diaphragm drift ratios from the diaphragm test (Tests #6 - #9) (Cohen and Klingner 2001a).

Figure 4.13 shows the three parameter model hysteretic curves (see Section 2.3.4.1) associated with Tests #1 - #5. The initial stiffness of the loading and unloading paths in Fig. 4.13, is larger than the actual stiffness of the diaphragm due to the frictional

forces between the diaphragm and steel test frame assembly shown in Fig. 4.10 (Cohen and Klingner 2001a). Cohen estimated that the frictional force totaled about 0.5 kips. In this work, a frictional force of 0.4 kips is used to obtain a hysteretic curve that passes through the origin at low levels of deflection in the linear-elastic range as shown in Figs. 4.14 and 4.15. Thus, the measured hysteretic force is separated into a frictional force and the diaphragm force, as shown in Fig. 4.15.

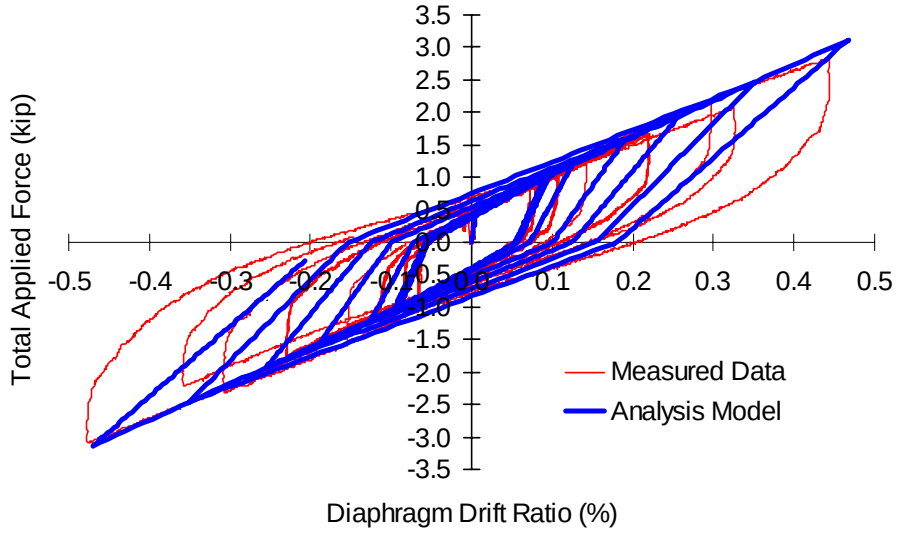

Figure 4.13: Comparison of measured and analysis model for low diaphragm drift ratios (Tests #1 - #5) from the diaphragm test.

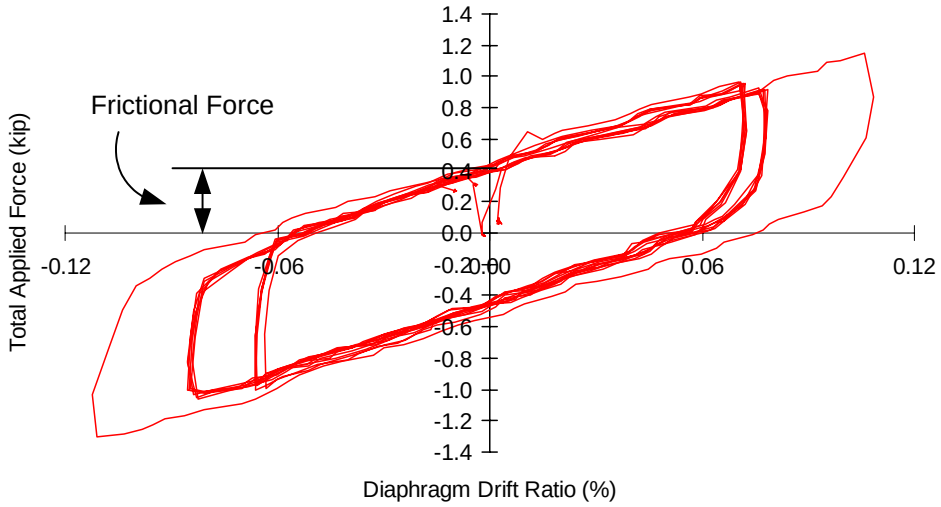

Figure 4.14: Frictional force for low diaphragm from the diaphragm test (Tests #1 and #2).

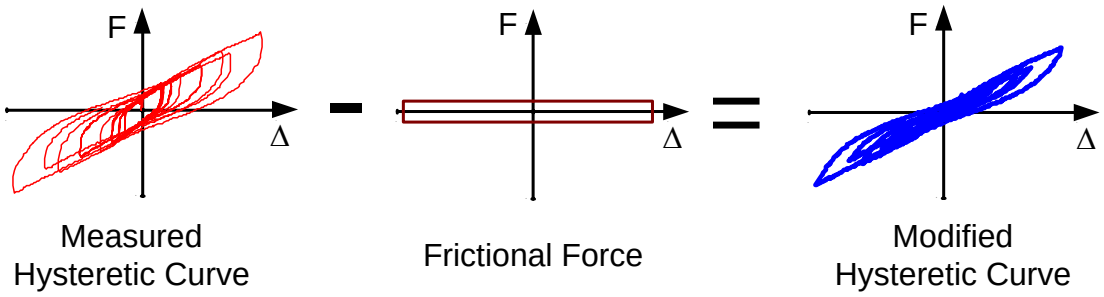

Figure 4.15: Contribution of friction to hysteretic curve (Cohen and Klingner 2001a).

4.3.2.2 Estimated diaphragm stiffness, strength and hysteresis model

Figures 4.16 and 4.17 compare the original experimental hysteretic curves and the modified ones in which the frictional forces have been numerically extracted (see Fig. 4.15). The diaphragm hysteretic properties are obtained from the modified hysteretic curves shown in these figures. The three-parameter model discussed in Section 2.3.4.1 is implemented to characterize the diaphragm hysteresis behavior. Figures 4.18 and 4.19 compare the results of the selected three parameter hysteretic model to the modified hys-

teretic curves.

It must be recognized that this diaphragm was damaged during the previous shaking table tests (Cohen 2001). Even if the visually damaged components of this diaphragm were removed and replaced, the stiffness and strength of the diaphragm in the shaking table test building may be slightly larger. Therefore, the stiffness and strength properties of the diaphragm are increased 10% over those of the measured hysteretic properties. The backbone curve is shown in Fig. 4.20.

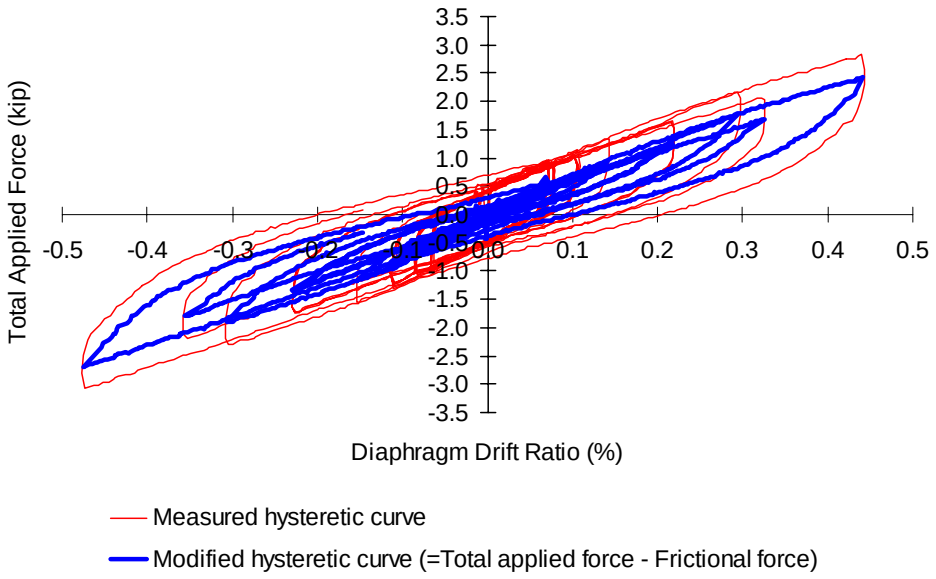

Figure 4.16: Comparison of measured and modified hysteretic curve in which frictional forces are extracted from measured forces for low diaphragm drift ratios (Tests #1 - #5).

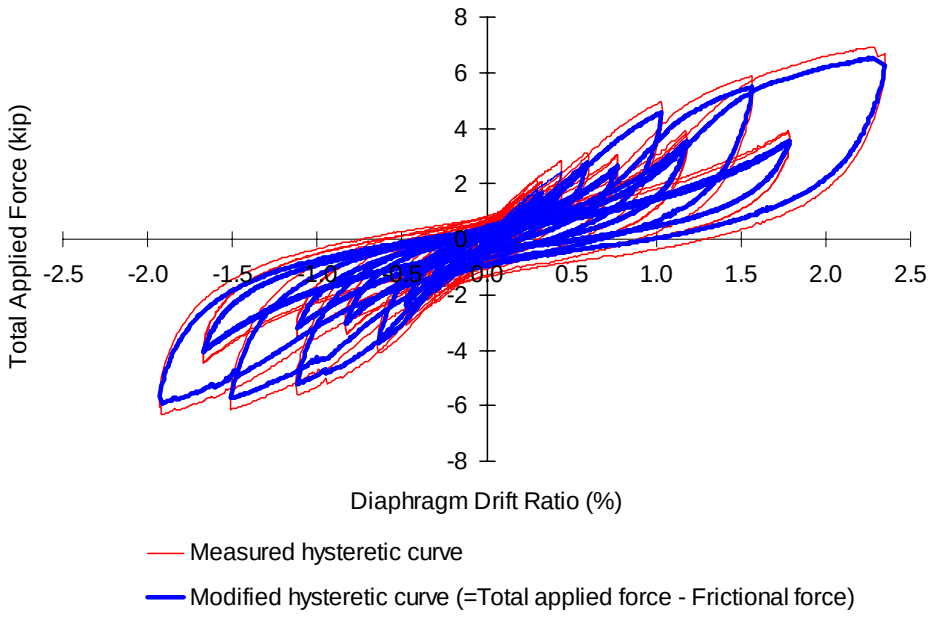

Figure 4.17: Comparison of measured and modified hysteretic curve in which frictional forces are extracted from measured forces for low diaphragm drift ratios (Tests #6 - #9).

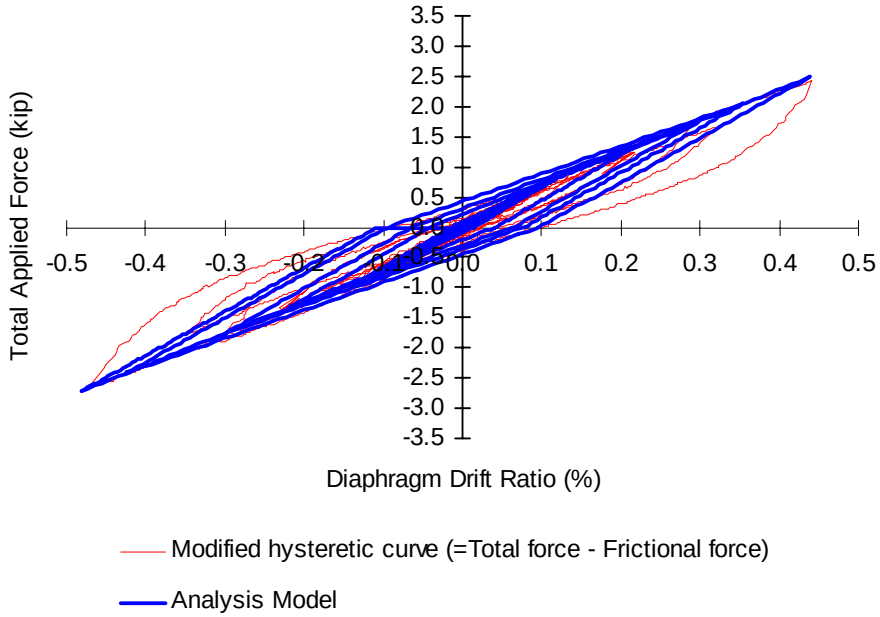

Figure 4.18: Diaphragm analysis model associated with the modified hysteretic curve for Tests #1- #5.

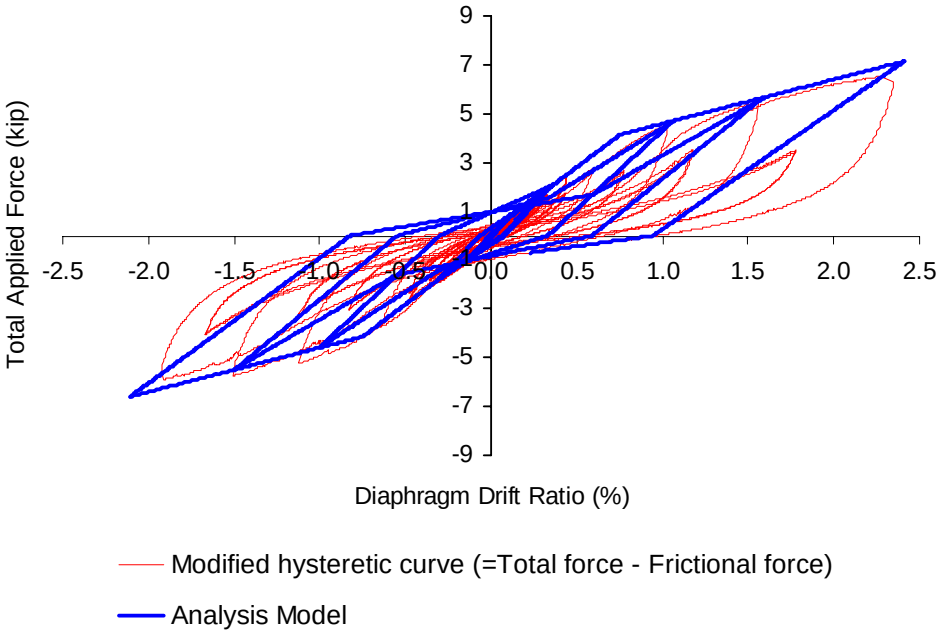

Figure 4.19: Diaphragm analysis model associated with the modified hysteretic curve for Tests #6- #9.

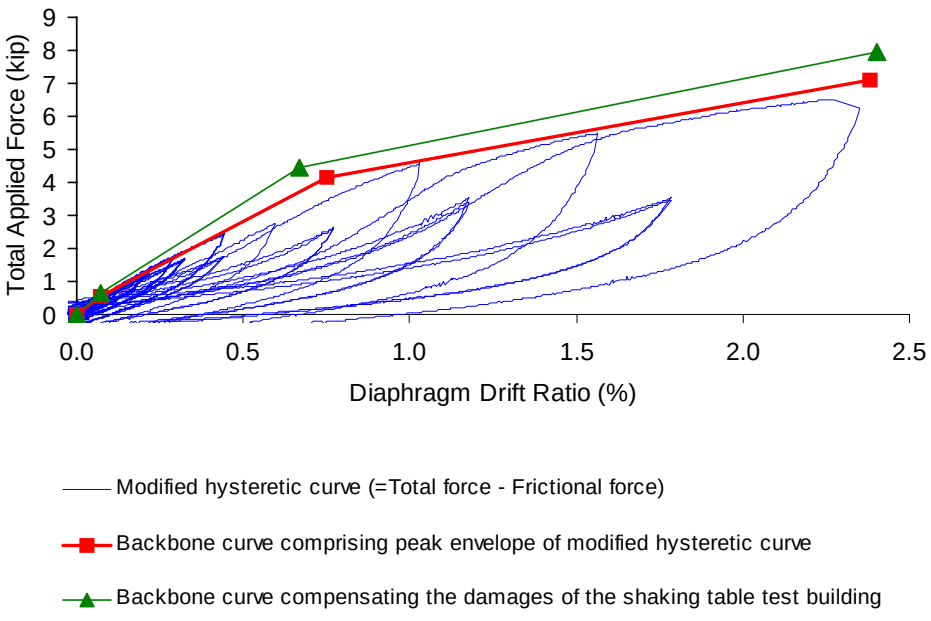

Figure 4.20: Comparison of hysteresis envelopes.

The final selected stiffness and strength properties of the diaphragm are shown in Fig. 4.21. The elastic stiffness of the diaphragm is 9.05 kips per one percent drift. This calculated total stiffness the diaphragm is 7.41 kips/in. This stiffness value is similar to G_{d_FEMA356} (8 kips/in) for a chorded single diagonally sheathed diaphragm (see Table 2.2).

In Cohen's research, the structure was idealized as a two-degrees-of-freedom system as shown in Fig. 2.1. The first degree of freedom was associated with the in-plane deformation of the north and south walls, and the second one is associated with the in-plane deformation of the flexible diaphragm. The estimated diaphragm stiffness of the two DOF model was 24 kips/in (Cohen 2001). The difference between 24 and 7.41 kips/in may be due to the effects of the out-of-plane wall. In the two DOF model, the out-of-plane wall stiffness was not considered. The diaphragm properties selected from the quasi-static diaphragm tests are used in the current work.

The equivalent shear properties of the diaphragm (see Section 2.3.5.4) are calculated from the modified backbone curve shown in Fig. 4.20. The behavior of this diaphragm is governed by shear deformation. The equivalent width of the diaphragm is calculated from the mid-thickness of the walls. The equivalent shear stiffness, $G_e t$, and the equivalent shear stress is calculated from these equivalent properties and these values are used in the analysis input discussed in Section 2.3.

The calculated effective elastic and tangent shear stiffness for the three parameter hysteretic model are 8.82 kips/in $(G_e t)_1$ and 1.95 kips/in $(G_e t)_3$, respectively, as shown in Fig. 4.21. The first (F_1) and second shear stresses (F_2) at the points where the stiffness changes, as explained in Sections 2.4.3, are 0.1 ksi (0.65kips) and 0.69 ksi (4.46 kips), respectively. The α, β and γ parameters are 3.0, 0.01, and 0.478, respectively.

4.3.3 Wall modeling

The dimensions of the north and south walls are 55 (B) x 84 (H) in, and the east

wall and west walls are 264 (L) x 84 (H) in as shown in Figs. 4.1 and 4.22. There were openings in the east wall. The strength of materials models discussed in Section 2.4 apply only to unreinforced masonry shear walls. The strengths and stiffnesses of the in-plane and out-of-plane reinforced masonry walls are estimated using the mechanics of materials type equations from FEMA 356 (ASCE 2000a) and ACI 530-99 (MSJC 1999b) in this Section. In order to obtain estimates of the actual properties of the test structure in this research, a model calibration process shown in Fig. 4.34 is used.

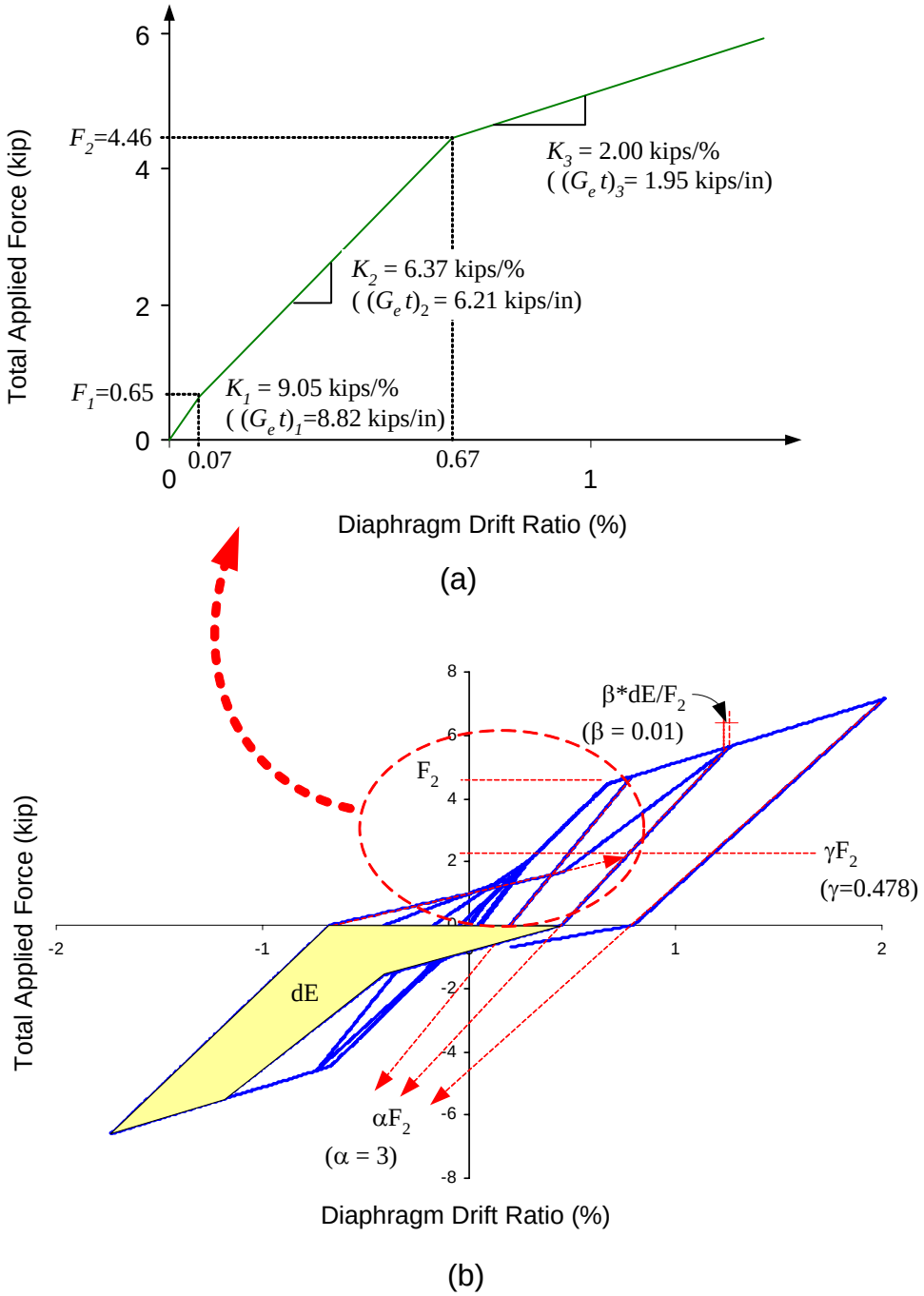

Figure 4.21: Summary of hysteretic properties of three parameter model for diaphragm element: (a) Stiffness and strength, (b) Hysteresis model.

4.3.3.1 Material properties from prism masonry compression tests versus predicted values

Compression tests were performed by CERL personnel. Measured mechanical properties of the masonry used in the test building were provided in (Cohen 2001). Table 4.2 summarizes the experimental test of the CMU used in the test building. The masonry compression prism tests from Cohen (2001a) showed that the grouted and ungrouted strengths were 1.4 ksi and 0.9 ksi, respectively. The elastic moduli of the grouted and ungrouted half-scale concrete masonry units (CMU) were 330 ksi and 320 ksi, respectively (Cohen 2001). When Eq. 2.66 is used along with f_m' = 1.4 ksi from Table 4.2, a value of E_m = 770 ksi is obtained for the grouted compressive strength. It can be concluded that Eqs 2.66 to 2.69 do not provide an accurate estimate of the elastic modulus of the masonry in compression, E_m, for this test. In the analyses subsequently reported in this chapter, the average values of E_m = 325 ksi and f_m' = 1.15 ksi from Table 4.2 are used for the subsequent analyses.

Table 4.2: Masonry prism compression tests (Cohen 2001).

Construction	Compressive strength (f_m')	Elastic modulus (E_m)	Usable strain
grouted	1,400 psi	330 ksi	0.0029
ungrouted	900 psi	320 ksi	0.0029

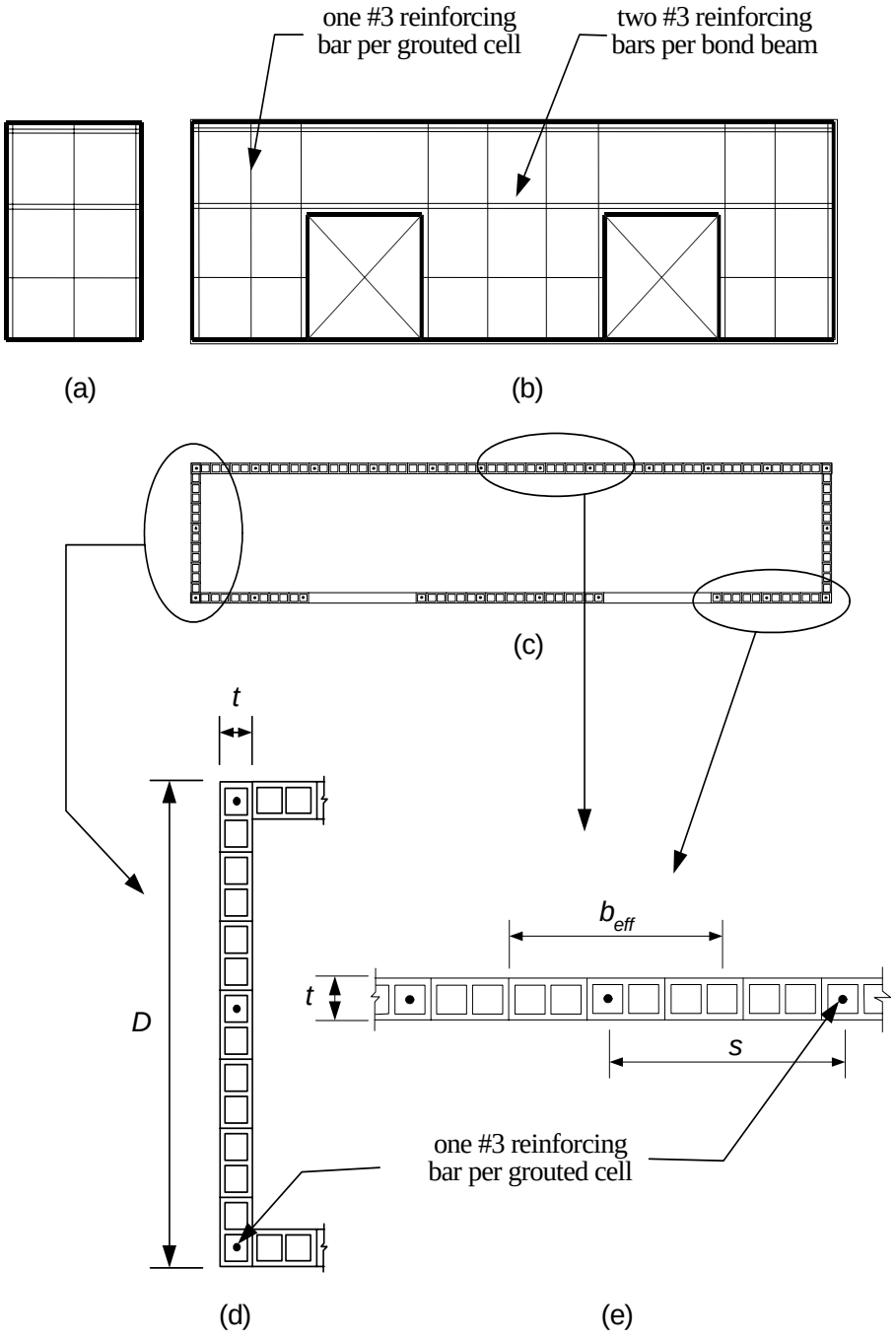

Figure 4.22: Reinforcement of masonry walls: (a) North and south wall; (b) East wall; (c) Plan; (d) North and south wall detail; and (e) East and west wall detail (Cohen 2001).

4.3.3.2 Stiffness and strength of in-plane walls

In Sections 2.4.4, the modeling of the flange effects from out-of-plane walls is discussed. The initial stiffnesses and cracking forces as a function of a variable effective flange width are summarized in Table 4.3. When the effective flange length L_f (see Fig. 4.23) is equal to the thickness of in-plane walls (3.5 in), i.e., zero flange effects, the in-plane wall stiffness of north and south wall is 53 kips/in using Eq. 2.72. When L_f is equal to 10.5 in, the in-plane stiffness is 70 kips/in. The in-plane stiffness, 50 kips/in, obtained from the model calibration process, as discussed in Sections 4.4.1, is similar to that of the in-plane stiffness without the flange. However, it must be recognized that the calculated values in Table 4.3 depend on the material properties (E_m and G_m).

Table 4.3: In-plane wall stiffness and flexural cracking strength varying L_f in Fig. 4.23.

L_f	Cracking force (V_{cr}: kip)	Stiffness (K_{ip}: kip/in)
t	1.3	53
$2t$	1.7	62
$3t$	2.0	70
$4t$	2.3	78

1. t = 3.5 in, $n = E_s/E_m$ = 89, E_s = 29,000ksi, E_m = 325 ksi, $G_m = 0.4E_m$ = 130 ksi, f_r = 68 psi (Allowable flexural tension according to mortar type M - ACI 530-99, Table 2.2.3.2 (MSJC 1999a).

2. $V_{cr} = M_{cr}/H$, where V_{cr} = strength at cracking, $M_{cr} = (f_r I_{gt}) / y_t$, M_{cr} = cracking moment, I_{gt} = moment of inertia gross transformed uncracked section, and y_t = distance from centroidal axis.

The shear strength of the in-plane wall can be calculated from Eq. 4.2 (ASCE 2000a).

$$V_{mL} = \left[4.0 - 1.75\left(\frac{M}{Vd_v}\right)\right]A_n\sqrt{f_m'} + 0.25P_L \text{ : Eq. 7-11 in FEMA 356} \qquad (4.2)$$

where

V_{mL} = Lower bound shear strength provided by masonry

A_n = Area of net mortared / grouted section

M = Moment on the masonry section

V = Shear on the masonry section

d_v = Wall length in direction of shear force

P_L = Lower-bound vertical compressive force in pounds due to gravity loads

If $M = VH$, Eq. 7-11 in FEMA 356 becomes

$$V_{mL} = \left[4.0 - 1.75\left(\frac{H}{d_v}\right)\right]A_n\sqrt{f_m'} + 0.25P_L \qquad (4.3)$$

V_{mL} is 5.2 kips using Eq. 4.3 with H = 84 in, d_v = 53 in, and P_L = 656 lb. Since the shear strength is from this calculation is greater than the flexural cracking strength from Table 4.3, it is apparent that the primary damage within the wall will be flexural cracking.

The yield strength of the in-plane wall without flange effects from the east and west walls is calculated from Fig. 4.23. The fraction of the structural depth of the wall in compression is calculated as

$$k = \frac{d_c}{d}$$

$$= \frac{[-3nA_s + \sqrt{nA_s(9nA_s - 2d_1 t_{eff} + 2d_3 t_{eff} + 4dt_{eff})}]}{df_m' t_{eff}} = 0.312 \quad (4.4)$$

Where

A_s = area of nonprestressed tension reinforcement (0.11 in^2)

d = structural depth (53.13 in)

d_2 = distance between compression reinforcements in Fig. 4.23 (27.44 in)

d_3 = distance from extreme compression fiber to centroid of compression reinforcement (1.75 in)

t_{eff} = effective thickness of hollow CMU (2.2 in)

The specified yield strength of the nonprestressed reinforcement is 31.92 ksi, which is 30 percent larger than the allowable strength of 24 ksi. The calculated values of the forces T_{s1}, T_{s2}, and C_s shown in Fig. 4.23 are 3.51, 0.87, and 1.43 kips, respectively. The yielding moment, M_y, is 190 kips-in, and the shear strength, V_y, is 2.26 kips. When the flange effect is considered, this strength value is increased depending on the magnitude of L_f. However, the flange effect is assumed to be zero in this work for the purpose of obtaining a lower-bound estimate of the in-plane wall properties (flange effects from the out-of-plane walls are considered within the calibration process).

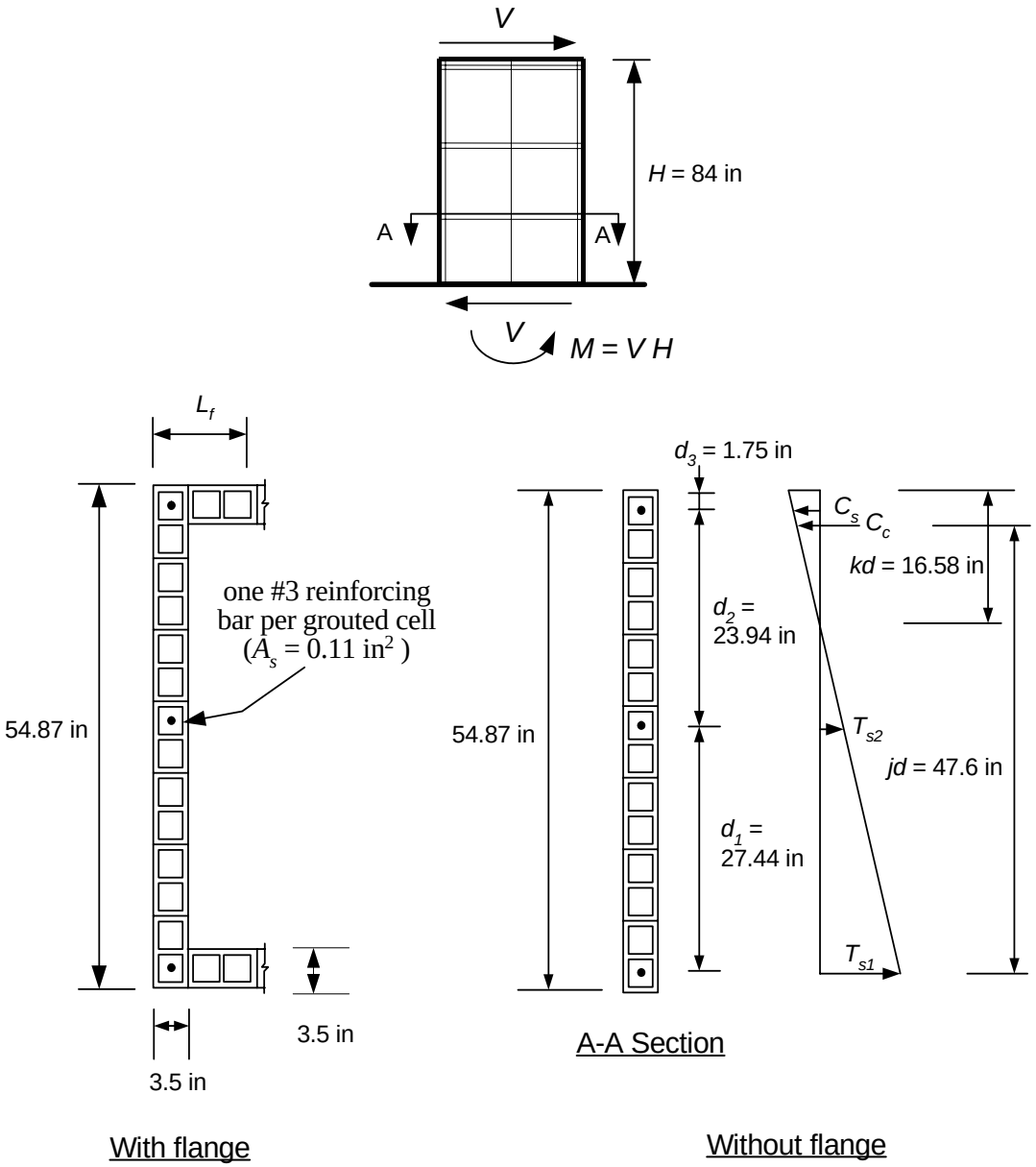

Figure 4.23: In-plane wall detailed section.

4.3.3.3 Stiffness and strength of out-of-plane walls

Strength of out-of-plane walls

The strength contribution from the out-of-plane walls is calculated based on Fig. 4.24. Flexural cracking of the out-of-plane masonry wall may lead to significant damage. The effective compression width per bar as b_{eff} in Figs. 4.22 and 4.24, is 21 in. This value is obtained as the smallest of the center-to-center bar spacing (22 in), six times the wall thickness (21 in), or 72 in (ACI 530-99 Section 2.3.3.3) (MSJC 1999b). The calculated flexural cracking moment M_{cr} is 2.8 kips-in per effective width using the information in the footnotes to Table 4.3. The cracking strength is 1.62 lb/in. When this strength is applied to the total length of out-of-plane wall (427 in), the flexural cracking force V_{cr} is 0.691 kips.

The fraction of the structural depth of the wall in compression $k = d_c/d$ is 0.137 from Fig. 4.24. The yielding moment M_y is 280 lb-in per in. The yielding force per unit length is 3.33 lb, and the total flexural yielding force, V_y, is 1.42kip.

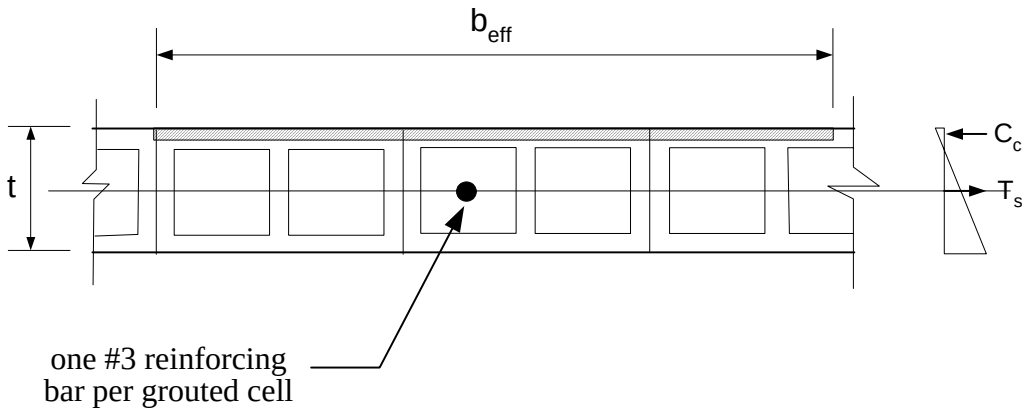

Figure 4.24: Compressive area for out-of-plane masonry wall.

Effects of out-of-plane walls and diaphragm flexibility

For the proposed MDOF model, two structures with a rigid diaphragm and one structure with a flexible diaphragm, as shown in Fig. 4.25, are examined to determine the approximate lateral stiffness of the in-plane walls and out-of-plane walls. The out-of-plane wall stiffnesses are influenced by the diaphragm flexibility. For these FEA models, the measured material properties are obtained from Cohen (2001a). In these analyses, an elastic modulus of 325 ksi is used for the masonry and the reinforcement is not considered. The resulting effective thickness, t_{eff}, is 2.25 in for the in-plane walls and 3.5 in for the out-of-plane masonry walls, because the CMU walls are partially hollow (Cohen 2002). Regarding these structures, thick shells are needed in cases where transverse shear flexibility of the masonry walls is important. Thus, the S8R element in ABAQUS (HKS 2000) is used. To define the total lateral stiffness of the structures, a unit load is applied to the center of the diaphragm in the E-W direction. The displacement at the center of the diaphragm is obtained to calculate total lateral flexibility of the structure. This flexibility coefficient is inverted to obtain the stiffness.

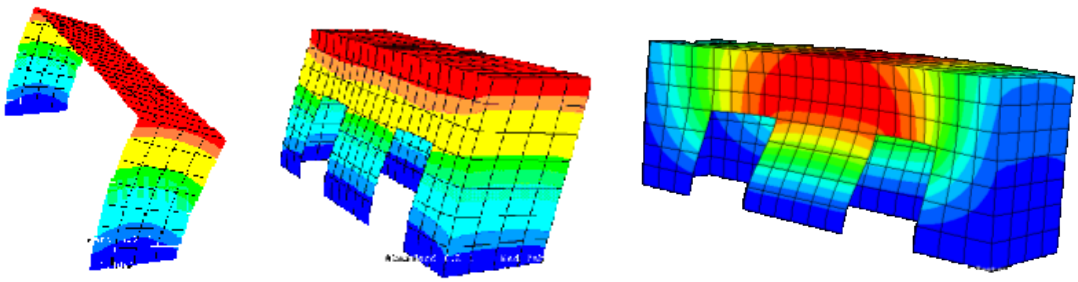

(a) (b) (c)

Figure 4.25: Deformed shaped of the structure: (a) structure with rigid diaphragm, (b) structure with rigid diaphragm and east and west wall, and (c) structure with flexible diaphragm.

Of the three FEA analysis models shown in Fig. 4.25, the structure that has no out-of-plane wall (see Fig. 4.25 (a)) gives a lower bound of the total lateral stiffness. The total

lateral stiffness of north and south in-plane walls in this model is 80 kips/in. This value is the same as that calculated from the simplified mechanics of materials types of approaches using Eq. 2.72. The total lateral stiffness of the structure with the rigid diaphragm (see Fig. 4.25 (b)) is 257 kips/in. The lateral stiffness of the second structure is almost three times larger than that of first structure that has no out-of-plane walls. The reason is that the shear stiffness and axial effect in east and west out-of-plane walls contributes to the total lateral stiffness, as shown in Fig. 4.26.

Figure 4.25 (c) shows the deformed shape of the structure with a flexible diaphragm. This deformed shape is more complex than the previous ones. The north and south walls are twisted due to the bending of the flexible diaphragm. The out-of-plane wall stiffness and strength is affected by the out-of-plane bending associated with the diaphragm deformation. It is difficult to determine the wall properties by simple principles in this case.

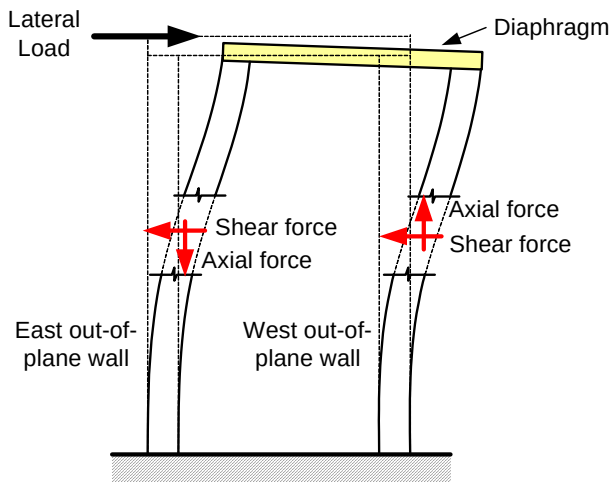

Figure 4.26: Shear and axial force contribution of out-of-plane walls.

The stiffnesses of these structures are summarized in Table 4.4. The total lateral stiffness of the structure with flexible diaphragm is estimated by using the model calibration process discussed in Sections 4.4. The total lateral stiffness from the model calibra-

tion process is 23 kips/in including in-plane and out-of-plane wall stiffness. These stiffnesses are discussed subsequently in Sections 4.4. It is apparent that the total lateral stiffness is dramatically decreased due to the diaphragm flexibility. The detailed out-of-plane wall effects are discussed in Sections 4.4 and 4.5.

Table 4.4: Comparison of stiffnesses in terms of diaphragm flexibility and out-of-plane walls without considering reinforcement.

Model	Total lateral stiffness	Note
In-plane walls with a rigid diaphragm	80 kips/in	See Fig. 4.25 (a)
In-plane and out-of-plane wall with a rigid diaphragm	257 kips/in	See Fig. 4.25 (b)
In-plane and out-of-plane wall with a flexible diaphragm	23 kips/in	See Fig. 4.25 (c) and Table 4.8

Observed wall damage and hysteretic models

In this work, the damage sustained by the building is characterized using drift ratios. The drift ratios of the in-plane and out-of-plane walls are captured at the top of the walls. The wall drift ratio is defined by

$$\delta_{wall} = \frac{\Delta_{wall}}{H} \tag{4.5}$$

where Δ_{wall} = wall lateral deflection at the top of the walls.

The hysteresis models for masonry walls discussed in Section 2.4.3 are applied to these reinforced masonry walls. A rocking hysteresis model, as shown in Fig. 2.41, is used for the in-plane walls, which have significant bed-joint cracking characteristic of wall rocking, as discussed in Section 4.2.3. Based on the observed damage of the out-of-

plane walls, the behavior of out-of-plane walls is governed by several patterns of response. The out-of-plane bending of the walls associated with the flexible diaphragm may crack the upper part of the out-of-plane walls. The central lower part of the walls is governed by the rocking response at the base. Both ends of the out-of-plane walls provide the flange effects to the in-plane walls. It is difficult to idealize the complex behavior of the out-of-plane walls. However, the rocking model is more appropriate to idealize the behavior for the simplified modeling. This is due to the fact that the dynamic response of the central lower out-of-plane walls exhibits the characteristics of rocking behavior.

4.3.4 Ground motions

Three E-W directional accelerations are recorded at the top of lifting frame, i.e., the pedestal that the building is constructed on. Figure 4.27 shows the locations of accelerometers on the lifting frame. The recorded motions on the top of the lifting frame were in general different for locations that were expected to have the same motion. The peak ground motions recorded at the lifting frame are listed in Table 4.5. The acceleration at A4 is slightly higher than at A6 for each test. Also, the recorded motions show slightly higher acceleration and relatively larger displacement at the top of south wall than at the top of north wall. The differences in the above indicate that there could be some twisting behavior in the lifting frame in each test. The average value of the three E-W directional accelerations is used in this study. It is not possible to apply the three recorded motions to the simplified analysis model due to a limitation associated with baseline correction. This limitation is explained in Section 4.3.7.

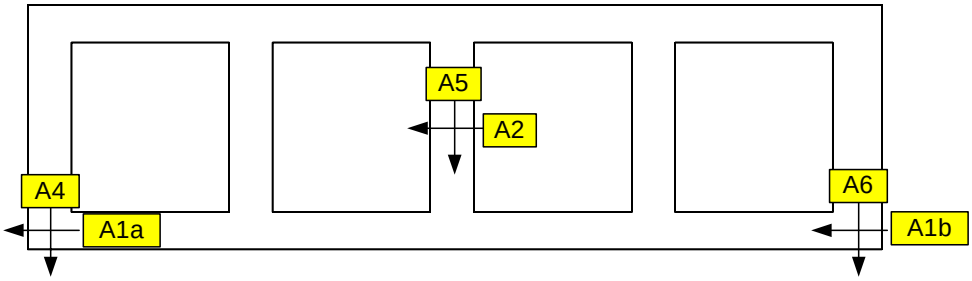

Figure 4.27: Instrument two corners and mid-frame in two directions for measuring horizontal acceleration at lifting frame.

Table 4.5: Measured E-W directional acceleration at lifting frame.

Instrument (Original Index)	Peak Acceleration (g)		
	Test 3	Test 5	Test 9
A4 (AY106)	0.5667	0.7989	1.1552
A5 (AY100)	0.5070	0.6536	0.9538
A6 (AY102)	0.5065	0.6371	0.9172

4.3.5 Mass

The masses are lumped at the corresponding degrees-of-freedom of the wall and diaphragm element shown in Table 4.6 and Fig. 4.7. A density of 120 pcf for the masonry wall and an uniform distributed load of 2.42 psf for the diaphragm are used. For the lumped mass calculation, an effective thickness of 2.2 in, which accounts for the 3.5 in hollow masonry units, is used for the calculation of the wall masses.

Table 4.6: Lumped masses at the node location in Fig. 4.7.

Direction	Node	Weight (lb)
E-W	104	1028
	105	1519
	106	1028
	Total	3576
N-S	101	1540
	102	422
	103	1614
	Total	3576

4.3.6 Damping

The calculated responses of the two story building discussed in the previous chapter are insensitive to damping assumptions, since the overall behavior is predominantly elastic. However, the calculated responses of this one story building are more sensitive when significant damage is encountered. Therefore, this section discusses more detailed considerations regarding the damping model for the one story building studied in this chapter.

Quantification of the true (physical) viscous velocity-dependent damping is difficult. Damping mechanisms are in general not well understood. The state variables relevant to calculation of the damping forces are not well known (Adhikari and Woodhouse 2001). The most common approach is to assume that the instantaneous generalized velocities are the only relevant state variables that determine damping. Modal or Rayleigh damping is often used to approximate the energy dissipation from various sources. Rayleigh damping, which is proportional to the stiffness and mass of the structure, is suggested primarily for

mathematical convenience (Adhikari and Woodhouse 2001). However, when structures have nonproportional damping and/or exhibit nonlinear response, their response can not be obtained by modal superposition. Therefore, strictly the damping can not be expressed by modal damping ratios, but it must be expressed by an explicit damping matrix (Clough and Penzien 1993). The concepts of hysteretic damping for nonlinear response and non-proportional damping are discussed below.

Hysteretic damping for nonlinear analysis

To take into account the energy (or force) dissipation via inelastic response, it is better to use hysteretic damping rather than viscous damping. However, it is difficult to estimate the hysteretic damping factor of a building. In order to use hysteretic damping, the nonlinear response of each structural component in the building, which indicates the dissipation forces or the dissipated energy per cycle, should be measured by testing. Therefore, hysteretic damping is difficult to consider in analysis modeling.

Nonproportional damping

In the analysis of a building made up of two types of materials (i.e., buildings with flexible diaphragms and reinforced masonry walls), the two different materials provide different energy dissipation (Clough and Penzien 1993).

The construction of the nonproportional damping matrix is similar to that in developing proportional damping matrices. Rayleigh damping coefficients, a_0 and a_1, in Eq. 1.2 are determined for two damping ratios from linear analysis. The coefficients are given by

$$\begin{Bmatrix} a_0 \\ a_1 \end{Bmatrix} = 2\frac{\omega_m \omega_n}{\omega_n^2 - \omega_m^2}\begin{bmatrix} \omega_n & -\omega_m \\ -1/\omega_n & 1/\omega_m \end{bmatrix}\begin{Bmatrix} \xi_m \\ \xi_n \end{Bmatrix} \tag{4.6}$$

where, ξ_m, ξ_n = damping ratio associated with the two specific frequencies, ω_m, ω_n.

For $\xi_{wall} \neq \xi_{diaphragm}$, different Rayleigh coefficients a_0 and a_1 (see Eqs. 4.7 and 4.8) are assigned to flexible diaphragms and reinforced masonry walls (Bathe 1996). These coefficients depend on the frequencies determined by solving the eigenproblem of the building using the combined initial elastic stiffness and mass matrices of masonry walls and diaphragms (Clough and Penzien 1993). Thus the diaphragm and wall damping sub-matrices are given by

$$C_{diaphragm} = a_{0\_\text{diaphragm}} M_{\text{diaphragm}} + a_{1\_\text{diaphragm}} K_{\text{diaphragm}} \tag{4.7}$$

$$C_{wall} = a_{0\_\text{wall}} M_{\text{wall}} + a_{1\_\text{wall}} K_{\text{wall}} \tag{4.8}$$

When the nonproportional damping matrix of the structure is constructed as shown in Fig. 4.28, the common DOFs (X in Fig. 4.28) include contributions from the diaphragm and the wall damping matrices.

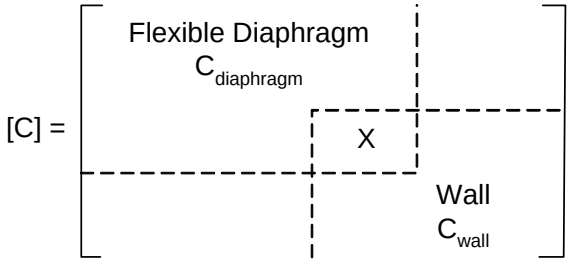

Figure 4.28: Assembly of combined damping matrices.

When the damping ratios ξ_{wall} and $\xi_{diaphragm}$ are known (or specified), the simplest way to formulate a non-proportional damping matrix is to construct it by combining the proportional matrices developed for each diaphragm and wall using Eqs. 4.7 and

4.8 (see Fig. 4.28) (Clough and Penzien 1993). The damping model of the two-story building discussed in the previous chapter does not consider the walls and the diaphragm damping ratios separately. This is because the specific damping ratios of the wall and diaphragm applied to the two story building do not affect the calculated response significantly due to its overall elastic behavior. However, the one-story building studied in this chapter has significant damage in the latter tests, and therefore the non-proportional damping model is necessary to give results comparable to the observed response of the physical structure.

The coefficients are calculated using the corresponding first and third modes (see Fig. 4.29) because the analytical model has three degrees of freedom for the E-W and N-S directions and the same damping ratio is desired approximately for the corresponding three modes in the E-W direction, i.e., m = 1, and n = 3 in Eq. 4.6 (Chopra 1995). The same damping ratios for the first and higher mode, i.e., $\xi_1 = \xi_3$ are assumed to calculate the Rayleigh damping coefficients for a practical linear analysis with proportional damping matrix. Therefore, given the first (ω_1) and third frequencies (ω_3) calculated from linear analysis of 75 and 141 rad/sec, respectively, and the same damping ratio of 3% for the first and third modes is assumed to calculate the proportional damping matrix of the diaphragm structure, the Rayleigh damping coefficients a_0 and a_1 are 2.932 and 0.000278 (see Fig. 4.30 to see the variation of damping ratio and frequency for Rayleigh damping). If a damping ratio of 6% for the first and third modes is assumed to calculate the proportional damping matrices of the walls, the Rayleigh damping coefficients a_0 and a_1 are 5.864 and 0.000556. The coefficients for 6% damping are two times higher than those for 3% damping. As shown in Fig. 4.29, the first mode shape is associated with the diaphragm displacement and the second and third mode shapes are associated with the in-plane wall displacements. When the damping ratios ξ_m and ξ_n are not same, the coefficients differ significantly from those calculated based on $\xi_m = \xi_n$. If the damping ratio of the first mode is 3% and the damping ratio of the third mode is 4%, the Rayleigh damp-

ing coefficients a_0 and a_1 are 1.832 and 0.000475, respectively. If the damping ratio of the first mode is 3% and the damping ratio of the third mode is higher than 5.67%, the coefficient a_0 will be a negative value and a_1 will be higher than 0.00166. Any non-negative value of a_0 is a possible candidate for a damping model. Figure 4.30 summarizes graphically the Rayleigh damping coefficients discussed above.

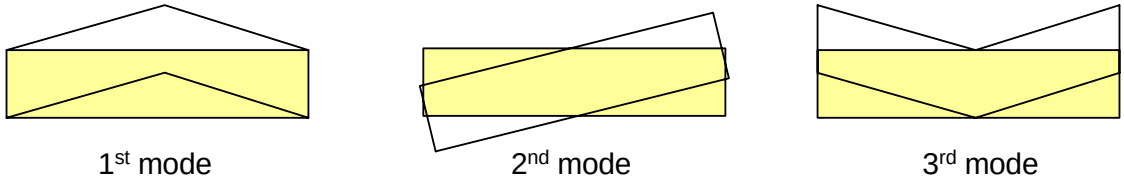

Figure 4.29: Eigenmode shapes of the building.

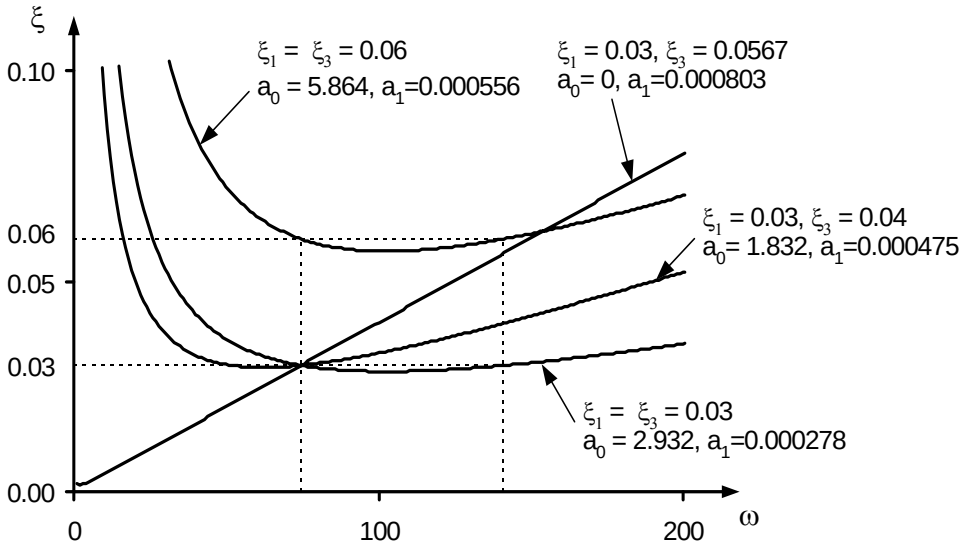

Figure 4.30: Variation of damping ratio and frequency for Rayleigh damping.

Recommended procedure for the MDOF models.

In this research, a nonproportional damping is used for linear and nonlinear analy-

sis. The proportional damping matrix is calculated for each of the parts because of the resulting simplicity and computational advantages. Rayleigh damping is a velocity-dependent damping. Therefore, it is necessary for structural engineer to pay attention to what velocity (relative or absolute velocity) is used to solve the linear equation of motion because some programs use absolute values. In the view of the authors, relative velocity is a more appropriate choice to approximate the seismic responses of buildings. The Rayleigh damping coefficients are calculated from linear analysis and are used to approximate unknown energy dissipation within the structure. The damping matrix for a structure should be determined from its modal damping ratios estimated from available data.

The CERL personnel performed three sine-decay tests in the three principal directions (E-W, N-S and vertical direction) to estimate the equivalent viscous damping within the elastic structure. The building was excited and abruptly halted to capture the decay of the accelerations. An equivalent damping ratio of 3% was taken from the E-W directional sine-decay test (Cohen 2001). However, it is possible that more than one damping ratio may represent the system response equally well, so that an identified damping becomes non-unique (Adhikari and Woodhouse 2001). It can be concluded that the assumption of 3% damping ratio is not appropriate for all the structural components of the building based on the analysis results reported subsequently in this chapter.

Although the damping matrices do not strictly combine in the same way as the stiffness matrices, the procedure illustrated in Fig. 4.28 is the simplest way to determine the structure nonproportional damping matrix (Clough and Penzien 1993). For the simplified MDOF modeling of the building, the lumped masses of the analytical MDOF model shown in Fig. 4.6 are associated with the common DOFs at the interface between the diaphragm and the wall elements (see Fig. 4.28). Although it is possible that more than one damping ratio may represent the response of the building, the viscous Rayleigh damping coefficients $a_{0\_diaphragm}$ and $a_{1\_diaphragm}$ are calculated from the equivalent damping ratio of 3% taken from the E-W directional sine-decay test. The coefficient $a_{0\_diaphragm}$

is applied to the lumped masses. Thus, the damping contribution from the masses in Eqs. 4.7 and 4.8 are assumed to be equal (i.e. $a_{0\_wall} = a_{0\_diaphragm}$) for simplicity.

When the effects of force loss and energy dissipation are assumed to be small, hysteretic damping of masonry walls can be approximately modeled as viscous damping with an equivalent coefficient of viscous damping. In this work, the Rayleigh damping coefficient a_{1_wall}, which is proportional to stiffness, is calibrated to take into account the energy dissipated by local damage within the wall during nonlinear time history analyses. This procedure is discussed further in Section 4.4.

4.3.7 Difficulties of linear and nonlinear time history analysis

4.3.7.1 Baseline correction

The integration of the acceleration record through time may result in a relatively large displacement at the end of the event when an acceleration history is specified for analysis. This behavior typically occurs due to mechanical errors or an insufficient sampling frequency such that the actual acceleration history is not accurately captured. To compensate for these errors, a base line correction technique proposed by Newmark (1973) can be applied to the ground motion for time history analysis (HKS 2000). However, when more than one ground motion is applied to the structure in a given direction, it is not appropriate to correct the approximate acceleration histories by using the baseline correction technique (i.e., different base excitation at each of the in-plane walls in the CERL test structure).

The measured accelerations at the lifting frame in the E-W direction are not symmetrical as shown in Table 4.5. The peak acceleration at the corner of the lifting frame below the south wall (0.56 g) is larger than that at the north corner and center of the lifting frame (0.50 g). Figures 4.31 and 4.32 show the measured and calculated relative displace-

ments, when three measured accelerations are applied to the bottom of the structures associated with the measured location at the lifting frame. The calculated peak acceleration is 1.59 g compared to the measured acceleration, 1.60 g. Even though the comparison of the three measured accelerations shows good comparative results in peak acceleration as shown in Fig. 4.35, the relative displacement from 8 to 9 sec (see Fig. 4.32) is larger than the measured one. The baseline correction method may not be used when different accelerations are applied to DOFs that have the same direction. In this study, this problem is surmounted by using the average input acceleration in the E-W direction to represent the test excitation in the analysis.

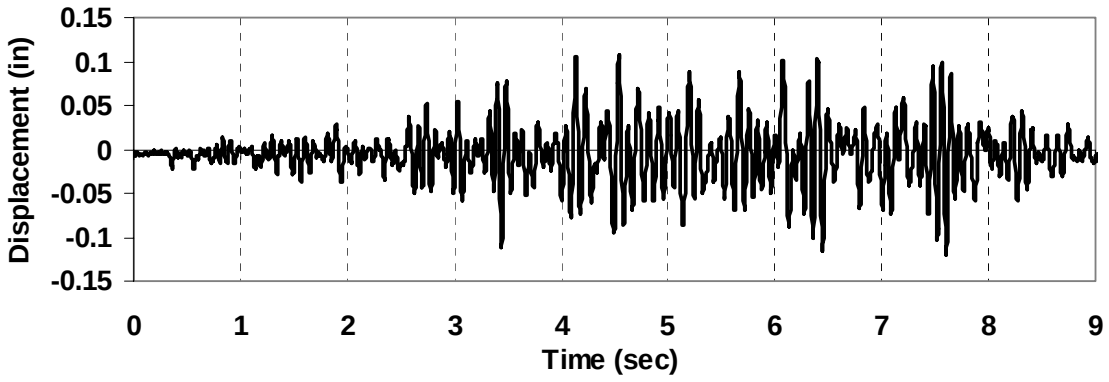

Figure 4.31: Recorded relative displacement at the center of the diaphragm.

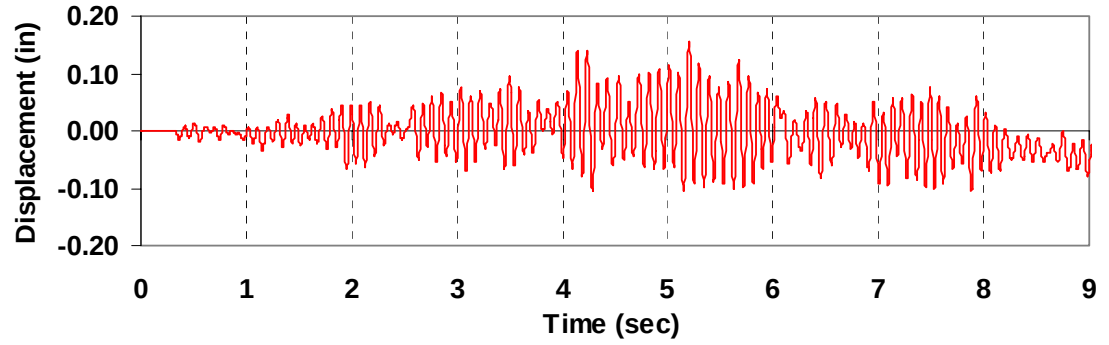

Figure 4.32: Calculated relative displacement at the center of the diaphragm applying three measured acceleration at the lifting frame.

4.3.7.2 Time step

The issue of choosing suitable time steps is a difficult problem to resolve in the case of linear and nonlinear dynamic analysis. The recorded incremental time step in the physical test is 0.005 sec. In the analysis model, it is always necessary to provide suitable steps to allow an acceptable level of accuracy. In order to insure accurate representation of the effects of this discretized time history, the time step must be smaller than 0.005 sec. Figure 4.33 shows the comparison of measured and calculated accelerations at the center of the diaphragm based on three different time steps of 0.005, 0.0025, and 0.001 sec., respectively, in the time history analyses. The differences in the results of the analyses with increments of 0.005 and 0.0025 sec. are much larger than that between those 0.0025 and 0.001sec. Thus, for the consistent linear and nonlinear dynamic analyses, a time step of 0.0025 sec. is used for linear analysis, and a time step of 0.001 sec. is used for non-linear dynamic analysis.

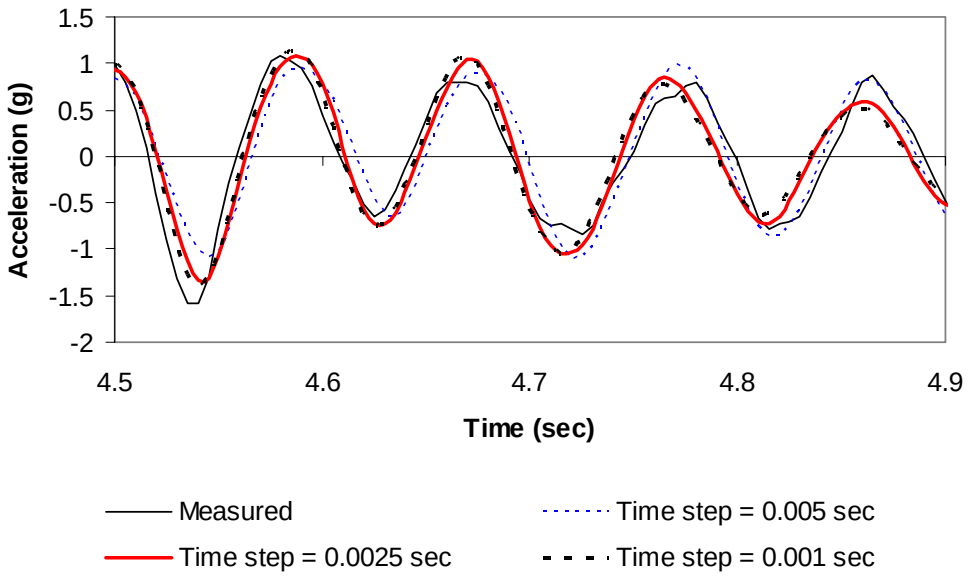

Figure 4.33: 1/2 second comparison of measured and calculated history varying time step from 0.005sec to 0.001sec.

4.4 Calibration of analytical model based on shaking table test results

The test building is idealized using the simplified multi-degree-of-freedom (MDOF) approach discussed in Section 4.3.1. The diaphragm element properties are obtained from the experimental diaphragm test results discussed in Section 4.3.2. However, it is difficult to estimate the response characteristics of masonry in-plane and out-of-plane walls, as discussed in Section 4.1. The calibration process is targeted at determining in-plane and out-of-plane wall stiffnesses, strengths, and damping.

The model calibration process (see Fig. 4.34) is applied to predict the system properties, which involve complex interactions between the in-plane wall, out-of-plane wall and diaphragm DOFs. The model calibration procedure is based on comparison of analytical model predictions to the shaking table test results. The studies focus on the acceleration and displacement in the E-W direction at the top of the south and north walls (nodes 104 and 106 in Fig. 4.6) and at the center of the roof diaphragm (node 105 in Fig. 4.6). Key unknown wall parameters are varied and examined in each analysis until good comparisons are achieved. The comparison includes the peak response and the history of the responses throughout the tests. The detailed process is discussed in Sections 4.4.1 to 4.4.3.

Section 4.4.1 presents the linear analysis step of the model calibration (see Fig. 4.34) to determine the wall stiffness. The results of Test 3 from (Cohen 2001) are used to identify the in-plane and out-of-plane wall stiffness. In Section 4.4.2, the results of Test 5 from (Cohen 2001) are used to capture the strength of the walls. In Section 4.4.3, Tests 9 and 10 from (Cohen 2001) are used to assess the hysteresis of the structural elements for the nonlinear time history analysis.

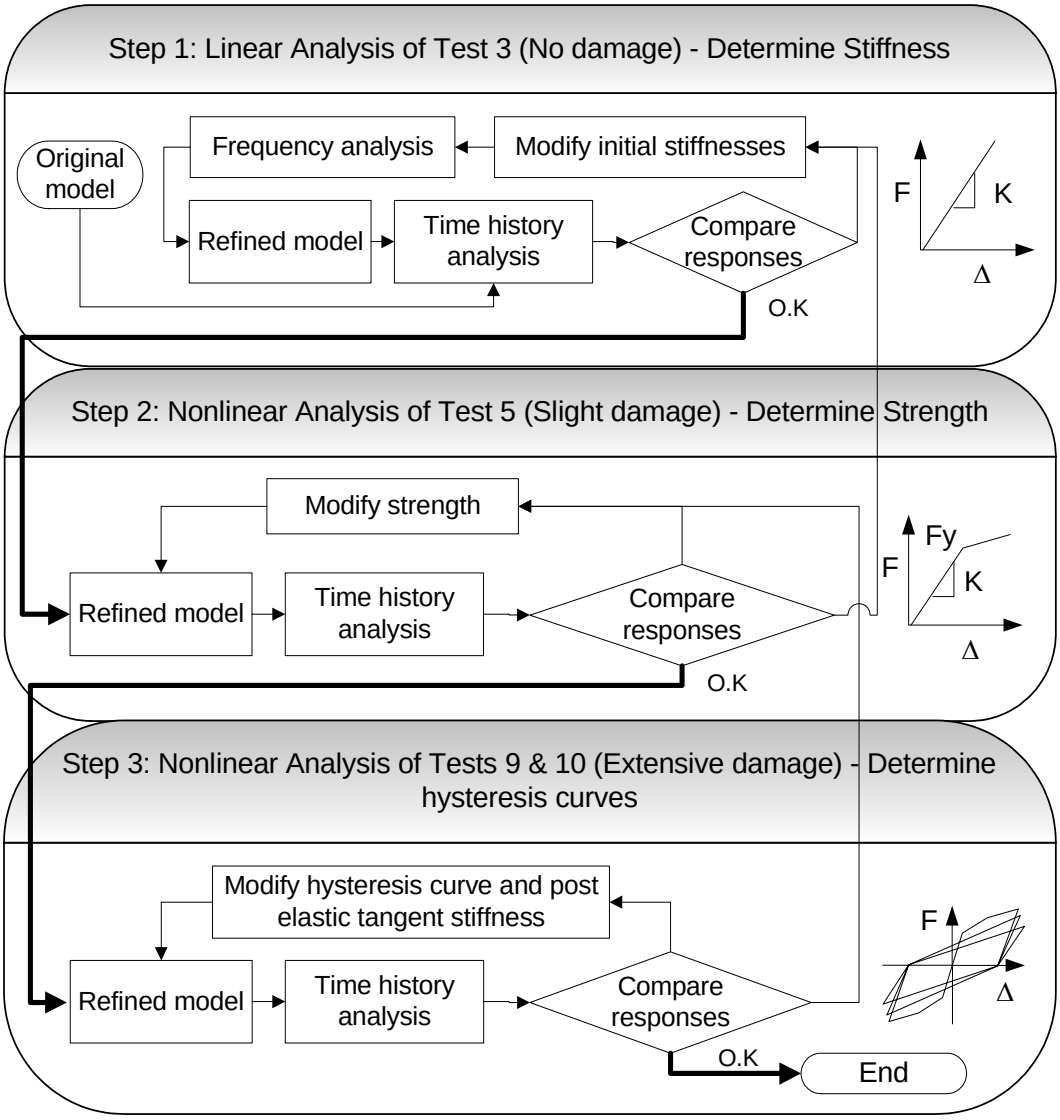

Figure 4.34: Model calibration process used for wall properties.

4.4.1 Calibration of in-plane and out-of-plane wall initial stiffness using PGA = 0.5g

The first step of the model calibration process shown in Fig. 4.34 is applied to find the elastic stiffness of in-plane and out-of plane walls. The peak acceleration of the input ground motion of Test 3 is 0.5 g. This input motion, selected from the Carbondale suite

(Wen and Wu 1999), is the modified record with its acceleration ordinates scaled by 75%. Test 3 provides the basis for the linear analysis model because there was no damage during the test. (see Table 4.1) (Cohen 2001).

The in-plane stiffnesses of the north and south walls is assumed initially as 40 kips/in, which is calculated using Eq. 2.72. During this calibration process, the in-plane stiffness is increased from this initial values and the out-of-plane wall stiffness is increased from zero. At each iteration of the calibration process, the Rayleigh damping coefficients are recalculated using the results of the frequency analysis with the modified stiffness values. The initial in-plane and out-of-plane stiffnesses are determined by comparing the overall history of the measured and calculated responses.

Section 4.4.1.1 summaries the peak measured responses of Test 3. Section 4.4.1.2 presents the predicted stiffness values obtained from this calibration. Section 4.4.1.3 shows the comparison of the measured and predicted responses.

4.4.1.1 Measured responses

Table 4.7 summarizes the peak measured responses corresponding to the locations shown in Fig. 4.4. The complete measured time history responses are plotted in Figs. C.5 through C.16 of Appendix C. The peak acceleration and displacement at the center of the diaphragm are 1.60 g and 0.12 in, respectively. The difference between the measured north (0.72 g) and south wall (0.78 g), shown in Table 4.7, may be attributed to experimental errors in the lifting frame, as discussed in Section 4.3.4. The measured acceleration at the top of south wall is 0.06 g higher than that of north wall. The relative peak displacements of the top of the north and south walls are 0.026 in.

Table 4.7: Summary of measured accelerations and displacement in the E-W direction.

Location	Peak Acceleration (g)		Peak displacement (in)	
	Instrument	Test 3	Instrument	Test 3
South wall	A104a	0.7363	D104	0.026
	A104b	0.7756		
Diaphragm	A105	1.6002	D105	0.120
North wall	A106a	0.7162	D106	0.026
	A106b	0.6922		

4.4.1.2 Summary of predicted properties

The predicted properties from Step 1 are summarized in Table 4.8. The predicted in-plane and out-of-plane wall stiffnesses are 50 kips/in and 16 kips/in, respectively. The predicted in-plane wall stiffness of 50 kips is higher than the stiffness of 40 kips/in calculated by using the simplified mechanics of materials types of approach without considering the flange effects from the out-of-plane walls and without reinforcing bar (see Table 4.4). The difference, 10 kips/in, may be attributed to the flange effects from the east and west walls or reinforcement. The predicted in-plane stiffness is similar to the in-plane stiffness with reinforcement and without flange, 53 kips/in, summarized in Table 4.3.

The estimated total lateral stiffness of Cohen's two DOF model was 320 kips/in (Cohen 2001). This total lateral stiffness of the test building is bigger than that (257 kips/in) of FEA analysis with rigid diaphragm shown in Fig. 4.25 (b). However, the total lateral stiffness of the shear wall building must be smaller than 257 kips/in due to the flexibility of the diaphragm. The total lateral stiffness from this calibrations process is 23 kips/in obtained as the sum of the in-plane and out-of-plane stiffnesses shown in Table 4.8. Based on these estimated stiffnesses, the detailed comparisons of measured and calculated responses are summarized in Section 4.4.1.3.

Table 4.8: Predicted properties from Step 1.

Component	Stiffness
In-plane Walls	50 kips/in
Out-of-plane Wall	16 kips/in (=East + West Wall)
Equivalent diaphragm stiffness $(G_e t)_1$	8.82 kips/in (see Section 4.3.2.2)

4.4.1.3 Comparison between measured and calculated responses

Of the two recorded accelerations, the one that has larger peak value is selected to compare with the analysis results. Table 4.9 summarizes the comparison of the measured and calculated response of the structure using the two damping ratios for the masonry walls and the diaphragm (see Section 4.3.6).

The measured fundamental period of the structure was 0.07sec. The fundamental period obtained in this study is 0.08 sec. The period of 0.10 sec for the two DOF model developed by (Cohen 2001) is slightly higher than the measured period. The first (ω_1) and third frequencies (ω_3) are 75 and 141 rad/sec, respectively. As discussed in Section 4.3.6, 3% damping is used to calculate Rayleigh damping coefficients for the diaphragm. The Rayleigh damping coefficients a_{0_wall} and $a_{0\_diaphragm}$ of the lumped masses at the common DOFs (X in Fig. 4.28) are 2.932. Two different damping ratios (3% and 10%) are used to calculate the Rayleigh damping coefficients a_{1_wall} of the in-plane masonry walls for investigating the effect of the damping ratio within the masonry walls. The damping coefficients a_{1_wall} are 0.00028 and 0.00097 for the damping ratios of 3% and 10%, respectively. The damping coefficient a_{1_wall} of out-of-plane wall is 0.00028.

Table 4.9: Comparison of measured and calculated response using PGA = 0.5 g.

Compared Item		Measured	Calculated			
			Refined FEM model (Cohen 2001)	2-DOF RSA (Cohen 2001)	MDOF model	
					Damping $\xi_{dia} = 3\%$ $\xi_{wall} = 3\%$	Damping $\xi_{dia} = 3\%$ $\xi_{wall} = 10\%$
Fundamental Frequency		14 Hz (0.07sec)	12 Hz (0.08 sec)	10.5 Hz (0.10sec)	12 Hz (0.08 sec)	
Diaphragm deflection		-	-	-	0.096 in	0.093 in
Center of diaphragm (105)	Acc.	1.6 g	1.8 g	1.5 g	1.48 g	1.45 g
	Disp.	0.12 in	0.13 in	0.15 in	0.11 in	0.10 in
North wall (106)	Acc.	0.72 g	-	-	0.86 g	0.70 g
	Disp.	0.026 in			0.022 in	0.020 in
South wall (104)	Acc.	0.78 g			0.86g	0.70g
	Disp.	0.026 in			0.022 in	0.020 in

The reason for showing the results of two damping ratios in Table 4.9 is the consideration of the subsequent nonlinear time history analysis of the building, as discussed in Section 4.3.6. The comparison of the analyses using two different damping ratios shows that the linear responses of the building are not sensitive to this variable. The change in the damping ratio doesn't significantly affect the displacement and acceleration at the center of the diaphragm, as shown in Figs. 4.40 and 4.45 and Table 4.9. The change from 3% to 10% damping slightly decreases the calculated peak response of in-plane walls, as shown in Table 4.9. However, when the in-plane wall is damaged, the effects of damping will be significant for the strong excitation of Tests 9 and 10 (see Section 4.4.3.3).

The peak acceleration, 1.48 g, at the center of the diaphragm is slightly smaller than the measured acceleration, 1.60 g, due to the average input motion discussed in Sec-

tion 4.3.7.1. As discussed in Section 4.3.7.1, the peak acceleration of the average ground motion (0.53g) is smaller than the measured peak acceleration at the bottom of south wall (0.57g) (see Table 4.5). When the three different input accelerations measured at the base of north and south walls and at the center of the lifting frame shown in Table 4.5 are used in this analysis, the peak acceleration is changed from 1.48 g to 1.53 g, as shown in Fig. 4.35. Therefore, it is concluded that the increased acceleration (1.53g) is due to the input ground motion. This trend appears to result from the fact that the measured acceleration at the center of the diaphragm is dynamically amplified due to the input accelerations. The three different input motions are not used in this model calibration process due to the limitation of the baseline correction discussed in Section 4.3.7.1. However, the difference compared to the measured peak value is acceptable, since the behavior of the test building is predominantly symmetric and each portion of the overall time history curve matches well without any shift phase, as shown in Figs. 4.35 and 4.39.

The calculated displacement at the center of the diaphragm is 0.11 in compared to the measured value of 0.12 in (see Table 4.9). Due to the average input ground motion discussed above, the calculated responses are slightly smaller than the measured responses. Figures 4.41 and 4.44 show the comparison of the measured and calculated relative displacement at the center of the diaphragm.

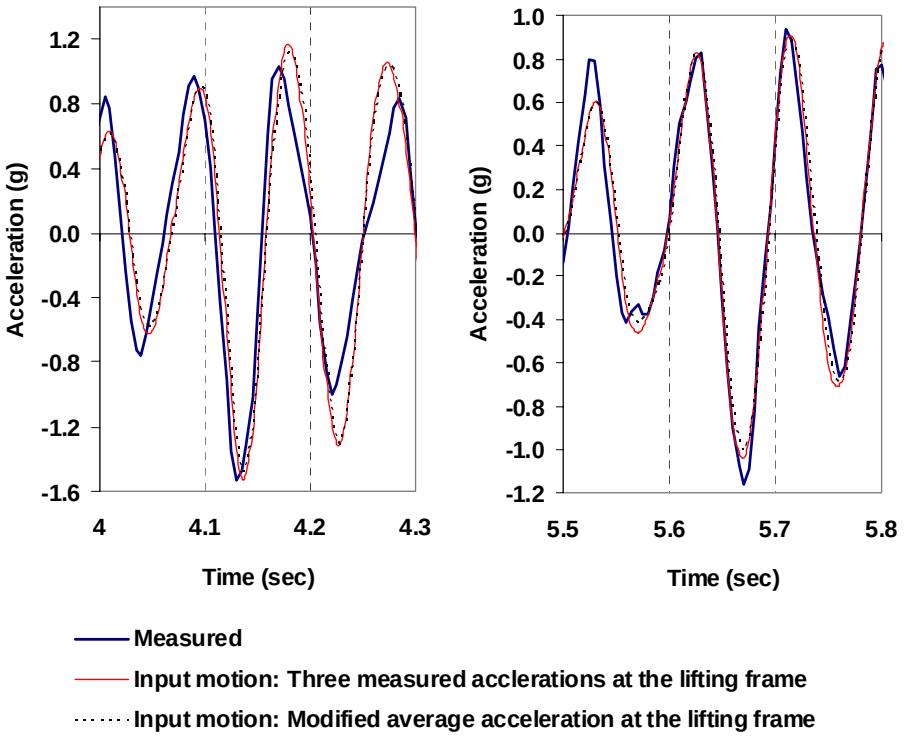

Figure 4.35: 0.3 second comparisons of measured and calculated response (Damping: ξ_{dia} = 3%, ξ_{wall} = 3%).

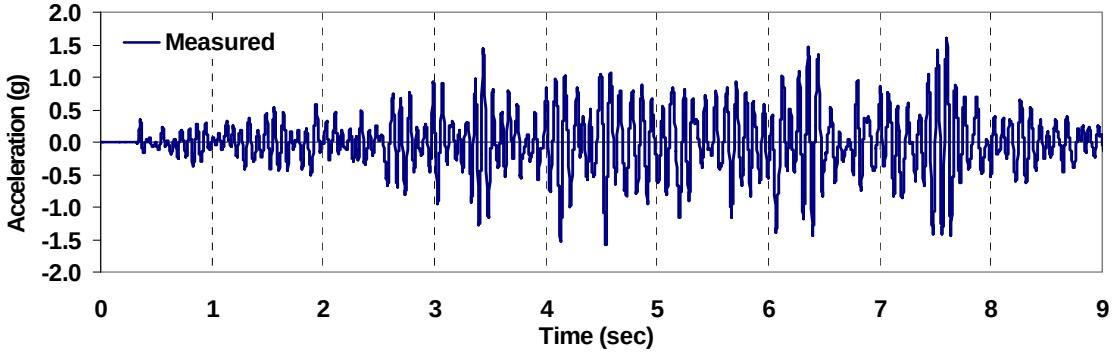

Figure 4.36: Measured acceleration at the center of the diaphragm employed in the analysis with PGA =0.5g.

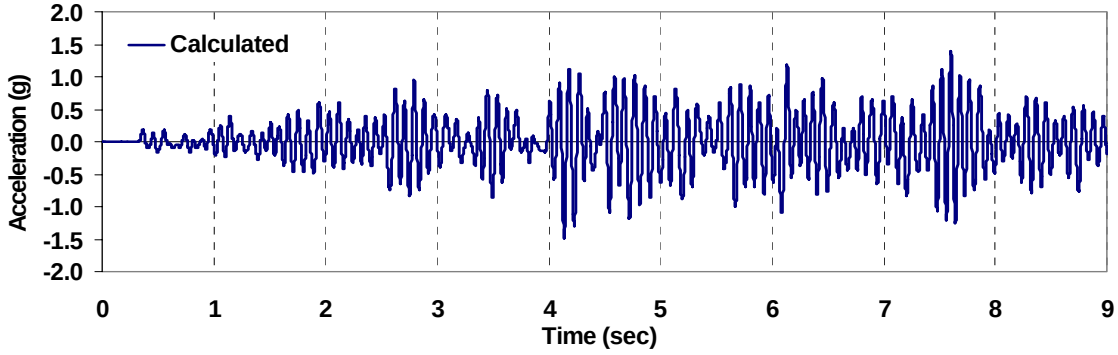

Figure 4.37: Calculated acceleration at the center of the diaphragm applying the average acceleration employed in the analysis with PGA =0.5g (Damping: ξ_{dia} = 3%, ξ_{wall} = 3%).

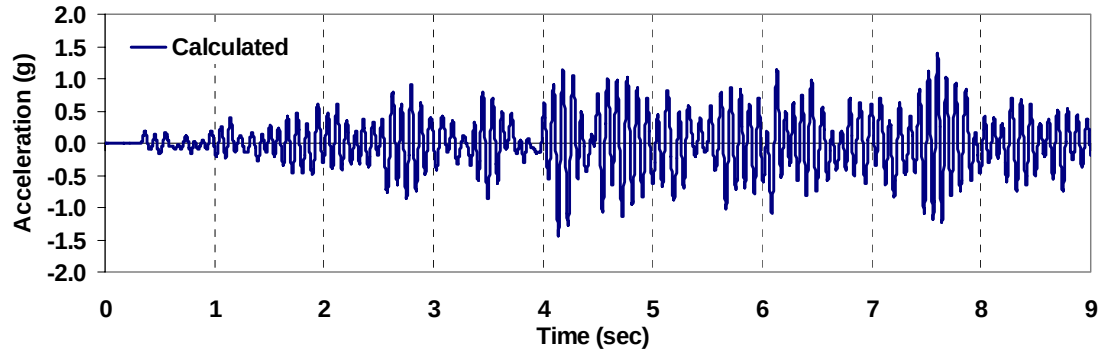

Figure 4.38: Calculated acceleration at the center of the diaphragm applying the average acceleration employed in the analysis with PGA =0.5g (Damping: ξ_{dia} =3%, ξ_{wall} = 10%).

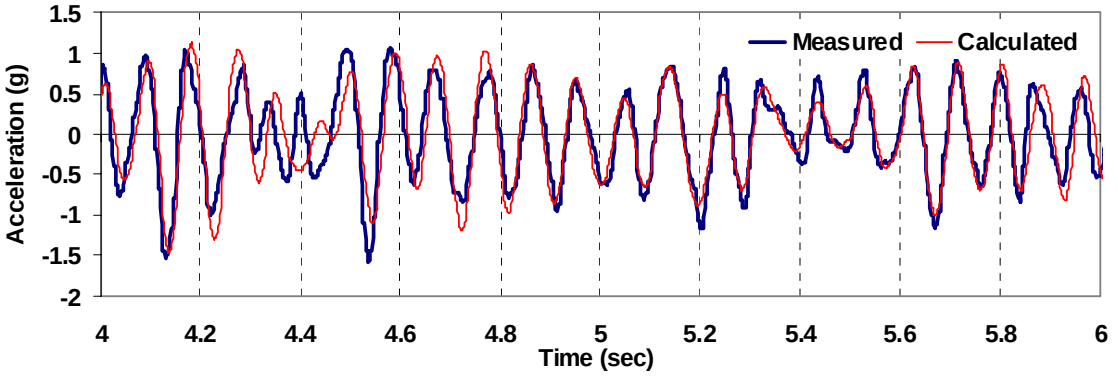

Figure 4.39: Two-second comparison of acceleration at the center of the diaphragm applying the average acceleration with PGA = 0.5g (Damping: ξ_{dia} = 3%, ξ_{wall} = 3%).

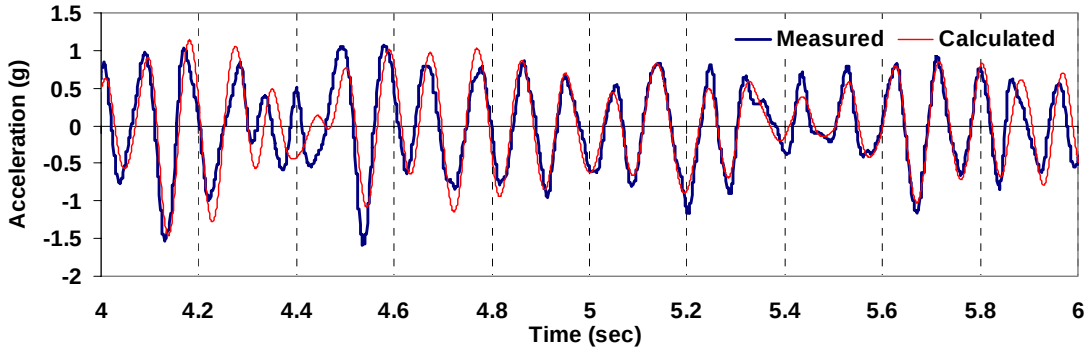

Figure 4.40: Two-second comparison of acceleration at the center of the diaphragm applying the average acceleration with PGA = 0.5g (Damping: ξ_{dia} = 3%, ξ_{wall} = 10%).

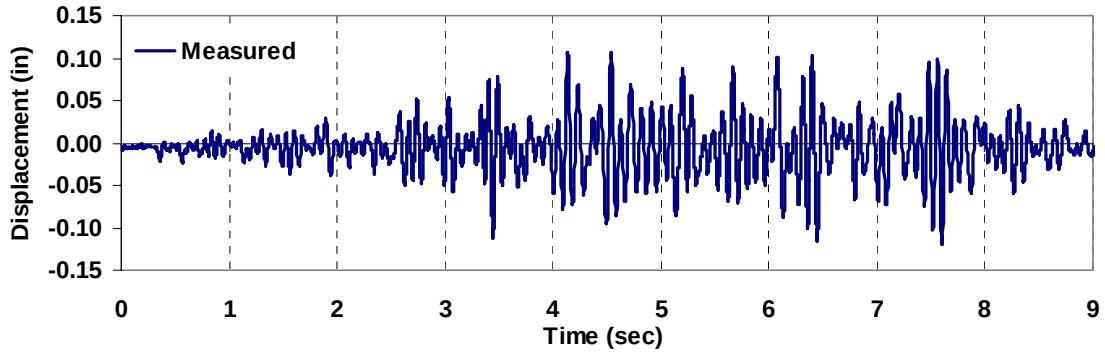

Figure 4.41: Measured displacement at the center of the diaphragm for Test 3 with PGA = 0.5g.

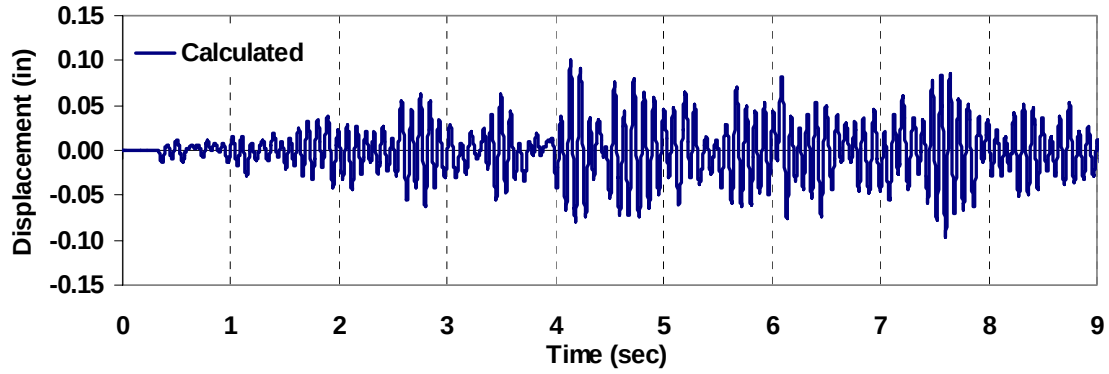

Figure 4.42: Calculated displacement at the center of the diaphragm for Test 3 with PGA = 0.5g. (Damping: ξ_{dia} = 3%, ξ_{wall} = 3%).

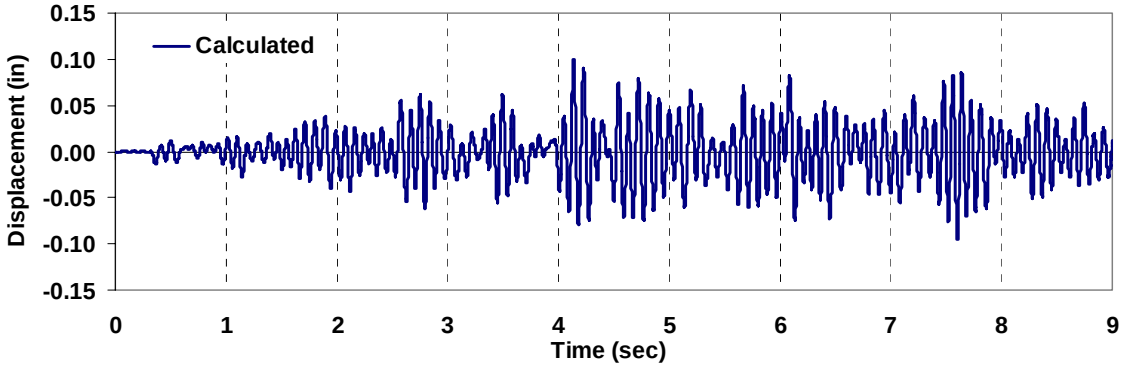

Figure 4.43: Calculated displacement at the center of the diaphragm for Test 3 with PGA = 0.5g. (Damping: ξ_{dia} = 3%, ξ_{wall} = 10%).

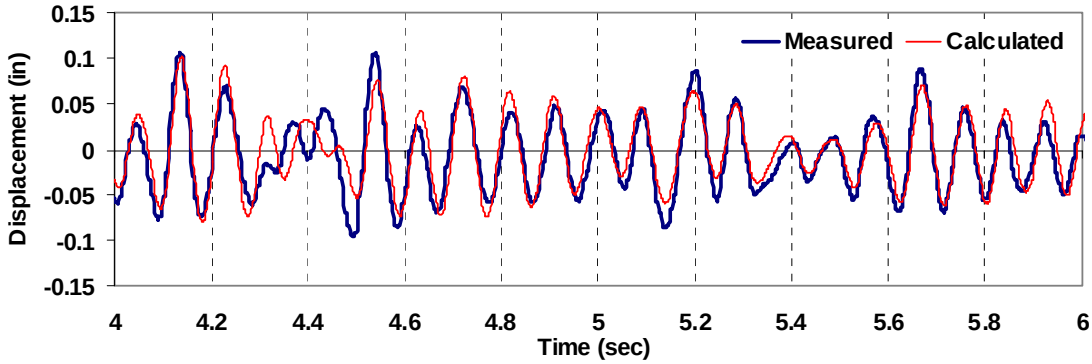

Figure 4.44: Two-second comparison of displacement at the center of the diaphragm for Test 3 with PGA = 0.5g. (Damping: ξ_{dia} = 3%, ξ_{wall} = 3%).

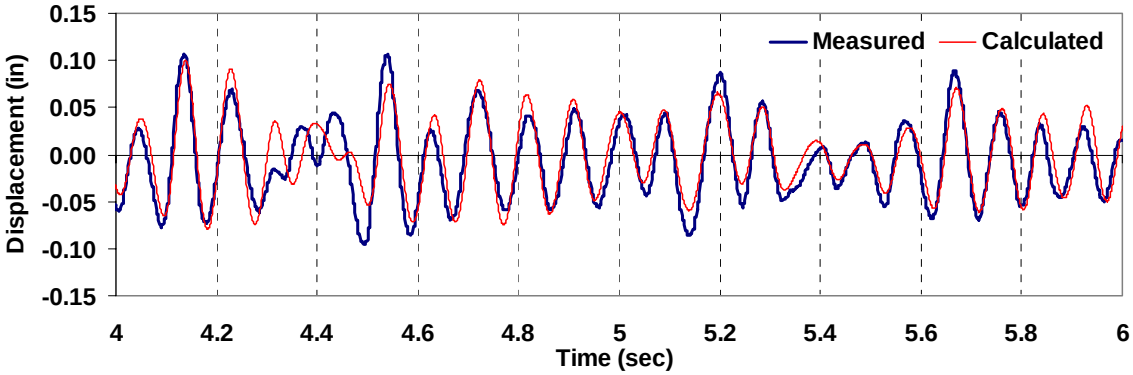

Figure 4.45: Two-second comparison of displacement at the center of the diaphragm for Test 3 with PGA = 0.5g. (Damping: ξ_{dia} = 3%, ξ_{wall} = 10%).

Effects of out-of-plane walls

When the out-of-plane wall is removed, the peak acceleration at the center of diaphragm is changed to 1.59 g (see Figs. 4.46 to 4.47), and the overall responses are also changed (see Figs. 4.48 to 4.49). This acceleration are not changed considerably compared to the computed value of 1.48 g given in the previous section, but the peak displacement (0.385 in) is 3 times larger than the previously calculated value of 0.11 in. It is concluded that the contribution of the out-of-plane wall in this type of building is important to reduce the diaphragm deflection. A detailed sensitivity analysis of the effect of the out-of-plane walls is discussed in Section 4.5.3.

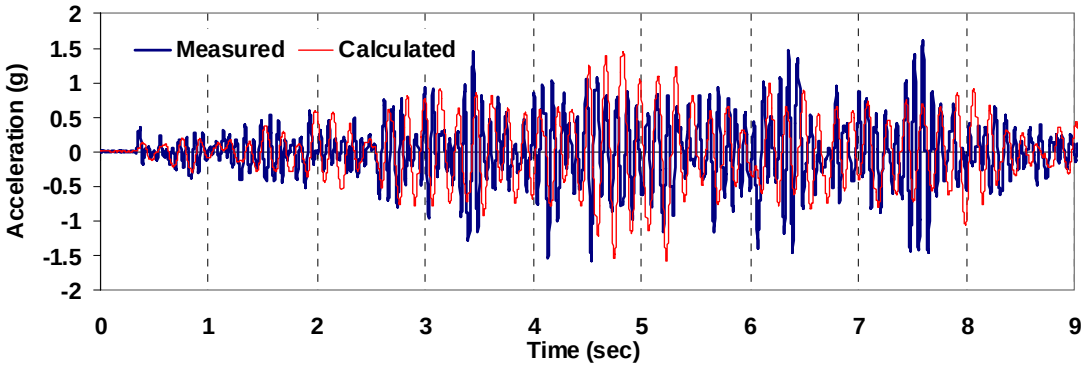

Figure 4.46: Comparison of acceleration at the center of the diaphragm without the out-of-plane wall for PGA = 0.5g. (Damping: ξ_{dia} = 3%, ξ_{wall} = 3%).

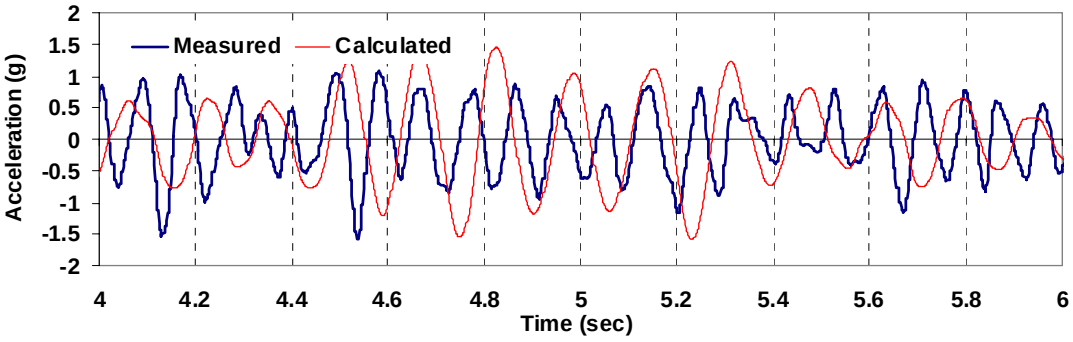

Figure 4.47: Two second comparison of acceleration at the center of the diaphragm without the out-of-plane wall for PGA = 0.5g. (Damping: ξ_{dia} = 3%, ξ_{wall} = 3%).

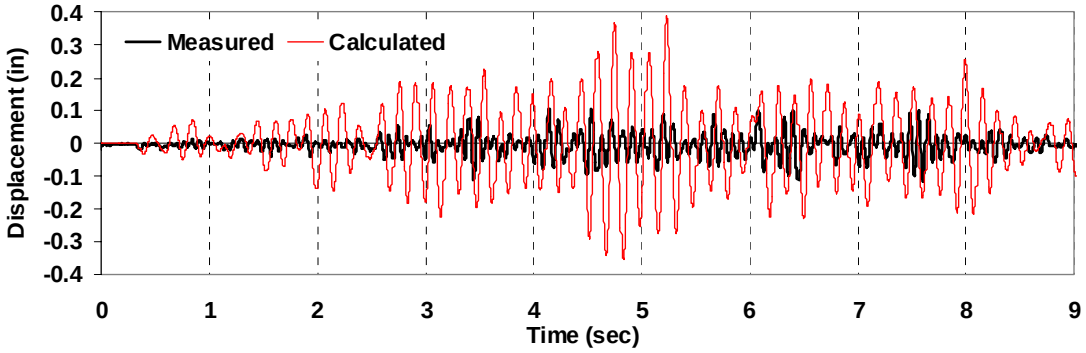

Figure 4.48: Comparison of displacement at the center of the diaphragm without the out-of-plane wall for PGA = 0.5g. (Damping: ξ_{dia} = 3%, ξ_{wall} = 3%).

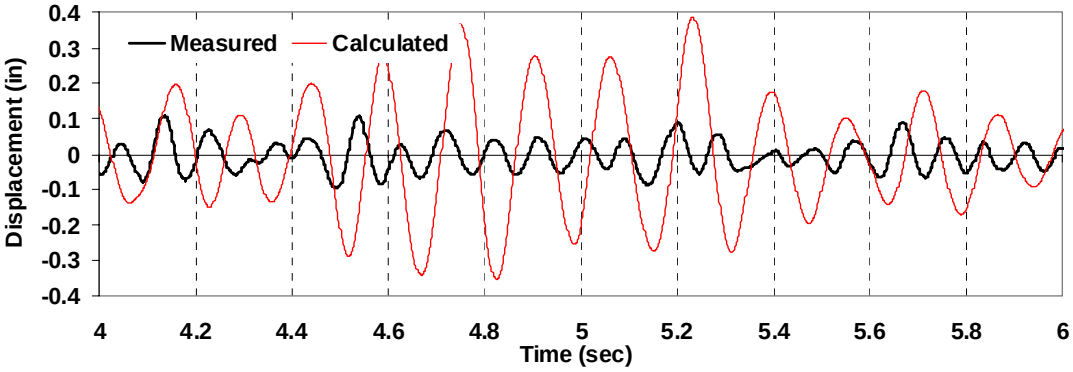

Figure 4.49: Two second comparison of displacement at the center of the diaphragm without the out-of-plane wall for PGA = 0.5g. (Damping: ξ_{dia} = 3%, ξ_{wall} = 3%).

Discussion of shear forces

Table 4.10 summarizes the calculated wall shear forces. The total shear force of the out-of-plane walls (east and west wall) is larger than those of the north and south walls. The relative displacement of the out-of-plane wall is larger than that of the in-plane walls due to the diaphragm flexibility. The total base shear of the simplified MDOF model matches well with that of the FEM and 2-DOF models considered in the previous research (see the bottom two rows of Table 4.10) (Cohen 2001). When the damping ratio of the masonry walls is changed from 3% to 10%, the shear force is decreased about 10%. The

in-plane wall strengths estimated using the mechanics of materials type equations from FEMA 356 (ASCE 2000a) and ACI 530-99 (MSJC 1999b) are summarized in Table 4.3. The calculated in-plane wall shear forces (1.08 and 0.91 kips in Table 4.10) are smaller than the flexural cracking force (1.3 kips shown in Table 4.3). However, the out-of plane wall shear force, 1.6 kips, is higher than the estimated flexural cracking force (0.69 kips shown in Section 4.3.3.3) and the yielding force (1.42kips) of the out-of-plane wall. However, there is no observed damage during this test.

Table 4.10: Calculated shear force at the base using PGA = 0.5 g.

Element		Shear force (lb)	
		Damping ξ_{dia} = 3% ξ_{wall} = 3%	Damping ξ_{dia} = 3% ξ_{wall}=10%
1.South wall		1,078	913
2.North wall		1,078	913
3.out-of-plane wall (= East + West wall)		1,618	1,608
Total Base Shear	MDOF model(=1+2+3)	3,774	3,434
	FEM model (Cohen 2001)	3,600	
	2-DOF model (Cohen 2001)	3,700	

The diaphragm shear forces are summarized in Table 4.11. Using the MDOF model, the diaphragm shear at both ends is 335 lb, and the shear force contribution from the out-of-plane walls is 1,618 lb. The shear force and displacement calculated from the two DOF model (Cohen 2001) is much higher than those of the refined FEM model developed by (Cohen 2001) and the MDOF model proposed in this research. The effects of out-of-plane wall were not considered in the two DOF model.

Table 4.11: Calculated shear force at the roof diaphragm level (ξ_{dia} and ξ_{wall} = 3%).

Element		Shear Force	Overall drift ratio at the center of diaphragm
a. Diaphragm shear		335 lb	0.074% (Diaphragm Drift)
b. Out-of-plane wall		1,618 lb	0.13% (0.11 in)
Diaphragm shear	MDOF model (=2*a +b)	2,288 lb	0.13% (0.11 in)
	Refined FEM model (Cohen 2001)	2,500 lb	0.15% (0.128 in)
	2-DOF Response Spectrum Analysis model (Cohen 2001)	3,200 lb	0.18% (0.148 in)

4.4.2 Calibration of out-of-plane wall strength using PGA = 0.67g

The second step of the model calibration process shown in Fig. 4.34 is applied to find the strength of out-of plane walls. The peak acceleration of the input ground motion of Test 5 is 0.67 g. Test 5 provides the basis for the nonlinear analysis model because there was slight cracking in east and west walls during the test. (see Table 4.1) (Cohen 2001).

As shown in Fig. 4.6, the out-of-plane of east and west walls are modeled by a single wall element. During this calibration process, the total out-of-plane strength of east and west walls is determined from the estimated flexural cracking force V_{cr} (0.691 kips) (see Section 4.3.3.3). The initial stiffnesses of the in-plane and out-of-plane walls predicted from the previous step (see Section 4.4.1) are used in this step. The total strength of out-of-plane walls is determined by comparing the overall history of the measured and calculated responses.

Section 4.4.2.1 summarizes the peak measured responses of Test 5. Section 4.4.2.2 presents the predicted strength values obtained from this calibration. Section 4.4.2.3 shows the comparison of the measured and predicted responses.

4.4.2.1 Measured responses

Table 4.12 summarizes the peak measured response corresponding to the location shown in Fig. 4.4. The complete measured history responses are plotted in Figs. C.17 through C.30 in Appendix C. The peak acceleration and displacement at the center of the diaphragm are 2.51 g and 0.225 in, respectively. The difference between the measured north (0.87g) and south wall (0.97g) shown in Table 4.12, may be attributed to experimental errors in the lifting frame, as discussed in Section 4.3.4. The measured acceleration at the top of south wall is 0.1 g higher than that of north wall.

Table 4.12: Summary of measured accelerations and displacement in the E-W direction.

Location	Peak Acceleration (g)		Peak displacement (in)	
	Instrument	Test 5	Instrument	Test 5
South wall	A104a	0.9501	D104	0.036
	A104b	0.9752		
Diaphragm	A105	2.5121	D105	0.225
North wall	A106a	0.8665	D106	0.028
	A106b	0.8666		

The measured peak relative displacements at the top of north and south wall are 0.028 in and 0.036 in, respectively. The relative peak displacement at the center of the diaphragm associated with the out-of-plane wall displacement is 0.225 in. The peak in-plane and out-of-plane wall displacements show 39% and 88% increase, respectively, over the measured responses of Test 3.

4.4.2.2 Summary of predicted properties

The predicted properties from Step 1 and 2 are summarized in Table 4.13. The predicted strength F_s' and stiffness K_2 is assessed by comparing the measured with the computed responses of the building. The predicted total out-of-plane wall strength F_s' and stiffness K_2 are 0.6 kips and 9 kips/in, respectively. The predicted total out-of-plane wall strength of 0.6 kips is slightly lower than the estimated flexural cracking force V_{cr} (0.691 kips) calculated by using the simplified mechanics of materials types of approach (see Section 4.3.3.3).

Table 4.13: Predicted properties from Step 2.

Component	Stiffness	Strength
In-plane Walls	50 kips/in	-
Out-of-plane Wall	K_1 = 16 kips/in, K_2 = 9 kips/in (=East + West Wall)	0.6 kips
Equivalent diaphragm stiffness $(G_e t)_1$	8.82 kips/in (see Section 4.3.2.2)	-

The initial stiffnesses of diaphragm, in-plane walls and out-of-plane walls, are not changed from Test 3. It is assumed that there is no accumulated damage from the previous tests and that the north and south walls remain elastic because no significant damage is observed during Test 5.

Effect of out-of-plane wall shear strength

To investigate the effect of out-of-plane wall, a series of nonlinear time history analyses are performed. The overall time history response is considered by varying the second stiffness K_2 and strength of the out-of-plane wall F_s', as shown in Fig. 4.50.

The shear strength, F_s' in Figs. 4.50 and 4.52, is the point where stiffness changes in the bi-linear curve. The K_2 stiffness (9 kips/in) is also found from the sensitivity analysis varying the shear strength of the out-of-plane wall. Figures 4.50 to 4.52 show the effect of the bi-linear curve in Figs. 4.50 and 4.51. As the out-of-plane wall shear strength is decreased from 1.0 to 0.9 kips, the acceleration and out-of-plane displacement at the center of the diaphragm is not changed significantly as shown in Figs. 4.50 and 4.51. In this range of the out-of-plane wall shear strength, the diaphragm is predominantly elastic as shown in Fig. 4.52. When the shear strength is changed from 0.8 to 0.6 kips, the responses of acceleration and displacement at the center of the diaphragm match well with the measured ones, as shown in Figs. 4.50 and 4.51. Therefore, as the shear strength is decreased from 0.8 to 0.6 kips, the diaphragm begins to show inelastic behavior (see Fig. 4.52). In the range between the shear strengths of 0.6 and 0.4 kips, the response is not largely changed. Based on this sensitivity analysis, the out-of-plane wall strength, F_s', and tangent stiffness, K_2 are predicted as 0.6 kips and 9 kips/in, respectively.

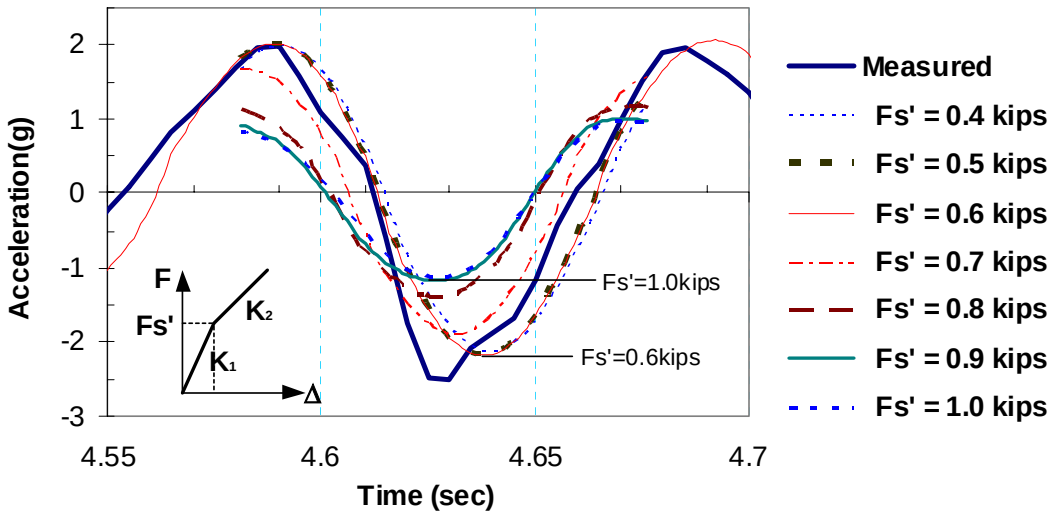

Figure 4.50: 0.15 second comparison of accelerations at the center of the diaphragm with changing F_s' in the bi-linear curve (K_1 = 16kips/in, K_2 = 9kips/in, Damping: ξ_{dia} = 3%, ξ_{wall} = 3%).

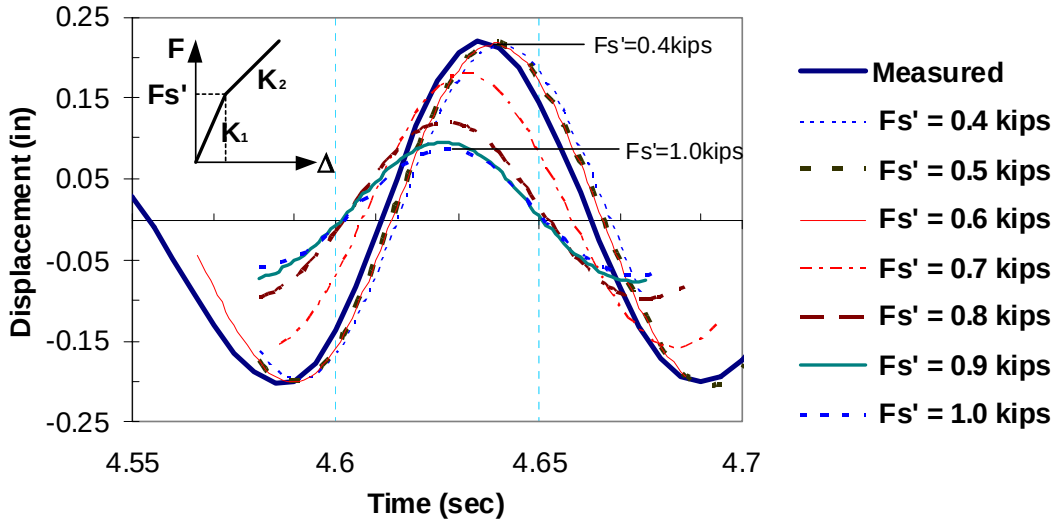

Figure 4.51: 0.15 second comparison of displacements at the center of the diaphragm with changing F_s' in the bi-linear curve (K_1 = 16kips/in, K_2 = 9kips/in, Damping: ξ_{dia} = 3%, ξ_{wall} = 3%).

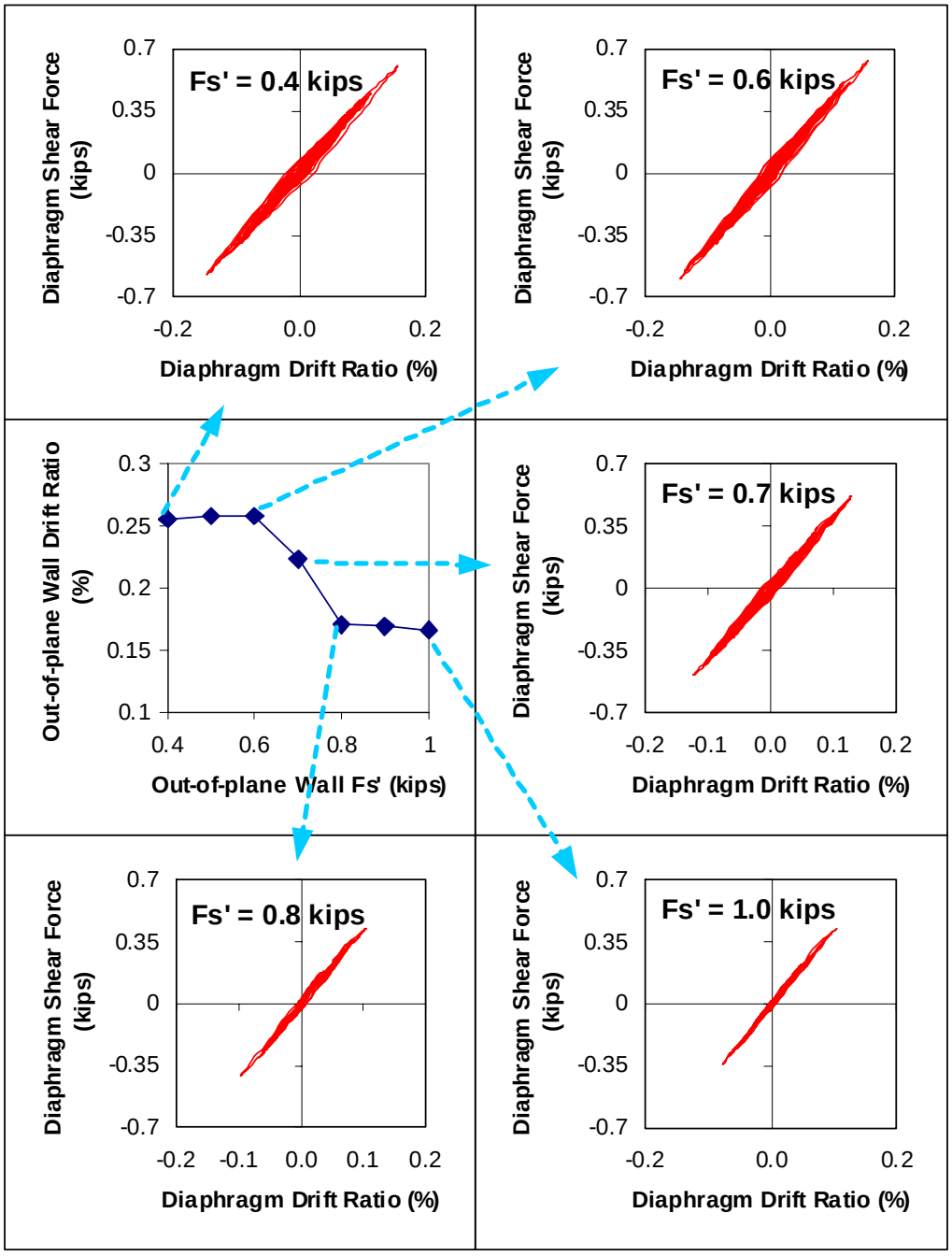

Figure 4.52: The diaphragm response with changing the out-of-plane wall shear strengths (K1 = 16kips/in, K2 = 9kips/in, Damping: ξ_{dia} = 3%, ξ_{wall} = 3%).

4.4.2.3 Comparison between measured and calculated responses

Table 4.14 summarizes the comparison of the measured and calculated responses of the structure using the two damping ratios for the masonry walls and the diaphragm (see Section 4.3.6). The change in the damping ratio doesn't significantly affect the displacement and acceleration at the center of the diaphragm due to the slight damage of the out-of-plane walls. When 10% damping is used for the in-plane walls, the calculated responses at the center of the diaphragm are slightly increased and the ones at the top of in-plane walls are decreased compared to the 3% damping.

Table 4.14: Comparison of measured and calculated response using PGA = 0.67 g.

Compared Item		Measured	Calculated (MDOF model)	
			Damping ξ_{dia} = 3% ξ_{wall} = 3%	Damping ξ_{dia} = 3% ξ_{wall}=10%
Fundamental Frequency		13 Hz (0.077 sec)	12 Hz (0.08 sec)	
Diaphragm deflection		-	0.20 in	0.22 in
Center of diaphragm (105)	Acceleration	2.51g	2.22 g	2.32 g
	Displacement	0.23 in	0.22 in	0.23 in
North wall (106)	Acceleration	1.0g	1.2 g	1.0 g
	Displacement	0.036 in	0.032 in	0.026 in
South wall (104)	Acceleration	0.82g	1.2g	1.0g
	Displacement	0.028 in	0. 032 in	0. 026 in

The measured fundamental period of Test 5 is increased to 0.077 sec compared to that of Test 3 (see Table 4.9). However, the calculated fundamental period (0.08 sec) is not changed due to the same elastic properties of the MDOF model used in the analysis model

of Test 3 (see Section 4.4.1.2). The Rayleigh damping coefficients of the diaphragm and in-plane walls used in Step 1 (see Section 4.4.1.3) are not changed. The damping coefficient (a_{1_wall}) of the out-of-plane wall is reduced to 0.0001 to match the measured peak relative displacement and acceleration at the center of the diaphragm. Figure 4.53 summarizes the Rayleigh damping coefficients used in constructing the non-proportional damping matrix. The coefficient a_{1_wall} is varied to investigate the effects of the stiffness proportional part of the damping matrix. The out-of-plane wall damping coefficients a_{1_wall} of 0.0001 to 0.00097 correspond to damping ratios of 1% to 10%, respectively. The Rayleigh damping curves obtained by varying a_{1_wall} from 0.00028 to 0.00097 are between the 3% and 10% damping curves. Three different out-of-plane wall damping coefficients are considered in Fig. 4.53 and are discussed below.

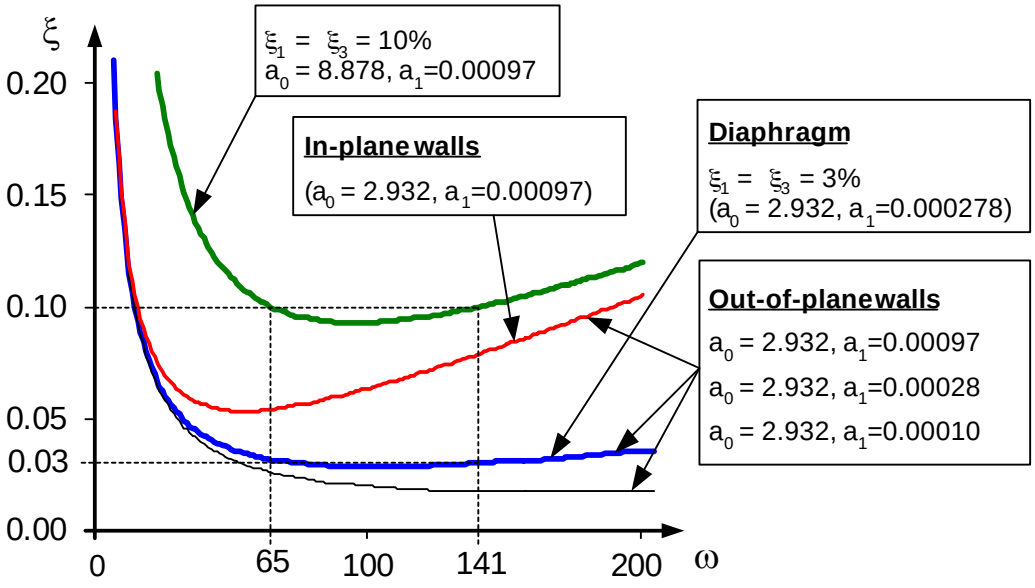

Figure 4.53: Summary of Rayleigh damping coefficients.

Figures 4.54 through 4.57 present the effects of the stiffness proportional damping coefficient a_1 of the out-of-plane wall. The overall phases of the calculated time history

responses match well with the measured ones in these figures. However, when a damping ratio of 10% ($a_{1\_wall} = 0.00097$) is used for the out-of-plane wall, the peak relative displacement and acceleration at the center of the diaphragm (0.17 in and 1.72 g, respectively) are smaller than the measured ones (0.22 in and 2.51g, respectively) (see Fig. 4.54 (d) and 4.55 (d)). When the damping coefficient ($a_{1\_wall} = 0.00028$) based on the damping ratio of 3% is used, the peak relative displacement and acceleration at the center of the diaphragm are 0.22 in and 2.21 g, respectively. A possible cause of the above differences may be an increase in the effective damping ratio in the damaged out-of-plane walls, since the response of the out-of-plane walls is associated with the response at the center of the diaphragm. When the damping coefficient ($a_{1\_wall} = 0.0001$) is used, the calculated peak relative displacement at the center of the diaphragm (0.23 in) is equal to the measured one (see Table 4.14). However, the calculated peak acceleration at the center of the diaphragm (2.32g) is less than the measured acceleration (2.51g). It must be recognized that the damping coefficient ($a_{1\_wall} = 0.0001$) is used to match only the peak displacement. The discrepancy between the calculated and measured acceleration is significant when the strong ground motion (PGA > 1.0g) is applied. A possible cause of the discrepancy is discussed in detail in Section 4.4.3.3.

As mentioned above, it is difficult to determine what representative values of a_0 and a_1 should be used to predict the response of the physical structure. These values are used to construct the non-proportional damping matrix of the building only for mathematical convenience. If a small stiffness proportional damping coefficient is used, the responses between 0 and 4 sec, where the behavior of the building is elastic, will be overestimated (see the two 0.3 sec comparisons in Fig. 4.54 (d)).

However, the responses at the top of the in-plane walls are not affected by the variation of the out-of-plane wall damping coefficient a_{1_wall} (see Fig. 4.56 and 4.57). The calculated peak relative displacements at the top of the north and south walls (0.026 in) in the E-W direction match well with the south wall (0.028 in). Due to the increased damage

of the out-of-plane walls during Test 5, the out-of-plane wall displacement with the damping coefficient ($a_{1\_wall} = 0.0001$) increases 100%, and the in-plane wall displacement increase 45% compared to those of Test 3.

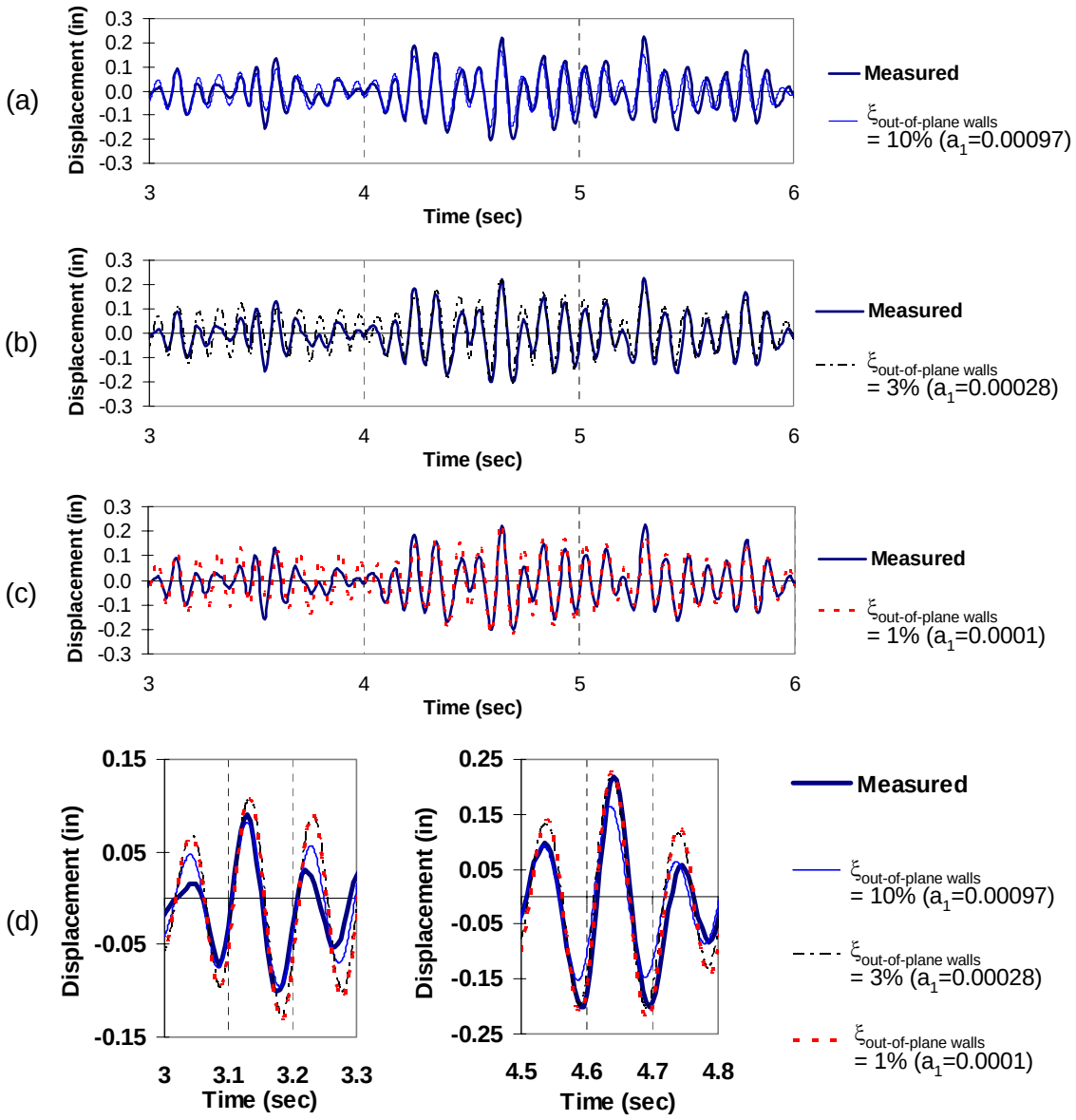

Figure 4.54: Comparison of the relative displacement at the center of the diaphragm varying the stiffness proportional damping of the out-of-plane wall: (a) a_1=0.00097, (b) a_1=0.00028, (c) a_1=0.0001, (d) 0.3 second comparison.

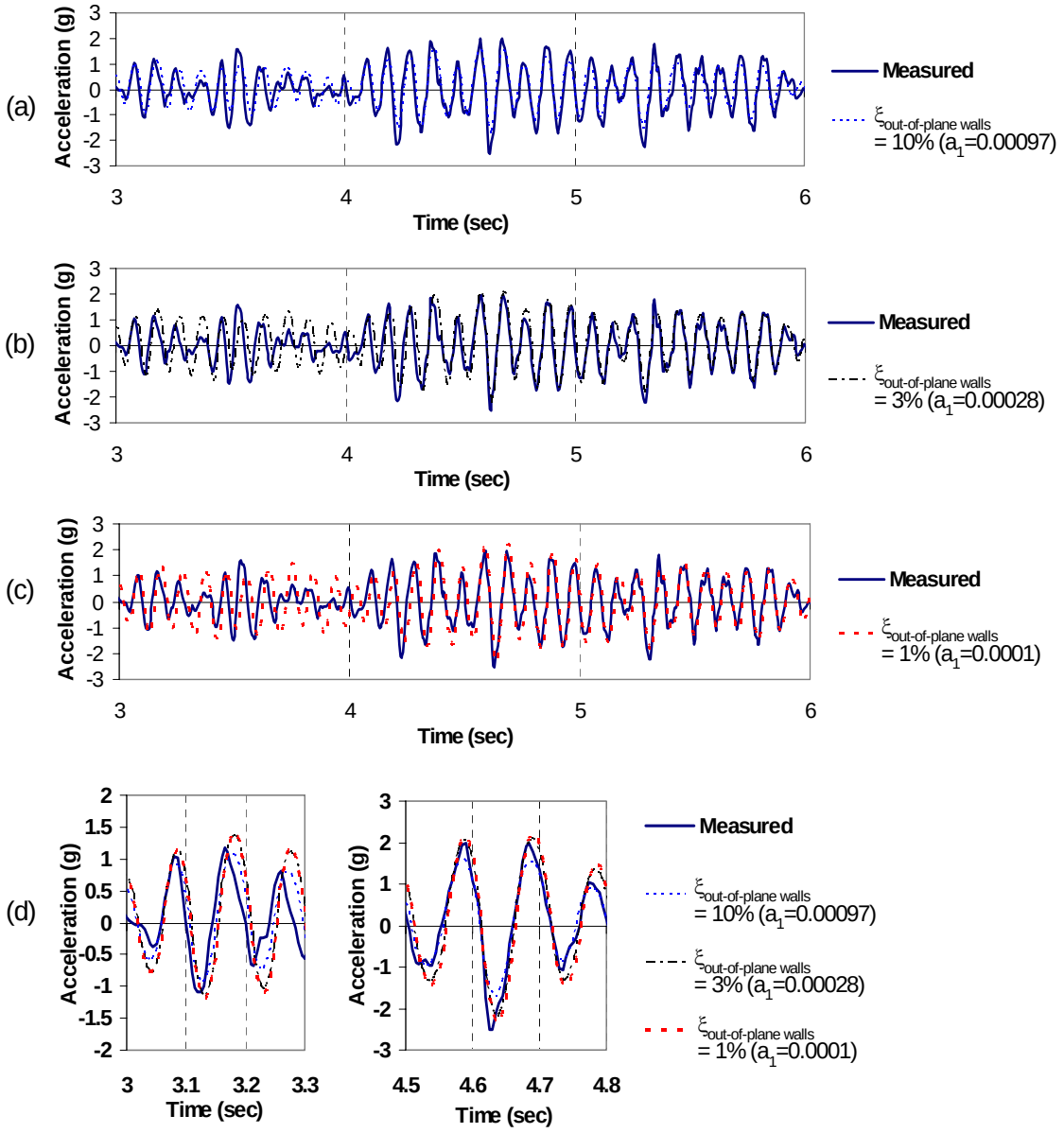

Figure 4.55: Comparison of the acceleration at the center of the diaphragm varying the stiffness proportional damping of the out-of-plane wall: (a) a_1=0.00097, (b) a_1=0.00028, (c) a_1=0.0001, (d) 0.3 second comparison.

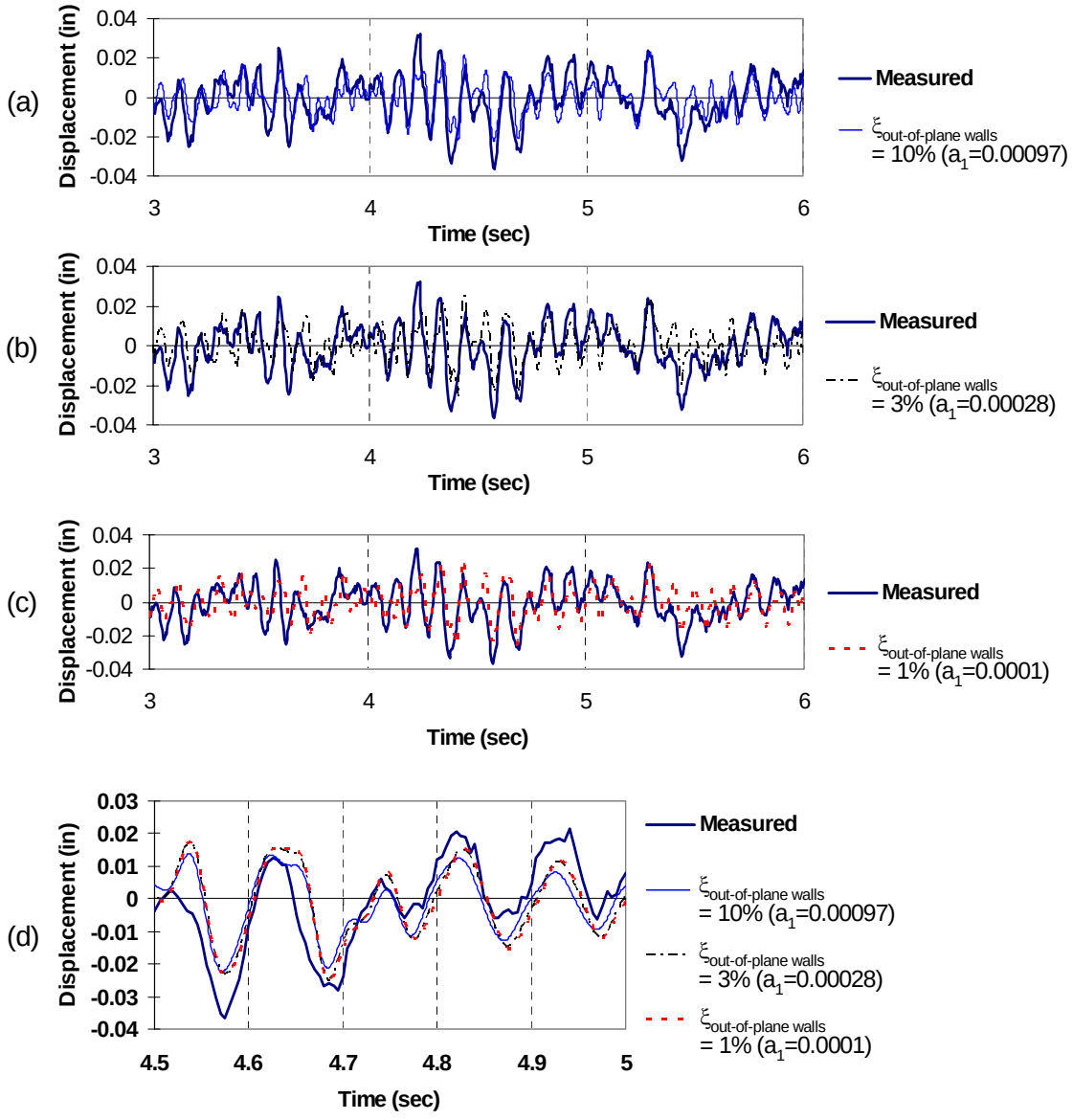

Figure 4.56: Comparison of the relative displacement at the top of the south wall varying the stiffness proportional damping of the out-of-plane wall: (a) a_1=0.00097, (b) a_1=0.00028, (c) a_1=0.0001, (d) 0.5 second comparison.

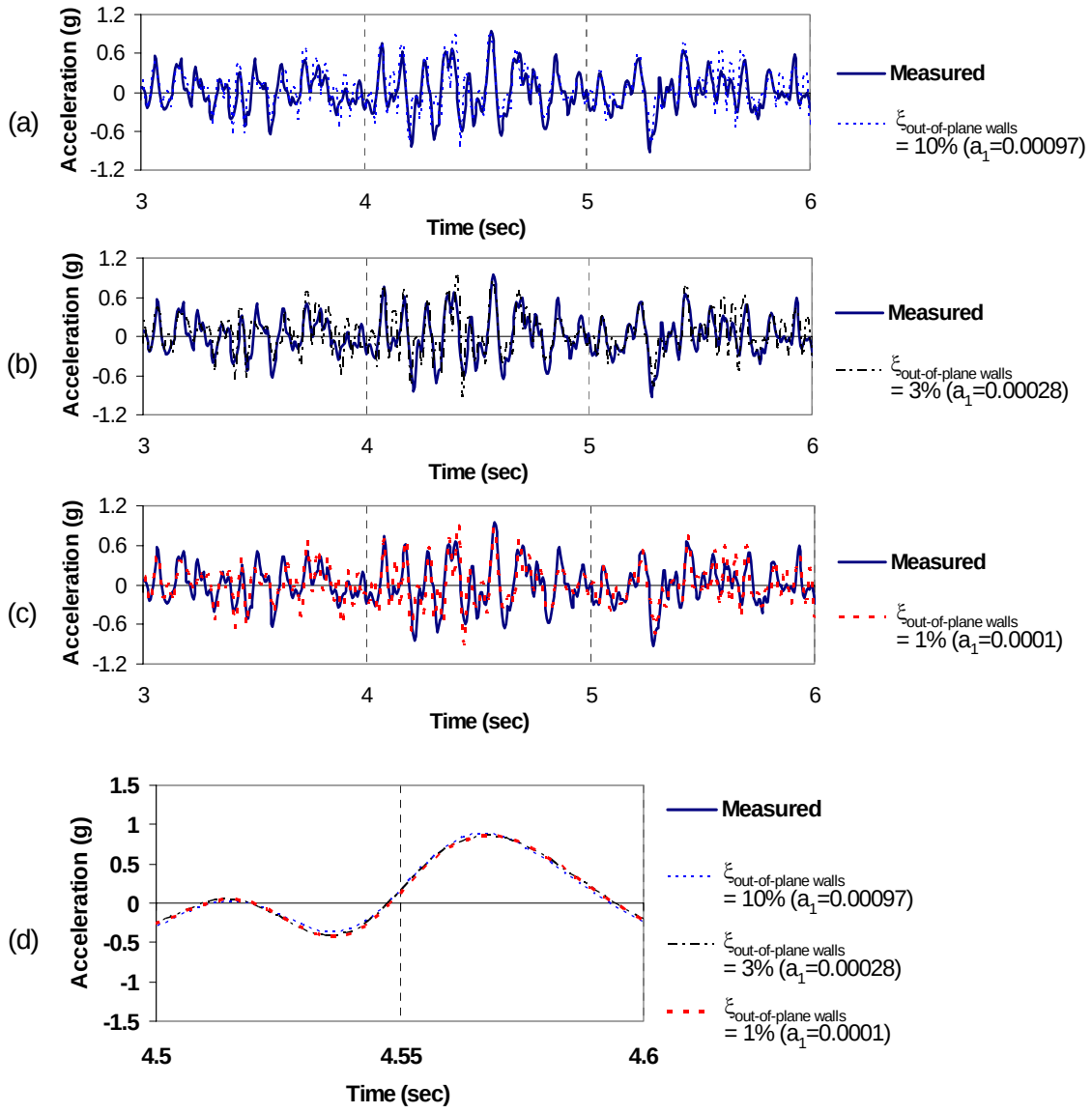

Figure 4.57: Comparison of the acceleration at the top of the south wall varying the stiffness proportional damping of the out-of-plane wall: (a) a_1=0.00097, (b) a_1=0.00028, (c) a_1=0.0001, (d) 0.2 second comparison.

Figures 4.58 and 4.60 show the comparison of the measured and calculated acceleration at the center of the diaphragm. Figures 4.61 and 4.63 show the comparison of the measured and calculated relative displacement at the center of the diaphragm. The responses using 10% damping are not plotted here because that they are only slightly dif-

ferent compared to the responses for 3% damping.

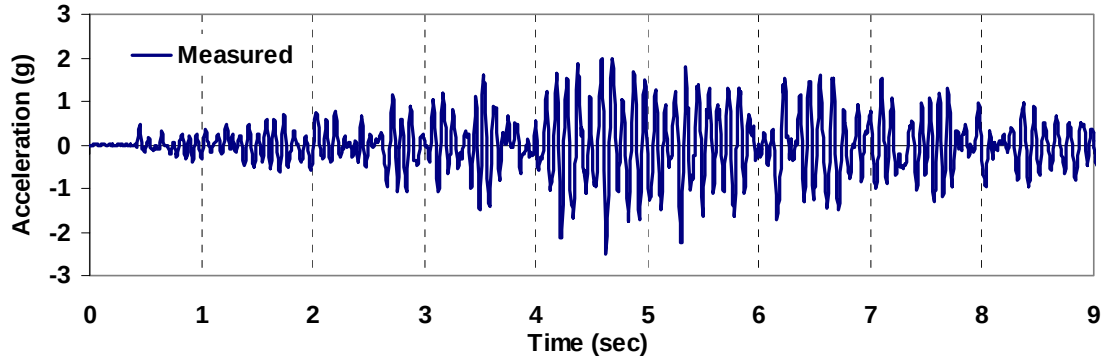

Figure 4.58: Measured acceleration at the center of the diaphragm with PGA =0.67g (Damping: ξ_{dia} = 3%, ξ_{wall} = 3%).

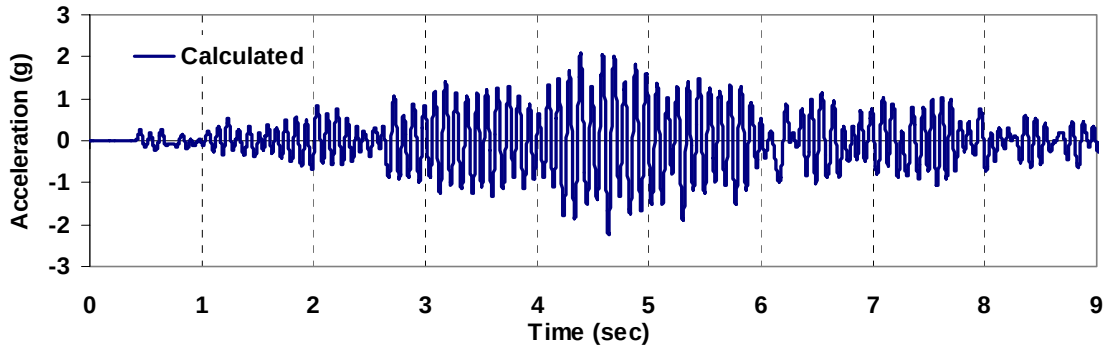

Figure 4.59: Calculated acceleration at the center of the diaphragm with PGA =0.67g (Damping: ξ_{dia} = 3%, ξ_{wall} = 3%).

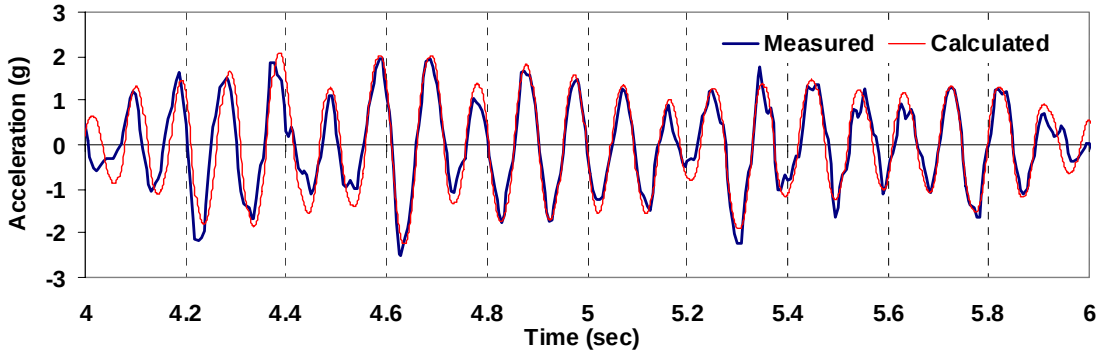

Figure 4.60: Two-second comparison of acceleration at the center of the diaphragm with PGA = 0.67g (Damping: ξ_{dia} = 3%, ξ_{wall} = 3%).

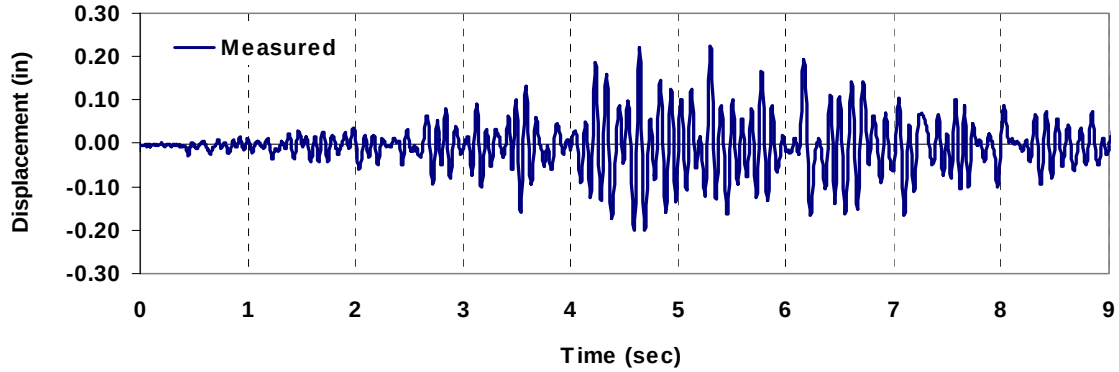

Figure 4.61: Comparison of displacement at the center of the diaphragm with PGA = 0.67g (Damping: ξ_{dia} = 3%, ξ_{wall} = 3%).

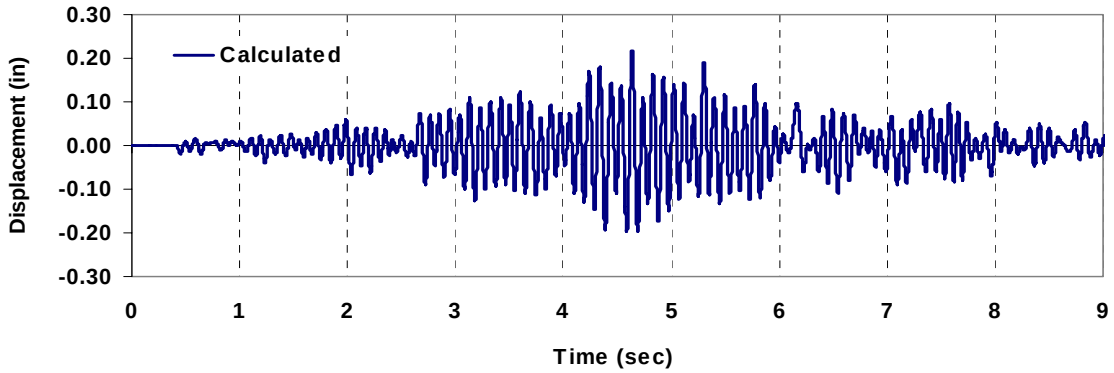

Figure 4.62: Comparison of displacement at the center of the diaphragm with PGA = 0.67g (Damping: ξ_{dia} = 3%, ξ_{wall} = 3%).

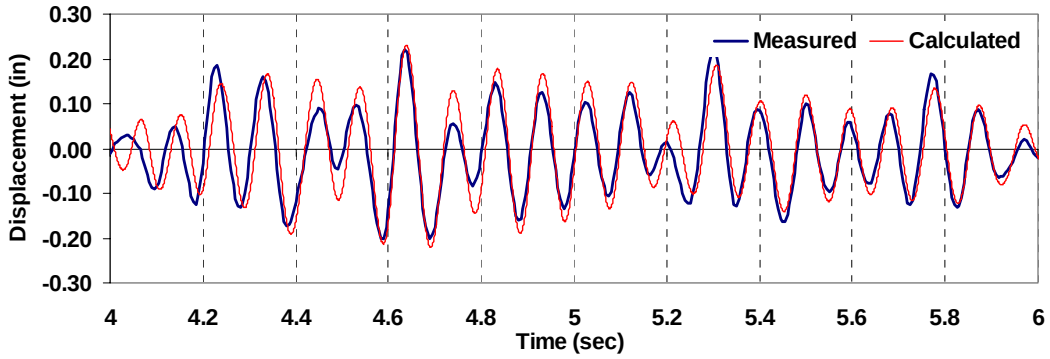

Figure 4.63: Two-second comparison of displacement at the center of the diaphragm applying the average acceleration employed in the analysis for PGA = 0 67g (Damping: ξ_{dia} = 3%, ξ_{wall} = 3%).

The peak shear forces at the base of the in-plane and out-of-plane walls are summarized in Table 4.15. The calculated peak in-plane shear force (1.59 kips) of the 3% damping is higher than the cracking force (1.3 kips) without flange effects shown in Table 4.3. However, the shear force of the 10% damping is similar to the estimated cracking force. The calculated peak out-of-plane shear force, 2.2 kips shown in Table 4.15, is higher than the estimated yielding force, 1.42 kips (see Sections 4.3.3.3). The total peak base shear increases 43% compared to Test 3 (see Table 4.10). The peak shear force of in-plane walls increases 48% and the shear force of out-of-plane walls increases 36%. As the damping of in-plane wall increase from 3% to 10%, the peak in-plane shear forces decrease about 18%.

From the behavior of the out-of-plane and in-plane walls, the following observation can be made. Due to the damaged out-of-plane walls, the peak relative displacement of the out-of-plane wall is much larger than that of the in-plane wall in the E-W direction. The in-plane wall shear forces are increased due to the decreased out-of-plane wall stiffness.

Table 4.15: Calculated shear force at the base using PGA = 0.67 g.

Element	Shear force (lb)	
	Damping ξ_{dia} = 3% ξ_{wall} = 3%	Damping ξ_{dia} = 3% ξ_{wall}=10%
1.South wall	1,590	1,305
2.North wall	1,590	1,305
3.out-of-plane wall (= East + West wall)	2,203	2,290
Total Base Shear (=1+2+3)	5,383	4,900

4.4.3 Calibration of in-plane and out-of-plane wall strengths and stiffnesses using PGA greater than 1.00g

The second and third steps of the model calibration process shown in Fig. 4.34 are applied to find the strengths and inelastic stiffnesses of in-plane and out-of plane walls. The peak accelerations of the input motion of Test 9 and 10 are approximately 1.00g. and 1.33g (Cohen 2001). These input motions of Test 9 and 10 are the modified record with its acceleration ordinates scaled by 150% and 200%, respectively. The measured data of Test 9 are used to find the inelastic properties of the in-plane and out-of-plane walls. The experimental data of Test 10 are used to verify the strength of in-plane walls and the hysteric behavior of in-plane walls, out-of-plane walls and diaphragm.

The in-plane and the out-of-plane wall stiffnesses and the out-of-plane wall strength are predicted using the first and second steps in Figure 4.34. At the high level excitations whose PGA is greater than 1.0g in the previous research (Cohen 2001), there were the extensive cracking in east and west out-of-plane walls and the prominent bed-joint cracks in south in-plane walls (Cohen 2001). This bed joint cracking may be characteristics of pier rocking. Even though extensive cracking propagated throughout the out-of-plane of east and west walls, no visible damage occurred to the roof diaphragm during Test 9. The visual damage of the roof diaphragm are observed during Test 10 (Cohen 2001). Based on the observed damage discussed above and the measured data, the total out-of-plane wall shear strength of the east and west walls and the south in-plane wall strengths are determined by using the second and third step in Fig. 4.34. It is assumed that the behavior of the north wall remain in elastic range.

Section 4.4.3.1 summarizes the peak measured responses of Test 9 and 10. Section 4.4.3.2 presents the predicted stiffness values. Section 4.4.3.3 shows the comparison of the measured and predicted responses.

4.4.3.1 Measured responses

Tables 4.16 and 4.17 summarizes the peak measured responses of Tests 9 and 10, respectively, corresponding to the locations shown in Fig. 4.4. The complete measured time history responses are plotted in Figs. C.31 through C.44 in Appendix C. The peak acceleration and displacement at the center of the diaphragm are 3.28 g and 0.46 in, respectively for Test 9. The test shows slight different peak acceleration between the north (1.26g) and south wall (1.37g). The difference may be attributed to experimental errors in the lifting frame, as discussed in Section 4.3.4. The measured peak relative displacements at the top of north and south walls are 0.053 in (see Table 4.16). The peak relative displacement, 0.92 in (Test 10) at the center of the diaphragm is higher than 0.46 in (Test9) (see Tables 4.16 and 4.17). It is due to the extensive damage of the out-of-plane walls.

Table 4.16: Summary of measured accelerations and displacements in the E-W direction (PGA = 1.0g).

Location	Peak Acceleration (g)		Peak displacement (in)	
	Instrument	Test 9	Instrument	Test 9
South wall	A104a	1.3105	D104	0.053
	A104b	1.3736		
Diaphragm	A105	3.2862	D105	0.457
North wall	A106a	1.2585	D106	0.053
	A106b	1.2555		

Table 4.17: Summary of measured accelerations and displacements in the E-W direction (PGA = 1.33g).

Location	Peak Acceleration (g)		Peak displacement (in)	
	Instrument	Test 10	Instrument	Test 10
South wall	A104a	1.768	D104	0.076
	A104b	1.801		
Diaphragm	A105	4.810	D105	0.921
North wall	A106a	1.547	D106	0.072
	A106b	1.222		

4.4.3.2 Summary of predicted properties

The predicted properties are summarized in Table 4.18. The initial stiffnesses of the in-plane and out-of-plane walls are obtained from Tests 3 and 5, (see Tables 4.8 and 4.13). For the nonlinear time history analyses, the rocking model discussed in Section 4.3.2 is applied to the in-plane and out-of-plane wall elements and the three parameter model is applied to the diaphragm element (see Sections 4.3.2 and 4.3.3). The in-plane wall damping ratio of 10% is used to obtain the predicted values

By comparing the overall history of the measured and calculated responses, the in-plane wall strength and out-of-plane stiffnesses and strength are calibrated. The estimated in-plane stiffness and strength of south wall are 50 kips/in and 1.75 kips, respectively. The predicted strength, 1.75 kips is higher than the estimated cracking strength, 1.3 kips, but smaller than the yield strength, 2.26 kips (see Section 4.3.3). The out-of-plane strength and inelastic stiffness are reduced to 0.4 kips and 2 kips/in compared to the previous predicted properties, 0.6 kips and 9 kips/in (see Table 4.13). This is due to the accumulated damage in the out-of-plane walls during Tests 6 to 7, which are done between Test 5 and 9.

Table 4.18: Predicted properties from the calibration process (PGA=1.0g).

Component	**Stiffness**	Strength
In-plane Walls	50 kips/in	1.75 kips
Out-of-plane Wall	K_1 = 11 kips/in, K_2 = 2 kips/in (=East + West Wall)	0.4kips
Equivalent diaphragm stiffness $(G_e t)_1$	8.82 kips/in (see Section 4.3.2.2)	F_1 = 0.1 ksi, F_2 = 0.69 ksi

The comparison of the analyses using two different damping ratios shows that the nonlinear responses of the building are sensitive to this variable. Because 3% damping corresponds to essentially elastic response, the effective damping should be increased when hysteretic behavior occurs. Two different damping ratios (3% and 10%) are used to investigate the effect of the damping ratio within the masonry walls. The sensitivity of the damping ratio is now discussed.

Effects of masonry wall damping ratios

A frequency analysis is performed to find the Rayleigh damping coefficients using the predicted properties (see Table 4.18). Due to the decreased out-of-plane wall stiffness, the frequencies of the first and third modes (65 and 140 rad/sec, respectively) are changed. The Rayleigh damping coefficients a_{0_wall} and $a_{0\_diaphragm}$ of the lumped masses at the common DOFs (X in Fig. 4.28) are 2.67. The Rayleigh damping coefficients of the diaphragm $a_{1\_diaphragm}$ is 0.00029 for a damping ratio of 3%

Figure 4.64 shows the comparison of the time history responses varying the in-plane wall damping ratios. When a damping ratio of 3% ($a_{1\_wall} = 0.00029$) is used for the in-plane walls, the time history response shows the unstable curves between 4.4 and 4.7 sec shown in Figs. 4.64 (c) and (d). When a damping ratio of 5%

($a_{1\_wall} = 0.00049$) is used for the in-plane walls, the peak response is reduced but is unstable compared to the measured history responses. The time history response with 10% damping ($a_{1\_wall} = 0.00098$) for the in-plane walls fit well with the measured response (see Figs. 4.64 (a) and (d)). It appears that the 3% damping ratio obtained from the sine-decay tests (see Section 4.3.6) can be applied to the diaphragm element and can not be applied to the in-plane walls for the non-linear time history analysis. The 10% damping ratio of the in-plane walls is an appropriate choice to give results comparable to the observed response of the physical structure. However, the responses of the diaphragm are not changed due to the changes in the damping ratios of the in-plane walls, as shown in Fig. 4.65.

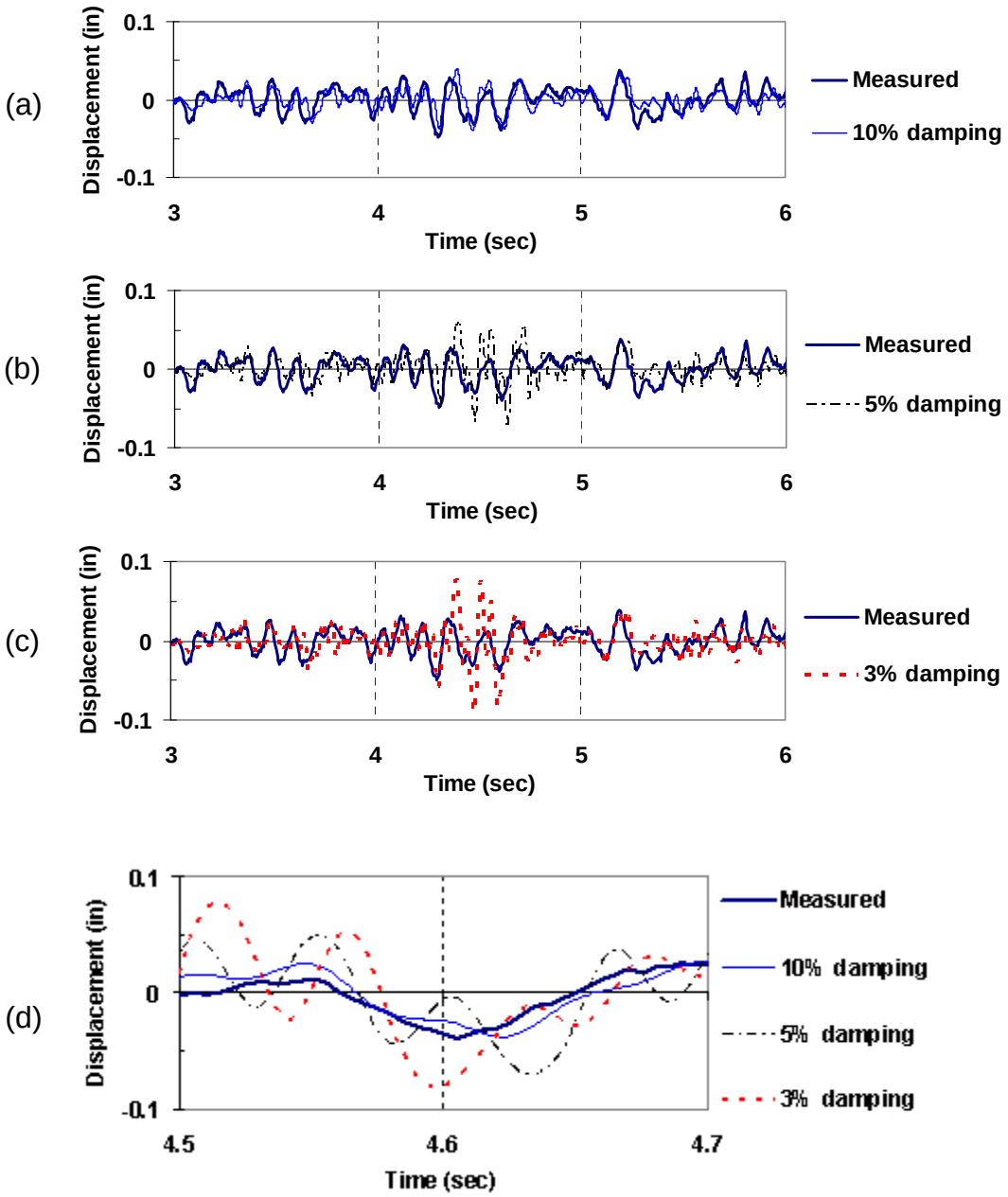

Figure 4.64: Comparison of relative displacement at the top of south wall using three different in-plane wall damping ratio: (a) 10% damping; (b) 5% damping; (c) 3% damping; and (d) 0.2 sec comparison of three different damping.

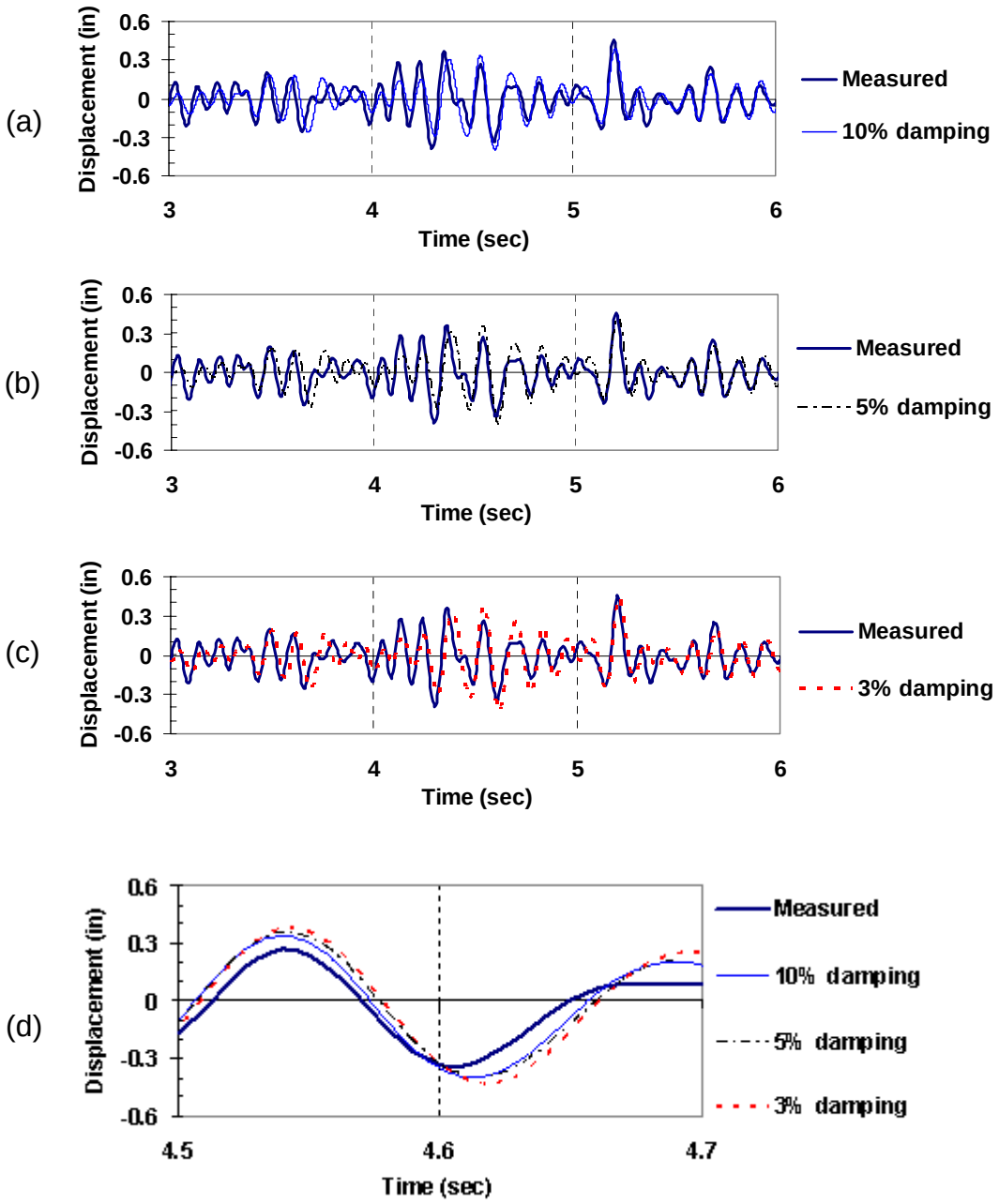

Figure 4.65: Comparison of relative displacement at the center of diaphragm using three different in-plane wall damping ratio: (a) 10% damping; (b) 5% damping; (c) 3% damping; and (d) 0.2 sec comparison of three different damping.

In summary, the above studies as well as the studies discussed in Sections 4.4.1.3 and 4.4.2.3 indicate that the following damping assumptions provide good correlation

with all of the results from tests 3, 5 and 9:

- 3% damping for the diaphragms and for the out-of-plane walls. This leads to damping coefficients of $a_{0\_diaphragm}$ = 2.932, $a_{1\_diaphragm}$ =0.000278 , a_{0_wall} =2.932 and a_{1_wall} = 0.000278.
- 10 % damping for the in-plane walls. This leads to damping coefficients of a_{0_wall} = 2.932 and a_{1_wall} = 0.00097.

In-plane wall strength

The rocking hysteresis model developed in this research is used for the masonry walls. The predicted hysteretic curve of south wall is shown in Fig. 4.66. The in-plane north wall is assumed to be elastic based on the observed damage, as shown in Fig. 4.67. The properties of south wall are determined by decreasing shear strength as shown in Fig. 4.68. When the in-plane strength of south wall is reduced from infinite (elastic) to 2.0 kips, the peak relative displacements of the south wall, 0.043 in, are not changed. Because the nonlinear action of the south wall is not significant, it does not affect the response of the building. When the in-plane strength of south wall reduced to 1.75 kips, the peak relative displacement increases to 0.051in compared to the measured value of 0.053 in.

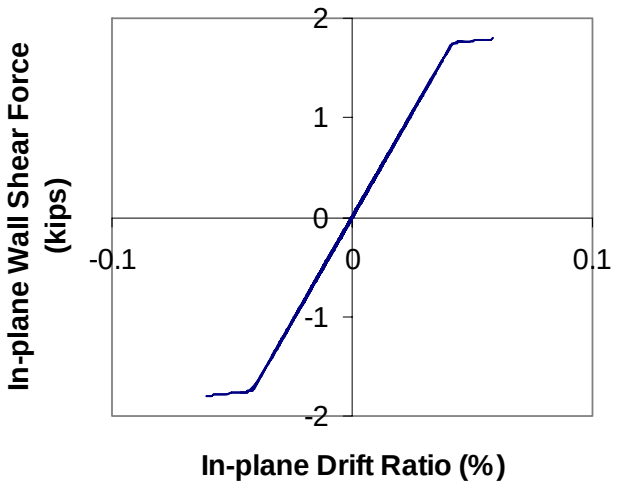

Figure 4.66: In-plane south wall hysteresis curve employed in the analysis for PGA = 1.0g (Damping: ξ_{dia} = 3%, ξ_{wall} = 10%).

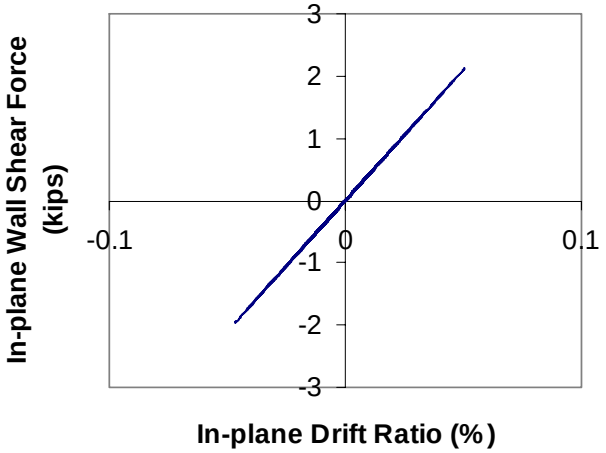

Figure 4.67: In-plane north wall hysteresis curve employed in the analysis for PGA = 1 0g (Damping: ξ_{dia} = 3%, ξ_{wall} = 10%).

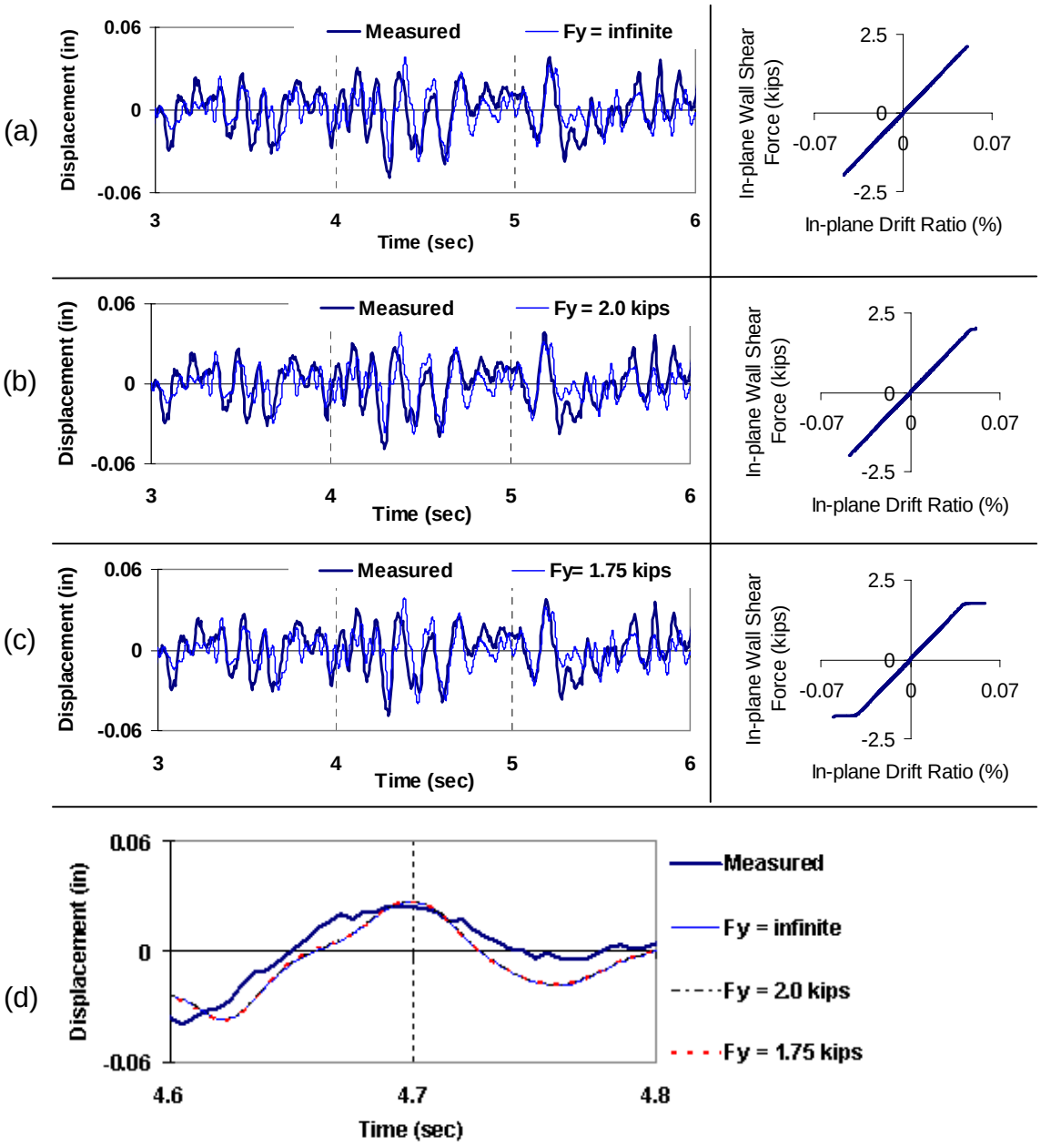

Figure 4.68: Comparison of force and displacement at the south wall using three different in-plane wall strength: (a) F_y = infinite; (b) F_y = 2.0 kips; (c) F_y = 1.75 kips; and (d) 0.2 sec comparison of three different strength. (Damping: ξ_{dia} = 3%, ξ_{wall} = 10%).

Out-of-plane wall strength and stiffness

The predicted initial and second tangent stiffness of out-of-plane wall are decreased to 11 and 2 kips/in, respectively, because the accumulated damage of the out-of-plane walls during the previous tests (Tests 6, 7, and 8) (see Table 4.13). The predicted strength of the out-of-plane wall also decreases 0.4 kips compared to the shear strength of 0.6 kips in Table 4.13. The hysteretic behavior of the out-of-plane east and west walls is shown in Fig. 4.69. As the in-plane and out-of-plane walls are damaged, the visible inelastic behavior of diaphragm can occur during Test 9, as shown in Fig. 4.70. Time history responses are compared in Section 4.4.3.3.

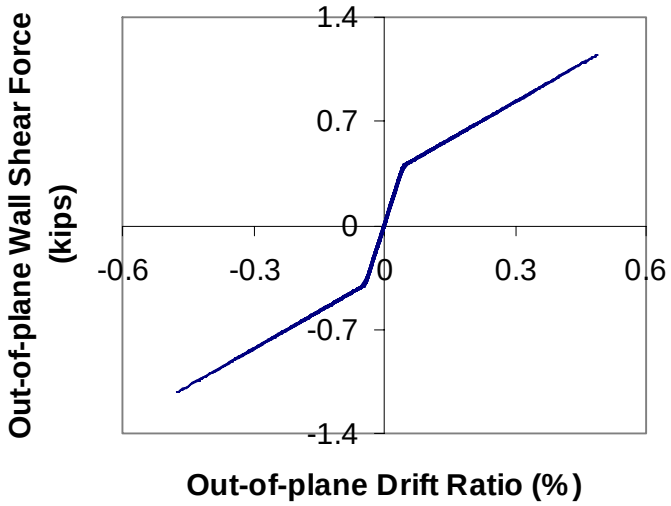

Figure 4.69: Out-of-plane wall hysteresis curve employed in the analysis for PGA = 1 0g (Damping: ξ_{dia} = 3%, ξ_{wall} = 10%).

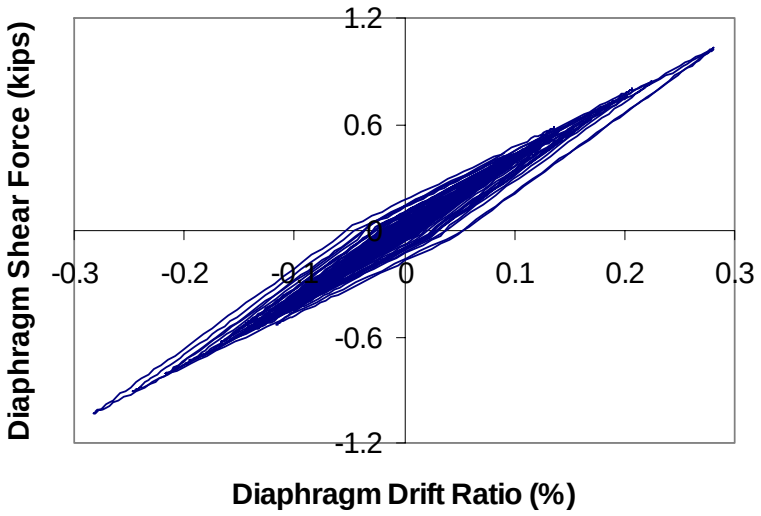

Figure 4.70: Diaphragm Hysteresis curve employed in the analysis for PGA = 1.0g (Damping: ξ_{dia} = 3%, ξ_{wall} = 10%).

4.4.3.3 Comparison between measured and calculated response

Table 4.19 summarizes the comparison of the measured and calculated peak responses of the structure using the damping ratio of 10% for the masonry walls and the damping ratio of 3% for the diaphragm. The non-linear analysis uses the predicted properties shown in Table 4.18.

Table 4.19: Comparison of measured and calculated response using PGA = 1.0 g (ξ_{dia} = 3%, ξ_{wall} = 10%).

Compared Item		Measured	Calculated (MDOF model)
Center of diaphragm (105)	Acceleration	3.28 g	2.10 g
	Displacement	0.45 in	0.41 in
North wall (106)	Acceleration	1.32 g	1.39 g
	Displacement	0.053 in	0.043 in
South wall (104)	Acceleration	1.37 g	1.38 g
	Displacement	0.053 in	0.051 in

The peak relative displacement at the top of the south wall is 0.051 in compared to the measured one, 0.053in. The calculated and measure drift ratios of the in-plane south wall is 0.06%. The drift ratio is much lower than the drift limitation (0.4%) of the immediate occupancy level in FEMA 356 (see Table 4.20). However, there is significant bed-joint cracking along the bottom of the south in-plane wall. The comparison of the calculated and measured displacement time history responses is shown in Figs. 4.71 and 4.73. The peak acceleration at the top of the south wall (1.38 g) is compared with the measured one (1.37g) (see Figs. 4.74 and 4.76). The calculated acceleration and displacement at the top of south wall are matched well with the measured ones. The calculated peak acceleration at the top of the north wall (1.39g) is slightly higher than the measured one (1.26g).

The calculated relative displacement at the center of the diaphragm is 0.41 in compared to the measured value of 0.45 in. The drift ratios of the out-of-plane wall associated with the diaphragm displacement is 0.54%. The drift ratio is much lower than the drift limitation (2%) of the immediate occupancy level in FEMA 356 (see Table 4.20). However, the building shows extensive cracking. Figures 4.77 to 4.79 show the comparison of displacement at the center of the diaphragm. The initial time range (from 3 to 4 sec) shows

that the predicted structural property seems to be overestimated. As the stiffness of the diaphragm is degraded after 4 seconds, the overall displacement time history responses are matched well with measured response, as shown in Fig. 4.79 However, the peak acceleration at the center of the diaphragm (2.01 g) is less than the measured acceleration (3.28 g). Figures 4.80 to 4.82 show the comparison of acceleration at the center of the diaphragm.

Table 4.20: Structural performance criteria for RM structure in FEMA356 (ASCE 2002a).

Masonry	Element	Immediate Occupancy	Life Safety	Collapse Prevention
Reinforced (7.4.5.3 in FEMA356)	In-plane wall (Controlled by shear)	0.4%	0.6%	0.75%
	Out-of-plane wall	2%	3%	5%
Reinforced Masonry walls (Table C1-3 in FEMA 356)		0.2%	0.6%	1.5%
Damage states		Minor cracking	Extensive cracking	Crushing

The relative displacement is captured at the top of the west wall and the acceleration is measured at the center of the diagonally sheathed diaphragm, as shown in Figs. 4.3 and 4.4. At strong excitation (PGA > 1.0g), damage of the diaphragm were observed (Cohen 2001). This nonlinear behavior of the diagonally sheathed diaphragm shown in Fig. 4.3 may cause the discrepancy between the measured and calculated acceleration, because the acceleration instrument was located on the diagonal sheathing, as shown in Figs. 4.3 and 4.4. When the peak input ground motion of 1.33 g (Test 10) is applied to this building, the problem is significant. The calculated acceleration of Test 10 is 2.6g com-

pared to the measured one, 4.8g. The comparison of these accelerations is shown in Figs. 4.83 to 4.85.

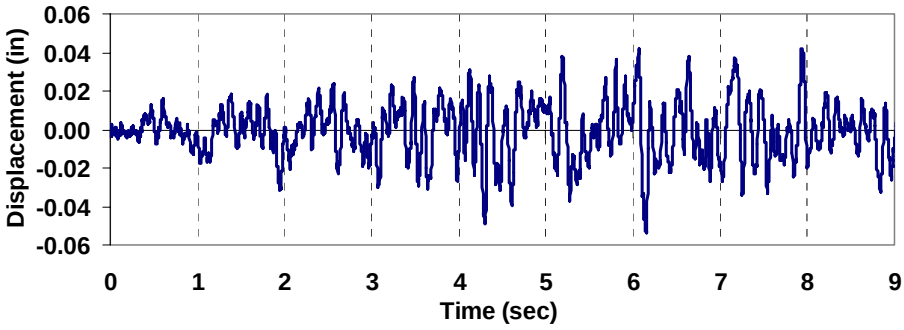

Figure 4.71: Measured displacement at the top of south wall with PGA = 1.0g (Damping: ξ_{dia} = 3%, ξ_{wall} = 10%).

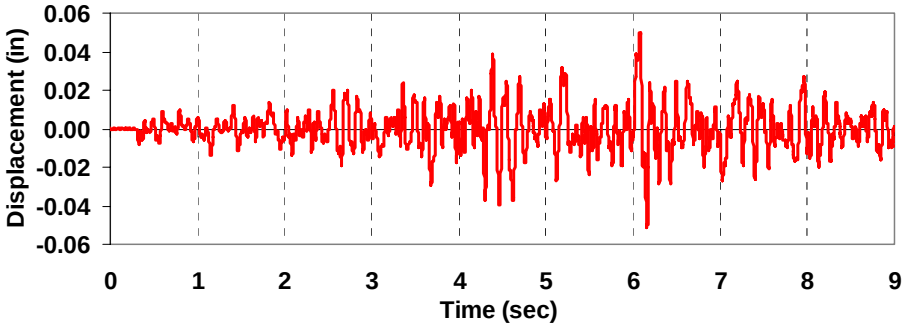

Figure 4.72: Calculated displacement at the top of south wall with PGA = 1.0g (Damping: ξ_{dia} = 3%, ξ_{wall} = 10%).

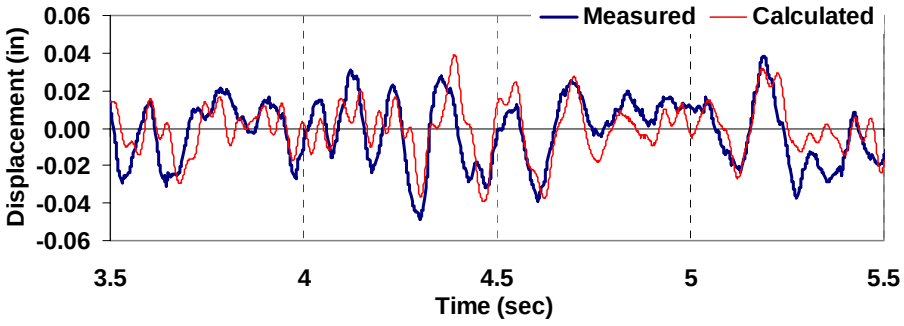

Figure 4.73: Two-second comparison of displacement at the top of south wall with PGA =1.0g (Damping: ξ_{dia} = 3%, ξ_{wall} = 10%).

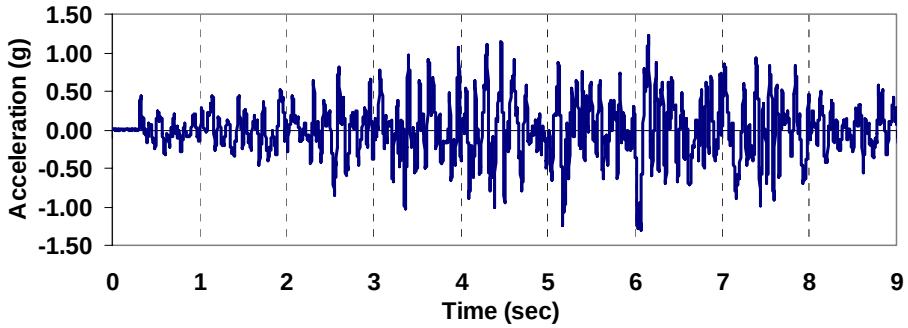

Figure 4.74: Measured acceleration at the top of south wall with PGA = 1.0g (Damping: ξ_{dia} = 3%, ξ_{wall} = 10%).

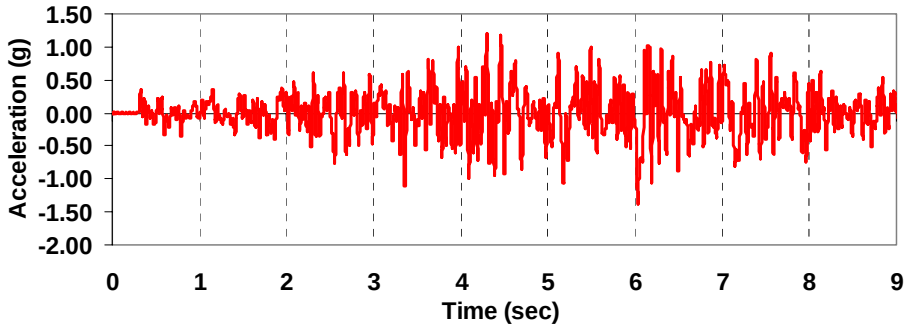

Figure 4.75: Calculated acceleration at the top of south wall with PGA = 1.0g (Damping: ξ_{dia} = 3%, ξ_{wall} = 10%).

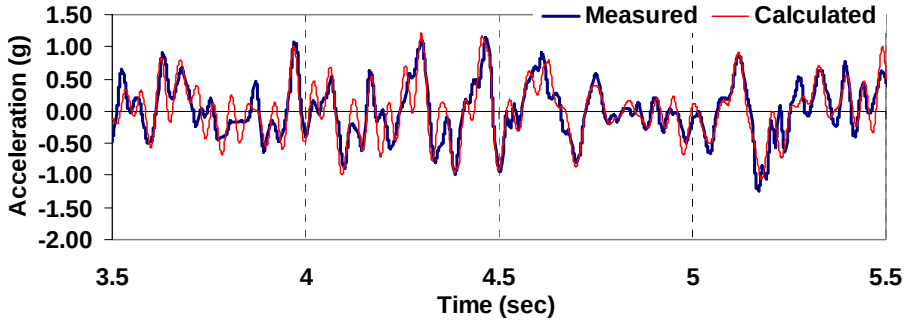

Figure 4.76: Two-second comparison of acceleration at the top of south wall with PGA =1.0g (Damping: ξ_{dia} = 3%, ξ_{wall} = 10%).

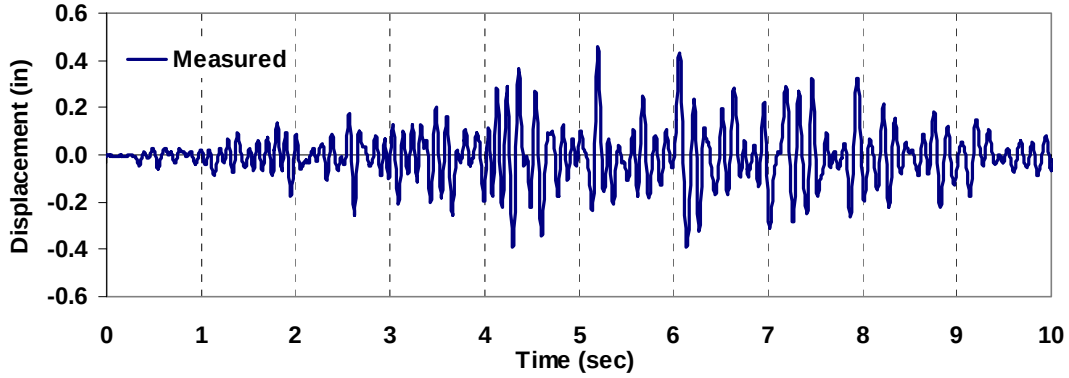

Figure 4.77: Measured displacement at the center of the diaphragm with PGA = 1.0g (Damping: ξ_{dia} = 3%, ξ_{wall} = 10%).

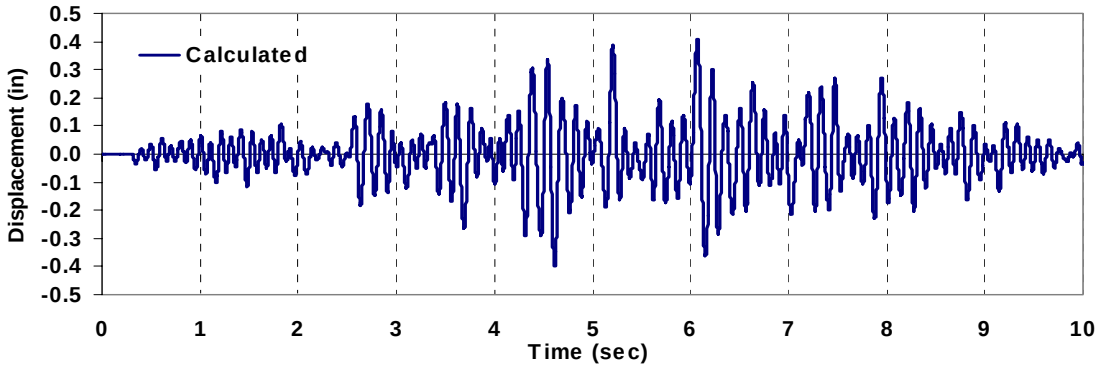

Figure 4.78: Calculated displacement at the center of the diaphragm with PGA = 1.0g (Damping: ξ_{dia} = 3%, ξ_{wall} = 10%).

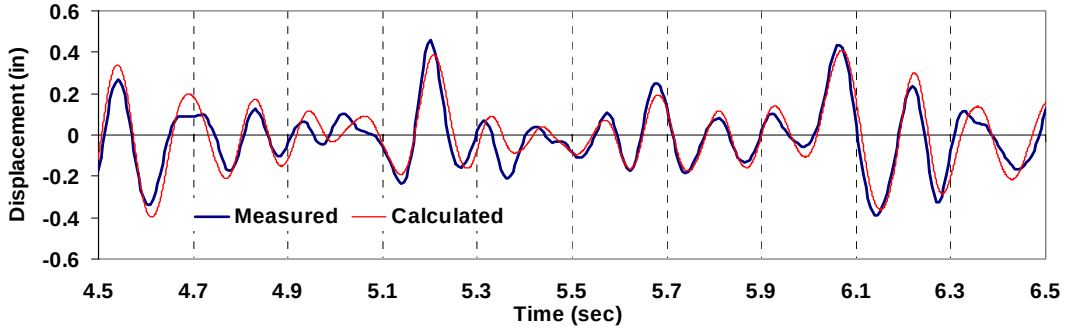

Figure 4.79: Two-second comparison of displacement at the center of the diaphragm with PGA = 1.0g (Damping: ξ_{dia} = 3%, ξ_{wall} = 10%).

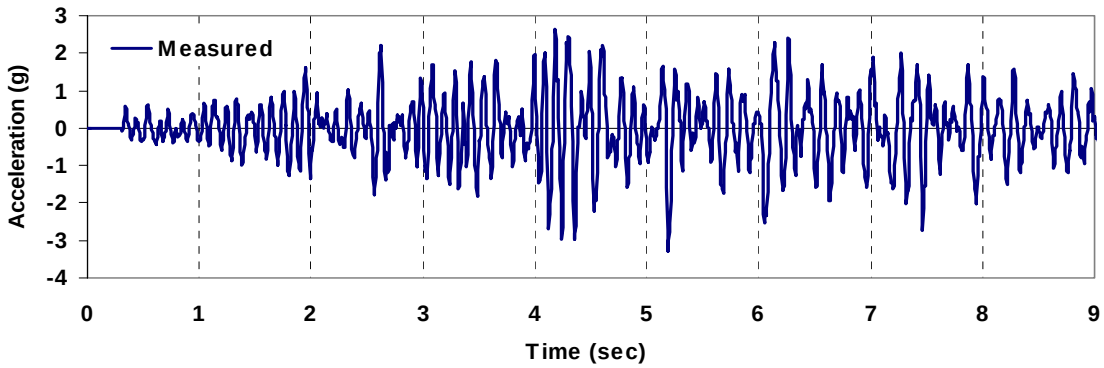

Figure 4.80: Measured acceleration at the center of the diaphragm with PGA = 1.0g (Damping: ξ_{dia} = 3%, ξ_{wall} = 10%).

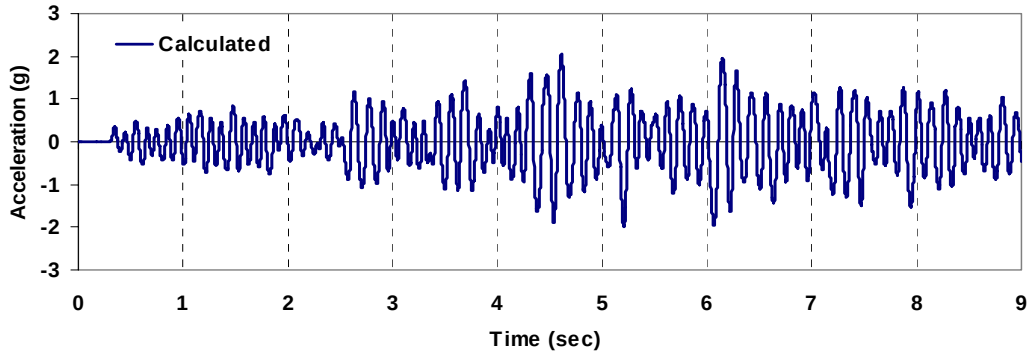

Figure 4.81: Calculated acceleration at the center of the diaphragm with PGA = 1.0g (Damping: ξ_{dia} = 3%, ξ_{wall} = 10%).

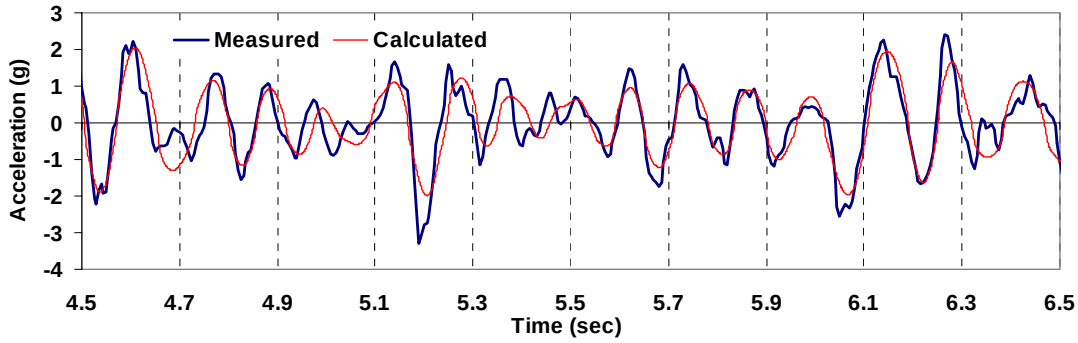

Figure 4.82: Two-second comparison of acceleration at the center of the diaphragm with PGA = 1.0g (Damping: ξ_{dia} = 3%, ξ_{wall} = 10%).

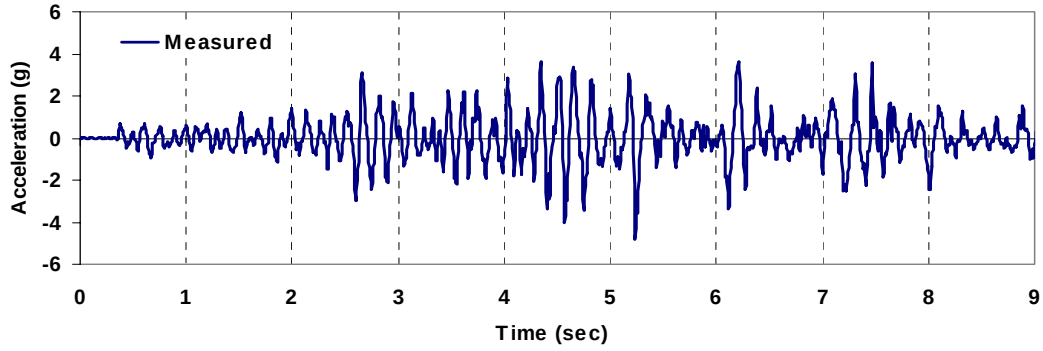

Figure 4.83: Measured acceleration at the center of the diaphragm with PGA = 1.33g (Damping: ξ_{dia} = 3%, ξ_{wall} = 10%).

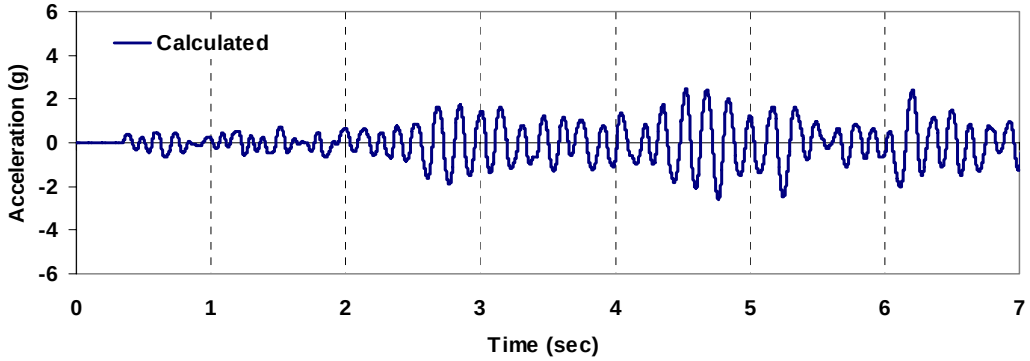

Figure 4.84: Calculated acceleration at the center of the diaphragm with PGA = 1.33g (Damping: ξ_{dia} = 3%, ξ_{wall} = 10%).

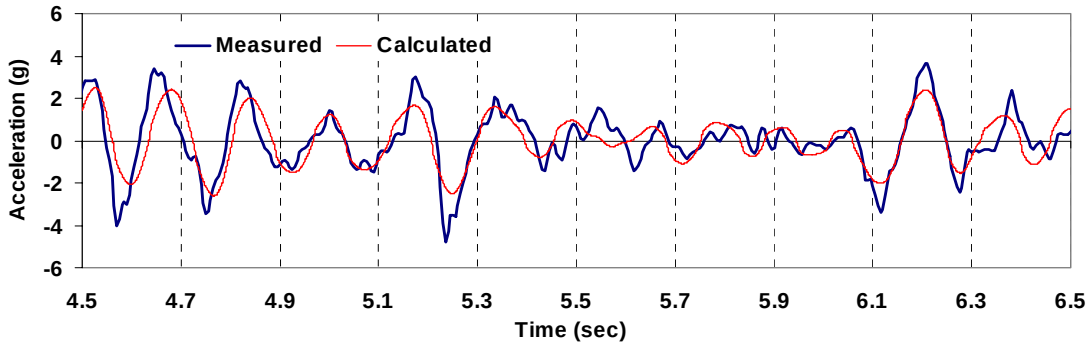

Figure 4.85: Two-second comparison of acceleration at the center of the diaphragm with PGA = 1.33g (Damping: ξ_{dia} = 3%, ξ_{wall} = 10%).

The calculated shear forces at the base are summarized in Table 4.21. The total base shear increases 66% compared to Test 3 as shown in Table 4.10. The shear force of in-plane walls increases 138%, but the shear force of out-of-plane walls decrease 29%. Due to the extensive damage of the out-of-plane wall, the increased lateral force of the structure is much more distributed to the in-plane walls than to the damaged out-of-plane walls.

Table 4.21: Calculated seismic shear at the base using PGA = 1.0 g (Damping ξ_{dia} = 3% ξ_{wall}= 10%).

Element	Shear Force (lb.)
1. North wall	1,797 lb.
2. South wall	2,125 lb.
3. out-of-plane wall (= East + West wall)	1,147 lb.
4. East wall	165 lb.
5. West wall	156 lb.
Overall Base Shear (=1+2+3)	5,069 lb.

4.5 Sensitivity Analysis

In this section, parametric sensitivity analyses are performed using the structural properties obtained from the model calibration process as base reference values. In these analyses, the stiffness and strength of the backbone curves for the diaphragm, the out-of-plane walls, and the in-plane walls are varied as illustrated in Figs. 4.86 and 4.88. Figure 4.86 shows the backbone curves for a number of the analyses that span the complete range of parameters considered. The hysteresis properties of the varied curves are unchanged from those selected by the calibration procedure. The model maxima are computed using

the nonlinear time history analysis with two different ground accelerations (PGA = 0.5g and 1.0g) obtained from Tests 3 and 9. The main objective is to capture the nonlinear dynamic characteristics of the building under the moderate and strong earthquakes. The analytical results in these figures are normalized to the predicted element properties obtained from the model calibration process. In each figure, the normalized parameter versus the out-of-plane and in-plane drift ratios in percent is plotted. Each of the figures focuses on illustrating the effects on the out-of-plane and in-plane wall drift. The mass properties are assumed to be the same in all the models of the sensitivity study for purposes of simplicity. In these sensitivity analyses, 3% damping is applied to diaphragm and 10% damping is applied to the masonry walls (see Section 4.4.3.2).

4.5.1 Effect of diaphragm flexibility

The diaphragm stiffness (K_d) is normalized by the obtained diaphragm stiffness from the quasi static test results (K_d*) (see Section 4.3.2.2). The normalized diaphragm stiffness (K_d/K_d*) is used to plot the backbone curves of the diaphragm. The normalized diaphragm stiffness (K_d/K_d*) is plotted against the out-of-plane and in-plane drift ratios in percent. Figures 4.89 through 4.94 summarize the displacement and acceleration results from all the sensitivity studies varying diaphragm flexibility. The following trends can be observed from the plots.

- For both 0.5g and 1.0g input ground motions, as the diaphragm stiffness is increased from K_d/K_d* = 1 to 5, the out-of-plane wall drift ratio is decreased, as shown in Figs. 4.89 and 4.90, but the in-plane wall drift ratio is increased, as shown in Fig. 4.92.
- For 0.5 g input ground motion, the overall response of the building is elastic between K_d/K_d* = 3 to rigid diaphragm. As the diaphragm goes from K_d/K_d* = 3 to very flexible diaphragm, the behavior of out-of-plane walls becomes inelastic. As the diaphragm goes from K_d/K_d* = 3 to 1, the in-plane wall drift

ratios are slightly increased. As the diaphragm goes from $K_d/K_d^* = 1$ to very flexible diaphragm, the in-plane wall drift ratios are not changed as rapidly as the out-of-plane wall drift ratio. As the diaphragm goes from $K_d/K_d^* = 0.7$ to 2 (see Fig. 4.90), the in-plane and out-of-plane wall drift ratios are increased compared to the results of $K_d/K_d^* = 2.9$.

- For 1.0g input ground motion, as the diaphragm stiffness ratio (K_d/K_d^*) is increased from 0.4 to 2.9, the out-of-plane drift ratio is gradually decreased (see Fig. 4.90), but the in-plane wall drift is increased above the immediate occupancy level in FEMA356, as shown in Figs. 4.91 and 4.92 (a). However, as the diaphragm stiffness ratio is increased from 3, the in-plane wall drift ratio is decreased, but after passing 25, the drift ratio remains about 0.11%. From the point where diaphragm stiffness ratio equals 6 to rigid diaphragm, the behavior of the diaphragm is elastic (see Fig. 4.92(d)). The behavior of the diaphragm is inelastic for diaphragm stiffness ratios between 0.4 and 3. The out-of-plane and in-plane wall are in inelastic range on the whole. The in-plane drift ratio has a maximum value at a stiffness ratio of 3. The peak in-plane drift ratio of 3 can be treated as the similar phenomenon, as shown in the SDOF spectral response in Fig. 4.95. Spectral displacement value is maximized around 0.1sec. The calculated natural period of the test building is 0.08sec (Table 4.9). As the stiffness of out-of-plane and in-plane walls are degraded, the period of the structure will be increased around 0.10 sec. In addition, if the assumed stiffness proportional damping for non-linear analysis is increased, the corresponding maximum value where stiffness ratio is 3 will be decreased in the analytical model.

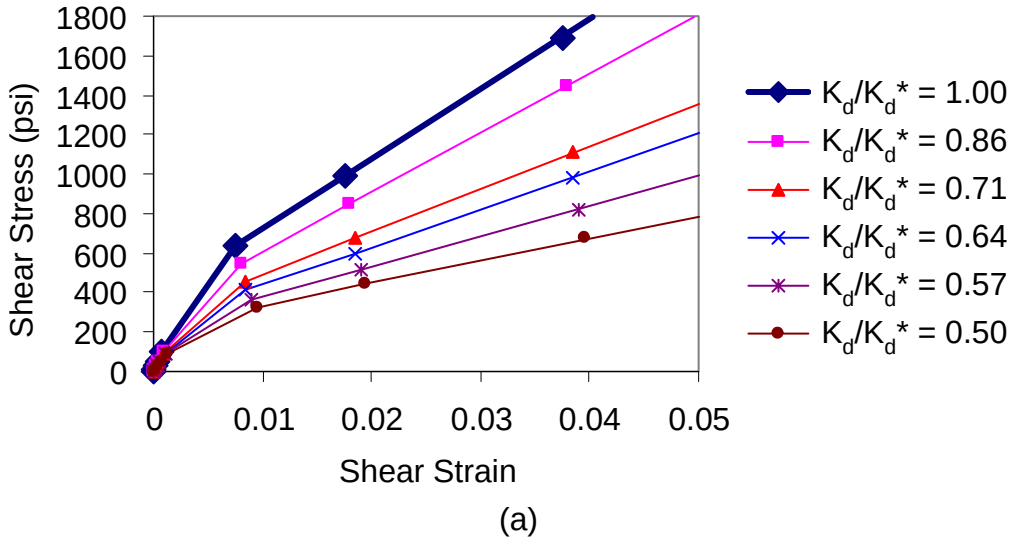

(a)

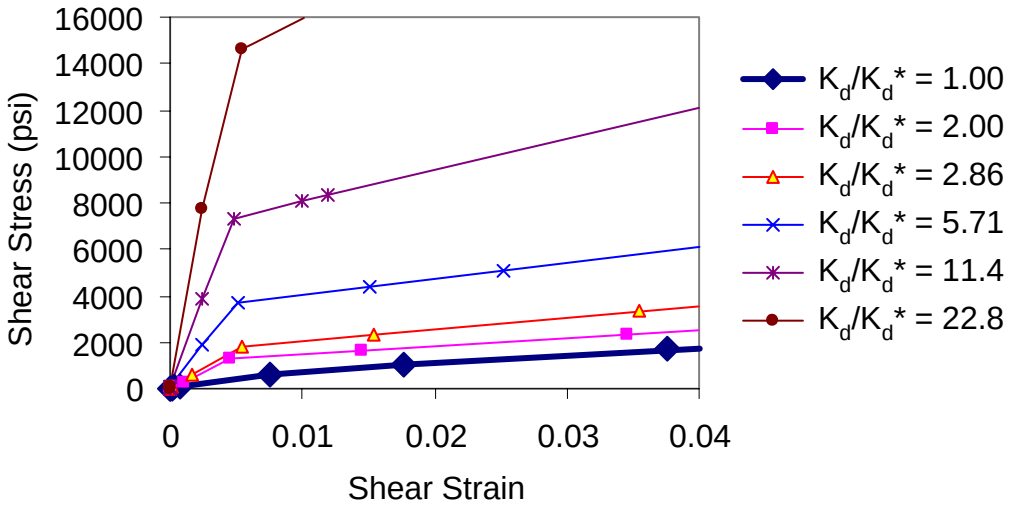

(b)

Figure 4.86: Variation of the diaphragm backbone curves corresponding to (a) the decreased initial stiffnesses and (b) the increased initial stiffnesses.

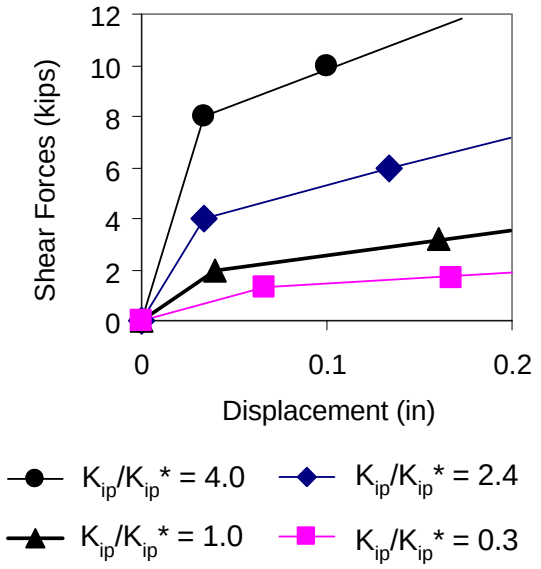

Figure 4.87: Variation of the in-plane wall backbone curves corresponding to the increased initial stiffnesses and strength.

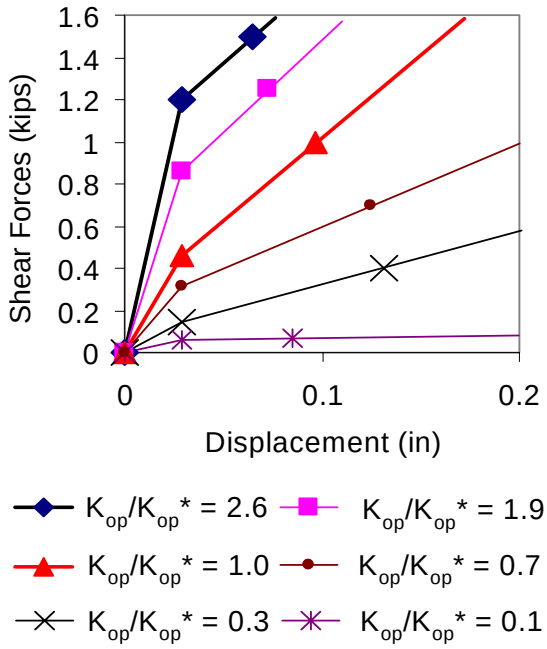

Figure 4.88: Variation of the out-of-plane wall backbone curves corresponding to the increased initial stiffnesses and strength.

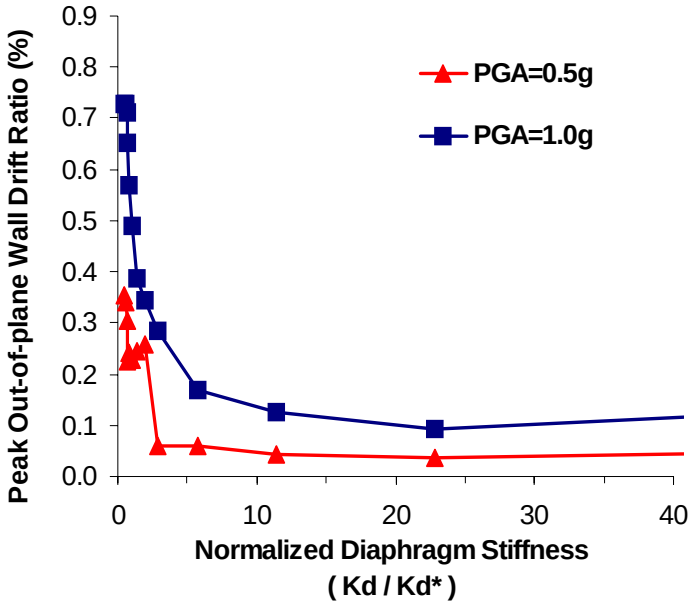

Figure 4.89: Peak out-of-plane wall drift ratio varying the diaphragm stiffness from K_d/ K_d* = 0.4 (flexible diaphragm) to 40 (rigid diaphragm).

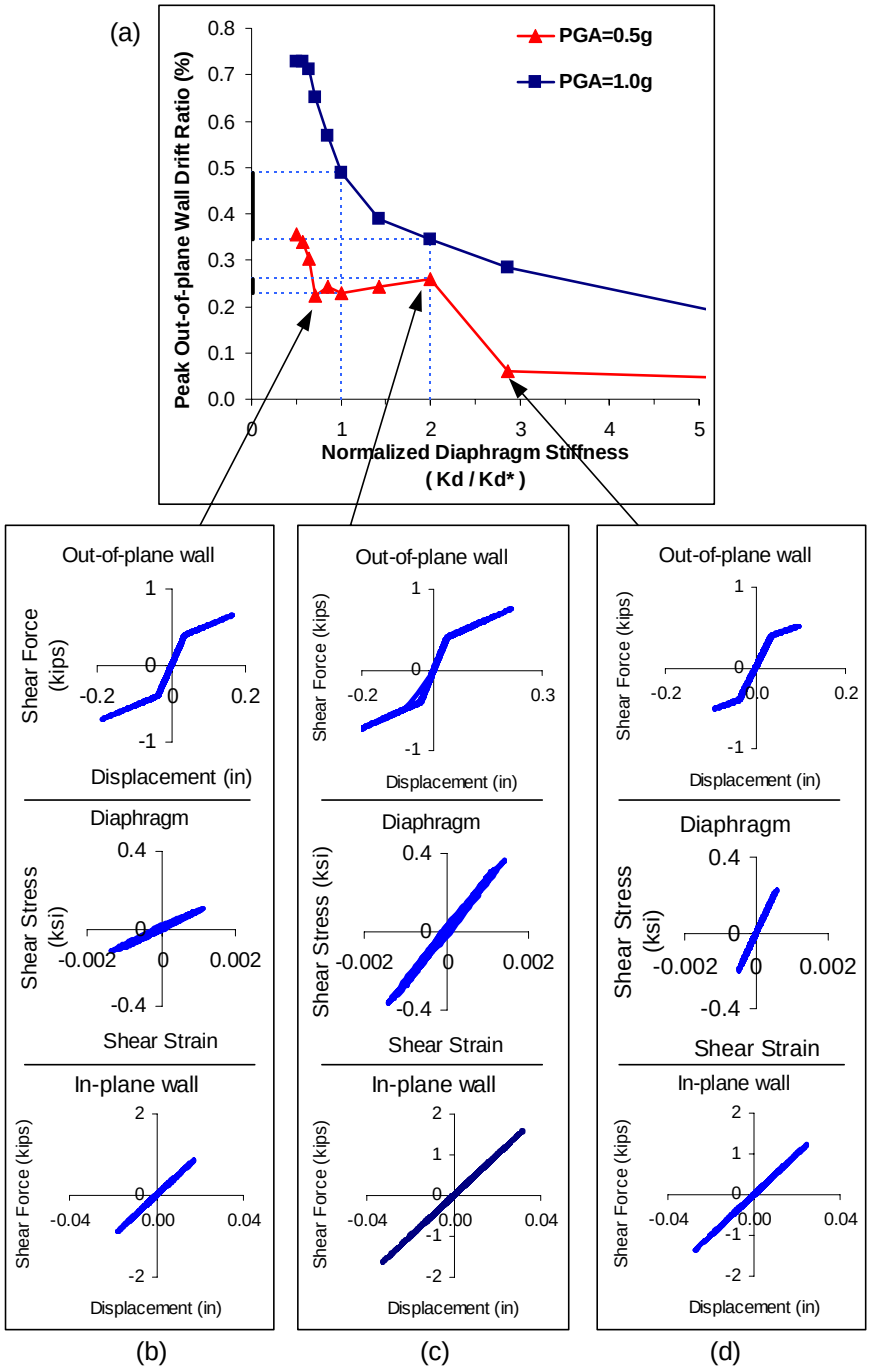

Figure 4.90: (a) Peak out-of-plane wall drift ratio varying the diaphragm stiffness from $K_d/K_d^* = 0.4$ (very flexible diaphragm) to 5 (flexible diaphragm), (b) Hysteretic curves of structural components for $K_d/K_d^* = 0.7$; (c) for $K_d/K_d^* = 2$; and (d) for $K_d/K_d^* = 2.9$.

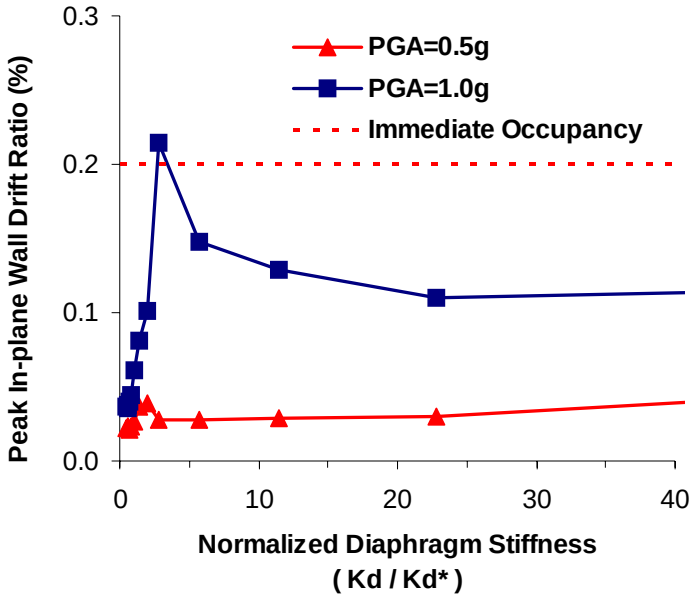

Figure 4.91: Peak in-plane wall drift ratio varying the diaphragm stiffness from K_d/K_d^* = 0.4 (flexible diaphragm) to 40 (rigid diaphragm).

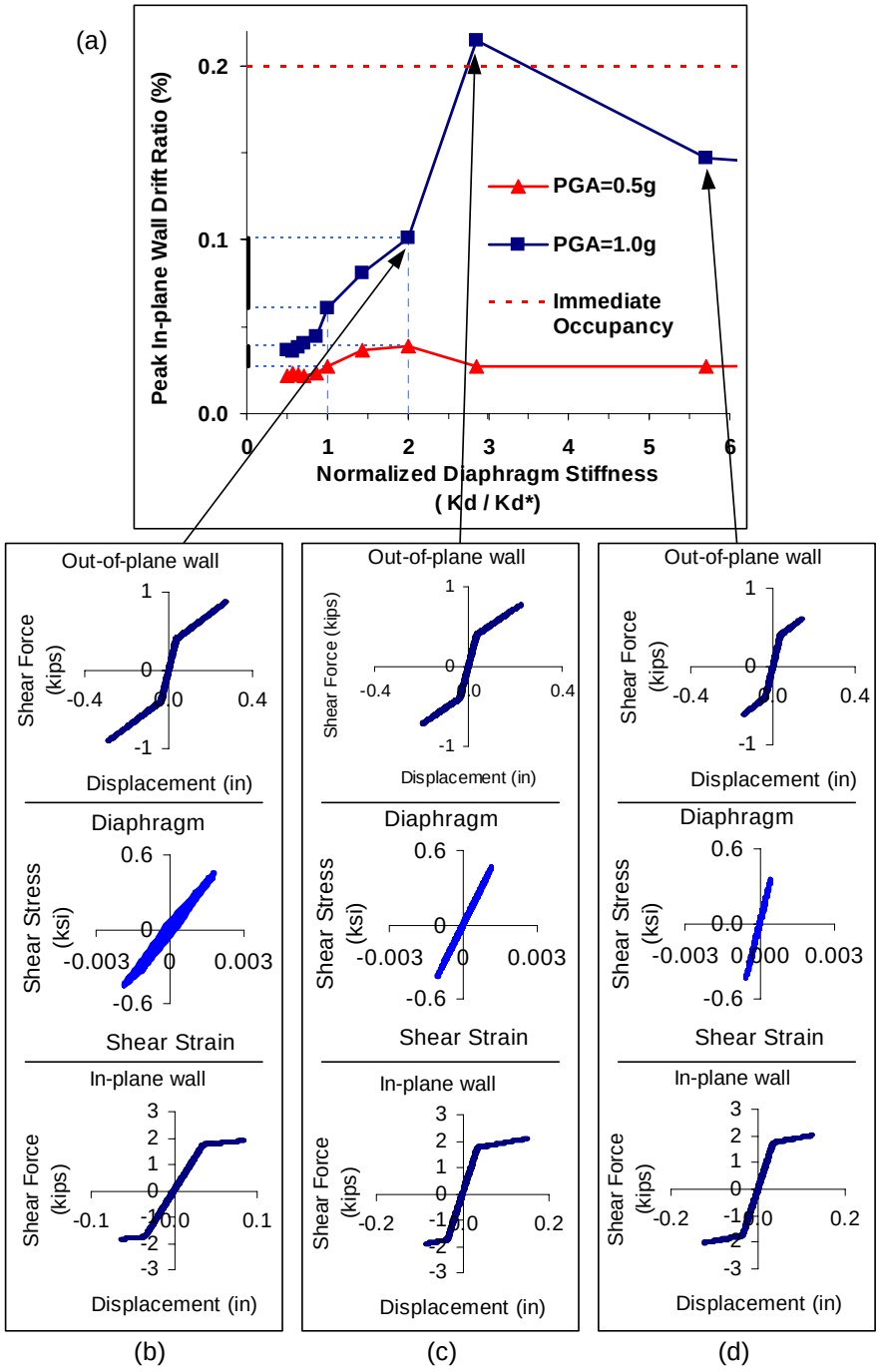

Figure 4.92: (a) Peak in-plane wall drift ratio varying the diaphragm stiffness from K_d/K_d^* = 0.4 (very flexible diaphragm) to 6 (flexible diaphragm) (b) Hysteretic curves of structural components for K_d/K_d^* = 2; (c) for K_d/K_d^* = 2.9; and (d) for K_d/K_d^* = 5.7.

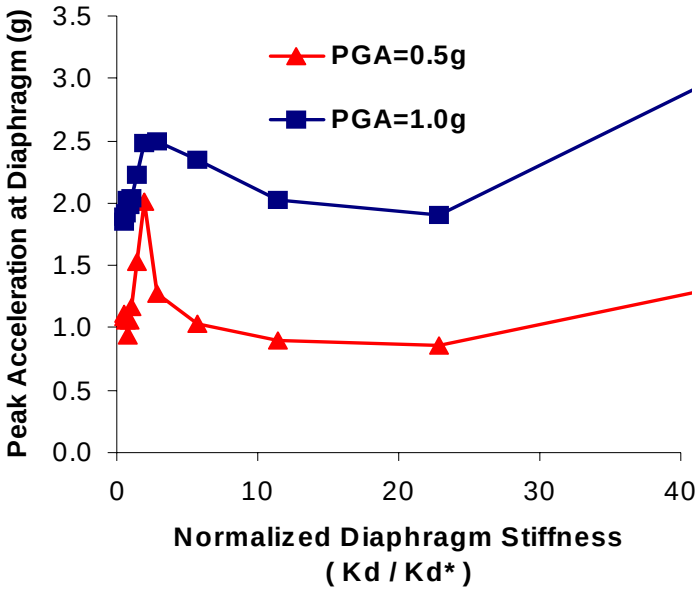

Figure 4.93: Peak acceleration at diaphragm varying the diaphragm stiffness from K_d/K_d^* = 0.4 (flexible diaphragm) to 40 (rigid diaphragm).

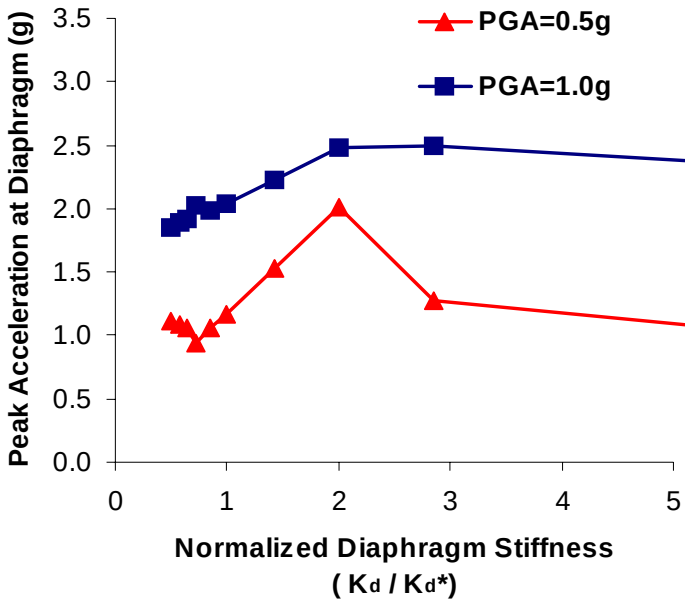

Figure 4.94: Peak acceleration at diaphragm varying the diaphragm stiffness from K_d/K_d^* = 0.4 (very flexible diaphragm) to 5 (flexible diaphragm).

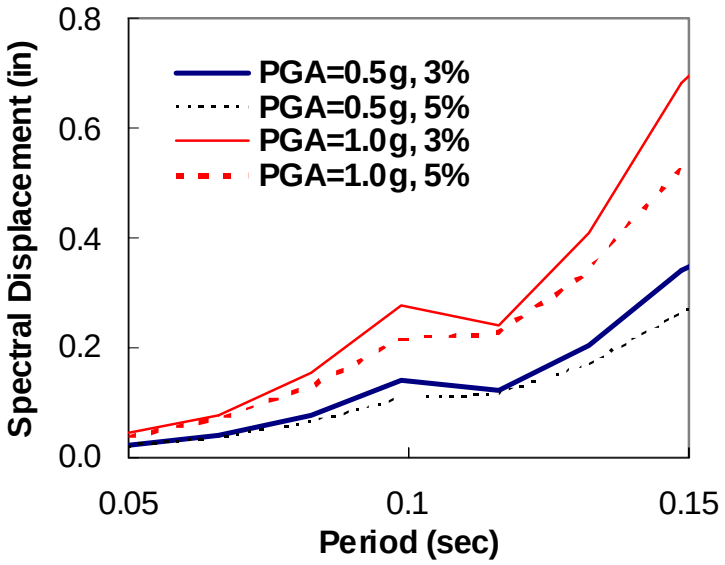

Figure 4.95: Displacement response spectrum of time-scaled (factor = 0.5) input record used for ground excitation.

4.5.2 Effect of in-plane wall stiffness and strength

Figures 4.96 through 4.98 summarize the displacement and acceleration results from all the sensitivity studies varying in-plane wall stiffness. The normalized in-plane wall stiffness ratio (K_{ip}/K_{ip}*) is plotted against the out-of-plane, in-plane drift ratios in percents. K_{ip}* is the in-plane wall stiffness obtained from the model calibration process (see Table 4.18). The following characteristics can be observed from the plots in Figs. 4.96 through 4.98.

- For both 0.5 g and 1.0g input ground motion, as the in-plane wall stiffness ratio is increased from 0.33 to 4, both the out-of-plane and in-plane wall drift ratios are decreased.
- For 0.5g input ground motion, the out-of-plane wall drift ratios, as shown in Fig. 4.96, are not significantly influenced by changing the in-plane wall stiffness ratio from 0.5 to 4.

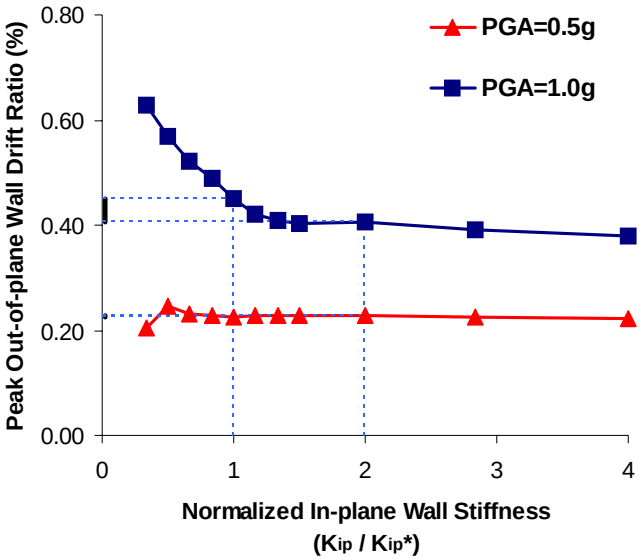

Figure 4.96: Peak out-of-plane wall drift ratio varying the in-plane wall stiffness from $K_{ip}/K_{ip}^* = 0.33$ to 4.

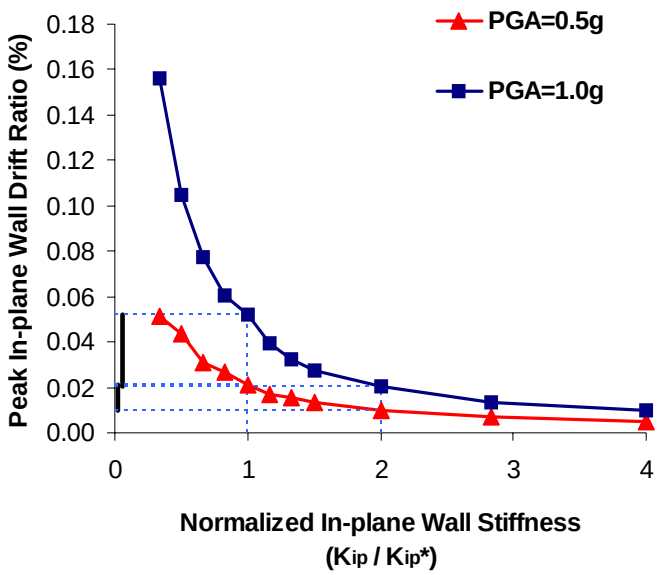

Figure 4.97: Peak in-plane wall drift ratio varying the in-plane wall stiffness from $K_{ip}/K_{ip}^* = 0.33$ to 4.

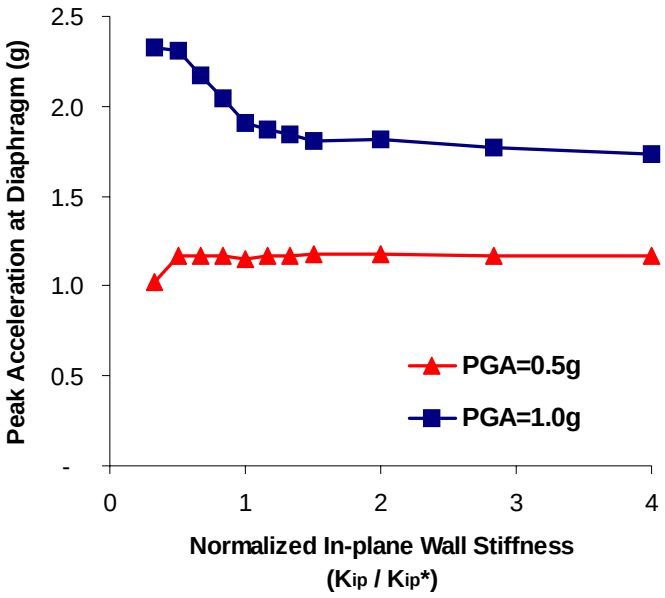

Figure 4.98: Peak acceleration at diaphragm varying the in-plane wall stiffness from $K_{ip}/K_{ip}^* = 0.33$ to 4.

4.5.3 Effect of out-of-plane wall stiffness and strength

Figures 4.99 through 4.101 summarize the peak displacement and acceleration results from all the sensitivity results varying out-of-plane wall stiffness. The normalized out-of-plane wall stiffness ratio (K_{op}/K_{op}^*) is plotted versus the out-of-plane, in-plane drift ratios in percents. K_{op}^* is the out-of-plane wall stiffness obtained from the model calibration process (see Table 4.18). The following trends can be observed from the plots in Figure 34 and 35.

- For 0.5g input ground motion, as the out-of-plane wall stiffness ratio is increased from 0.05 to 3, the out-of-plane wall drift ratio is decreased (see Fig. 4.99). However, the in-plane wall drift ratio is not changed significantly (see Fig. 4.100). There are abrupt changes from 1.2 to 1.5 due to a dynamic characteristic.
- For 1.0g input ground motion, as the out-of-plane wall stiffness ratio is increased

from 0.05 to 3, the out-of-plane and in-plane wall drift ratios are decreased.

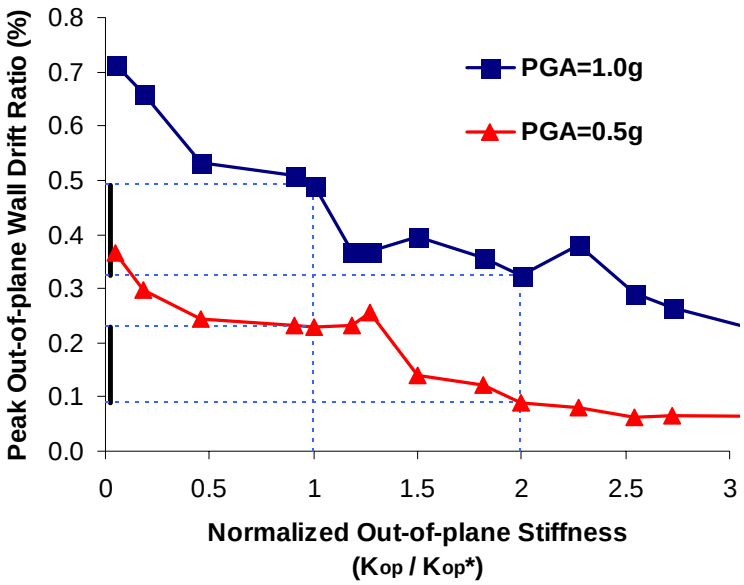

Figure 4.99: Peak out-of-plane wall drift ratio varying the out-of-plane wall stiffness from $K_{op}/K_{op}^* = 0$ (neglecting out-of-plane wall) to 3.

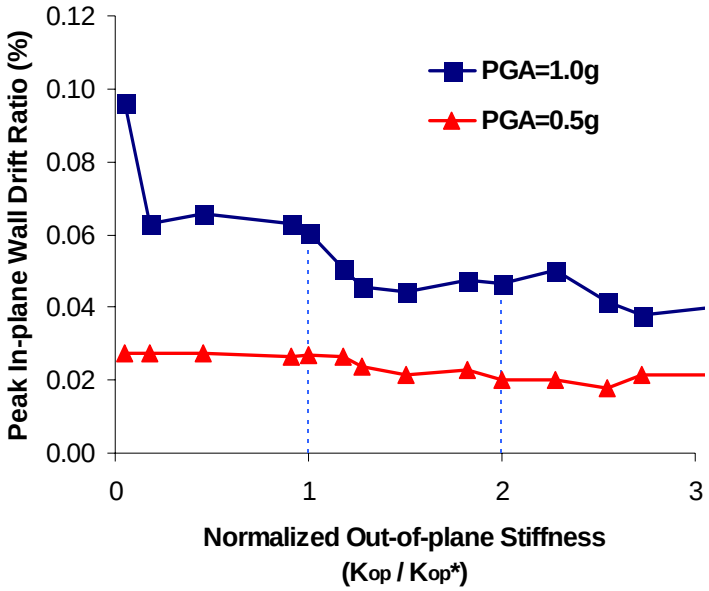

Figure 4.100: Peak in-plane wall drift ratio varying the out-of-plane wall stiffness from $K_{op}/K_{op}^* = 0$ (neglecting out-of-plane wall) to 3.

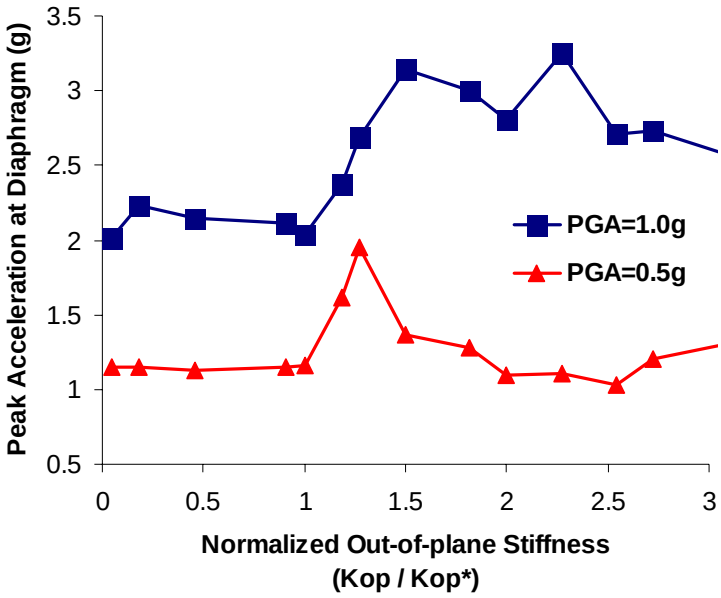

Figure 4.101: Peak acceleration at diaphragm varying the out-of-plane wall stiffness from $K_{op}/K_{op}^* = 0$ (neglecting out-of-plane wall) to 3.

4.6 Summary

A one-half scale one-story reinforced shear wall building with a flexible diaphragm is investigated using a MDOF modeling approach proposed in Chapter II. The overall behavior of the structure is considered by comparing the simplified MDOF analysis model and the experimental shaking table test results. The overall response of this building is dominated by the diaphragm behavior and out-of-plane wall, since the stiffness of these components is much smaller than that of the in-plane walls. It is recognized that buildings such as the one studied here do not behave as SDOF systems. The dynamic behavior of the out-of-plane wall and the flexible diaphragm can be predicted well when the proposed MDOF approach is used with appropriate values of the structural properties. By comparing the analysis results with measured data, the following observations and rec-

ommendations may be made:

- When the applied input ground motion is increased from moderate to strong, the out-of-plane wall is damaged first. The out-of-plane wall drift ratio is much higher than the in-plane wall drift ratio. When the out-of-plane wall stiffness and strength are decreased in the calibration studies, the diaphragm responds in a more non-linear fashion and larger lateral shear forces are distributed to the in-plane walls. The relative lateral force taken by the in-plane and out-of-plane walls depends significantly on their relative stiffnesses.
- For test 3, approximately one-third of the total base shear is taken by the two out-of-plane walls and by each of the in-plane walls. However, in test 5, where the out-of-plane wall starts to experience some damage, a larger fraction of the base shear is taken by the in-plane walls. In test 9 where there is significant damage to the out-of-plane walls, an even higher fraction of the total base shear is distributed to the in-plane walls, in spite of the fact that the south wall also experiences damage in this test.
- The response of the out-of-plane walls is influenced significantly by the diaphragm flexibility. For both moderate and strong ground motions, the out-of-plane wall drift ratio is increased significantly when the out-of-plane wall stiffness is decreased in the calibration studies. However, the out-plane-wall drift ratio is not affected greatly by the changes in the in-plane wall stiffnesses. Increases in the diaphragm stiffness significantly decrease the out-of-plane wall drift ratio but increase the in-plane wall drift ratio for the strong ground motion test.
- The above results indicate that one of the most effective ways of improving the performance of these types of buildings would be to increase the out-of-plane wall stiffnesses and strengths. The out-of-plane wall stiffnesses and strengths

might be enhanced in general by retrofit measures such as steel bracing, fiber reinforced polymer (FRP) adhered with epoxy to the surface of the wall, reinforced or prestressed vertical cores, or reinforced shotcrete overlay bonded to the surface of the wall.

- The above results also indicate that damage to the out-of-plane walls may be reduced most effectively in general by increasing the diaphragm stiffnesses and strengths. The diaphragm stiffnesses and strengths might be enhanced by applying wood structural panels directly to wood diaphragms, strengthening the connections between the diaphragms and the walls, or installing and anchoring new diaphragms or bracing frames below existing diaphragms.
- In general, it is difficult to determine the effective flange width of out-of-plane walls, since this width depends on the connected condition at the intersection of the in-plane and out-of-plane walls as well as on the relative flexibility of the diaphragm and the walls. In this study, the flange effect from the out-of-plane walls appears to be negligible. The in-plane wall stiffness and strength estimated using mechanics of materials type equations from FEMA 356 and ACI 530-99 (MSJC 1999) are similar to the properties of the in-plane walls obtained from the calibration study assuming zero flange effects from the out-of-plane walls.
- While the out-of-plane reinforced masonry walls showed extensive cracking, they were strong enough to resist the lateral loads that resulted from diaphragm flexibility and out-of-plane dynamic loads. Because, the out-of-plane wall drift is associated highly with the diaphragm and the lateral loads of the diaphragm will be distributed to in-plane walls corresponding to the degree of the out-of-plane wall damage.
- In this work, Rayleigh damping is used to approximate the energy dissipation from various sources. The Rayleigh damping is based on linear theory. This

simple model may not be appropriate, when the structure shows extensive non-linear actions (e.g., the south wall of the test building). The linear equation of motion must include additional terms describing the non-linear damping affected by the non-linearities of the system. Damping models should be developed specifically for nonlinear dynamic analysis.

- Sine decay tests on the undamaged elastic structure such as performed on the CERL building are useful to establish damping ratios for analysis models. However, good correlation can be obtained with the measured results in this type of test using nonproportional damping models involving the assumption of different damping ratios for different materials. The studies within this paper indicate that different damping values need to be assumed for the combined response of the diaphragms and the out-of-plane walls versus that of the in-plane walls. The different damping ratios account for different energy dissipation in the different structural components.

CHAPTER V

SIMPLIFIED LINEAR STATIC PROCEDURES FOR LOW-RISE BUILDINGS WITH FLEXIBLE DIAPHRAGMS

5.1 Introduction

The main purpose of this chapter is to propose and investigate a simple and practical procedure for seismic assessment and design of low-rise shear wall buildings with flexible diaphragms, referred to in Chapter I as the structural separation method. The applicability of this simplified approach for these types of structures is demonstrated.

In rigid diaphragm structures with regular geometries, the lateral story shear forces are distributed through the diaphragms (e.g., the concrete slabs) to the shear walls in proportion to the rigidities of the walls. For these types of buildings, an equivalent single degree-of-freedom (SDOF) model may be used to estimate the total story shear force. However, this solution is not suitable for typical low-rise flexible diaphragm structures (e.g., low-rise shear wall buildings with wood or steel deck diaphragms). Flexible diaphragms generally have multiple dominant modes, and each of the diaphragms within the structure tends to respond in each of their principal directions largely in an independent fashion. This chapter proposes and investigates a simple and practical procedure for seismic analysis of low-rise shear wall buildings with flexible diaphragms using an approach termed the structural separation method. The qualities and limitations of this simplified approach are considered for these types of structures.

As discussed in Chapter I, the structural separation method entails the modeling of each of the diaphragms and their adjacent walls within a building as separate subassem-

blies. In many cases, it may be assumed that the displacements of the in-plane walls are small compared to that of the flexible diaphragms to the extent that the in-plane walls may be modeled as rigid elements. However, the method does not require the in-plane walls to be modeled as rigid elements. The in-plane wall lateral forces are calculated by summing the lateral forces from the adjacent diaphragm subassemblies with the lateral forces due to the direct inertial effects within each wall

In this chapter, the proposed simplified linear static procedure is applied to a single-story reinforced masonry test building with a single flexible diaphragm and to a two-story unreinforced masonry historic building with interior walls and multiple diaphragms in each story considered previously in Chapters III and IV. The results using the structural separation method with a linear static procedure are compared to the results from time history analysis using the best models determined from the Chapter III and Chapter IV studies.

This chapter is organized as follows. Section 5.2 explains the limitations of the current seismic codes and the motivation for the proposed simplified linear static approach for assessment and design of low-rise buildings with flexible diaphragms. Section 5.3 discusses the approximate period calculation and the lateral load distribution for the separated diaphragm subassemblies in a simplified linear static procedure by this method. Section 5.4 discusses the application of the linear static procedure to the one-story CERL test building (see Chapter IV). In this case, the structure has only one diaphragm and therefore no structural separation is required. Section 5.5 shows an example of the structural separation method and its application to the two-story Gilroy firehouse (see Chapter III).

5.2 Motivation for the structural separation method

5.2.1 Summary of the linear static procedure in current seismic codes

The national model codes (UBC, BOCA, SSBC) and FEMA 273 and 356 employ a linear static procedure as the simplest design or assessment method. This procedure can be summarized as follows:

- The fundamental period of the structure is estimated using a simplified period calculation.
- The required lateral load is determined using smoothed design response spectra in conjunction with the estimated period of vibration.
- The lateral load is distributed vertically and horizontally to each of the floor levels according to the mass distribution and an assumed distribution of the maximum accelerations.
- The strength is checked based on the estimated lateral load.

This procedure is targeted primarily at multiple story buildings with rigid diaphragms. As discussed in Section 1.2.2, there is no specific procedure that addresses the characteristics of nonrigid diaphragm structures, of which flexible diaphragm structures are a sub-group.

5.2.2 Limitations of the current seismic codes for assessment of low-rise buildings with flexible diaphragms

For buildings with flexible diaphragms, the linear static procedures in the current seismic codes such as IBC 2000 and UBC 97 have the following limitations:

- These codes focus on the use of the fundamental period for characterizing the seismic response. The fundamental period calculation is not meaningful for a structure with multiple dominant modes. To the extent that a building's diaphragms respond independently of one another, each of the individual diaphragm periods is important to the overall structural response.
- The story shear calculated from the total base shear in the linear static (pseudo lateral load) procedure of these codes is effectively applied at the center of mass at each floor (see Fig. 1.4 (a)). The base shear is generally distributed to the shear walls in proportion to their relative rigidities. This procedure is reasonable for regular buildings with rigid diaphragms but is not reasonable for nonrigid diaphragm structures. The story lateral force must be distributed appropriately to represent the effects of the distributed mass within the corresponding diaphragms as well as the distributed mass of the in-plane and out-of-plane walls (see the proposed simplified MDOF model of a one-story single-diaphragm building in Fig. 1.4 (b)).

FEMA 356 suggests that the period and pseudo lateral load should be calculated for each diaphragm span and at each floor level for unreinforced masonry buildings with flexible diaphragms. However, this standard does not provide any explicit guidance regarding this type of calculation for other types of flexible diaphragm structures. Furthermore, FEMA 356 does not address the fact that the motion of the in-plane walls is generally different than that of the flexible diaphragm. The FEMA 356 procedure considers only the period of the diaphragm spans. If the fundamental period calculated at the each flexible diaphragm is used for all the in-plane walls and diaphragm for each span, the calculated in-plane wall lateral forces will tend to be overestimated. The peak accelerations at the top of the in-plane walls are usually much smaller than those at the center of the diaphragm in these types of buildings. The accelerations at the top of the in-plane walls and

the center of the diaphragm should be considered separately.

5.2.3 Multiple mode effects and structural separation

The stiffnesses of the flexible diaphragms within a low-rise masonry building are typically much smaller than those of the shear walls. For these types of buildings, there are typically several dominant modes, each associated with the structural components that have the smaller stiffness. An example of this behavior is discussed in Section 3.4.1 (see Fig. 3.23 (b)).

These types of buildings can be assessed approximately by considering individual separated structures at each diaphragm location (see Fig. 1.5(c)). In this simplified procedure, lumped masses are located at the center of the diaphragm and the top of the shear walls as shown in Fig. 1.4 (b). Compared with the behavior of the building with rigid diaphragms, the displacements at the center of each flexible diaphragm are significantly larger than the corresponding displacements at the shear walls. The first two mode shapes from the eigenvalue analysis of a building are shown in Fig. 1.5 (b). The first mode is dominated by bending of the left diaphragm and the second mode is dominated by bending of the right diaphragm. The behavior of the left diaphragm does not affect the behavior of the right diaphragm significantly, and vice versa. Based on these independent multiple mode effects, the structural separation approach of the building can be considered as shown in Fig. 1.5 (c). The individual subassemblies are considered separately, and the base shear forces of the original structure are obtained by summing the base shears of the separated subassembly models.

5.3 Linear static procedure using the structural separation method

Figure 5.1 outlines the overall linear static procedure proposed in this chapter. The

first step of this method is to separate a structure with multiple flexible diaphragms into individual diaphragm subassemblies as discussed in Section 1.5. Lumped masses are calculated at the center of the diaphragm and at the intersections between the diaphragm and walls (see Fig. 5.2 (b)).

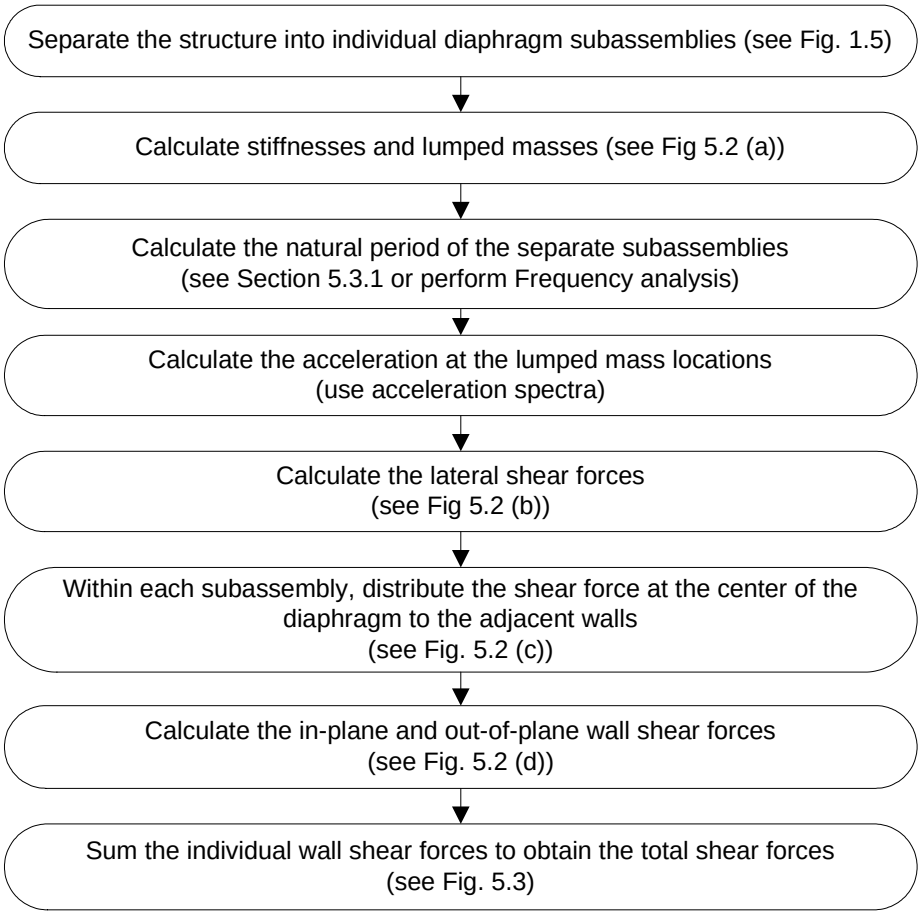

Figure 5.1: Simplified procedure for low-rise building with flexible diaphragms.

The fundamental period is calculated based on the lumped masses and the subassembly stiffnesses (see Section 5.3.1). The calculation of the period is discussed in detail in Section 5.3.1. When both the in-plane and out-of-plane walls are considered in calculating the period, a frequency analysis is required. In the proposed structural separation

approach, the influence of in-plane shear wall flexibilities on the inertial effects is approximated using a separate analysis model of each of the shear walls, including the mass from the walls as well as that from an assumed tributary area of the diaphragms. When the in-plane walls are stiff enough such that they may be assumed to be rigid relative to the diaphragms, only the separated diaphragm subassembly models need to be analyzed.

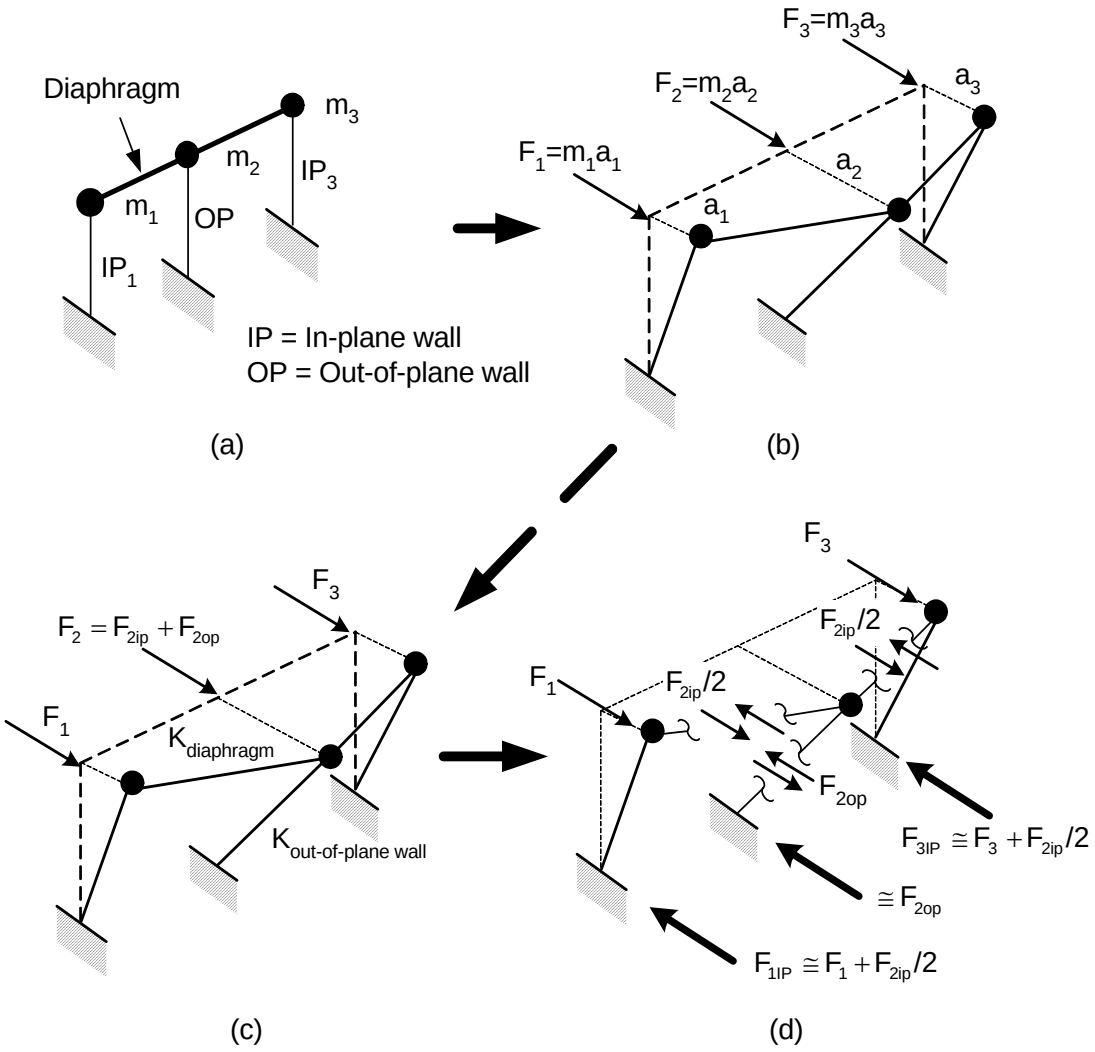

Figure 5.2: Base shear calculation for the MDOF system of a one-story building with a flexible diaphragm and out-of-plane walls: (a) MDOF system; (b) Acceleration and inertial forces; (c) Diaphragm load distribution to in-plane and out-of-plane walls, and (d) Approximate calculation of reactions.

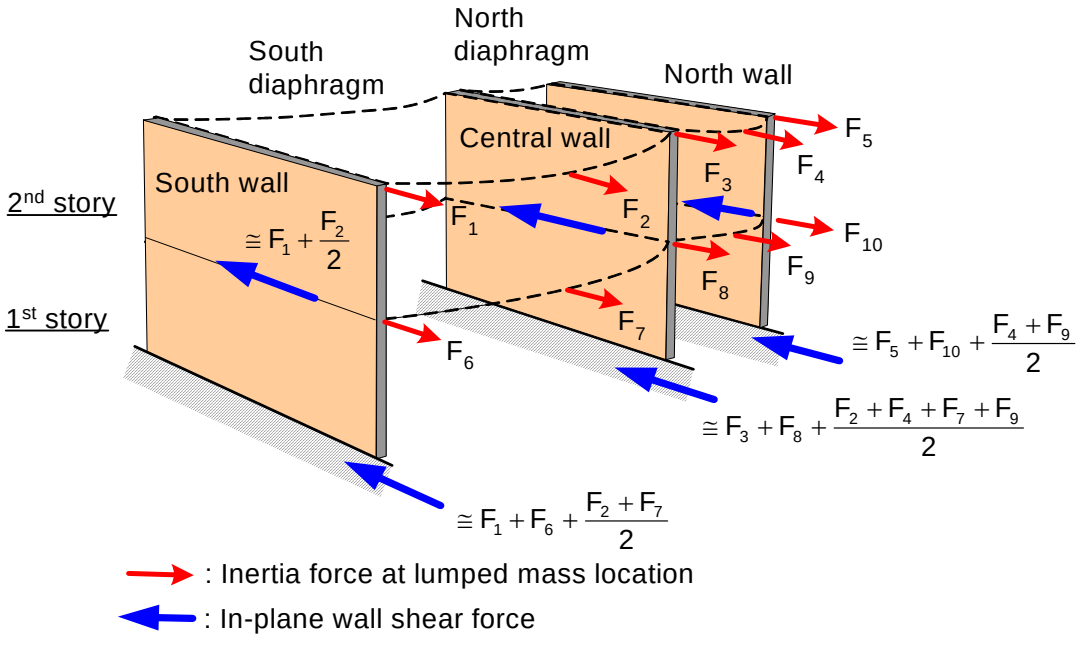

Figure 5.3: Approximate calculation of lateral forces of the two-story building with flexible diaphragms.

The accelerations at the lumped mass locations are determined using either smoothed design or specific response spectra (see Section 5.3.2). The lateral forces are calculated in the manner shown in Fig. 5.2 (b). The diaphragm lateral forces are distributed to the adjacent in-plane and out-of-plane walls (see Fig. 5.2 (c)). The base lateral forces of the separated subassemblies are calculated (see Fig. 5.2 (c)) and summed to obtain the total base shear of the structure with multiple diaphragms (see Fig. 5.3). The detailed calculation of the lateral forces is discussed in Section 5.3.2.

5.3.1 Approximate period calculation for the separated diaphragm subassemblies

The approximate fundamental period calculation for a single-story structure with a single nonrigid diaphragm is discussed in FEMA 273 and 356 (ASCE 2000a). FEMA 356 provides the following equation:

$$T = (0.1\Delta_w + 0.078\Delta_d)^{0.5} \quad \text{Eq. 3-8 in FEMA 356} \tag{5.1}$$

where, Δ_w and Δ_d are the in-plane wall and diaphragm displacements in inches "due to a lateral load in the direction under consideration, equal to the weight of the diaphragm." Use of this equation is permitted for one-story buildings with multiple-span flexible diaphragms. A lateral load equal to the weight tributary to the diaphragm span under consideration, applied to calculate a separate period for each diaphragm span. However for unreinforced masonry (URM) buildings with single-span flexible diaphragms, six stories or less in height, use of the following simpler formula is permitted (ASCE 2000a)

$$T = (0.078\Delta_d)^{0.5} \quad \text{Eq. 3-9 in FEMA 356} \tag{5.2}$$

where Δ_d is the maximum diaphragm displacement in inches, due to a lateral load in the direction under consideration, equal to the weight tributary to the diaphragm.

It is important for engineers to understand the origin of Eqs. 5.1 and 5.2 for proper interpretation of their applicability to general structures. Equation 5.2 is obtained by performing a Ritz analysis for the free vibration of a simply-supported beam with uniformly distributed mass along its length, as shown in Fig. 5.4 (b), using Euler-Bernoulli beam theory (i.e. zero shear deformations). Precisely speaking, a coefficient of 0.081 is obtained based on this model. Also, in the limit of a rigid diaphragm $(\Delta_d = 0)$, the other portion of Eq. 5.1 is obtained by applying just the lumped diaphragm inertial loading at the top of the walls, assuming symmetry of the structure and loading. The summation in Eq. 5.1 then gives a coarse approximation of the fundamental period of the three degree-of-freedom system composed of a Euler-Bernoulli beam of uniformly distributed mass, simply-

supported on flexible transverse springs (representing the wall flexibilities). Equation 5.2 effectively predicts the diaphragm natural period for the case of rigid structural walls.

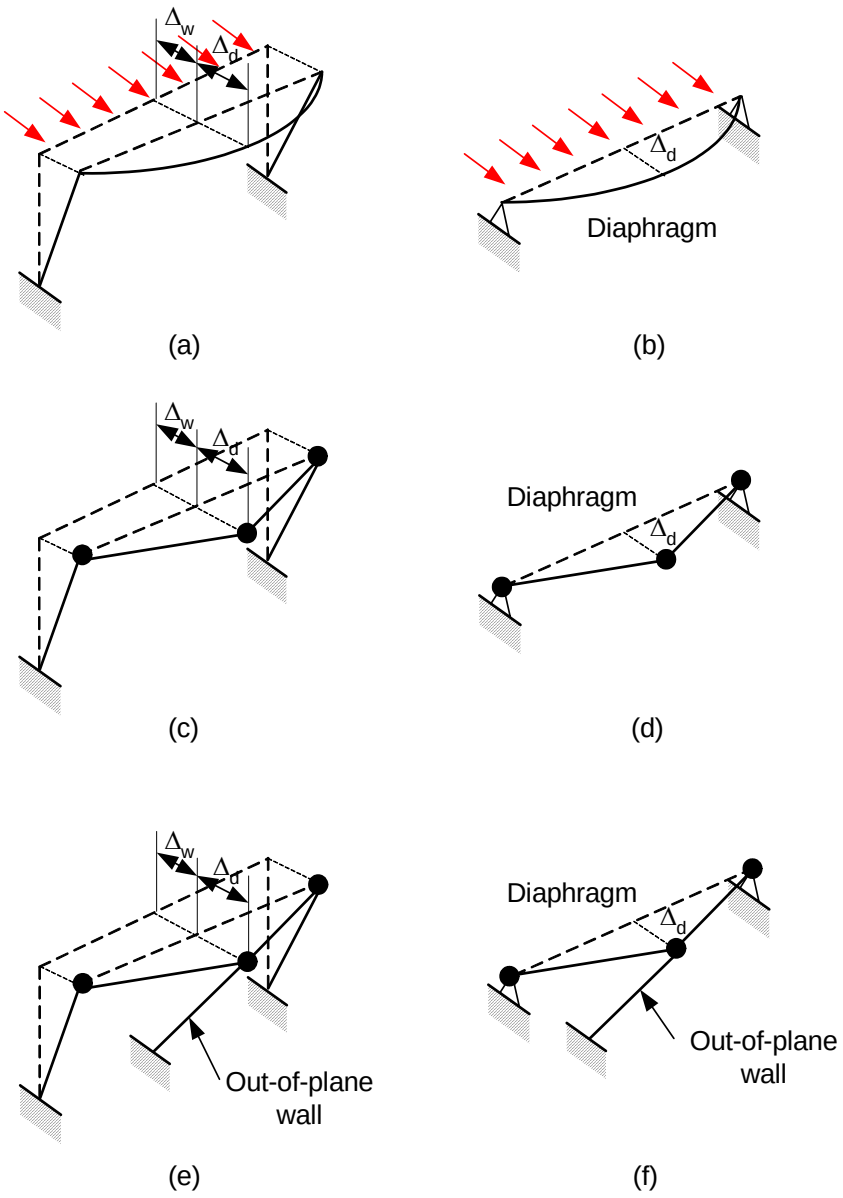

Figure 5.4: Displacements of one bay one-story building with a flexible diaphragm.

It should be noted that if the natural period of the diaphragm is calculated based on lumping of the mass at the diaphragm mid-span, as shown in Fig. 5.4 (d), a Ritz analysis predicts a coefficient of 0.1 instead of 0.078 in Eqs. 5.2 and 5.4. This is obtained as:

$$T = 2\pi\sqrt{\frac{m}{k}} \tag{5.3}$$

$$T = 2\pi\sqrt{\frac{m}{\left(\frac{mg}{\Delta_d}\right)}} \cong (0.1\Delta_d)^{0.5} \tag{5.4}$$

FEMA 356 suggests that the diaphragm displacement, Δ_d shown in Fig. 5.4 (a) and (b), should be based on the likely distribution of the inertial forces, and suggests a parabolic distribution with a maximum magnitude of 1.5 F_d/L, where F_d is the total inertial load applied to the diaphragm, for the equivalent static loading. FEMA 356 gives an illustration similar to that of Fig. 5.4 (a) implying that only the diaphragm stiffness need be included in the calculation of the diaphragm bending displacements.

The FEMA 356 model associated with Eq. 5.1 is reasonable for structures in which the out-of-plane wall stiffnesses are negligible. However, the use of lumped masses is more convenient and is considered to be sufficiently accurate for buildings in which there are significant stiffness and strength contributions from both the in-plane and out-of-plane walls, such as shown in Fig. 5.4(c) and in more general cases in which there are significant three-dimensional (torsional) responses. This model simplifies to the one shown in Fig. 5.4(d) when the in-plane walls are assumed to be rigid. The inertial effects of the in-plane wall masses do not influence the period, if the in-plane walls are effectively rigid, but, are important to calculate the in-plane wall forces. Furthermore, it should be recognized that, in general, both the mass as well as the stiffness of the out-of-plane walls influences the response significantly. The mass of the masonry walls is typically much higher than that of the diaphragm, and the behavior of the diaphragm generally includes a contribution from the out-of-plane walls, as shown in Fig. 5.4 (e). The added mass from out-of-plane shear walls increases the natural period and the stiffness of out-of-plane walls decreases the natural period. Therefore, the models shown in Figs. 5.4 (e) and (f) are a more accu-

rate representation of this type of structure in general than those shown in Figs. 5.4 (a) and (b). In light of the various approximations associated with the representation of the type of structure considered in these figures, the period calculation using Eq. 5.3 is preferred. However, if Equations 5.1 or 5.2 are employed, in general both the mass as well as the stiffness of the out-of-plane walls should be included in the calculation of Δ_d.

5.3.2 Lateral load calculations

5.3.2.1 Lateral load calculation within the separated subassemblies

Figure 5.2 (a) shows an individual isolated diaphragm subassembly separated from a multi-story structure with multiple diaphragms. When the in-plane shear walls connected to the diaphragm have significantly larger stiffness than that of the diaphragm and the stiffness of the out-of-plane wall is negligible (e.g., the approximation suggested by FEMA 356 for typical unreinforced masonry walls), the subassembly can be idealized as shown in Fig. 5.4(d). When the stiffness of the out-of-plane walls is not negligible (i.e., reinforced masonry walls), the subassembly can be idealized as shown in Fig. 5.4(f) and the stiffness contribution from the out-of-plane wall is included to calculate the natural period. In either case, based on the assumption that the acceleration at the top of the in-plane walls is equal to that at the base (i.e., rigid in-plane walls), the acceleration at the center of the diaphragm is determined using either smoothed design or specific response spectra in conjunction with the estimated period of vibration (see Section 5.3.1).

The lateral forces at the diaphragm level are calculated from the lumped mass and acceleration at each DOF location, as shown in Fig. 5.2 (b). The lateral force at the center of the diaphragm F_2 (see Fig. 5.2 (c)) is written as

$$F_2 = F_{2ip} + F_{2op} \tag{5.5}$$

where F_{2ip} = lateral force distributed to the in-plane wall

F_{2op} = lateral force distributed to the out-of-plane wall

Based on the relative stiffness of the diaphragm and the out-of-plane walls, the lateral force distribution to the in-plane and out-of-plane walls is calculated as

$$F_{2op} = \frac{F_2}{1 + \frac{K_{\text{diaphragm}}}{K_{\text{out-of-plane wall}}}} \tag{5.6}$$

$$F_{2ip} = \frac{F_2}{1 + \frac{K_{\text{out-of-plane wall}}}{K_{\text{diaphragm}}}} \tag{5.7}$$

The lateral forces of the in-plane walls (see Fig. 5.2 (d)) are finally determined as

$$F_{1ip} = F_1 + \frac{F_{2ip}}{2} \tag{5.8}$$

$$F_{3ip} = F_3 + \frac{F_{2ip}}{2} \tag{5.9}$$

5.3.2.2 Total in-plane and out-of-plane wall lateral force calculation

Figure 5.3 shows the approximate calculation of the total shear wall forces for an example two-story two-bay building with flexible diaphragms. It is assumed that the stiffnesses of the out-of-plane walls are negligible in this example (e.g., unreinforced masonry walls or shear walls with large openings). The lateral forces at the center of the diaphragms, calculated from the separated subassemblies, are distributed and added to the lateral forces from the lumped mass models at the tops of the adjacent shear walls. That is, the lateral force at the second story in the south wall is the sum of the inertia force of

the second story in the south wall (F_1) and the half of the inertia force from the lumped mass at the center of the south roof diaphragm (F_2). The wall lateral forces from the upper story add to those from the lower story.

If out-of-plane walls are considered in a multiple story structure such as the example shown in Fig. 5.3, the lateral load distribution discussed above will be more complex. In this case, the lateral force distribution at the center of the diaphragms is influenced significantly by the rigidity of the diaphragms and out-of-plane walls. When the proposed structural separation method is applied to multiple-story structures, any coupling between diaphragms that are located one above the other is neglected and it is assumed that the out-of-plane wall stiffness effects are small relative to the diaphragm stiffness. Otherwise, the subassembly concept must be modified.

5.4 Application of linear static procedure to the one-story CERL test building

In this example, the one-story half-scale test building, which is assessed in Chapter IV, is studied using the proposed simplified linear static procedure outlined in the Section 5.3. This building is investigated in the manner shown in Fig. 5.2. The mass properties are the same as those of the time history analysis model in Section 4.3.5. The effective damping is taken equal to 3% for the diaphragm subassembly, and an effective damping of 10% is used for the in-plane masonry walls in the E-W direction, as discussed in Section 4.3.6. The out-of-plane walls are included in this assessment as illustrated in Fig. 5.2. Test 3, one of the three experimental tests of the test building considered in Chapter IV, is used to investigate the simplified procedure, and the results from linear time history analysis are compared with those of the simplified method.

5.4.1 Acceleration spectra

In order to assess the one-story low-rise building, a set of acceleration response spectra that represent the earthquake motions used in the test are employed. The artificially scaled ground motion developed by Wen and Wu (1999) is used for test 3 (PGA = 0.5g). The acceleration spectra are obtained using the representative 2% in 50 years artificial ground motion (C02_09s) for that site. The acceleration spectra are calculated using the Utility Software for Earthquake Engineering (USEE Version 0.9.8) developed by Aschheim et al. (1999). Figures 5.5 and 5.6 show the half-time-scaled and unscaled acceleration spectra for various damping ratios. The test building was a half-scale model whose natural periods are one-half those of the full-scale prototype structure. Thus, in order to investigate the building using the simplified linear static procedure, the acceleration spectra are obtained using the half-scaled input time that was used in the experimental tests. The results of the simplified procedure using these spectra are compared with linear time history analysis results of the test.

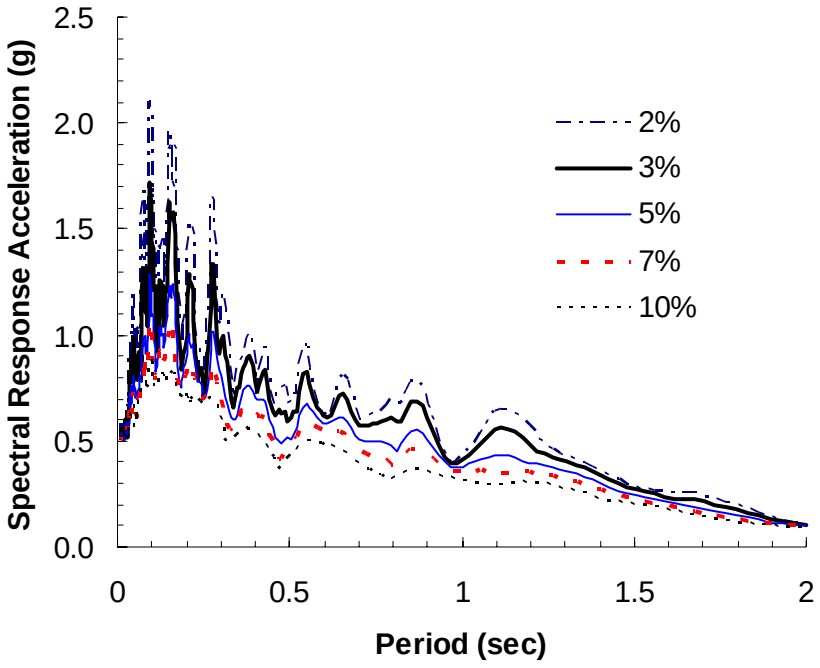

Figure 5.5: Half-time-scaled acceleration response spectra of 2% in 50 years Carbondale, IL artificial ground motion (C02_09s) for representative soil profile.

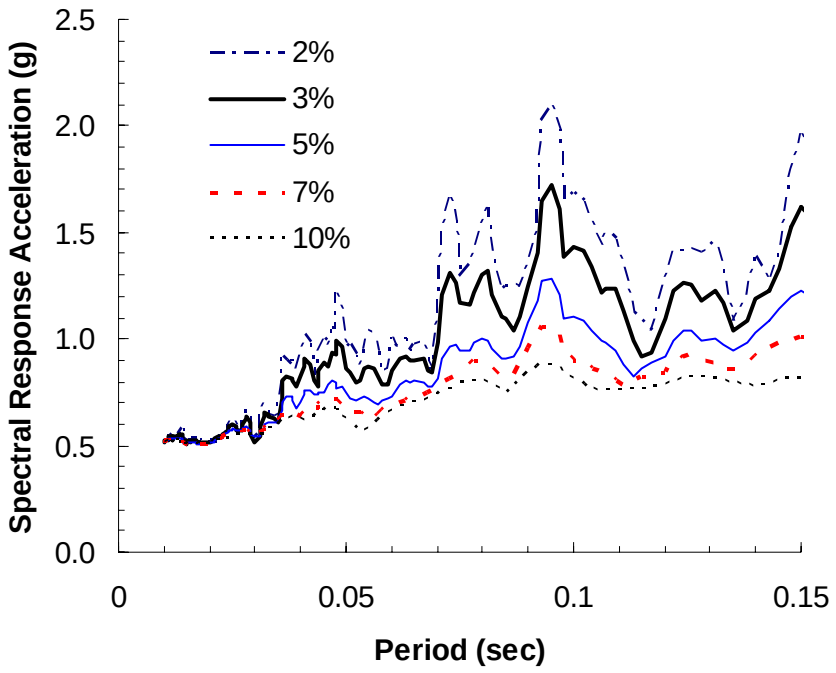

Figure 5.6: Half-time-scaled acceleration response spectra of 2% in 50 years Carbondale, IL artificial ground motion (C02_09s) for representative soil profile, plotted over a period range of zero to 0.15 sec.

5.4.2 Force calculation

The lateral forces calculated at the top of in-plane walls and the center of the diaphragm are shown in Table 5.1. The period of the diaphragm subassembly is calculated including the out-of-plane walls and assuming rigid in-plane walls, as shown in Fig. 5.4(f). The stiffnesses of diaphragm and out-of-plane wall are 7.41 and 16 kips/in, respectively, as shown in Table 4.13. The weight at the center of the diaphragm is 1,519 lb. The period is 0.082 sec calculated from Eq. 5.4. Equations 5.1 and 5.2 are not comparable because the natural periods is a coarse approximation based on the maximum diaphragm displacement. The acceleration, 1.32g shown in Table 5.1, is obtained from the acceleration spectrum, as shown in Fig. 5.6, corresponding to the period (0.082 sec) and 3% damp-

ing.

Two different calculations are considered for the periods of the north and south in-plane walls. The first and most basic calculation is based on the simple assumption that the in-plane walls are rigid, in which case, the accelerations at the tops of these walls are the same as the wall base accelerations (PGA of 0.5 g). The second calculation is based on the assumption of that the diaphragms are rigid. In this analysis, the finite in-plane and out-of-plane wall stiffnesses are included and the period (0.056 sec in the third column in Table 5.1) is calculated using the Ritz method considering the mass at the roof level and the stiffness from the in-plane and out-of-plane walls (see the note under Table 5.1). The spectral acceleration obtained from this analysis is 0.62g at the top of the in-plane walls. This is somewhat larger than the PGA of 0.5g.

The lateral forces shown in the fifth column in Table 5.1 are calculated in the manner shown in Fig. 5.2 (b). The lateral force at the center of the diaphragm (2.01 kips) is distributed to the in-plane and out-of-plane walls using Eqs. 5.6 and 5.7. The lateral force of the out-of-plane walls is 1.37 kips. The lateral force of the in-plane wall, including the contribution from the lateral force at the center of the diaphragm, is 0.95 kips. The total lateral forces at the base are shown in the sixth column of the Table 5.1.

Table 5.1: Calculated lateral forces from the simplified linear static procedure in the E-W direction.

Location	Mass (lb-sec^2/in)	Period (sec)	Acceleration (g)	Max. inertial loads[a] (kips)	Wall shear forces[b] (kips)
South wall	2.66	0.056[b]	0.50[c] 0.62[d] 0.70[e]	0.52[c] 0.64[d]	0.84[c] 0.95[d]
out-of-plane wall (at the center of the diaphragm)	3.94	0.082	1.32 1.45[e]	2.01	1.37
North wall	2.66	0.056[b]	0.50[c] 0.62[d] 0.70[e]	0.52[c] 0.64[d]	0.84[c] 0.95[d]

a. Max inertial loads (F_1, F_2, and F_3) in Fig. 5.2(b).
b. Wall shear forces (F_{1IP}, F_{2OP}, and F_{3IP}) in Fig. 5.2(d).
c. PGA assuming rigid in-plane shear walls.
d. Period calculated from the Ritz method assuming rigid diaphragm ($K = K_{op} + 2\ K_{ip} =$ 116 kip/in, $M = 9.26$ (lb sec^2/in).
e. Analysis results from linear time history analysis (see Table 4.9).

5.4.3 Comparison of the simplified procedure and linear time history analysis

Table 5.2 compares the lateral base shear forces from the simplified procedure (see Table 5.1) and linear time history analysis (see Table 4.11). The in-plane wall lateral force from the simplified procedure (0.95 kips) matches well with the one from the linear time history analysis (0.91 kips). The out-of-plane wall force (1.37 kips) is somewhat smaller than the one from the linear time history analysis (1.61 kips).

The lateral forces shown in the fifth column in Table 5.1 are applied to the CERL

test building model (see Figs. 4.6 and 5.2 (b)) and a linear static analysis is performed to calculate the displacements. The static analysis differs from these of the simplified procedure results due to the lateral load distribution from the center of the diaphragm to the in-plane and out-of-plane walls. These results are closer to the time history analysis results than those of the simplified procedure. The results of the linear static analysis match well with those of the linear time history analysis, as shown in Fig. 5.7 and Table 5.2, although the lateral force (1.49 kips) at the out-of-plane wall is slightly underestimated compared to that (1.61 kips) of the linear time history analysis. The north and south wall reaction forces (0.90 kips) compare with the peak reaction forces (0.913 kips) calculated from the linear time history analysis, as shown in Fig. 5.8. The out-of-plane wall reaction force is compared in Fig. 5.9. The in-plane and out-of-plane displacements (0.018 and 0.093 in, respectively) are matched well with the peak displacements (0.02 and 0.1 in, respectively) from the linear time history analysis (see Table 5.2). The results of the simplified procedure are considered accurate in spite of its simplicity.

Table 5.2: Comparison of analysis results.

Location	Simplified procedure	Linear static analysis		Linear time history analysis	
	Force (kips)	Force (kips)	Disp. (in)	Force (kips)	Disp. (in)
South wall	0.95	0.90	0.018	0.91	0.02
Out-of-plane wall	1.37	1.49	0.093	1.61	0.10
North wall	0.95	0.90	0.018	0.91	0.02

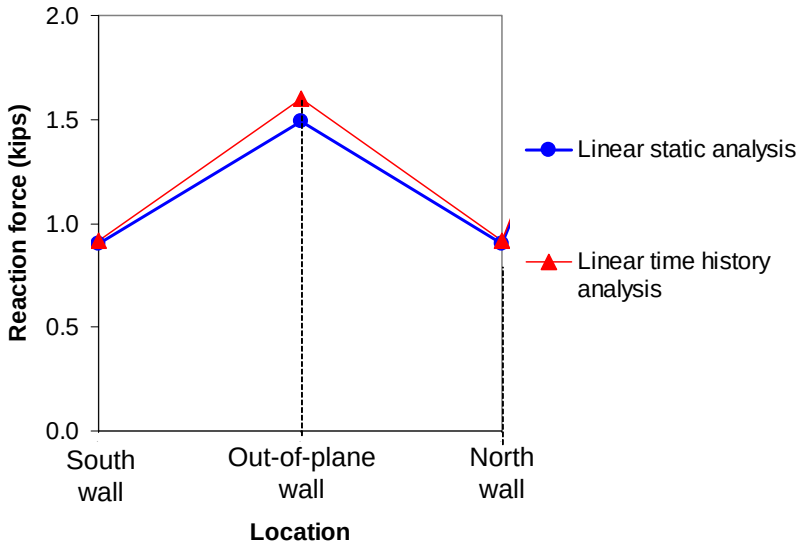

Figure 5.7: Comparison of analysis results.

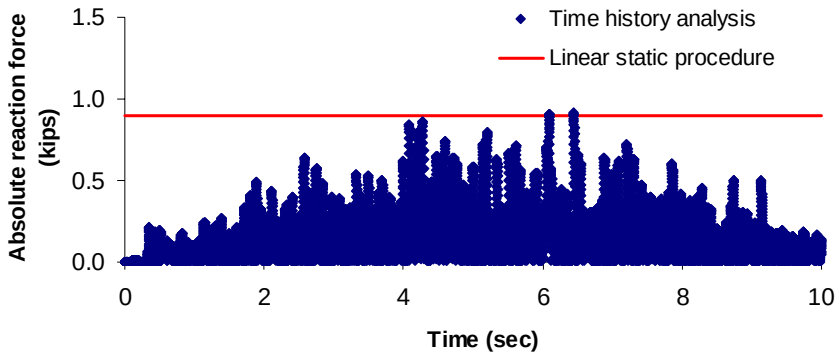

Figure 5.8: Comparison of reaction forces at the south and north wall.

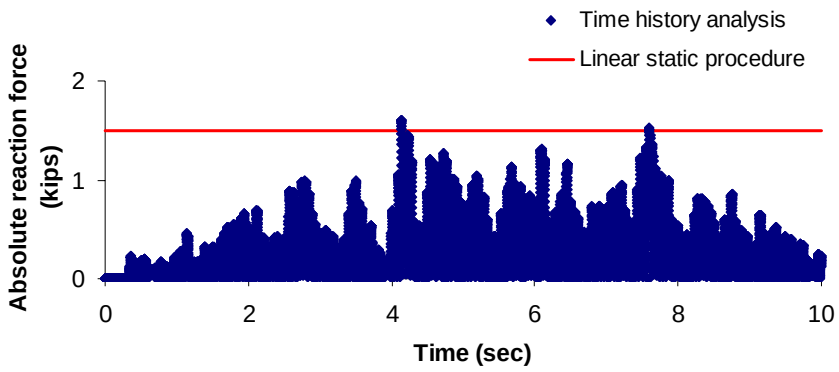

Figure 5.9: Comparison of reaction forces at out-of-plane wall.

5.5 Application of linear static procedure to the Gilroy firehouse using structural separation method

The main purpose of this assessment is to investigate the applicability of the simplified procedure discussed in Section 5.2 for a multi-story building with multiple flexible diaphragms. The two-story URM shear wall building with flexible diaphragms investigated in Chapter III is used to demonstrate the structural separation method and apply the simplified linear static procedure.

Section 5.5.1 compares the time history analysis results using the structural separation method with those from the model of the complete two-story structure. Section 5.5.2 shows the comparison of the simplified procedure and the linear time history analysis results.

5.5.1 Validation of the structural separation method

The structural separation method (see Section 5.2.3) is applied to the two-story

building with multiple diaphragms (see Fig. 3.1). Linear time history analyses are performed using each one-story single diaphragm subassembly. The summed reaction forces and displacements from the subassembly analyses are compared with the results from the complete building model.

Section 5.5.1.1 explains how the two-story structure is separated into the single-story single-bay subassemblies. Section 5.5.1.2 discusses the validation of the structural separation method by comparing the linear time history analysis results from the separated subassemblies with the results from the analysis of the complete two-story building.

5.5.1.1 Structural separation of the two-story building with multiple diaphragms

The response of two-story building (see Fig. 3.1) is considered into the separate the E-W and N-S directions (see Figs. 5.10 and 5.11). The out-of-plane URM walls are neglected in these models. The lumped masses are located at the center of the diaphragm and the top of the shear walls. The structure is displaced due to the lateral seismic ground motion in the E-W and N-S directions, as shown in Figs. 5.10 and 5.11.

The first four mode shapes from the eigenvalue analysis of the building are shown in Fig. 3.23. As discussed in Section 3.4.1, it appears that the flexible diaphragms have considerably smaller stiffnesses compared to the stiffnesses of masonry walls. The diaphragms effectively respond independently of one another. Based on this observation, the structural separation method of the building can be considered. The structural separation (see Figs. 5.10 and 5.11) is based on the one-story subassemblies with single diaphragm. The separate models in Figs. 5.10 and 5.11 are used to calculate their natural periods. The story shear forces of the buildings are calculated at the lumped mass locations on each diaphragm. The natural periods are used to calculate the maximum inertial forces at the center of the diaphragms. The maximum inertial forces at the top of the in-plane walls are calculated from the peak accelerations at the top of the in-plane walls. In this section, these peak accelerations are assumed to be equal to the PGA.

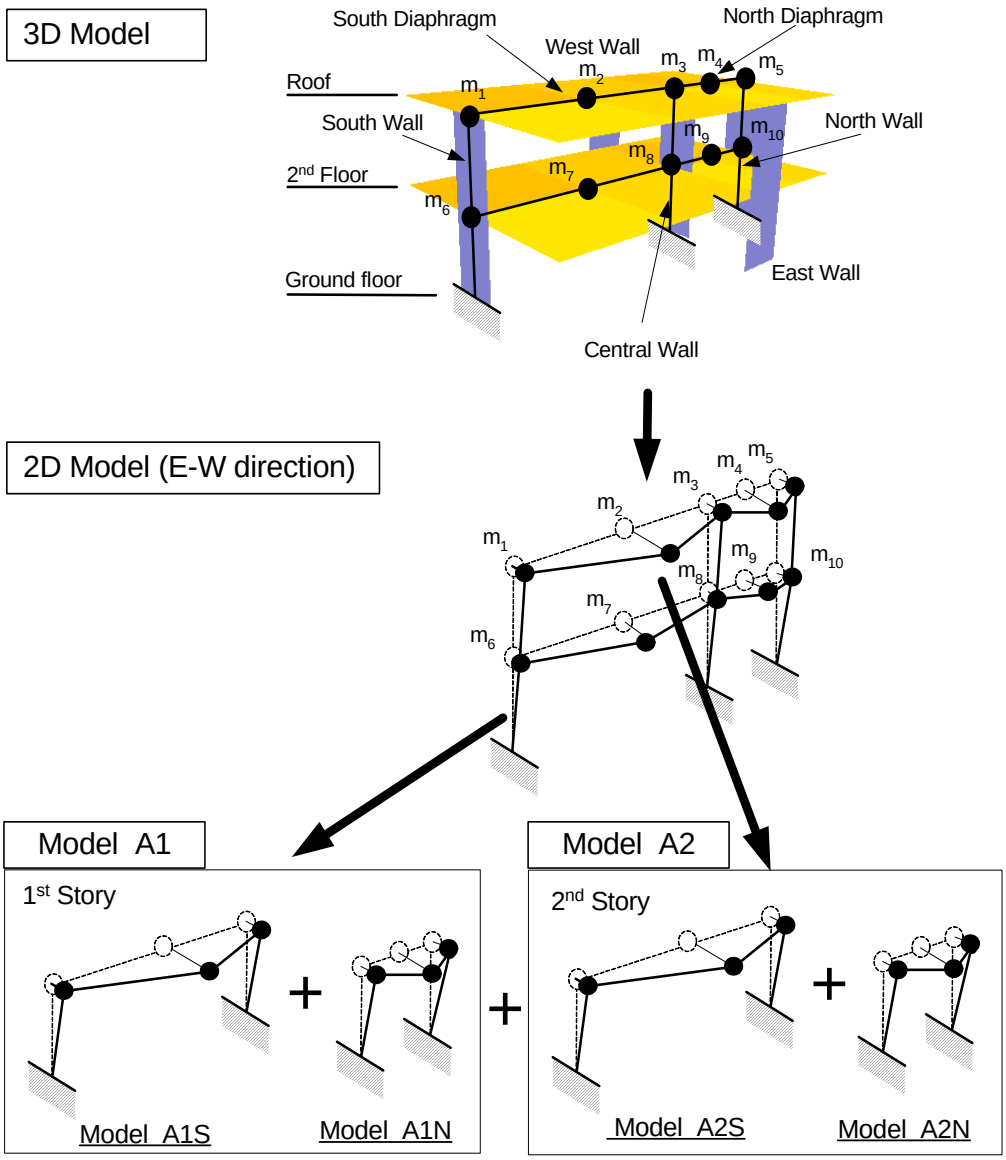

Figure 5.10: Structural separation of the two-story building in the E-W direction.

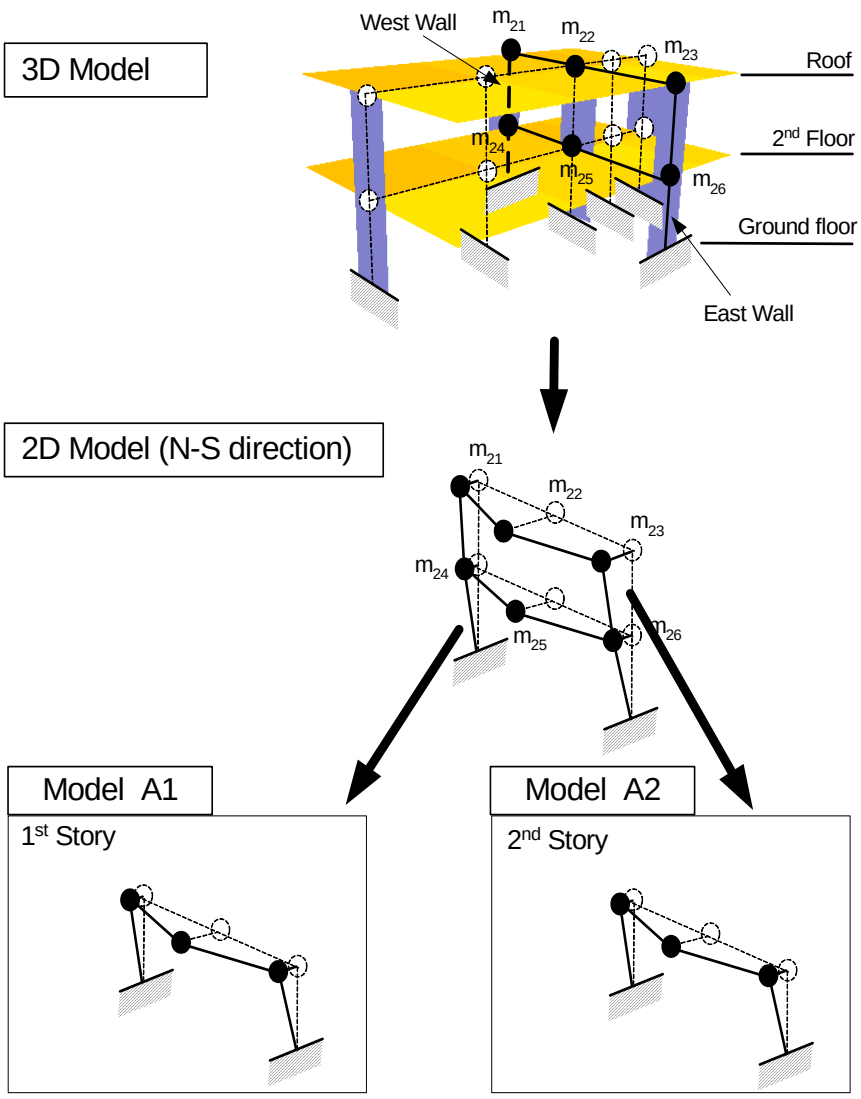

Figure 5.11: Structural separation of the two-story building in the N-S direction.

5.5.1.2 Comparison of linear time history analysis results

The purpose of these comparisons with the results of two-story building model is to assess if the building can be separated into the subassemblies (see Figs. 5.10 and 5.11) at each story level. In order to assess the independent behavior of the multiple flexible diaphragms in the building, time history analyses are performed to obtain the response of the

one-story subassemblies shown in Figs. 5.10 and 5.11. The lumped mass properties shown in Table 3.14 are summarized in Tables 5.3 and 5.4 in accordance with the lumped mass locations in Figs. 5.10 and 5.11. The properties of diaphragm and in-plane shear walls are the same as the two-story three-dimensional model used in Section 3.5. The lateral forces and displacements are calculated from the analysis results of the subassemblies (Models A1 and A2). The total lateral forces and displacements are compared as follows.

Table 5.3: E-W directional lumped mass according to the MDOF system of Gilroy firehouse.

Floor	Location	Mass (lb-sec2/in)	Note
Roof	m_1	280	South wall
	m_2	270	Center of south diaphragm
	m_3	342	Central wall
	m_4	128	Center of north diaphragm
	m_5	203	North wall
2nd	m_6	279	South wall
	m_7	318	Center of south diaphragm
	m_8	339	Central wall
	m_9	144	Center of north diaphragm
	m_{10}	208	North wall

Table 5.4: N-S directional lumped mass according to the MDOF system of Gilroy firehouse.

Floor	Location	Mass (lb-sec2/in)	Note
Roof	m_{21}	417	West wall
	m_{22}	395	Center of diaphragms
	m_{23}	412	East wall
2nd	m_{24}	450	West wall
	m_{25}	435	Center of diaphragms
	m_{26}	403	East wall

Comparison of diaphragm displacements.

The displacement results of the one-story models (A1 and A2) are summarized in Table 5.5. The diaphragm displacement of the separated one-story buildings are compared with those of the two-story building. The diaphragm displacements are calculated using Eq. 2.3 and Fig. 2.6. The E-W directional displacements at the center of the south and north diaphragms match well with the ones of the two-story structure. The E-W directional displacements of the north and south diaphragms in the separated first story structure are 1.151 and 0.092 in, respectively, compared to 1.166 and 0.096 in of two-story building analysis (see Table 5.5). The N-S directional displacements are not changed significantly as well. It is concluded that the flexible diaphragms of the two-story building behave independently.

Table 5.5: Comparison of peak relative diaphragm displacements for the subassemblies (see Fig. 5.10) and the complete two-story building.

Direction	Floor	Location	Diaphragm displacement (in)		
			Model A2	Model A1	Complete MDOF model
E-W	Roof	South	1.123	-	1.142
		North	0.083		0.088
	2nd	South	-	1.151	1.166
		North		0.092	0.096
N-S	Roof	South	0.401	-	0.414
		North	0.401		0.414
	2nd	South	-	0.579	0.598
		North		0.579	0.598

Comparison of in-plane wall lateral forces.

Table 5.6 shows the comparison of the lateral forces of the in-plane masonry walls. The summed in-plane wall lateral forces of the subassemblies match well with those of the second story building. The sum of the south wall lateral force (60 kips) in Model A2 and the lateral force (62 kips) in Model A1 match well with the shear reaction (130 kips) at the south wall of the two-story structure. It is concluded that the in-plane lateral forces of the two-story building can be calculated accurately by summing the in-plane forces calculated from the subassemblies and using the structural separation method.

Table 5.6: Comparison of shear wall displacement and lateral force for the subassemblies (see Fig. 5.10) and the complete two-story building (unit: kips).

Direction	Story	Location	Model A2	Model A1	Reaction forces (A1+A2)	Complete MDOF model
E-W	2nd	South	60	-	-	65
		Central	66			66
		North	30			32
	1st	South	-	62	**122**	**130**
		Central		69	**135**	**135**
		North		31	**61**	**64**
N-S	2nd	East	74	-	-	76
		West	76			76
	1st	East	-	64	**138**	**145**
		West		71	**147**	**149**

5.5.2 Calculations using the simplified linear static procedure

The individual models of Step A in Figs. 5.10 and 5.11 are analyzed to check the lateral forces using the simplified linear static procedure. The results calculated from the subassemblies are compared to those of the linear time history analysis to assess the qualities and limitations of the procedures for low-rise multiple story buildings with multiple flexible diaphragms.

5.5.2.1 Acceleration spectra

The two recorded ground motions in the E-W (U_3) and the N-S direction (U_1) are measured at the base of the two-story building (see Section 3.2). These records are used to derive acceleration spectra for different levels of damping from 2 to 10%. The acceleration spectra, as shown in Figs. 5.12 and 5.15, are calculated using Utility Software for

Earthquake Engineering (USEE Version 0.9.8) developed by Aschheim et al. (1999). The number of steps is 300 from 0.01 to 2 sec concentrating in low period range. Figures 5.12 and 5.14 show the E-W and N-S direction acceleration spectra, respectively. Figures 5.13 and 5.15 show the acceleration spectra in low period range.

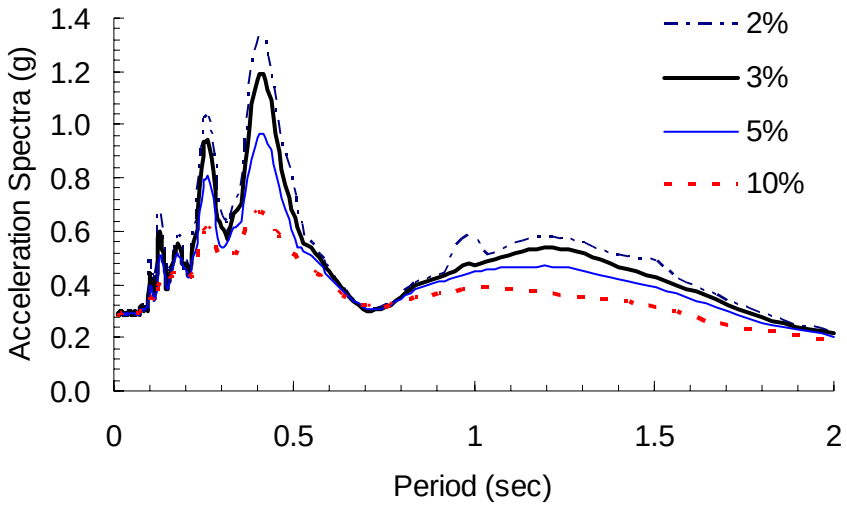

Figure 5.12: Acceleration spectra of recorded E-W directional (U_6) ground motion. (ch3m2a).

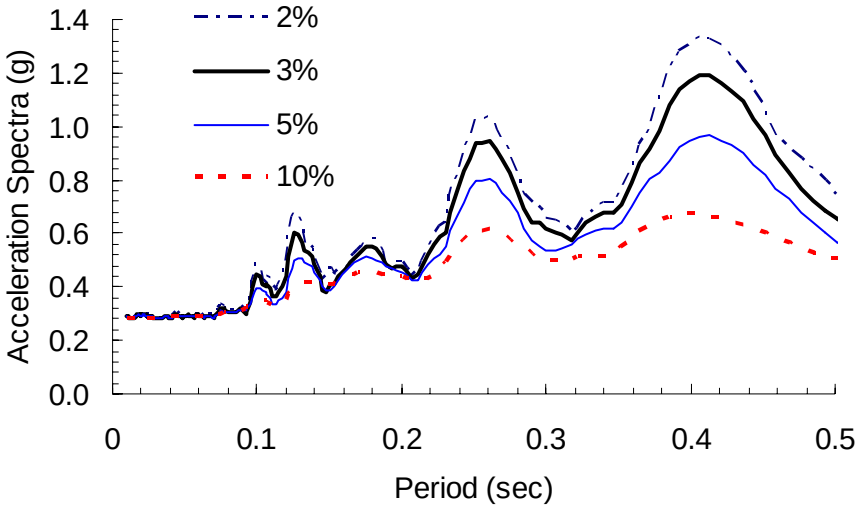

Figure 5.13: Acceleration spectra for the first 0.5 seconds of recorded E-W directional (U_6) ground motion. (ch3m2a).

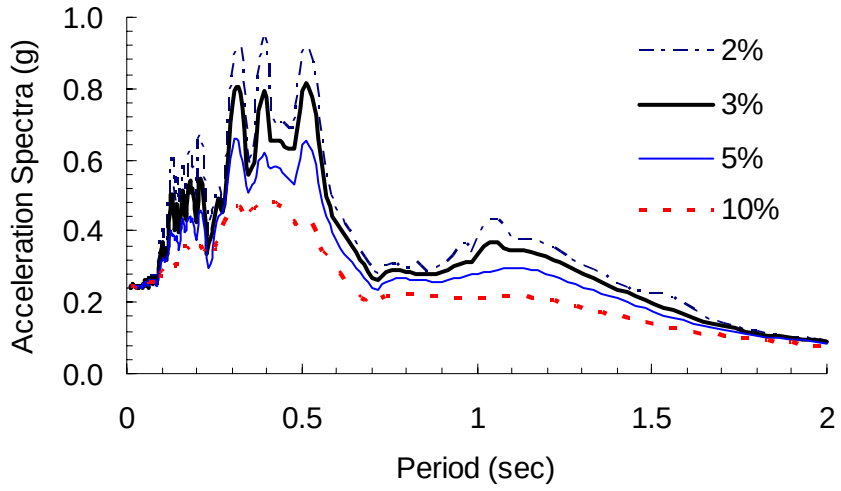

Figure 5.14: Acceleration spectra of recorded N-S directional (U_1) ground motion. (ch1m2a).

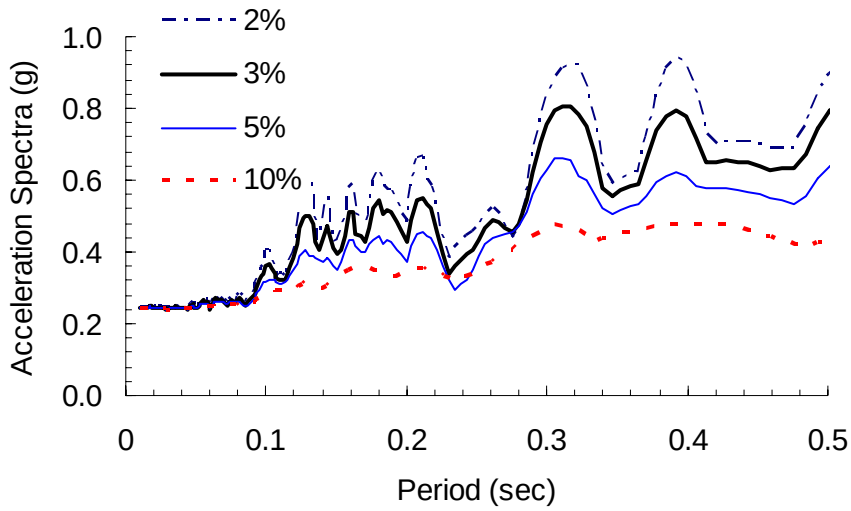

Figure 5.15: Acceleration spectra for the first 0.5 seconds of recorded N-S directional (U_1) ground motion. (ch1m2a).

5.5.2.2 Force calculation

For the assessment of the building in the E-W and N-S direction (see Figs. 5.10 and 5.11), natural periods of the separated subassemblies are calculated. The diaphragm stiffness and the lumped masses at the center of the diaphragms (see Tables 5.7 and 5.8)

are used to calculate the period using the Ritz method. The E-W directional natural periods of the separated structures (A1S, A1N, A2S, and A2N in Fig. 5.10) are summarized in Table 5.7 and the N-S directional natural periods of separated structures (see Fig. 5.11) are summarized in Table 5.8. The stiffnesses of in-plane masonry walls are assumed to be rigid for the approximate period calculation. The natural period (0.412 sec) calculated from the south roof diaphragm subassembly is quite similar to the fundamental period (0.415 sec) of the two-story MDOF model discussed in Chapter III.

The accelerations shown in Tables 5.9 and 5.10 are calculated from the response spectra (see Figs. 5.13 and 5.15) for different levels of damping from 2 to 10%.

Table 5.7: Diaphragm period calculation of structures in the E-W direction.

Story	Model	Mass ($lb\text{-}sec^2/in$)	Stiffness (kips/in)	Period (sec)
1st	A1S	318	70	0.423
	A1N	144	233	0.156
2nd	A2S	270	62.7	0.412
	A2N	128	233	0.147

Table 5.8: Diaphragm period calculation of structures in N-S direction.

Story	Mass ($lb\text{-}sec^2/in$)	Stiffness (kips/in)	Period (sec)
1st	435	136	0.355
2nd	395	176	0.298

Table 5.9: Acceleration obtained from response spectra shown in Fig. 5.13. .

Story	Structure	Period (sec)	Acceleration (g)		
			3% damping	5% damping	10% damping
1st	A1S	0.423	1.132	0.930	0.650
	A1N	0.156	0.455	0.443	0.427
2nd	A2S	0.412	1.188	0.966	0.665
	A2N	0.147	0.412	0.388	0.408

Table 5.10: Acceleration obtained from response spectra shown in Fig. 5.15.

Story	Period (sec)	Acceleration (g)		
		3% damping	5% damping	10% damping
1st	0.355	0.575	0.522	0.455
2nd	0.298	0.755	0.630	0.471

The lateral forces shown in Tables 5.11 and 5.12 are calculated by multiplying the masses by the acceleration at lumped mass locations, (see Figs. 5.10 and 5.11). For simplicity, the in-plane walls are assumed to be rigid and the acceleration at the tops of in-plane masonry walls is assumed to be equal to the measured peak accelerations at these bases. This is reasonable for a simplified procedure in this type of building. The accelerations calculated from this simple assumption do not significantly differ from the measured peak acceleration of the in-plane walls shown in the fourth column of Table 5.11. The acceleration at the top of the south wall (0.319 g) is slightly higher than the measured peak acceleration (0.29 g) in the E-W direction.

The lateral force (80 kips) at the center of the south diaphragm is much larger than that of the in-plane wall lateral forces (31 kips). Half of the lateral force (80 kips) calculated at the center of the south diaphragm is distributed to the south and central shear walls

as shown in Fig. 5.3. Half of the lateral forces calculated at the center of the north diaphragm (24 kips) are distributed to central and north walls. The in-plane wall lateral forces are summarized in the sixth column of Tables 5.11 and 5.12 for the E-W and N-S directional assessment, respectively.

Table 5.11: Calculated lateral forces from the linear static procedure in -E-W direction.

Model	Location	Mass (lb-sec2/in)	Acceleration (g)	Max. inertial loads (kips)	Wall shear forces (kips)
A1	South wall	279	0.290 0.319[a]	31	71
	Center of south diaphragm	318	0.650 0.672[a]	80	-
	Central wall	339	0.290 0.299[a]	38	90
	Center of north diaphragm	144	0.427 0.431[a]	24	-
	North wall	208	0.290 0.293[a]	23	35
A2	South wall	280	0.290 0.345[a]	31	66
	Center of south diaphragm	270	0.665 0.699[a]	69	-
	Central wall	342	0.290 0.312[a]	38	83
	Center of north diaphragm	128	0.408 0.445[a]	20	-
	North wall	203	0.290 0.309[a]	23	33

a. obtained from linear time history analysis of MDOF model.

Table 5.12: Calculated lateral forces from the linear static procedure in N-S direction.

Model	Location	Mass (lb-sec2/in)	Acceleration (g)	Max. inertial loads (kips)	Wall shear forces (kips)
A1	West wall	450	0.240	42	80
	Center of diaphragm	435	0.455	76	-
	East wall	403	0.240	37	76
A2	West wall	417	0.240	39	75
	Center of diaphragm	395	0.471	72	-
	East wall	412	0.240	38	74

5.5.2.3 Comparison of the analysis results of the simplified procedure and linear time history analysis.

In this section, the analysis results calculated from the simplified linear static procedure are compared with the linear time history analysis results discussed in Chapter III. The total lateral forces of the in-plane masonry walls in the E-W direction are compared with the peak lateral forces from the linear time history analysis, as shown in Table 5.13. Figures 5.16 through 5.21 compare the time history of the wall shear forces to the maximum shear force estimates from the simplified procedure. The dots in these figures show the absolute lateral forces distribution in time domain. The lateral force (137 kips) in the first story south wall (see the fourth column of Table 5.13) is the sum of the second story (66 kips) and the first story lateral forces (71 kips) (see Table 5.11). The lateral force distribution of the south wall is plotted in Fig. 5.16. The lateral forces of south and north walls show good results; however, the central wall lateral force (173 kips) is overestimated compared to that (135 kips) from the linear time history analysis (see Table 5.11 and Fig.

5.22).

The total lateral forces of the in-plane walls in the N-S direction are compared in Table 5.14. Figures 5.23 to 5.26 compare the in-plane lateral forces of the simplified linear static procedure and the shear force histories from the linear time history analyses. The lateral forces in the east and west walls match well with those of linear time history analysis (see Fig. 5.27 and Table 5.14). The lateral forces of the east and west walls (140 and 144 kips, respectively) are compared with those of the time history analysis (150 and 154 kips, respectively).

Table 5.13: Comparison of in-plane wall lateral forces in the E-W direction.

Story	Wall (Position)	Lateral forces (kips)	
		Linear time history analysis[a]	Linear static procedure[b]
2nd	South (1)	65	66
	Central (2)	66	83
	North (3)	32	33
1st	South (1)	130	137
	Central (2)	135	173
	North (3)	64	68

a. The peak lateral forces are obtained from the linear time history analysis of the two-story MDOF model discussed in Chapter III.
b. Combined total lateral forces of walls calculated from Table 5.11, assuming that each diaphragm structure moves separately.

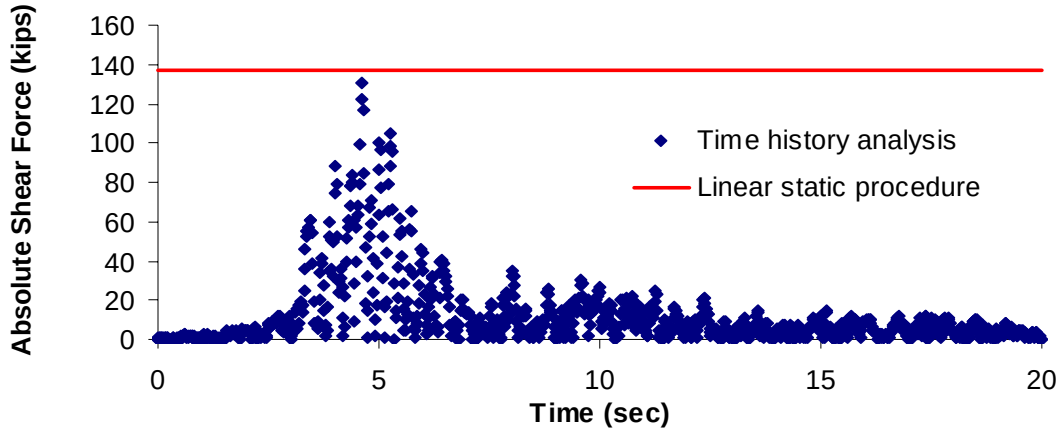

Figure 5.16: Comparison of lateral force of south shear wall at first story.

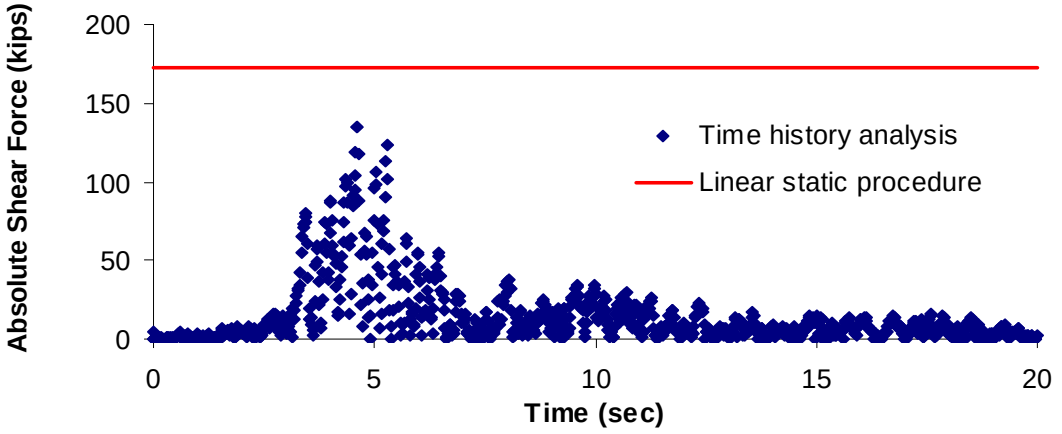

Figure 5.17: Comparison of lateral force of central shear wall at first story.

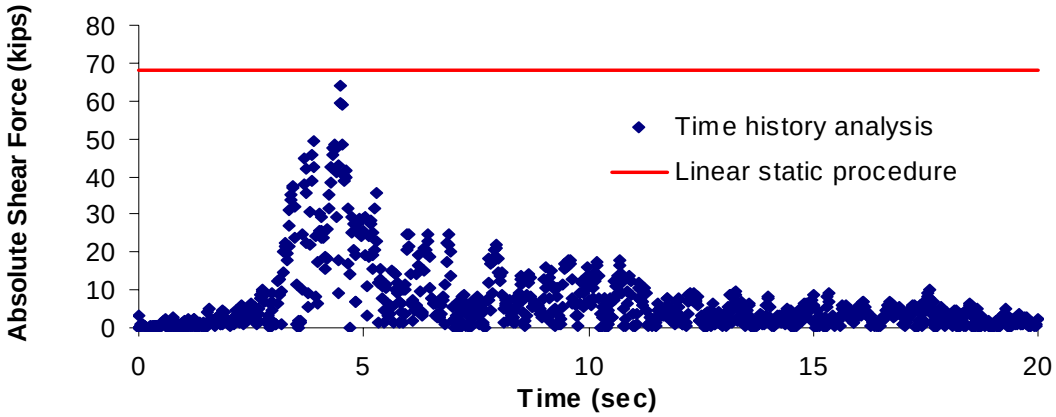

Figure 5.18: Comparison of lateral force of north shear wall at first story.

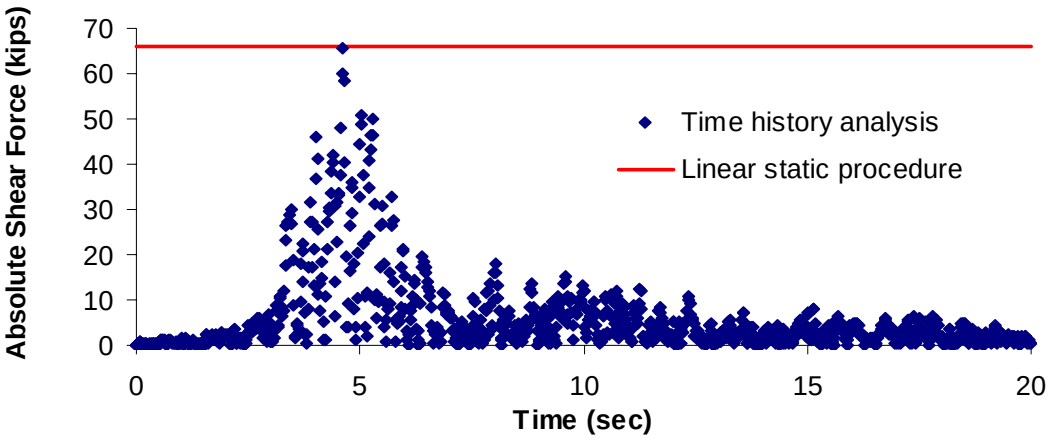

Figure 5.19: Comparison of lateral force of south shear wall at second story.

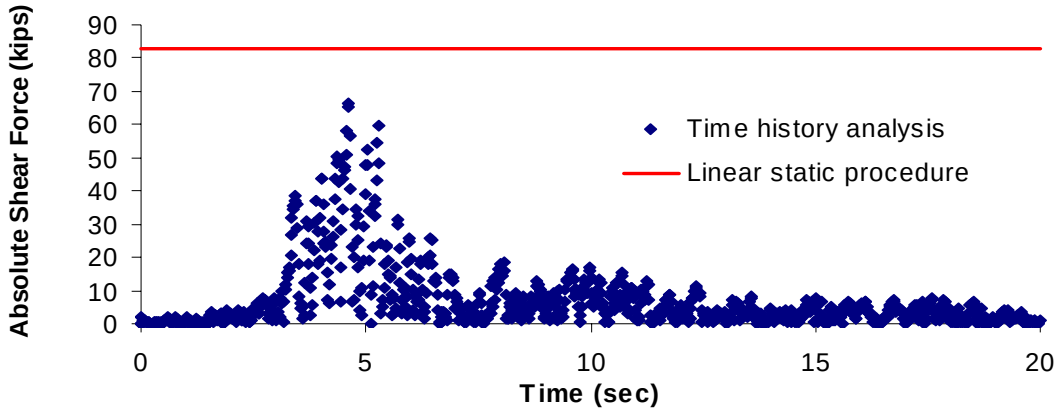

Figure 5.20: Comparison of lateral force of central shear wall at second story.

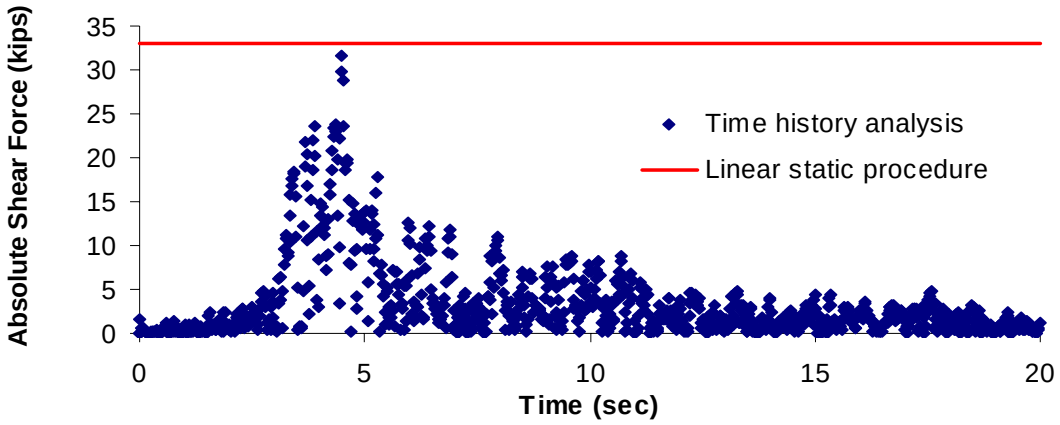

Figure 5.21: Comparison of lateral force of north shear wall at second story.

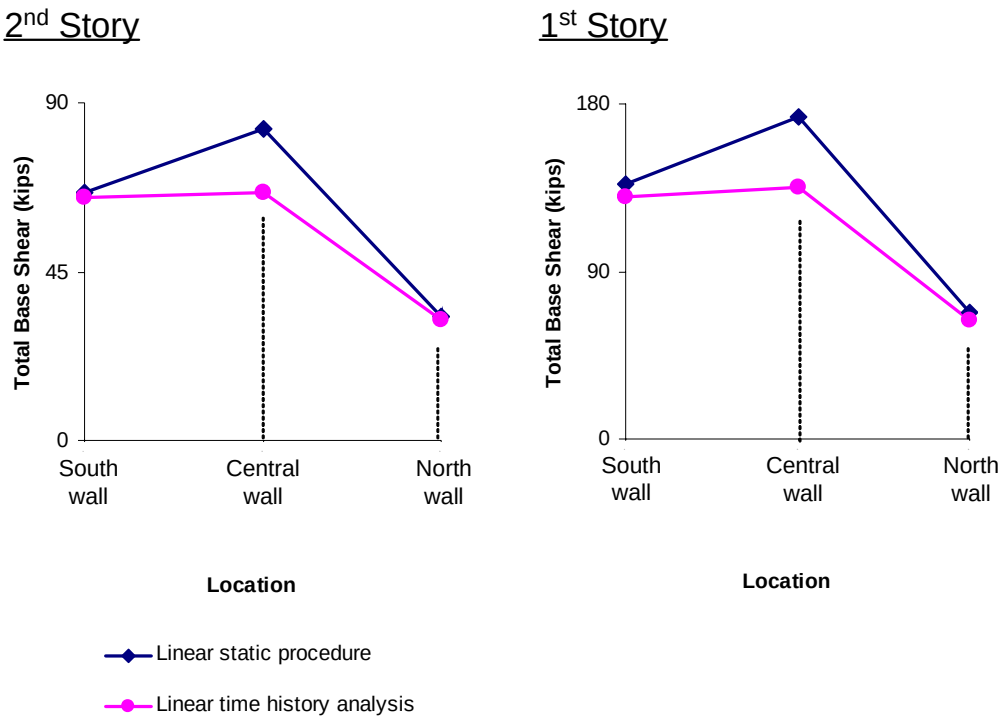

Figure 5.22: Comparison of lateral forces in the E-W direction.

Table 5.14: Comparison of in-plane wall lateral forces in N-S direction.

Story	Wall (Position)	Lateral forces (kips)	
		Linear time history analysis[a]	Linear static procedure[b]
2nd	East	76	74
	West	77	76
1st	East	140	150
	West	144	154

a. The lateral forces are obtained from linear time history analysis of two-story MDOF model.
b. Combined total base lateral forces of walls calculated from Table 5.11, assuming that each diaphragm structure moves separately.

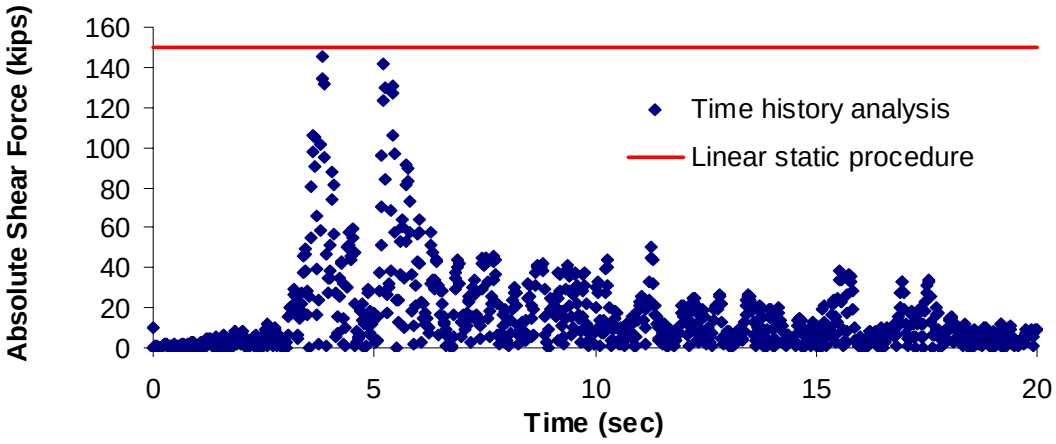

Figure 5.23: Comparison of lateral force of east shear wall at first story.

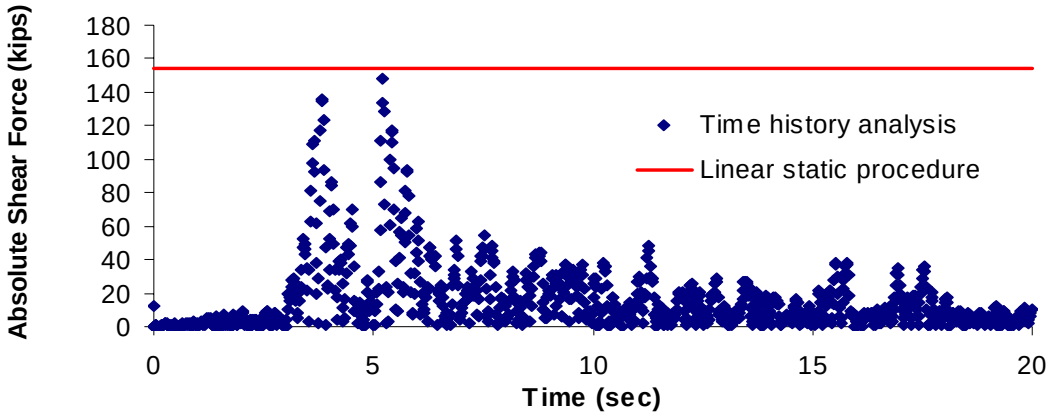

Figure 5.24: Comparison of lateral force of west shear wall at first story.

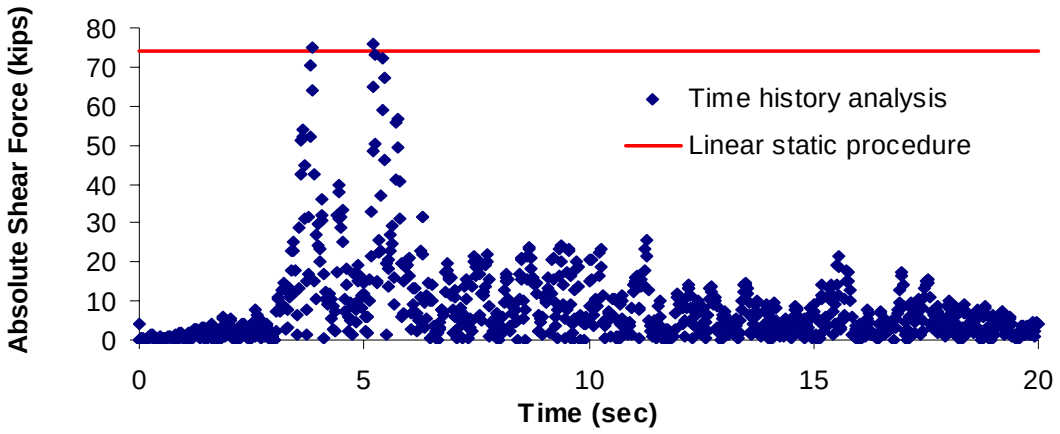

Figure 5.25: Comparison of lateral force of east shear wall at second story.

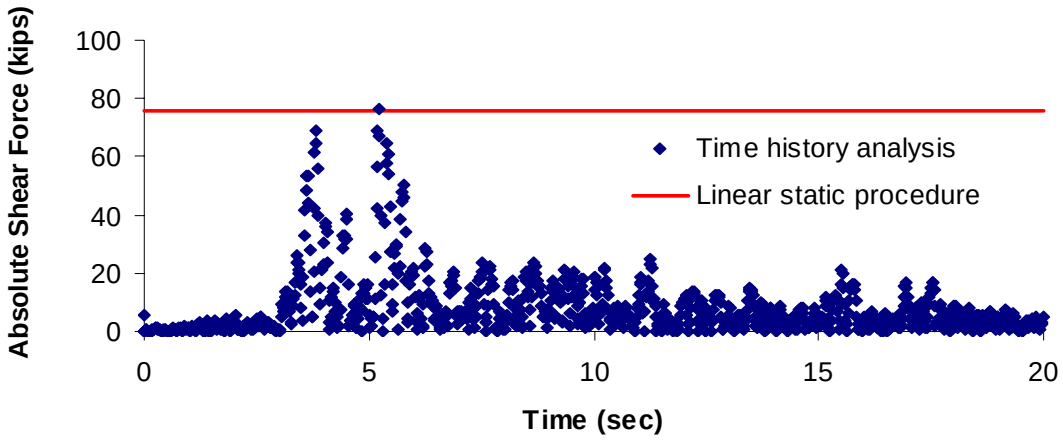

Figure 5.26: Comparison of lateral force of west shear wall at second story.

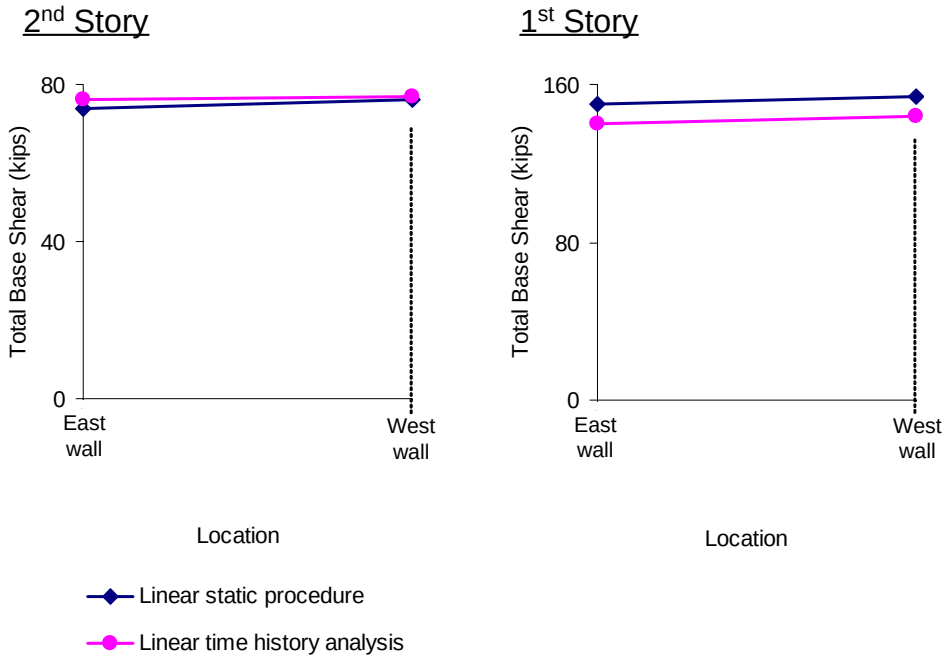

Figure 5.27: Comparison of lateral forces in N-S direction.

Tables 5.15 and 5.16 compare the displacements calculated from the simplified linear static procedure and linear time history analysis. The element displacements are calculated from dividing lateral forces shown in Tables 5.11 and 5.13 by the stiffnesses shown in Table 5.15. The displacement of the second story central wall (0.55 in) is overestimated as much as 20% compared to that of linear time history analysis (0.044 in). The lateral force of the central wall (173 kips) is overestimated as much as 28 % compared to that of linear time history analysis (135 kips) (see Table 5.13). However, the overall responses match well with those of time history analysis in the E-W and N-S directions.

Table 5.15: Comparison of displacement in the E-W direction.

Story	Location	Stiffness (kips/in)	Simplified linear static procedure		Linear time history analysis[c] (in)
			Element displacement[a] (in)	Nodal displacement[b] (in)	
2nd	South wall	1,654	0.040	0.108	0.103
	Center of south diaphragm	63	1.105	1.136	1.218
	Central wall	3,739	0.022	0.055	0.044
	Center of north diaphragm	233	0.086	0.105	0.110
	North wall	2,170	0.015	0.025	0.023
1st	South wall	2,008	0.068	0.068	0.064
	Center of south diaphragm	70	1.140	1.190	1.216
	Central wall	5,263	0.033	0.033	0.026
	Center of north diaphragm	233	0.102	0.123	0.104
	North wall	7,005	0.010	0.010	0.009

a. displacement obtained from the separated structure assuming that each structural components move separately.
b. displacement at the top of walls and the center of diaphragms of the two-story building.
c. displacement obtained from linear time history analysis of two-story MDOF model.

Table 5.16: Comparison of displacement in N-S direction.

Story	Location	Stiffness (kips/in)	Simplified linear static procedure		Linear time history analysis[c] (in)
			Element displacement[a] (in)	Nodal displacement[b] (in)	
2nd	East wall	1,835	0.021	0.060	0.078
	Center of diaphragm	176	0.408	0.425	0.453
	West wall	6,038	0.012	0.028	0.027
1st	East wall	3,820	0.039	0.039	0.036
	Center of diaphragm	136	0.562	0.589	0.613
	West wall	9,806	0.016	0.016	0.015

a. displacement obtained from the separated structure assuming that each structural components move separately.
b. displacement at the top of walls and the center of diaphragms of the two-story building.
c. displacement obtained from linear time history analysis of two-story MDOF model.

5.6 Implications for General Seismic Assessment

The above analysis solutions are all based on linear elastic response. However, for general seismic assessment, the influence of potential nonlinear structural actions must be considered. Based on the above analysis results, it is apparent that the out-of-plane walls are typically damaged at an early stage due to the relatively large out-of-plane displacements associated with the flexible diaphragms. The authors are not aware of any research that has investigated the in-plane hysteretic response of wall components that are simultaneously subjected to out-of-plane damage. Given this lack of knowledge about the wall responses, it may be wise to consider in-plane unreinforced masonry walls as force-controlled components, while handling the potentially significant out-of-plane hysteretic

response as a deformation-controlled problem. In the context of this philosophy, the application of the structural separation method is relatively straightforward. The out-of-plane walls can be handled using equivalent linear properties based on their expected response.

Alternatively, the effects of inelasticity might be incorporated in the calculation of the lateral forces within the structural separation method, step 5 of Fig. 5.1, by using the FEMA 356 pseudo lateral load equation in each of the subassemblies, that is Eq. (3-10) of FEMA 356. In this case, appropriate modification factors C_1, C_2, C_3 and C_m must be determined. Further research is necessary to determine precisely what values should be used for these coefficients in flexible diaphragm structures.

However, if one of in-plane walls in a story (e.g., one of the walls in the two story building discussed in this paper) is damaged, the force distribution within the structural system will tend to be significantly changed from that of the elastic model. For example, if the south wall of the two-story building is severely damaged due to in-plane wall action, a larger fraction of the south wall shear force is taken by the east, west, and central walls, and a small fraction of the force is taken by the north wall due to the flexible diaphragm (via shear raking within the south diaphragm and overall torsion of the structure). If the central wall (interior wall) is severely damaged, a larger fraction of the central wall shear is taken by all exterior walls. In these cases, the force or displacement calculation of the walls and diaphragms can not be considered by using the simplified procedure discussed in this chapter. In order to investigate such an extensively damaged structure, a nonlinear dynamic analysis using the 3D MDOF model of Chapter II is recommended. The gravity load within the structure must be included in this MDOF model.

5.7 Summary and Conclusion

A simplified linear static procedure for structures with flexible diaphragms, termed the structural separation method is studied. Acceleration spectra calculated from the

recorded ground motions are used to determine the accelerations at the lumped mass locations. The natural periods of the diaphragms are obtained from the subassemblies assuming rigid in-plane walls. The spectral accelerations at the tops of the in-plane walls are calculated based on either of two idealizations as appropriate. The first idealization uses a separate analysis model of each of the in-plane walls, including the mass from the walls as well as that from an assumed tributary area of the diaphragms. The second idealization is that the accelerations at the tops of the in-plane walls are equal to those at the base, based on the assumption that the in-plane walls are rigid. The second idealization can be applied to the in-plane walls in many shear wall structures with flexible diaphragms.

The wall lateral forces are obtained by summing the maximum values obtained from the separate diaphragm subassemblies with those obtained from one of the two idealizations of the in-plane walls. The calculated lateral forces match well with those of time history analysis results. The following general conclusions can be made from this study.

- Low-rise shear wall buildings with nonrigid diaphragms do not behave as SDOF systems. These types of buildings must be assessed as MDOF structures explicitly considering the in-plane and out-of-plane walls associated with the nonrigid diaphragms.
- The proposed simplified procedure can accurately and simply investigate the response of buildings with flexible diaphragm including the out-of-plane wall stiffness and mass. This method is predicated on the judgment that, due to the fact that wall damage in the out-of-plane directions is likely to occur first and is not easily prevented by retrofit measures, damage in the in-plane wall directions generally should be limited. The walls should be investigated as force-controlled elements in their in-plane directions and as deformation-controlled elements in their out-of-plane directions.

CHAPTER VI

SUMMARY AND RECOMMENDATIONS

6.1 Summary

This research provides information on the seismic assessment of low-rise buildings with nonrigid diaphragms. These types of buildings generally do not behave as SDOF systems. The multiple-mode effects associated with bending of the separate diaphragms along with their associated out-of-plane walls must be considered directly in some fashion in order to improve methods of seismic assessment for these types of structures. In this research, a simplified linear or non-linear three-dimensional MDOF analysis approach is developed for these types of buildings. This analysis tool is applied in two time history analysis case studies. The accuracy and validity of this approach is evaluated by comparing the analysis predictions to recorded data. The proposed MDOF approach provides reasonable predictions of the behavior. Also, a simplified linear static procedure is proposed for use in the seismic assessment of flexible diaphragm shear wall structures. The results of the procedure are compared to the results from linear time history analysis using the best models determined from the above two case studies.

Diaphragm and wall elements are developed for the proposed three-dimensional modeling approach. The diaphragm element consists of six DOFs. It is assumed that the bending behavior of nonrigid diaphragms is similar to that of a horizontal plate girder. In addition to the diaphragm bending response, this element also represents the actions of the diaphragms as shear panels that provide torsional coupling between the walls within the structural system. The diaphragm element stiffness matrix is derived from a flexibility

approach based on three independent deformational modes (two bending modes and a shear raking mode) in two horizontal directions.

Consistent with the basic diaphragm model in FEMA 356, it is suggested that in many cases the chord deformations of the diaphragms are small relative to the overall diaphragm shear deformations. An equivalent shear model is used to define the properties of various types of horizontal wood and metal deck diaphragms. A general hysteresis model is proposed that accounts for stiffness degradation, strength deterioration and pinching characteristics in diaphragms.

The elastic in-plane wall element stiffnesses for the MDOF approach are obtained either using a flexibility method along with the results of detailed plane stress FEA of the walls, or using basic mechanics of materials equations. It is shown that the strength of materials type stiffness predictions for general perforated walls are often significantly different than the more rigorous predictions using plane stress FEA solutions. The piers of perforated walls are modeled using parallel springs to track the post-elastic response of the different wall components in detail. The wall hysteresis models incorporate the effects of pier rocking, bed-joint sliding, toe crushing and diagonal tension failure.

The three-dimensional MDOF model is used to study a two-story unreinforced masonry historic building that survived the Loma Prieta earthquake as well as a half-scale one-story single-diaphragm reinforced masonry shear wall building subjected to a suite of ground motions on the shaking table. The two-story building, originally investigated by Tena-Colunga and Abrams (1992a), is studied to demonstrate the use of the suggested three-dimensional MDOF approach, to investigate its qualities and limitations, and to investigate why this building withstood the ground shaking during the Loma Prieta earthquake with little damage. The three-dimensional inelastic response of the building is studied by simultaneously applying the two horizontal ground motions measured in orthogonal directions at the level of the floor slab. It is observed that the wood diaphragm stiffnesses are much smaller than those of the in-plane shear walls, and that the seismic

response of the overall structure is dominated by the separate responses of its flexible diaphragms. Each of the flexible diaphragms moves largely in an independent fashion due to the relative rigidity of the in-plane walls. Sensitivity studies are conducted to investigate the influence of variations in the flexible diaphragm stiffness. The out-of-plane wall displacements are reduced significantly due to increases in the diaphragm stiffnesses, but the in-plane wall forces are affected little by these changes.

A half-scale shaking table test building originally studied by Cohen (2001) is subjected to a suite of ground motions taken from the shaking table tests. This building was one story and had a single diaphragm. The elastic and inelastic responses of the test building are analyzed and compared with the experimental results. A calibration process is performed to predict the structural properties of the out-of-plane and in-plane walls based on the results of the shaking table tests. Sensitivity analyses are performed to determine the influence of the nonrigid diaphragm, the in-plane walls and the out-of-plane walls. The dynamic behavior of the out-of-plane wall and flexible diaphragm are predicted well when the proposed MDOF approach is used and the diaphragm and wall properties are appropriately calibrated. It is found that the strength and stiffness of the out-of-plane walls are the key factors in addition to the strength and stiffness of the diaphragm to limit the drift at the middle of the building's diaphragm. However, the increases in the diaphragm stiffness led to increased in-plane wall shear forces, while decreasing the out-of-plane wall forces.

A simplified linear static procedure using an approach referred to as the structural separation method is applied for the two buildings discussed above. It is found that this procedure gives reasonably accurate solutions relative to the results from time history analyses using the three-dimensional MDOF procedure and the best models determined from Chapters III and IV.

6.2 Recommendations

The recommendations from this research are as follows.

6.2.1 Approximate period calculation for structures with flexible diaphragms

The approximate period formulas (Eqs. 5.1 and 5.2 in Section 5.3.1) recommended in FEMA 356 may be used to estimate the period of one-bay single-story diaphragm structures. However, in general both the out-of-plane wall masses as well as the out-of-plane wall stiffnesses must be considered when applying these equations. These equations are valid to calculate the acceleration and lateral force at the center of single flexible diaphragms. The accelerations at the tops of the in-plane walls are generally smaller than those at the center of the diaphragms, and therefore the period discussed above should not be used to calculate the acceleration at the tops of the in-plane walls.

For more general flexible diaphragm structures involving multiple bays and/or multiple stories, a more general approach is needed for calculation of the periods. The diaphragms within typical masonry shear wall buildings are so flexible compared to the in-plane walls that their periods should be calculated from separate isolated subassembly models of the individual diaphragms along with the assumption of rigid or flexible in-plane walls. This aspect is discussed further in Section 6.2.2.

Use of the fundamental period within the each diaphragm structures determined from Eqs. 5.1 and 5.2 to calculate the lateral in-plane wall forces, as suggested in FEMA 356, generally will lead to an overconservative design. If the in-plane walls are assumed to be rigid when the walls are sufficiently stocky, the period of the diaphragm depends only on the diaphragm and out-of-plane wall stiffnesses and the mass calculated from the tributary wall and diaphragm areas. Also, the accelerations at the tops of the walls are equal to the wall base accelerations in this case. If the in-plane walls are flexible, the periods at the tops of the in-plane walls may be calculated by analyzing each of the individual walls as an isolated subassembly, including the wall masses and the masses from the adja-

cent diaphragms based on simple tributary area concepts.

FEMA 356 does not discuss the inclusion of the out-of-plane wall stiffnesses in Eqs. 5.1 and 5.2, and in fact implies in one of its figures that the out-of-plane wall stiffnesses are neglected. In general, the stiffness of the out-of-plane walls significantly affect the displacements at the center of the diaphragms. When the out-of-plane wall stiffnesses are not considered, the period of the structure is much larger than when these stiffnesses are included. For a structure with a nonrigid diaphragm, a decrease in the out-of-plane wall stiffness results in an increase in the period and an increase in the in-plane wall base shear. All of the computational results discussed in this research indicate this. Therefore, if Eqs. 5.1 and 5.2 are employed, the out-of-plane wall stiffness contributions should be considered in general in addition to the contributions from the out-of-plane wall masses.

Equation 5.3 can be used to calculate the natural period of the diaphragm based on the diaphragm and out-of-plane wall stiffnesses and the lumped mass calculated from the tributary wall and diaphragm areas at the diaphragm mid-span.

6.2.2 Recommended linear static procedure for low-rise buildings with flexible diaphragms

FEMA 357 states that flexible wood diaphragms in shear wall buildings might need special treatment (Global Issues 3-8 in FEMA 357, ASCE 2000b). In this research, it is confirmed that low-rise buildings with nonrigid diaphragms do not behave as SDOF systems. These types of buildings must be considered as MDOF structures. The suggested pseudo lateral-load procedure in FEMA 356 may not be applied to these types of buildings because this linear static analysis procedure is associated with rigid diaphragm structures and the suggested period equation in these guidelines should be defined as discussed in the previous section. The performance of these types of buildings can be assessed in terms of specific component distortions calculated using the MDOF modeling approach, or using

the structural separation method. The multiple mode effect of multi-story buildings with flexible diaphragms can be considered using individual separated subassemblies at each diaphragm location using the structural separation method as discussed in the next section.

6.2.3 Recommended linear and nonlinear dynamic procedure for low-rise buildings with nonrigid diaphragms in FEMA 356

The behavior of individual components such as in-plane, out-of-plane walls, wall anchorages, and nonrigid diaphragms depends on the overall system behavior. Particularly, URM buildings with nonrigid diaphragm have unique deformation modes as illustrated in Fig. 1.1. FEMA 356 suggests that linear and nonlinear time history methods may be used for evaluation of complex structures. However, specific guidelines for the linear dynamic procedure (LDP) and non-linear dynamic procedure (NDP) are not included in these standards. Refined finite element approaches are too expensive, as discussed Section 1.2.1. The proposed MDOF approach discussed in Chapter II can be practical for these analysis procedures. It can capture the linear and non-linear behavior of the key modes of low-rise buildings with nonrigid diaphragms. However, it must be acknowledged that the direct use of three-dimensional linear and nonlinear time history analyses requires a significantly greater effort on the part of the engineer to establish additional required information such as a suite of site-specific ground motion records as well as additional reliable calculations of detailed structural properties.

6.2.4 Recommendations for calculation of diaphragm model properties in FEMA 356

In Section 2.3.5.2, the diaphragm stiffnesses were discussed in accordance with FEMA 356. The suggested equation and stiffness values in the FEMA documents may not be appropriate to estimate the deflections in a wide variety of diaphragm types.

Peralta et al. (2001) reports recent test results for several representative wood floor

diaphragms. The tests showed that FEMA 356 tended to underpredict stiffness and overpredict yield displacement and deformation levels. The FEMA 356 equation (Eq. 2.52) is believed to provide the best estimate of the stiffness for diaphragms with aspect ratios less than about three. The engineer should be cautioned about the use of Eq. 2.52 particularly for diaphragms with aspect ratios larger than about three. For diaphragms with larger aspect ratios, Eq. 2.52 may overpredict the diaphragm stiffness.

When the diaphragm stiffness is overestimated in the analysis model of a structure, a larger fraction of the base shear is taken by the in-plane walls. Thus, the design of the in-plane walls will be more conservative and the out-of-plane wall responses will be underestimated. The design of the in-plane walls will be more conservative if the stiffness of the out-of-plane wall is underestimated or not considered in the analysis model. However, in order to prevent the damage to out-of-plane walls, it is more conservative if the flexible diaphragm stiffness is underestimated.

6.2.5 Out-of-plane wall limitation of shear walls with nonrigid diaphragms

Out-of-plane walls are affected by the out-of-plane bending associated with the diaphragm deformations as well as the displacements of the in-plane walls. The damage to out-of-plane walls may happen at the early stage of seismic response. In general, it is apparent that the out-of-plane walls can contribute substantial stiffnesses associated with the diaphragm bending deflections. Since this damage is likely influenced significantly by the flexibility of diaphragm, the behavior of out-of-plane wall is difficult to predict.

Consideration of the out-of-plane wall contributions may be merited at least for low to possibly moderate earthquake excitations. If the out-of-plane wall drifts are larger than some limit, the current FEMA 356 approach of neglecting out-of-plane URM wall stiffnesses altogether may be merited. However, when the out-of-plane stiffness is neglected for practical reasons, the lateral forces within in-plane walls and the displace-

ment at the center of the diaphragms are overestimated. The out-of-plane stiffness of masonry walls should not be neglected in nonlinear dynamic models in the orthogonal direction (ASCE 2000). FEMA 356 also does not provide out-of-plane deformation limits, such as in collapse prevention or immediate occupancy limits, for the acceptable performance of various types of walls. Based on the results of this research, it is apparent that the assessment of reinforced masonry out-of-plane walls as force-controlled elements will often be prohibitive, since the out-of-plane wall may often be damaged well before significant damage to the in-plane walls, and also these walls have a large amount of deformation capacity. Issues which need to be considered in establishing these limits must include the potential effects of combined in-plane and out-of-plane lateral and vertical seismic excitation of the wall elements. The tests by Peralta et al. (2001) and others indicate that wood floor diaphragms may be able to sustain extensive deformations themselves, at least for a small number of cycles, without substantial loss in resistance.

6.3 Future Research

In this section the needs for further research to better understand the general multi-story buildings with flexible diaphragms and to improve the present building codes are discussed. Potential future studies include the following:

- The strength of each pier of perforated walls can be categorized according to the pier-type collapse mechanism in FEMA 356, but, the strength calculation based on the multiple-story type collapse mechanism of masonry shear walls has not been corroborated by experimental test. The interaction between the out-of-plane and in-plane walls within buildings with nonrigid diaphragms has not been studied. Further research should address the need to predict the combined stiffness and strength of in-plane and out-of-plane walls and the effective flange length provided by the out-of-plane walls within shear wall buildings

with nonrigid diaphragms.

- In order to predict the detailed behavior of unreinforced out-of-plane walls, the stability of the out-of plane walls should be studied using non-linear time history analysis.
- The response of masonry structural components subjected to combined in-plane and out-of-plane excitation is required for improved assessment of buildings with flexible diaphragms. As discussed in the previous section, out-of-plane wall damage may happen at the early stage of seismic response. This damage is associated with the diaphragm flexibility as well as the in-plane wall responses. When buildings are excited also in the orthogonal direction to the out-of-plane walls, the effect of this motion on the combined in-plane actions may be significant.
- The mechanisms of force transmission between the walls and floor diaphragms through anchorages, etc. needs to be better understood. Generally, both shear and axial forces need to be transmitted between these components. Anchorages need to be designed to support these forces.
- Non-proportional damping is used to approximate the damping properties for linear and non-linear dynamic analysis of the buildings studied in this research. However, Rayleigh damping is based on a linear combination of a fraction of the mass and stiffness matrices. An improved damping model is needed to represent the effects of the associated nonlinear actions. There is little information pertaining to the damping properties of low-rise shear wall buildings with flexible diaphragms at the present time, particularly for levels of excitation causing significant damage. A combined viscous and non-viscous damping model may give improved results for these types of building. Specific damping models should be developed for linear and nonlinear dynamic analysis.

APPENDICES

APPENDIX A

THREE-PARAMETER MODEL

The hysteretic model (Three parameter model) that has been developed for use in ABAQUS user subroutine is illustrated. A variety of hysteretic properties are obtained through the combination of the trilinear skeleton curve and the three parameters 'α', 'β' and 'γ'. The challenge in using the three-parameter model lies in the physical identification of its three parameter. The actual hysteretic responses of reinforced concrete element and unreinforced masonry element are uncertain. The values of these parameters determine the properties of stiffness degradation, strength deterioration and pinching behavior, respectively. Most of the controlled parameters are determined empirically. The required data was determined through experimental analyses of different reinforced concrete components under a variety of cyclic loads. When the parameters assume program defaults values, i.e. $\alpha \to \infty$, $\beta = 0$ and $\gamma \to \infty$, a hysteretic property similar to the Clough model is obtained. The hysteretic model is quite similar to the Takeda model, except for strength deterioration, and may be exclusively used for the flexural strings of various components.

A.1 α Parameter

This parameter, as shown in Fig. A.1, controls the amount of stiffness reduction. The stiffness degradation is introduced by setting a common point on the extrapolated initial skeleton curve line. The unloading path targets this common target point until they

reach the horizontal deformation x-axis. More importantly, the area enclosed by the hysteresis loops clarifies how the parameter changes the hysteresis loops. The instantaneous element stiffness drops accordingly compared to its original elastic stiffness.

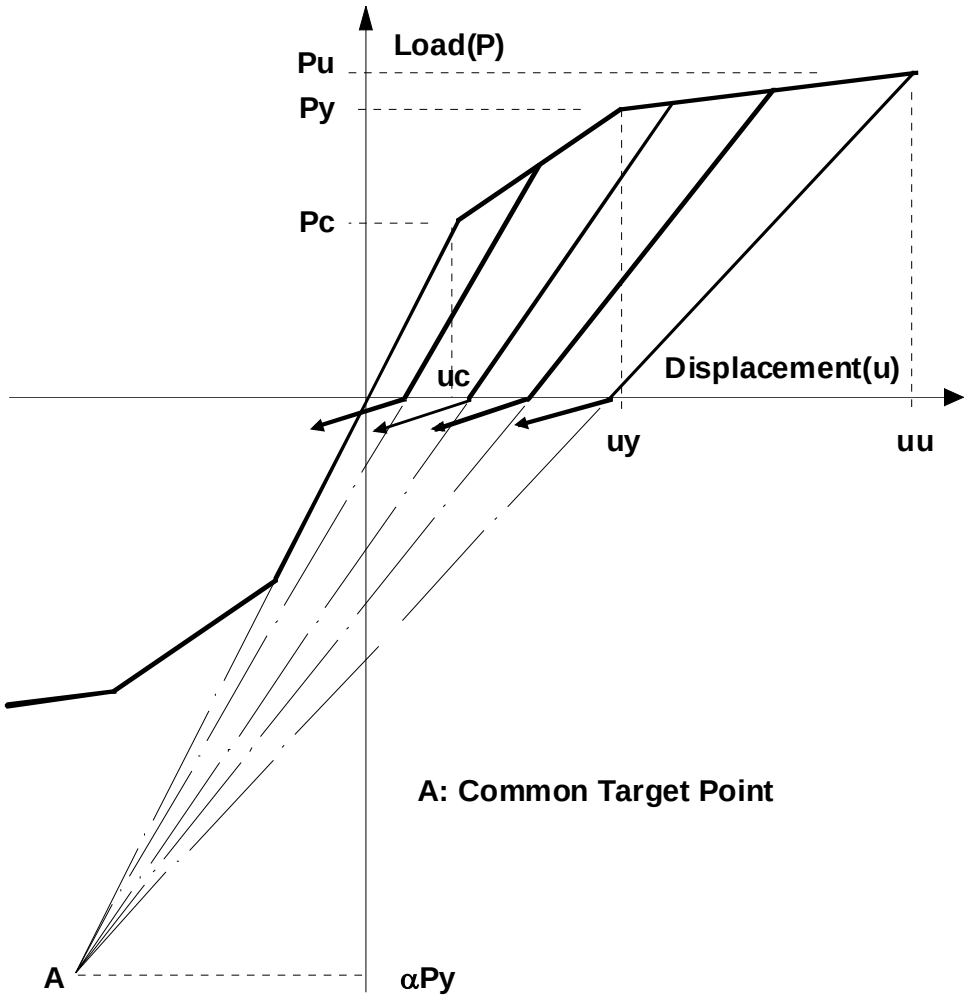

Figure A.1: α Parameter.

A.2 β Parameter

This parameter, as shown in Fig. A.2, specifies the rate of strength degradation. Strength deterioration does not allow the element to regain its full load capacity under repetitive loads. It also controls the amount of energy dissipated in the hysteretic cycles

and used in the damage computation of the structure components. The same parameter ‘β’ may be found in the definition of the damage index .D. which defines the earthquake structural damage as a linear combination of the maximum deformation ‘δ_m’ and the absorbed hysteretic energy as shown Fig. A.2.

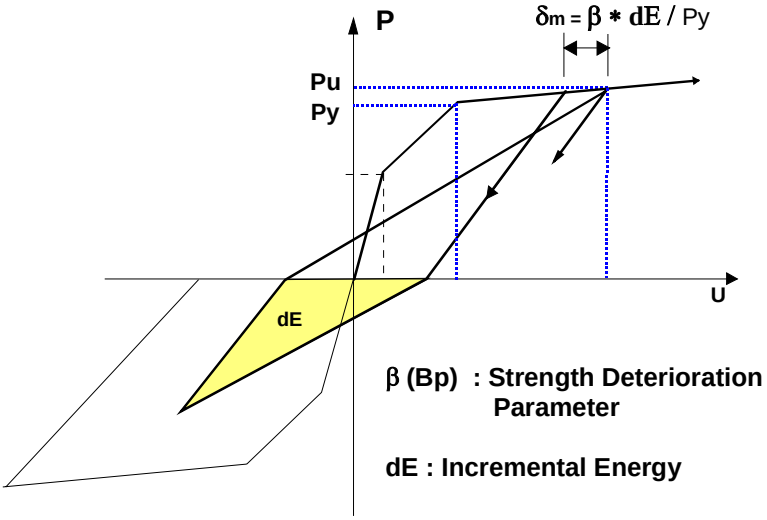

Figure A.2: Parameter.

A.3 γ Parameter

The pinching behavior, as shown in Fig. A.3, arises due to the shear crack closing mechanism during cyclic and reversal loading. It is introduced by lowering the target maximum point to a straight level of ‘γP_y’ along the previous unloading line. After cracking occurs, an element experience a low level of instantaneous stiffness until its deformation reaches the crack closing point. Reloading points aim this new target point “C” until they reach the crack closing deformation. The stiffness of reloading paths is changed at this point to aim the previous target maximum point ‘B’. The introduction of such a pinching behavior also leads to a reduction of hysteresis loop areas and indirectly, the amount of dissipated energy. The pinching behavior is common in shear walls and unreinforced

masonry walls.

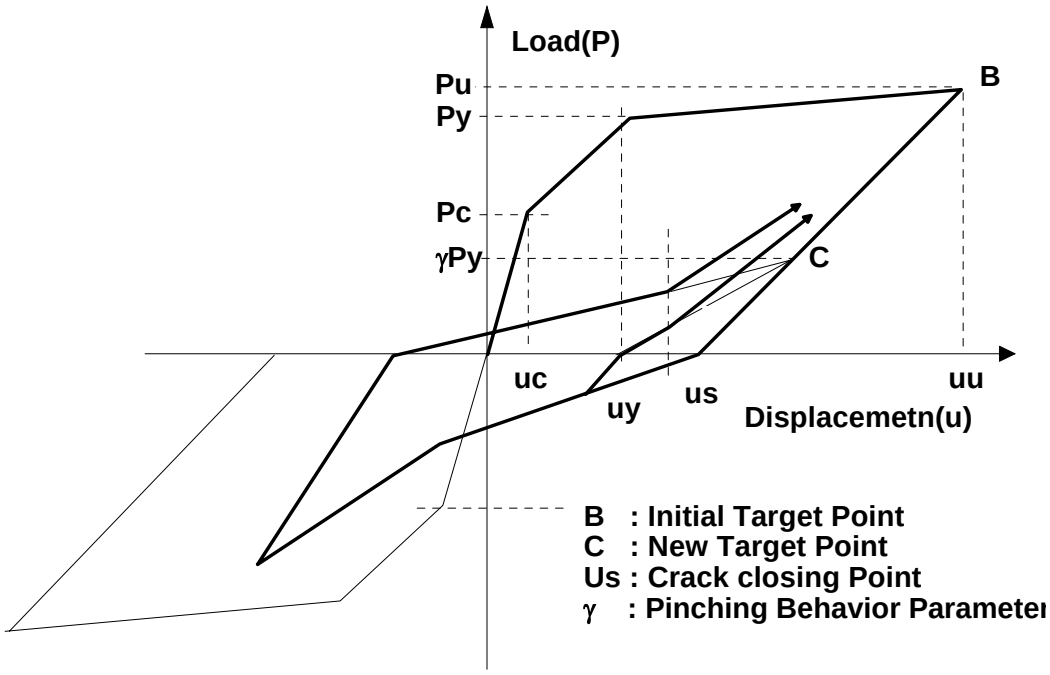

Figure A.3: γ Parameter.

A.4 Hysteresis rules

The three-parameter model defines the force-deformation relationship of a reinforced concrete element through several different hysteretic branches as shown in Fig. A.4. It detects any stiffness change in the element and immediately updates its physical properties. At the start of the analysis the element is assumed to behave linearly and free of residual stress. The model is force input/deformation output and uses the nonsymmetrical trilinear skeleton curve of the element. To understand the different hysteretic rules the following variables must be defined:

Because of the different branches in the model, the hysteretic rules were expressed in a logical format. The instantaneous stiffness is defined to be the slope of the branch

associated with the instantaneous location on the force deformation curve.

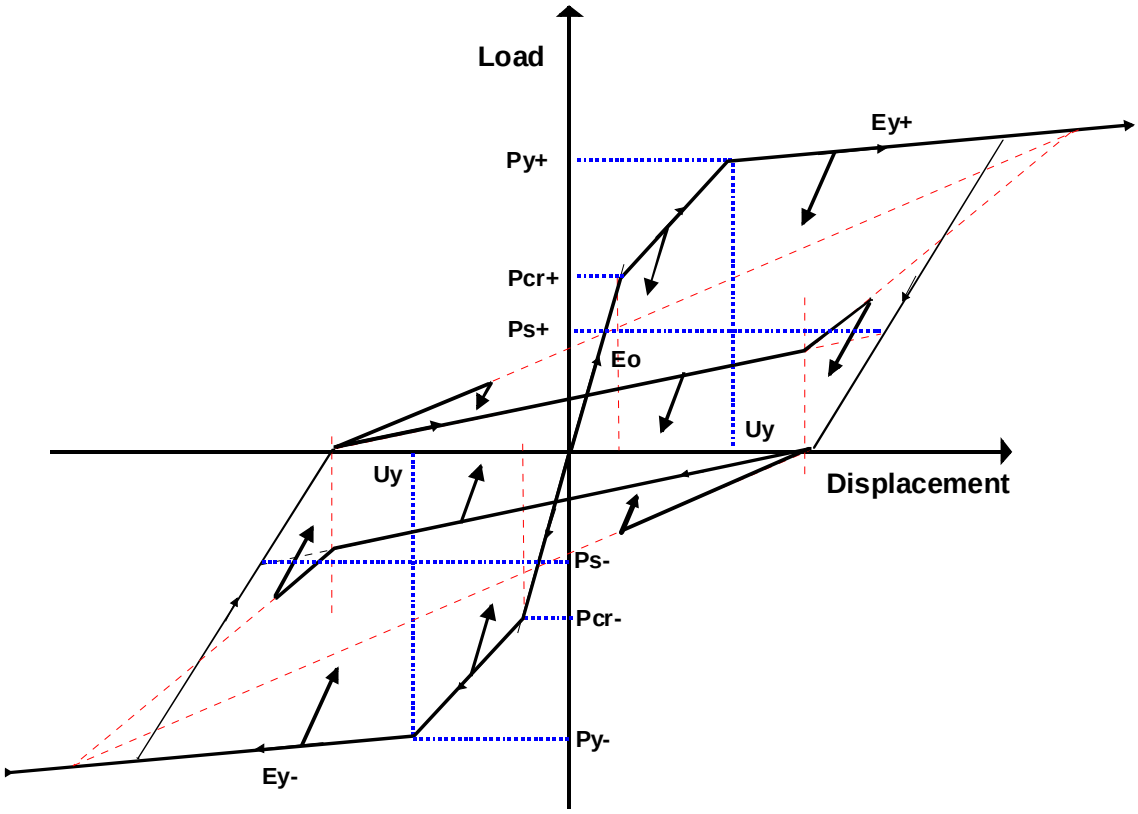

Figure A.4: Hysteresis rules.

APPENDIX B

TWO-STORY BUILDING

B.1 Gilroy Fire House Plan

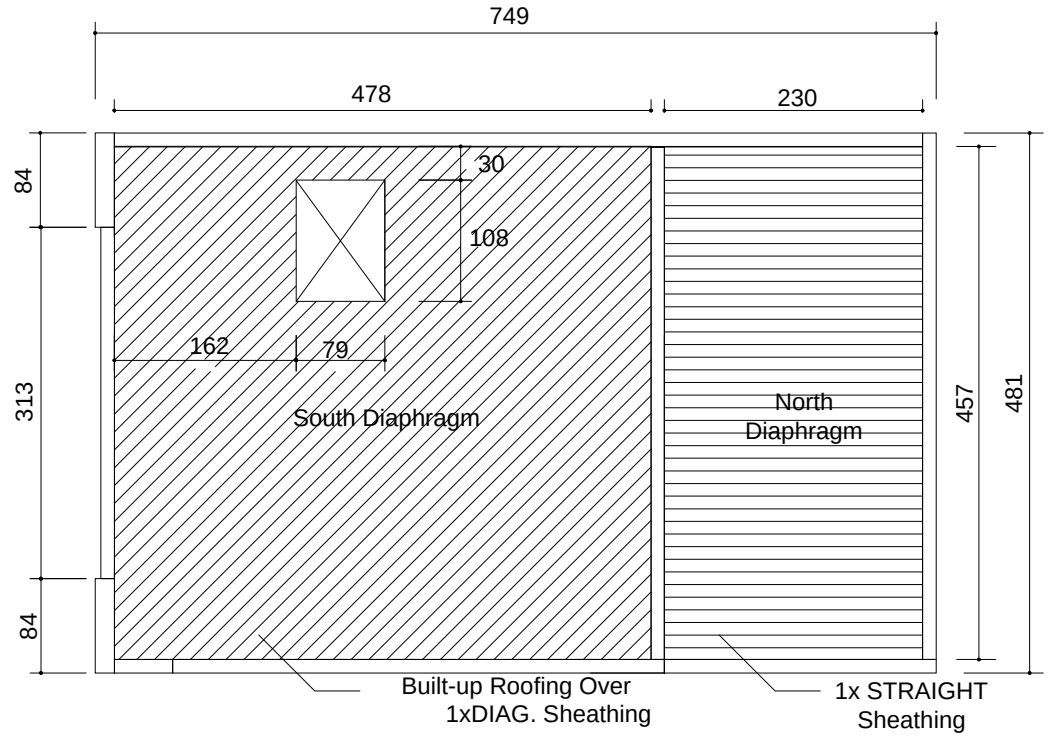

Figure B.1: Diaphragm layout of Roof Level.

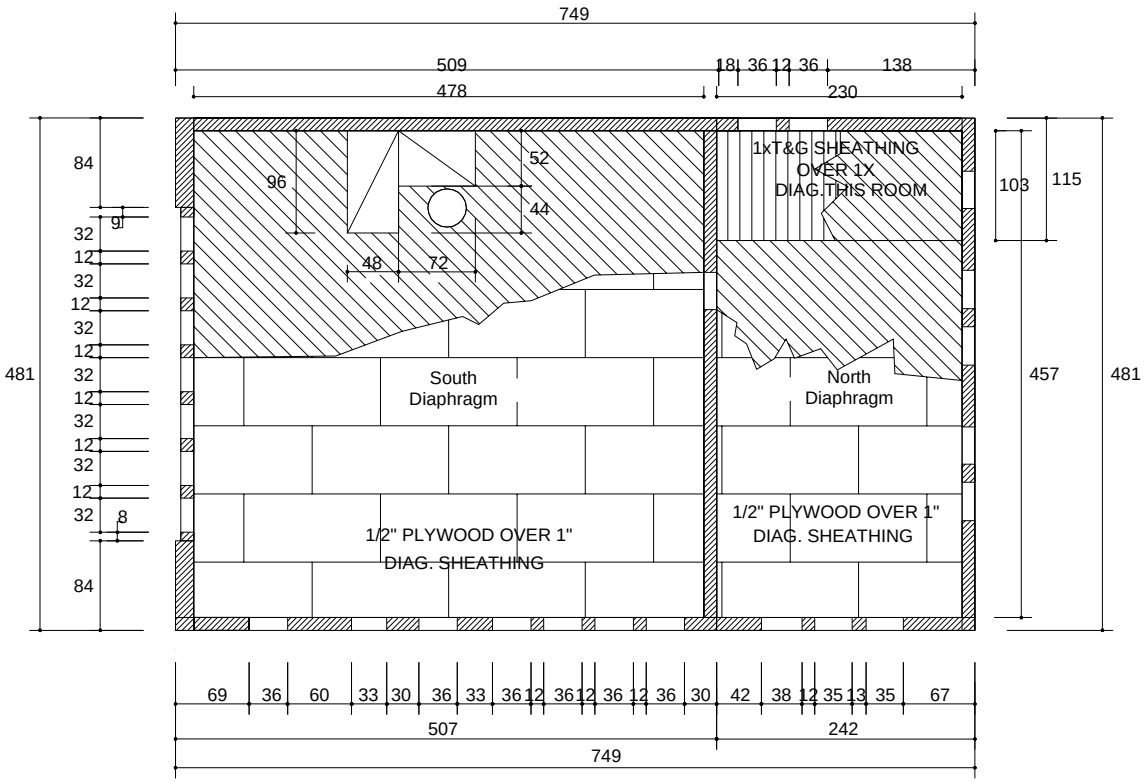

Figure B.2: Diaphragm layout of 2nd Floor Level.

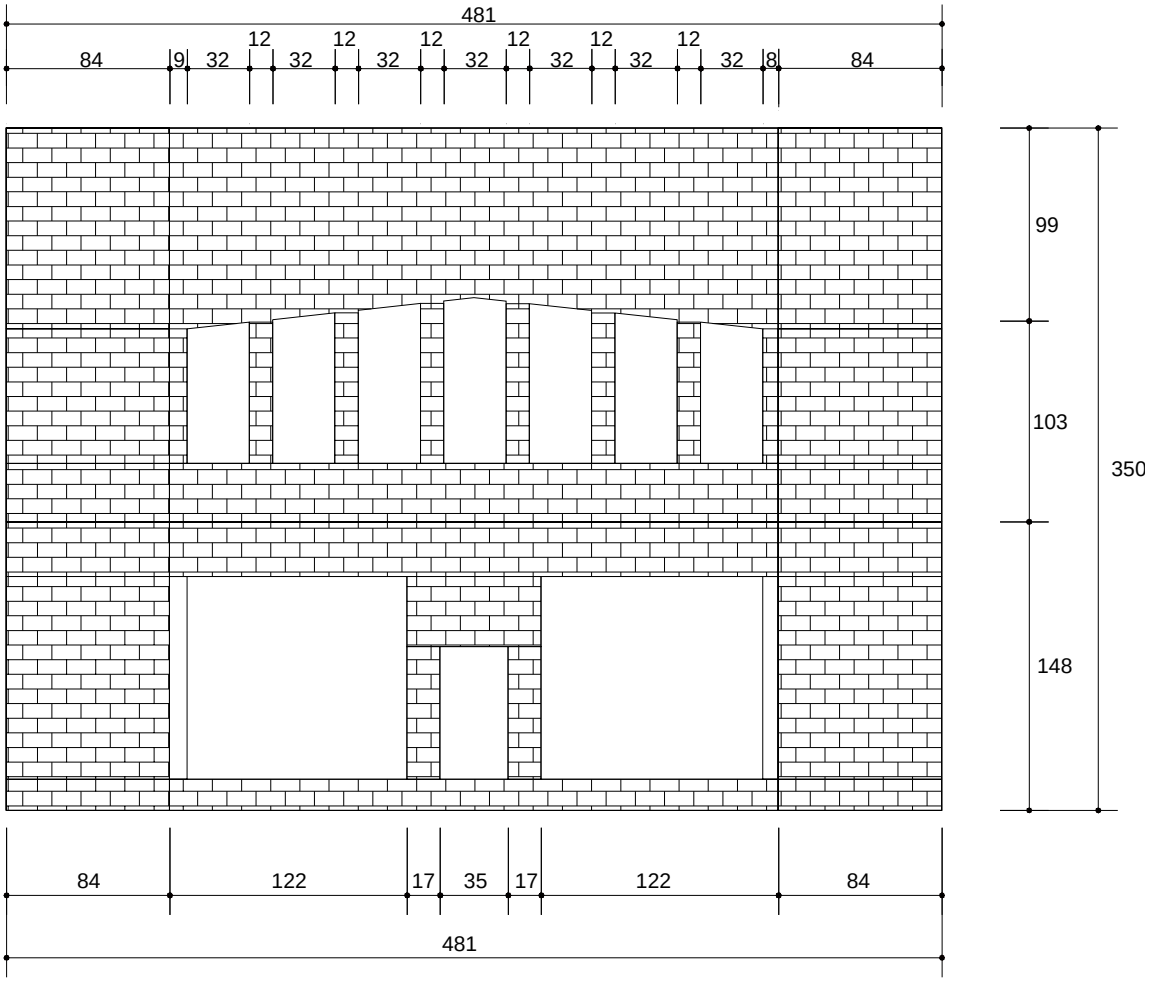

Figure B.3: South Wall, Firehouse of Gilroy.

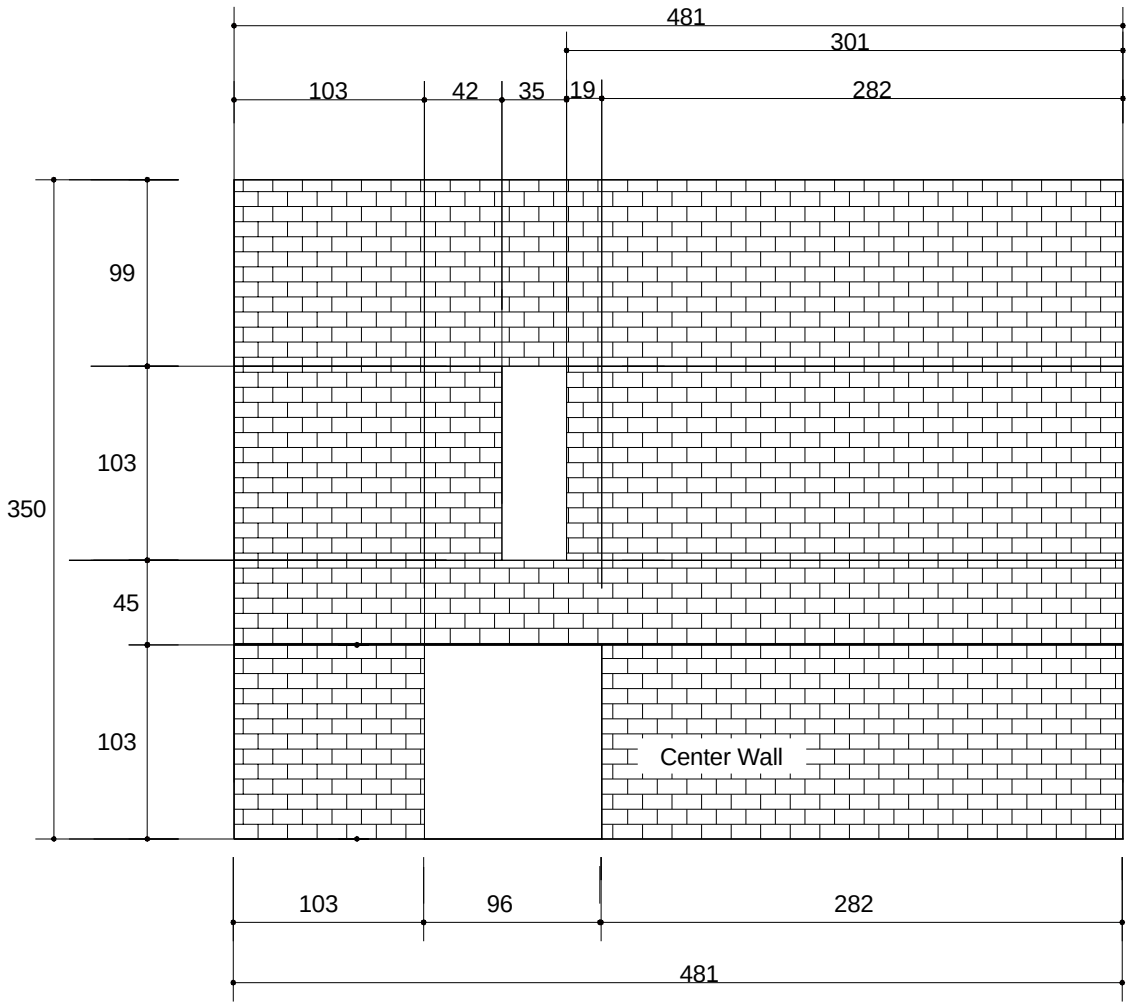

Figure B.4: Central Wall, Firehouse of Gilroy.

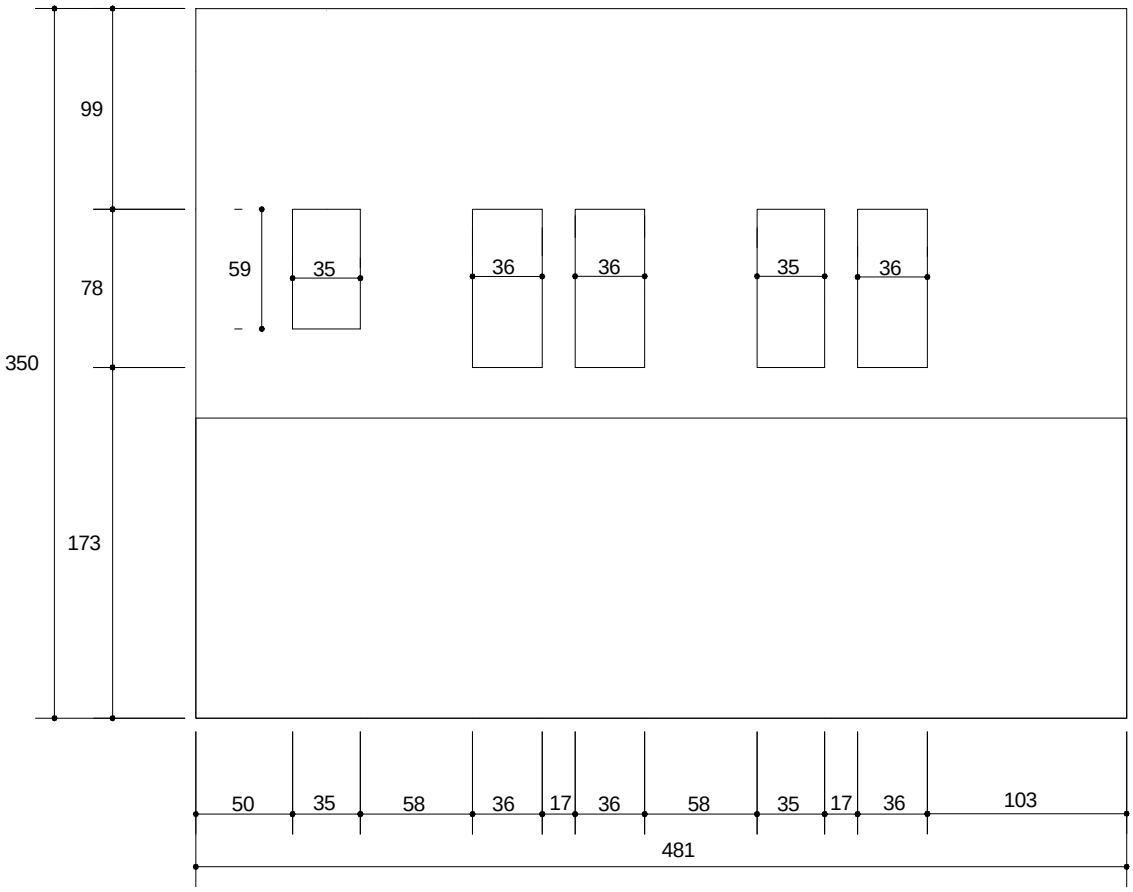

Figure B.5: North Wall, Firehouse of Gilroy.

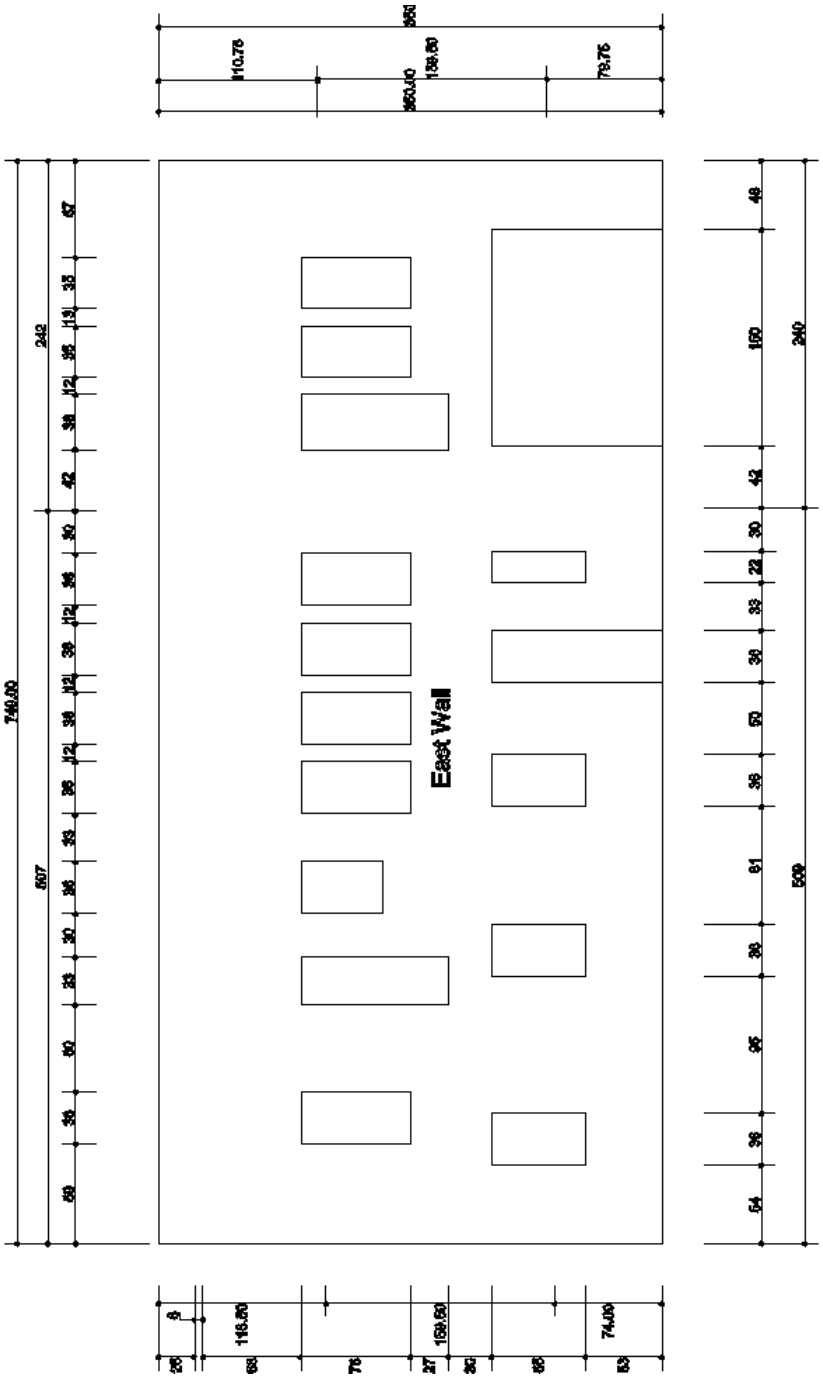

Figure B.6: East Wall, Firehouse of Gilroy.

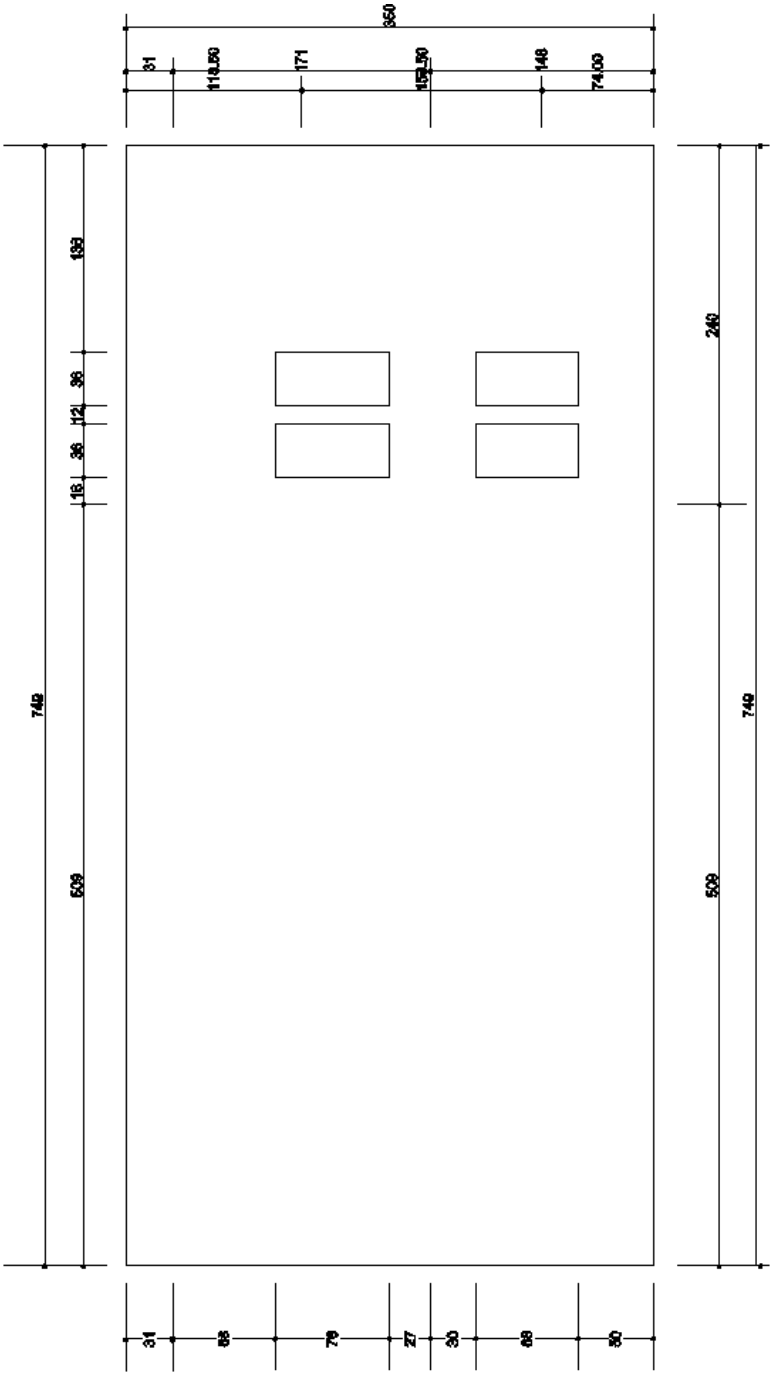

Figure B.7: West Wall, Firehouse of Gilroy.

B.2 Pier Modeling using Pier-type collapse mechanism

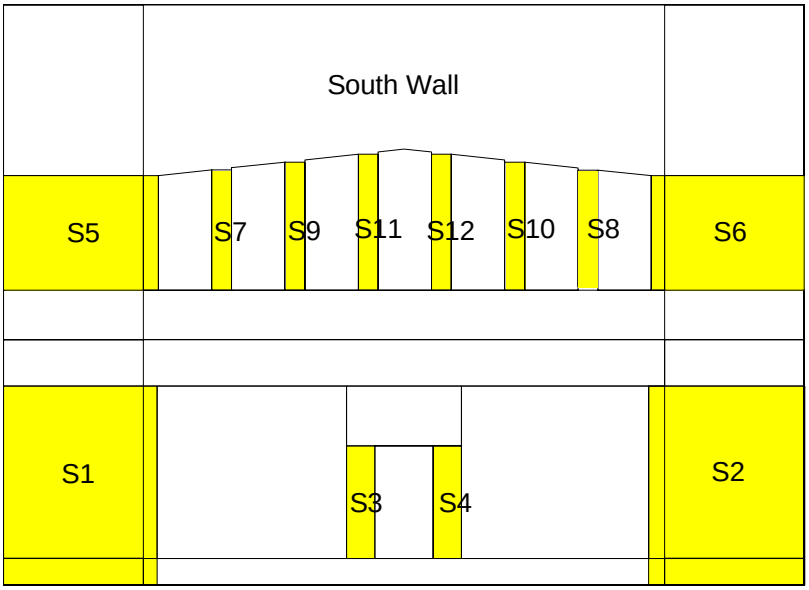

Figure B.8: Piers of south wall using the pier-type collapse mechanism.

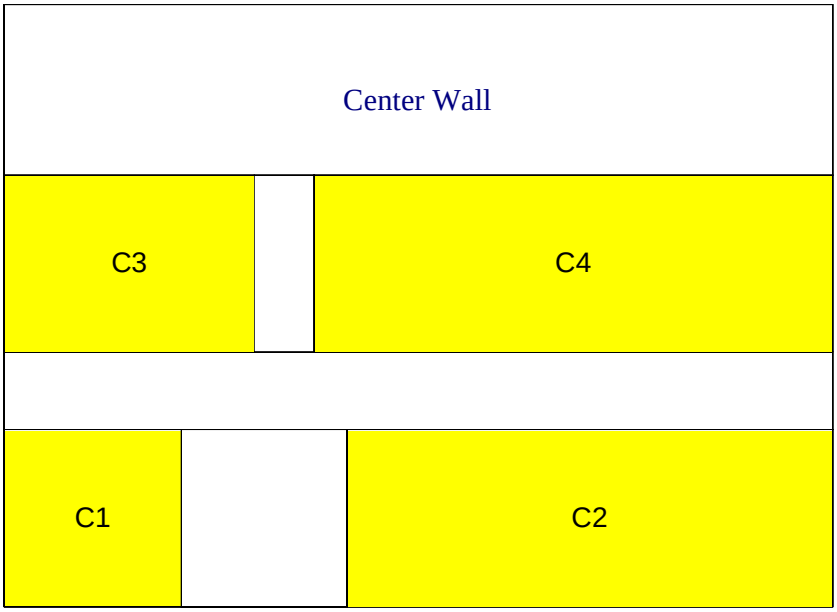

Figure B.9: Piers of central wall using the pier-type collapse mechanism.

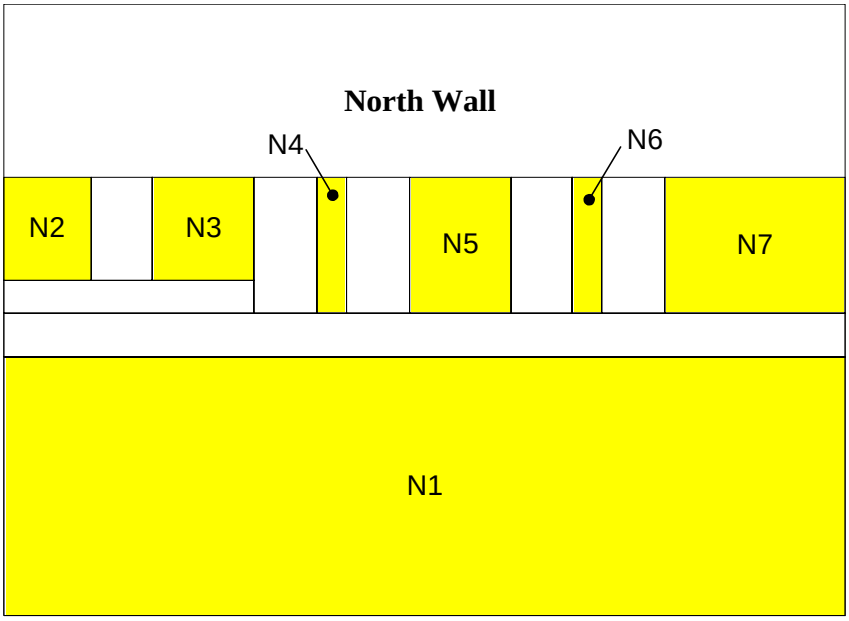

Figure B.10: Piers of north wall using the pier-type collapse mechanism.

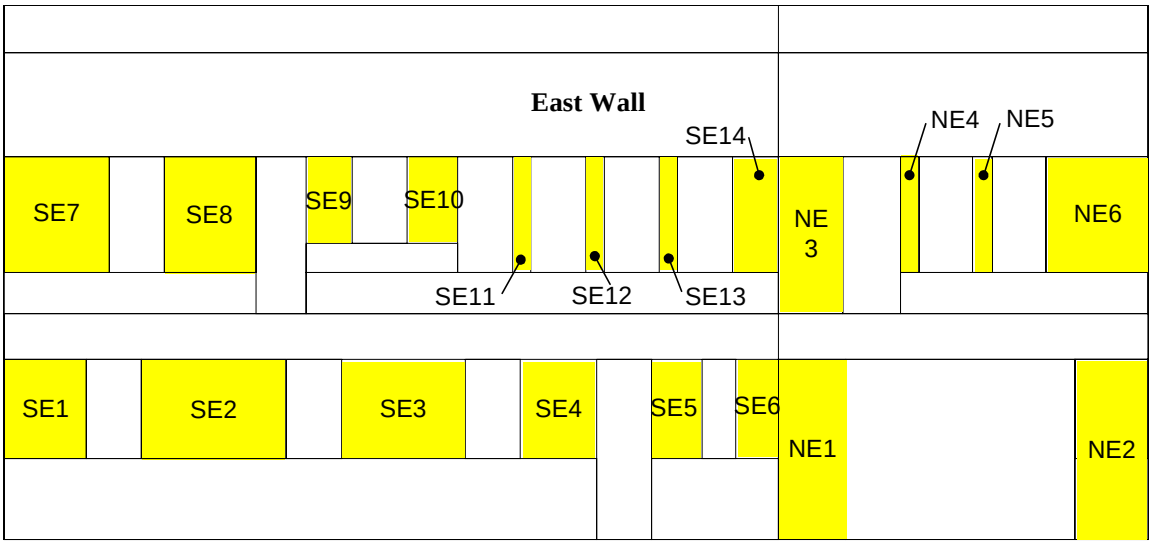

Figure B.11: piers of east wall using the pier-type collapse mechanism.

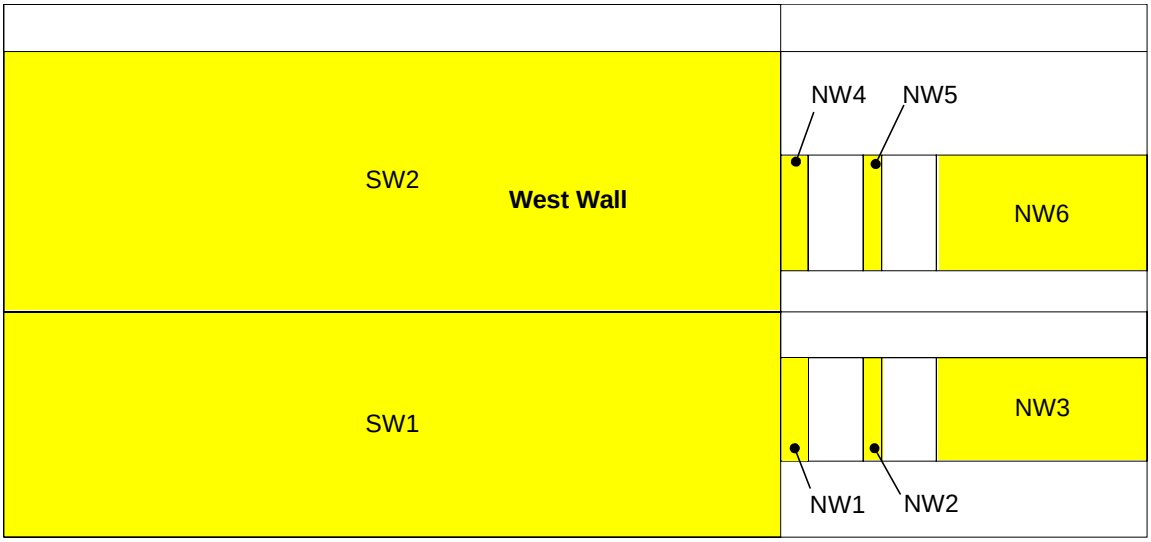

Figure B.12: Piers of west wall using the pier-type collapse mechanism.

APPENDIX C

ONE-STORY TEST BUILDING

C.1 As-built dimensions (plan)

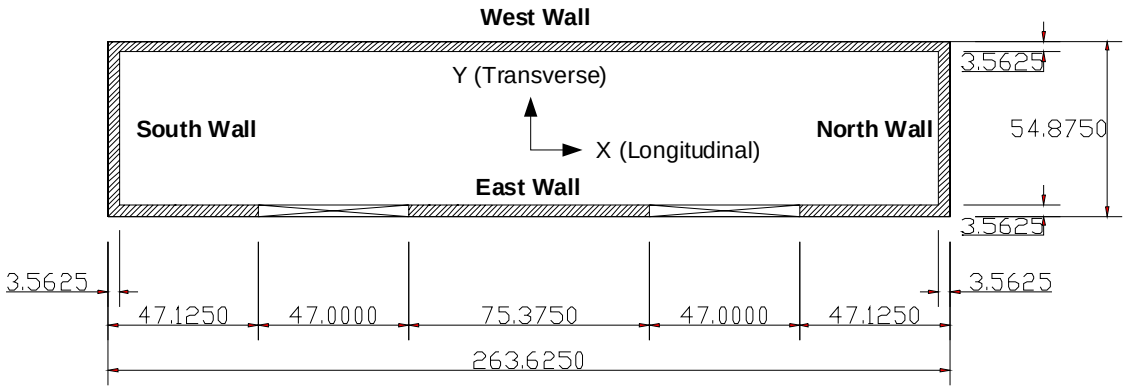

Figure C.1: Plan of Test Building.

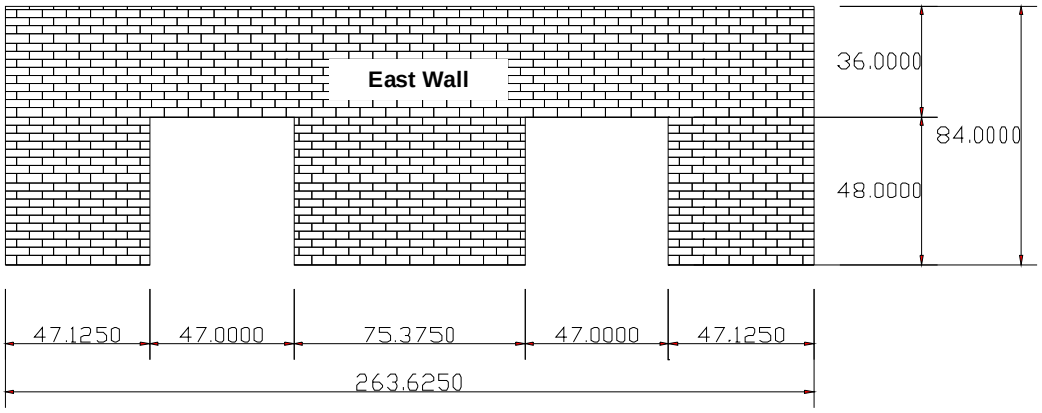

Figure C.2: East Wall of Test Building.

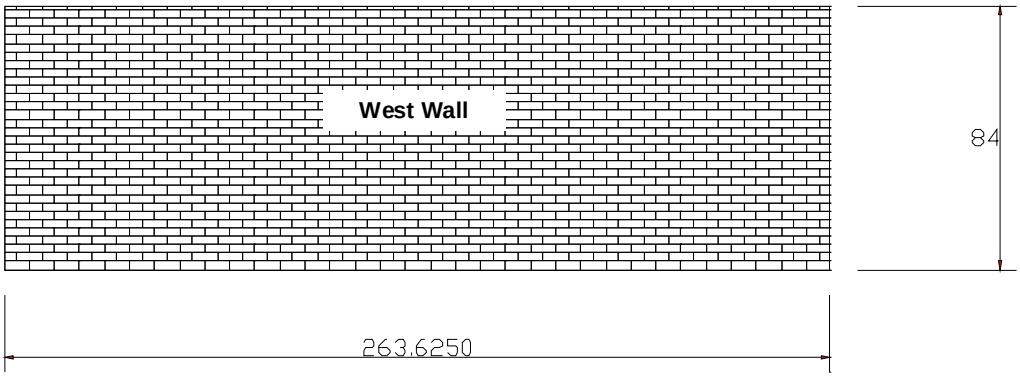

Figure C.3: West Wall of Test Building.

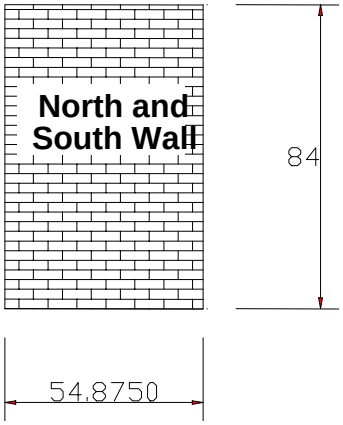

Figure C.4: North and South Wall of Test Building.

C.2 Measured Response of Experimental Test 3 (PGA = 0.5g)

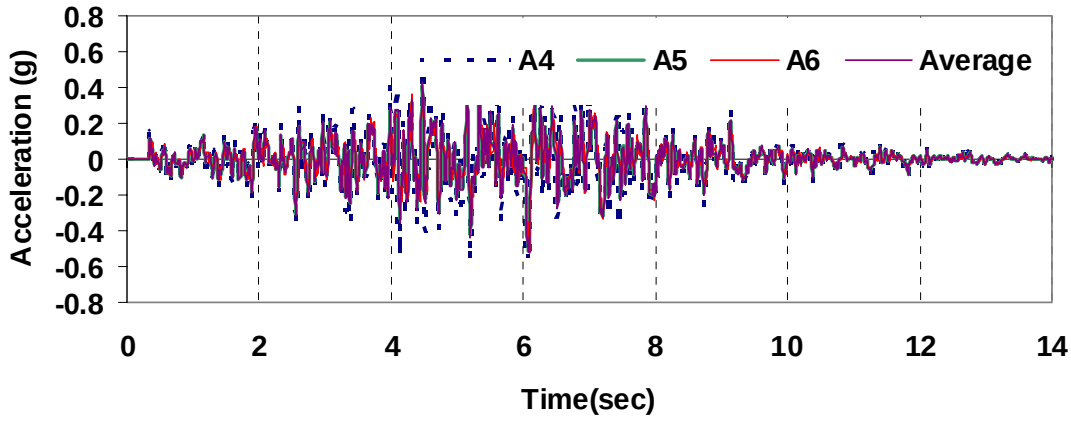

Figure C.5: Measured accelerations in the E-W direction at lifting frame (Specimen #1 Test 3) (Cohen 2001).

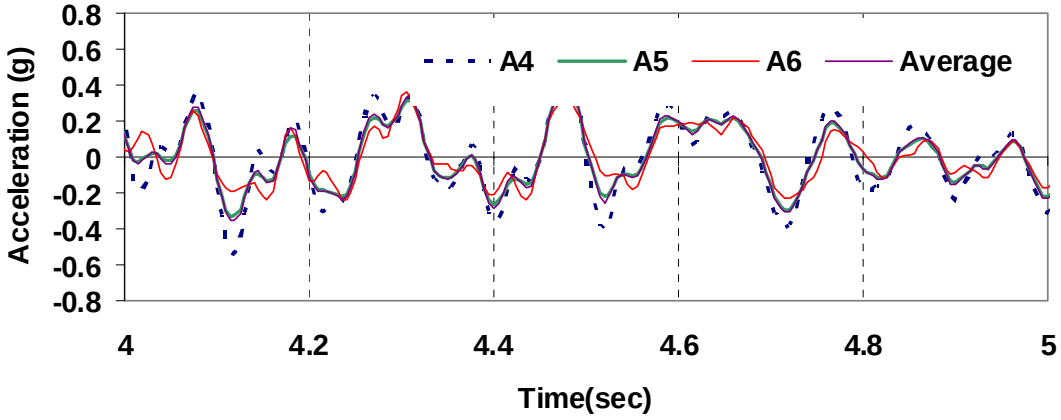

Figure C.6: One-second comparisons of measured accelerations in the E-W direction at lifting frame (Specimen #1 Test 3) (Cohen 2001).

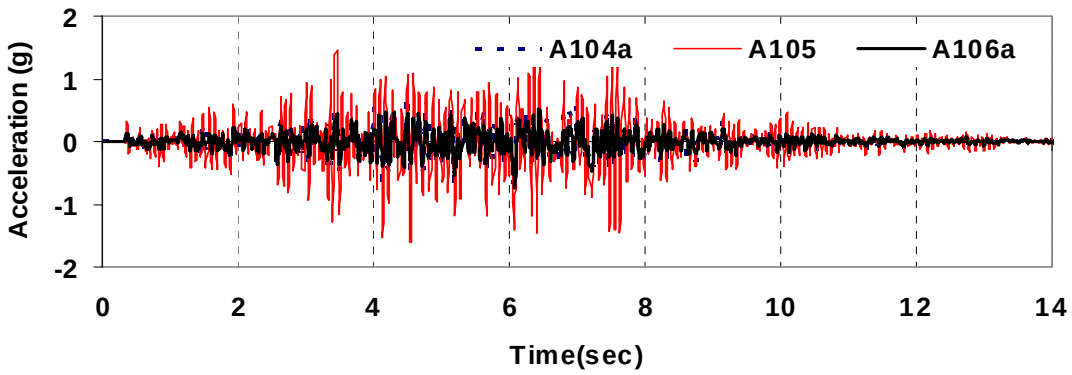

Figure C.7: Comparison of measured accelerations in the E-W direction at the center of diaphragm and the top of the north and south wall (Specimen #1 Test 3) (Cohen 2001).

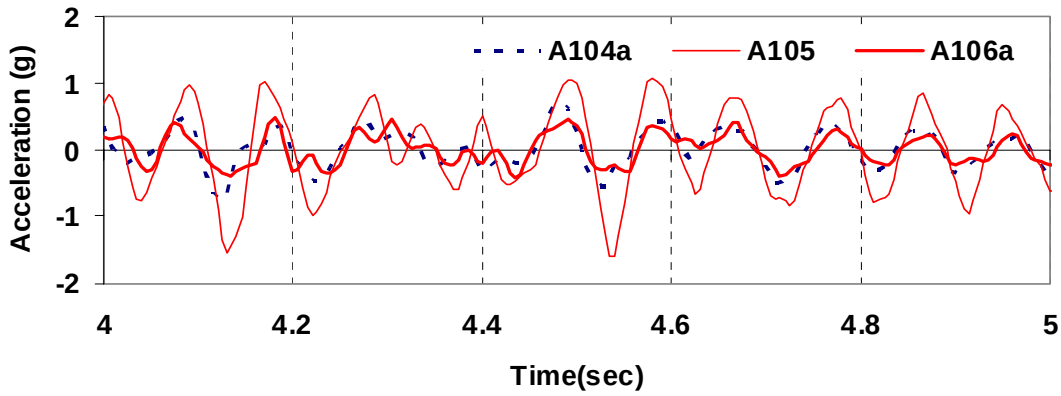

Figure C.8: One-second comparison of measured accelerations in the E-W direction at the center of diaphragm and the top of the north and south wall (Specimen #1 Test 3) (Cohen 2001).

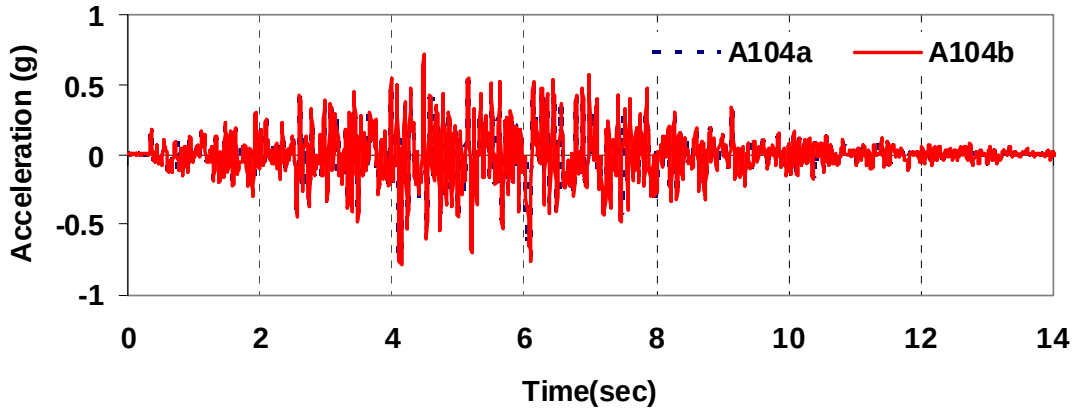

Figure C.9: Comparison of measured accelerations in the E-W direction at the top of the south wall (Specimen #1 Test 3) (Cohen 2001).

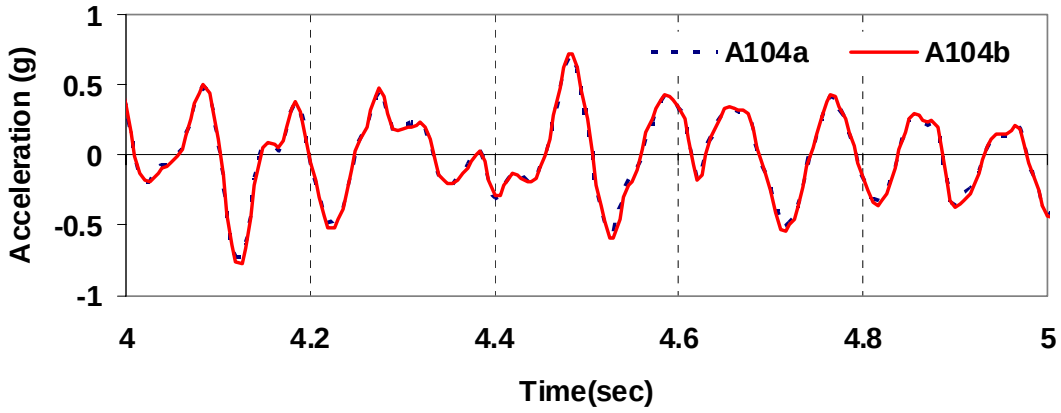

Figure C.10: One-second comparison of measured accelerations in the E-W direction at the top of the south wall (Specimen #1 Test 3) (Cohen 2001).

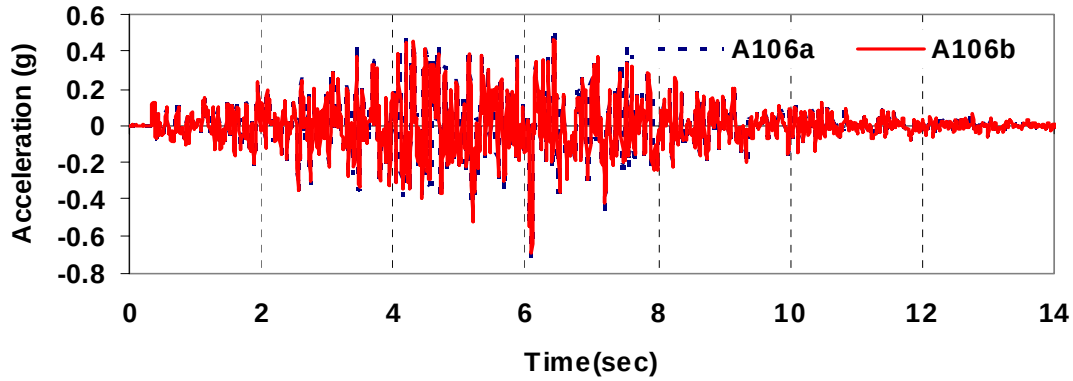

Figure C.11: Measured accelerations in the E-W direction at the top of the north wall (Specimen #1 Test 3) (Cohen 2001).

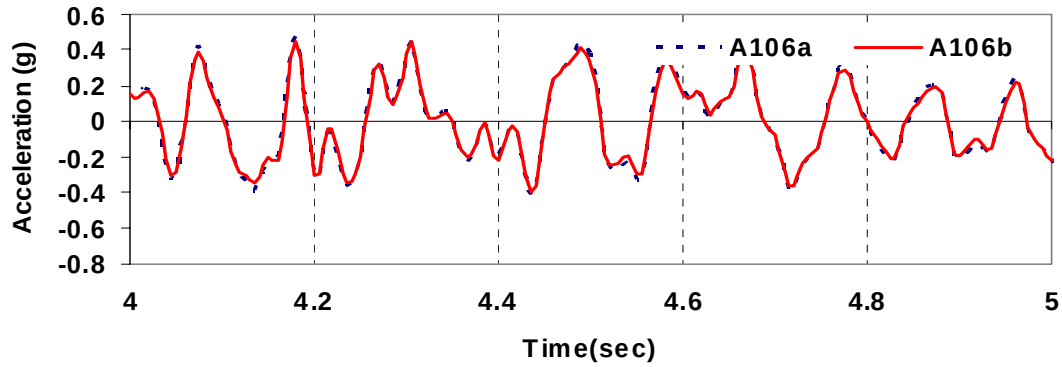

Figure C.12: One-second comparison of measured accelerations in the E-W direction at the top of the north wall (Specimen #1 Test 3) (Cohen 2001).

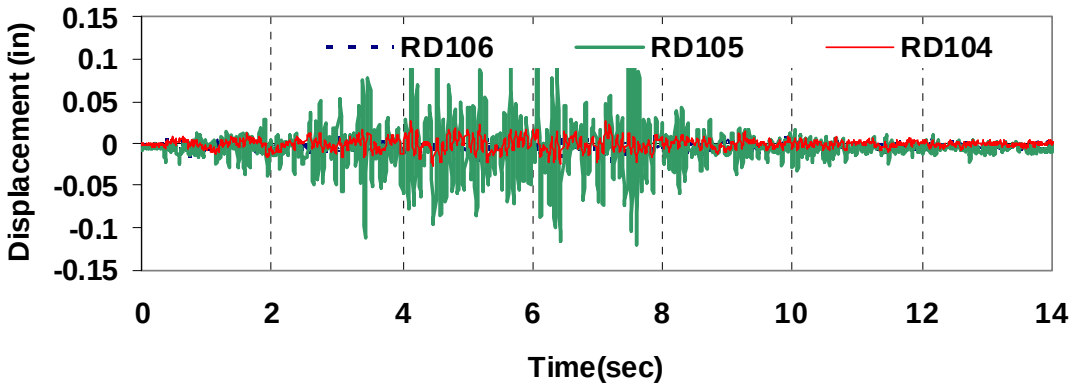

Figure C.13: One-second comparison of measured displacements in the E-W direction (Specimen #1 Test 3) (Cohen 2001).

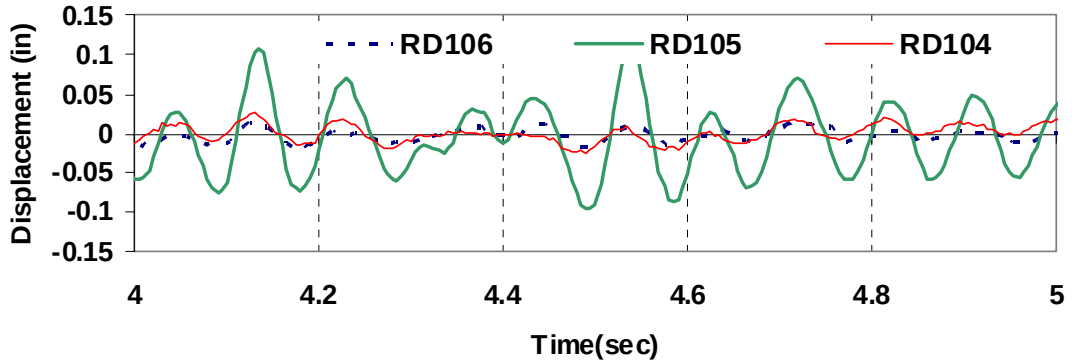

Figure C.14: One-second comparison of measured displacements in the E-W direction (Specimen #1 Test 3) (Cohen 2001).

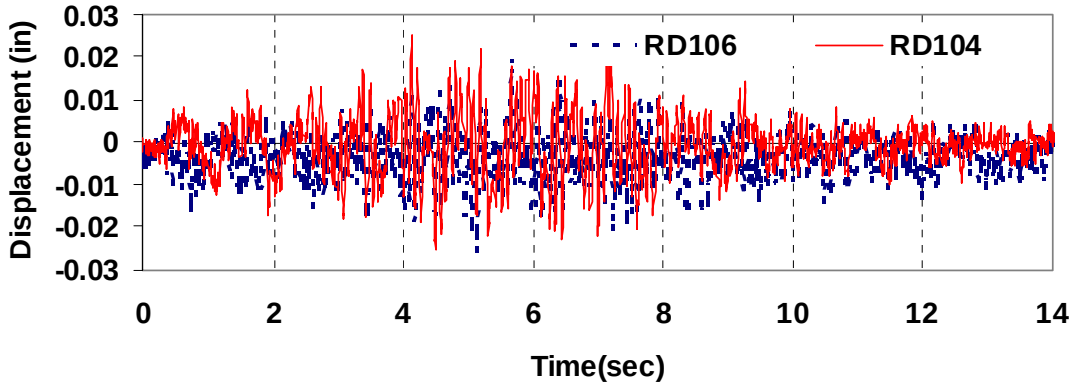

Figure C.15: Comparison of measured displacements in the E-W direction at the top of the north and south wall (Specimen #1 Test 3) (Cohen 2001).

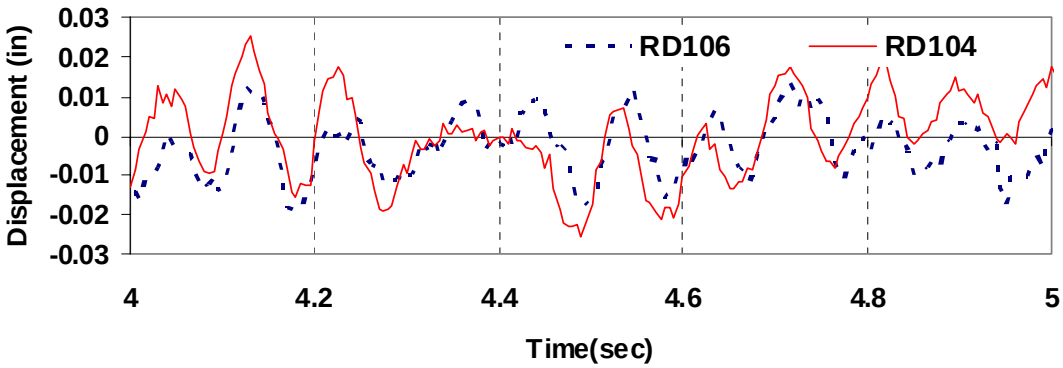

Figure C.16: One-second comparison of measured displacements in the E-W direction at the top of the north and south wall (Specimen #1 Test 3) (Cohen 2001).

C.3 Measured Response of Experimental Test 5 (PGA = 0.67g)

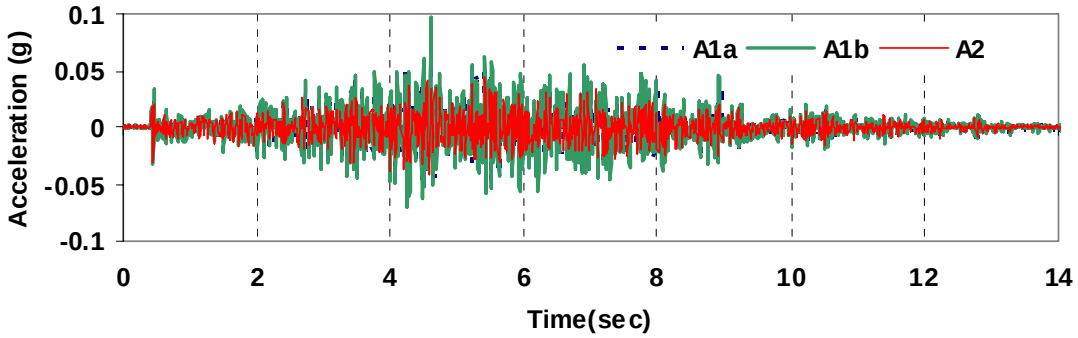

Figure C.17: Measured acceleration in the N-S direction at lifting frame (Specimen #1 Test 5) (Cohen 2001).

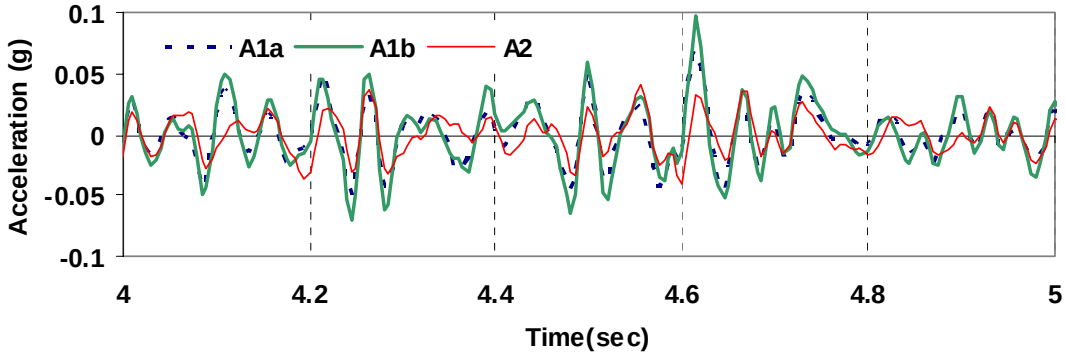

Figure C.18: One-second comparison of measured acceleration in the N-S direction at lifting frame (Specimen #1 Test 5) (Cohen 2001).

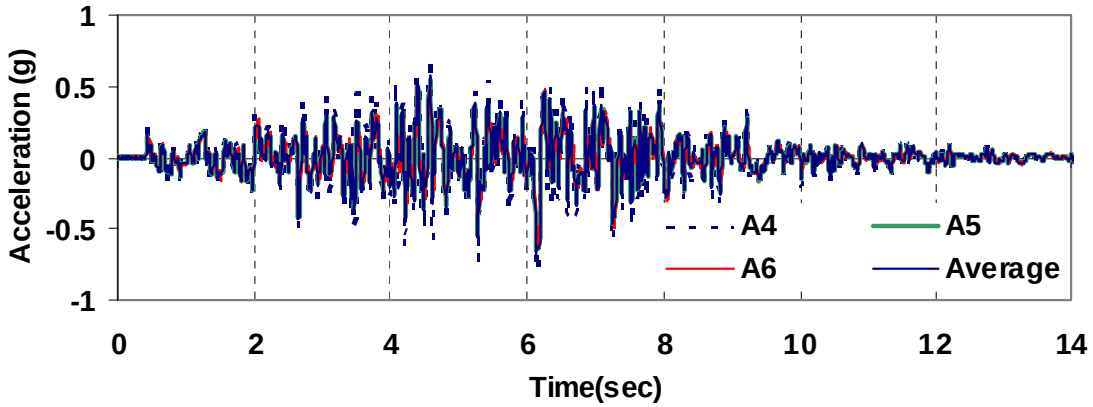

Figure C.19: Measured acceleration in the E-W direction at lifting frame (Specimen #1 Test 5) (Cohen 2001).

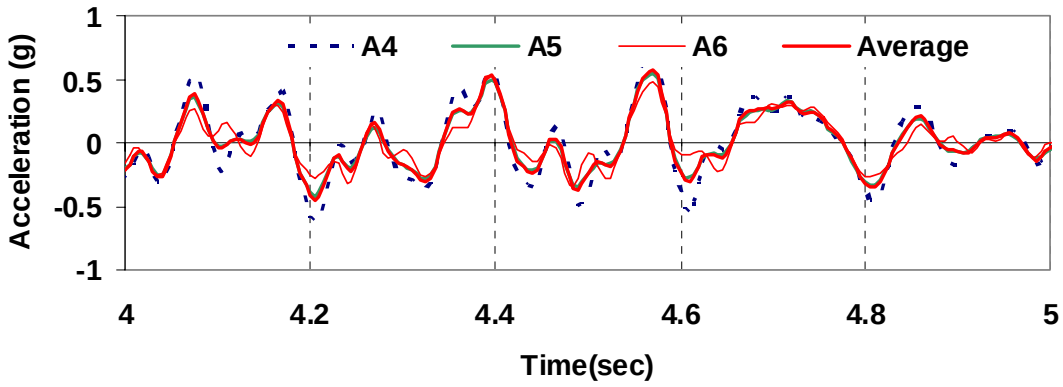

Figure C.20: One-second comparison of measured acceleration in the E-W direction at lifting frame (Specimen #1 Test 5) (Cohen 2001).

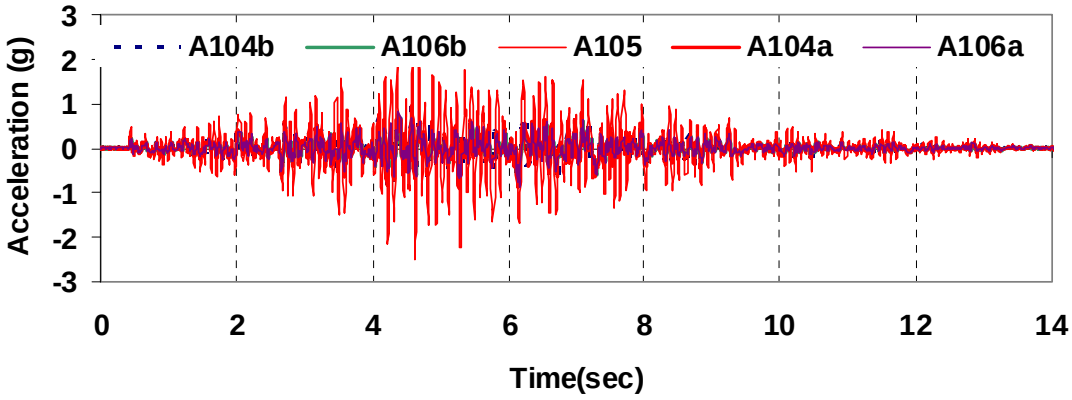

Figure C.21: Comparison of measured accelerations in the E-W direction at diaphragm (Specimen #1 Test 5) (Cohen 2001).

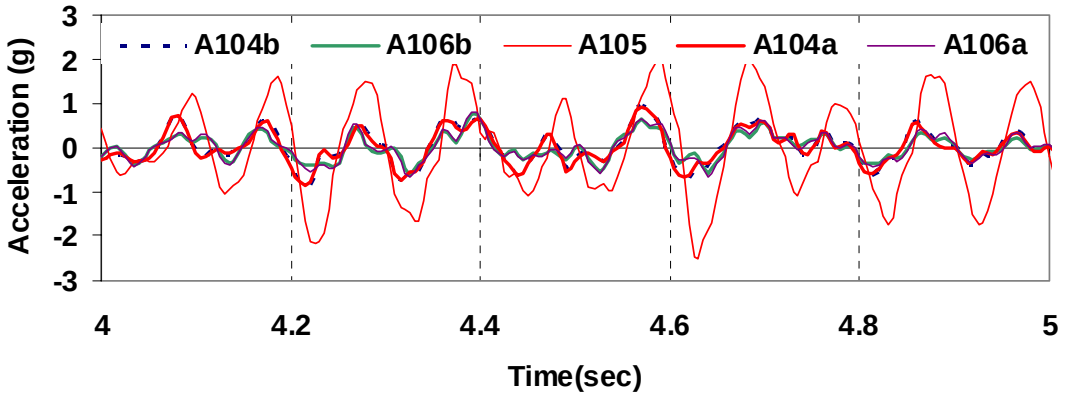

Figure C.22: One-second comparison measured accelerations in the E-W direction at diaphragm (Specimen #1 Test 5) (Cohen 2001).

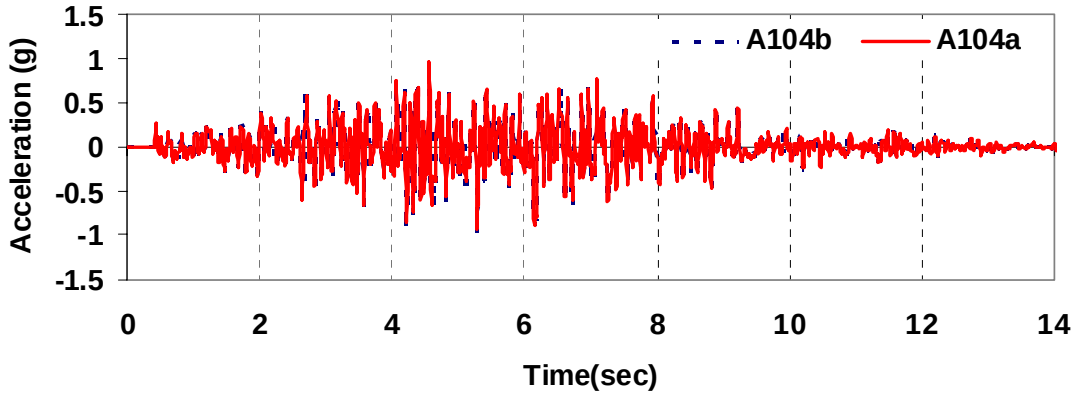

Figure C.23: Measured accelerations in the E-W direction at the top of south wall (Specimen #1 Test 5) (Cohen 2001).

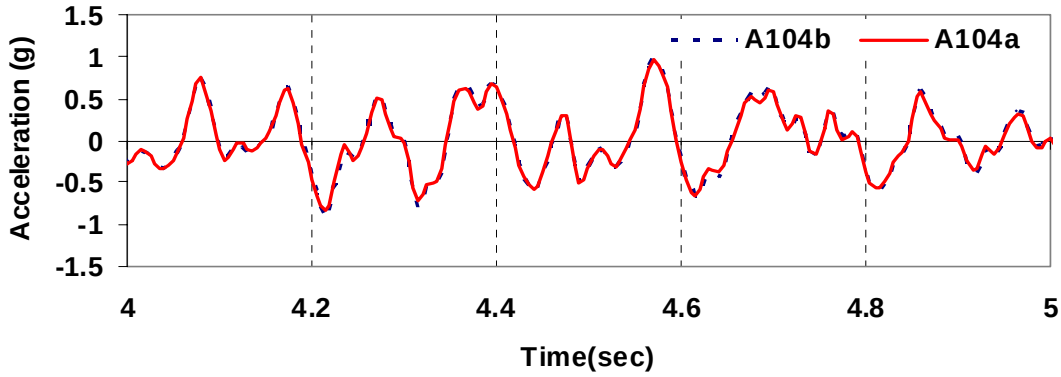

Figure C.24: One-second comparison of measured accelerations in the E-W direction at the top of south wall (Specimen #1 Test 5) (Cohen 2001).

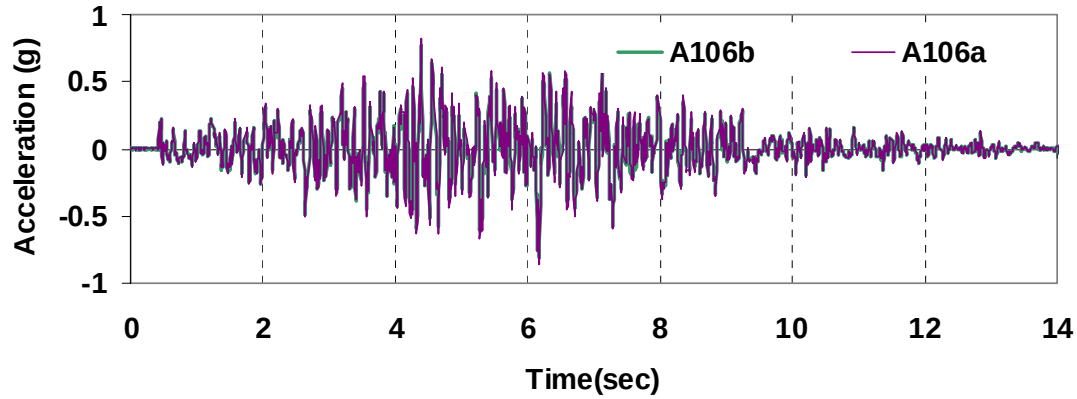

Figure C.25: Measured accelerations in the E-W direction at the top of north wall (Specimen #1 Test 5) (Cohen 2001).

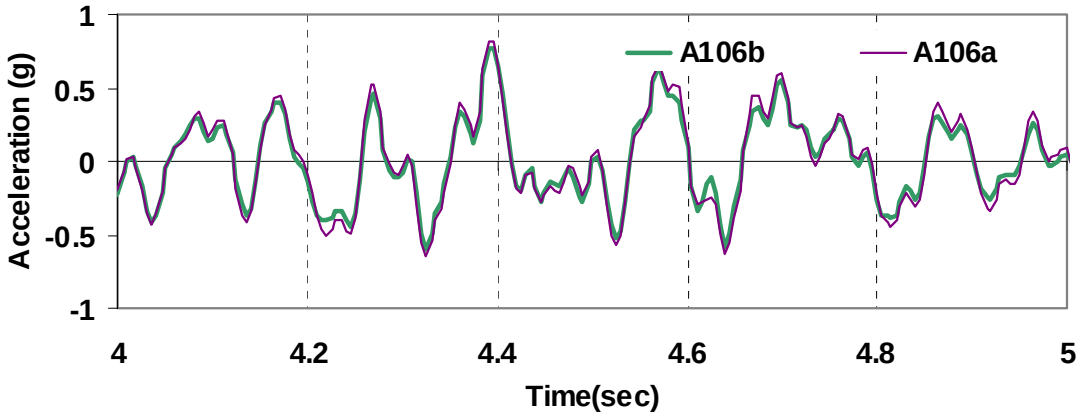

Figure C.26: One-second comparison of measured accelerations in the E-W direction at the top of north wall (Specimen #1 Test 5) (Cohen 2001).

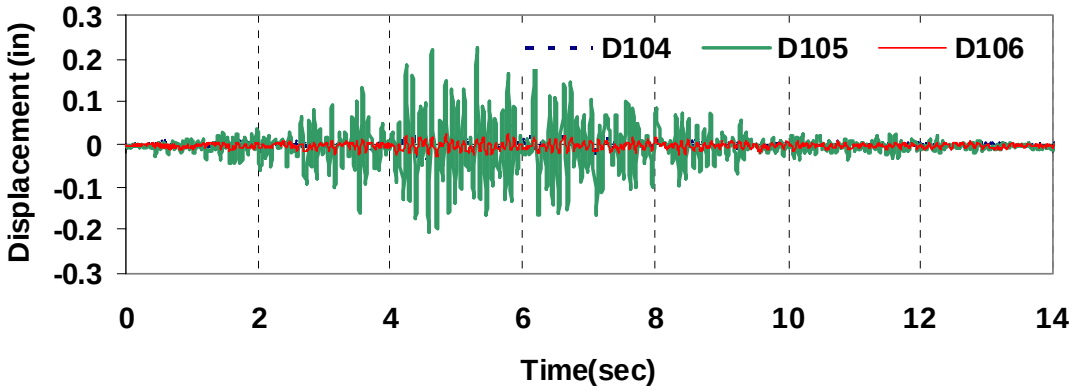

Figure C.27: Measured displacements in the E-W direction (Specimen #1 Test 5) (Cohen 2001).

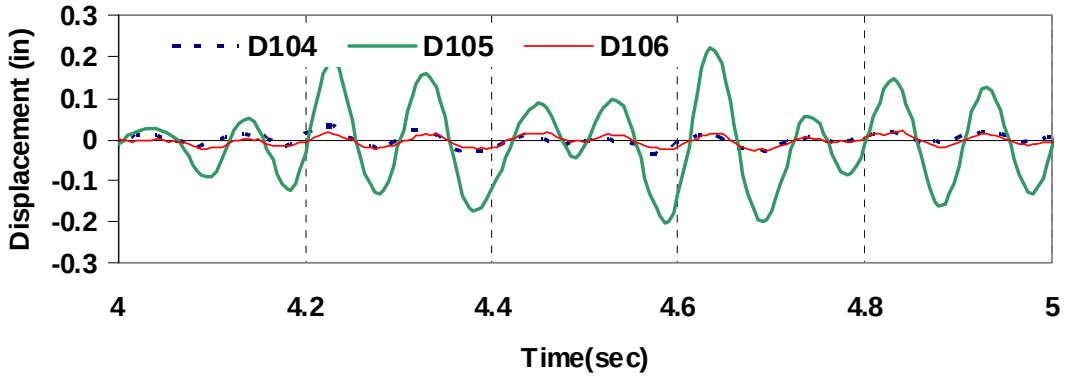

Figure C.28: One-second comparison of measured displacements in the E-W direction (Specimen #1 Test 5) (Cohen 2001).

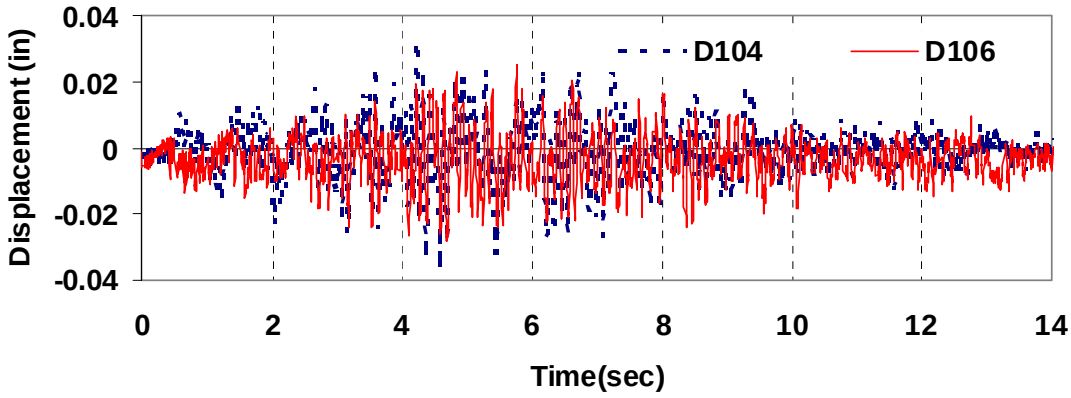

Figure C.29: Measured displacements in the E-W direction at the top of the north and south wall (Specimen #1 Test 5) (Cohen 2001).

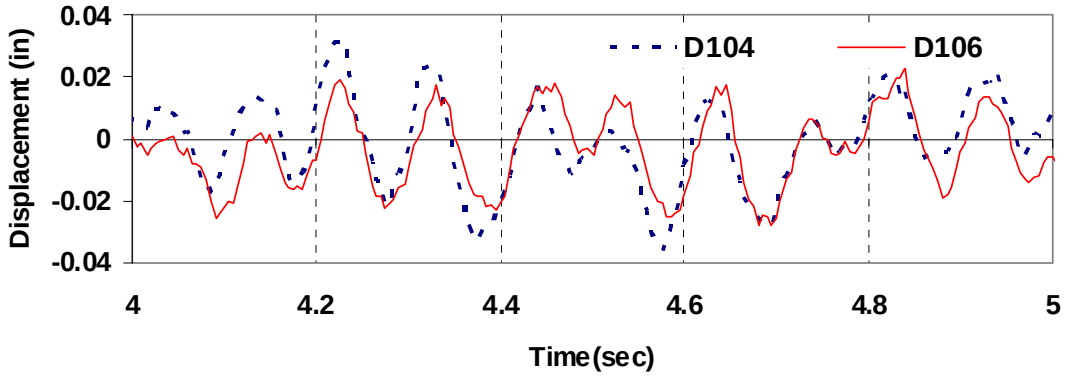

Figure C.30: One-second comparison of measured displacements in the E-W direction at the top of the north and south wall (Specimen #1 Test 5) (Cohen 2001).

C.4 Measured Response of Experimental Test 9 (PGA = 1.0 g)

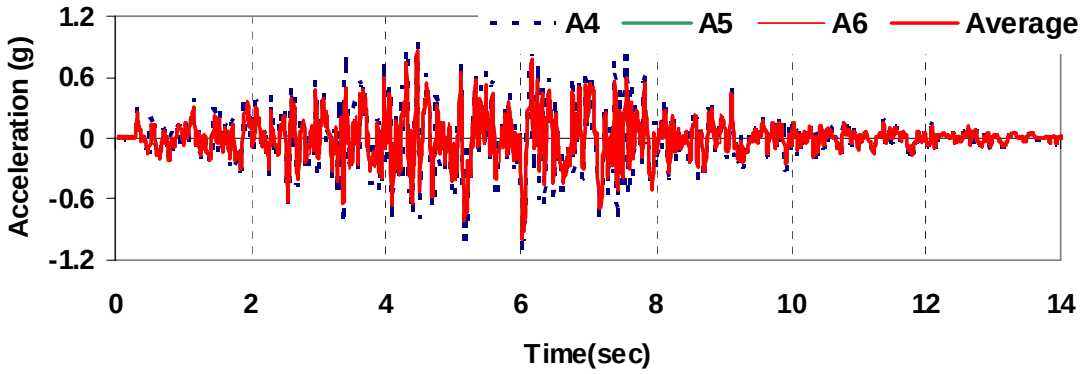

Figure C.31: Measured accelerations in the E-W direction at lifting frame (Specimen #1 Test 9) (Cohen 2001).

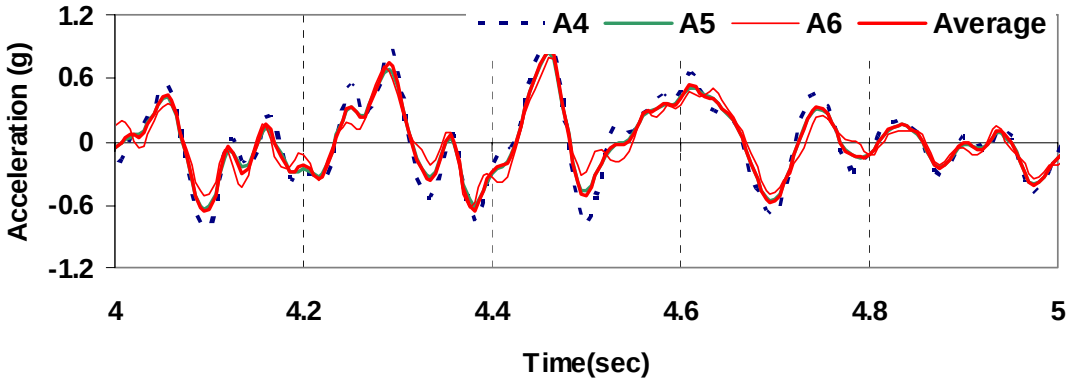

Figure C.32: One-second comparisons of measured accelerations in the E-W direction at lifting frame (Specimen #1 Test 9) (Cohen 2001).

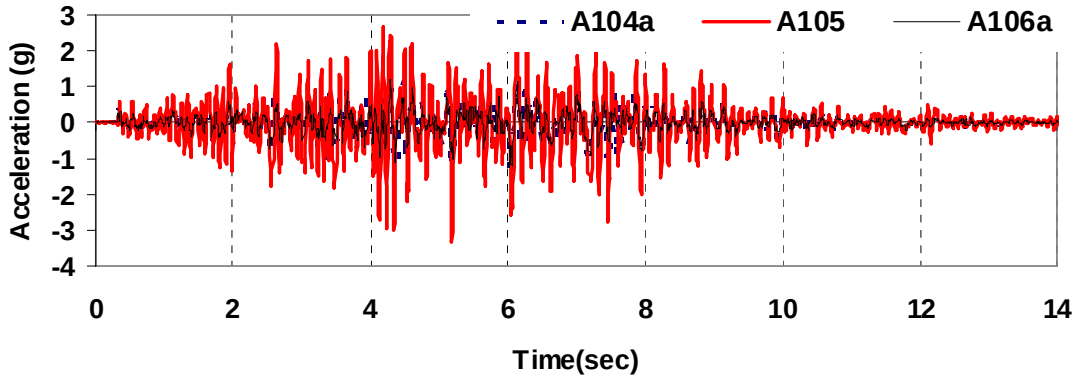

Figure C.33: Comparison of measured accelerations in the E-W direction at the center of diaphragm and the top of the north and south wall (Specimen #1 Test 9) (Cohen 2001).

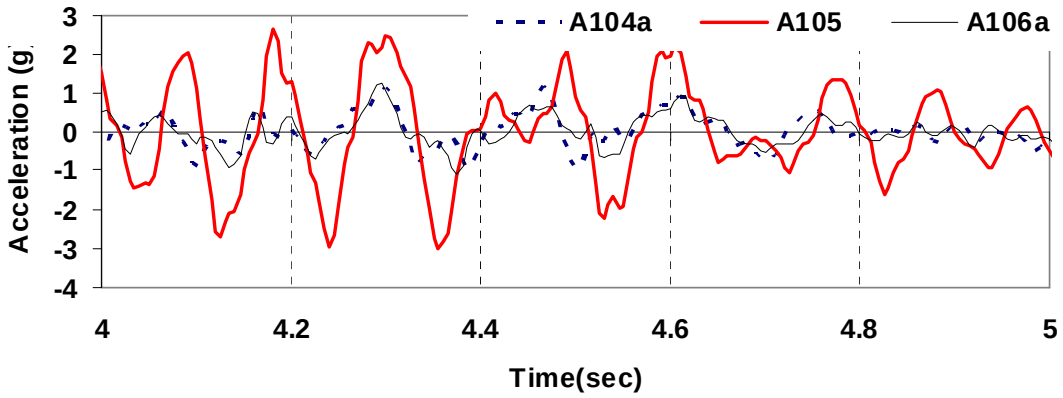

Figure C.34: One-second comparison of measured accelerations in the E-W direction at the center of diaphragm and the top of the north and south wall (Specimen #1 Test 9) (Cohen 2001).

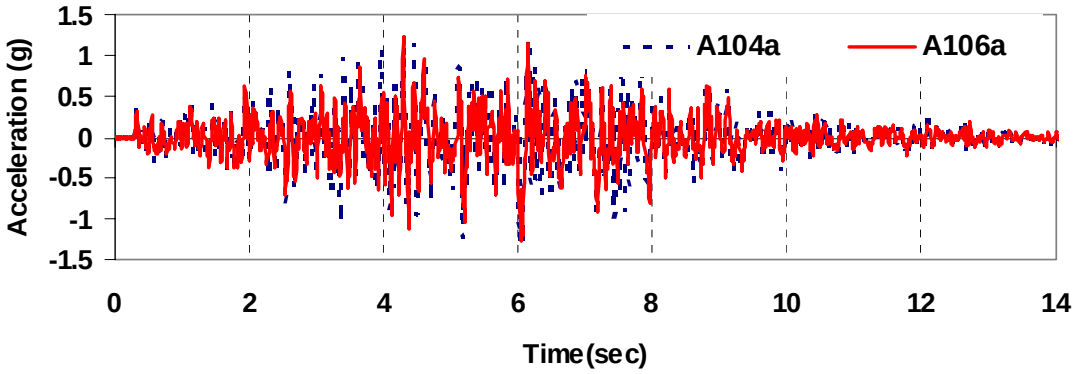

Figure C.35: Comparison of measured accelerations in the E-W direction at the top of north and south wall (Specimen #1 Test 9) (Cohen 2001).

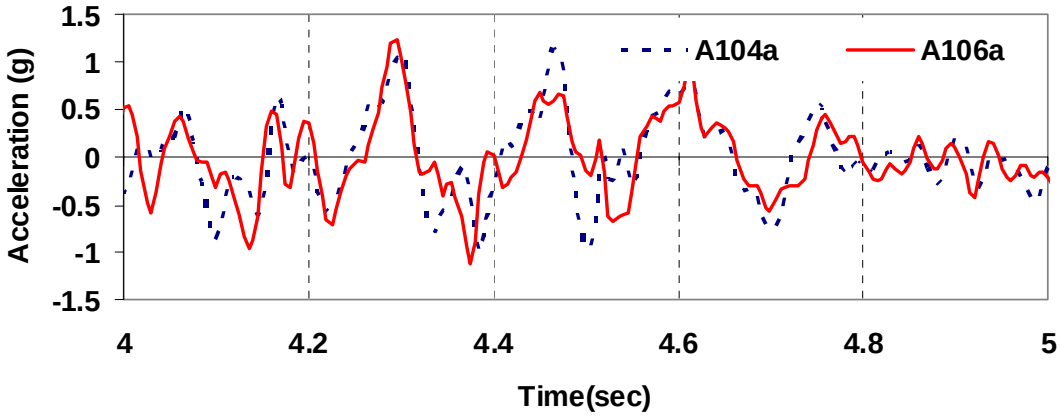

Figure C.36: One-second comparison of measured accelerations in the E-W direction at the top of north and south wall (Specimen #1 Test 9) (Cohen 2001).

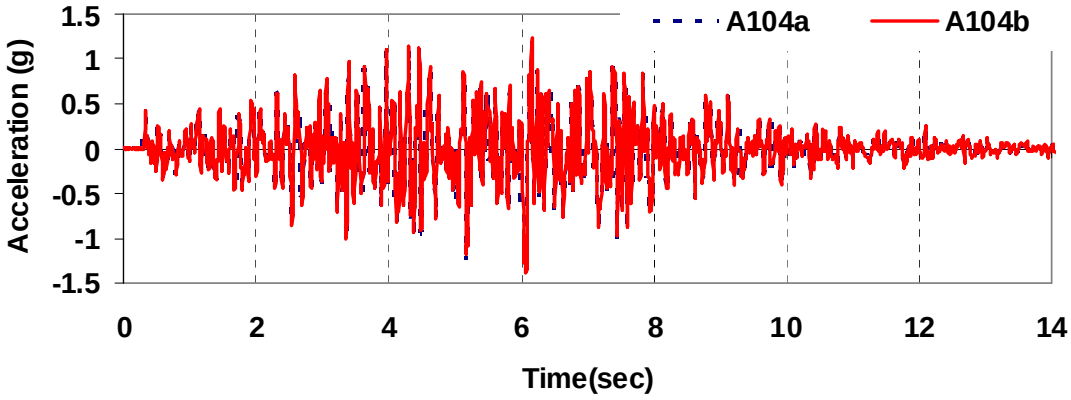

Figure C.37: Comparison of measured accelerations in the E-W direction at the top of south wall (Specimen #1 Test 9) (Cohen 2001).

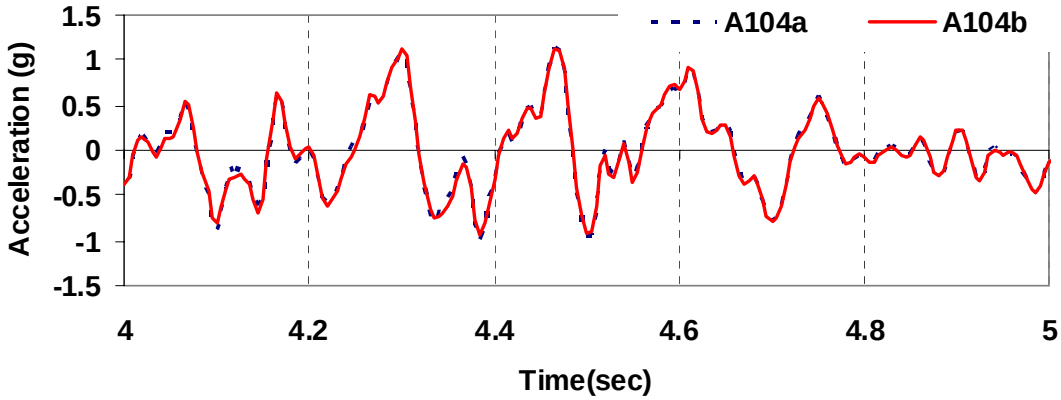

Figure C.38: One-second comparison of measured accelerations in the E-W direction at the top of south wall (Specimen #1 Test 9) (Cohen 2001).

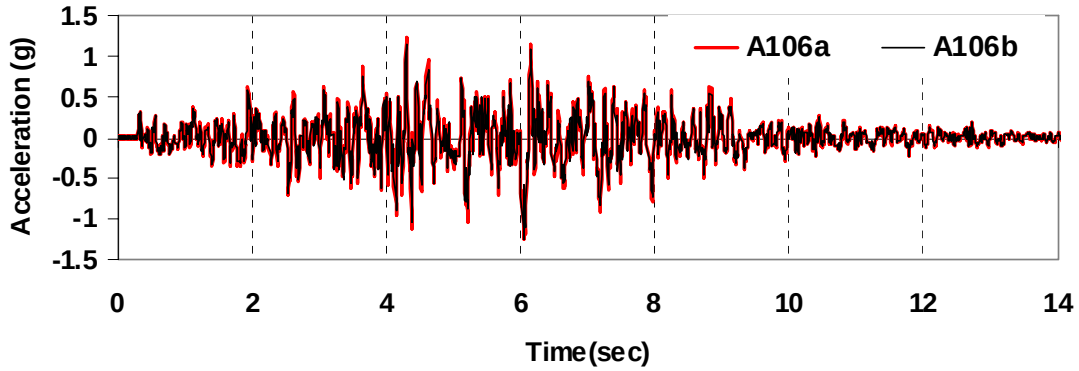

Figure C.39: Comparison of measured accelerations in the E-W direction at the top of north wall (Specimen #1 Test 9) (Cohen 2001).

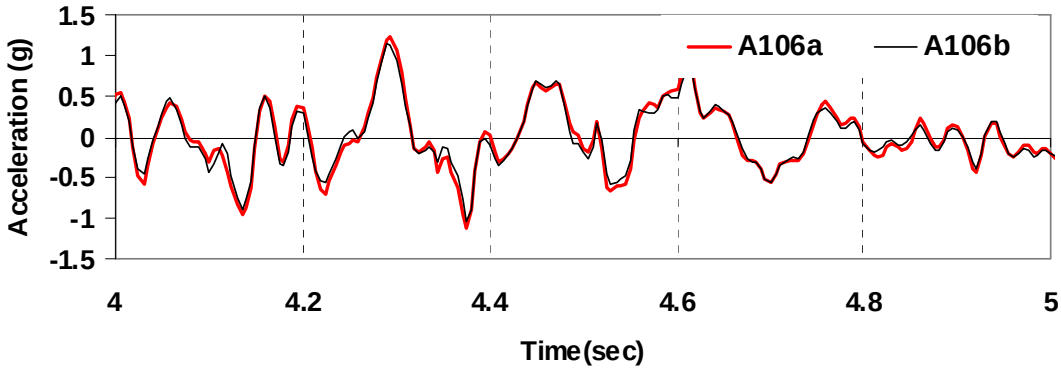

Figure C.40: One-second comparison of measured accelerations in the E-W direction at the top of north wall (Specimen #1 Test 9) (Cohen 2001).

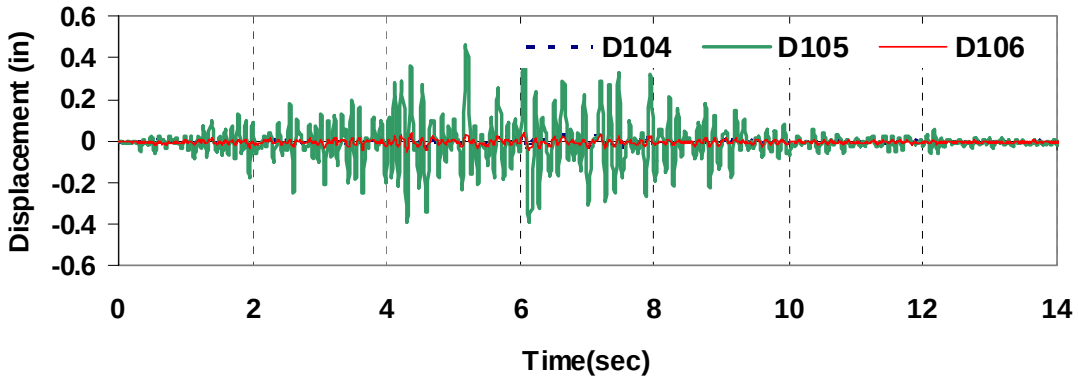

Figure C.41: Measured displacements in the E-W direction (Specimen #1 Test 9) (Cohen 2001).

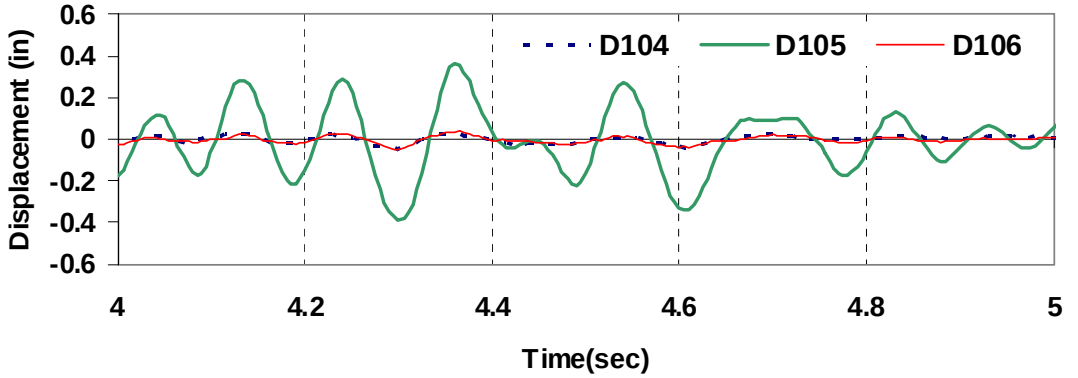

Figure C.42: One-second comparison of measured displacements in the E-W direction (Specimen #1 Test 9) (Cohen 2001).

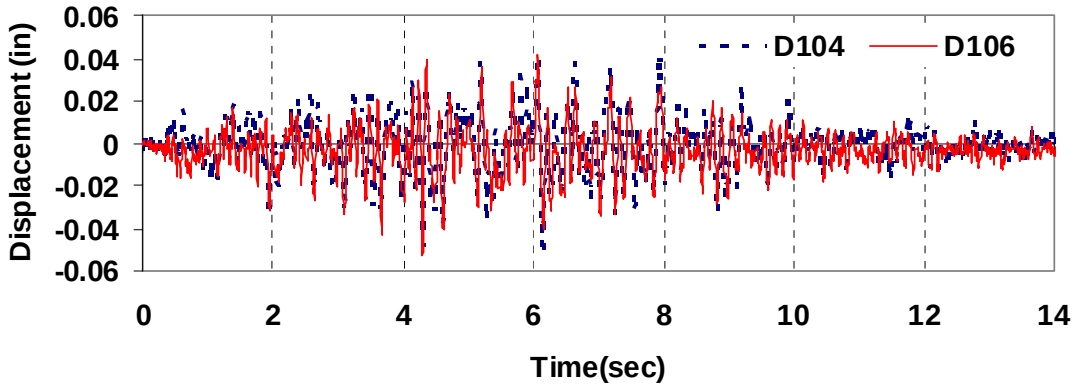

Figure C.43: Measured displacements in the E-W direction at the top of the north and south wall (Specimen #1 Test 9) (Cohen 2001).

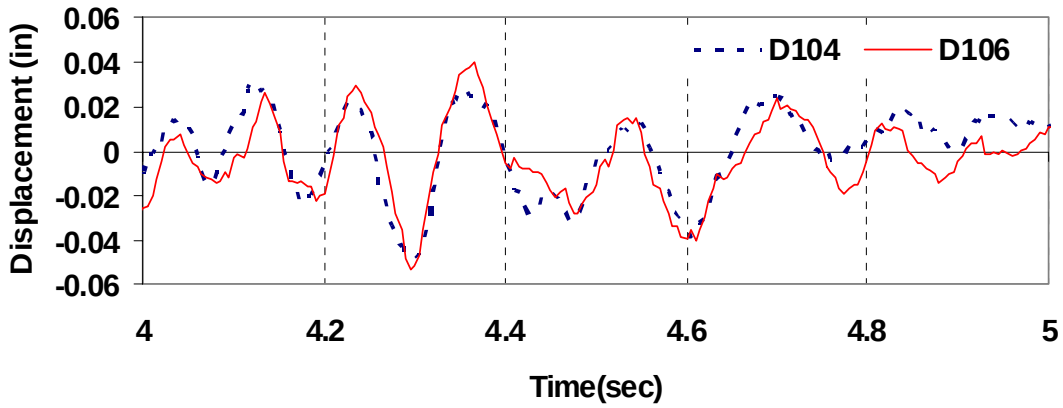

Figure C.44: One-second comparison of measured displacements in the E-W direction at the top of the north and south wall (Specimen #1 Test 9)(Cohen 2001).

C.5 Comparison of Measured and Calculated Response using PGA = 0.5 g

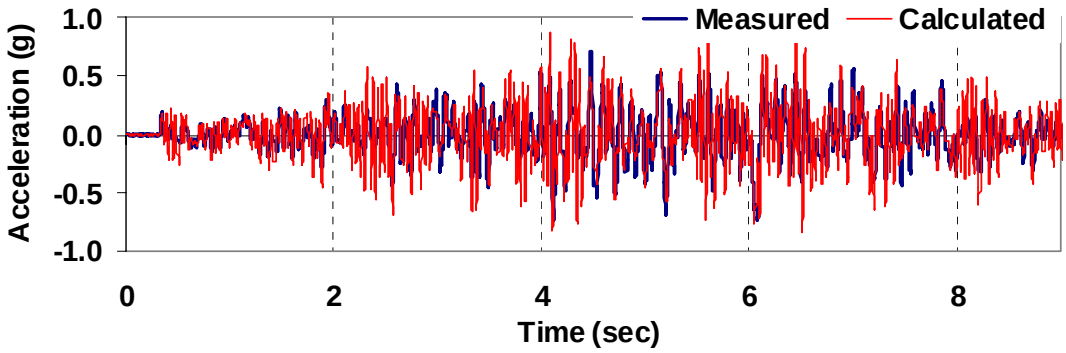

Figure C.45: Comparison of acceleration in the E-W direction at the top of south wall (PGA =0.5g).

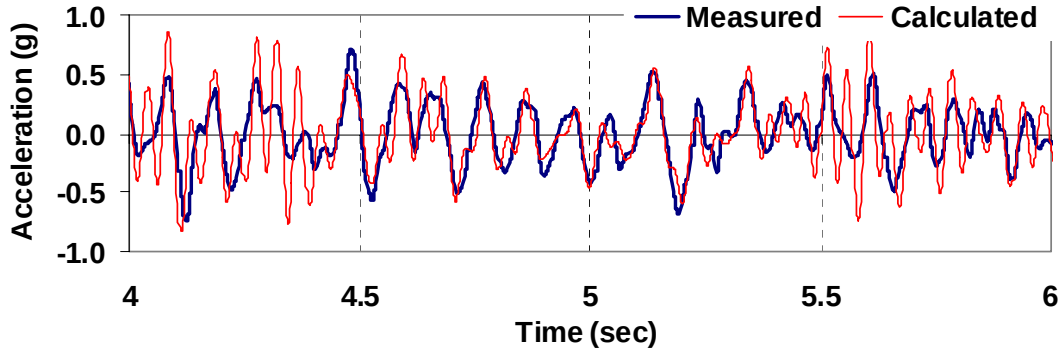

Figure C.46: Two-second comparison of acceleration in the E-W direction at the top of south wall (PGA =0.5g).

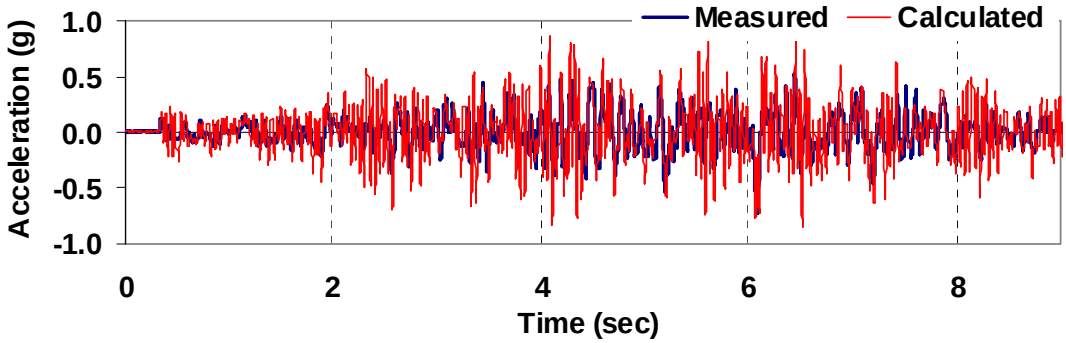

Figure C.47: Comparison of acceleration in the E-W direction at the top of north wall (PGA =0.5g).

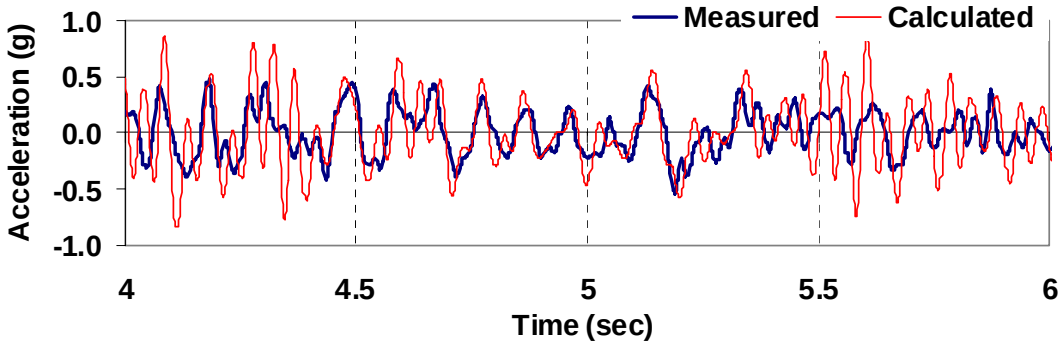

Figure C.48: Two-second comparison of acceleration in the E-W direction at the top of north wall (PGA =0.5g).

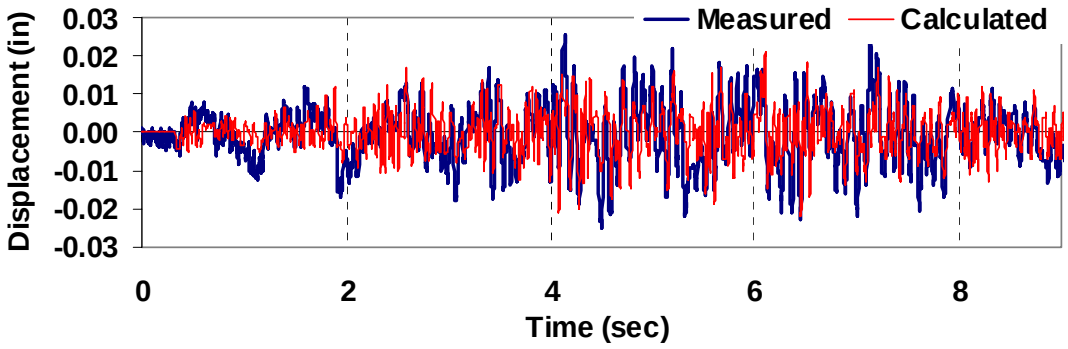

Figure C.49: Comparison of displacement in the E-W direction at the top of south wall (PGA =0.5g).

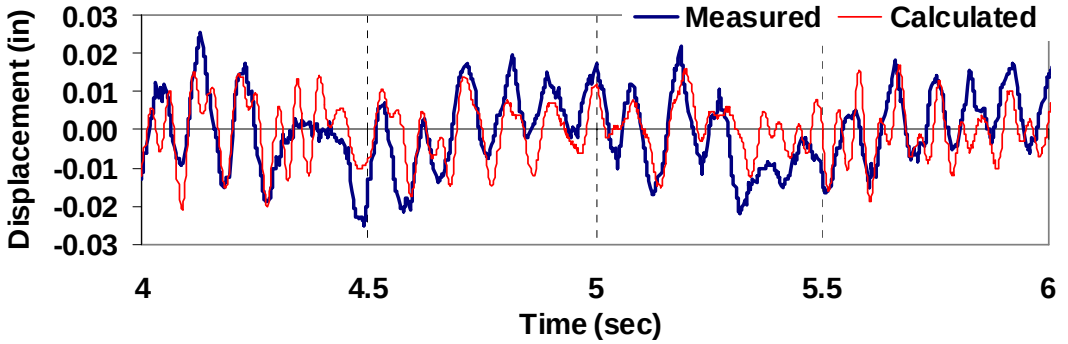

Figure C.50: Two-second comparison of displacement in the E-W direction at the top of south wall (PGA =0.5g).

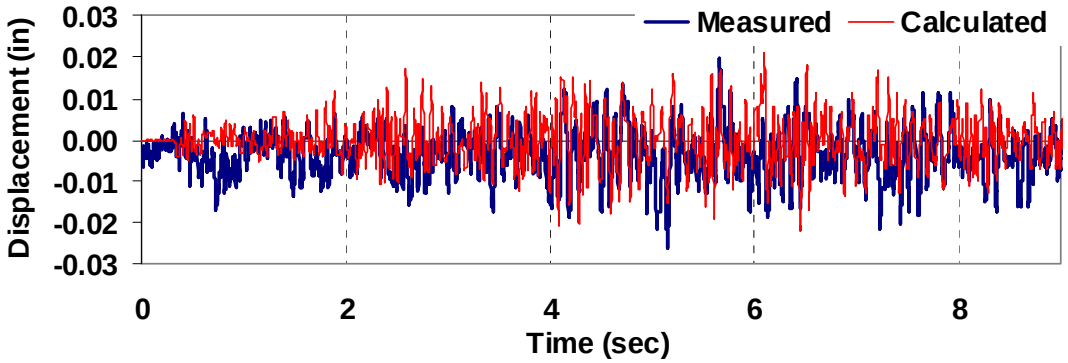

Figure C.51: Comparison of displacement in the E-W direction at the top of north wall (PGA =0.5g).

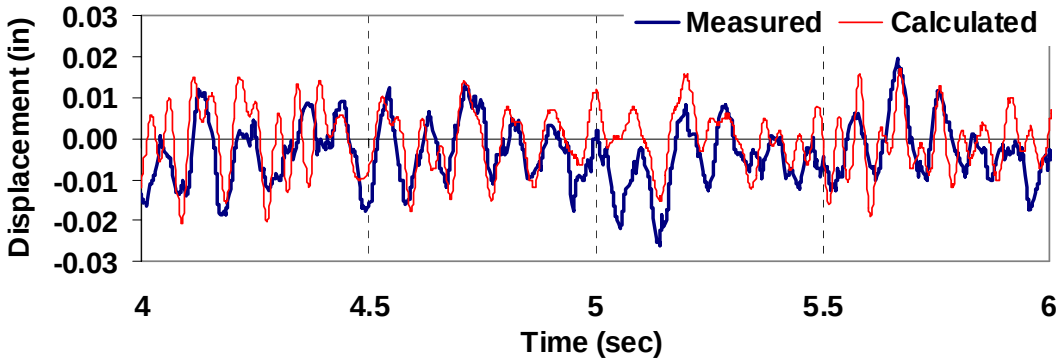

Figure C.52: Two-second comparison of displacement in the E-W direction at the top of north wall (PGA =0.5g).

C.6 Comparison of Measured and Calculated Response using PGA = 0.67 g

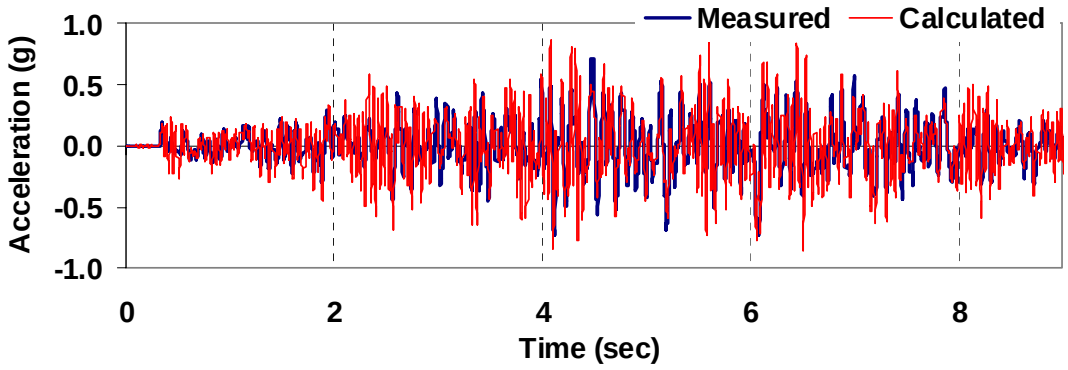

Figure C.53: Comparison of acceleration in the E-W direction at the top of south wall (PGA =0.67g).

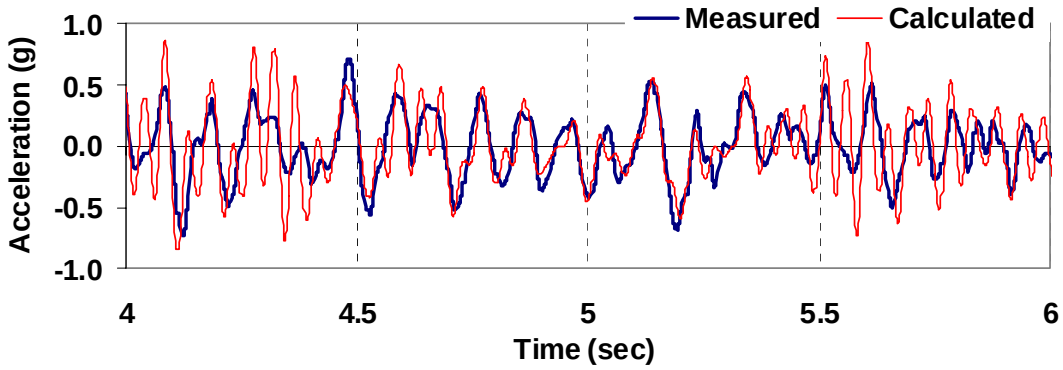

Figure C.54: Two-second comparison of acceleration in the E-W direction at the top of south wall (PGA =0. 67g).

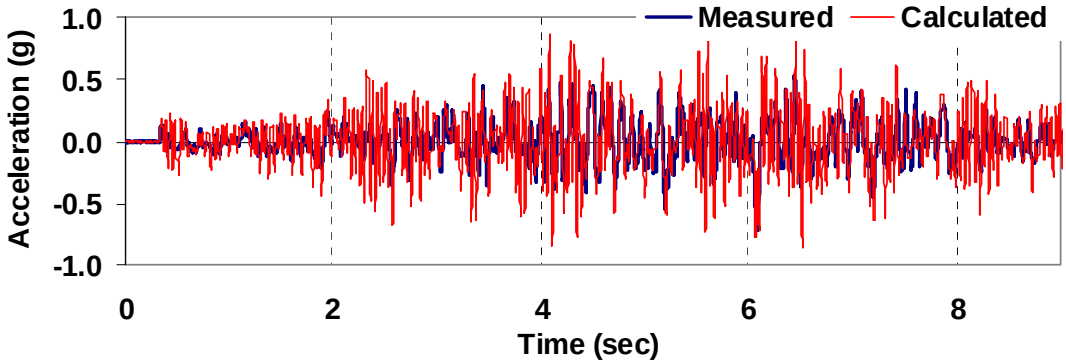

Figure C.55: Comparison of acceleration in the E-W direction at the top of north wall (PGA =0. 67g).

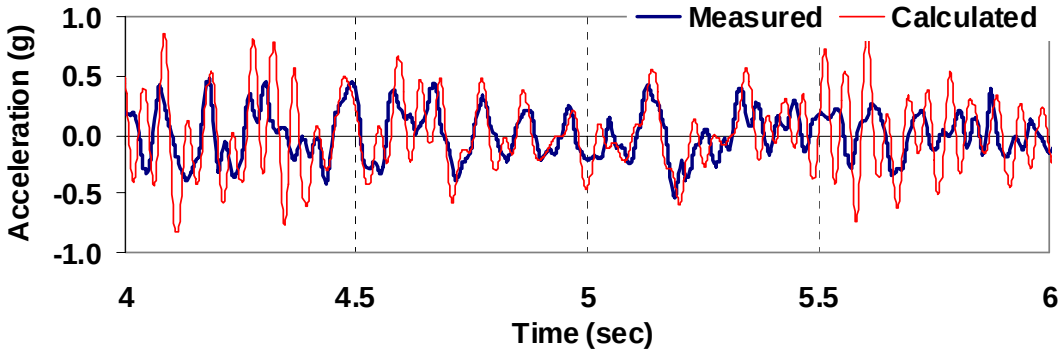

Figure C.56: Two-second comparison of acceleration in the E-W direction at the top of north wall (PGA =0.67g).

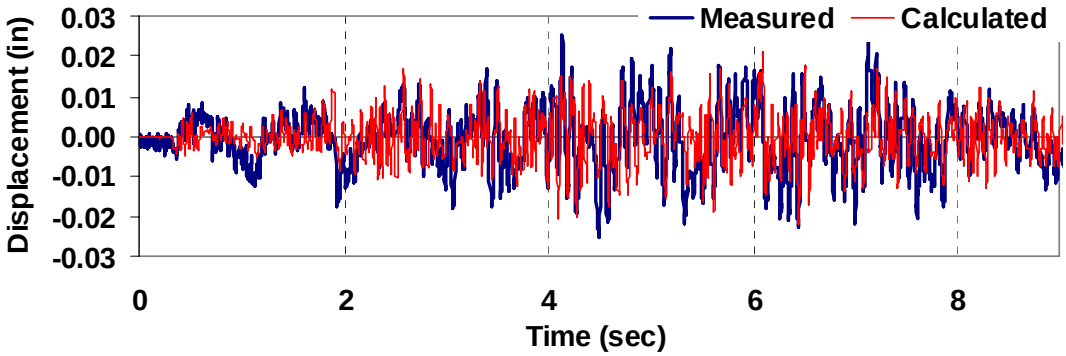

Figure C.57: Comparison of displacement in the E-W direction at the top of south wall (PGA =0. 67g).

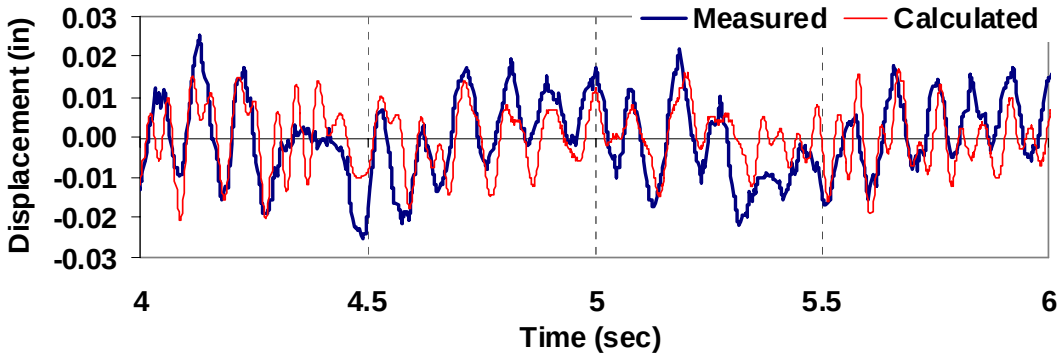

Figure C.58: Two-second comparison of displacement in the E-W direction at the top of south wall (PGA =0. 67g).

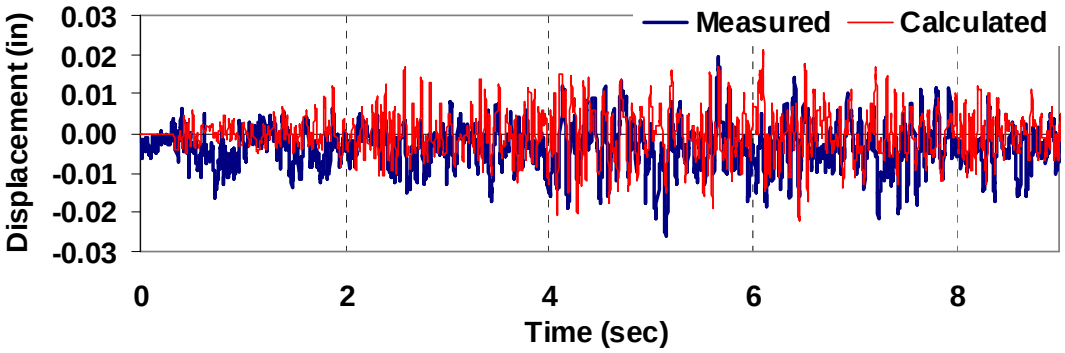

Figure C.59: Comparison of displacement in the E-W direction at the top of north wall (PGA =0. 67g).

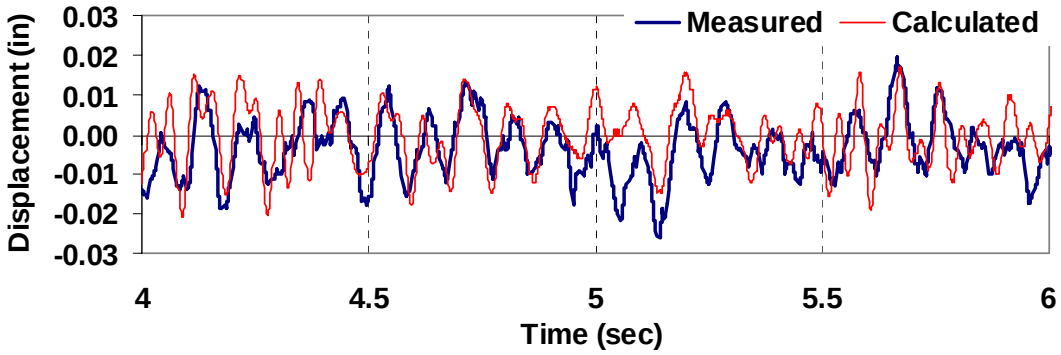

Figure C.60: Two-second comparison of displacement in the E-W direction at the top of north wall (PGA =0. 67g).

C.7 Comparison of Measured and Calculated Response using PGA = 1.0 g

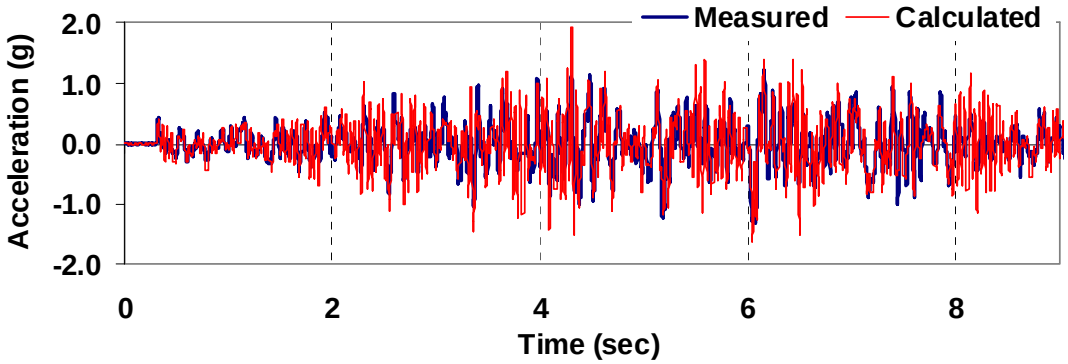

Figure C.61: Comparison of acceleration in the E-W direction at the top of south wall (PGA =1.0g).

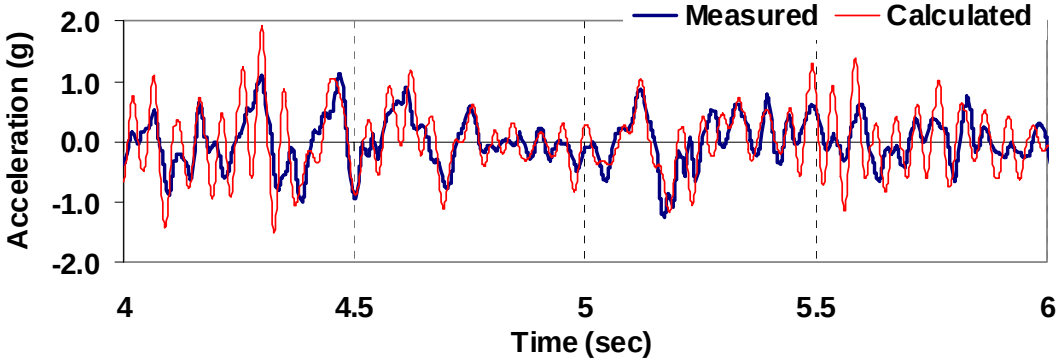

Figure C.62: Two-second comparison of acceleration in the E-W direction at the top of south wall (PGA = 1.0g).

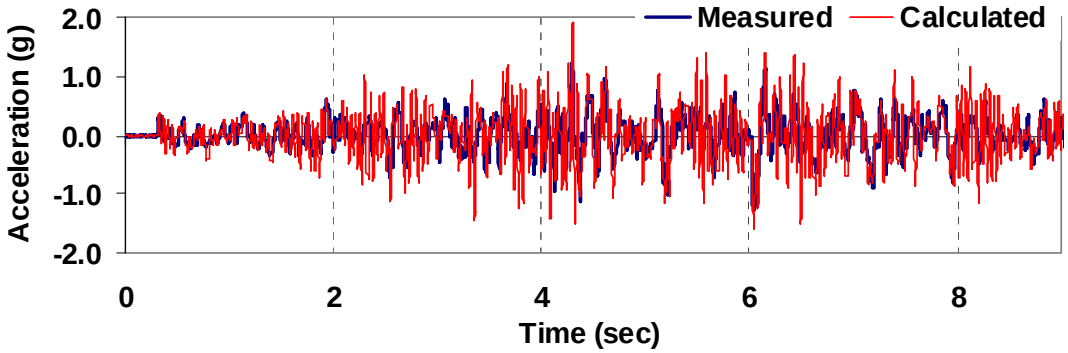

Figure C.63: Comparison of acceleration in the E-W direction at the top of north wall (PGA = 1.0g).

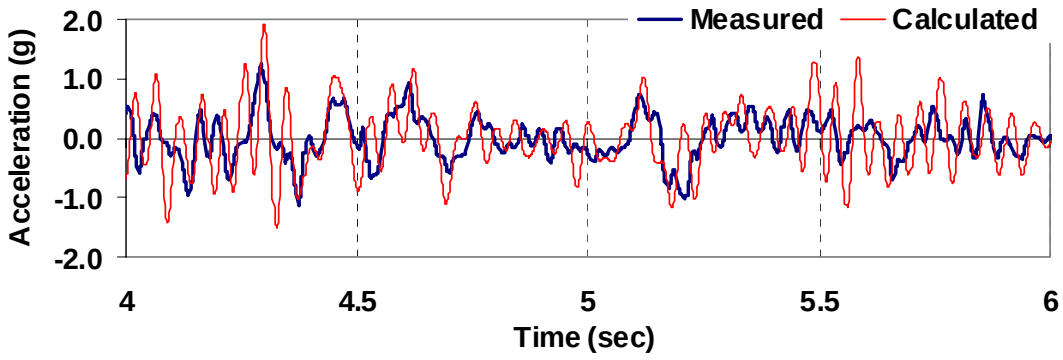

Figure C.64: Two-second comparison of acceleration in the E-W direction at the top of north wall (PGA = 1.0g).

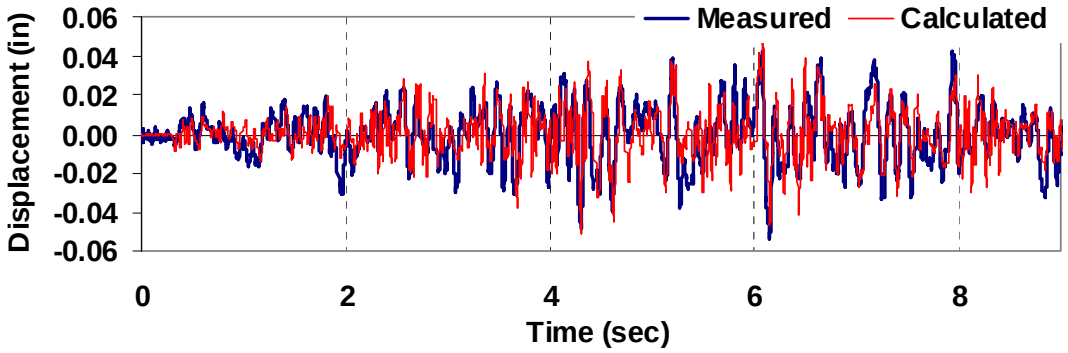

Figure C.65: Comparison of displacement in the E-W direction at the top of south wall (PGA = 1.0g).

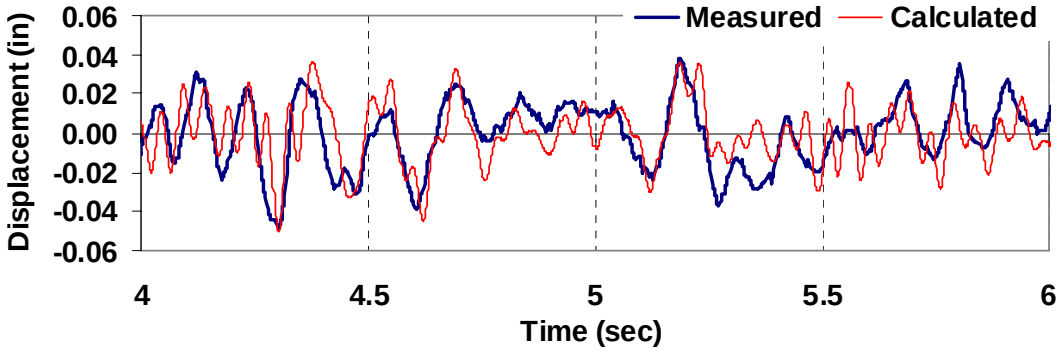

Figure C.66: Two-second comparison of displacement in the E-W direction at the top of south wall (PGA = 1.0g).

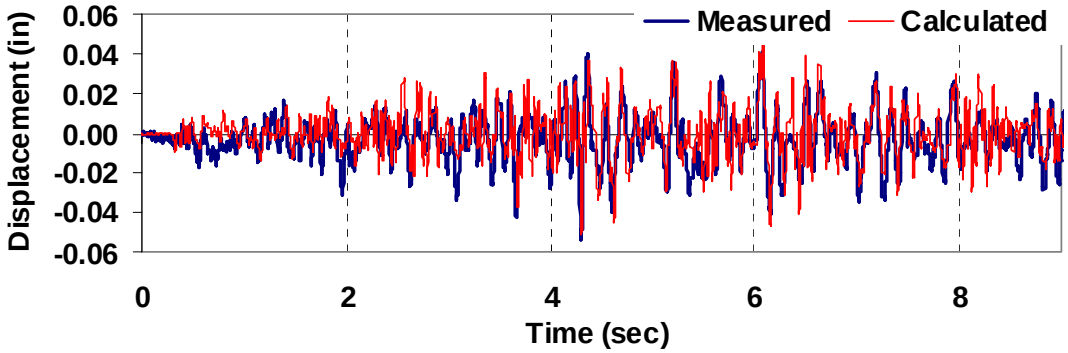

Figure C.67: Comparison of displacement in the E-W direction at the top of north wall (PGA = 1.0g).

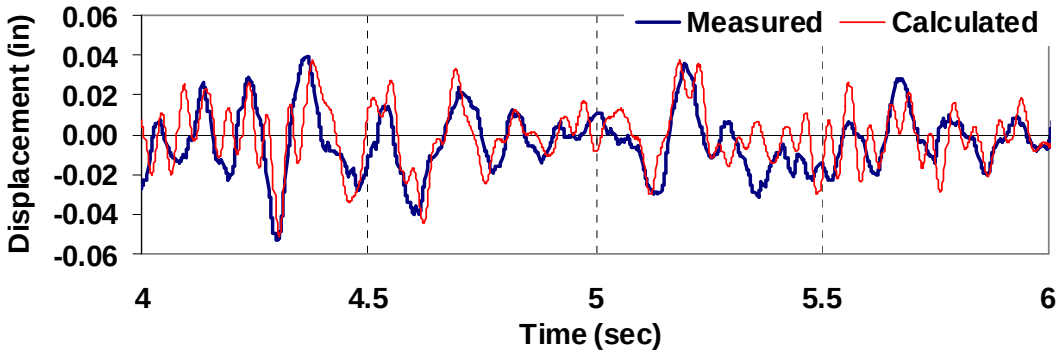

Figure C.68: Two-second comparison of displacement in the E-W direction at the top of north wall (PGA = 1.0g).

APPENDIX D

ANALYSIS SYSTEM

D.1 Overview of ABAQUS user element library

The ABAQUS finite element system has been used as a general-purpose finite element program. This system is operational on Windows NT and UNIX systems. ABAQUS/ Standard is a versatile analysis tool with a large number of element libraries that allows analysis of complex structural problems. And it has an interface that allows users to implement linear and nonlinear finite elements. User subroutines that are available in ABAQUS gives an extremely powerful and flexible tool for analysis. These subroutines (UEL, UMAT, UMATHT, UMATHT, UGENS, and so on) are typically written as FORTRAN code and are used to extend the capabilities of ABAQUS. UEL subroutine is used to make User-defined elements which are invoked in the same way as native ABAQUS elements (ABAQUS 1998).

The wall and diaphragm elements discussed in previous chapters were implemented in a user subroutine UEL. The interface makes it possible to define any element of arbitrary complexity. Multiple user elements can be implemented in a single UEL routine and can be utilized together.

The software developed in this project, as shown in Fig. D.1, can model three-dimensional Low-Rise buildings with flexible floor diaphragms. Currently, one nonlinear wall and one diaphragm element are included in the code. A schematic model of a representative low-rise building is shown in Fig. D.2. The nonlinear wall element is designed to represent a bearing wall under shear loadings. Diagonal shear, bed joint sliding, rocking and toe crushing behavior of shear walls are considered in the wall element.

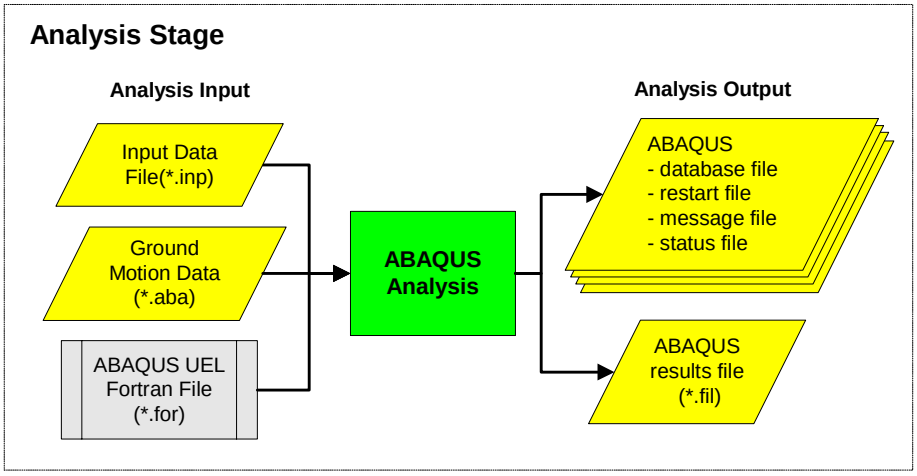

Figure D.1: General ABAQUS Implementation Concepts.

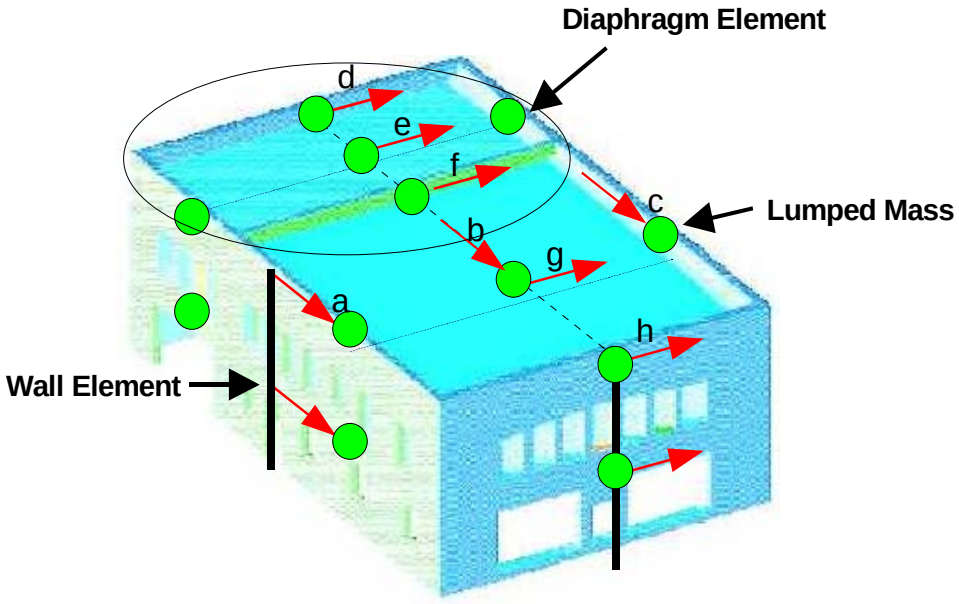

Figure D.2: A schematic modeling of an arbitrary structure.

The diaphragm element is based on a plate girder analogy as discussed in Section 3.5. Detailed formulation of the usage of UEL element libraries is shown in the ST5 UEL Manual: Diaphragm and Wall Elements for Analysis of Low-Rise Building Structures. To

use the manual, it is assumed that reader is familiar with the nonlinear time history analysis and the format of ABAQUS input data files.

D.1.1 Types of analysis

The software developed in this project has the capability of the static and dynamic analysis (Nonlinear Time history analysis) with any combination of several static or dynamic loading conditions. For the static analysis, there are two types of analysis: linear and nonlinear static analysis. Linear static analysis involves the specification of load cases and appropriate boundary conditions. In most nonlinear analyses the loading variations over the step follow a prescribed displacement or force history.

For the nonlinear time history analysis, the general direct-integration method provided in ABAQUS/Standard, called the Hilber-Hughes-Taylor operator, is used (Hilber et al, 1978). The integration method is an extension of the trapezoidal rule. A set of simultaneous nonlinear dynamic equilibrium equations must be solved at each time increment. ABAQUS/Standard generally uses Newton's method to solve the nonlinear equilibrium equations. The principal advantage of the Hilber-Hughes-Taylor operator is unconditionally stable for linear systems.

Damping.

ABAQUS is using an artificial damping, which is purely numerical. The ALPHA parameter introduces damping that grows with the ratio of the time increment to the period of vibration of a mode. In this project, the Newmark β-Method is used. Since the Newmark β-Method, which gives no artificial damping, is exactly the trapezoidal rule, the ALPHA parameter in ABAQUS is set to zero.

Baseline correction.

For a dynamic analysis, when an amplitude definition, such as earthquake acceleration history, is used, the integration of the acceleration record through time may result in a relatively large displacement at the end of the event. This behavior typically occurs because of instrumentation errors or a sampling frequency that is not sufficient to capture the actual acceleration history. It is possible to compensate for it by using "baseline correction."

ABAQUS allows an acceleration history to be modified to minimize the overall drift of the displacement obtained from the time integration of the given acceleration. The use of more correction intervals provides tighter control over any “drift” in the displacement at the expense of more modification of the given acceleration trace. In either case, the modification begins with the start of the amplitude variation and with the assumption that the initial velocity at that time is zero.

Absolute and Relative Response.

Research engineers use two types of energy equations to study single-degree-of-freedom systems subject to earthquake induced ground motions. The first method uses an absolute energy formulation; the second method uses a relative energy formulation. While the relative energy formulation has been used in the majority of previous investigations. The reference study shows that the absolute energy equation is physically more meaningful (Chia-Ming Uang et al, 1990).

The use of an ‘absolute’ energy equation rather that a ‘relative’ energy equation has the advantage that the physical energy input is reflected. For certain types of earthquake ground motion, the absolute input energy spectra are sensitive to the variation of ductility ratio. Except for the highly harmonic earthquakes, the absolute input energy spectra for a constant ductility ratio can be predicted reliably by the elastic input energy spectra using Iwan’s procedure which takes into consideration the effect of increasing

damping ratio and natural period. For steel dual systems of medium rise buildings it is possible to estimate with sufficient accuracy the input energy for a multi-story building structure from the absolute input energy spectra for a SDOF system and the fundamental period of the multi-story structure.

The first objective of this paper is to analyze the physical meaning of two energy equations that are derived and used in the literature. The second objective is to use these two definitions to construct inelastic input energy spectra for a SDOF system.

D.1.2 ABAQUS user element definitions

Defining a User Element

Before a UEL routine can be written, the following key characteristics of the element must be defined: The number of nodes on the element, the number of coordinates present at each node and the degrees of freedom active at each node. In addition, the following properties must be determined: 1) the number of element properties need to be defined external to the UEL for each element type, and 2) the number of solution-dependent state variables (SDVs) must be stored for each element type. These items need not be determined immediately: they can be added easily after the basic UEL subroutine is completed.

User Elements

In this project, three wall elements and two diaphragm elements are developed. These elements are defined as follows:

1. Combined Kinematic and Isotropic Hardening Wall Element
2. Rocking Wall Element
3. Park's Three Parameter Wall Element

4. Combined Kinematic and Isotropic Hardening Diaphragm Element

5. Park's Three Parameter Diaphragm Element

The diaphragm elements can be categorized into two types. The first type considers the effect of the bending and shear of the diaphragm at the same time, and the second type accounts for only shear of the web.

D.1.3 UEL Interface (Input file variables)

A user element is defined with the *USER ELEMENT option. This option must appear in the input file before the user element is invoked with the *ELEMENT option.

The syntax for interfacing to UEL is as follows:

* USER ELEMENT TYPE=Un , NODES= , COORDINATES= ,

PROPERTIES= , I PROPERTIES= , VARIABLES=, UNSYMM

Data line(s)

*ELEMENT,TYPE=Un, ELSET=UEL

Data line(s)

*UEL PROPERTY,ELSET=UEL

Data line(s)

*USER SUBROUTINE, (INPUT=filename)

Example)

*UEL PROPERTY,ELSET=UTRUSS

1.0, 10000000., 0.2, 10., 100000., 20000., 0.0

AREA, E, NU (poisson's ratio), RHO (material density), Et (inelastic tangent modulus of matl), Fyi, (initial yield stress of matl) , AISO (Isotropic hardening fraction)

Table D.1: Outline UEL Input Variables.

VARIABLES	NOTE
TYPE	(User defined) element type of the form Un, where n is a number
NODES	Number of nodes on the element
COORDINATES	Maximum number of coordinates at any node
PROPERTIES	Number of floating point properties
I-PROPERTIES	Number of integer properties
VARIABLES	Number of SDVs
UNSYMM	Flag to indicate that the Jacobian is non symmetric

D.2 Definition of earthquake accelerations

As shown in Fig. D.1, a dynamic analysis in ABAQUS is defined by two input file: model data and history data. To define the earthquake acceleration in model data file, the *amplitude option is used.

Example)

*amplitude, definition=tabular, value=relative, input=ch3m2a.acc, name=earth

The earthquake acceleration loading is prescribed as a function of time, so called “Amplitude curves”. This feature is used to prescribe a seismic event. The INPUT option is used to specify an external file that contains history definition data. When the option is encountered, ABAQUS will immediately process the input data within the file specified by the INPUT parameter. When the end-of-file is reached, ABAQUS returns to processing the original file.

D.3 Overview of JAV (JAVA Based ABAQUS Viewer)

D.3.1 OVERVIEW

For the development of MDOF modeling of Low-Rise Building with ABAQUS UEL, ABAQUS CAE and Post do not support UEL (User Element Library) well. Because of that, it is not efficient to handle the analysis output files from ABAQUS. In addition, ABAQUS nonlinear time history analysis output files (i.e. *.dat, *.fil, or *.res) are too big to be handled for a number of analysis in this research. So, it is needed to develop a light-weight program like this program.

C.2 Software systems employed by JAV

In order to develop this application, the used software and library are shown below.

- Main Development Platform: VisualAge for Java, Ver. 3.5
- Java compiler: JDK1.3
- Three-Dimensional Graphic Library: Java 3D Ver. 1.2.1
- XY-Plot library: Ptolemy Ver. 1.3
- Excel Plot Macro Language: Visual Basic.

C.3 Overall Dataflow

Figure C.1 shows the overall dataflow of the analysis. As mentioned early, there are several analysis output files generated from ABAQUS. Among them, the ABAQUS results file (job-name.fil) can be read by ABAQUS/Post to produce - plots or printed tabular output. The result file is converted into jobname.fia file using the data extraction program. This extraction module is written in Fortran. The main purpose of this process is to extract the essential data from the ABAQUS result file. The size of the extracted file from the results file is reduced from the process. It will be used for the Java-based ABAQUS

viewer (JAV) program to handle the analysis results. In JAV program there are several capabilities: X-Y plotting of nodal relative and absolute displacement, velocity, and acceleration history; X-Y plot of wall element force and displacement history; and animation of the whole structure. The hardcopy of example snaps captured from the screen are shown in next section.

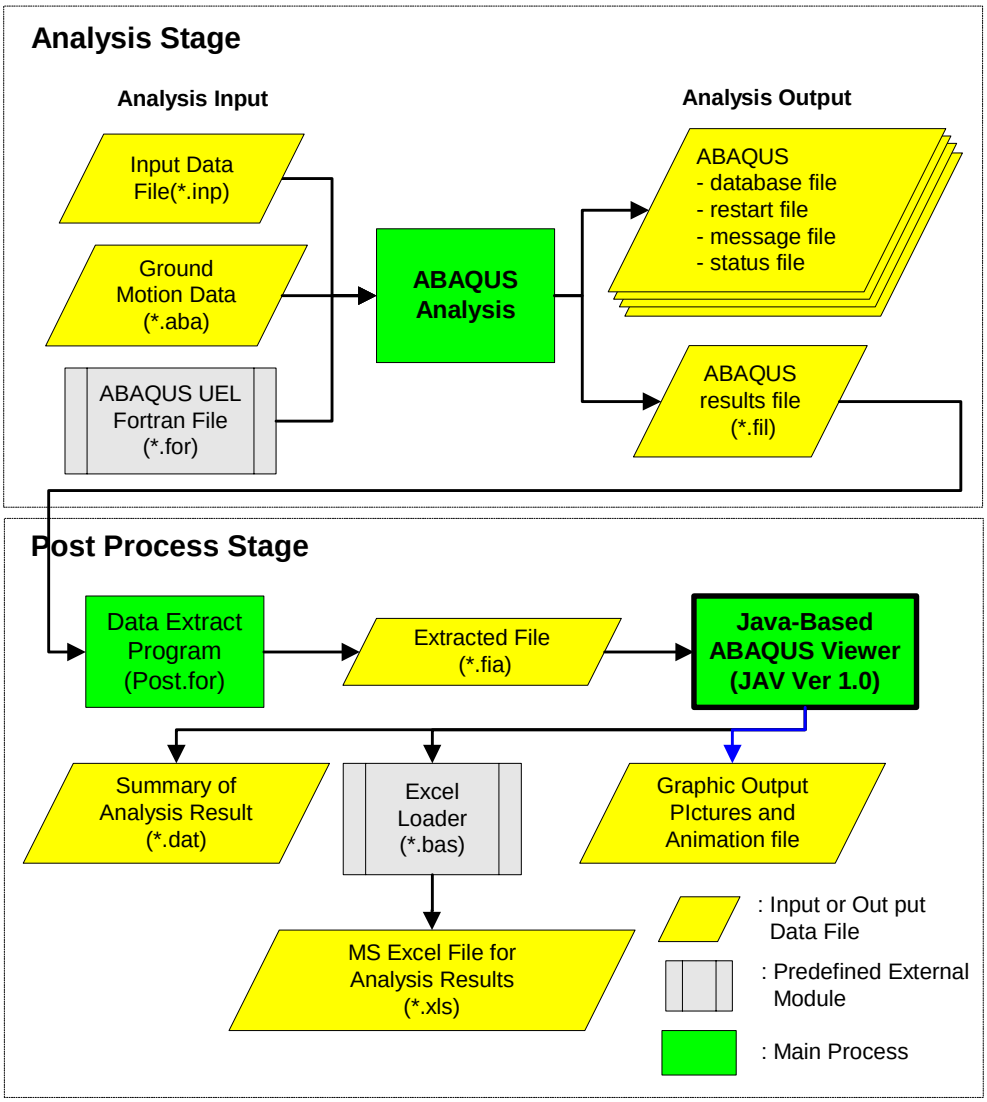

Figure D.3: Overall Dataflow.

D.3.2 Main Program

The 3D graph of this program is constructed by a Java 3D program. The mouse utility behavior package contains behavior classes in which the mouse is used as input for interaction with visual objects. Included are classes for translating (moving in a plane parallel to the image plate), zooming (moving forward and back), and rotating visual objects in response to mouse movements

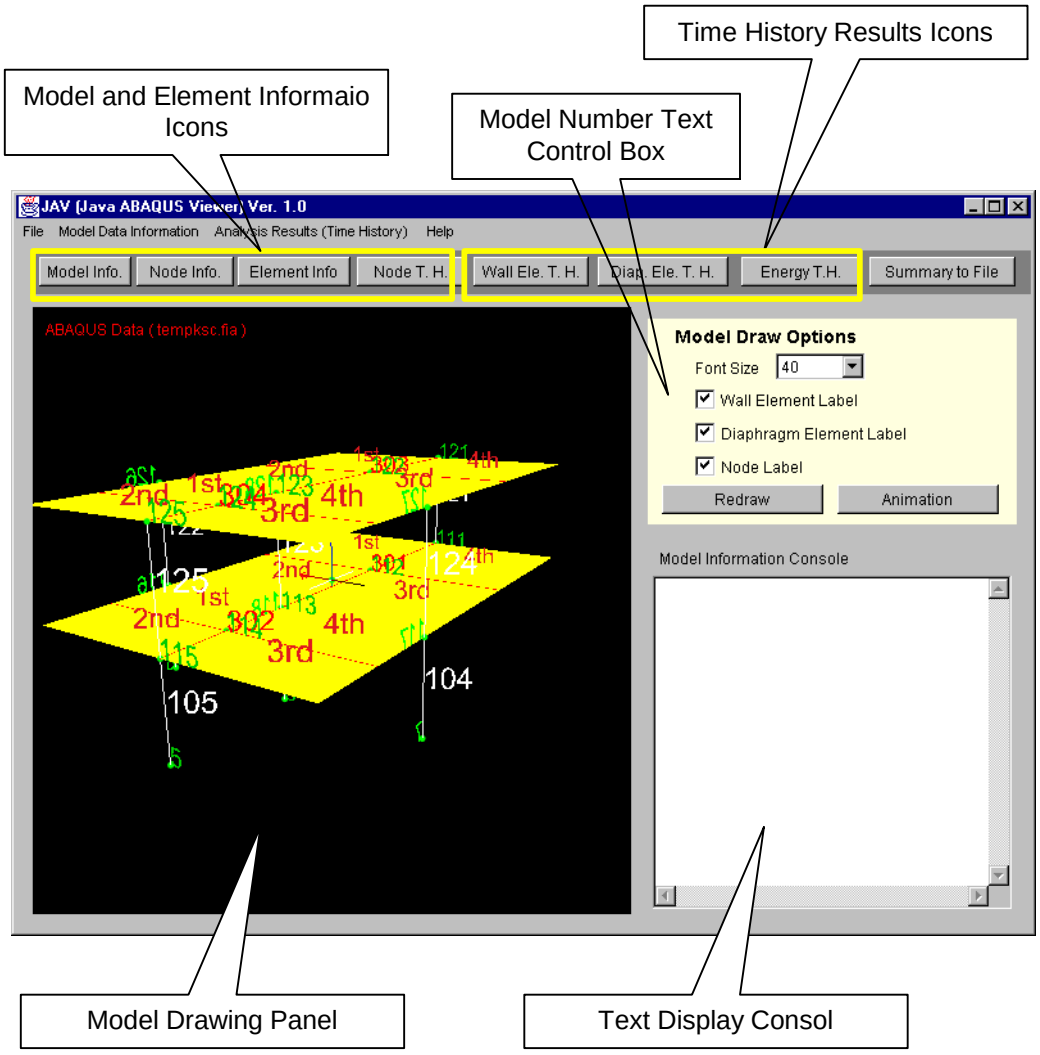

Figure D.4: Main Program.

REFERENCES

ABK (1981a). “Methodology for mitigation of seismic hazards in existing unreinforced masonry buildings: Categorization of buildings.” *ABK Tech. Rep. 01*, ABK, A Joint Venture, El Segundo, Calif.

ABK (1981b). “Methodology for mitigation of seismic hazards in existing unreinforced masonry buildings: Diaphragm testing.” *ABK Tech. Rep. 03*, ABK, A Joint Venture, El Segundo, Calif.

ABK (1984). “Methodology for mitigation of seismic hazards in existing unreinforced masonry buildings: Diaphragms: the methodology.” *ABK Tech. Rep. 08*, ABK, A Joint Venture, El Segundo, Calif.

Abrams, D. P. (1992). “Strength and behavior of unreinforced masonry elements.” *Proc. 10th World Conf. on Earthquake Engineering*, Madrid, Spain, Vol. 10, 3475-3480.

Abrams, D. P. (2001). “Performance-based engineering concepts for unreinforced masonry building structures.” Progress in Structural Engineering and Materials, Vol. 3, Issue 1, pp. 48-56.

Adhikari, S. and Woodhouse, J. (2001) “Identification of Damping: Part 1, Viscous Damping.” Journal of Sound and Vibration, 243(1), 43-61

Ali, S. S. and Page, A. W. (1988). “Finite element model for masonry subjected to concentrated loads.” J. Struct. Engrg., ASCE, 114(8), 1761 - 1784.

Anand, S.C. and Yalamanchili, K.K. (1996). “ Three-dimensional failure analysis of composite masonry walls.” J. Struct. Engrg., ASCE, 122(9), 1031-1039

APA (1997a). “DIAPHRAGMS AND SHEAR WALLS.” American Plywood Association, Tacoma, Wash.

APA (1997b). “Plywood Design Specification” American Plywood Association, Tacoma, Wash.

Argyris, J. H. et al. (1978). “Finite Element Method - the Natural Approach.” Comput Methods in Applied Mechanics and Engineering, Vols. 17/18, 1-106

ASCE (2000a). “FEMA 356: Prestandard and Commentary for the Seismic Rehabilitation of Buildings.” Publication No. 356, prepared by the American Society of Civil Engineers, funded by the Federal Emergency Management Agency,American Society of Civil Engineers, Washington, DC.

ASCE (2000b). “FEMA 357: Global Topics Report on The Prestandard and Commentary for The Seismic Rehabilitation of Buildings.” Publication No. 357, prepared by the American Society of Civil Engineers, funded by the Federal Emergency Management Agency,American Society of Civil Engineers, Washington, DC

ATC (1981). “Guidelines for the Design of Horizontal Wood Diaphragms.” Applied Technology Council, ATC 7, Washington, D.C.

ATC (1987). “Tentative Provisions for the Development of Seismic Regulations for Buildings.” ATC 3-06, NBS Special Publication 510, Washington D.C.

ATC (1998). “FEMA 306: Evaluation of Earthquake Damaged Concrete and Masonry wall buildings-Basic Procedures Manual.” Applied Technology Council, ATC-43 Project, Redwood City, CA.

Bathe, K., (1996). “ Finite Element Procedures”, Prentice Hall, Englewood Cliffs, New Jersey.

Benedetti, D., and Castellani, A. (1980). “Dynamic versus static behavior of a masonry structure under lateral loads.” Eng. Struct, Vol. 2, 163-170

Button, M. R., Kelly, T. E., and Jones, L. R. (1984). “The influence of diaphragm flexibility on the seismic response of buildings,” *Proc. 8th World Conf. on Earthquake Engineering,* Vol. 4, San Francisco, CA, 759-766.

Calvi, G. M. and Kingsley, G. R. (1995). “Displacement-based seismic design of multi-degree of-freedom bridge structures.” Earthquake Engineering and Structural Dynamics, Vol. 24, 1247-1266

Carney, J.M. (1975). “Bibliography on wood and plywood diaphragms.” *Journal of the Structural Division*, ASCE, 101(ST11), 2433 - 2436.

Chopra, A. K. (1995). “Dynamics of Structures – Theory and Applications To Earthquake Engineering.” Prentice Hall, Englewood Cliffs, New Jersey

Clough, R.W. and Penzien, J. (1993) “ Dynamics of Structures - 2nd Ed.” McGraw-Hill Inc., New York.

Cohen, G.L. (2001). “Seismic Response of Low-Rise Masonry Buildings with Flexible Roof Diaphragms.” M.S Thesis, University of Texas, Austin.

Cohen, G.L. and Klingner, R. E. (2001a). “Seismic Behavior and Evaluation of Flexible Roof Diaphragms.” US Army CERL report, University of Texas, Austin.

Cohen, G.L. and Klingner, R. E. (2001b), personal communication

Cohen, G.L. (2002), personal communication.

Coil, J. (1999), personal communication.

Cook, R. D., Malkus, D. S., and Plesha M. E. (1989). “Concepts and Applications of Finite Element Analysis - 3rd Ed.” John Wiley & Sons, New York

Costley, A. C., Abrams, D.P., and Calvi, G. M. (1994). “Shaking-Table Testing of An Unreinforced Brick Masonry Building.” Proc., Fifth U.S. National Conference on Earthquake Engrg.,Vol. I, EERI, Chicago, Ill, 127-146.

Costley, A. C. and Abrams, D.P. (1996). “Dynamic response of unreinforced masonry buildings with flexible diaphragms.” *Tech. Rep. NCEER-96-0001,* Nat. Ctr. for Earthquake Engrg. Res., Buffalo, N.Y.

Davies, J. M. (1976). “Simplified diaphragm analysis.” J. Struct. Div., ASCE, 103(11), 2093-2109

DenHartog, J.P. (1985) Mechanical Vibrations - 4th Edition, Dover

Dolce, M., Lorusso, V.D., and Masi, A. (1994). “Seismic response of building structures with flexible inelastic diaphragm.” Struct. Design Tall Build., John Wiley & Sons, Ltd, 3, 87-106

Easterling, R.G.(1999). “A Framework for Model Validation.” Report No: SAND99-0301C, Sandia National Laboratories, Albuquerque, NM, and Livermore, CA.

Easterling, W.S. and Porter, M.L. (1994a). “Steel-Deck-Reinforced Concrete Diaphragm. I.” J. Struct. Engrg., ASCE, 120(2), 560 - 576.

Easterling, W.S. and Porter, M.L. (1994b). “Steel-Deck-Reinforced Concrete Diaphragm. II.” J. Struct. Engrg., ASCE, 120(2), 577 - 596.

Erbay, O. O. and Abrams, D.P.(2002). “Seismic rehabilitation of unreinforced masonry shear walls.” Proc. Seventh U.S. National Conference on Earthquake Engrg., EERI, Boston, Massachusetts.

CEN (1995). “Eurocode 6: Design of masonry structures, Part 1-1: General rules for buildings. Rules for reinforced and unreinforced masonry.” European Committee for Standardization, ENV 1996-1-1, Brussels

Ewing, R. D., El-Mustapha, A. M., and Kariostis, J. C. (1987). “FEM / I: A finite element computer program for the nonlinear static analysis of reinforced masonry building components.” EKEH (Ewing / Kariostis / Englekirk & Hart Ewing & Associates), CA

Falk, R. H. and Itani, R. Y. (1987). “Dynamic Characteristics of wood and gypsum diaphragms.” J. Struct. Engrg., ASCE, 113(6), 1357-1370.

Falk, R. H. and Itani, R. Y. (1989). “Finite element modeling of wood diaphragms.” J. Struct. Engrg., ASCE, 115(3), 543 - 559.

FEMA (1992a). “Evaluation of unreinforced masonry bearing wall buildings.” NEHRP handbook for the seismic evaluation of existing buildings; *Federal Emergency Mgmt. Agency, Rep. No. 178*, Build. Seismic Safety Council, Washington, D.C.

FEMA (1992b). “NEHRP Handbook for the Seismic Evaluation of Existing Buildings.” *Federal Emergency Mgmt. Agency, Rep. No. 178*, Washington, D.C.

FEMA (1997a). “NEHRP Guidelines for the Seismic Rehabilitation of Building.” *Federal Emergency Mgmt. Agency, Rep. No. 273*, Build. Seismic Safety Council, Washington, D.C.

FEMA (1997a). “NEHRP Commentary on the Guidelines for the Seismic Rehabilitation of Building.” *Federal Emergency Mgmt. Agency, Rep. No. 274*, Washington, D.C.

FEMA (1997c). “NEHRP Recommended Provisions For Seismic Regulations for New Buildings and Other Structures, Part 1-Provisions.” *Federal Emergency Mgmt. Agency, Rep. No. 302*, Washington, D.C.

FEMA (1997d). “NEHRP Recommended Provisions For Seismic Regulations for New Buildings and Other Structures, Part 2-Commentary.” *Federal Emergency Mgmt. Agency, Rep. No 303*, Washington, D.C.

Goldberg, J. E. and Herness, E. D. (1965). “Vibration of Multistory buildings considering floor and wall deformations.” Bulletin of the seismological society of America, 55(1), 181-200.

HKS (1998). “ABAQUS *theory and user’s manual-Version 5.8.”* Hibbit, Karlsson & Sorensen, Inc., Providence, R.I.

Hilber, H.M., Hughes, T.J.R. and Taylor, R.L. (1978). “Collocation, Dissipation and ‘Overshoot’ for Time Integration Schemes in Structural Dynamics.” Earthquake Engineering and Structural Dynamics, 6, 99-117

Hjelmstad, K.D., and Foutch, D.A. (1988). “Response Spectrum Analysis of Buildings with Flexible Bases.” Unpublished Paper, University of Illinois at Urbana-Cham-

paign, IL.

ICC (2000). "*International Building Code."* International Code Council, Falls Church, VA.

Itani, R. Y. and Cheung, C. K. (1984). "Nonlinear Analysis of sheathed wood diaphragms." J. Struct. Engrg., ASCE, 110(9), 2137 - 2147.

Jain, S. K., and Jennings, P. C. (1985). "Analytical models for low-rise buildings with flexible floor diaphragms." Earthquake Engng. & Struct. Dynam., Vol. 13, 225-241.

Jain, S. K., and Sharma, R. (1988). "Dynamic response of a setback building with a flexible floor diaphragm." *Proc. 9th World Conf. on Earthquake Engineering*, Tokyo-Kyoto, Japan, Vol. 5, 479-484.

Kappos, A.J., Penelis, G. G., and Drakopoulos, C. G. (2002). "Evaluation of simplified models for lateral load analysis of unreinforced masonry buildings." J. Struct. Engrg., ASCE, 128(7), 890 - 897.

Karadogan, H. F. (1980). "Earthquake analysis of 3D structures with flexible floors." *Proc. 7th World Conf. on Earthquake Engineering*, Istanbul, Turkey, 261-266

Kariostis, J. C., Rahman, A. M. D., Waqfi, O. M., and Ewing, R. D. (1992a). "LPM/I: A computer program for the nonlinear, dynamic analysis of lumped parameter models." US - Japan coordinated program for masonry building research, EKEH

Kariostis, J. C., Waqfi, O. M., and Ewing, R. D. (1992b). "LPM/II: A computer program using beam elements for the nonlinear, dynamic analysis of lumped parameter models." US - Japan coordinated program for masonry building research, EKEH

Kim, S. C.and White, D. W (2001). "Seismic Assessment of Existing Unreinforced Masonry Buildings." KEERC-MAE Joint Seminar on Risk Mitigation for Regions of Moderate Seismicity, University of Illinois at Urbana-Champaign, August 5-8.

Klingner, R. E., Villablanca, R., Blondet, M., and Mayes, R. L. (1990). "Masonry structures in the Chilean earthquake of March 3, 1985: behavior and correlation with analysis." The Masonry Society Journal, 9(1), 20-25.

Krawinkler, H. and Seneviratna, G.D.P.K. (1998). "Pros and cons of a pushover analysis of seismic performance evaluation." Eng. Struct., Elsevier Sci. Ltd. Engl., 20(4-6) 452-464.

Kunnath, S. K., Mehrain, M., and Gates, W. E. (1994). "Seismic damage-control design of gypsum-roof diaphragms." J. Struct. Engrg., ASCE, 120(1), 120 - 138.

Kunnath, S. K., Panahshahi, N., and Reinhorn, A. M. (1991). "Seismic response of RC

buildings with inelastic floor diaphragms." J. Struct. Engrg., ASCE, 117(4), 1218 - 1237.

Kunnath, S. K., Reinhorn, A. M., and Park, Y. J. (1990). "Analytical modeling of inelastic seismic response of R/C structures." J. Struct. Engrg., ASCE, 116(4), 996 - 1017.

Lee, D.-G. and Moon, S.-K. (1989). "Seismic response of multistory building structures with flexible floor diaphragms." Structural Design, Analysis and Testing Proceedings of the sessions at Structures Congress '89, San Francisco, CA, 547-556

Leiva, G. and Klingner, R. E. (1994). "Behavior and design of multi-story masonry walls under in-plane seismic loading." The Masonry Society Journal, 13 (1), 15-24.

Lopez, O. A., Raven, E., and Anichiarico, W. (1994). "Effect of floor plan shape on the seismic response of building." Proc., The fifth U.S. national conference on earthquake engineering, EERI, ChicagoEl Cerrito, CA, Vol. 1, 147-156

Lourenco, P. B., Rots, J. G., and Blaauwendraad, J. (1998). "Continuum model for masonry: Parameter estimation and validation." J. Struct. Engrg., ASCE, 124(6), 63-80

Magenes, G. and Calvi, G. M. (1994) "Shaking table tests on brick masonry walls." 10th European Conf. Earthquake Engng, Vienna, 2419-2424

Magenes, G and Calvi, G..M. (1997). "In-plane seismic response of brick masonry walls." Earthquake Engineering and Structural Dynamics, John Wiley & Sons, Ltd., Vol. 26, 1091-1112.

Masi, A., Dolce, M., and Caterina, F. (1997). "Seismic response of irregular multi-storey buildings with flexible inelastic diaphragms." Struct. Design Tall Build., John Wiley & Sons, Ltd, 6, 99-124

Medhekar, M.S. and Kennedy, D.J.L. (2000a). "Displacement-based seismic design of buildings-theory." Engineering Structures, Elsevier Science Ltd, Vol. 22, 201-209.

Medhekar, M.S. and Kennedy, D.J.L. (2000b). "Displacement-based seismic design of buildings-application." Engineering Structures, Elsevier Science Ltd, Vol. 22, 210-221.

Moroni, M.O., Astroza, M., and Gomez, J. (1992). "Seismic force reduction factor for masonry building." *Proc. 10th World Conf. on Earthquake Engineering*, Madrid, Spain, 4521-4524

MSJC (1999a). "Building Code Requirements for Masonry Structures." ACI 530-99 / ASCE 5-99 / TMS 402-99, by The Masonry Standards Joint Committee.

MSJC (1999b). “Commentary on Building Code Requirements for Masonry Structures.” ACI 530-99 / ASCE 5-99 / TMS 402-99, by The Masonry Standards Joint Committee.

MSJC (1999c). “Specification for Masonry Structures.” ACI 530.1-99 / ASCE 6-99 / TMS 602-99, by The Masonry Standards Joint Committee.

MSJC (1999d). “Commentary on Specification for Masonry Structures.” ACI 530.1-99 / ASCE 6-99 / TMS 602-99, by The Masonry Standards Joint Committee.

Nakashima, M, Huang, T, and Lu, L.W. (1982). “Experimental study of beam-supported slabs under in-plane loading.” J. American Concrete Institute, 79, 59-65

Nilson, A. H. and Ammar, A. R. (1974). “Finite element analysis of metal deck shear diaphragms.” J. Struct. Div., ASCE, 100(ST4), 711 - 726

Page, A. W. (1998). “Masonry research for the 21st century - An australian perspective.” Conf. on Structural engineering world wide, San Francisco, Calif.

Panahshahi, N., Reinhorn, A. M., Kunnath, S. K., Lu, L.-W., Huang, T., and Yu, K. T. (1991). “Seismic response of a 1:6 reinforced concrete scale-model structure with flexible floor diaphragms.” ACI Structural Journal, 88(3), 315-324

Paquette, J. and Bruneau, M. (2000). “Pseudo-dynamic testing of unreinforced masonry buildings with flexible diaphragm.” *Proc. 12th World Conf. on Earthquake Engrg.*, Auckland, New Zealand, Paper No. 1367 (CD-ROM)

Paquette, J., Bruneau, M., and Filiatrault, A. (2001). “Out-of-plane seismic evaluation and retrofit of turn-of-the-century north American masonry walls.” J. Struct. Engrg., ASCE, 127(5), 561 - 569

Paulson, T. J., and Abrams, D. P. (1990). “Correlation between static and dynamic response of model masonry structures.” Earthquake Spectra, 6 (3), 573-591

Peralta, D. F., Bracci, J. M. and Hueste M. B. D. (2000). “Seismic Performance of Rehabilitated Floor and Roof Diaphragms.” ST-8 project final report, Mid-America Earthquake Center, National Science Foundation, Texas A&M Univ. Dept. of Civil Eng. College, Texas.

Pomonis, A., Spence, R. J. S., Coburn, A. W., and Taylor, C. (1992). “Shaking table tests on strong motion damagingness upon unreinforced masonry.” *Proc. 10th World Conf. on Earthquake Engineering,* Madrid, Spain, Vol. 10, 3533-3538

Priestley, MJN. (1993). “Myths and fallacies in earthquake engineering-conflicts between design and reality.” Bulletin of the New Zeal and National Society for Earthquake Engineering, 26 (3):

Roper, S. C. and Iding, R. H. (1984). “Appropriateness of the rigid floor assumption for building with irregular features.” *Proc. 8th World Conf. on Earthquake Engineering,* Vol. 4, San Francisco, CA, 751-758.

Rutenberg, A. (1969). “Laterally loaded flexible diaphragm buildings.” J. Struct. Div., ASCE, 106(ST9), 1969-1973

Saffarini, H. S. and Qudaimat, M. M. (1992). “In-plane floor deformations in RC structures.” J. Struct. Engrg., ASCE, 118(11), 3089 - 3102

Scawthorn, C., and Becker, A. (1986). “Relative benefits of alternative strengthening methods for low strength masonry buildings.” Proc., The third U.S. national conference on earthquake engineering, EERI, 3, El Cerrito, CA, 2023-2034

Schneider, R. R., and Dickey, W. L. (1994). “Reinforced Masonry Design.” Prentice Hall, Third Edition, 419 – 484

SDI (1995). “DIAPHRAGM DESIGN MANUAL.” Steel Deck Institute, Fox River Grove, IL.

Seible, F., Hegemier, G. A., Igarashi, A., and Kingsley, G. R. (1994). “ Simulated seismic-load tests on full-scale five-story masonry building.” J. Struct. Engrg., ASCE, 120(3), 903 - 924

Shepherd, R. and Donald, R. A. H. (1967). “The influence of in-plane floor flexibility on the normal mode properties of buildings.” J. Sound Vib., 5(1), 29-36.

Shing, P. B., and Cao, L. (1998). “Analysis of partially grouted masonry walls.” Conf. on Structural engineering world wide, San Francisco, Calif.

Shing, P. B., and Klingner, R. E. (1998). “Nonlinear Analysis of Masonry Structures.” Conf. on Structural engineering world wide, San Francisco, Calif.

Suto, F. and Asayama, S. (1988). “Experimental considerations on earthquake behaviours of a large long strip-type of actual structure.” *Proc. 9th World Conf. on Earthquake Engineering,* Tokyo-Kyoto, Japan, Vol. 5, 503-508.

Tena-Colunga, A., and D. Abrams (1992a). “Response of an unreinforced masonry building during the Loma Prieta Earthquake.” Struct. Res. Ser. No. 576, Dept. of Civ. Engrg., Univ. of Illinois at Urbana-Champaign, Urbana, Ill

Tena-Colunga, A., and D. Abrams (1992b). “Response of an instrumented unreinforced masonry shear wall building with flexible diaphragms during the Loma Prieta Earthquake.” Struct. Res. Ser. No. 576, Dept. of Civ. Engrg., Univ. of Illinois at Urbana-Champaign, Urbana, Ill

Tena-Colunga, A., and D. Abrams (1992c). “Response of an unreinforced masonry building during the Loma Prieta Earthquake.” *Proc. 10th World Conf. on Earthquake Engineering,* Madrid, Spain, 79-84

Tena-Colunga, A., and D.P. Abrams (1995). “Simplified 3-D dynamic analysis of structures with flexible diaphragms.” Earthquake engineering and structural dynamics, Vol. 24,No. 2. 221-232

Tena-Colunga, A.(1998). , personal communication.

Tena-Colunga, A., and D. Abrams (1996). “Seismic behavior of structures with flexible diaphragms.” J. Struct. Engrg., ASCE, 122(4), 439 - 445

Tissell, J. R. (1979). “Design considerations for plywood diaphragms in seismic zone 4.” Proc. of the 2nd US Natl. Conf. on Earthquake Eng., Stanford Univ., Calif.

Tissell, J. R. and Elliott, J. R. (1983). “PLYWOOD DIAPHRAGMS.” Research Report 138, , APA (The Engineered Wood Association), Tacoma, Washington.

Tissell, J.R. and Elliott, J.R (1997). "Diaphragms and Shear Walls." American Plywood Association (APA).

Tissell, J. R. and Rose, J. D. (1993). “Roof Diaphragms for Manufactured Homes.” Research Report No. 146, APA (The Engineered Wood Association), Tacoma, Washington.

Tomazevic, M. (1987). “Dynamic modelling of masonry buildings: Storey mechanism model as a simple alternative.” Earthquake engineering and structural dynamics, Vol. 15, 731-749

Tomazevic, M. (1999). “Earthquake-Resistant Design of Masonry Buildings – Series on Innovation in Structures and Construction: Vol. 1.” Imperial College Press, London

Tomazevic, M. and Klemenc, I. (1997). “Verification of seismic resistance of confined masonry buildings.” Earthquake Engineering and Structural Dynamics, Vol. 26, 1073-1088

Tomazevic, M., Lutman, M., and Petkovic, L. (1996a). “Seismic behavior of masonry walls: experimental simulation.” J. Struct. Engrg., ASCE, 122(9), 1040-1047

Tomazevic, M., and Lutman, M. (1996b). “Seismic behavior of masonry walls: modeling of hysteresis rules.” J. Struct. Engrg., ASCE, 122(9), 1048-1054

Tomazevic, M., Modena, C., Velechovsky, T., and Weiss (1990). “ The influence of structural layout and reinforcedment on the seismic behaviour of masonry buildings: An Experimental Study.” The Masonry Society Journal, 9(1), 26-50.

Tomazevic, M., and Velechovsky, T. (1992). “Some aspects of testing small-scale masonry building models on simple earthquake simulators.” Earthquake Engineering and Structural Dynamics, Vol. 21, 945-963

Tomazevic, M., and Weiss, P. (1994). “Seismic behavior of plain- and reinforced- masonry buildings.” J. Struct. Engrg., ASCE, 120(2), 323-338

Uang, C. M., and Bertero, V. V. (1990). “ Evaluation of Seismic Energy in Structures.” Earthquake Engineering and Structural Dynamics, Vol. 19, 77-90

Unemori, A. L., Roesset, J. M., and Becker, J. M. (1980). “Effect of inplane floor slab flexibility on the response of crosswall building systems.” Reinforced concrete structures subjected to wind and earthquake forces, ACI Publication SP-63, 113-134

Uniform building code (1997), International conference of building of ficials, Whittier, CA

Weaver, W., Jr., and Gere, J. M. (1990). “Matrix Analysis of Framed Structures.” Chapman & Hall, New York

Wen, Y.K. and Wu, C.L. (1999). "Generation of Ground Motions for Mid-America Cities." Projects RR-1 and RR-2, Mid-America Earthquake Center, University of Illinois, Urbana-Champaign. IL.

Yamazaki, Y., Kaminosono, T., Teshigawara, M., and Seible, F. (1988a). “The Japanese 5 Story Full Scale Reinforced Concrete Masonry Test - Pseudo Dynamic and Ultimate Load Test Results.” The Masonry Society Journal, 7(2), T1-T18.

Yamazaki, Y., Seible, F., Mizuna, H., Kaminosono, T., and Teshigawara, M. (1988b). “The Japanese 5 Story Full Scale Reinforced Concrete Masonry Test - Forced Vibration and Cyclic Load Test Results.” The Masonry Society Journal, 7(1), T1-T17.

Yang, C. and Liu, D (1988). “The effect of stiffness degradation of shear wall and floor horizontal deformation on the frame-shear wall buildings.” *Proc. 9th World Conf. on Earthquake Engineering,* Tokyo-Kyoto, Japan, Vol. 4, 17-22.

Zhuge, Y, Thambiratnam, D., and Corderoy, J. (1998). “Nonlinear Dynamic Analysis of Unreinforced Masonry.” J. Struct. Engrg., ASCE, 124(3), 270 - 277.